

OBSERVATOIRE DE GRENOBLE
et
LABORATOIRE DE GEOPHYSIQUE INTERNE ET TECTONOPHYSIQUE

HABILITATION A DIRIGER DES RECHERCHES

Présentée par

STEPHANE GARAMBOIS

UNIVERSITE JOSEPH FOURIER – GRENOBLE I

Spécialité Géophysique – Géochimie - Géomécanique

**INVESTIGATIONS GEOPHYSIQUES DE LA SUBSURFACE : MILIEU BIPHASIQUE
ET ALEAS NATURELS**
(version provisoire)

Date de présentation prévue: 28 octobre 2010

Composition du jury

Rapporteurs :	Dominique Gibert	Professeur	Institut de Physique du Globe, Paris
	Klaus Holliger	Professeur	Université de Lausanne
	Andreas Kemna	Professeur	Université de Bonn
Examineurs:	Jean Virieux	Professeur	Université Joseph Fourier, Grenoble
	Michel Dietrich	DR CNRS	Institut Français du Pétrole
	Yves Guglielmi	Professeur	Université de Provence, Aix-Marseille

TABLE DES MATIERES

Curriculum Vitae	1
Introduction	7
Chapitre 1 – Hydrogéophysique et milieux poreux	15
1.1 Introduction	15
1.2 Travaux effectués pour des problématiques du milieu bi-phasique	19
1.3 Faisabilité de l'imagerie acoustique pour la caractérisation in-situ de l'injection de ciment frais dans les sols superficiels	54
1.4 Perspectives : Imageries sismique des milieux poreux par inversion des champs d'ondes complets et approche différentielle	70
1.5 Références.....	74
Chapitre 2 – Etudes sur les conversions d'ondes sismo-électromagnétiques dans les milieux poreux	79
2.1 Introduction	79
2.2 Travaux effectués sur le sujet	84
2.3 Perspectives	124
2.4 Références	125
Chapitre 3 – Investigations et suivi temporel géophysiques des glissements de terrain	129
3.1 Introduction	129
3.2 Investigations géophysiques multi-méthodes dans différents contextes	134
3.3 Exemples de l'intérêt d'un suivi sismologique temporel sur les mouvements de terrain de type rocheux	171
3.4 Perspectives Générales	194
3.5 References	198
Chapitre 4 – Intérêt du Géoradar pour l'imagerie et la caractérisation des fractures dans le contexte de stabilité des falaises	201
4.1 Introduction – Problématique	201
4.2 Imagerie des fractures dans le contexte de stabilité des falaises	203
4.3 Caractérisation des fractures : inversion des courbes AVO dispersives	227
4.4 Perspectives	244
4.5 Références	246
Perspectives générales	249

CURRICULUM VITAE

GARAMBOIS Stéphane
Né le 25 septembre 1970
Maître de Conférences – Classe normale
Date de promotion : passage à l'échelon 5 le 1er avril 2010
Université Joseph Fourier – Grenoble I
Section CNU : 36
Titulaire de la PEDR en [2004-2008] puis PES [campagne 2009]

1 PARCOURS

1.1. Résumé.

- Janvier 2007 – présent* **Maître de conférences à l'université Joseph Fourier, LGIT (UMR 5559)**, équipe Mouvements de Terrain, puis équipes Risques
- Octobre 2001 à décembre 2006* **Maître de conférences à l'université Joseph Fourier, LIRIGM**, équipe risques naturels, Ecole Polytechnique de l'université Grenoble I. Titularisation le 1^{er} octobre 2002.
- Octobre 1999 à septembre 2001* **Séjour post-doctoral CNRS à l'université de Pau et des Pays de l'Adour**, laboratoire d'Imagerie Géophysique (UMR 5831)
- Avril 1999* **Doctorat en géophysique, géochimie, géomécanique de l'université Joseph Fourier, Grenoble I**
Titre : « Etudes expérimentales et théoriques des conversions d'ondes sismo-électriques dans les milieux poreux superficiels », directeur de thèse : Michel Dietrich (LGIT, UJF Grenoble), mention très honorable avec félicitations du jury.
- Septembre 1994 à août 1995* **Service militaire** effectué au Bureau Gravimétrique International : stage de recherche en géodésie spatiale, Observatoire Midi-Pyrénées, Toulouse,
- Juin 1994* **DEA Mécanique des Milieux Géophysiques et Environnement, UJF Grenoble**, mention Bien.

1.2. Encadrement doctoral et scientifique

Depuis ma soutenance de thèse j'ai officiellement co-encadré 10 thèses (4 sont en cours) et 10 stages de M2R.

Nom	Soutenance	Titre	%	Co-encadrant
E. Rey	2005, UJF	Caractérisation de sols hétérogènes par méthodes géophysiques	33	D. Jongmans & P. Gotteland
M. Jeannin	2005, UJF	Etude des processus d'instabilités des versants rocheux par prospection géophysique. Apport du radar géologique	50	D. Jongmans
F. Nguyen	Juin 2005, Univ. Liège	Imaging slow-active faults with combined geophysical methods in Provence, France	50	D. Jongmans
O. Méric	2006, UJF CIFRE	Etudes de mouvements de terrain par méthodes géophysiques	50	D. Jongmans
J. Deparis	3 Juillet 2007, UJF	Etudes des éboulements rocheux par méthodes géophysiques	50	D. Jongmans
L. Tatard	8 février 2010, UJF	Statistical analysis of triggered landslides: implication for earthquake and weathering controls	33	J. R. Grasso et T. Davies
B. Dupuy	10/2011, UJF - ANR	Inversion du champ d'ondes sismique complet en milieux poreux	50	J. Virieux
S. Beauprêtre	10/2012, UJF	Identification des forts séismes passés par imagerie géophysique de sub-surface	50	I. Manighetti
L. Chaumont	02/2013, UJF - ANR	Dynamique du mouvement de terrain de Séchilienne et réponse à des forçages externes (séismes, pluie), en couplant sismologie, géodésie et données hydrogéophysiques	33	A. Helmstetter & D. Amitrano
A. Asnaashari	04/2013, UJF - TOTAL	Quantitative 4D seismic in complex media using 2D full-waveform inversion	33	J. Virieux & P. Thore

TABLE 1. ENCADREMENT DOCTORAL

Nom	Soutenance	Thématique	%	Co-encadrant
O. Méric	Juin 2003	Landslides	50	D. Jongmans
J. Deparis	Juin 2003	Rockfalls	50	D. Jongmans
H. Cadet	Juin 2004	Landslides	50	P. Guéguen
L. Tatard	Juin 2006	Landslides	50	P. Guéguen
V. Allègre	Juin 2007	Hydrogeophysics	100	
L. Sanchez	Juin 2008	Landslides	50	A. Helmstetter
B. Dupuy	Juin 2008	Hydrogeophysics	50	J. Virieux
A. Quintero	Février 2009	Landslides	50	C. Voisin
F. Lavoué	Juin 2010	GPR	50	J. Virieux
L. Eymard	Juin 2010	Active faults	25	Manighetti I. & C. Larroque

Table 2. Encadrement stages de Master

2. ACTIVITES DE RESPONSABILITES

2.1 Responsabilités au sein du laboratoire

- Responsable de l'équipe « *Caractérisation et comportement des matériaux hétérogènes naturels (massifs montagneux)* » du LIRIGM entre février 2003 et décembre 2006. Cette équipe regroupait en moyenne 8 enseignants/chercheurs permanents, 2 ITA et 5 doctorants. J'ai servi d'adjoint au responsable de l'équipe mouvements de terrains du LGIT (L. Baillet, 2007-2009).

- Membre élu du conseil de laboratoire du LGIT (UMR 5559) depuis janvier 2007.

2.2 Commissions de spécialistes

- membre élu de la commission de spécialistes de l'UJF section 35-36-37 [2003-2006]

- membre de la commission de spécialistes de l'université de Pau et des Pays de l'Adour, section 35-36 [2004-2008]

- membre de la commission de spécialistes de l'université Paul Sabatier, Toulouse, section 36 [2004-2008]

- membre nommé de la Commission de spécialiste d'Aix-Marseille en 2008.

2-3 Rayonnement scientifique et relations avec le monde industriel

- Prix. Young Scientist Best paper award accordé à J. Deparis & S. Garambois au 11th International Conference on Ground Penetrating Radar, 2006.

- Invitation par l'université de Canterbury (Nouvelle Zélande) pour séjours et collaborations en 2007-2008.

- Rapporteur de deux thèses étrangères de l'université du New Brunswick (Canada, 2008) et de l'université de Curtin (Perth, Australie, 2007)

- Partenariats avec la Société Alpine de Géotechnique (SAGE) sous la forme de projets de recherche locaux et d'une bourse CIFRE (Ombeline Méric, embauchée depuis en CDI à la SAGE).

- Expertises pour le RTM Haute-Savoie (Restauration des Terrains en Montagne), EDF et préfecture Haute-Savoie dans le cadre de problématiques glaciers.

- Projet ANR JETPHI (2007-2009) sur l'imagerie de colonnes géotechniques dans le sol obtenues par le JET-GROUTING, dont la coordination est assurée par le groupe Soletanche-Bachy. Je suis responsable d'un Work-package et d'une post-doctorante (P. Sénéchal).

- Projet TOTAL, inversion 4D ; thèse d'Amir Asnaashari (2010-2013)

2-4 Participation à des Programmes de recherche

- Nationaux

- o ACI Catastrophes Naturelles : SAMOA, GACH2C (2005-2007)
- o ACI Eau et environnement
- o ANR : coordinateur du projet SLAMS (2010-2013), ANR RISKMAT 2009. Participation à SIGMA (2006-2009), JETPHI (2007-2009) responsable d'un WP, « Ecou-Pref » (2007-2009), HPPP-C02 (2008-2011), CENTURISK (2010-2014)
- o INSU : projet 3F (2007)
- o GDR FORPRO (ANDRA/INSU)
- o Ministère de l'environnement, projet RDT (2003-2005)

- **Locaux** : Conseil général de l'Isère : 3 projets coordinateur, 2 autres projets participants ; projet biodiversité avec l'ONF ; pôle TUNES (2008), BQR LGIT.

- **Observatoire INSU**: responsable du site de Séchilienne dans le service d'observation OMIV (Observatoire Multidisciplinaire des Instabilités de Versants, responsable J.-R. Grasso) labellisé par l'INSU en 2008.

- **Internationaux** : Projet Européen SAFE (2001-2004) sur failles actives

2.5 Responsabilités administratives et pédagogiques

J'effectue depuis mon arrivée en octobre 2001 à l'Ecole Polytechnique de l'université Grenoble I un service d'enseignement complet, excepté en 2008-2009 où j'ai bénéficié d'une année CRCT.

- Matières enseignées (C, TD, TP, Terrain): prospection géophysique, modélisation par différences finies, mécanique des roches, traitement du signal, interventions dans l'enseignement de l'anglais.

- Mon activité d'enseignement s'est récemment focalisée vers la reconnaissance géophysique en se partageant pour les 2/3 à la filière Ingénieur Géotechnique de Polytech' Grenoble et pour 1/3 à différentes formations de l'OSUG (Observatoire des Sciences de l'Univers de Grenoble) en niveau M2P et M2R principalement.

Responsabilités de filières d'enseignement

- Responsable de la 1^{ère} année de la filière d'ingénieur géotechnique de l'Ecole Polytechnique de l'université Grenoble I entre février 2002 et septembre 2007 (entre 45 et 50 étudiants).

- Co-responsable du M2R européen MEEES (Master in Earthquake Engineering and Engineering Seismology) de l'OSUG depuis septembre 2006 (entre 18 et 25 étudiants « mondiaux »). Cette formation est un programme européen "Erasmus Mundus" s'adressant aux étudiants hors-Europe.

Responsabilités de modules d'enseignement

- responsable du module « Field survey » du Master MEEES de l'OSUG depuis 2005

- responsable du module « Géophysique de site » du M2P « Géologie, Exploration, Risques » de l'OSUG en commun avec le M2R « STUE » de l'OSUG depuis 2005.

PRODUCTION SCIENTIFIQUE : PUBLICATIONS DE RANG A

- (1) GARAMBOIS, S., DIETRICH, M., « Seismo-electric wave conversions in porous media: Field measurements and transfer function analysis », Geophysics, 2001, n° 66, pp. 1417-1430.
- (2) GARAMBOIS, S., DIETRICH, M., 2002, « Full-waveform numerical simulations of seismo-electromagnetic wave conversions in fluid-saturated stratified porous media », Journal of Geophysical Research, 107, No B7.
- (3) PRIDE, S., GARAMBOIS, S., 2002, « The role of Biot slow waves in electroseismic wave phenomena », Journal of Acoustical Society of America, 111, 697-706.
- (4) GARAMBOIS, S., SENECHAL, P. & H. PERROUD, 2002, « On the use of combined geophysical methods to assess water content and water conductivity of near-surface », Journal of Hydrology, 259, pp 32-48.
- (5) LUTZ, P., GARAMBOIS, S., & PERROUD, H., 2003, Influence of antenna configurations for GPR surveys: information from polarization and amplitude offset measurements, Special Publication of the Geol. Soc. of London, 211, pp 295-308.
- (6) NGUYEN, F., GARAMBOIS, S., JONGMANS, D., PIRARD, E. & M. LOCKE, 2005, Image processing of 2D resistivity data to locate precisely faults, Journal of Applied Geophysics, 57, pp 260-277.
- (7) PRIDE, S. & S. GARAMBOIS, 2005, Electroseismic wave theory of Frenkel and more recent developments, Journal of Engineering Mechanics, pp 898-907.
- (8) MERIC, O., GARAMBOIS S., JONGMANS D., VENGEON J.-M. & J.-L. CHATELAIN, 2005, Application of geophysical methods for the investigation of the large gravitational mass movement of Séchilienne (France), Canadian Geotechnical Journal, 42, pp 1105-1115.
- (9) REY, E., JONGMANS D., GOTTELAND, P. & S. GARAMBOIS, 2006, Characterization of heterogeneous soils using geoelectrical measurements, Journal of Applied Geophysics, 58, pp 188-201.
- (10) JEANNIN, M., GARAMBOIS S., GREGOIRE C. & JONGMANS D., 2006, Multi-configuration GPR measurements for geometrical fracture characterization in limestone cliffs (Alps), Geophysics, 71, pp B85-B92.
- (11) BORDES C., JOUNIAUX, L., DIETRICH, M., POZZI J.-P. & S. GARAMBOIS, 2006, Laboratory measurements of seismo-magnetic conversions in fluid-filled sand, Geophys. Res. Lett., VOL. 33, L01302, doi:10.1029/2005GL024582.
- (12) GUEGUEN, P., CORNOU, C., GARAMBOIS, S. and J. BANTON, 2007, On the limitation of the H/V spectral ratio using seismic noise as an exploration tool: Application to the Grenoble valley (France), a small apex ratio basin, PAGEOPH, 164(1), 115-134..
- (13) MERIC O., GARAMBOIS S., MALET J.-P., CADET H., GUEGUEN P. & D. JONGMANS, 2007, Seismic-noise based methods for soft-rock landslides characterization, Bull. Soc. géol. france, 2007, n 2, pages 137-148.
- (14) JONGMANS D. & S. GARAMBOIS, 2007, Surface geophysical investigation and monitoring of landslides: a review, BSGF, n2, pages 101-112.
- (15) NGUYEN, F., GARAMBOIS S., CHARDON, D., BELLIER O., HERMITTE D. & D. JONGMANS, 2007, Subsurface electrical imaging of anisotropic formations affected by a slow active reverse fault, Provence, France, Near surface Geophysics, 62, pages 338-353.
- (16) DEPARIS J., GARAMBOIS S. & D. HANTZ, 2007, On the potential of Ground Penetrating Radar to help rock fall hazard assessment of a limestone scale, Engineering geology, 94, 89-102.

- (17) BORDES C., JOUNIAUX L., GARAMBOIS S., DIETRICH M., POZZI J.-P. & S. GAFFET, 2008, Evidence of the theoretically predicted seismo-magnetic conversion, Geophysical Journal International, doi: 10.1111/j.1365-246X.2008.03828.x.
- (18) DEPARIS, J. & GARAMBOIS S., 2009, On the use of APVO GPR curves for thin-bed properties estimation : theory and application to fracture characterization, Geophysics, 74, 1, J1-J12.
- (19) HELMSTTETER A. & S. GARAMBOIS, 2010, Seismic activity of Séchilienne rockslide (french Alps) and its correlation with rainfalls, Journal of Geophys. Res (September), in press.
- (20) DEPARIS J. & S. GARAMBOIS, 2010, Inversion methodology of dispersive amplitude and phase versus offset curves (DAPVO) for thin-beds, SEG books, in press.
- (21) VINCENT C., GARAMBOIS, S., E. THIBERT, E. LEFÈBVRE, E. LE MEUR AND D. SIX, 2010, Origin of the outburst flood from Tete Rousse glacier in 1892 (Mont-Blanc area, France), Journal of Glaciology, in press.

EN REVISION (ACCEPTES AVEC MODIFICATIONS)

- (22) SENECHAL, P., GARAMBOIS S. & BORDES C., 2010, Feasibility of acoustic imaging for in-situ characterization of fresh concrete injected into soil subsurface", Journal of Applied Geophysics, accepted.
- (23) LEGCHENKO, A., CLEMENT, R., GARAMBOIS, S., MAURY, M., MIC, L.-M., LAURENT, J.-P., DESPLANQUE C. & GUYARD H., 2010, Locating water storage of Luitel lake peat bog using MRS, ERT and GPR, Near Surface Geophysics, accepted.
- (24) TATARD, L., GRASSO, J.-R., HELMSTETTER, A., & S. GARAMBOIS, 2010, Characterization and comparison of landslide dynamics in different tectonic and climatic settings, Journal of Geophys. Res., accepted.

ARTICLES SOUMIS

- (25) GRANDJEAN G., GOURRY J.C., SANCHEZ O., BITRI A & S. GARAMBOIS, 2009, Structural study of the Ballandaz landslide (Savoie) using geophysical imagery, Journal of Applied Geophysics, submitted.

ARTICLES à SOUMETTRE

- (26) GARAMBOIS S., QUINTERRO A., MASSEY C. & C. VOISIN, 2010a, Spatial and azimuthal variabilities of seismic site effect patterns due to a landslide located in a high-seismicity region: The Utiku landslide (New-Zealand), to be submitted to Journal of Geophys. Res.
- (27) GARAMBOIS S., VINCENT C., DESCLOITRES M., LEGCHENKO A., LE MEUR E., 2010b, GPR Velocity pushdown due to a large water reservoir within a temperate glacier : example of the outburst risk in the Tete-Rousses glacier (Mont-Blanc massif), to be submitted to Geophysics.
- (28) DUPUY B., DE BARROS L., GARAMBOIS S. & J. VIRIEUX, 2010, Wave propagation in heterogeneous porous media formulated in the frequency-space domain, to be submitted to Geophysics.

INTRODUCTION

Les premières dizaines à centaines de mètres du sous-sol constituent ce qu'on appelle communément la subsurface, qui est la partie terrestre marquée par la plus forte hétérogénéité, que ce soit au niveau lithologique que de part les paramètres qui la constituent (fluides, espace poreux et/ou fracturés). C'est une échelle fondamentale sur le plan sociétal car elle concentre nombre de problèmes affectant directement l'humain et les activités économiques qui s'y réfèrent. On peut par exemple citer les problèmes de ressources naturelles, de ressources en eau, de risques naturels et/ou environnementaux et de géotechnique. C'est pourquoi sa caractérisation dans des contextes et à des échelles divers reste et constituera un enjeu important à l'avenir, qui nécessite l'emploi et le développement de techniques d'imagerie géophysiques spécifiques ou de forages. De la même manière qu'en médecine, où le développement des techniques d'imagerie a réduit le besoin d'opérations invasives, les méthodes géophysiques ont ce potentiel de caractérisation de la subsurface, de manière rapide, non-invasive et à grande échelle.

Les moyens liés à l'exploration géophysique ont été principalement concentrés au cours du siècle dernier au niveau de l'industrie pétrolière, qui développe principalement des techniques de sismique réflexion à grande échelle et, depuis récemment, qui voit l'émergence de techniques électromagnétiques basses fréquences à source contrôlée (CSEM). A plus petite échelle, l'étude géophysique de la subsurface était plutôt cantonnée à des problématiques d'ingénierie, menées en forte relation avec les travaux de génie civil de caractérisation des sols ou d'hydrologie. Depuis quelques années, une forte demande sociétale (environnementale, liée aux risques naturels et géotechnique) a généré un accroissement des besoins en techniques d'investigation qui soient adaptées à la première centaine de mètres, cette échelle étant marquée par une forte complexité et une forte hétérogénéité. Suivant les problèmes à résoudre, en plus de l'imagerie du sous-sol, un besoin de quantification de ses propriétés constitutives s'est accru. Ainsi le développement de techniques originales a vu le jour, par exemple la Résonance Magnétique Protonique (RMP) qui permet d'apporter des réponses aux besoins de quantification hydrologique. Que cela soit pour les techniques émergentes ou les techniques plus classiques, ce sont les fréquents allers et retours entre données réelles ou de laboratoire, approches théoriques et numériques qui peuvent permettre de caractériser plus finement les matériaux rencontrés grâce à de nouvelles observables ou des relations pétrophysiques reliant les observables aux propriétés constitutives. Il faut noter que nombre de processus de produisant dans la subsurface évoluent au cours du temps, que ce soit de manière naturelle qu'anthropique (ressources en eau, pollutions, instabilités gravitaires). Un des principaux enjeux de l'avenir en géophysique sera de développer des systèmes d'acquisitions continus ou discrets de suivi temporel, et de mettre en œuvre les techniques de traitement et d'interprétation adaptées à cette problématique.

Au cours de mes activités conduites pendant dix ans depuis ma thèse de doctorat, j'ai été emmené à travailler sur différentes problématiques qui ont en commun des enjeux importants liés aux phénomènes de subsurface. Je me suis intéressé au caractère biphasique (voire multiphasique) des formations rencontrées, notamment par la prise en compte de la phase fluide dans les phénomènes de propagation d'ondes (sismiques, électromagnétiques, sismo-électromagnétiques). Cette thématique a eu des incidences environnementales, hydrologiques mais également de ressources naturelles (pétrole, CO₂). Je me suis également intéressé par des approches multi-méthodes aux problématiques d'imagerie ou de caractérisation géophysique de différents aléas naturels, tels que les instabilités gravitaires et les failles tectoniquement actives.

Ces travaux ont été menés le plus souvent à partir de données réelles et de manière plus éparse d'études de laboratoire. Des développements méthodologiques ont été parfois proposés en combinant des approches théoriques et/ou numériques et par l'intermédiaire de l'inversion.

Parmi l'ensemble des travaux effectués au cours de ces années, et par rapport aux perspectives envisagées, j'ai choisi de regrouper les recherches les plus significatives sur les quatre grandes thématiques suivantes: i) hydrogéophysique et milieux poreux, ii) conversions d'ondes sismo-électromagnétiques, iii) géophysiques et glissements de terrain et iv) intérêt du géoradar pour la caractérisation des fractures dans le contexte d'instabilités rocheuses. Dans chacune des thématiques présentées, j'ai tenté d'introduire les principales questions posées et les travaux importants qu'y si sont référés pour mettre en perspective les activités de recherche que j'ai pu mener. Egalement, des perspectives concrètes sont proposées qui dessinent quelque peu les grandes orientations que je compte prendre à moyen terme. Celles-ci seront synthétisées dans une dernière partie résumant les perspectives générales.

Au vu de la dispersion des méthodes et des objets que j'ai été amené à étudier, j'ai dû me résoudre à ne pas présenter l'ensemble des problématiques que j'ai pu aborder. J'ai notamment laissé de côté les travaux pour lesquels je n'étais pas vraiment moteur, notamment ceux concernant les approches statistiques sur le déclenchement des mouvements de terrain de part le monde (Tatard et al., 2010), ceux concernant les problèmes de risque sismique (Guéguen et al., 2007) et enfin les développements méthodologiques pour la caractérisation de sols hétérogènes par tomographies électriques (Rey et al., 2006). Ces activités peuvent être néanmoins accessibles sous la forme de publications dans des revues internationales (cf. Curriculum Vitae). Par un souci de synthèse, j'ai également choisi de ne pas présenter la problématique de la reconnaissance géophysique des failles actives, qui aurait pu constituer un chapitre dans ce mémoire. Celle-ci avait fait l'objet de la thèse de F. Nguyen (Nguyen et al., 2005, 2007) pour la reconnaissance géophysique des failles en Provence. Cette problématique fait actuellement l'objet de la thèse en cours de S. Beauprêtre dans le cadre d'une ANR (CENTURISK, [2010-2014], coordinatrice I. Manighetti) sur les failles en décrochement de Nouvelle-Zélande et les failles normales en Italie centrale. Je présenterai néanmoins les grandes lignes de ce projet de recherche à la fin de cette introduction ainsi que les travaux envisagés.

Comme introduit auparavant, l'aspect multiphasique des formations composant la subsurface m'a conduit à essayer de mieux comprendre les phénomènes de propagation des ondes sismiques et électromagnétiques dans les milieux poreux et également leur couplage électrocinétique.

Je présenterai dans le **chapitre 1** quelques contributions à la problématique hydrogéophysique. Cette approche multiphasique a été principalement abordée pour la caractérisation du contenu en eau des formations superficielles, pour des problèmes environnementaux, écologiques ou de risque glaciaire. J'aborderai notamment une démarche combinée d'étude de la zone non-saturée par comparaison quantitative de méthodes différentes méthodes géophysiques (Géoradar, tomographies électriques et acquisitions sismiques) et leur interprétation conjointe en termes de propriétés constitutives (Garambois et al., 2002). Je présenterai rapidement dans un second paragraphe une étude comparative entre différentes méthodes d'estimation par géoradar (GPR) de la teneur en eau dans un milieu gorgé d'eau que constituent les tourbières et leur validation par d'autres méthodes (RMP et TDR). Dans un contexte de risque en montagne qui peut-être lié au changement climatique, j'ai tenu à présenter une étude GPR non finalisée (Garambois et al., 2010b), mais dont les analyses ont permis d'identifier et de localiser la présence importante d'eau dans le glacier de Tête-Rousses (massif du Mont-Blanc). Sa vidange brutale en 1892 avait provoqué la mort de près de 200 personnes en

aval. Les données GPR ont été comparées avec une interprétation 3D RMP et des forages creusés a posteriori.

Dans un second temps, une application géotechnique de mesures acoustiques en laboratoire sera également proposée dans la problématique d'injection de fluides dans le sous-sol (Jet-Grouting), procédé qui vise à consolider un sol ou à circonscrire une pollution. Ces travaux ont été conduits dans le cadre d'un financement ARN « Réseau Génie Civil et urbain » qui visait à imager en temps quasi-réel (contrôle) la géométrie de la colonne cylindrique créée. Les caractéristiques acoustiques du mélange homogénéisé ont pu être déterminées en laboratoire en fonction de son temps de durcissement, et montrent la fenêtre temporelle optimale d'acquisition au niveau de l'atténuation ainsi que la meilleure configuration (source, fréquence, positions sources-récepteurs) souhaitée pour l'imagerie (Sénéchal et al., 2010). Ces activités de recherche sur la propagation des ondes sismiques en milieux poreux se poursuivent actuellement dans le cadre de l'ANR HPPP-CO2. Elles visent à proposer une inversion du champ d'onde sismique complet qui permettrait de déduire à partir d'acquisitions sismiques « lourdes » de type les propriétés composant le milieu multiphasique. Les paramètres importants à investiguer seront principalement la nature du fluide saturant (densité, viscosité), la porosité et la perméabilité de l'espace poreux et dans un deuxième temps la saturation. Les applications potentielles visent à la fois des applications de sismique profonde (séquestration du CO2, pétrole), de sismique haute-résolution (hydrogéophysique) et en forages à partir de mesures de sondes dédiées (exemple sources hydro-mécaniques, ANR HPPP-CO2). Il faut noter qu'en parallèle à ces travaux, les imageries différentielles par sismique réflexion dans des contextes différents (séquestration de CO2, réservoirs) demandent également des développements d'inversion différentielle pour accéder aux modifications de l'espace poreux et du fluide saturant.

J'arborai dans le **second chapitre** les couplages électrocinétiques dynamiques entre ondes sismiques et électromagnétiques dans les milieux poreux, en se focalisant sur les principaux développements réalisés depuis ma thèse de doctorat. L'approche adoptée sur cette thématique consistait à évaluer le potentiel de ces effets pour la détection et la caractérisation de fluides dans la subsurface (eau, huile, gaz) en conservant la résolution des méthodes de sismiques réflexions. Après avoir mesuré ces effets sur le terrain dans différents contextes tout en développant des techniques de traitement du signal appropriées et en comparant les données à la théorie (Pride, 1994) (Garambois & Dietrich, 2001), nous avons également mené une étude numérique qui nous a permis une meilleure compréhension des phénomènes et notamment de la sensibilité des ondes générées en profondeur lorsqu'une onde sismique traverse une interface (Garambois & Dietrich, 2002). Ces travaux ont été poursuivis par la suite de manière plus théorique en évaluant l'influence de l'onde de Biot lente sur ces phénomènes (Pride & Garambois, 2002) puis en revisitant la théorie de Frenkel (Pride & Garambois, 2005). Pour mieux caractériser ces phénomènes, les travaux ont été poursuivis à l'échelle du laboratoire, sur des expériences contrôlées menées dans le Laboratoire à Très bas Bruit de Rustrel, ce qui a notamment permis l'étude des champs magnétiques associés aux ondes S (Bordes et al., 2006; 2008). A l'heure actuelle, les travaux en cours sur cette problématique concernent principalement l'aspect dispersif du phénomène en comparant les signatures fréquentielles des ondes sismiques et celles des champs électriques (laboratoire, données de terrain) avec la théorie. Nous travaillons également sur le potentiel des conversions sismo-électriques pour mettre en évidence, de manière indirecte, la signature électrique de la propagation de l'onde lente de Biot dans sa partie diffuse (basse fréquence). Celle-ci demeure très difficilement accessible à l'heure actuelle en laboratoire ce qui empêche toute avancée théorique.

Outre les problématiques liées au caractère poreux de la subsurface, celle dernière est également le siège d'instabilités gravitaires dont les conséquences socio-économiques peuvent être catastrophiques que ce soit en termes d'emménagement du territoire que de dommages directs ou indirects sur les infrastructures ou l'humain. Ces objets géologiques qui évoluent au cours du temps ont donné lieu à de nombreux travaux d'ingénierie visant principalement à caractériser l'état de l'aléa en termes de stabilité à partir de mesures en forage, d'essais géotechniques et de modélisation numérique. Si cette approche est et reste fondamentale, elle souffre du manque de reconnaissance des objets, tant d'un point de vue géométrique que de ses caractéristiques. Par exemple, dans le cas bien instrumenté des mouvements de terrain de grande ampleur à risque, la surveillance des déplacements et l'approche classique de surface (géologique, essais géotechniques), qui est dans certains cas combinée à des données de forage, représente un effort considérable tant sur les plans humains que financiers. Ces approches combinées ne peuvent pas rendre compte des hétérogénéités présentes au sein de la masse en mouvement (lithologiques, fluides, géométriques, structurales). Ceci rend toute tentative de modélisation de la dynamique présente et de l'impact de potentiels facteurs externes aggravants (séismes, pluie) relativement vaine. De plus, ces hétérogénéités spatiales sont également susceptibles d'évoluer au cours du temps. C'est également le cas pour les problèmes d'éboulements en falaises, pour lesquels l'expertise de stabilité repose principalement sur les observations géologiques de surface visant à établir des analyses de fracturation et de stratification, sans aucune certitude sur le prolongement de celles-ci vers la profondeur. Dans ce contexte, un intérêt croissant s'est manifesté vers les techniques d'imagerie géophysiques conduites à un instant « t » et leur potentiel suivant le problème rencontré (Jongmans & Garambois, 2007).

Je présenterai ainsi dans le **chapitre 3** les études de reconnaissance et de suivi temporel géophysiques spécifiques aux mouvements de terrain. Après un rappel sur les techniques classiquement utilisées pour cette problématique, je montrerai le potentiel de nombreuses méthodes géophysiques pour déterminer la géométrie des masses en mouvement dans un contexte rocheux (donc fracturé, Meric et al., 2005) et un contexte plus visqueux (sols, Méric et al., 2007) pour lequel les méthodes de reconnaissance par bruit sismique sont efficaces. Pour les glissements rocheux de grande échelle (la centaine de mètres de profondeur), nous avons mené une étude comparative sur le site emblématique de Séchilienne, qui a montré entre autres que les techniques de tomographies sismiques et électriques étaient fortement sensibles à la fracturation du massif, et permettaient ainsi de délimiter des zones plus ou moins affectées par le mouvement (Méric et al., 2005). Cette forte fracturation semble également modifier l'amplitude du bruit de fond sismique, mais diffracte fortement les ondes de surface ce qui rend difficile les approches basées sur les ondes de cisaillement par inversion des ondes de surface ou par bruit de fond sismique. A l'opposé, nous avons pu montrer sur deux glissements argileux que dans le cas de mouvements de sols, ce sont les techniques d'imagerie basées sur les ondes de cisaillement (bruit de fond H/V, réseaux, ondes de surface) qui permettaient de délimiter les limites du mouvement (Méric et al., 2007). Dans les deux cas, les études électriques passives (polarisation spontanée), fortement utilisées sur les édifices volcaniques, restent difficiles à interpréter.

L'imagerie et la caractérisation géophysique appliquée à un temps « t » vont être étendues à l'avenir vers un suivi temporel afin d'identifier les zones les plus réactives en profondeur. Dans ce contexte, un observatoire multidisciplinaire sur les mouvements de terrain (OMIV) a été créé et labélisé au sein de l'INSU depuis 3 ans. Il consiste à acquérir, archiver et diffuser des données fiables et continues (géodésiques, sismologiques, météorologiques, autres) sur quatre mouvements de terrain Alpains, afin de mieux comprendre les paramètres influençant leur dynamique. Cet effort a notamment permis d'établir l'intérêt de la surveillance sismologique sur le site de Séchilienne, fortement surveillé par ailleurs. En effet, il est possible de distinguer les signaux sismologiques créés par des chutes de blocs (et de les caractériser) de ceux produits par

de la fracturation au sein du massif. Les corrélations et relaxations de ces évènements par rapport à des chutes de pluies ont pu être établies finement (Helmstetter & Garambois, 2010). Leur localisation précise nécessitera une meilleure connaissance de la répartition 3D des vitesses sismiques au sein de ce massif fortement hétérogène. La réactivité de ces glissements de terrains, hétérogènes, en réponse à des sollicitations sismiques, constitue également une autre difficulté pour tout calcul numérique de prévision (Tatard et al., 2020). Pour avoir une meilleure connaissance des propriétés des effets de site et pour étudier la linéarité de ceux-ci par rapport aux caractéristiques spatiales des séismes, un glissement de terrain a été instrumenté dans une région présentant une sismicité forte (Utiku, Ile du Nord, Nouvelle-Zélande). Les fortes variabilités au niveau de la fréquence de résonance et surtout de l'amplification semblent dépendre principalement de la structure géométrique du mouvement, mais également de la méthode d'analyse employée (bruit de fond ou rapport spectraux) et des propriétés de la sollicitation (azimut). Ces observations montrent la complexité et la variabilité de l'effet de site produit, et donc la difficulté d'évaluer ceux-ci sur des zones potentiellement actives mais à sismicité très modérée (Garambois et al., 2010a). Les perspectives sur cette problématique « glissements de terrain » sont nombreuses et diverses. Au niveau de l'imagerie, il conviendra de mener un effort vers la quantification, que ce soit au niveau des propriétés mécaniques (porosité, fracturation) que celles des fluides qui jouent un rôle considérable dans la dynamique des mouvements de terrain. Ceci rejoint les problématiques du Chapitre 1. Dans le cadre de l'ANR SLAMS [2010-2013] que je coordonne, le site choisi d'études multi-disciplinaire est le mouvement de Séchilienne, site intégré à l'observatoire national OMIV que je présenterai. Ce projet de recherche ainsi que l'instrumentation non-pérenne d'autres sites permettront de mieux comprendre les interactions complexes entre dynamique des mouvements, l'évolution de leurs propriétés mécaniques et hydrologiques, de leur activité sismologique (énergie, fréquence, localisation) et sollicitations externes. Outre ces aspects scientifiques, un travail interdisciplinaire concernant les grandes questions posées par la gestion d'un tel risque (communication, transparence, gouvernance) seront abordées en collaboration avec les acteurs opérationnels et des sciences humaines et sociales.

Le **chapitre 4** abordera la problématique de la stabilité de masses rocheuse notamment de l'intérêt de techniques d'acquisitions GPR pour son évaluation. Jusqu'à présent, la plupart des expertises étaient conduites à partir d'observations depuis la surface de falaise (fracturation, stratification) ou à partir d'observations en retour, post-éboulement, qui ont permis d'évaluer les conditions menant à la rupture. Nous avons mené des études comparatives de différentes méthodes géophysiques (tomographie électriques et sismiques, bruit de fond, GPR par réflexion et tomographie) sur des sites sans risque réel, qui visaient à évaluer leur potentiel dans l'imagerie des discontinuités (Jeannin et al., 2005). En se concentrant sur les données GPR acquises en paroi, nous avons pu évaluer le pourcentage maximal de ponts rocheux restants et leur localisation en pseudo-3D sur le site problématique des Gorges de la Bourne (Deparis et al., 2007). Ceci a permis une aide à la décision, de minage de l'écaille concernée.

Dans un deuxième temps, nous avons tenté de proposer une méthodologie de caractérisation des fractures à partir des données géoradar, et notamment dans le cas où celles-ci étaient trop fines pour pouvoir individualiser par imagerie radar chacun de leur lobe. Pour cela, nous avons développé des méthodologies d'inversion originales qui utilisent les propriétés dispersives des paramètres constitutifs. La première approche, basée sur des rapports spectraux de données mono-offset, a rencontré des difficultés pratiques d'applicabilité, celle-ci nécessitant un signal de référence. Nous nous focaliserons donc sur la méthode utilisant les propriétés spectrales des courbes d'amplitude de la réflectivité en fonction de l'offset, ceci dans le cas de couches fines. Cette approche a été utilisée à la fois sur des données synthétiques (Deparis & Garambois, 2010) et des données réelles (Deparis & Garambois, 2009) en utilisant des acquisitions en Point Milieu

commun (CMP) et a permis de retrouver les propriétés de l'encaissant et de la couche fine (ouverture, remplissage). Ce travail pourra être étendu à l'avenir sur toutes zones de contact (glaciers par exemple) et plus généralement une approche d'inversion en champ d'onde complet des données GPR sera proposée, comme proposé en sismique dans le chapitre 1..

Pour terminer cette introduction, j'aimerais également résumer mes activités concernant le risque sismique, même si cette problématique n'a pas fait l'objet d'un chapitre. Outre les effets de site (Guéguen et al., 2007), la caractérisation des failles actives a toujours constitué une problématique importante pour la compréhension de la tectonique active. Les investigations géophysiques menées sur les failles ont souvent été conduites jusqu'alors comme outil préliminaire de positionnement de tranchées paléosismologiques, et dans certains cas comme caractérisation géophysique de zones de gouges par exemple. Dans ce contexte, nous avons montré que les images extraites de processus d'inversion électriques pouvaient s'avérer fausses en cas d'anisotropie des formations, ce qui rendait difficile l'interprétation notamment dans le cas de failles inverses (Nguyen et al., 2007). De même, le lissage inhérent aux méthodes de tomographie rend difficile la localisation précise des failles, à moins d'employer des techniques adaptées d'analyses d'images (Nguyen et al., 2005). Ces travaux initiés sur des sites marqués par une déformation faible (Trévaresse, Moyenne Durance) et une anthropisation forte (Projet européen SAFE) sont actuellement étendus à d'autres chantiers tectoniquement et sismiquement plus actifs, mais avec d'autres objectifs que l'imagerie de la zone de faille.

Nous proposons dorénavant de rechercher des marqueurs enfouis par sédimentation, qui seraient décalés par des séquences de séismes (Fig. 1).

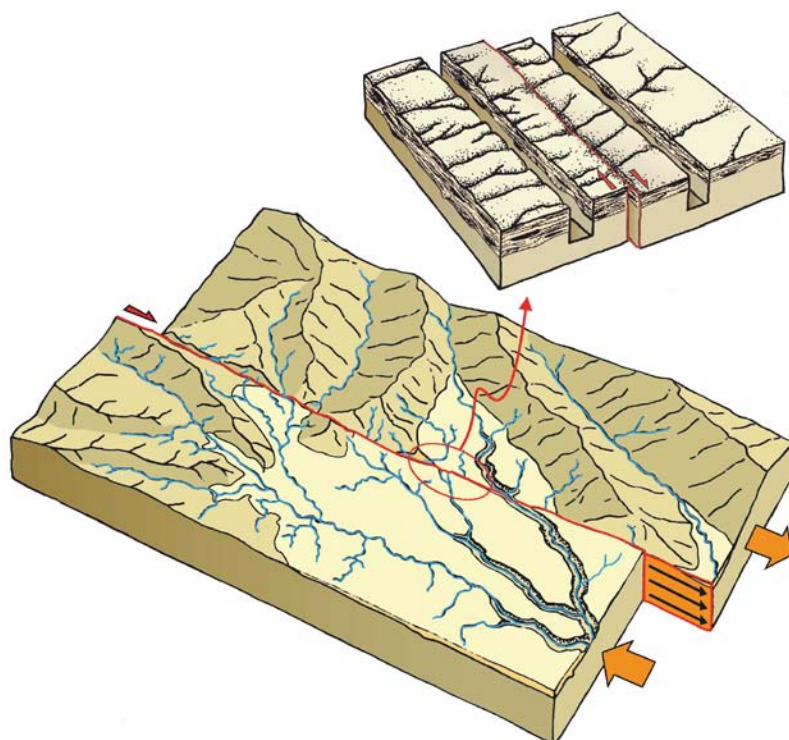


Fig. 1. Schéma illustrant le décalage de marqueurs superficiels générés par des ruptures de failles en décrochement (d'après Malavieille, ANR CENTURISK, 2010).

En effet, pour mieux appréhender le risque sismique lié à une faille donnée, mais aussi mieux comprendre le fonctionnement de cette faille au cours de ses cycles répétés, il est fondamental d'obtenir des informations précises sur les forts séismes qui ont rompu cette faille par le passé: quelle(s) partie(s) de la faille ont-ils rompu, quelles quantités de déplacement ont-ils produit tout au long de la faille, quelles

ont été leurs magnitudes, quels intervalles de temps ont séparé chacune des fortes ruptures ? Pour tenter de répondre à ces questions, nous utilisons des méthodes très haute résolution sur deux chantiers différents. Dans le cas de failles en décrochement de Nouvelle-Zélande, les investigations sont faites de part et d'autre de la faille sur de très longs profils en pseudo-3D, et c'est la technique GPR qui est privilégiée lorsqu'elle est applicable (terrains peu conducteurs). La difficulté réside alors dans la reconnaissance de marqueurs similaires de part et d'autre de la faille, et leur éventuelle mesure de rejet. Dans le cas de failles normales (autour du bassin de Fucino, Italie) ces marqueurs seraient situés au pied de l'escarpement, ce qui nécessite peu de profils traversant la zone de faille, mais qui doivent présenter une très forte résolution et une sensibilité adaptée à de très légers changements de compaction ou de granulométrie, par exemple. Dans ce cas, les méthodes GPR et sismique très haute résolution ont été privilégiées. Pour les deux méthodes, le développement discuté dans les chapitres 1 et 4 des techniques d'inversion en champ d'onde complet, pourraient permettre, outre l'obtention d'images plus fines, une caractérisation précise des propriétés diélectriques et/ou sismiques des marqueurs, et donc ainsi faciliter la visualisation de leur extension spatiale.

Pour conclure, à l'avenir, les méthodes d'investigations ou de surveillance géophysiques vont continuer à jouer un rôle primordial au niveau de la subsurface, celle échelle devenant sans doute le théâtre de risques naturels ou environnementaux à enjeux croissants. Il faudra ainsi continuer les développements de nouvelles méthodes ou l'analyse plus fine de méthodes plus classiques. Pour ce faire, seule une forte relation entre recherches expérimentales (laboratoire, terrain) et développements théoriques et numériques pourront apporter des avancées intéressantes. De même, à la multiplication des systèmes d'observations et d'imageries différentielles, il faudra proposer des techniques d'interprétations plus fines et qui tentent d'exploiter le maximum d'informations contenues dans les signaux enregistrés. C'est donc vers ces perspectives que j'aimerais me placer et que je proposerai dans une dernière partie synthétique, tout en gardant une forte variabilité (ou dispersion suivant le regard porté) dans les applications potentielles.

CHAPITRE 1

HYDROGÉOPHYSIQUE ET MILIEUX POREUX

1.1. Introduction.

1.1.1. Méthodes et paramètres hydrogéophysiques

La constitution poreuse de la subsurface de la Terre en fait une zone majeure d'intérêt socio-économique, que ce soit en termes de ressources d'énergie (huiles, gaz), de ressources vitales (eau, agriculture) mais aussi de contaminations potentielles (déchets industriels, contaminants d'origines multiples). Une utilisation raisonnée mais efficace de cet espace superficiel constitue un challenge majeur que la société va devoir relever, qui passe par une amélioration de la connaissance sur les processus d'échanges et de transport. Cet espace doit une partie de sa complexité à sa forte hétérogénéité, mais également à son caractère multi-phasique: mélange de grains solides autour desquels se dégage un espace poreux complexe, plus ou moins saturé et rempli par des fluides présentant des propriétés également variables.

Les techniques conventionnelles de prise d'échantillons pour caractériser ou suivre temporellement différentes propriétés des formations superficielles passent par des forages. Ces méthodes sont chères, longues à mettre en œuvre et invasives, ce qui peut modifier les propriétés d'écoulement. De plus, comme elles sont forcément très espacées, elles ne peuvent rendre compte des hétérogénéités hydrologiques ou environnementales à grande échelle spatiale. Cette faible caractérisation de la subsurface rend la gestion de l'eau, la délimitation de l'extension spatiale de contaminants, le suivi de tentatives de dépollution excessivement chers et peu efficaces. De la même manière qu'en médecine, où le développement des techniques d'imagerie a réduit le besoin d'opérations invasives, les méthodes géophysiques ont ce potentiel de caractérisation de la partie fluide de la subsurface, de manière rapide, non-invasive et à grande échelle. Pour tenter de répondre à ces enjeux, une nouvelle branche de la géophysique a vu le jour au début des années 2000, l'hydrogéophysique. Celle-ci regroupe l'ensemble des méthodes géophysiques qui permettent d'estimer des paramètres et/ou de suivre temporellement des processus considérés comme importants pour toute étude hydrologique (Hubbard and Rubin, 2005). Ceci inclut les processus associés aux ressources en eau, au transport de contaminants ou aux investigations écologiques. Outre son aspect non-destructif, la plupart des méthodes géophysiques est dorénavant capable d'apporter des informations – certes indirectes via des observables – à grande échelle comparé aux mesures in-situ (surface, forage) qui restent, par nature, ponctuelles.

Les principaux obstacles qui empêchent des succès routiniers de l'hydrogéophysique résident i) dans le manque de connaissance entre les observables géophysiques mesurées et les paramètres d'intérêt en hydrologie (perméabilité, porosité, ..) ou en géochimie, ii) les relations pétrophysiques généralement non-unicas entre ces paramètres et les problèmes d'homogénéisation qui permettent de les établir et iii) la difficulté d'intégration de données par essence disparates en termes de sensibilité, de résolution et de profondeur de pénétration (Hubbard, 2002). A ces difficultés, il convient également de rajouter les problèmes liés aux méthodes géophysiques en elles-mêmes, notamment en termes de sensibilité non-unique à un seul paramètre, de non-unicité des méthodes de potentiels, ceux liés à un passage par un processus d'inversion. Enfin, la résolution décroît en général avec la profondeur.

La sensibilité des observables géophysiques usuelles (résistivité électrique, vitesses sismiques, permittivité diélectrique, densité) aux constituants des milieux poreux a fait l'objet de nombreuses synthèses bibliographiques (Guéguen and Palciauskas, 1997; Mavko et al., 2003). C'est la résistivité électrique qui est le paramètre le plus utilisé en hydrogéophysique, car sensible à la fois à la teneur en eau et la conductivité de l'eau (chimie de l'eau). Cette dépendance est bien décrite par le modèle d'Archie (1942) en l'absence d'argiles. En présence d'argiles, il convient de rajouter un terme de conduction de surface, qui prédomine sauf dans le cas d'eau fortement conductrice. Cette dépendance non-unique va poser des problèmes d'interprétation quantitative dans les sols fins ou argileux. La résistivité électrique est aisément accessible par de multiples méthodes relativement classiques, qui diffèrent de part leur mise en œuvre, leur interprétation et leur résolution. Les méthodes électromagnétiques d'induction à basses fréquences permettent d'obtenir des cartes de la résistivité moyennées sur une certaine épaisseur.

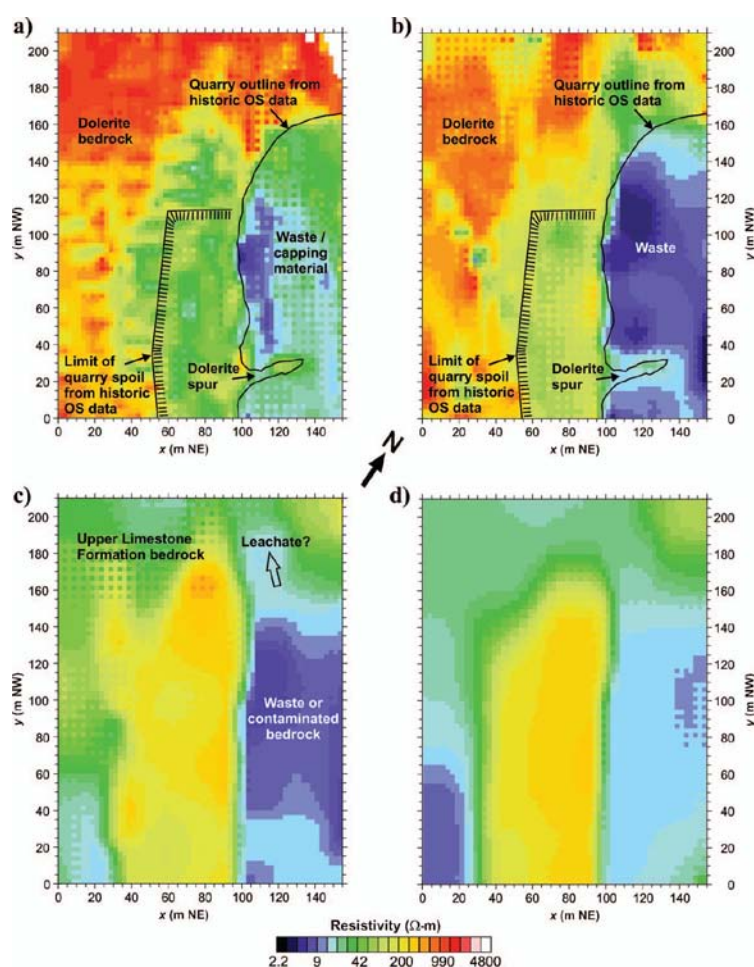


Fig. 1.1 Résultats de tomographies électriques 3D d'un site de décharge (Chambers et al., 2006) montrant les extensions latérales et en profondeur de contaminants (zones conductrices).

De nombreuses études ont été effectuées pour la problématique environnementale en utilisant cette méthode rapide. On peut citer la caractérisation de extension spatiale 2D d'une pollution industrielle (Guérin et al., 2004) ou de contamination au niveau d'intrusions salines (Dahlin et al., 2002), d'études multi-échelles de la zone non saturée (Descloitres et al., 2003; Massuel et al., 2006). Cependant, ces méthodes de cartographie apportent peu de contraintes sur la profondeur. C'est pourquoi, il est courant de combiner cette approche avec des tomographies électriques 2D ou 3D voir en suivi temporel, majoritairement depuis la surface et plus rarement

entre forages (par exemple, Binley et al., 2002; Guérin et al., 2004 ; Chambers et al., 2006 ; Dahlin et al., 2002). Les résultats d'une tomographie électrique 3D sont présentées Fig. 1.1 (Chambers et al., 2006). Ceux-ci ont permis de délimiter l'extension 3D du transport de contaminants issus d'une décharge (conducteurs) au sein d'une carrière. Dans les sols résistifs (secs, fracturés), les méthodes d'induction en temps (TEM) ont été privilégiées (Descloitres et al., 2000). Ces dernières méthodes nécessitent cependant une inversion qui peut donner des résultats non-unicques et montrent une décroissance forte de la résolution avec la profondeur. Bien que très populaire par leur facilité d'utilisation, un des problèmes inhérents aux méthodes de résistivité électrique réside dans la non unicité de l'interprétation. En effet, la présence d'argiles générant des conductances de surface, l'interprétation de conductivités élevées sera délicate dans les sols entre leur origine argileuse ou électrolytique. De plus, il existe également une non-unicité dans l'interprétation entre le contenu en eau et la chimie de l'eau. Leur utilisation en suivi temporel pourrait laisser penser une plus grande facilité d'interprétation, un seul des constituants (teneur eau, concentration de soluté) variant de manière dynamique, les autres restants statiques. Pourtant, comme constaté par Decloitres (2010), Kemna et al. (2004) ou Singha et Gorelick (2006), les images de résistivités obtenues par différence (post-inversion) ou en différentiel (pré-inversion) sont difficilement convertibles quantitativement en termes de variations de concentration de solutés ou de teneur en eau (suivant le contexte), en raison des problèmes de sensibilité aux acquisitions et aux paramètres d'inversion.

Une manière de contourner le problème de la non-unicité de l'interprétation peut résider dans l'emploi de méthodes géophysiques combinées, qui diffèrent en termes de sensibilité. Dans ce cas, l'utilisation de relations pétrophysiques adaptées peut permettre d'intégrer les observables déduites de chacune des méthodes pour en sortir les caractéristiques du milieu.

Parmi les méthodes directement sensibles à la teneur en eau, celles permettant d'accéder à la permittivité diélectrique des matériaux et la résonance magnétique protonique (RMP) sont privilégiées. En effet, comme la molécule d'eau est une molécule polaire, ses propriétés diélectriques sont beaucoup plus élevées que celles des autres constituants des matériaux naturels. Aux fréquences inférieures à quelques GHz, la constante diélectrique de l'eau avoisine 81 alors qu'elle se situe autour de 10 pour les autres matériaux et de 1 pour l'air (Topp et al., 1980). Pour cette raison, différentes techniques de mesures de la constante diélectrique ont été développées afin d'estimer, à différentes échelles, la teneur en eau. Pour des applications superficielles ou en forage, la TDR (Time-Domain Reflectometry, Robinson et al., 2003; Laurent et al., 2003) a été utilisée mais reste ponctuelle et destructive, alors que des mesures de télédétection radar (Dobson and Ulaby, 1986) fournissent des teneurs en eau très superficielles, mais à très grande échelle. Entre ces deux échelles, les mesures GPR peuvent accéder à cette observable, via les mesures de vitesses électromagnétiques, et ceci en employant différentes méthodes (Huisman et al., 2003 pour une synthèse) qui seront explicitées par la suite. Au niveau de la RMP, l'amplitude du signal mesuré en fonction de l'intensité du champ magnétique transmis à la fréquence de Larmor nous renseigne sur la teneur en eau dans le sous-sol et sur la profondeur et l'épaisseur de la nappe, tandis que les temps de relaxation nous renseignent sur la taille moyenne de pores dans la nappe (Legchenko et al., 2002).

Cette brève introduction aux méthodes hydrogéophysiques classiquement utilisées ne serait pas complète sans évoquer les phénomènes de polarisation spontanée, qui constitue la méthode permettant de caractériser la dynamique d'un écoulement d'eau (Suski et al., 2006, Jardani et al., 2008). Elle utilise la mesure et l'inversion de la distribution spatiale d'un champ électrique naturellement généré par l'écoulement de l'eau. Enfin, la partie complexe de la résistivité électrique, dénotée la polarisation induite, regroupe l'ensemble des phénomènes de relaxation se produisant dans le milieu. La dispersion de cette observable, utilisée à l'origine pour l'exploration de minéraux métalliques dans le sous-sol, est dorénavant adaptée à résoudre

problématiques hydrologiques, environnementaux et d'ingénierie, notamment en raison de sa sensibilité à la perméabilité (Slater et al., 2006 ; Kemna et al., 2004).

A plus grande profondeur, bien que l'aspect multi-phasique des couches géologiques soit un problème de premier ordre pour les problématiques pétrolières ou de séquestration de CO₂, les méthodes sismiques d'imagerie et d'inversion sont généralement reinteintes aux approximations acoustiques ou élastiques. A partir des vitesses d'ondes P (et parfois d'ondes S) obtenues, des relations pétrophysiques (par exemple Pride et al., 2003 ; Mavko et al., 2003) peuvent permettre, dans un second temps, de retrouver les caractéristiques de l'espace poreux et donc du fluide. Des techniques d'analyse de l'amplitude de la réflectivité (AVO) des ondes réfléchies ont également permis d'identifier la nature du fluide saturant (Simmons and Backus, 1994; Hall and Kendall, 2003; Mahob and Castagna, 2003; Stovas et al., 2006).

1.1.2 Travaux effectués

Par rapport à cette thématique, certains travaux que j'ai pu mener ont constitué une contribution – certes modeste - à la caractérisation de l'espace fluide ou de l'espace poreux. Ces travaux sont principalement axés sur les méthodes de propagation d'ondes (sismiques, électromagnétiques). Celles-ci ont parfois été combinées avec d'autres méthodes (tomographie électrique, RMP en collaboration avec M. Descloitres et A. Legchenko, LTHE Grenoble) pour des interprétations plus quantitatives en termes de propriétés de l'espace poreux.

Différents contextes ont été abordés et seront présentés ci-après. La première série de travaux porte sur les problématiques d'imagerie et de caractérisation de la teneur en eau des matériaux naturels par géoradar. Le premier milieu étudié porte sur la zone non-saturée et son étude par intégration de différentes méthodes dans la loi d'Archie. Cette approche a permis de caractériser l'évolution de la distribution 2D des teneurs en eau et de la conductivité de l'eau, ainsi que d'appliquer la théorie de Biot pour retrouver la porosité de la zone saturée à partir de données sismiques. Ce travail sera présenté sous la forme d'un article au Journal of Hydrology (Garambois et al., 2002). Je présenterai rapidement dans un second paragraphe une étude comparative entre différentes méthodes d'estimation GPR de teneur en eau dans un milieu saturé et gorgé de fluides que constituent les tourbières (GPR, comparaison RMP et TDR). Enfin, dans un contexte de changement climatique, j'ai tenu à présenter une étude GPR encore en cours sur la problématique du risque glaciaire lié à une brusque vidange potentielle. En effet, les analyses GPR puis RMP préliminaires ont permis d'identifier et de localiser la présence d'eau dans le glacier de Tête-Rousses (massif du Mont-Blanc). Sa vidange brutale en 1892 avait provoqué la mort d'environ 200 personnes en aval, sur St-Gervais. Ici, la détection d'eau est abordée de manière qualitative au niveau GPR, le milieu étant très hétérogène. En fait, les cavités remplies d'eau localisées au niveau du contact glacier-bedrock provoquent localement un important ralentissement des vitesses électromagnétiques (pushdown) et créent des sauts de continuité au niveau de cette interface. Les données GPR ont été comparées avec une interprétation 3D RMP, puis avec une vingtaine de forages thermiques effectués début juillet 2010. Ce travail, effectué en liaison avec la préfecture de Haute-Savoie, sera présenté en anglais, sous la forme d'un article en préparation.

Dans un second temps, une application géotechnique de mesures acoustiques en laboratoire sera proposée pour la problématique d'injection de fluides à haute-pression dans le sous-sol (Jet-Grouting), procédé qui vise à consolider un sol ou à circonscrire une pollution. Ces travaux ont été conduits dans le cadre d'un financement ARN « Réseau Génie Civil et urbain » qui visait à imager en temps quasi-réel (contrôle) la géométrie de la colonne cylindrique créée.

Les caractéristiques acoustiques du mélange homogénéisé ont pu être déterminées en laboratoire en fonction de son temps de durcissement, et montrent la fenêtre temporelle optimale d'acquisition en termes d'atténuation, ainsi que la meilleure configuration souhaitée pour une imagerie par sismique réflexion (source, fréquence, positions sources-récepteurs).

Les travaux en cours sur cette thématique seront détaillés dans la partie perspective. Ils se recentrent sur les problèmes d'imagerie sismique et GPR en privilégiant une approche d'inversion du champ d'onde complet. Une modélisation poro-élastique de la propagation des ondes sismiques en 2D est à l'étude actuellement (thèse B. Dupuy). Celle-ci permettra une inversion ciblée sur les paramètres d'intérêts (porosité, perméabilité, saturation, viscosité) suivant les applications hydrologiques, pétrolières ou d'enfouissement du CO₂ désirées, par la prise en compte de l'ensemble des paramètres constitutifs du milieu poreux. Un certain nombre de perspectives relatives à ces travaux seront détaillées (acquisitions de données terrain et de laboratoire, intégration de la saturation, d'une double porosité). Des travaux similaires seront également entrepris pour les ondes radar (thèse F. Lavoué), qui font suite aux travaux effectués sur l'inversion des propriétés fréquentielles des courbes AVO (Amplitude versus Offset) réalisés pour une problématique de caractérisation de fractures (détaillées dans le Chapitre 4). Enfin la problématique de l'inversion différentielle de champs d'ondes complets en sismique sera également abordée dans un contexte où la phase fluide évolue dans le temps. Ceci fait l'objet d'une collaboration avec Total dans le cadre d'une thèse (Amir Asnaashari).

1.2. Travaux effectués pour des problématiques du milieu bi-phasique

1.2.1. Caractérisation quantitative de la Zone non-saturée : apport de données géophysiques multi-méthodes



On the use of combined geophysical methods to assess water content and water conductivity of near-surface formations

Stéphane Garambois*, Pascale Sénéchal, Hervé Perroud

Laboratoire d'Imagerie Géophysique, IPRA, CNRS UMR 5831, Université de Pau et des Pays de l'Adour, 64000 Pau, France

Received 29 September 2000; revised 16 October 2001; accepted 12 November 2001

Abstract

We propose to deepen the interpretation of combined geophysical methods (georadar, seismic and electric) to assess physical properties characterizing the near-surface porous formations, especially the influence of water. Velocity analysis of multioffset georadar data are used together with seismic methods to estimate lateral and vertical ground water fluctuations. This enables us to identify transitions from non-saturated to fully saturated porous layers with certainty. Furthermore, the accurate knowledge of seismic velocities helps to estimate the porosity of the ground water formations. Finally, we show how the radar technique may be useful in solving the problem of trade-off between bulk resistivity, which is deduced from electrical measurements, and that of water ionic conductivity and water content. These theoretical considerations are illustrated using various measurements conducted at the same test site. Our interpretation is compared with a few laboratory measurements on water and soil samples. This study displays the impact of combined geophysical approaches for providing models of water and ionic transfers down to a depth of several metres. © 2002 Elsevier Science B.V. All rights reserved.

Keywords: Ground penetrating radar; Seismic and electrical methods; Water content; Water conductivity

1. Introduction

The knowledge of the geometry and the physical properties characterizing the subsurface is a contemporary challenge that society has increasingly to face, especially for ground water and its protection from sources of contamination of various kinds. Most physical properties of porous material (e.g. sedimentary rocks) are significantly influenced by the presence of water in pores and fissures and by their chemical properties (e.g. salinity). The use of classi-

cal, non-destructive, geophysical measurements should enable us to delineate changes of mineralogy, water content or chemistry and thus to develop optimum hydrological or geochemical investigations of the subsurface. The use of geophysical methods in such highly heterogeneous media is particularly problematic due to the fact that the physical parameters that can explain the observations are not unique, leading to an ambiguity in the interpretation. For example, seismic velocity variations can be due to changes in different physical properties (water content i.e. saturation, mineralogy, soil consolidation), thus making their interpretations ambiguous if there is no supplemental information. This problem can sometimes be reduced through the additional use of the multioffset ground penetrating radar (GPR) technique, its outcome (dielectric permittivity ϵ) being highly

* Corresponding author. Present address: LIRIGM, Université Joseph Fourier, 1381 rue de la Piscine, 38041, Grenoble Cedex 9, France. Tel.: +33-4-76-82-80-57; fax: +33-4-76-82-80-70.

E-mail addresses: stephane.garambois@ujf-grenoble.fr (S. Garambois), pascale.senechal@univ-pau.fr (P. Sénéchal), herve.perroud@univ-pau.fr (H. Perroud).

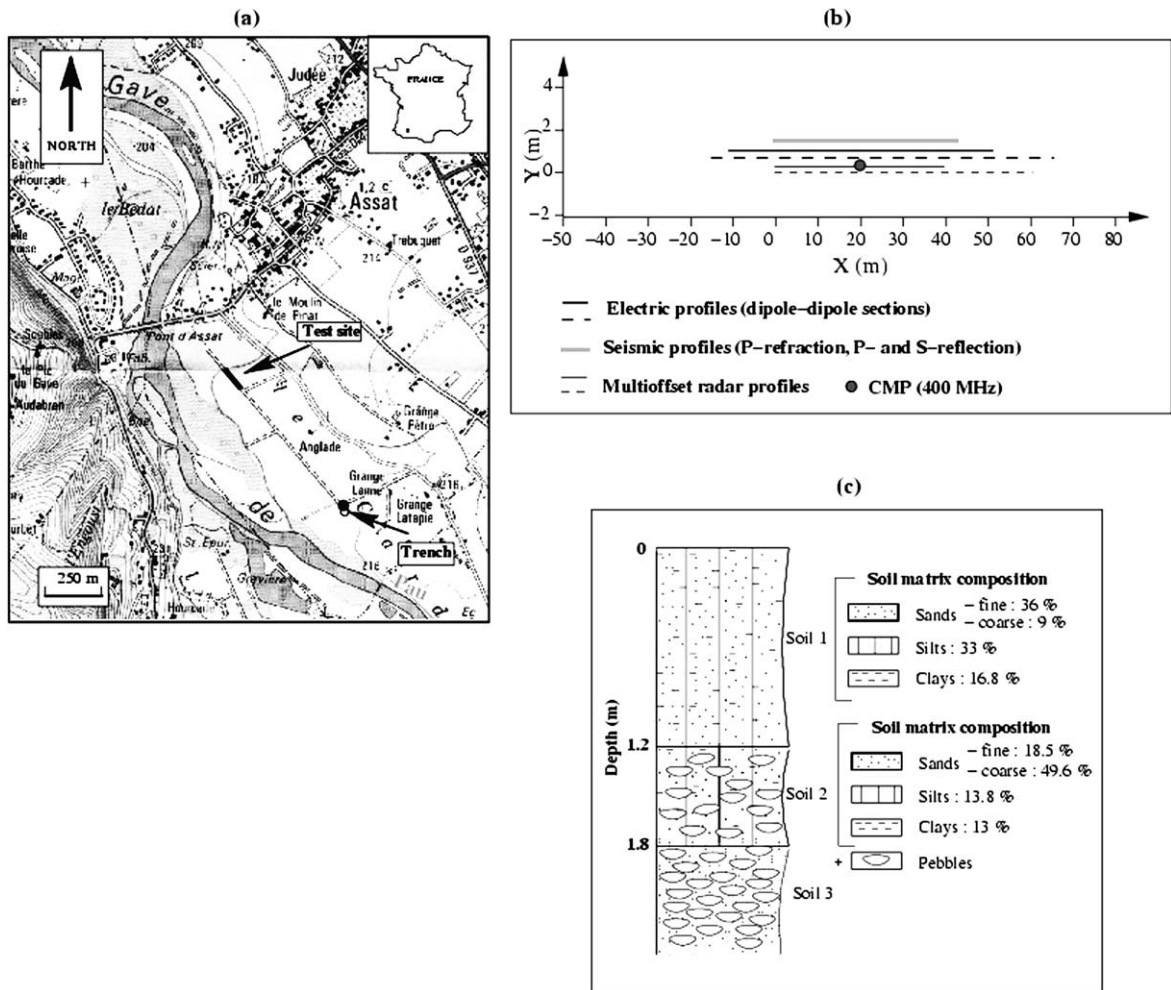


Fig. 1. (a) Test site location in the alluvial valley of the Gave de Pau river, in the South-West of France. (b) Location of the different geophysical profiles used in this study. The solid circle represents the location of the multioffset GPR section recorded using 400 MHz antennas at the middle of the 100 MHz multioffset GPR profile. Experiment A (solid line) was conducted in February 1999 and experiment B (dotted line) in December 2000. (c) Pedological log based on sample analysis of a trench located 600 m from the test site.

sensitive to the water content of granular sediments (Sen et al., 1981; van Overmeeren et al., 1997). As a matter of fact, several researches on the use of GPR as an in situ water detector have been published recently (e.g. Weiler et al., 1998; Dannovski and Yaramanci, 1999; Hagrey and Müller, 2000; Charlton, 2000).

The interpretation can be improved by combining information derived from different geophysical techniques. The approach presented here includes theoretical studies of the geophysical response linked to

each individual geophysical technique (GPR, geoelectrics, and seismics) for unsaturated porous materials of the vadose zone. The main outcome is to estimate quantitatively the soil moisture content from GPR and to compare these estimates with supplementary techniques, which are used also to improve interpretation. It also underlines the advantage of combining results of GPR with the electrical methods to solve the problem of trade-off between bulk resistivity, water resistivity (salinity) and water content in Archie law. This allows us to create an image of water conductivity

variations (and possible anomalies), as well as possible ionic transfers in the soil.

The present studies are illustrated using geophysical data acquired at the Anglade test site, near Pau (South-West France) in the alluvial valley of the Gave de Pau river (Fig. 1a). The studied formation belongs to the recent Würm glaciation period and is mainly composed of coarse deposits of pebbles and sands. The water table varies from 1 to 5 m in depth, depending on the weather and season. The field work was carried out on a gravel track separating agricultural fields where fertilizers were applied. We conducted two experiments, the first in February 1999 (experiment A) consisting of seismic studies (P-wave refraction, P and S-wave reflection), multi-offset GPR and dipole–dipole electrical profiles (Fig. 1b). The second experiment was conducted in December 2000 (experiment B), where GPR multi-offset and dipole–dipole electrical profiles were carried out. For experiment B, we performed sample analysis, (1) of the water table in a nearby well (conductivity and characterization of the solute ions and cations), and (2) of a 1 m depth soil located at $x = +3$ m along the profile (conductivity, pH, clay composition, nitrates proportion). These independent measurements helped us to interpret some of the geophysical data. Beside this, a 2 m deep trench located in the same formation, but 600 m away from the acquisition site, allowed us to analyse the composition of the soil matrix in the laboratory. The hole drilled on the profile during experiment B (at $x = +3$ m) revealed almost the same geological formation, thus indicating that the trench soil analyses are representative of the test site where the geophysical measurements were acquired. The only deviation along our profile was the presence of gravel track material from the surface down to about 0.4 m depth.

Three types of soil layers, all of them presenting low clay contents ($<17\%$), have been distinguished (Fig. 1c). The first layer, down to 1.2 m depth, consists of a mixture of very fine sands (44%), silts (33%) and clays (16.8%) and can be denoted loam (according to the textural triangle convention). The second layer, down to 1.8 m depth, is composed of sands (50% coarse sands + 18% of fine sands), mixed with silts (15.5%) and clays (13%) and is denoted sandy loam. It overlies a layer of pebbles (ophites, granites and quartzites) possessing a sandy matrix.

2. Water content estimations from GPR data

Microscopic fluid distribution can significantly affect dielectric properties of granular sediments. The GPR method has been used increasingly in the last few years to estimate directly the water content of near-surface rocks. For example, Greaves et al. (1996) showed field applications of multi-offset GPR data and interpreted subsurface variations of volumetric water content quantitatively. van Overmeeren et al. (1997) showed that GPR can provide reliable quantitative informations of the soil water content from the surface, both vertically and horizontally, and so avoids drilling. Proof of this was established after comparing water content estimates obtained using GPR and from a capacitance probe. In the same way, Hagrey and Müller (2000) successfully investigated the capability of GPR to determine accurately the pore water content of clean sands, both in the laboratory and at outdoor experimental sites. In this section, we summarize the different steps allowing us to quantify the pore water content from GPR data. To be more specific, we (a) present briefly the dependence of the radar wave velocity on soil dielectric permittivity and associated assumptions, (b) address the data acquisition and processing steps required to determine radar velocities precisely, and (c) discuss different expressions relating the dielectric properties of rocks to their pore water content. Some of these steps are illustrated by our field examples.

2.1. Propagation velocity of radar waves

In general, the radar wave velocity depends on the dielectric permittivity ϵ , the magnetic permeability μ , and the electrical conductivity σ of the considered material, which are all complex and frequency-dependent tensor parameters.

Nevertheless, it has already been shown (e.g. Davis and Annan, 1989) that the radar wave velocity v can be approximated as

$$v = \frac{c}{\sqrt{\epsilon_r}} \quad (1)$$

where ϵ_r denotes the relative dielectric permittivity and c the velocity of free space. Relation (1) is valid for nearly homogeneous and isotropic formations and results from the hypothesis that $\epsilon = \epsilon_0 \epsilon_r$, where ϵ_0

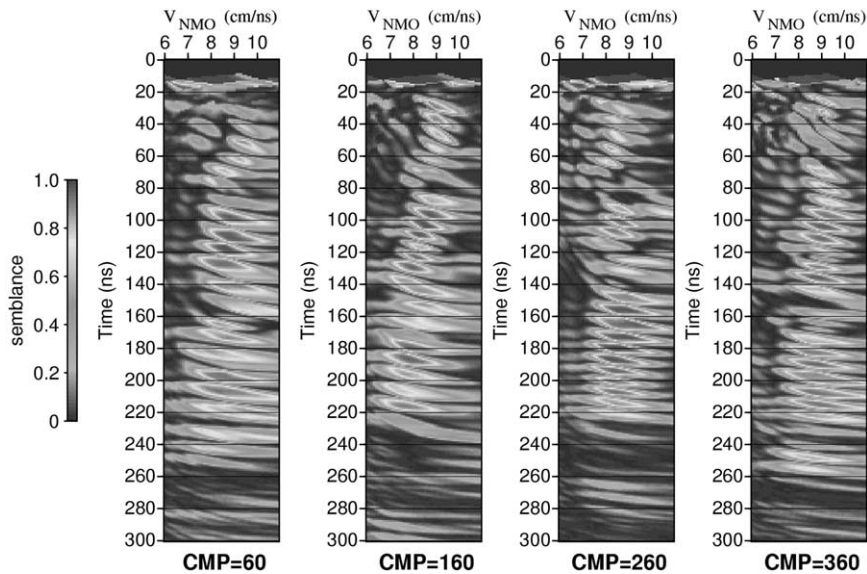


Fig. 2. Semblance panels obtained from four super-CMPs after preprocessing of GPR data collected at the test site (experiment A).

denotes the permittivity of free space ($= 8.854 \times 10^{-12}$ F/m). The major assumptions leading to this approximation are (i) that the material is a good dielectric, i.e. the conduction current density is negligible compare to the displacement current density [$\sigma/\omega\epsilon_0\epsilon_r \ll 1$], where ω is the angular frequency and, (ii) that the dispersive effects that appear through ϵ are negligible, which is usually the case in the 50–1000 MHz frequency range. The good dielectrics assumption for soils is often encountered in nature, especially when no metallic objects or minerals are present, or when rocks possess a low clay content. Considering our test site, inversion of electrical data, presented later, show resistivities in the range between 50 and 2250 Ohm m^{-1} . We used 100 MHz electric antennas for GPR data acquisition, and thus $\sigma/\omega\epsilon_0\epsilon_r \ll 1$. In any case, if this assumption was not satisfied, there would be no strong reflected waves on GPR sections.

An important consequence is that the GPR wave velocity is invariant in this frequency range, depending only on the dielectric constant of the medium of propagation.

However, as pointed out by Greaves et al. (1996), in addition to the major assumptions discussed before, some other factors have been omitted. These include scattering losses and possible signal variations caused

by the technique used. Nevertheless, such possible disturbances are expected to produce second-order effects, as compared to velocity variations in the ground, especially when strong reflections are found on GPR sections.

2.2. Electromagnetic velocities derived from GPR data

The common mid point (CMP) soundings, obtained by varying the radar antenna spacing at a fixed central location and measuring the change in the two-way traveltimes to the reflectors, can be used to determine a 2D stacking velocity field. In the CMP configuration, this stacking velocity field is extracted from normal-moveout velocities deduced from standard reflections analysis applied to radar waves (e.g. Yilmaz, 1987).

The corresponding detailed processes are now described and discussed.

2.2.1. GPR processing

The GPR measurements were conducted using a RAMAC/GPR unit system (MALA Geosciences) connected to 100 MHz antennas. For experiment A, radar data were collected with a set of 8 transmitters to receiver offsets, ranging from 1 to 8 m, such that, after

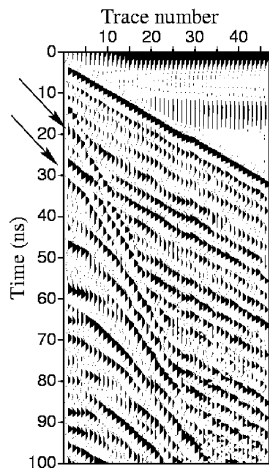


Fig. 3. 400 MHz antennas CMP gather used to support the resolution of the NMO velocity model in the first layer (experiment A). Two reflected waves are identified at approximately 19 and 29 ns (arrows).

re-arrangement, 401 CMPs of 8 traces spaced every 0.1 m on a 40 m long profile were available. For experiment B, CMP radar data were recorded every 4 m on a 60 m long profile with transmitter to receiver offsets ranging from 0.6 to 10 m, every 0.2 m.

Some preprocessing steps needed to be applied to the data before velocity analysis. To reduce noise and undesirable signals, a 15–250 MHz zero-phase band-pass filter was applied to the data, followed by a top mute of first arrivals corresponding to the direct waves. Next, the amplitudes were normalized by dividing each trace of a constant offset section by the average of the envelope traces of that section. For experiment A, the normal moveout was analysed in a first stage using the semblance maxima approach. Such an approach, well-known in seismic processing (Yilmaz, 1987), yields the stacking normal moveout (NMO) velocity V_{NMO} , that provides the normal moveouts appropriate for the offsets of the traces being examined as a function of arrival time. The semblance between the traces is determined, and this process is repeated until the semblance has been determined as a function of both stacking velocity and arrival time. To improve the picking resolution in the velocity spectra, traces from a few gathers around each CMP chosen for velocity analysis were combined (super-CMP). Fig. 2 displays the semblance panels of 4 chosen super-CMP collected at the

Anglade test site (Exp. A), obtained after combining traces from 7 CMP gathers (for the entire profile, this process has been repeated every 20 CMP gathers, i.e. every 2 m). For each super-CMP, the NMO velocity of each reflector was determined using the maximum corresponding semblance. The studied reflections are mainly between 45/50 ns and 240 ns, and are associated to NMO velocities between 7.6 and 9.6 cm/ns. A difficulty of this approach concerns the velocity spreading of the semblance, associated to the stretching effect of the NMO correction. The second stage of the process to refine these estimates consists of superimposing the hyperbolae corresponding to the obtained NMO velocities on the central CMP gather. This was done to refine the fit with the GPR data (if necessary), which improves the precision to ± 0.2 cm/ns. Another problem concerns the lack of information until 45 ns, which is principally due to the fact that at 100 MHz reflected waves destructively interfere with the direct wave propagating in the ground, which can lead to substantial errors in the interval velocity estimates. To overcome this problem, one can use higher frequency antennas, which can provide more information on superficial layers. Fig. 3 shows a 400 MHz central acquisition CMP gather, where reflected waves appear at approximately 19 and 29 ns. The corresponding NMO velocities have been added to the NMO velocity model with the assumption that they are laterally constant along the entire profile. Fig. 4a shows the resulting 2D NMO velocity field obtained from interpolation of the various 1D velocity models computed for every 20 CMP gathers. The NMO velocity field has been superimposed on the stacked CMP section (described in the next paragraph) to show the consistency between reflections and velocity variations. The 2D model appears relatively smooth, and artifacts due to the poor resolution of semblance spectra have been removed.

After applying the normal-moveout corrections computed using the derived 2D NMO velocity field, the multioffset data were stacked to produce the simulated zero offset section shown in Fig. 4b. In comparison to single-channel recordings, the stacking step has improved the signal-to-noise ratio significantly. It has also increased the depth of penetration and the quality of interpretation of structural and stratigraphic details (Fisher et al., 1992).

The same analyses were performed to derive the

NMO velocity model corresponding to the experiment B (which is not presented here) except that we obtained near-surface lateral variations without using higher frequency antennas. This was possible thanks to the larger number of traces available in every CMP, making the recognition of the first reflections possible. In addition, the larger number of traces results in a higher confidence in NMO velocity estimates (± 0.05 cm/ns).

2.2.2. Interval velocity

The average interval velocity $V_{i,j}$ between times t_i and t_j , can be computed from the NMO velocity using the Dix formula (Dix, 1955)

$$V_{i,j}^2 = \frac{V_{\text{RMS},j}^2 t_j - V_{\text{RMS},i}^2 t_i}{t_j - t_i}; \quad (2)$$

$$i = 1, 2, \dots, n - 1; \quad j = i + 1.$$

Here $V_{\text{RMS},j}$ is the NMO velocity at zero-offset arrival time t_j , corresponding to the j th reflection. The use of this formula is only valid for almost horizontally stratified media, which is approximately the case for our test site (see Fig. 4b). Application of this formula (classical in seismic processing) can provide non-real velocities, if the traveltime intervals are small or if the NMO velocity change is large. Such problems were not encountered in our case. The obtained interval velocities after smoothing are presented in Fig. 4c and d for experiments A and B, respectively. Both figures show relatively similar velocity sections, ranging from 6 to 11 cm/ns, that consist of successive horizontal layers. From top to bottom we can distinguish on Fig. 4c a moderate velocity layer (< 8.5 cm/ns) between 0 and 1.2 m depth, followed by a high velocity layer (> 9 cm/ns) between 1.2 and 2.5 m depth overlying a low velocity layer (between 5 and 8 cm/ns). The latter presents substantial lateral variations. For experiment B, the first layer does not appear so clearly, as it presents lateral variations. The second layer seems to be thicker down to 3 m depth and the low velocity layer appears more homogeneous than the one deduced from experiment A. The reliability of both models depends on the accuracy of the NMO velocity estimates based on the Dix

formula. We shall see in Section 2.3 how this 2D velocity field can be used to estimate the water content in the layers.

2.3. Sensitivity of the dielectric permittivity to the water content

The effective dielectric constant of a porous material is highly sensitive to its volumetric water content θ because the relative dielectric constant of water ($\epsilon_{r,w} \approx 80$) is several orders in magnitude higher than the dielectric constant of most minerals forming a rock matrix ($\epsilon_{r,g} = 3 - 5$) and of air ($\epsilon_{r,a} = 1$). Thus, the knowledge of the variations of the dielectric constant allow the determination of the water content distribution in the soil.

Several models can be found in literature (e.g. Sen et al., 1981; Shen et al., 1985) that propose a relationship between the dielectric constant and properties characterizing the water content θ , i.e. porosity ϕ and water saturation S_w ($\theta = \phi S_w$). This relation can be derived from capillary tube or network models and from percolation and effective medium theories.

One such formula is derived from the electromagnetic analogue of the time-average Wyllie equation for seismic velocities, and is known as the complex refractive index method (CRIM, Freedman and Vogiatzis, 1979). As pointed out by Dvorkin and Nur (1998), this approach consists of simply assuming that the total traveltime of a wave (seismic or electromagnetic) in a multicomposite medium is the sum of the traveltimes along the individual components (as if the components were arranged in layers normal to the direction of propagation and the wavelengths were small compared to the thickness of an individual layer). For a water–air–mineral mixture, this model leads to the dielectric constant

$$\sqrt{\epsilon_r} = (1 - \phi)\sqrt{\epsilon_{r,g}} + \phi S_w \sqrt{\epsilon_{r,w}} + \phi(1 - S_w)\sqrt{\epsilon_{r,a}}, \quad (3)$$

where subscripts g, w and a denote grain, water and air respectively. The major problem with the above relationship is that it does not take into account the geometrical information on the internal structure of rocks and on microscopic fluid distribution. As shown in Endres and Knight (1992), this has a significant effect on dielectric properties of partially saturated rocks. The above restriction may be overcome

by using another differential mixing expression, the Hanai–Bruggeman formula. It allows the determining of (1) the effective relative dielectric constant of a water/air mixture $\epsilon_{r,w/a}$, and (2) the effective relative dielectric constant of the total rock by mixing the mineral grains into the water/air mixture. The resulting relative dielectric constant is found to be

$$\epsilon_r = \epsilon_{r,w/a} \phi^{m_2} \left(\frac{1 - \frac{\epsilon_{r,g}}{\epsilon_r}}{\frac{\epsilon_{r,w/a}}{1 - \frac{\epsilon_{r,g}}{\epsilon_r}}} \right)^{m_2}, \quad (4)$$

$$\epsilon_{r,w/a} = \epsilon_{r,w} S_w^{m_1} \left(\frac{1 - \frac{\epsilon_{r,a}}{\epsilon_r}}{\frac{\epsilon_{r,w}}{1 - \frac{\epsilon_{r,a}}{\epsilon_r}}} \right)^{m_1}. \quad (5)$$

Here m_1 and m_2 are the cementation exponents. m_1 is related to the microgeometry of the water/air mixture that fills the pore space and may vary with the level of water saturation (Endres and Knight, 1992) whereas m_2 is related to the shape of the mineral grains. The main problem with the two previous approaches is that it is not possible to derive both the porosity and the water content from the dielectric constant. We cannot therefore obtain information about the water content without strong a priori assumptions. For this reason, it is preferable to use the well-known empirical equation derived in Topp et al. (1980) regarding the study of the dielectric response ϵ_r of various soil samples (presenting different degrees of saturation), as a function of their net water content θ . This formula is given by

$$\epsilon_r = 3.03 + 9.3\theta + 146.0\theta^2 - 76.7\theta^3. \quad (6)$$

Topp et al. (1980) propose a reciprocal expression for estimating θ in terms of a polynomial function in ϵ_r

$$\theta = -5.3 \times 10^{-2} + 2.92 \times 10^{-2} \epsilon_r - 5.5 \times 10^{-4} \epsilon_r^2 + 4.3 \times 10^{-6} \epsilon_r^3. \quad (7)$$

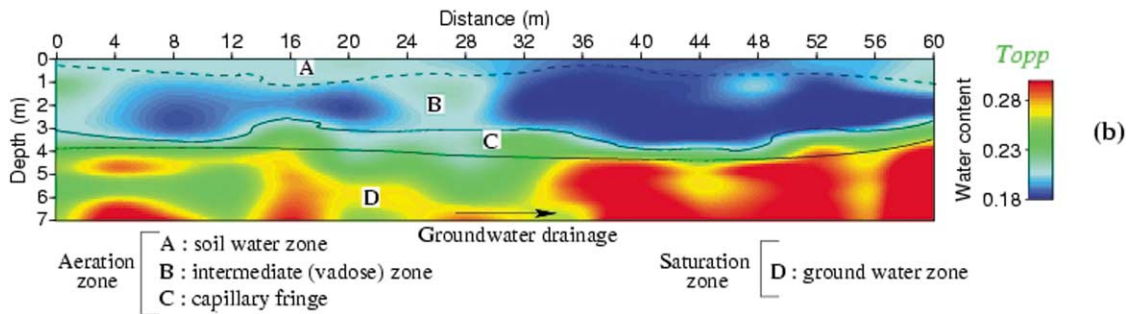
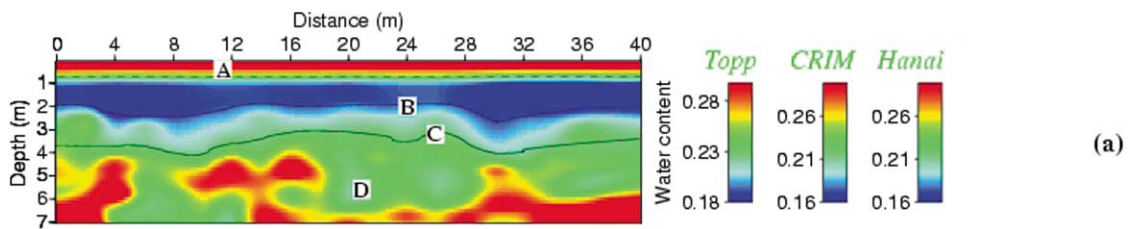
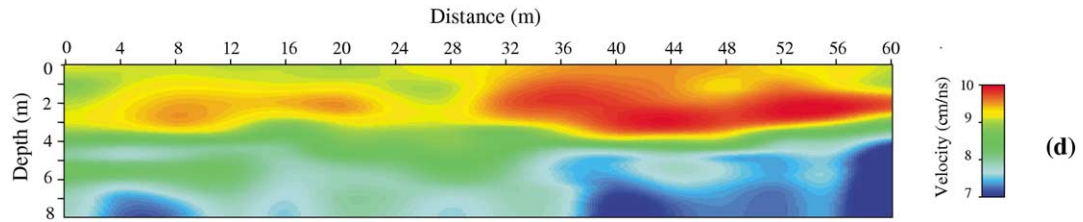
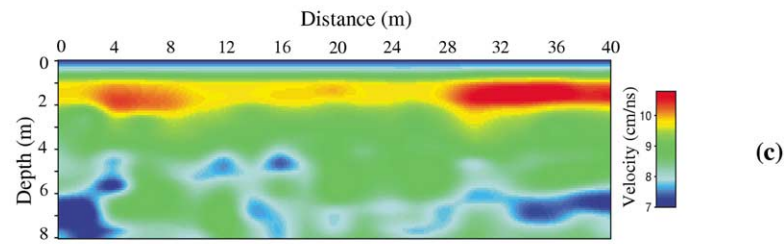
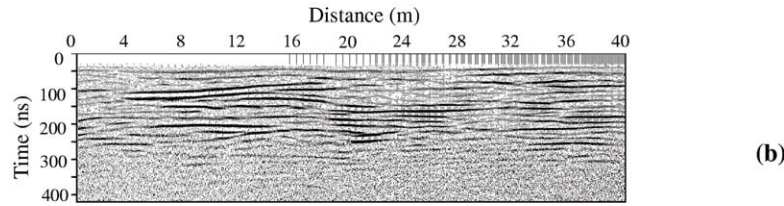
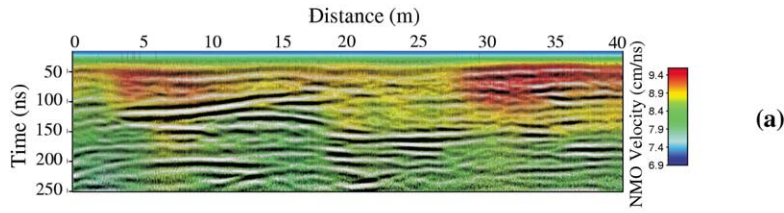
Greaves et al. (1996) compared the results predicted by the Hanai–Bruggeman formula (4) with those predicted using the Topp relation (7), and noted the good correlation between the two models. Greaves et al. (1996) considered the cementation exponent to vary from $m_1 = 2$ to $m_1 = 1.5$ when the water saturation increases. In practice, m_2 is related to the grain shape and varies from 1.5 (well-rounded grains) to more than 2 (oblate grains).

The three models presented above, directly expressing the dielectric constant as a function of the porosity and the water saturation, have been applied to the data recorded in our Anglade test site. The 2D velocity models presented in Fig. 4c and d have already been converted into dielectric constant models using Eq. (1). Fig. 5a displays 2D estimates of the volumetric water content θ for experiment A using (a) the Topp empirical relation (7), (b) the CRIM formulation in a saturated porous medium (Eq. (3), with $S_w = 1$), and (c) the Hanai–Bruggeman relation in a saturated porous medium with $m_2 = 1.5$ (Eqs. (4) and (5), with $S_w = 1$). The choice of m_2 comes from the analysis of samples down to 2 m depth (Fig. 1c), which shows the predominance of well-rounded unconsolidated sand grains or gravels. The three models show similar estimations on the water content of the medium (see legend colour axis), except when it drops to low values. In this case, the approximation of fully saturated material seems to be less valid, and only the Topp relation should be considered. For experiment B, we present on Fig. 5b only the results obtained using the Topp empirical relation (7).

Fig. 5a displays a first layer going from surface to

Fig. 4. (a) Superimposition of the 8-fold stacked CMP section with the 2D NMO final velocity model obtained after semblance analysis, hyperbola adjustment and 400 MHz central CMP analysis (experiment A). (b) Unmigrated 8-fold stacked CMP section (offsets from 1 to 8 m). (c) and (d) Final interval velocity 2D model obtained from the NMO velocity model using the Dix formula for experiments A and B, respectively.

Fig. 5. (a) Water content estimates from the velocity analysis of multioffset GPR data for experiment A. The colour bars display whether the water content has been estimated using the Topp equation or from the water-saturated CRIM or Hanai–Bruggeman ($m = 1.5$) equations. In the last two cases, the volumetric water content is equal to the material porosity. (b) Water content estimates for experiment B, using only the Topp equation.



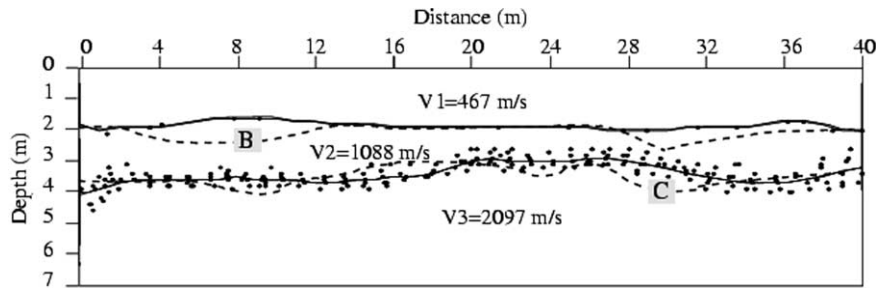


Fig. 6. 2D P-wave velocity model obtained after inversion of the first arrival time in the refraction experiment (experiment A). The dots represent the incident and emergent refraction points along the interface, for all point-source and receiver positions. The dotted lines represent the horizons B and C deduced from GPR multioffset.

approximately 1 m depth presenting a mean water content of 28%, which does not appear as clearly in Fig. 5b. This zone (denoted A), which is adjacent to the surface, is highly affected by conditions at the ground surface (mostly by seasonal and diurnal fluctuations of precipitation, air temperature and air humidity). Experiment A was conducted after strong precipitation, and the soil in this zone was almost saturated (infiltration process), contrary to Experiment B, which was conducted on dry soil. These surface conditions can explain the fluctuations obtained from GPR analysis in this near-surface zone. Fig. 5a shows that this zone is followed by a layer (denoted B) going from 1 m depth to 2.5 m depth with a 17% mean water content, that we interpreted as the intermediate (vadose) zone presenting lateral variations. This zone appears to extend deeper in Fig. 5b, but we can observe the same relative lateral variations as in Fig. 5a (higher water content around positions of $x = 0$ to $x = 2$ m and $x = 22$ to $x = 28$ m). We can also distinguish another intermediate zone, denoted C, which presents a gradual increase in moisture content with depth (between 2.5–3 and 4 m depth). We interpreted this zone, whose upper limit has an irregular shape, as the capillary fringe. It appears thicker in experiment A during the water infiltration process. Finally, the last layer, denoted D, is interpreted as the ground water, a zone where the pores are saturated and that presents a mean water content around 25–26%. It is noticeable that the transition between the capillary fringe and the saturated layer does not appear very clearly throughout the length of the model (especially between positions of $x = 18$ and $x = 28$ m). A discussion about the consistency

of these results with those obtained from seismic methods will follow below. It is advisable in any case, as pointed out by Greaves et al. (1996), to consider such images as relative changes of the water content rather than absolute values.

3. Information from P and S-wave data

Seismic refraction and reflection methods have been used successfully for mapping water tables and aquifers in unconsolidated sandy formations. The effect of saturation and pore fluids on seismic velocities has been extensively studied both theoretically (Gassmann, 1951; Biot, 1956, 1962) and experimentally (Domenico, 1974; Murphy, 1984). Bachrach and Nur (1998), using high-resolution field experiments in sands, have recently confirmed the potential of seismic waves to provide a real-time image of the hydrological process. In particular, they showed that, both the reflections and refractions are influenced by partial saturation and do not follow the phreatic surface and that the wave velocity in porous sand can be inverted directly into water saturation. In this section, we want to assess the advantages of using seismic methods to create images of depth interfaces and to get information about the fluid content of near-surface layers. This quantitative information will then be compared to those of GPR.

3.1. Seismic data analysis

In February, 1999, we conducted high-resolution P-wave seismic refraction, P-wave reflection and S-wave reflection experiments in the Anglade test site, to

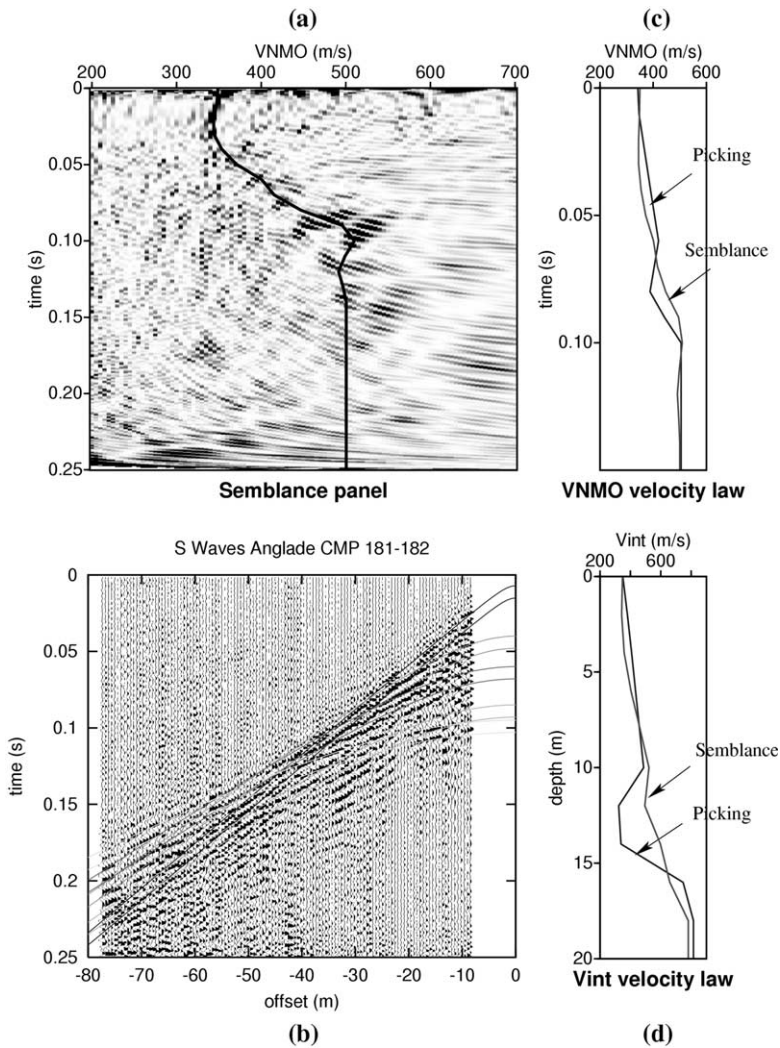


Fig. 7. S-wave reflections analysis for experiment A: estimates of S-wave velocities were performed using the same process than the one used for GPR multioffset data, i.e. NMO velocity extraction from a semblance analysis of reflected S-waves (a), and from a manual time picking (b). (c) NMO velocity models (c) and (d) interval velocity models calculated using the Dix formula (d).

gather information about both P and S-wave velocities at different depths (experiment A). The acquisition of refraction data was conducted using several 50-Hz vertical geophones (48) located every 1 m along a profile centred around the 100 MHz GPR profile (see Fig. 1b). Seven shots (hammer blows) were recorded for every 12 m. The picking of first breaks for each record shows three major slopes, namely, the direct P-wave and two refracted waves. The inversion of the time breaks was performed using the delay-time method (Parkiser and Black, 1957) to obtain a tenta-

tive model, which was refined by a ray tracing process and adjusted after various iterations to minimize the variations between experimental and modeled data in a least square sense (Scott, 1973). The obtained model presented in Fig. 6 clearly shows three almost horizontal layers whose velocities increase with depth (from top to bottom 467, 1088 and 2097 m/s, respectively). The superimposition of horizons B and C deduced from GPR multioffset (dotted lines) shows a good consistency between the seismic and GPR methods. There are some deviations, which disappear

Table 1

Properties used to compute seismic velocities (bulk moduli K and densities ρ) of quartz, water and air (denoted by subscripts s, w and a, respectively)

Properties	K_s (GPa)	K_w (GPa)	K_a (GPa)	ρ_s (kg/m ³)	ρ_w (kg/m ³)	ρ_a (kg/m ³)
Sand gravels	35	2.27	0.00015	2.6	1	0.0012

near the centre of the profile, where the 400 MHz antenna has been used to provide supplemental information near the surface. Therefore, we suspect that these weak deviations are due to the EM velocity heterogeneity near the surface, which appears clearly on experiment B (Fig. 5b). The difference in resolution of these methods can also induce such deviations.

The similarity can be explained by geological and/or mineralogical considerations. Nevertheless, as the water content plays a major role for the different physical parameters influencing the seismic velocities and to an even greater extent the dielectric permittivity, we believe that hydrologic parameters are the most likely explanation for this consistency.

The seismic P-wave reflection profile does not give information at a depth of less than about 20 m. This is not the case for the S-wave reflection profile, which has been conducted under an SH configuration, using several 50-Hz horizontal geophones (60) every 0.6 m, and a prototype horizontal vibrator (OYO GEOSPACE), which sweeps from 30 to 300 Hz. Around 150 shots have been recorded, the geophones being fixed and centred on the GPR profile, with offsets ranging from 0.3 to 80 m. Fig. 7b displays a CMP gather obtained at the centre of the refraction profile, where reflected waves can be identified and analyzed using two different methods. The first consists of manually identifying the hyperbolae associated to each reflection (Fig. 7b). The second consists of a semblance spectra analysis, as already discussed for GPR radar data (Fig. 7a). In any case, from these estimations, NMO velocity model can be deduced, and the application of Dix formula (2) yields an interval velocity versus depth relationship. The two velocity models obtained are similar, especially in the near-surface zone (0–5 m depth), where the S-wave velocity (centred around 370 m/s) does not show strong variations (Fig. 7c and d).

3.2. Biot–Gassmann model predictions

Combining information obtained from P-wave refraction and S-wave reflection profiles provides estimates on some properties of the porous layers. The presence of a strong P-wave velocity contrast, associated with the absence of a corresponding S-wave velocity contrast around 3–4 m depth, can be explained by saturation variations. Indeed, as predicted by the Biot–Gassmann theory or measured by ultrasonic velocity experiments (as performed on Massilon sandstones by Murphy (1984)), and by field experiments in sand by Bachrach and Nur (1998), S-wave velocity is almost insensitive to water saturation when the saturating fluid is composed of an air–water mixture. In opposition, P-wave velocity greatly increases when water saturation reaches 100%. Using the Biot–Gassmann theory, which will not be reviewed here (see e.g. Pride et al., 1992; Bachrach and Nur, 1998), it is possible to assess some soil properties using S-wave and P-wave velocities as a function of saturation variations. In a water–rock mixture, the slight decrease of both P and S-wave velocities, when water saturation remains lower than a certain value, which can reach 99%, may be due to density effects. When the water saturation exceeds this value, it is well-known that there is a strong increase of P-wave velocity due to a jump in the fluid frame modulus of the considered material. We think that such a mechanism can explain the observed P-wave velocity contrasts in our test site, as the transition from a partially saturated to a fully saturated layer.

In addition to the saturation jump, seismic velocities mainly depend on porosity and consolidation of the frame material, via its frame bulk and shear moduli (Murphy et al., 1993). By assuming the third layer to be water saturated, an inversion process of both S and P-wave velocity changes as a function of these three properties can be better constrained. There is no explicit form of the inversion process leading to porosity estimates of the saturated layer as a function

of velocity. We applied the well-known poro-elastic velocity model derived from the Biot–Gassmann theory (e.g. Bachrach and Nur, 1998) using the bulk modulus K and the density ρ of quartz, water and air displayed in Table 1.

If a 2% confidence estimate is assumed for these velocities, the solution space is quite restricted. We found in this case that porosity ranges from 0.23 to 0.26, frame shear modulus (G_{fr}) ranges from 0.3 to 0.31 GPa and frame bulk modulus (K_{fr}) ranges from 2 to 2.26 GPa. Unfortunately, the estimation of seismic velocities is not precise enough to constrain the saturation transition (the saturation in the second layer). Note that the porosity estimates are consistent with those predicted by GPR radar data (mean porosity of 0.25–0.26). Moreover, the access to relatively precise soil consolidation estimates can be very interesting, particularly in civil engineering or for horizontal borehole applications. The present study shows the potential of high-resolution P and S-wave reflection methods to identify properties of aquifers in a porous medium at greater depth as compared to the use of the GPR method.

4. Water conductivity estimations from combined electric and GPR data

Electrical surveys measure the distribution of electrical currents generated by an applied direct electric field and are interpreted in terms of the apparent resistivity of the ground. Electrical monitoring techniques have been used successfully for environmental purposes because of their ability to observe the change in resistivity due to migration of contaminants and/or water in the vadose zone (e.g. Greenhouse and Harris, 1983; Kean et al., 1987; Van et al., 1991).

The dipole–dipole array provides both lateral and vertical coverage of the ground. A sequence of source dipoles of length a and receiving dipoles of the same length are laid out on the ground. By varying the spacing between the dipoles, their length, and by moving the array laterally over the ground, it is possible to construct an electrical pseudo-section of the subsurface. This can be inverted to calculate a 2-D resistivity (or conductivity) model of the ground.

4.1. Conductivity law in unsaturated porous media

At low frequencies ($f < 10^3$ Hz), grain or gas phases can be considered as insulator material as compared to an electrolyte. In this case, the macroscopic conductivity of porous rocks results from two mechanisms: (i) bulk conduction which represents electromigration of the ions in the interconnected pore space, and (ii) surface conduction resulting from various conduction processes near the interface separating the pore fluid from the grains, where an electric double layer develops (Pride, 1994; Revil and Glover, 1997). This macroscopic effective conductivity σ can be expressed as (Guéguen and Palciauskas, 1992; Pride, 1994)

$$\sigma = \frac{1}{F} \left(\sigma_w + 2 \frac{\sigma_s}{\Lambda} \right). \quad (8)$$

Here F is the formation factor taking into account microscopic reduction processes associated to the tortuous way of electric charges migration in the fluid phase, σ_w represents the fluid conductivity, σ_s denotes the surface conductivity, and Λ a characteristic length of the pore space microgeometry. As the presence of clay sediments in our test site is limited, we will assume in the following that the contribution of surface conductance can be ignored. Therefore, the effective conductivity depends only on the electrolyte's conductivity and on the microstructure of the mixture, via the formation factor F .

The formation factor F characterizes the reduction in conductivity of a water volume that is caused by the presence of a non-conducting matrix and/or of an insulating second fluid phase (or gas). For clean water-saturated sands and sandstones, an expression relating the formation factor F to the effective porosity ϕ

$$F = \phi^{-m}, \quad (9)$$

was experimentally obtained by Archie (1942). The empirical exponent m can be close to 1 in the case of cracked granite, and is more typically in the range of $1.5 \leq m \leq 2.5$ for sedimentary rocks (for granular sediments, $m \leq 1.5$). This value depends strongly on the pore microgeometry, particularly on tortuosity (which changes with porosity) and on lithology. It is possible to account for the partial saturation case (air/water mixture), by considering the gas phase and rock

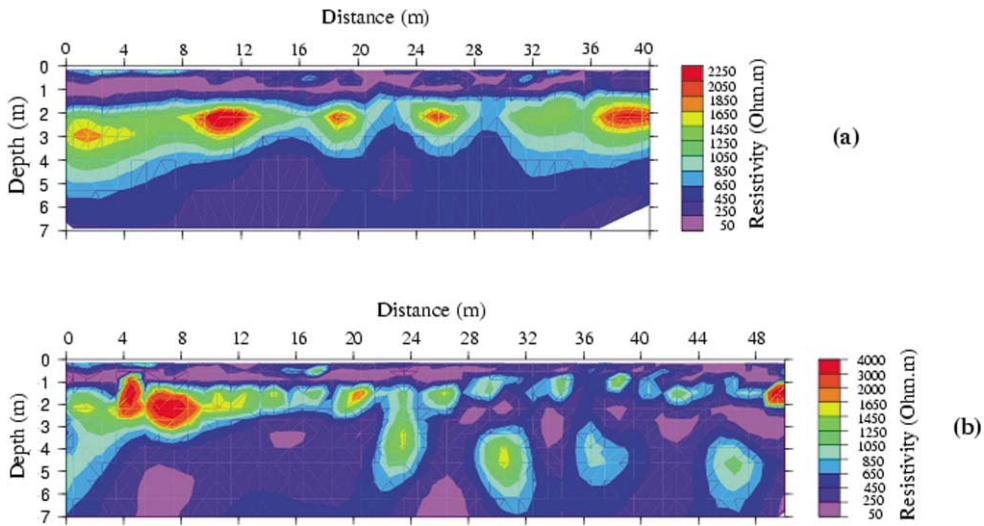


Fig. 8. 2D electrical resistivity models obtained after the inversion of apparent resistivity measurements acquired in the dipole–dipole configuration for experiments A (a) and B (b).

matrix as insulators. When surface conductance is neglected, an extension of Archie’s law (see, e.g. Waxman and Smits, 1968) leads to

$$\sigma = S_w^n \phi^m \sigma_w, \quad (10)$$

where the saturation exponent n is a function of the microgeometry of the gas/water mixture. The

efficiency of extended Archie’s law has been confirmed by many experimental studies when rocks have a low-clay content, and particularly when the fluctuations of microporosity and microsaturations are small, which is not the case for chemically unstable rocks, such as carbonates (Sen, 1997). In general, the determination of m and n can only be

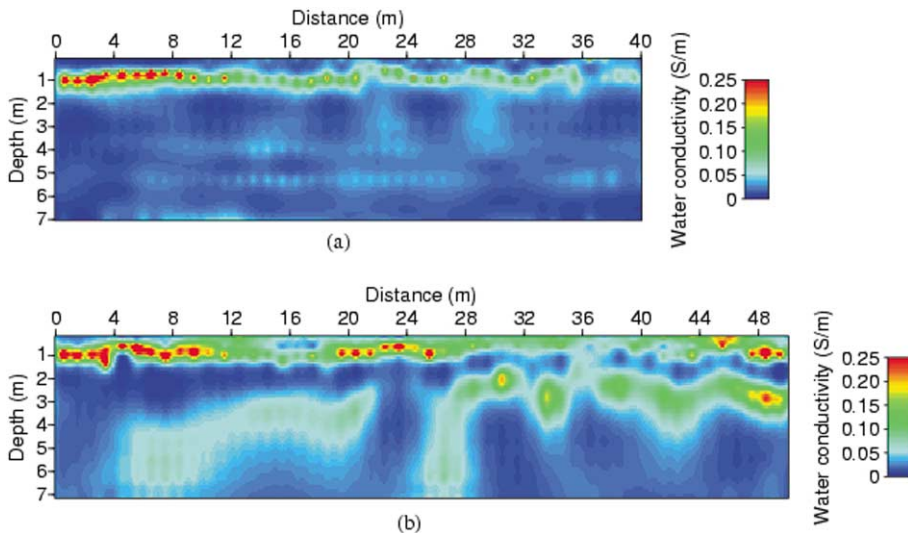


Fig. 9. 2D models of water conductivity estimates obtained by replacing the 2D electrical bulk resistivity models and the volumetric water content influence, which was estimated through multioffset GPR data in the Archie equation. The cementation exponent of the extended Archie’s law is assumed to be equal to $m = n = 2$. (a) Experiment A. (b) Experiment B.

achieved by laboratory experiments. Yaramanci and Flach (1992) obtained a good consistency between empirical predictions of rock conductivity computed using $m = n = 2$ in Eq. (10), and measurements on rock-salt samples. In practice, the values $m = n = 2$ are often adopted for various types of rocks (e.g. Edwards, 1997; Dannovski and Yaramanci, 1999).

4.2. Water conductivity model

The 2D electrical profiles, centred around the CMP radar profile in the Anglade test site (Fig. 1b), were acquired using 64 electrodes (experiment A) and 80 electrodes (experiment B) spaced every 1 m using the dipole–dipole configuration. The program RES2DINV (Loke and Barker, 1996), based on the smoothness-constrained least-squares method (deGroot-Hedlin and Constable, 1990), was used in order to invert the 622 and 1028 resistivity measurements acquired for experiments A and B, respectively. The 2D resistivity models obtained after 7 iterations with a final RMS error below 2.6%, are displayed in Fig. 8. The resistivity sections show clearly an alternation of horizontal layers with high and low resistivities. A laboratory resistivity measurement performed on the 1 m depth soil sample located at a position of $x = +3$ m along the profile during experiment B displays a resistivity of 250 Ohm m^{-1} , which presents a good consistency with the value proposed after the inversion process (Fig. 8b).

The horizontally and vertically varying resistivity and water content models (obtained from Topp equation) are combined using Archie's law (Eq. (10)). We only present the water conductivity estimates obtained from Archie's law using $m = n = 2$ for both experiments (Fig. 9), although we also computed Archie's law with different values of m and n ranging from 1 to 2.5. In fact, the absolute estimates of water conductivity were highly fluctuating as a function of m and n , which was not the case of the relative images presenting a higher stability. This fact indicated that soil moisture variations can be considered as second-order effects compare to water conductivity variations into Archie's law.

Both models show a higher water salinity intrusion near the surface, and possible salinity transfers along preferential zones at depths. Below 1.2 m depth, except in the preferential flow zones, the water

conductivity appears relatively homogeneous. These results will be interpreted more precisely in Section 5.

5. Discussion

We shall briefly discuss the water content and water conductivity distributions obtained from GPR measurements and its combination with electrical and seismic measurements, respectively.

The use of multioffset GPR data to estimate the soil water content has been shown to be reliable, and can replace extensive sample analysis.

Three to four quasi-horizontal layers can be recognized from GPR data (Fig. 5a) and three similar layers are observed in seismic refraction studies (Fig. 6). This illustrates the advantage of combining different methods which are based on different physical parameters and possess different sensitivity and resolution. In our case, it is not possible to determine if the seismic contrasts are due to mineralogy, consolidation or water content changes. Only a combined analysis of GPR and seismic results clearly identifies the water table around 4 m depth and its lateral fluctuations (which do not appear very clearly in some zones on Fig. 5a and b, using GPR only).

Nevertheless, in another test site, one can encounter some formations where the transition zone does not yield strong seismic reflected or refracted waves. In the same way, there are some regions where the identification of the transition zone is easier by GPR, because of the strong EM reflected waves.

From the high resolution GPR measurements even the capillary fringe is observed (Fig. 5a) which does not appear on seismic interpretation (the gradient in velocity appears to be too weak). There is a satisfactory consistency in quantitative water content predictions of the saturated layer when analyzing both GPR and seismic velocities using the Biot–Gassmann theory.

Finally, we would like to emphasize that GPR can monitor accurately both lateral and vertical water content variations, and that such large-scale images, if repeated over time, should help hydrologists to map and interpret water transfers and preferential flow paths in the vadose zone during infiltration, as well as water movement, both qualitatively and quantitatively. By using higher-frequency antennas, the higher

Table 2
Chemical analysis of a water table sample (ppm) in experiment B

Anions/cations	Ca ⁺⁺	Mg ⁺⁺	Na ⁺⁺	K ⁺	NH ₄ ⁺	Cl ⁻	NO ₃ ⁻	SO ₄ ⁻⁻
	81	4.5	2.8	1.4	0.15	3.5	9.9	11

resolution images of water content will provide useful applications in various domains, such as studies on the water absorption by plants, although the penetration depth will decrease.

For the water conductivity models presented on Fig. 9, the first point concerns the reliability of the quantitative values. The water sample analysis conducted in a well during experiment B indicates a water conductivity of 45 mS/m. The average water conductivity obtained using Archie's law, shows an almost constant water conductivity of 40 mS/m from 1.4 m depth. It is important to note that if we had used a value of $m = n = 1.5$, the mean constant water conductivity under 1.4 m depth would have been 8 mS/m.

It is also noticeable that the mean bulk resistivity presents strong variations between 1 to 4 m depth in both experiments, as well as the water content in this zone. After applying Archie's law, the water conductivity appears almost constant in this zone, thus emphasizing the role of soil moisture on bulk resistivity and the validity of Archie's law. It also illustrates the advantage of combining two geophysical methods. Otherwise, the resistivity increase at 2 m could have been interpreted as due to mineralogic variations. Both 2D water conductivity models (Fig. 9) display a high conductivity zone between 0.4 and 1.2 m, which varies laterally and does not show significant fluctuations as a function of time. A key question is the origin of this high concentration zone: is it due to artifacts in the proposed methodology, to natural or to anthropological causes? As discussed before, the employed methodology seems to give consistent results with sample analysis beyond 1.2–1.4 m depth. For the near-surface area, there may be two causes that could lead to errors in water conductivity estimates. Firstly, as we used 100 MHz antennas for GPR measurements, the resolution near the surface is poor and thus water content estimates in this zone only provides a mean water content from the surface to the first reflection (occurring around 1 m depth). If

there is a water infiltration process in the soil, the vertical infiltration front can modify water conductivity estimates. As this high water conductivity zone appears in both experiments, where surface conditions were extremely different, this explanation seems unsatisfactory. The most likely explanation of this higher conductivity is the presence of a higher concentration of clay in the first soil (to 1.2 m depth, as observed from sample measurements presented in Fig. 1c). This clay content can generate artifacts in water conductivity estimates, because the contribution of surface conductances to the bulk conductivity is no more negligible, and the choice of $m = n = 2$ may be less convenient, Archie's law is no longer applicable. In this case, the water conductivity estimates using Archie's law represent mainly an apparent water conductivity and no longer the intrinsic water conductivity, which will be much lower depending on the clay content of the formation, as proposed by Keller (1987). Moreover, such a surface conductance, resulting from cations adsorption (carbonates), can explain the high value of the pH measured on a 1 m depth soil sample (pH = 7.85). The adsorptive properties of these clays (composed of 58% of illite, 23% of chlorite, 11% of kaolinite and 7% of interstratified), can lead to trap salts which tend to concentrate in the root zone due to the twin processes of evaporation and transpiration, and thus participate to an increase in conductivity. The weak lateral heterogeneity observed in both experiments (Fig. 9), which is stable over time, can thus be due to heterogeneity, common in this alluvial context where fluvial streams have been observed.

We also tested another possibility, i.e. the impact of the agricultural activity. The ground water sample analysis conducted during experiment B (Table 2) showed that the concentration of nitrates, sulphates or chlorides were normal. It is also noticeable that no unusual proportion of nitrates were measured on the 1 m depth soil sample, making this hypothesis unrealistic.

Therefore, the textural formation of deposits and its fluctuations, combined with the adsorptive properties of clays, can explain the water conductivity anomalies observed in the uppermost soil layer. Moreover, such a hypothesis can explain the stability of these anomalies over more than one year.

Fig. 9 also highlights preferential flows, below a depth of 1.5 m down to the water table, which varies a lot over time. In fact, during its passage through the soil, the infiltrated water tends to dissolve additional solutes, including products of mineral and organic matter, as well as residues of fertilizers and pesticides. As they move vertically, solutes are adsorbed, taken up by plants and react among themselves. These phenomena depend on different parameters, including water transfer, temperature, acidity, which fluctuate with time. Our proposed model can be considered as a rough estimate of these transfers in the soil. Such large scale images are important for the understanding or interpreting both qualitatively and quantitatively of these transfers. They can be applied to contaminated areas, to assess the quality of aquifers used for human consumption, and/or to monitor the efficiency of eventual remediation methods with very limited drilling.

6. Conclusion

In this research, we used a multioffset GPR data set to estimate the water content of near-surface rocks over an area of 40×7 m, with a satisfactory resolution, in a fast and non-destructive manner. The obtained results are consistent both geometrically and quantitatively with those deduced from various seismic methods. The seismic methods benefited from strong reflections and refractions within the unsaturated vadose zone. We emphasize that a GPR study is easy to conduct in the field (and will now be even easier with the use of multichannel GPR systems). By repeating these measurements over time, it is possible to follow the fluctuation of aquifers and water content in response to natural and/or anthropological impacts. It can therefore be a valuable tool for hydrological purposes.

Using the obtained water content estimates, we were able to propose a solution to the problem of trade-off between bulk and water conductivities. For that we needed the additional assumption that grain

surface conductances could be neglected. As a result, we obtained an image of ionic water transfer based on electrical and multioffset GPR measurements, that permitted access to geochemical information on a large scale. This information, in turn, can be used to track natural chemical reactions and/or monitor possible ionic contaminants in situ. If the relative image can be considered as reliable, the absolute water conductivity estimates highly depend on the cementation exponents used in Archie's law, and should not be considered. This is also a consequence of the complexity of the parameters involved and of the lack of calibrating existing empirical or theoretical models with macroscopical sample data. These problems concern the sensitivity of the dielectric permittivity and the bulk conductivity to the water content and to a certain degree, to the ionic concentrations. It would be preferable in future to refine this calibration, but the overall approach used here appears very useful, especially when considering the time variation of the measured geophysical parameters.

Acknowledgements

We are grateful to S.A. al Hagrey and to an anonymous reviewer for their comments which greatly improved the manuscript. We also thank C. Doussan from INRA of Avignon, D. Cussey and R. Sabrier from Pau University for helpful discussion, A. Daudignon, B. Fasentieux and E. Landat for sample analysis, as well as all those who helped us with field experiments. S. Garambois and P. Sénéchal thank Elf Exploration Production for their financial support. The S wave experiment was made possible thanks to the help of J. Muller, from Elf Exploration Production.

References

- Archie, G.E., 1942. The electrical resistivity log as an aid in determining some reservoir characteristics. *Trans. AIME* 145, 54–62.
- Bachrach, R., Nur, A., 1998. High-resolution shallow-seismic experiments in sands, Part I: Water table, fluid flow and saturation. *Geophysics* 63, 1225–1233.
- Biot, M.A., 1956. Theory of propagation of elastic waves in fluid saturated porous solid. I low frequency range, II higher frequency range. *J. Acoust. Soc. Am.* 28, 168–191.

- Biot, M.A., 1962. Mechanics of deformation and acoustic propagation in porous media. *J. Appl. Phys.* 33, 1482–1498.
- Charlton, M., 2000. Small-scale soil-moisture variability estimated using ground penetrating radar. Proceedings of Eighth International Conference on Ground Penetrating Radar, Gold Coast, Australia, 23–26 May 2000, pp. 798–804.
- Dannovski, G., Yaramanci, U., 1999. Estimation of water content and porosity using combined radar and geoelectrical measurements. *Eur. J. Environ. Engng Geophys.* 4, 71–85.
- Davis, J.L., Annan, A.P., 1989. Ground penetrating radar for high-resolution mapping of soil and rock stratigraphy. *Geophys. Prospect.* 37, 531–552.
- deGroot-Hedlin, C., Constable, S., 1990. Occam's inversion to generate smooth, two dimensional models from magnetotelluric data. *Geophysics* 55, 1613–1624.
- Dix, C.H., 1955. Seismic velocities from surface measurements. *Geophysics* 20, 68–86.
- Domenico, S., 1974. Effect of water saturation on seismic reflectivity in sand reservoirs encased in shale. *Geophysics* 39, 759–769.
- Dvorkin, J., Nur, A., 1998. Time-average equation revisited. *Geophysics* 63, 460–464.
- Edwards, R.N., 1997. On the resource evaluation of marine gas hydrate deposits using sea-floor transient electric dipole–dipole methods. *Geophysics* 62, 63–74.
- Endres, A.L., Knight, R., 1992. A theoretical treatment of the effect of microscopic fluid distribution on the dielectric properties of partially saturated rocks. *Geophys. Prospect.* 40, 307–324.
- Fisher, E., McMechan, G.A., Annan, A.P., 1992. Acquisition and processing of wide-aperture ground-penetrating radar data. *Geophysics* 57, 495–504.
- Freedman, R., Vogiatzis, J.P., 1979. Theory of microwave dielectric constant logging, using the electromagnetic propagation method. *Geophysics* 44, 969–986.
- Gassmann, F., 1951. Über die Elastizität poröser Medien. *Vierteljahrsschr. Naturforsch. Gesellschaft, Zürich* 96, 1–23.
- Greaves, R.J., Lesmes, D.P., Lee, J., Toksöz, N.M., 1996. Velocity variations and water content estimated from multi-offset, ground-penetrating radar. *Geophysics* 61, 683–695.
- Greenhouse, J.P., Harris, R.D., 1983. Migration of contaminants in groundwater at a landfill: A case study. 7. DC, VLF, and inductive resistivity surveys. *J. Hydrol.* 63, 177–197.
- Guéguen, Y., Palciauskas, V., 1992. In: Hermann (Ed.). *Introduction à la Physique des Roches*. p. 299.
- Hagrey, S.A., Müller, C., 2000. GPR study of pore water content and salinity in sand. *Geophys. Prospect.* 48, 63–85.
- Kean, W.F., Walter, M.J., Layson, H.R., 1987. Monitoring moisture migration in the vadose zone with resistivity. *Ground Water* 25, 562–571.
- Keller, G.V., 1987. Rock and mineral properties. In: Nabighian, M.N. (Ed.). *Electromagnetic Methods in Applied Geophysics*. Series: Investigations in Geophysics 3, vol. 1. Society of Exploration Geophysics, Tulsa, Oklahoma.
- Loke, M.H., Barker, R.D., 1996. Rapid least-squares inversion of apparent resistivity pseudosections using a quasi-Newton method. *Geophys. Prospect.* 44, 131–152.
- Murphy III, W.F., 1984. Acoustic measures of partial gas saturation in tight sandstones. *J. Geophys. Res.* 89, 11549–11559.
- Murphy III, W.F., Reisher, A., Hsu, K., 1993. Modulus decomposition of compressional and shear velocities in sand bodies. *Geophysics* 58, 227–239.
- Parkiser, L.C., Black, R.A., 1957. Exploring for ancient channels with the refraction seismograph. *Geophysics* 22, 32–47.
- Pride, S.R., 1994. Governing equations for the coupled electromagnetics and acoustics of porous media. *Phys. Rev. B* 50, 15678–15696.
- Pride, S.R., Gangi, A.F., Morgan, D.F., 1992. Deriving the equations of motion for porous isotropic media. *J. Acoust. Soc. Am.* 92, 3278–3290.
- Revil, A., Glover, P.W.J., 1997. Theory of ionic surface electrical conduction in porous media. *Phys. Rev. B* 55, 1757–1773.
- Scott, J.H., 1973. Seismic refraction modeling by computer. *Geophysics* 38, 271–284.
- Sen, P.N., 1997. Resistivity of partially saturated carbonate rocks with microporosity. *Geophysics* 62, 415–425.
- Sen, P.N., Scala, C., Cohen, M.H., 1981. A self-similar model for sedimentary rocks with application to the dielectric constant of fused glass beads. *Geophysics* 46, 781–795.
- Shen, L.C., Savre, W.C., Price, J.M., Athavale, K., 1985. Dielectric properties of reservoir rocks at ultra-high frequencies. *Geophysics* 50, 692–704.
- Topp, G.C., Davis, J.L., Annan, A.P., 1980. Electromagnetic determination of soil water content: measurements in coaxial transmission lines. *Water Resour. Res.* 16, 574–582.
- Van, G.P., Park, S.K., Hamilton, O., 1991. Monitoring leaks from storage ponds using resistivity methods. *Geophysics* 56, 1267–1270.
- Van Overmeeren, R.A., Sariowan, S.V., Gehrels, J.C., 1997. Ground penetrating radar for determining volumetric water content; results of comparative measurements at two test sites. *J. Hydrol.* 197, 316–338.
- Waxman, M.H., Smits, L.J.M., 1968. Electrical conductivities in oil-bearing shaly sands. *Soc. Pet. Engng J.* 8, 107–122.
- Weiler, K.W., Steenhuis, T.S., Boll, J., Kung, K.-J.S., 1998. Comparison of ground penetrating radar and TDR as soil water sensors. *Soil Sci. Soc. Am. J.* 62, 1237–1239.
- Yaramanci, U., Flach, D., 1992. Resistivity of rock-salt in ASSE (Germany) and petrophysical aspects. *Geophys. Prospect.* 40, 85–100.
- Yilmaz, O., 1987. *Seismic Data Processing*. Society of Exploration Geophysics, Tulsa.

1.2.2. Plusieurs approches d'estimation de la teneur en eau dans une tourbière par les vitesses électromagnétiques

INTRODUCTION

Le géoradar a été utilisé à de nombreuses reprises pour la mesure du contenu en eau dans les sols. En effet, comme explicité auparavant (Garambois et al., 2002), les propriétés constitutives régissant la propagation des ondes électromagnétiques, et en particulier la permittivité diélectrique, sont directement sensibles à ce paramètre hydrologique. La permittivité diélectrique est également liée à d'autres paramètres du sous-sol, comme la porosité, la proportion d'argiles ou la salinité (Hagrey et Müller, 2000), mais de manière secondaire. En utilisant des relations calibrées à partir d'échantillons locaux ou des relations empiriques plus générales (Topp et al., 1980), il est alors possible de remonter à la teneur en eau à partir des mesures de vitesse électromagnétique. Comme le rappellent Huisman *et al.* (2003) dans un article synthétisant différentes approches, les estimations de teneur en eau peuvent être obtenues à partir de tomographies entre forage (Hubbard et al., 1997; Binley et al., 2001), d'analyses des ondes se propageant directement entre sources et récepteurs (Grote et al., 2003) ou à partir des ondes réfléchies (Van Overmeeren et al., 1997).

Pour la méthode utilisant des ondes directes, les expériences sont souvent conduites à haute fréquence (supérieures à 200 MHz), ce qui permet une séparation plus facile entre ondes directes se propageant dans l'air et celles se propageant dans le sol. L'avantage de cette méthode réside dans le fait que l'on peut utiliser les profils à offset constant qui sont acquis pour des besoins d'imagerie. Par contre, il peut s'avérer difficile de pointer le début de l'onde que l'on veut analyser, notamment lorsque les distances source-récepteur sont faibles. Avec ces méthodes, l'extension en profondeur de l'information sur la teneur en eau dépend du type de sol et de l'antenne considérée, mais reste de l'ordre de la longueur d'onde. Les analyses des ondes réfléchies acquises par Point Milieu Commun (CMP) permettent l'accès à une moyenne de la teneur en eau entre deux réflecteurs horizontaux (Van Overmeeren, 1997 ; Garambois et al., 2002) et donc à la distribution de la teneur en eau en fonction de la profondeur. Outre le problème du temps d'acquisition plus important pour des données multi-offset, il est nécessaire dans les milieux hétérogènes de convertir les vitesses NMO mesurées en vitesses d'intervalle par la formule de Dix (1955) qui peut s'avérer très instable et reste limitée aux milieux 1D. Il faut noter que des méthodes utilisant les ondes réfléchies acquises à offset constant ont été également développées depuis quelques années. Certaines supposent que le réflecteur considéré est de profondeur constante, ce qui peut être raisonnable dans le cas de milieux non naturels (bétons), et ainsi permettre l'accès aux variations latérales de teneur en eau (Grote et al., 2003) par mesure de la variation des temps réfléchis. D'autres chercheurs utilisent cette technique pour effectuer des suivis temporels en milieu naturel, le seul paramètre supposé varier étant la teneur en eau (Lunt et al., 2004). Plus récemment, Lambot et al. (2008) inversent la réflectivité de la réflexion entre l'air et la surface de sol considérée, ce qui permet de maximiser l'information et de ne pas se réduire à la seule vitesse, qui peut s'avérer dispersive dans certains milieux et difficile d'accès pour les acquisitions à offset constant.

L'étude présentée ci-après découle d'une collaboration avec l'ONF. Elle a pour objectifs de mieux comprendre le fonctionnement de l'éco-complexe tourbeux que constitue l'ensemble des

compartiments de la tourbière ombrotophe du col du Luitel (elle ne bénéficie que des apports de pluie), et de comparer les relations entre paléotopographie et carte de végétation. Nous présenterons ici quelques images GPR de la tourbière, puis nous montrerons l'intérêt des analyses par CMP, avec une estimation des barres d'erreur, pour l'estimation moyennée des teneurs en eau au sein de la tourbière gorgées d'eau. Celles-ci seront comparées quantitativement avec celles déduites de mesures par RMP (Legchenko et al., 2010). Dans un second temps, nous illustrerons la méthodologie d'utilisation des profils à offset constant pour l'estimation de la teneur en eau superficielle, en comparant ces résultats avec ceux déduits des analyses CMP et de mesures par TDR (Time Domain Reflectometry, Laurent et al., 2003).

PALEOTOPOGRAPHIE DE LA TOURBIERE

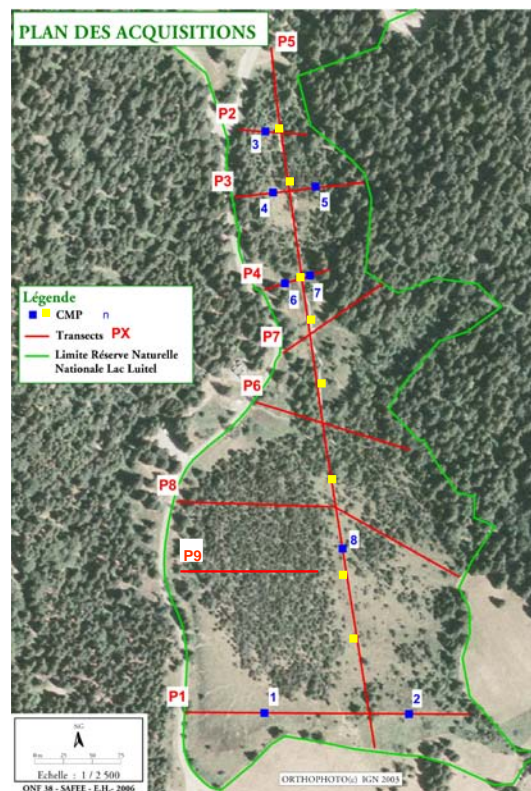


Fig. 1.2. Localisation des profils radar et des points CMP nécessaires à l'obtention des vitesses EM.

La tourbière du col Luitel, est située à 30 km à l'Est de Grenoble et fût la première réserve naturelle de France, ainsi nommée en 1961. Elle se situe dans le sud du massif de Belledonne, légèrement au Nord de Séchilienne, au niveau de l'accident médian de Belledonne. L'érosion glaciaire a façonné ces paysages et la tourbière est une relique de cet âge glaciaire qui forme le comblement d'un ancien lac, laissé par le retrait du glacier. On peut encore observer la présence de moraines sur ces bords ainsi qu'une très faible étendue d'eau, un petit lac restant non comblé à l'heure actuelle (au Nord de la figure 1.2). Cette réserve naturelle demande à être protégée des impacts anthropiques et la compréhension de la paléotopographie et de la distribution de l'eau

représentent des enjeux écologiques importants, notamment pour mieux comprendre la répartition des végétaux observés. Les premières couches sont composées du matériau tourbeux saturé, parfois d'un milieu poreux de faible épaisseur (roches altérées, moraines, dépôts fins) et du socle rocheux. Son extension relativement petite (17 ha) en fait un site test intéressant pour évaluer l'efficacité et le développement de diverses méthodes géophysiques qui s'appliquent à la première dizaine de mètres.

Des études préliminaires avaient été conduites afin de sélectionner parmi l'arsenal des méthodes géophysiques disponibles, celles les plus adéquates (pénétration, résolution) permettant l'imagerie de l'interface tourbière – socle rocheux. Les tests, qui ont inclus des méthodes de bruit de fond sismique (H/V), des méthodes sismiques actives, de tomographie électrique et de radar, ont été entrepris dans la partie Nord de la tourbière, au niveau de l'actuel profil P3 (figure 1.2). Ceux-ci ont permis de dresser les premières conclusions et de diriger les choix du projet en termes géophysiques : seuls la tomographie électrique et le géoradar ont réussi à imager correctement l'interface cherchée (Fig. 1.3). L'atténuation très importante des ondes sismiques, due à l'absence de squelette solide du milieu a rendu inopérante toute méthode sismique, quelle soit passive ou active.

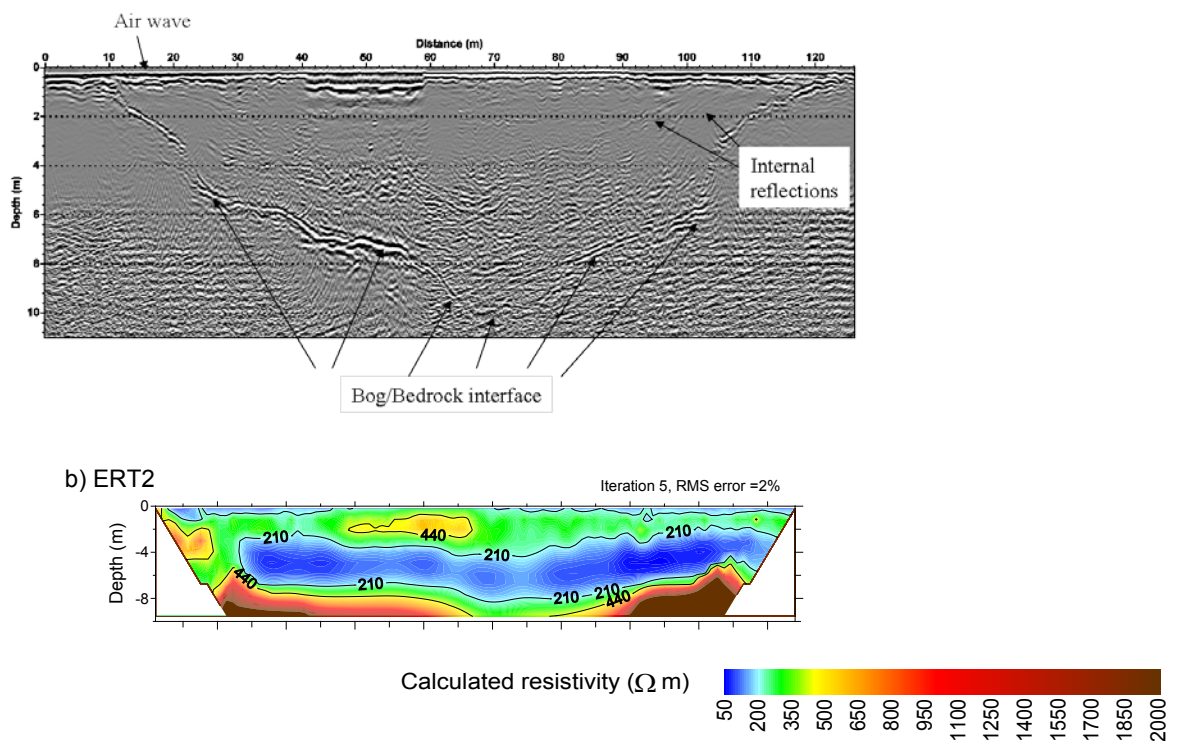


Fig. 1.3. Profil GPR obtenu le long du profil P3 avec une antenne de 100 MHz (haut) et tomographie électrique obtenue en combinant acquisitions Wenner-Schlumberger et dipôle-dipôle (bas), après inversion (Legchenko et al., 2010).

Les profils GPR ont été effectués avec un système RAMAC connecté en général à des antennes 100 MHz non blindées. Différents profils (offset de 1 m) et CMP ont été réalisés dans différentes parties de la tourbière. Le choix de la fréquence a été dicté par la pénétration désirée (10 m) tout en gardant une résolution verticale intéressante (12.5 cm pour une vitesse de 5 cm/ns). Pour

chaque image fournie, le même processus de traitement des données a été appliqué, à savoir : i) suppression de la composante continue, ii) un filtre passe-bande [10-250 MHz], iii) une analyse des vitesses CMP, iv) migration f-k à vitesse constante, v) conversion temps-profondeur et vi) une égalisation des gains dynamique (fenêtre de 400 ns). Sur l'exemple comparatif produit figure 2.2, la tomographie électrique a été acquise en considérant 95 électrodes espacées de 1 m, une acquisition dipôle-dipôle combinée à une configuration Wenner-Schlumberger, puis une inversion via le logiciel RES2DINV (Loke et Barker, 1996).

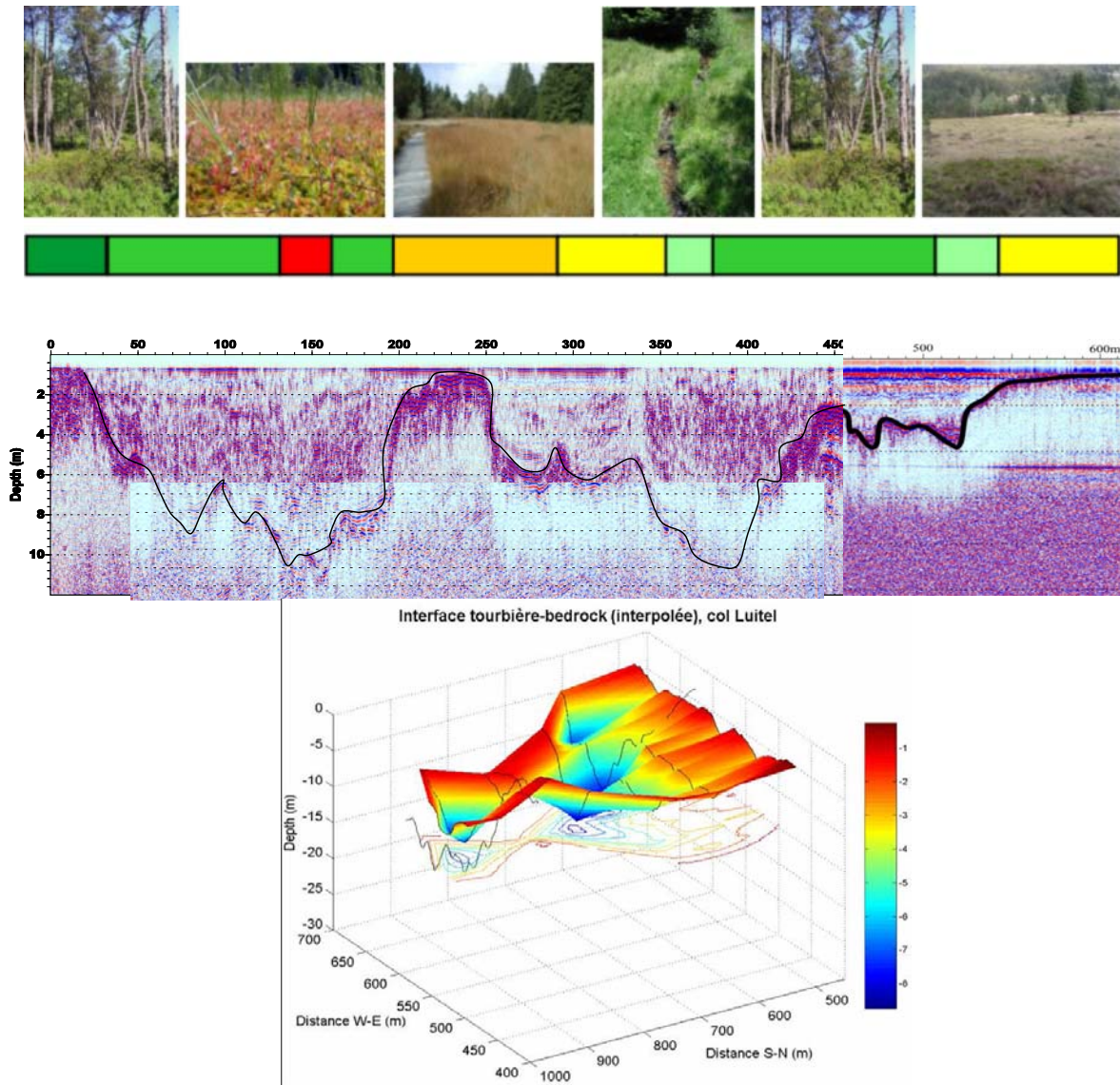


Figure 1.4. Profil GPR P8 (milieu). Carte 3D obtenue par interpolation des profondeurs de l'interface tourbière-bedrock (bas). Les lignes noires correspondent aux profils utilisés. En haut, photos des formations végétales caractéristiques des différentes zones.

Ces deux méthodes donnent des résultats similaires, que ce soit au niveau de la profondeur de la paléotopographie du socle que de la présence de deux couches distinctes au sein de la tourbière, une étant plus résistive (avec moins d'eau). Cet exemple comparatif illustre très bien l'intérêt du

GPR en terme de résolution, qui image beaucoup plus finement les contrastes abrupts, notamment lorsque les interfaces sont fortement inclinées, par rapport à la tomographie électrique, qui lisse ces contrastes. La figure 1.4 montre un second profil GPR (P5) qui traverse la tourbière du Nord au Sud, ainsi qu'une image pseudo-3D qui synthétise l'ensemble des épaisseurs de la tourbière, interpolées par les différents profils (Allègre, 2007).

On peut observer sur le profil P5 l'existence de deux cuvettes très distinctes séparées par un col et également une limite en terme de profondeur de pénétration entre les distances 350 et 400 m. Ceci est dû à une forte conductivité locale de la tourbière et/ou à une très grande épaisseur. Cette forte conductivité pourrait mettre en évidence une zone de très forte proportion d'eau (ruisseau souterrain) ou une eau de minéralisation plus forte. La carte montre un fond de la tourbière particulièrement accidenté. Elle met en évidence les deux zones très profondes pouvant atteindre 10 mètres de profondeur (au Nord et au Sud), et des zones dont le remplissage n'excède guère un mètre, notamment aux bords de tourbière et au niveau du col, qui sépare ces zones profondes. Trois vallées apparaissent dans la partie Sud, alors qu'après le passage du col, une seule vallée a été reconnue au Nord. La question de l'origine de ces vallées reste en suspens à l'heure actuelle, même si une origine glaciaire pourrait être privilégiée. Le resserrement observé au centre de la carte, au niveau du col, est sous-jacent à des moraines affleurant en surface. Ce point peut constituer un verrou glaciaire.

ANALYSES DE LA TENEUR EN EAU PAR GPR

Pour estimer la teneur en eau au sein de la tourbière, nous allons comparer deux approches, qui peuvent s'avérer complémentaires : (i) analyse des ondes réfléchies et (ii) analyse de l'onde directe dans le sol.

Pour une acquisition CMP, les antennes sont mobiles et graduellement éloignées l'une de l'autre d'une même distance, autour d'un point central. Dans ce cas, les temps de trajets augmentent donc au fur et à mesure, et correspondent à la même réflexion en profondeur. L'enregistrement de ces arrivées forme une hyperbole de réflexion que l'on va analyser pour déduire une vitesse au sein de la couche et à l'endroit considérés. L'exemple de la figure 1.5, acquis à 170 m du début du profil 5 montre très clairement les différentes ondes possibles : (i) onde directe dans l'air ; (ii) onde directe dans le sol ; (iii) réflexions internes à la tourbière et (iv) réflexion à l'interface socle-tourbière. Ces ondes réfléchies, dont la forme et l'équation hyperbolique dépendent à la fois des vitesses des ondes dans le milieu considéré, de la profondeur de la couche étudiée et de la distance source-récepteur (offset). Leur étude permet donc de remonter très précisément à la vitesse des ondes EM dans le milieu, ainsi qu'à l'épaisseur des couches considérées.

Une synthèse des résultats des études de vitesse effectuées pour l'ensemble des profils CMP acquis le long du profil P5 est fournie dans le tableau 1.1. Les techniques d'analyses des ondes réfléchies sont identiques à celles présentées dans l'article précédent (Garambois et al., 2002). Ici, le milieu étant plus homogène, l'application de la formule de Dix (1955) ne pose pas de problème. Les résultats montrent une forte variabilité des vitesses, la partie Sud semblant être légèrement moins saturée ou moins poreuse que la partie Nord montrant des vitesses plus faibles.

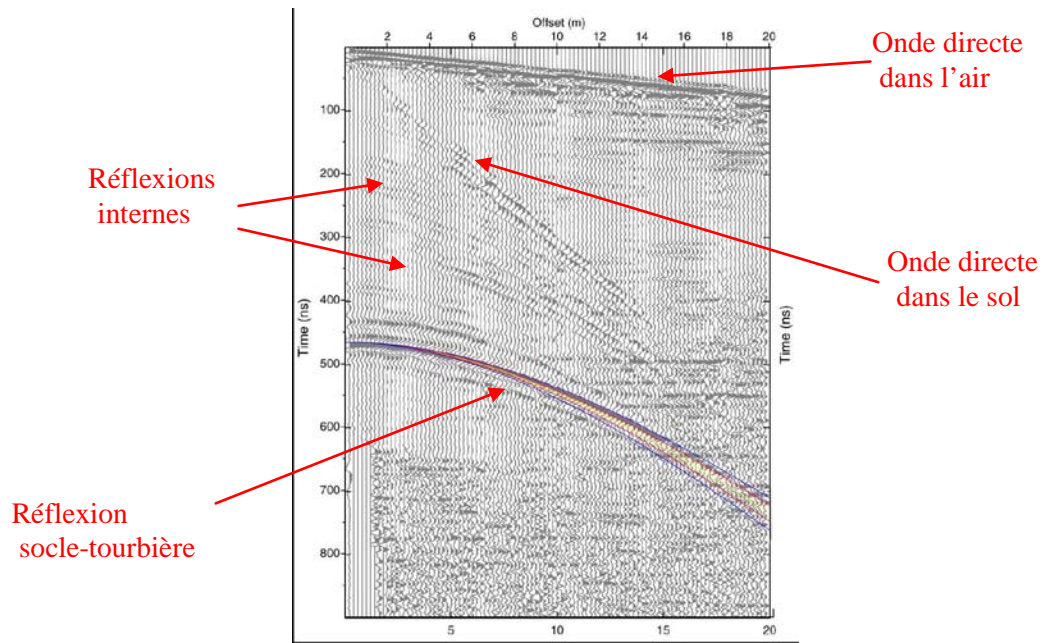


Figure 1.5. Exemple de données acquises en mode CMP. On observe les ondes directes et la forme hyperbolique des ondes réfléchies.

CMP	90m	170m	280m	330m	380m	430m	470m
v (cm/ns)	[3.3,3.7]	[3.3,3.6]	[3.25,3.65]	[3.25,3.6]	[3.45,3.85]	[3.2,3.6]	[3.5,3.75]
ϵ_r	73.47	75.61	75.61	77.85	64	69.44	69.44
	± 4.2	± 4.4	± 4.4	± 4.6	± 3.4	± 3.9	± 3.9

Tableau 1.1. Résultats déduits de l'analyse des ondes radar réfléchies acquis par CMP le long du profil P5 et erreur associée (Allègre, 2007). Les vitesses sont moyennées entre la surface et l'interface.

Si ces résultats sont intéressants, une couverture plus large d'analyse des CMP serait très coûteuse en temps, à la fois au niveau de l'acquisition que du traitement des données. Ayant effectué un grand nombre de profils à offset constant pour imager la paléotopographie du bedrock, nous proposons d'utiliser l'onde directe dans le sol pour obtenir des informations quantitatives sur la variation latérale de la teneur en eau. Le problème dans ce type d'approche est illustré figure 1.6 : comment pointer le début des temps d'arrivée de cette onde directe, qui est presque toujours confondue avec l'onde directe dans l'air ? Pour cela, nous proposons de pointer la fin du signal de l'onde directe se propageant dans le sol. Une analyse de l'onde directe déduite des CMP nous donne ponctuellement la vitesse de celle-ci ainsi que forme d'onde. Il est alors possible de déduire les temps exacts de début de l'onde sur l'ensemble du profil étudié, si l'on suppose que la variabilité des phénomènes de dispersion affectant la forme d'onde est négligeable sur un même site. Ceci revient à supposer que les variations des pointés correspondent uniquement à des variations de vitesses.

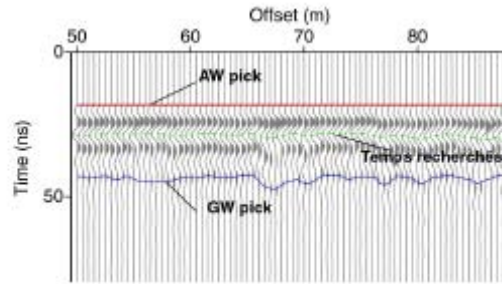


Figure 1.6. Signaux enregistrés le long du profil P5 à l'aide d'antennes 100 MHz. Les lignes rouge et bleue représentent respectivement le pointé de l'onde directe dans l'air et celui de l'onde directe dans le sol (la fin). Après correction de la vitesse en un point (par analyse CMP), il est possible de retrouver la courbe des temps de départ recherchés (verte).

Un exemple de résultat est fourni le long du profil longitudinal P5 (figure 1.7). Les résultats sont confrontés à ceux déduits d'autres analyses de l'onde directe, à la fois par CMP et par mesure TDR, qui moyenne les résultats sur les 40 premiers cm.

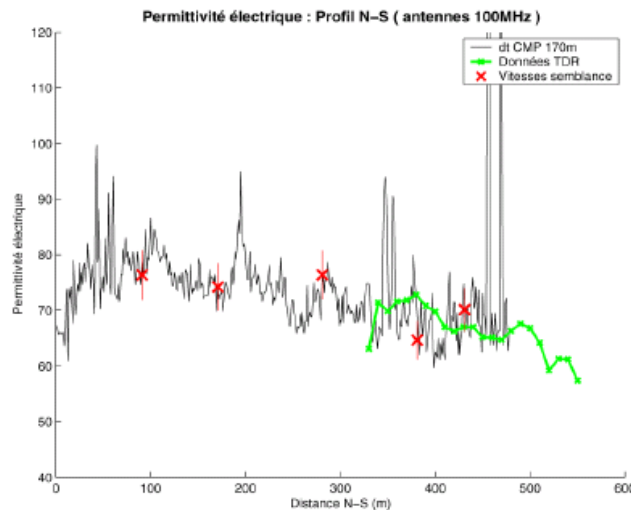


Figure 1.7. Permittivités diélectriques (courbe noire) calculées à partir des temps corrigés des premières arrivées dans le sol. Les croix rouges (avec barres d'erreur) montrent les résultats déduits des analyses CMP. La courbe verte montre les résultats des données TDR, sous-échantillonnées spatialement.

On remarque que les permittivités déterminées à partir de l'onde directe dans le sol se corrént parfaitement avec celles déduites des quatre autres CMP, et de manière satisfaisante avec les mesures de TDR, malgré des effets potentiels de dispersion. Quelques soit le CMP utilisé pour effectuer la correction des temps pointés, les résultats sont stables. On retrouve globalement une lente décroissance de la permittivité lorsque l'on se dirige vers le Sud, comme en témoignaient les analyses des vitesses, mais alors moyennées sur l'ensemble de l'épaisseur de la tourbière (table 1.1.). Ceci semble donc dû à un changement de porosité. Des variations importantes à courte longueur d'onde sont observées, sans doute correspondant à des variations importantes de la saturation et de la porosité, le milieu étant presque fluide en surface à certains endroits. Quelques points aberrants sont dus à un mauvais pointé.

CONCLUSIONS

Dans un futur très proche, il faudra généraliser l'approche utilisant l'onde directe avec des données de plus grand offset (3 m), ce qui va lisser les variations latérales, mais produira une meilleure robustesse du pointé du début des ondes directes dans le sol, alors mieux séparées de l'onde dans l'air. On peut alors s'affranchir des corrections via des CMP, et donc atténuer des problèmes liés à l'atténuation ou la dispersion des ondes, sans doute importants dans un tel milieu.

L'ensemble des résultats a été comparé à des mesures RMP effectuées a posteriori et donné lieu à un article, accepté dans *Journal of Applied Geophysics* (Legchenko et al., 2010). Les variations 2D à la fois de la topographie du socle et de la distribution en eau a donné lieu à un développement 2D pour l'inversion RMP, dont les résultats sont synthétisés figure 1.8 (centrés sur le profil P3).

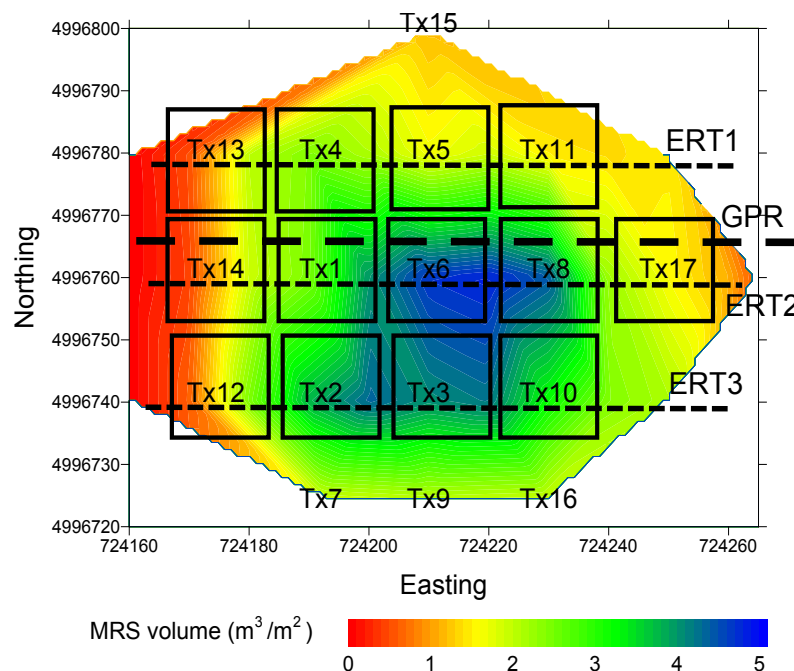


Fig. 1.8. Estimation du volume d'eau présent dans la tourbe d'après les mesures RMP.

Si le contenu en eau maximum est estimé entre 64 et 70 % dans la partie centrale de la tourbière avec les deux méthodes d'estimation (RMP et GPR), une forte différence s'observe au Nord sur les estimations RMP, qui peut être due à un effet 3D sur l'inversion RMP ou sur le processus d'estimation des teneurs en eau, la paléotopographie remontant vers la surface.

Pour conclure cette étude d'un point de vue écologique, la relation paléotopographie-teneur en eau-végétation a été étudiée par C. Desplanques (conservateur du Luitel). Pour elle, le secteur profond "porte" le groupement végétal le moins évolué en termes de dynamique végétale (dépression à Scheuchzérie des marais et lâche des bourbiers), également caractérisé par le caractère ombrotrophe (alimentation par des eaux de pluie). Les secteurs de profondeur intermédiaire (4 m de profondeur environ) portent la forêt de pins à crochets. Parmi les moins profonds, un secteur "porte" un groupement dit de dégradation de la tourbière (prairie à Molinie bleue et canche flexueuse) au niveau du col Luitel (Fig. 1.4, photos).

1.2.3. Risques liés à la présence d'eau dans les glaciers tempérés : exemple de Tête-Rousse (massif du Mont-Blanc)

Paper to be submitted to geophysics

GPR Velocity pushdown due to a large water reservoir within a temperate glacier: example of the outburst risk in the Tete-Rousses glacier (Mont-Blanc massif)

by S. Garambois, C. Vincent, M. Descloitres, A. Legchenko & E. Lemeur

A. INTRODUCTION

Outburst floods from water trapped within intraglacial cavities can lead to extreme discharge events (Haeberli, 1983, Mathews, 1963). In densely populated mountainous areas, such abrupt floods can have catastrophic consequences on life and property (Haeberli et al., 1989). Most observed outburst floods come from intraglacial cavities in Icelandic ice caps and are also referred to as jökulhlaups (Björnsson, 1998; Björnsson, 2002; Gudmundsson et al., 1997). These meltwater reservoirs result from a combination of a hydraulic pressure gradient, local topography and sometimes geothermal or hydrothermal heat (Björnsson, 1974; Nye, 1976).

The outburst flood from the Tête Rouse glacier (Mont Blanc area), France, in 1892, was however one of the deadliest disasters ever caused by glaciers (Fig. 1.9). Since that catastrophe, many surveys and costly investigations have been carried out to prevent similar disasters from occurring. However, the causes of the outlet excavation and outburst flood have until now remained unknown.

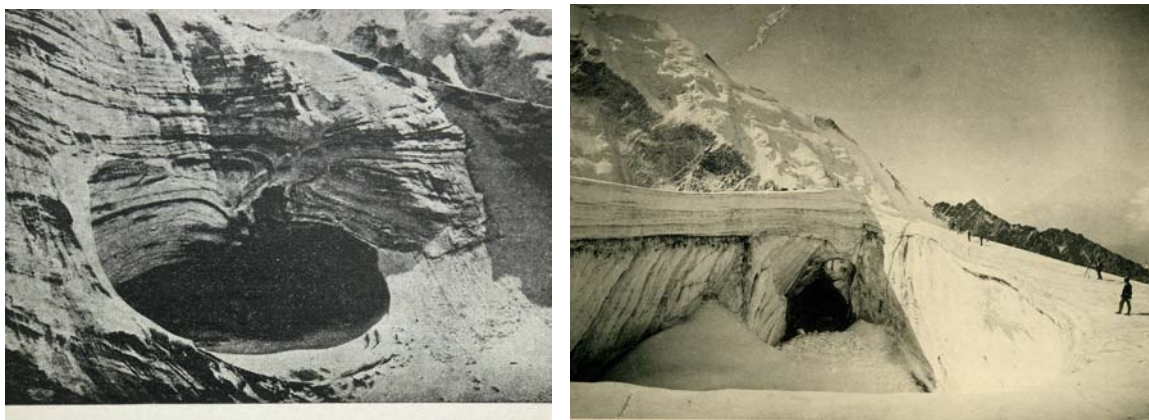


Fig. 1.9. The lower cavity at the terminus of the glacier. A part of the snout has been torn from the glacier (left). Photograph by Pelloux, September 1892. The upper cavity at the centre of the glacier (right). Photograph by Kuss, 13 August 1893.

We conducted a previous study (Vincent et al., 2010) focused on the origin of the reservoir that stored the meltwater within the Tête Rouse glacier, by (i) reviewing the historical data (ii) analysing this event from new field data, including bedrock topography deduced from GPR data

and (iii) proposing an explanation on the origin of the meltwater reservoir. All these results and observations suggested that the origin of the upper cavity was very likely a supraglacial lake and that the outburst flood hazard could be related to change in mass balance.

Originally, the preliminary GPR study was designed to image the bedrock topography and to evaluate the potential presence of an intraglacial lake. However, the first GPR images underlined large anomalies (mainly large scattering), especially in the centre and deepest part of the glacier, which prevented to follow the continuity of glacier/bedrock interface for all the surveys, despite migration was applied. The presence of these anomalies, which seems to attenuate the GPR signal, led us to imagine the presence of water at the glacier-bedrock contact. This assumption was confirmed a year later by preliminary RMP measurements. Consequently, complementary studies have been ordered by people in charge of the risk in Haute-Savoie.

B. PRELIMINARY INVESTIGATIONS

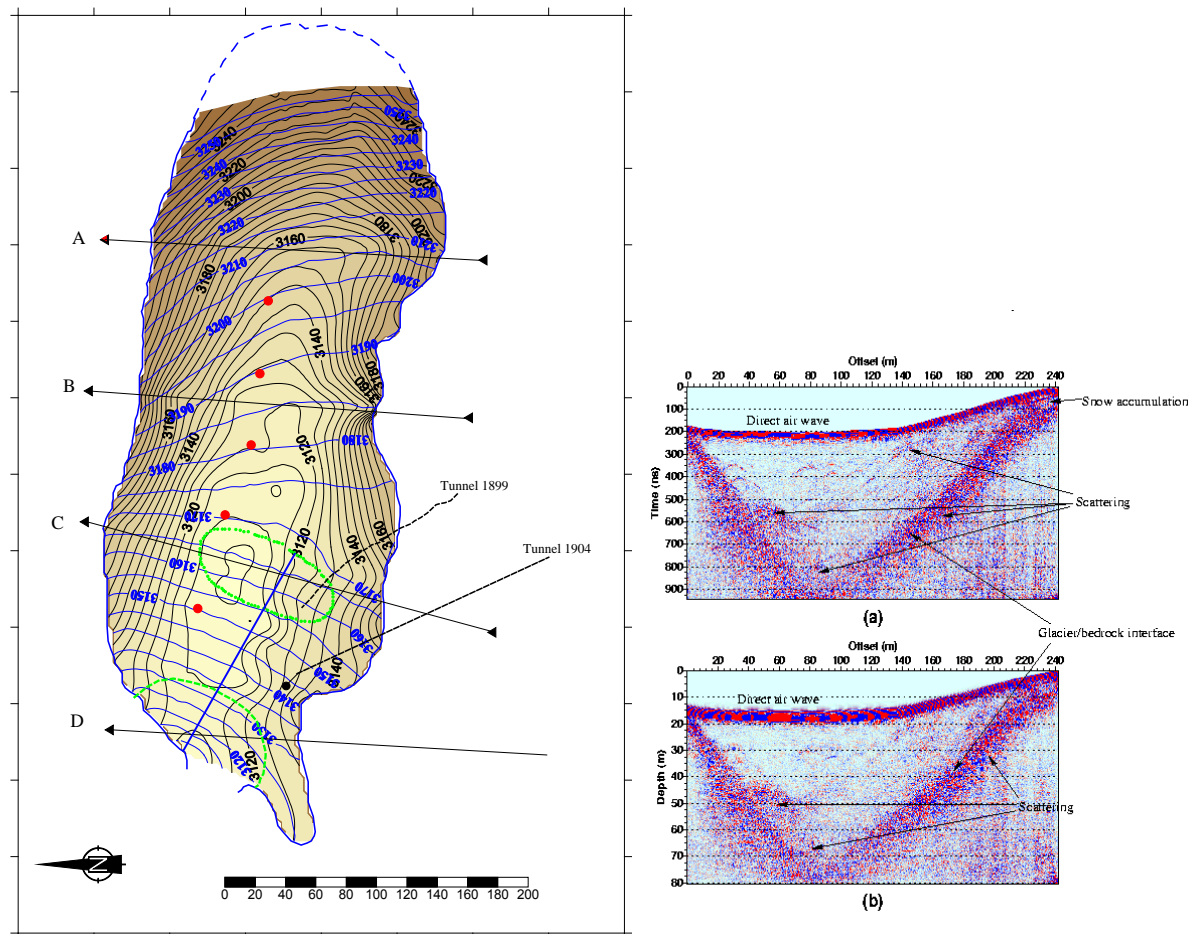


Fig. 1.10. Map of surface and bedrock topography in 2007. The locations of the upper cavity and lower cavity (green dashed line) are shown (left). On the right, North-South GPR data using 250 MHz antennas. (a) Data after elevation corrections and amplitude equalization. (b) Data derived from (a) after f-k migration and time to depth conversion (with a velocity of 175 m/ μ s).

Ground Penetrating Radar has been successfully used on temperate glaciers to map bedrock geometry (Arcone and others, 1995) or to study the distribution of water in polythermal glaciers (for example, Moran and others, 2000; Murray and others, 1997; Irvine-Flynn and others, 2006, Barrett and others, 2008). The bedrock topography of Tête Rousse glacier was first determined in 2007 using a 250 MHz shielded antenna (antenna spacing of 36 cm) connected to a RAMAC/GPR system (MALA Geosciences) along eight profiles (six were performed in the transverse direction, separated by 50 m, and two in the longitudinal direction). Figure 1.10 (right) shows a transverse N-S GPR profile obtained after static corrections and migration (bottom) performed with a 17.5 cm/ns constant velocity. It shows numerous un-clustered scatterers located within the glaciers as well as the interface between the glacier and the bedrock. Figure 1.10 (left) shows the deduced map of the surface of the glacier and of the bedrock topography, derived from GPR profiles.

The presence of the large scattering hyperbolae on the Northern side of the glacier, as well as larger anomalies marked by strong scattering hyperbolas, more or less continuous, around the deepest region of the glacier, suggested the potential presence of water within a relatively large zone. This potential presence of water was not expected and was also suggested by the presence of several reflectors on the only CMP survey available, notably between 40 and 80 m depth.

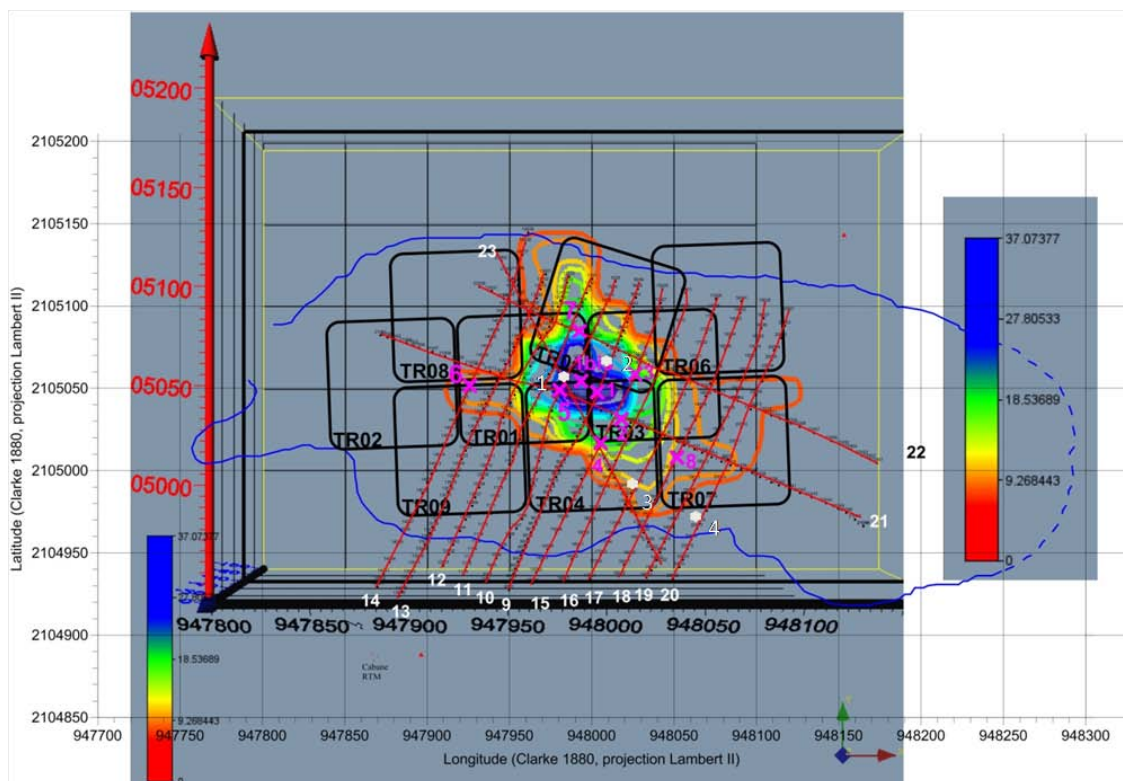


Fig. 1.11. GPR profiles (red lines), CMPs (white crosses) conducted before the interpretation of RMP measurements (black square loops). 3D RMP interpretation is superimposed and shows the percentage of water between 40 and 80 m depth.

Considering these preliminary results and RMP first measurements conducted in 2008, which also confirmed the presence of water, complementary studies have been ordered by people in charge of the risk (St-Gervais mayor and Haute-Savoie prefect).

C. THE SECOND PHASE OF INVESTIGATIONS

The supplemental GPR studies consist in denser GPR profiles (twelve transverse profiles separated each other by 15 m and two long longitudinal profiles, with 40 cm between each trace), four CMPs and supplemental RMP measurements conducted by Descloitres et Legchenko (LTHE). A map of the different profiles is provided Fig. 1.11 together with the RMP loops and associated RMP interpretation in terms of water content computed between 40 and 80 m. GPR data have been acquired using 100 MHz Rough Terrain Antennas (RTA) from MALA Geosciences, whose all in-line design provides improved performance for deeper penetration. Here, the acquisition mode is Transverse Magnetic, which differs from the more classical Transverse Electric acquisition mode in terms of reflectivity sensitivity to offset and of radiation pattern. It is acknowledged that under this mode, the electric field is more focalized under the antenna compares to TE mode and that energy strongly decrease when emission angle is greater than 30° (Deparis, 2007). In our case, this property should limit potential 3D effects and out-of-plane reflections in such heterogeneous object.

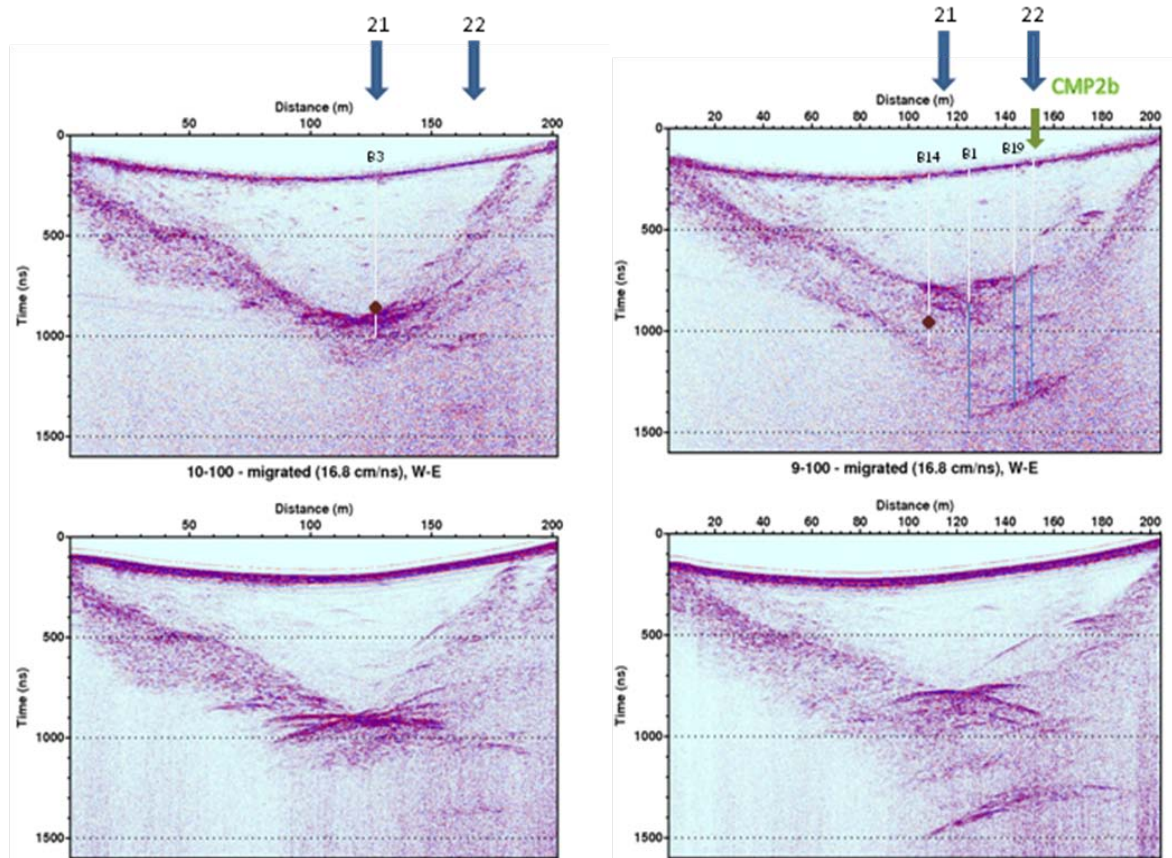


Fig. 1.12. Unmigrated (bottom) and migrated (top) South-North GPR profiles P10 & P9. The white line corresponds to the conversion of glacier thickness as deduced from boreholes into TWT considering a velocity of 17 cm/ns. The blue lines correspond to the conversion of water-filled cavity thickness as deduced from boreholes into TWT, with a adjusted velocity of 9 cm/ns. The brown diamond indicates the presence of rock debris within the glacier, as seen from boreholes. Also the CMP TWT is indicated.

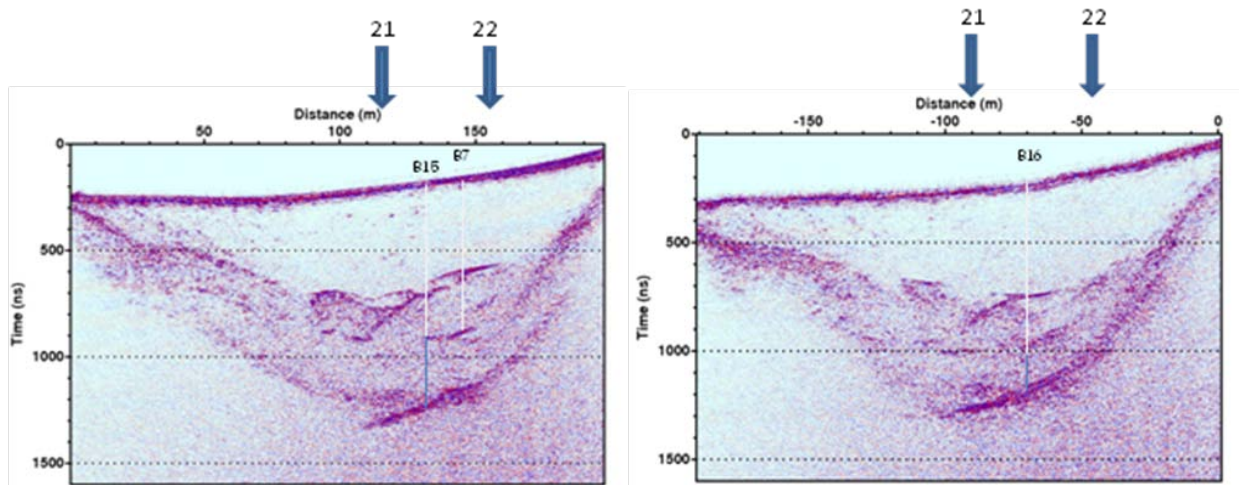


Fig. 1.13. Migrated South-North GPR profiles P15 & P16. The white line corresponds to the conversion of glacier thickness as deduced from boreholes into TWT considering a velocity of 17 cm/ns. Here, the blue line corresponds to the conversion of an estimated water-filled cavity thickness (with a velocity of 9 cm/ns) as deduced from TWT consideration as the borehole was blocked before.

The 100 MHz frequency choice of the antennas was made to increase penetration depth, a necessity due to the larger thickness of the glacier and to the potential presence of water, which will attenuate GPR signals. Vertical resolution is about 37 cm when considering glacier velocity.

A second purpose of the combined GPR and RMP study was also to propose different locations for borehole reconnaissance. Raw GPR data were processed considering i) the suppression of DC currents, ii) filtering using a [20-350 MHz] frequency pass-band, iii) static corrections with a velocity of 16.8 cm/ns, iv) amplification of late arrivals with an exponential gain and v) 2D Stolt migration with a constant velocity of 16.8 cm/ns.

Figure 1.12 shows the effect of migration on profiles P9 and P10, which appears to correctly focalize scattering energy and to re-locate dipping reflected events. Data are presented as a function of the two-way travel time, as we suspected large interval velocity changes within the glacier and problematic time to depth conversion. When comparing both migrated profiles, one can note the large difference between the two images, a very large deepening of the central part and the presence of a deep and large reflected event between 120 and 165 m on the P9 profile. Also, the continuity of the glacier-interface appears to be broken in this location. On P10, it seems to be a rather simple geometry of the glacier, with the presence of a N-S dipping reflection on the Northern side of the glacier, supposed to be generated by rock avalanches coming from the crest. Another observation is the homogeneity of the glacier on P10 and the large amount of scattered energy in the lower part of the image on P9. This vertical contrast is also present on all GPR profiles and must represent a high proportion of small water pockets or bubbles beneath this diffuse boundary.

On Figure 1.13, profiles 15 and 16 show the same features than on profile 9, but with less depth deepening. Profiles P21 and P22 displayed on figure 1.14 are more complex to interpret. Both profiles exhibit a lack of continuity in terms of the deeper reflectors, which disappear in the deepest parts where it was detected on the transverse profiles. The cause of this un-consistency between transverse and longitudinal views is still an open question, but abrupt longitudinal

changes of the rugosity of both the bedrock paleotopography and of potential cavities may cause destructive interferences within the first Fresnel zone and strongly decrease their reflectivity as well as decrease efficiency of migration process. It must also be noted that the deeper reflector observed on the transverse profiles is unfortunately almost exactly located between profiles P21 and P22 and do present weak extension under these longitudinal profiles.

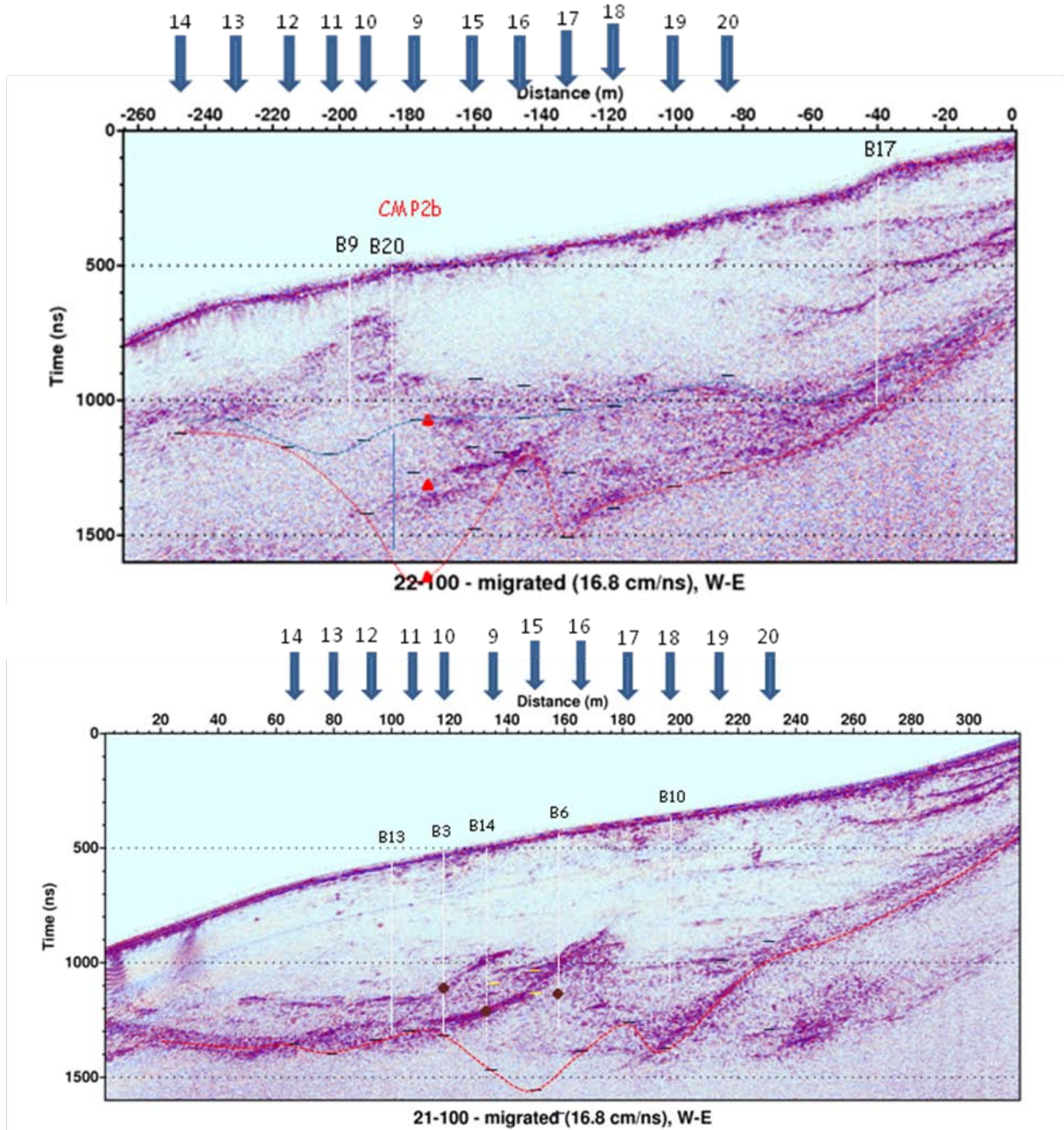


Fig. 1.14. Migrated West-East GPR longitudinal profiles P21 (bottom) & P22 (Top). The white line corresponds to the conversion of glacier thickness as deduced from boreholes into TWT considering a velocity of 17 cm/ns. Information from the “deep” reflector observed on the transverse profiles is added (black small lines). An attempt to draw the roof (blue dots curve, P22) and the bottom (red dots curve) of the cavity has been tried.

In addition to the time information coming from boreholes (following paragraph), the time pickings of the transverse profiles have been added on the images. It allowed drawing a potential interface (red lines).

CMP ANALYSIS

One of the CMP survey located at the intersection of profiles P9 and P22 (Fig. 1.11) was acquired using a Transverse Magnetic mode (TM). The data are displayed on figure 1.15, together with an hyperbola picking and a semblance analysis (right). The zero-offset arrival times of the main picked reflectors are displayed on profiles P9 and P22 (Figs. 1.12 & 1.14) and show a satisfying consistency with constant-offset reflectors.

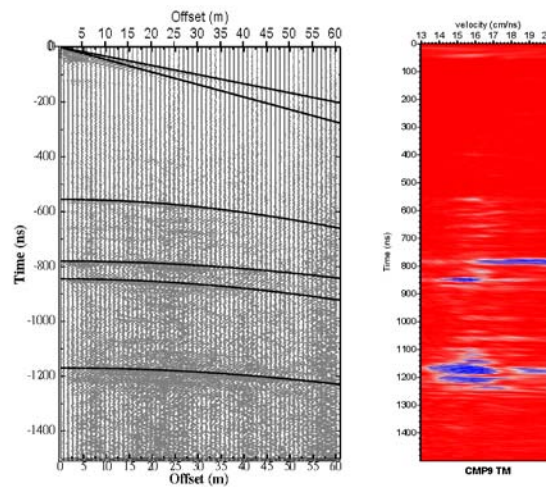


Fig. 1.15. Picked CMP data and associated semblance map.

In a qualitative way, it seems that, in this area, the glacier is rather homogeneous until 570 ns with a relatively constant velocity around 16.8 cm/ns. Below, different reflectors appear between 570 ns and 850 ns, which exhibit large NMO velocity contrasts on the semblance map (from 19 cm/ns to 15 cm/ns) over a very short time. It means that the interval velocities will present larger contrasts that Dix formula (1955) is unable to compute due to closely spaced reflectors generating instability. Anyway, these large velocity contrasts, if real, can only be explained by the presence predominance of air within the glacier until 850 ns, and by large water content between 850 ns and 1150 ns. From these CMP data, air-filled and water-filled layers seems to succeed beneath the ice body and below, water seems to predominate until the bedrock, as NMO velocity decreases to 15 cm/ns.

TRAVEL TIME ANALYSES

The complex transverse and longitudinal GPR data were interpreted thanks to the presence of boreholes, even if we already suspected that the abrupt “deepening “ of some layers observed on various transverse profiles could be due to the presence of a low-velocity body above the interface of the glacier-bedrock. Indeed, we benefited from the presence of 20 boreholes drilled within the first two weeks of July 2010 (Fig. 1.16). Some boreholes clearly

reached the bedrock and six of them discovered a water-filled cavity recognized thanks to a camera (Table 1.2). When comparing Two-Way Travel times (TWT) corresponding to glacier thicknesses derived from boreholes with GPR images, it appears that a few of boreholes were blocked before reaching the interface, due to the presence of rock debris within the glacier (B6, B7, B8, B9 & B16). In these locations, no conclusion could be derived concerning the presence of a cavity. The vertical distributions of temperature were measured at boreholes B10, B5, B2, B13, B4 and B18. They showed an abrupt temperature gradient between profiles P10 and P9: all temperatures increase to 0°C from B9 to the boreholes located Eastern.

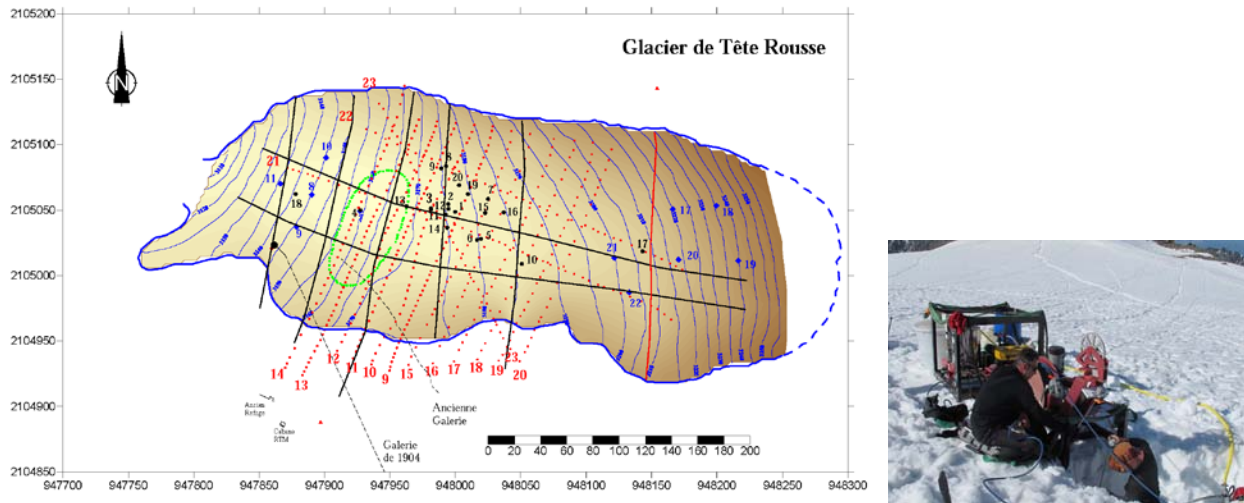


Fig. 1.16. Boreholes map (black) and permanent temperature measurements (blue). On the right, photograph of a 75-m depth borehole.

B	1	2	3	4	5	6	7	8	9	10	11	12	13	14	15	16	17	18	19	20
Cavity	51	65.5										64			61				49	53.5
Cavity thickness	25	8.5										10.2			11				29	18.7
Borehole depth	76	74	67.3	59.7	59.5	71.9	59.8	33	42	66.3	60	74.2	65	72.6	72	67.2	71	33.6	74	72.2

Table 1.2. Borehole results for glacier and cavity thicknesses. The values in red are suspected not to reflect the glacier thicknesses (compares to GPR data).

When the glacier presents a simple homogeneous geometry on GPR images, with a clear reflection at the depth, the thicknesses values of the glacier, derived from boreholes camera analyses, show a remarkable consistency with those deduced from GPR TWT. In fact, thicknesses were converted into TWT considering a constant velocity of 16.8 cm/ns (white lines on figures 1.12, 1.13 & 1.14). For the boreholes which lack consistency with GPR images, field drilling notes indicate that the drilling was blocked several times by rocks embedded within the glacier and that they certainly did not reached the bedrock.

A more interesting comparison in terms of TWT was made on boreholes which reached a water-filled cavity. The theoretical travel times displayed in white lines on GPR images represent the propagation time between the surface and the roof of the glacier, whereas the blue lines express the propagation time within the water-filled cavity. This travel time analyses appear very consistent with deep reflections on GPR images observed on transverse profiles, only when

cavity travel times were computed considering a velocity of 9 cm/ns. It means that the late arrival times related to deeper reflectors could be due to a velocity pushdown, which generated abrupt lateral and longitudinal changes in TWT. This velocity pushdown seems to be due to the presence of a large water-filled cavity, whose extension has been roughly drawn on the longitudinal profiles together with the roof of the cavity, when boreholes data permitted to achieve this goal (P22, Fig. 1.14). The consistency between cavity travel times and GPR images can only be explained assuming that water-filled cavity presents a velocity of 9 cm/ns. However, such a value does not correspond to the value expected from a 100 % water cavity (3.20 cm/ns at $T=0^{\circ}\text{C}$). It rather could represent a complex mixture of water, ice and air, whose proportions are unknown. If we assume a superimposition of air-filled and water-filled layers, application of simple time average formula of Wyllie lead to a water content of 30 %, whereas a superimposition of ice and water leads to 21 % of water. The apparent lack of consistency between this interpretation and the borehole observations, which suggest that the cavity is saturated, is still an open question. Are the camera observations concerning saturation reliable, i.e., when the hole is drilled to which extend does it modify fluid pressure? It is a consequence of the delay between GPR acquisitions (May) and boreholes measurements (July)? Does it come from the GPR acquisition which tends to homogenize information on a certain volume, due to radiation patterns? Numerical modeling of GPR propagation in such a situation should help in understanding and interpreting our data and analyses.

It must be noted that a 3D inversion of RMP data acquired on the glacier was performed by Legchenko and Descloitres and the results is shown Fig. 1.11. It reveals a body which presents an extension of 60 m in the N-S direction, 100 m in the W-E direction and localized between 25 to 85 m depth (Fig. 1.17). This body displays large variations in water content (Fig. 1.11), from a few % to 37 %, the largest water content value being consistent with GPR deduced velocities.

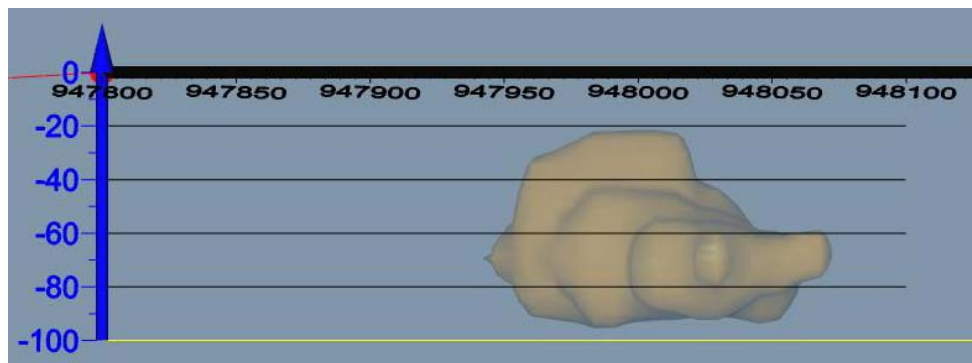


Fig. 1.17. Image of the unsaturated body deduced from the 3D RMP inversion.

CONCLUSIONS/FUTURE WORKS

The combined analysis of GPR, RMP and borehole data showed their efficiency to qualitatively located water-filled cavities within a complex temperate glacier. Estimated extension, thickness and apparent continuity of the cavity represent a large outburst risk in a highly vulnerable zone, which already experienced an outburst of 80,000 m³ of water in 1892. Only the lower part of the glacier appears cold and may act as a barrage against water-flow at present days. We anticipate that the decision of draining water out of the cavity will be urgently

made by people in charge of the risk. Besides the vulnerability problem, this glacier will represent an interesting case study permitting to monitor the cavity changes after this remediation, both with RMP and GPR data, and to work quantitatively on the differential data. Concerning GPR data, after these preliminary studies, we think that a more thorough analysis of the reflection attributes on common-offset data together with an AVO approach on CMP data should be conducted to improve the quantitative interpretation, notably to estimate the presence of the cavity roof, which is poorly imaged at this point. All the GPR analyses were limited to a constant velocity approach for migration. A careful study of NMO velocities from CMP and from scattering hyperbolae should improved the 2D NMO velocity distribution and should be introduced in a more robust migration process. Finally a 2D and then 3D numerical modeling should be made to better understand the data and the complex obtained images.

The other question of interest concerning the presence of intraglacial water is the following: how long will take water to rebuild and to fill a large cavity in the context of climatic change? Analysis of collected water samples will maybe bring responses about its age but we believe that recurrent GPR and RMP monitoring will be needed for the next few years to monitor the reformation of a water-filled cavity as well as its potential fluctuation depending on the season. Finally, we would like to stress that high-resolution seismic reflection may also be an interesting alternative to image the glacier.

1.3. Faisabilité de l'imagerie acoustique pour la caractérisation in-situ de l'injection de ciment frais dans les sols superficiels

Introduction. Cette problématique a été initiée dans le cadre d'un projet ANR « JETPHI » financé dans le cadre de l'appel d'offre « Risques Génie Civil et Urbain », et coordonné par le groupe Soletanche-Bachy. Le « jet-grouting » est un procédé de construction utilisant un jet de fluide à haute énergie cinétique pour déstructurer un terrain et le mélanger avec un coulis liquide, afin de former une inclusion en « béton de sol » dans la masse du terrain. Les caractéristiques de l'inclusion construite dans le sol (diamètre, composition, résistance mécanique) dépendent très fortement de l'interaction complexe entre les caractéristiques du terrain en place (nature, granulométrie, composition, compacité), les paramètres du traitement (vitesses de translation et de rotation des tiges, pressions et débit des fluides utilisés, dosage du coulis) et la méthode employée (jet simple, double ou triple). Il n'existe pas actuellement de moyen d'évaluer les caractéristiques de la colonne de jet pendant sa construction. Il existe donc pour les entreprises de construction un réel besoin de méthodes de caractérisation de l'inclusion, qui puissent délivrer un résultat au moment de la mise en place de la colonne, c'est-à-dire à un moment où il serait encore possible de remédier facilement à un éventuel défaut. L'objectif des travaux effectués dans ce contexte consistait à identifier et valider une méthode géophysique capable de déterminer le diamètre des colonnes de jet-grouting, si possible, pendant la phase de jet, ou au moins juste à la fin de la phase de jet. J'avais la responsabilité de cette partie et j'ai monté une collaboration entre le LGIT et le MIGP de l'université de Pau et des Pays de l'Adour qui développe des expériences acoustiques en laboratoire.

Après un tour d'horizon des différentes méthodes géophysiques disponibles, le choix s'est porté sur la sismique haute fréquence, idéalement avec un contrôle azimutal comme développé par ailleurs en forage par Valero et al. (2001). Une première série d'essais en laboratoire avec une

source émettrice existante à une fréquence de 500 kHz a été infructueuse, en raison de la trop grande absorption du signal par le matériau sol-ciment. La suite des travaux a donc consisté à construire une source capable d'émettre sur la plage 0-20 kHz, puis à caractériser la propagation des ondes dans le mélange, en fonction de son évolution dans le temps et à définir les caractéristiques optimales du système d'acquisition à utiliser in-situ. L'étude des ondes réfléchies a abouti à la détermination des configurations source-récepteur optimales pour l'enregistrement et l'analyse des ondes P réfléchies, nécessaires au calcul du rayon de la colonne de jet-grouting. Ces travaux sont l'objet d'un article présenté ci-après, accepté dans le *Journal of Applied Geophysics*. Cette étude est innovante et apporte de nouvelles connaissances susceptibles d'autres applications dans le domaine de la construction. Sur le plan du savoir-faire et des outils de mesure, le projet a permis au MIGP de mettre au point des sources sismiques adaptées au problème particulier posé par le béton de sol, et à Solétanche Bachy de construire une sonde sismique qui a trouvé ses limites dans le béton de sol, mais est susceptible de nouvelles applications en forage.

Paper accepted in *Journal of Applied Geophysics*.

Feasibility of acoustic imaging for in-situ characterization of subsurface soil injected with fresh mortar

Pascale Sénéchal^{1,2}, Stéphane Garambois¹ & Clarisse Bordes²

¹ Laboratoire de Géophysique Interne et Tectonophysique, CNRS, Université Joseph Fourier, Grenoble France

² MIGP, Université de Pau et des Pays de l'Adour, CNRS, Pau, France

Abstract.

This paper investigates the potential of acoustic imaging technologies to determine the spatial geometry of the soil-fresh mortar interface (water cement ratio > 2). The proposed study is first devoted to the characterization and monitoring of the acoustic properties of this evolving material. They were analysed in the laboratory using a specifically-designed experimental device for eight hours, in order to assess the evolution of the mixed material as a function of its maturity. The measured seismic dataset shows the very low P wave velocities and their evolution as a function of time (hardening), their large attenuation and low dispersion characteristics in the [0.5-6 kHz] frequency range. In particular, seismic attenuation remains the lowest when mortar mixture is younger than 90 minutes, which consequently constitutes the optimum time window for imagery

purposes. A comparison between the measured properties and existing theoretical models shows that the material can be considered as a fluid mixture with solid particles in suspension, which exhibits poorly compressible elastic behaviour during the first eight hours. In a second part, numerical seismograms are generated to assess the reflected P wave properties as a function of offset for a mortar/soil interface. Such study permitted to establish the optimum source-receiver configuration, which results from a compromise between acquiring large amplitudes for signal to noise ratio issues (reflectivity, attenuation), while to correctly analyse the P wave velocity using the hyperbola of the reflected wave. A correct assessment of the in-situ velocity, which depends on both the mixture characteristics (i.e. the soil conditions) and the mortar maturity, is a necessary step towards a correct 2D image of the interface.

Keywords: fresh mortar, elastic properties, acoustic imaging, monitoring

1. Introduction

Numerous civil engineering problems are solved by injection of mortar at depth in the ground. Quality control, which would allow assessing the compliance and effectiveness of the work done, is hardly approachable because of a lack of adapted imaging techniques. These techniques should be able to characterize the mortar and to image the interface between the mortar and the soil surrounding the zone where mortar was injected. Besides quality control, such imaging techniques could also allow, in certain cases, mortar injection properties such as direction, depth, volume and/or pressure to be adjusted, ideally in a lively manner. Consequently, it is necessary to develop imaging techniques which are efficient in fresh mortar and which present interesting resolution properties. Although electrical resistivity methods could be a potential techniques in surface and/or boreholes configurations, they provide too low resolution images mainly due to smoothing effects. Among the potential high-resolution geophysical methods, Ground Penetrating Radar cannot image the interface, due to the high electrical conductivity of the mortar mixture, which induces large attenuation of electromagnetic waves. In-situ imaging probes were developed by Valero et al. (2001) and Arroyo et al. (2006) for acoustic reflection techniques (see Figure 1).

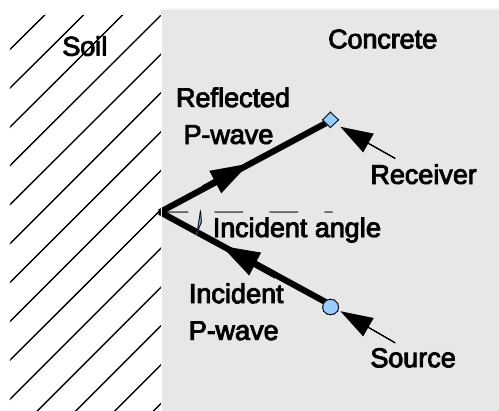


Figure 1: Schematic side view of the waited design needed for imagery of the interface between in-situ soil and mortar mixture.

Evaluation of its feasibility first requires a better assessment of the seismic properties of the fresh mortar mixture, and their time-dependence. Indeed, the progression of mortar from the initial fluid mixture into a consolidated medium induces large variations in physical properties of the mortar.

Numerous studies concerning the mechanical properties of cement-based materials were performed using elastic wave propagation (l'Hermite, 1955; van der Winden, 1990; Niyogi et al., 1990; Keating et al., 1989; Boutin and Arnaud, 1995; Arnaud and Thinet, 2003). All concluded that P wave velocity increases with the solidification state of mortar. Jonas (1991), Sayers and Dahlin (1993) and Reinhardt and Grosse (1996) showed that the amplitude and frequency content of the seismic signals depend on the age of the mortar. They exhibit low frequency content with high attenuation shortly after mixing, and broadband frequencies with strong increase of amplitude as age of the mortar increases. RILEM report 31 (2005) discusses the applicability of wave reflection methods to monitor the setting and the hardening of cement-based materials. In these studies, the cement-based materials present a water-cement ratio lower than 1 ($W/C < 1$). As they were developed essentially to evaluate directly the low-scale cement-based material quality and strengthening for civil engineering purposes, the methods were tested considering ultrasonic frequencies, which will hardly be useful in attenuating media when a larger scale is required. Only the vibroscope device (Arnaud and Thinet, 2003) considered lower frequencies, but for materials presenting a W/C ratio lower than 1. Here, we concentrate on infrequently studied mortar with a water-cement ratio larger than 2. It is a mixture of cement, water and soil surrounding the zone where mortar is injected, i.e. saturated or unsaturated sedimentary deposits.

The mortar was analysed in the laboratory for its seismic properties. Its composition was chosen to be representative of the mortar encountered in real conditions: a mixture of sands containing various gradings, cement and water. There are no additives in the mixture. As air bubbles were trapped during the mixing, the obtained mixture

can be considered a fluid with a suspension of solid particles and air bubbles. During the hardening of mortar, the chemical reactions between cement and water produce the appearance and development of hydrates, which increase the solid concentration, while decreasing fluid concentration. Progressively, the solid skeleton grows in the surrounding fluid and the material hardens. The duration of the process varies according to the initial mixture composition, temperature and the heat transfer conditions (Boumiz, 1995). Neuville (1995) distinguished two periods: i) the setting period, which refers to the change from a fluid to a solid state and ii) the hardening period, which corresponds to the strength increase of the mortar. The proposed study was focused on the setting period, the eight hours after injection. A laboratory measurement device, specifically designed for seismic wave propagation recording, was used to monitor acoustic waves during the setting of mortar. It allows mechanical characteristics to be determined from seismic wave properties (velocity, attenuation, dispersion, useful frequency content) and compared with existing empirical/theoretical mixture models.

In a second part, the derived properties of the mixture were used as input for a numerical study concerning the properties of a P wave reflection occurring at an interface separating the mortar mixture with soil. It enabled us to assess the optimum source-receiver configuration acquisition. The latter results from a compromise between the necessity to acquire large amplitudes for signal to noise ratio issues, while allowing a satisfying analysis of P wave velocity, a process which implies to get large offsets. The correct assessment of in-situ velocity, which depends on both the mixture characteristics and on the mortar maturity, is a necessary step towards a correct 2D image of the interface, and notably for the different processing which must be applied to the data, as time to depth conversions, stacking and migration.

2. Experimental device and data acquisition

The studied mortar was obtained by mixing sands of 0-4 mm grading range with cement CEM III/C 32.5 and water, in proportions which cannot be

announced for confidentiality reasons. The granulometric properties of sand, combined with the introduction of fine sand texture, allows a stable and homogeneous suspension to be obtained after mixing. It takes about 10 minutes to prepare the mixture. In the following experiments, the time zero corresponds to the instant of the introduction of water in cement. It must be noted that air bubbles were trapped during the mixing process. This stable suspension mixing has a volumetric mass of 1800 kg/m^3 and a water-cement ratio (W/C) larger than 2. The laboratory device was specifically designed to overcome difficulties associated with the fluidity of the mortar, mainly by sealing source and receivers and locating receivers within the mortar. The optimum frequency range results from a compromise between desired resolution, signal attenuation and minimization of scattering disturbances on aggregates. Preliminary tests using ultrasounds (around 500 kHz) showed large wave attenuation for a distance greater than 5 cm, which unfortunately condemns the use of this technology, despite its high resolution power. Indeed, the scale of applications that are envisaged implied that reflected waves must be recorded for greater distances than two meters of propagation for imaging of soil-mortar interface. Lower frequency tests were conducted using an acoustic source which generates signals reaching 20 kHz recorded using [0.001-17 kHz] accelerometers. They showed that wave propagation in mortar is largely attenuated, a property which shifts the measured signal's spectra towards low frequencies (a few kHz). Considering these preliminary results, the experimental device was constituted by the following elements (Figure 2):

- the acoustic source : a pendulum constituting of a stainless steel ball (diameter = 6 mm) attached to a nylon thread which is fixed to the frame (Figure. 2). The ball hits a granite cylinder which is in contact with the mortar. An accelerometer placed on the granite cylinder records the source time function. An optic sensor detects the path of the nylon thread and triggers the record. The obtained broad-band spectrum lies in the [0.005 - 20 kHz] frequency range. It is possible to change the stainless steel ball fall height, which allows control of the level of acceleration at the granite cylinder. Using this

configuration, the motion of the cylinder after the ball impact is in the direction of the main cylinder axis.

- the receivers: they should be suitable both for attenuating materials and frequencies below 10 kHz. Single component piezoelectric accelerometers (4513 B-002 from Brüel & Kjaer) were used in combination with built-in preamplifiers. They exhibited a flat response in the [1 Hz – 10 kHz] frequency range, a satisfying sensitivity of 500 mV/g and a measuring threshold of 10 g. Their characteristics make them particularly adaptable to measurements in attenuating materials.

- the recorder: dynamic signal acquisition modules PXI-4498 from National Instruments with 16 simultaneous 24-bit analog inputs per module were used.

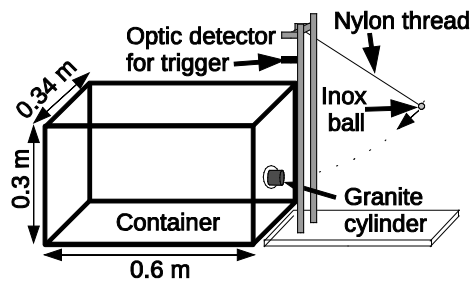


Figure 2: Acquisition device.

For the experiments presented here, fresh mortar was poured at ambient temperature (20° C) into a 0.60 m long, 0.28 m wide and 0.30 m high container. The bottom and lateral edges were covered with acoustic foam to attenuate refracted and reflected waves. A line of accelerometers was embedded in the fresh mortar just after mixing, while the mortar is still a fluid mixture. The accelerometers remained in the mortar for the whole experiment. At the beginning, the coupling between the mortar and the accelerometers was satisfying. Accelerometers were fixed on the rods, which are in turn mounted on a gantry. They were aligned with the axis of the granite cylinder and oriented in the same direction to obtain a null angle of incidence for the direct wave (Figure 3).

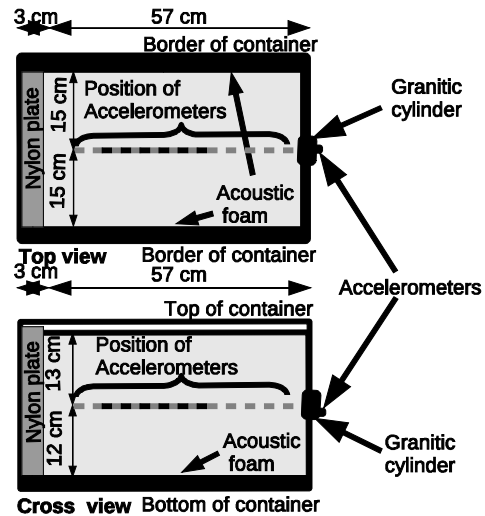


Figure 3: Top and Cross views of acquisition configurations. Black and grey lines respectively correspond to the position of accelerometers for configurations 1 and 2.

Two acquisition configurations were used: (1) using 10 accelerometers spaced every 2.5 cm from 20 cm to 42.5 cm from the source (offset) and (2) using accelerometers spaced every 1.25 cm with offsets ranging from 2 cm to 50.75 cm (four separate records were necessary). The system was designed to measure direct and reflected P-waves at null and low incidence angles (reflection is generated by the presence of a nylon plate located on the opposite side -Figure 3-). Data were acquired using configuration 1 from thirty minutes to eight hours after mixing. Shots were performed at 15 minute intervals, and were recorded to monitor seismic properties as a function of mixture hardening. A second and independent data acquisition was undertaken using configuration 2 during the first hour after mixing only.

3. Characterization of P-wave propagation

from direct wave:

The purpose is to characterize and monitor direct P-wave propagation properties within the fresh mortar (velocity, frequency and attenuation) during the first eight hours after mixing.

Figure 4 compares the source acceleration waveform recorded using the accelerometer placed on the granite cylinder (a) with the three

seismic traces acquired using configuration 1 which were recorded 30 minutes after the mixing for offsets of 20 cm (light grey line), 32.5 cm

(grey line) and 42.5 cm (black line) (b). The associated source and receiver amplitude spectra are shown on Figures 4c and 4d, respectively.

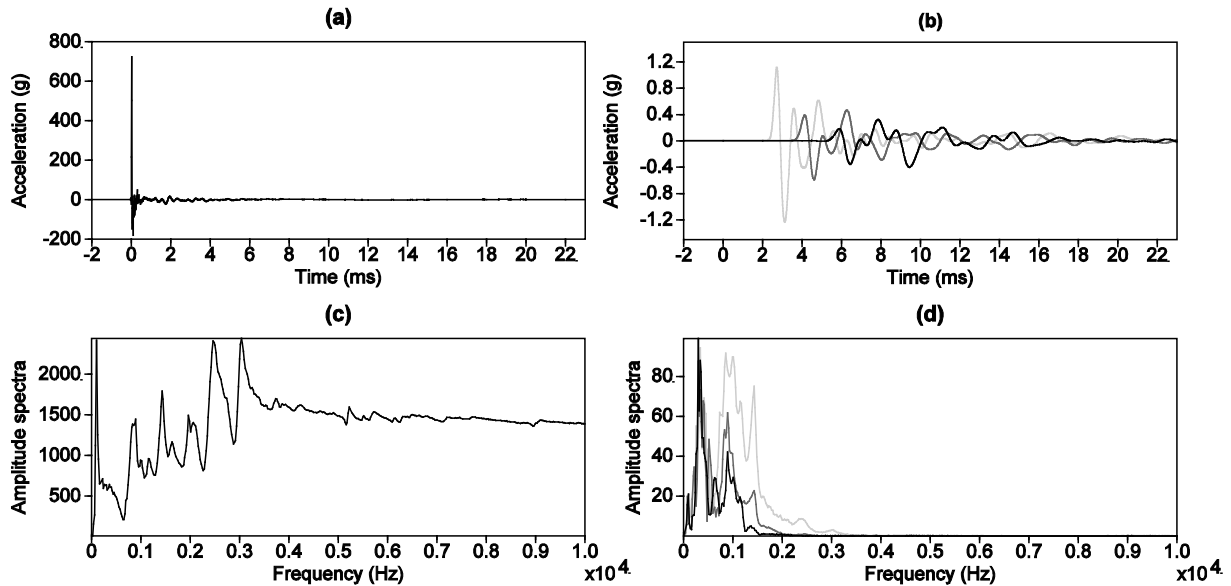


Figure 4: (a) source waveform and (c) the corresponding amplitude spectrum. (b) Seismic traces recorded 30 minutes after mixing for offsets of 20 cm (light grey line), 32.5 cm (grey line) and 42.5 cm (black line) and (d) the corresponding receiver amplitude spectra.

Figure 4 clearly shows the very high attenuation of seismic waves when comparing the acceleration recorded at the source and those recorded within the fresh mortar (at different offsets). Despite a source amplitude spectrum reaching 20 kHz, the obtained signals exhibit a low range of frequencies [0-4 kHz], showing that the fresh mortar acts as a low-pass frequency filter. One can also observe the attenuation effect within the mortar when comparing the three traces recorded at different offsets. The variation of time recording (from 30 to 525 min) does not induce any change in receiver amplitude spectrum. The full waveforms appear complex, highlighting a large number of seismic events, despite the presence of the attenuating acoustic loams.

3.1. Velocity analysis

Figures 5a and 5b show the evolution of a single seismic trace (offset of 20 cm and 40 cm, respectively) as a function of the setting duration

for the mortar (from 30 to 525 minutes after initial mixing).

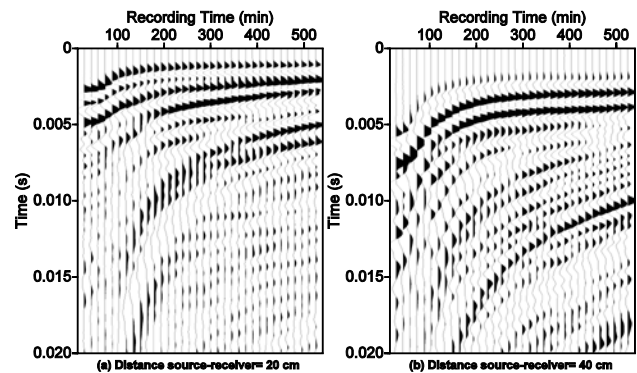


Figure 5: Evolution of the seismic data acquired for offsets of 20 cm (a) and 40 cm (b) at different times ranging from 30 to 525 minutes. The traces are normalized in amplitude.

The propagation times of the first arrivals show clear variations depending on the recording time,

the longer propagation times being observed during the first hour after mixing. The corresponding picked velocities (Figure 6a) range from 86 m/s to 287 m/s. The associated uncertainties on the velocities were computed from uncertainties linked to the propagation distance (± 0.5 cm) and the picking time ($\pm 2.10^{-5}$ s).

As the receptacle was covered by acoustic foams, only the free surface can generate waves which may interfere with direct waves. To verify if the picked events correspond to direct arrivals, simple analytical computations of the expected refracted arrival times can be easily made. This study shows that the refracted waves at the free surface can only reach receivers before direct waves when mortar velocities are lower than 150 m/s. Such case can occur only when offsets are larger than

30 cm (if $V=80$ m/s) or larger than 45 cm (if $V=150$ m/s). However, for real data, the first arrivals recorded soon after mixing ($T=60$ min) form a single slope for direct waves at all offsets (Figure 6b), which corresponds to a velocity of 90 m/s. The low reflection coefficient between air and fresh mortar (≈ 0.4) and the large attenuation of the signal can explain the absence of refracted waves. For all these reasons, it seems reasonable to assume that picked events are related to direct waves. The analytical modeling of the arrival times of the different waves observed shows that the second arrival, which clearly appears between 0.004 s and 0.006 s, corresponds to the reflected wave on the free surface. Also, the reflected wave observed between 8 and 12 ms is related to the reflection of the direct wave on the nylon plate.

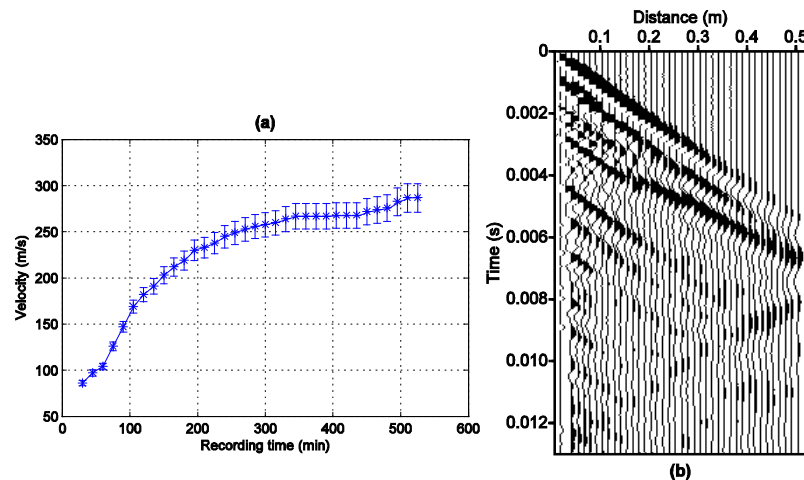


Figure 6: (a) First arrival velocities values obtained after time picking with their uncertainty. (b) Data obtained for a recording time of 60 min in configuration 2.

The low measured velocity values can be explained by the presence of air bubbles trapped during mixing process and by the large porosity of fresh mortar, which resembles a fluid suspension. Indeed, acoustic P-wave velocity is strongly dependent on porosity and water saturation, as the fluid's bulk modulus and density in equations by Gassmann (1951) and Biot (1956, 1962) depend on water saturation. As verified by Bachrach and Nur, (1998) and Bachrach et al (2000) on field experiments in sands, P-wave velocity greatly increases when water saturation exceeds a value of about 90-95 %. It was also used by Garambois et al. (2002) to estimate water content from seismic velocities in soils. Below

this range of saturation values, acoustic velocity is less sensitive to water saturation. Porosity also influences the acoustic velocities, as shown by Nur et al (1998), who introduced the notion of critical porosity. This value separates the mechanical and acoustic behaviours into two domains: (1) for low porosities, mineral grains are load-bearing and both bulk and shear modulus decrease quickly from the mineral values (at zero porosity) to the suspension values (at the critical porosity); (2) for large porosities, absence of contact between grains indicates that the fluid phase is load-bearing and that elastic properties are those of a fluid. In the context of our study, velocity variations as a function of hardening

from 86 m/s to 287 m/s, can be explained by the increasing development of hydrates in the mortar, and consequently of grains in contact. In term of image resolution, the most suitable configuration will be at earlier times, when velocity exhibits lower values (wavelength of 8 cm when $V=80$ m/s and $f \approx 1$ kHz).

Shortly after mixing, the fresh mortar can be considered as a fluid mixture, where heterogeneities are small compared to the wavelength. In this context, Wood's formula (1955), often applied for three-phase problems, was used to analyse measured velocities:

$$(1) V_P = \sqrt{\frac{K_R}{\rho}}$$

where V_P is the P-wave velocity and K_R denotes the Reuss average bulk modulus of the mixture given by:

$$(2) \frac{1}{K_R} = \sum_{i=1}^N \frac{f_i}{K_i}$$

and ρ denotes the average density, defined by

$$(3) \rho = \sum_{i=1}^N f_i \rho_i$$

In these relations, f_i , K_i and ρ_i denote the volume fractions, bulk moduli and densities of the different phases. In our study, the mortar properties can be estimated: $K_{\text{quartz}}=37$ GPa with $\rho_{\text{quartz}}=2.65$ g/cm³, $K_{\text{water}}=2.2$ GPa with $\rho_{\text{water}}=1.0$ g/cm³ and $K_{\text{air}}=0.00012$ GPa with $\rho_{\text{air}}=0.0012$ g/cm³. Density of cement was measured to $\rho_{\text{cement}}=2.95$ g/cm³. The exact bulk modulus of cement grain, K_{cement} is unknown and very difficult to obtain from the literature. Various tests conducted on K_{cement} values in Wood's formula show that K_R and V_P do not significantly change when air bubbles are present in the mixture. For example, with a K_{cement} value of 1.5 GPa or 40 GPa, K_R and V_P variations are lower than 0.4 % for a air fraction of 0.1 %.

Figure 7 shows the application of Wood's formula using $K_{\text{cement}}= 1.5$ Gpa and illustrates the sensitivity of velocity as a function of air fraction. It shows that the measured velocity range recorded at early times [86-100 m/s] can be explained if the volume fraction of air is in the vicinity of 1%. This value is consistent with the

hypothesis of Arnaud and Thinet (2003), who considered that air bubbles trapped during the mixing represent a volume concentration between 1% and 3%.

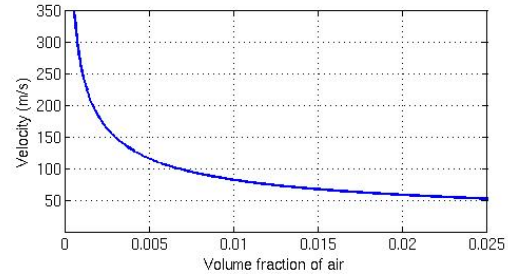


Figure 7: Velocity as a function of volume fraction of air using Wood's formula.

For an air volume fraction of 1 %, application of Wood's formula leads to: $K_R=0.012$ GPa, $\rho=1.78$ g/cm³ and $V_P=82$ m/s. This velocity is consistent with the measured velocity (86 m/s) obtained for mortar exhibiting a measured density of 1.8 g/cm³ just after mixing. The presence of air bubbles in the mortar considerably reduces the value of K_R compared to the value obtained without air bubbles ($K_R=3.39$ GPa with $K_{\text{cement}}= 1.5$ Gpa or $K_R=4$ GPa with $K_{\text{cement}}= 40$ GPa). These results indicate that mortar can be considered as a fluid suspension for early recording times.

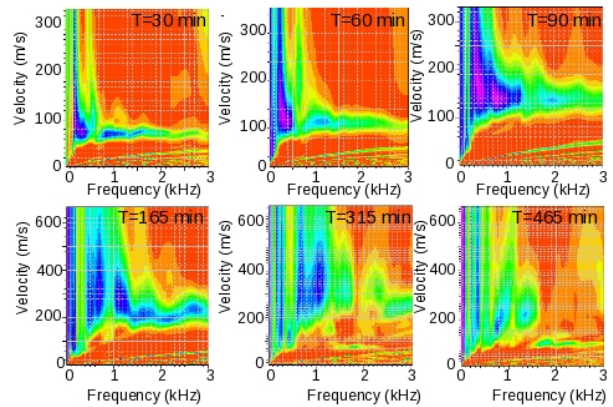


Figure 8: Semblance maps of phase velocity depending to frequency from raw data recorded with configuration 1 at various time recording (T). Maximum of semblance is in blue color and minimum of semblance in red color.

In order to gauge the sensitivity of velocity with frequency (dispersion), a classical frequency-wavenumber (f-k) approach was used, consisting

of semblance maps of phase velocity with frequency.

Figure 8 shows the semblance maps computed using GEOPSY software (Wathelet et al., 2004) obtained for various recording times. The low resolution obtained at low frequency can be due to the length in time of window used for the f-k analyses. Indeed, when the time increases, the wavelength grows and at low frequencies, few periods are used for the f-k analyses. These parameters induce a decrease of resolution of the dispersion diagram. They show that before 300 minutes, no dispersion phenomena can be detected. After 300 minutes, an energy splitting appears, marked by the appearance of a second lower velocity mode, which increases until 525 minutes. After 300 minutes, an energy splitting appears, marked by the appearance of a second lower velocity mode, which increases until 525 minutes. This second mode is also significant on Figure 5 which shows the presence of new propagation waves after 120 minutes. Its apparent velocity significantly increases with time. It could be related to S to P conversion at the free

surface and/or to surface waves, as it appears only after a certain hardening time due to hydrates development. This time transition reflects a mixture behaviour transition over time, going from a fluid mixture to a consolidated medium behaviour.

3.2. Amplitude analyses

Thanks to the absence of interferences between direct and refracted waves (§ 3.1), amplitude analyses can be possible and performed according to variations of (1) the hardening time of mortar for a given propagation distance at null incidence angle and (2) the propagation distance for a given recording time. In addition to mortar characterization, amplitude studies are important for evaluating the conditions (offsets, hardening time) suitable for seismic reflection imaging (in term of signal to noise ratio). Considering that the source time function is reproducible, maximum amplitudes of first arrivals were picked for all receivers and recording times for both configurations 1 and 2.

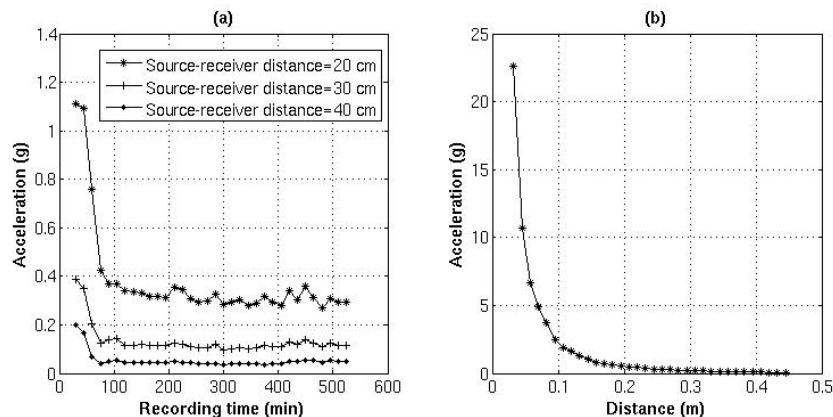


Figure 9: Variation of maximum amplitude (acceleration) with (a) the recording time (configuration 1) and with (b) the source-receiver distance at recording time of 60 minutes (configuration 2).

Figure 9a presents maximum amplitude variations as a function of hardening time for each receiver. Surprisingly, it shows that the highest amplitudes and variations appear for times soon after mixing – when the mortar can be considered as a fluid suspension - and that they are rather constant from 90 minutes to 525 minutes. The small fluctuations of amplitude observed on all receivers, as for example at 205 and 235 minutes, are due to small variations of the source energy. Attenuation

mechanisms are still being debated and their quantitative assessment remains far from being resolved. Bourbié et al (1986) qualitatively showed that wave attenuation is highly sensitive to saturation, frequency, fluid viscosity, fluid pressure and temperature. Their conclusions were based on laboratory experiments performed on various media (sandstone, granite, limestone and sand) by Murphy (1982), Jones and Nur (1983), Spencer (1981) Winkler and Nur (1982). They

notably showed that P-wave attenuation is higher when the saturation reaches a range of around 80-97 %, and is higher in the 5 to 10 kHz range of frequencies. They found that it is also sensitive to fluid viscosity (from the existence of attenuation peaks depending on the nature of the fluid) and that it decreases with increasing temperature and effective pressure. Boumiz (1995), who more specifically studied chemical and mechanical evolution of young mortar, showed that the evolution of mortar, due to the development of hydrates, induces variations in aforementioned parameters. The distribution of air bubbles in mortar varies during the hydration. Similarly, the accelerometers-mortar and granite plate-mortar couplings could change, due to the shrinkage effects during hydrate development. These factors may affect the recorded amplitudes, and could explain the strong attenuation variations observed at around 90 minutes.

It still remains very difficult to quantify independently the influence of all these parameters on amplitudes. In this study, the observed attenuation remains low at early times. Nevertheless, we cannot identify the exact contribution of each parameter.

Figure 9b shows the amplitude variations as a function of propagation distance at a recording time of 60 minutes. In order to compare the measured attenuations with those derived from an elastic behaviour, we used a classical elastic law expressed as following:

$$(4) \frac{A}{A_0} = \frac{X_0}{X} e^{-\alpha(X-X_0)}$$

or in another form:

$$(5) \ln\left(\frac{AX}{X_0}\right) = \ln(A_0) - \alpha(X - X_0)$$

Where A and A0 are the amplitude at a propagation distance of X and X0 respectively, and α the attenuation coefficient.

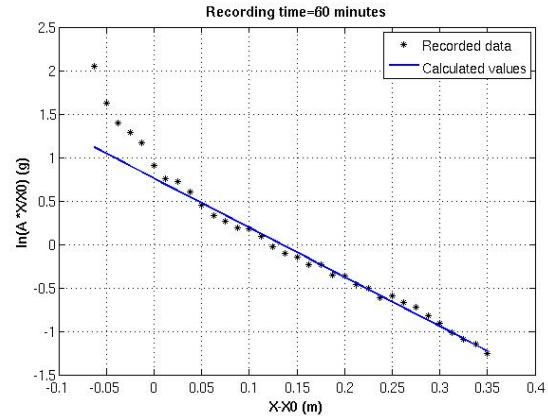


Figure 10: Data recorded in configuration 2 at recording time of 60 minutes and the values computed using expression 5, with $X_0=0.095$ m.

In the far field, the amplitude falls off by $1 / r$, contrary to the amplitude in the near field condition, which is defined as the region within a radius where λ is the wavelength. In the case where data were recorded using configuration 2 at a recording time of 60 minutes (Figure 9b), the obtained wavelength is around 0.095 m. By considering only the data in far field, Figure 10 compares the recorded and computed amplitudes for a propagation distance X_0 equal to 0.095 m. The best fit was obtained with an attenuation coefficient of 5.68. This corresponds to a quality factor (Q) lower than 10 if we apply a central frequency of 1000 Hz and a velocity of around 85 m/s in the following classical relation:

(6)

where f is the frequency, α the attenuation coefficient and V the phase velocity.

Not only the results highlight very strong attenuation, they also show that an elastic behaviour can reproduce the observed data in terms of amplitude attenuation.

4. Properties of reflected waves.

The purpose of this part is to characterize the properties of reflected waves and to evaluate their potential to image the interface between unconsolidated mortar and in-place soil. At early times, the data at low incidence angles clearly show a reflected wave (Figure 6b). The goal is to establish the optimum source-receiver configuration, a compromise between the

necessity to acquire large amplitudes for signal to noise ratio issues (depending on reflectivity and attenuation), and allowing a correct analysis of P wave velocity. First, we evaluate the amplitude variation of the reflected wave according to both the incidence angle (AVO) and the propagation distance in the mortar. Secondly, we investigate the uncertainties in P-wave velocity estimates, particularly as a function of the recording configuration (offsets).

4.1. AVO analysis.

Changes of reflection and transmission coefficients with incident angle are the fundamental basis for amplitude versus offset analysis (AVO). Here, AVO studies are not conducted to characterize the interface as in oil seismic reflection (Simmons and Backus, 1994) or fracture GPR characterization (Deparis and Garambois, 2009). They are only performed to evaluate the expected amplitude levels after wave energy splitting (Castagna, 1993). Reflection and transmission coefficients depend both on the incidence angle and on the material properties of the two media. Full solutions for their amplitudes were given by Zoeppritz equations (Knott, 1899; Zoeppritz, 1919) in which reflection and transmission coefficients are solved as a function of incident angle and elastic properties (densities, bulk and shear modulus). Aki and Richards (1980) presented these equations in matrix form. The most useful results are the P-to-P (R_{PP}) and P-to-S (R_{PS}) reflectivities, which were completely determined by the density and the P-wave and S-wave velocities of each medium (Mavko et al, 1998). Figure 11 presents R_{PP} AVO curves for a young mortar (when attenuation is low) presenting a P wave velocity of 80 m/s, a null S-wave velocity and considering different types of second layers (nylon, moist sand and saturated clay). The velocities and densities used for each media are summarized in Table 1 (deduced from Bourbié et al, 1986). The curves were computed by the CREWES Zoeppritz explorer 2.0 developed by the Consortium for Research in Elastic wave Exploration Seismology located at the University of Calgary with the exact equations of Zoeppritz.

Medium	Vp (m/s)	Vs (m/s)	Density (kg/m ³)
Concrete	80	0	1800
Nylon plate	2700	1350	1180
Moist sand	1750	500	2000
Clay	1100	200	2000

Table 1: Velocities (Vp and Vs) and densities used for the amplitude estimation of seismic reflected waves.

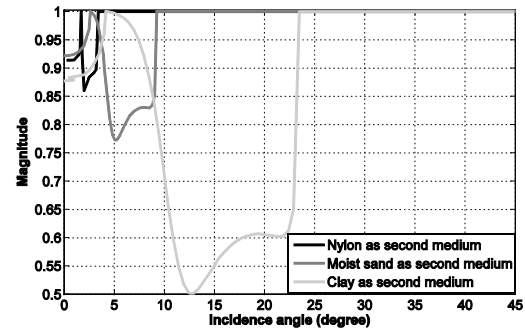


Figure 11: AVO curves R_{PP} AVO curves for a young mortar (P waves velocities equal to 80 m/s, null mortar S waves velocity) and considering different second media (nylon, moist sand and saturated clay with respectively P-wave velocities V_2 of 2700, 1750 and 1100 m/s, S-wave velocities of 1350, 500 and 200 m/s and densities of 1180, 2000 and 2000 kg/m³. Curves were obtained by the CREWES Zoeppritz Explorer 2.0 with the exact equations of Zoeppritz.

Figure 11 shows that the first maxima visible at low angles corresponds to the critical angle for the refracted P-wave. Beyond this first critical angle, there is no transmitted P wave energy, while the reflected P wave energy decreases. This decrease can be explained by an increase in P-to-S wave conversion in the elastic case. The second maximum corresponds to the critical angle for the refracted S-wave: beyond this second critical angle, there are no transmitted S-waves. Because of the absence of S-waves in fluid mortar, the reflectivity coefficient stays at 1 beyond this second critical angle.

From these curves, the optimum reflectivity coefficient R_{PP} is obtained for incidence angles lower than the first critical angle, or higher than the second critical angle. When P wave velocity contrast decreases, values of critical angles essentially increase. The first and second critical angles vary in ranges of [1.7-4.2 degrees] and [3.4-23.6 degrees] respectively, depending on the

properties of the second medium. Between the two critical angles, the reflectivity coefficient reaches the lowest value in the lower P wave velocity contrast case, i.e., to 0.5 for clays.

4.2. Reflected wave amplitude variations

Attenuation was characterized for young mortar (see §3.2) and reflectivity behaviour of the mortar was determined considering different interfaces (see §4.1). From these two studies, reflected wave amplitude can be modelled using the classical elastic law (equation 4). It was computed using an attenuation coefficient of 5.68 (measured for young mortar at 1000 Hz), which was combined with the reflectivity AVO curves shown earlier, for offsets varying from 0 to 1.5 m. The initial amplitude A_0 is 1 g for a corresponding propagation distance X_0 of 0.095 m. The model was defined using two flat layers (Figure 12a): a 1 m thick mortar and the second one a nylon plate (used for laboratory configuration), moist sand or clayey layer (consistent with the sedimentary deposits often encountered near the surface). The velocities and densities used are summarized in Table 1. Reflected P wave amplitudes (Figure 12b) clearly show high attenuation of the acceleration, ranging from $2.8 \cdot 10^{-7}$ to $1.4 \cdot 10^{-11}$ g when incidence angles vary from 0 to 45 degrees. For clays, reflectivity changes appear between 7 and 24 degrees. Attenuation remains the main parameter controlling amplitude of the reflected wave.

4.3. Estimation of in-situ P wave velocity of the mortar

A correct image of the interface between the mortar and in-place soil requires a precise knowledge of in-situ velocity, which may have large variability both in space (in-situ soil sensitivity) and time (mortar hardening). This implies that velocity must be derived directly from the seismic measurements, for example from the reflected hyperbola. Its normal move-out (NMO) can be analysed using the semblance maxima approach (Yilmaz, 1987), which is commonly used in seismic processing, yielding the stacking velocity. To apply this process to real data, and to evaluate the uncertainties on the derived velocities, numerical simulations were used considering the measured mortar properties, to determine the optimum source-receiver configuration. For this, we used an elastic modelling software of seismic wave propagation originally developed by Dietrich (1988), extended to porous media and seismo-EM coupling (Garambois and Dietrich, 2002). This code is based on the Kennett and Kerry reflectivity scheme (1983) for layered media, and begins by decomposing the wave fields into their plane wave (or more precisely cylindrical wave) components. The various decomposed plane-wave amplitudes are then determined, by satisfying the continuity conditions that hold at each interface. Consequently, proper modelling of how plane waves reflect and transmit at an isolated interface in the frequency-wavenumber domain is essential.

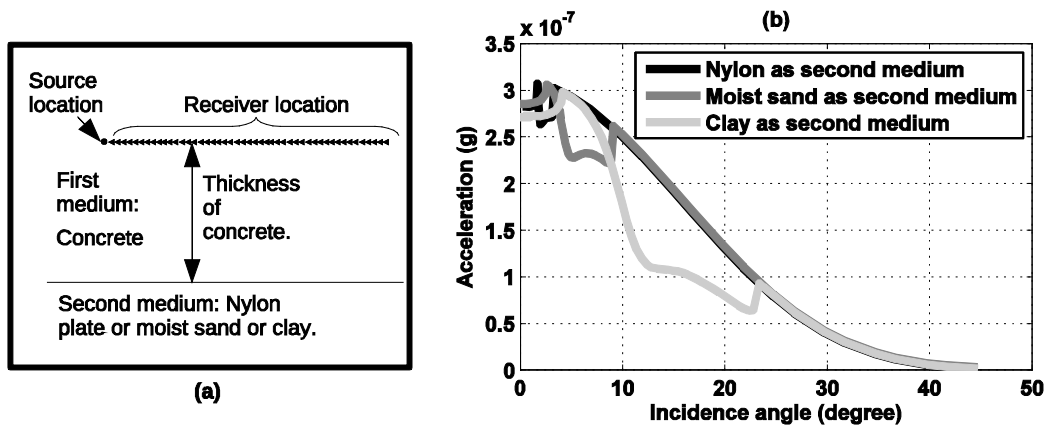


Figure 12: (a) Model and source-receiver geometry used for amplitude estimation of P reflected waves.(b) Amplitude (acceleration) of P reflected wave simulated for a mortar thickness of 1 m and incidence angle from 0 to 45 degrees.

A discrete wave number integration of the reflectivity (Bouchon and Aki, 1977), followed by application of Bessel functions and an inverse Fourier Transform, provides the response in time-space domain. The source is a Ricker function whose predominant frequency can be controlled. To better simulate the pendulum source used in our experiment, a simulated vertical force with a dominant frequency of 1000 Hz was applied. In the proposed simulations (Figure 12a), the soil thickness was considered to be 1 m, and 39 receivers every 0.05 m were spread along the horizontal axis, between 0.1 m and 2 m (incidence angles ranging from 2.86 degrees to 45 degrees). The model was defined by two stratified media: the first one corresponding to the young mortar ($V_p=80$ m/s, V_s around 0) and the second one corresponding to a nylon plate, to better reproduce laboratory configuration. An example of the reflected waves obtained with 20 % of additional Gaussian noise is presented on Figure 13.

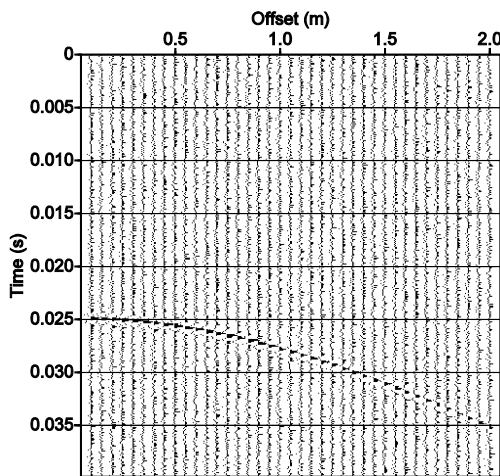


Figure 13: Synthetic seismogram of reflected waves with 20% added Gaussian noise.

In order to determine the minimum offset needed to derive correct estimation of velocity, semblance maps (Figure 14) were produced with

various maximum offset ranges from 2 m (Figure 14a) to 0.25 m (Figure 14e). The results show that it is not possible to constrain the velocity for a maximum offset lower than 0.5 m. For maximum offset larger than 0.5 m, the maximum semblance zone is centered on a velocity of 80 m/s, which corresponds to the velocity of medium. However, the uncertainties on velocity picking can vary from ± 1 m/s (for a maximum offset of 2 m) to ± 9 m/s (for a maximum offset of 0.5 m). These uncertainties generate possible errors in the estimation of the thickness of mortar, ranging from 0.13 m to 0.02 m (See Table 2).

Maximum offset (m)	0,25	0,5	1	1,5	2
Maximum incidence angle (degrees)	7	14	26,5	37	45
Velocity uncertainty (m/s)	-	± 9	± 4	± 2	± 1
Uncertainty on concrete thickness uncertainty	-	± 0.13	± 0.05	± 0.03	± 0.02

Table 2: Uncertainties of velocities and thickness of mortar obtained from semblance analyses for different maximum offsets (or incidence angles).

These results show that soon after mixing, a configuration with a maximum offset of 1 m, corresponding to an incidence angle of 26.5 degrees, appears appropriate to obtain a correct estimation of phase velocity and mortar thickness, with uncertainties of ± 0.05 m. An increase of maximum offset does not significantly reduce the uncertainties. It is noticeable that increasing the distance between receivers to 0.15 m does not produce significant changes in the results on semblance maps. Consequently, a distance of 0.15 m between receivers, with a maximum offset of 1 m, appears to be good compromise for deriving correct uncertainties on the velocity and mortar thickness, while ensuring satisfactory signal to noise signals.

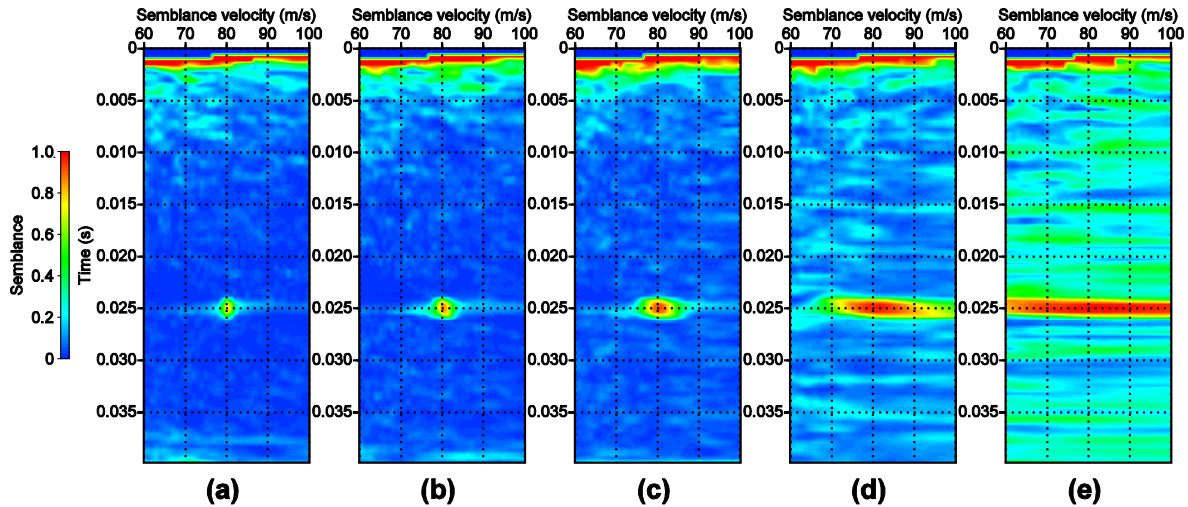


Figure 14: Semblance maps of velocity analysis for different maximum offsets of 2 m (a), 1.5 m (b), 1 m (c), 0.5 m (d) and 0.25 m (e) with receivers spread every 0.05 m.

5. Conclusions.

This study aimed at establishing the potential of acoustic methods for imaging of mortar and in-place soil. The first part was dedicated to assessing the seismic characteristics and behaviour of fresh mortar mixture and its time-dependence between 15 minutes and 8 hours after mixing. It shows (1) the very weak values of P waves velocities, whose variations appear after a certain curing time, and do not present any dispersion ; (2) very high attenuation of waves in the mortar, which decreased the signal's frequency content from 20 kHz (source frequency) down to 4 to 6 kHz. Lowest attenuation appears at early times (below 90 minutes), and increases after. Combining these two results, it suggests that for imagery purposes, acquisition would be better on fresh mortar in terms of wave resolution (lower velocity) and interesting signal to noise ratio (relatively low attenuation). Seismic monitoring also allowed detection of a second propagation mode after five hours of hardening, interpreted as the signature of new propagation modes (S to P conversion at the free surface and surface waves) linked to the evolution of mortar from a fluid mixture to a consolidated medium. Finally, velocity and attenuation studies conducted soon after mixing, show that the mortar mimics the characteristics of a fluid suspension and that it

exhibits an elastic behaviour, staying almost incompressible, even after eight hours. In a second part, we focused on the search for the best source-receiver configuration to detect and characterize the interface between in situ soil and mortar, via reflected waves. Amplitude Versus Offset (AVO) studies showed that reflectivity variations according to offset are not the main concern in term of signal to noise ratio, compared to the large amplitude decrease due to P wave propagation in such an attenuating material. In order to precisely locate the interface, an in situ velocity assessment may be conducted with semblance maps using a maximum incidence angle of 26 degrees, independent of distance between receivers (lower or equal to 0.15 m when mortar is less thick than 1 m). This ensures a satisfactory signal to noise ratio for reflected waves. This study showed the feasibility of in situ acoustic imaging for depth located mortar-soil interface imaging and assessed (1) practical characteristics and the changes in velocities, attenuation, resolution and amplitudes of waves and (2) optimum source-configurations (frequency, maximum offset) to be used for reflection imagery. The following issues will have to be addressed: (1) acquiring seismic data after injection on a real controlled test site, (2) imagery problems for more complex interfaces (roughness, 2D variation of interface geometry)

and (3) estimation of the spatial resolution in a real case. Complex structures problem must be studied using 2D simulations, which aim at evaluating the efficiency of the standard seismic reflection processing techniques (velocity analyses, dynamic corrections, stacking, migration). In future, it is envisaged that full waveform inversion may be utilised to reconstruct the complex geometry of the interface.

Acknowledgements:

This research project was made possible with the financial support of the “Agence Nationale pour la Recherche” (JETPHI project). The authors are grateful to J.-M. Martin for his help during the laboratory experiments and to Michel Dietrich, who initialized the current project. Also, constructive comments from two anonymous reviewers greatly improved the manuscript. We also thank Chris van Houtte (MEEES student) for its help for english corrections.

References:

Aki, K. and Richards, P.G., 1980. Quantitative seismology: Theory and methods: W. H. Freeman and Co., San Francisco, 932 pp.

Arnaud L. and Thinet S., 2003. Mechanical evolution of mortar during setting. *Materials and structures*. 36, 355-364.

Arroyo Franco M.A. Mercado Ortiz J.L., Gopa S. De, Renlie L. and Williams S., 2006. Sonic Investigations In and Around the Borehole. *Oilfield Review*. Vol. 18, no. 1, 14–33.

Biot, M.A., 1956. Theory of propagation of elastic waves in a fluid saturated porous solid. I. Low frequency range, II. Higher frequency range. *J. Acoust. Soc. AM.*, 28, 168-191.

Biot, M.A., 1962. Mechanics of deformation and acoustic propagation in porous media. *J. Appl. Phys.*, 33, 1482-1498.

Bachrach, R. and Nur, A., 1998. High-resolution shallow-seismic experiments in sands, Part I: water table, fluid flow and saturation. *Geophysics* 63, 1225-1233.

Bachrach R., Dvorkin J. and Nur A.M., 2000. Seismic velocities and Poisson's ratio of shallow unconsolidated sands. *Geophysics*, 65, 559-564.

Bouchon M. and Aki K. 1977. Discrete wave-number representation of seismic-source wave fields. *Bull. Seism. Soc. Am.*, 67, 259-277.

Boumiz A. 1995. Etude comparée des évolutions mécaniques et chimiques des pâtes de ciment et mortiers à très jeunes âges. Développement des techniques acoustiques. Thèse de doctorat. Université de Paris 7. 195 pp.

Bourbié, T., Coussy, O. and Zinszner, B., 1986. *Acoustique des milieux poreux*. Pub. de l'IFP. Ed. Technip. 339 pp.

Boutin, C., Arnaud, L., 1995. Mechanical characterization of heterogeneous materials during setting. *Eur. J. Mech., A/Solids* 14, No. 4, pp 633-656

Castagna, J.P., 1993. AVO analysis- tutorial and review, in *Offset Dependent Reflectivity- Theory and Practice of AVO analysis*, J.P. Castagna and M. Backus, eds. *Investigations in geophysics*, No 8, Society of Exploration Geophysicists, Tulsa, Oklahoma, 3-36.

Deparis J. and Garambois S., 2009, On the use of dispersive APVO GPR curves for thin-bed properties estimation: theory and application to fracture characterization, *Geophysics*, V. 74, 1, J1-J12.

Dietrich, M., 1988. Modeling of marine profiles in the t-x and tau-p domains. *Geophysics*, 53, 453-465.

Garambois S. and Dietrich M., 2002. Full waveform numerical simulations of seismo-electromagnetic wave conversions in fluid saturated porous media, *Journal of Geophysical Research*, 107, No B7, 10.1029/2001JB000316.

Garambois S., Sénéchal P. And Perroud H., 2002. On the use of combined geophysical methods to assess water content and water conductivity of near-surface», *Journal of Hydrology*, 259, pp 32-48.

Gassmann, F., 1951. Über die elastizität poröser medien. *Vier. Der Natur. Gesellschaft in Zürich*, 96, 1-23.

Jonas, M., 1991. Einsatzmöglichkeiten einer Ultraschall-Frequenzanalyse bei der Erhärtung anorganischer, mineralischer Bindemittel. *Forschungskolloquium DAfStb*, Bochum, pp. 187-191

Keating, J., Hannant, D.J., Hibbert, A.P., 1989a. Comparison of shear modulus and pulse velocity techniques to measure the build-up structure in fresh cement pastes used in oil well cementing. *Cem. Conc. Res.*, Vol 19, pp. 554-566.

Keating, J., Hannant, D.J., Hibbert, A.P., 1989b. Correlation between cube strength, ultrasonic pulse velocity and pulse velocity. *Cem. Conc. Res.*, Vol 19, pp. 567-574.

Knott, C.G., 1899. Reflexion and refraction of elastic waves with seismological applications: *Phil. Mag.*, 48, 64-97.

L'Hermite, R., 1955. Idées actuelles sur la technologie du béton. Documentation TBTP, Paris, pp. 193-200.

Mavko, G., Mukerji, T. and Dvorkin, J., 1998. *The Rock Physics Handbook. Tools for seismic analysis in porous media.* Cambridge University Press. 329 pp.

Niyogi, S.K., Das Roy, P.K., Roychaudhuri, M., 1990. Acousto-ultrasonic study on hydration of portland cement. *Cer. Trans.*, Vol. 16, pp. 137-145.

Nur A., Mavko G., Dvorkin J. and Galmudi D., 1998. Critical porosity: a key to relating physical properties to porosity in rocks. *The Leading Edge*. 17, 357-362.

Reinhardt, H.W. And Grosse, C., 1996. Setting and hardening of mortar continuously monitored by elastic waves. *Proc. Of the Int. RILEM Conferences.*

velocity and volume change for oil well cement slurries. *Cem. Conc. Res.*, Vol. 19, pp. 715-726.

Kennett B.L.N. And Kerry N.J., 1979. Seismic waves in a stratified half space. *Geophys. J. Roy. Astr. Soc.*, 57, 557-583.

1.4 Perspectives : Imagerie sismique des milieux poreux par inversion des champs d'ondes complets et approche différentielle

1.4.1. Utilisation du champ d'onde complet

Mes perspectives à court terme sur les problématiques hydrogéophysiques peuvent être résumées par les différentes thèses que je co-encadre à l'heure actuelle sur la problématique d'imagerie géophysique. Celles-ci ont toutes en commun l'imagerie par champ d'onde complet, que ce soit pour les ondes sismiques qu'électromagnétique, leur couplage étant le cœur du chapitre 2. Un des aspects crucial en hydrogéophysique est de recouvrer la distribution d'observables sensibles à la structure poreuse (ou fracturée) des matériaux étudiés ainsi qu'à la partie fluide (saturation, nature du fluide, porosité, contenu en eau, conductivité de l'eau). Des exemples divers ont montré que les vitesses électromagnétiques étaient très sensibles à la teneur en eau, et que différentes techniques (analyses de l'onde directe et des ondes réfléchies) permettaient de remonter aux distributions 2D du contenu en eau, aux échelles spatiales (extension latérale et profondeur) accessibles à cette technique. Des développements concernant la dispersion des courbes APVO (Amplitude and Phase vs Offset) de la réflectivité dans le cas de couches fines permettent également de retrouver des propriétés de ces couches fines au niveau du premier réflecteur (Chapitre 4). Néanmoins, dans toutes ces approches, une seule partie très limitée du signal (ondes réfléchies et/ou directe) n'est utilisée, restreignant ainsi fortement la potentialité d'information que pourrait apporter un champ d'ondes complet. Ainsi, que ce soit pour les ondes sismiques ou électromagnétiques, il faut généraliser l'étude à l'ensemble des formes d'ondes, ce qui permettra de tirer partie de la totalité des informations accessibles dans les enregistrements.

Pour répondre à ces besoins, les techniques d'inversion du champ d'onde complet (Full Waveform Inversion, FWI) ont connu un regain d'intérêt à partir des développements en fréquence proposés par Pratt (1999), bien que les travaux précurseurs datent de plus de 25 ans (Lailly, 1983; Tarantola, 1984). Ce délai s'explique d'une part par les besoins considérables de ces méthodes en moyens de calculs, et également par les progrès en termes d'acquisition des données (grands angles, multi-composantes, 3D). La démarche d'inversion en sismique vise à extraire de l'information quantitative des sismogrammes, à savoir les paramètres constitutifs décrivant le milieu, idéalement en prenant en compte l'ensemble des ondes se propageant à partir de sources actives (cf. synthèse de Virieux et Operto, 2009). Dans le chapitre 4, nous présenterons des perspectives d'inversion concernant les ondes électromagnétiques, qui pourront être appliquées aux problèmes hydrogéophysiques, en considérant des modèles constitutifs adaptés et la prise en compte du diagramme de rayonnement suivant les modes d'acquisition.

En sismique, les approches acoustiques permettent l'accès à la distribution 2D ou 3D des vitesses d'onde P et de la densité tandis que les approches élastiques ou visco-élastiques permettent de prendre en compte les phénomènes dissipatifs et fournissent la distribution des vitesses d'ondes P et S et à la densité (actuellement en 2D). La figure 4.1 illustre cette démarche par un exemple élastique synthétique calculé par Brossier et al. (2009). Dans ce cas, le problème direct est calculé dans le domaine spectral, par une méthode de Galerkin-discontinu (volumes finis) sur des cellules triangulaires, ce qui permet une prise en compte efficace de la surface libre et des effets de dispersion. L'inversion séquentielle est effectuée en montant en fréquence à partir d'un modèle initial qui joue un rôle primordial, souvent déduit d'une analyse tomographique.

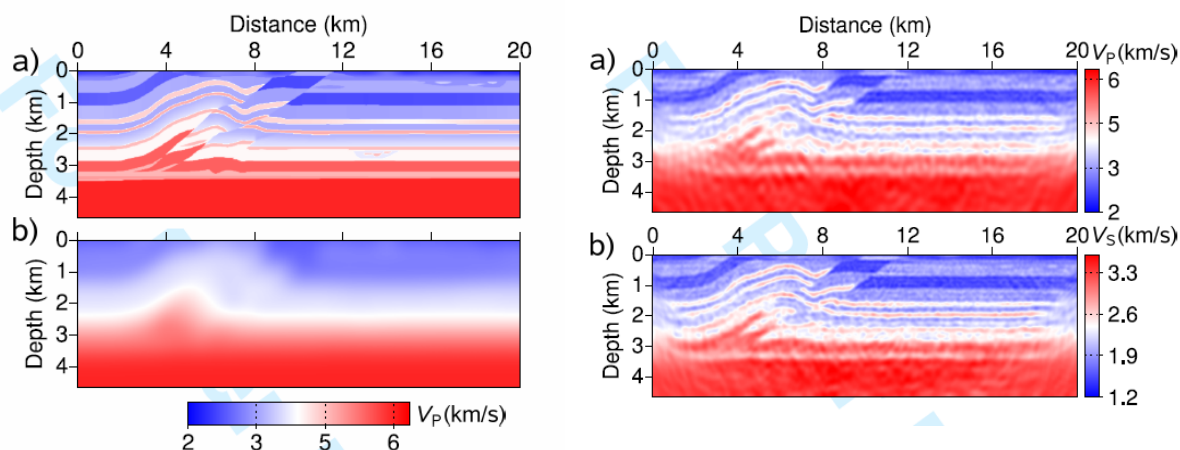


Fig. 4.1. A gauche le modèle direct test SEG/EAGE à reconstruire (a) et le modèle initial avant inversion en V_p (bas). A droite, résultats de l'inversion avec itération en fréquence pour V_p (a) et V_s (b). Les données ont été pré-conditionnées pour chaque inversion en fréquence (atténuation des ondes de surface). D'après Brossier et al. (2009).

A partir de la distribution des vitesses obtenues par inversion, il est courant d'effectuer, dans un second temps, une transformation pour recouvrer les propriétés constitutives du milieu poreux, via des relations pétrophysiques en général non-linéaires (down-scaling). Cette stratégie à deux temps, en général calibrée grâce à des mesures complémentaires en forages, permet d'estimer certains paramètres décrivant les formations réservoirs (porosité, nature du fluide, saturation). La prise en compte du caractère poro-élastique des formations réservoirs tout au long du problème, c'est-à-dire aux niveaux du problème direct et de la formulation du problème inverse, n'est pas très développée à ce jour. Pourtant, que ce soit pour des problèmes de réservoirs (huile, gaz, stockage de CO_2) ou hydrogéophysiques, la prise en compte du caractère bi-phasique (voir multiphasique) de la subsurface, et notamment l'interaction dynamique entre les phases solides et fluides, est une étape essentielle pour rendre compte correctement des amplitudes des ondes sismiques (Pride et al., 2003) et de leur contenu spectral. De plus, en adoptant cette stratégie, une seule étape serait alors nécessaire pour passer des sismogrammes aux propriétés caractérisant les formations poreuses.

Dans le cadre de la thèse de B. Dupuy [2008-2011], une tentative d'inversion des paramètres constitutifs du milieu poreux est tentée, en 2D. Cette démarche est également conduite avec une méthode Galerkin-Discontinu en fréquence, qui permet de prendre en compte l'ensemble des phénomènes de relaxation et d'atténuation prédits par le modèle de Biot (1956). On peut ainsi considérer à la fois les modes de propagation et de diffusion de l'onde de Biot, mode particulièrement important aux basses fréquences sismiques. De plus, comparé aux méthodes des éléments spectraux utilisées par Morency et Tromp (2008) ou à celle en différences finies proposée par Masson et Pride (2010), qui sont effectuées dans le domaine temporel, les simulations en fréquence sont moins coûteuses en termes de mémoires. A ce stade, la validation du modèle direct, conçu à partir des relations constitutives proposées par Pride (2005) en milieu saturé, a été effectuée par confrontation avec un algorithme de modélisation SKB, qui utilise la technique de réflectivité dans le domaine des fréquences-nombres d'ondes (De Barros and Dietrich, 2008). Une illustration de cette validation est fournie Fig. 4.2 (Dupuy et al., 2010a) et un article est en cours de préparation (Dupuy et al., 2010b).

La validation du modèle direct étant effectuée, les perspectives sont multiples. A court terme, une étude des noyaux de sensibilité des paramètres constitutifs (porosité, perméabilité, viscosité, ...) doit être menée, ce qui permettra un choix des paramètres à inverser, et sera une base pour une inversion différentielle en milieu poreux (cf. paragraphe suivant). L'inversion discrète dans le

domaine des fréquences pourra alors être testée sur des modèles 1D puis 2D synthétiques, pour les différentes problématiques envisagées (huile, gaz, CO₂, ressources en eau).

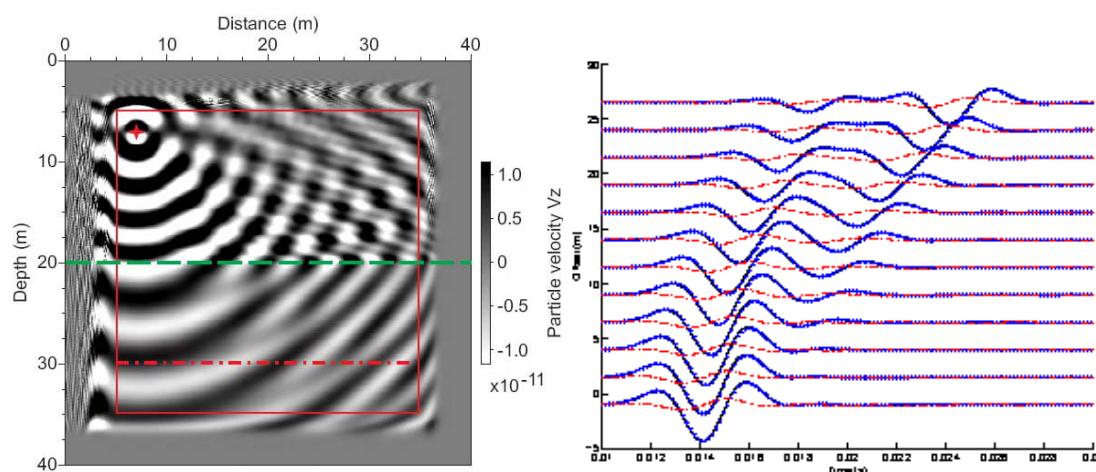


Fig. 4.2. Carte fréquentielle (598.8 Hz) de la vitesse de déplacement vertical des ondes sismiques générées par une source explosive (Ricker, 200 Hz) localisée dans le coin haut et à gauche dans un milieu stratifié. Les PML jouent leur rôle d'atténuation des ondes aux bords. A droite, superposition des sismogrammes obtenus avec la méthode Galerkin-Discontinu et la méthode de réflectivité. La différence en pointillés rouges est amplifiée d'un facteur 5. On observe que la répartition de l'énergie à l'interface (ondes P, S et de Biot) semble correcte.

Des inversions sur données réelles sont également envisagées. Je privilégierai dans un premier temps une approche 1D (milieux stratifiés), certes restrictive, mais dictée par les problèmes d'acquisition qui doivent rester à la portée des moyens universitaires et être conduits dans des zones difficiles d'accès. Celles-ci pourront être effectuées pour des problématiques hydrologiques appliquées à des milieux sédimentaires (nappes), des glissements de terrain de type sols ou à des glaciers, pour lesquels l'hypothèse 1D reste raisonnable. Dans ces problématiques, la distribution des zones saturées, de leur porosité et de la perméabilité associée est de première importance. La prise en compte de la dispersion et des phénomènes de relaxation étant un point fort de cette démarche, il sera intéressant d'élargir le domaine des fréquences sismiques aux fréquences en laboratoire. Ceci permettra d'analyser les résultats d'inversion obtenus pour des données issues d'expériences contrôlées en laboratoire, à plus haute fréquence, comme cela a été fait par Bretaudeau et al. (2009) en élastique pour des applications géotechniques. Ceci sera fait dans le cadre d'une collaboration avec C. Bordes et D. Brito (MIGP, université de Pau) qui fourniront des jeux de données sismiques acquises dans des milieux 1D (puis 2D) présentant des variations de porosité, de perméabilité et de nature du fluide saturant.

Dans un second temps, il faudra élargir ces analyses à des données réelles dans des milieux présentant de fortes variations 2D, que ce soit au niveau du terrain que du laboratoire. Plusieurs sites tests pourront être envisagés, qui regroupent les problématiques présentées dans d'autres chapitres : glaciers, géotechnique, faille active, glissement de terrain rocheux, par exemple Séchilienne (Chapitre 3) ou des glissements de type sols dans lesquels les ondes de surface sont prépondérantes à courte distance. Si un effort d'acquisition plus lourde pourra être mené ponctuellement au niveau du laboratoire, il me semble que des collaborations avec l'industrie pétrolière, qui acquiert régulièrement des données 4D (3D + suivi temporel), seront nécessaires, d'autant plus qu'ils bénéficient de forage de contrôles qui permettront d'analyser non seulement les vitesses sismiques, mais également les caractéristiques des formations réservoirs.

A plus long terme, pour toutes les problématiques présentées ci-avant, une nouvelle description du milieu poreux devra être envisagée, pour prendre en compte sa complexité. D'une part, la connaissance de l'état de saturation du milieu me paraît un enjeu crucial, que ce soit pour les problèmes d'écoulement fluide que de réservoirs (mélanges gaz/huiles, gaz/eau, CO₂). Pour cela, des théories d'homogénéisation permettent de prendre en compte cet effet via les relations constitutives, sans modifier la structure des équations de Biot, et devront être introduites dans notre formulation poro-élastique.

Enfin, les milieux réels, et en particuliers les formations réservoirs et les formations fracturées (karts, calcaires, mouvements de terrain fracturés), nécessitent une description qui dépasse la description poreuse telle que décrite par la théorie de Biot, qui d'ailleurs a du mal à expliquer les atténuations faibles observées dans les milieux réels hétérogènes. Les propriétés de transport des milieux en question peuvent être approchées comme des milieux poreux présentant une double porosité. L'une des porosités est associée aux fissures, qui jouent un rôle prépondérant dans le transport des fluides (vitesse élevée), alors que l'autre porosité, associée aux pores en place, sert au stockage du fluide. En effet, même si ces pores sont connectés, leur perméabilité globale est bien moindre que la perméabilité due aux fissures. De plus, un phénomène nouveau intervient : l'échange dynamique des fluides d'une porosité à l'autre. Cet aspect aura un impact très fort sur l'atténuation des ondes sismiques, l'onde de Biot jouant un rôle plus important dans les milieux de forte perméabilité. Pour prendre en compte ces effets, nous pourrions nous inspirer des travaux de Pride et Berryman (2003) qui ont proposé que les équations de double porosité et de perméabilité duale pouvaient être rassemblées sous la forme d'un milieu équivalent à porosité unique non saturée, moyennant des transformations au niveau du squelette solide. Il faudra donc que nous intégrions à moyen terme cette complexité dynamique dans la formulation des problèmes directs et inverses. Cette démarche aura des applications concrètes dans l'imagerie des réservoirs et des glissements de terrain rocheux, et s'inscrit pleinement dans l'ANR HPPP-CO₂ (coordinateur Y. Guglielmi), qui vise à améliorer l'estimation des propriétés mécaniques, hydrauliques et de l'état du milieu poreux dans un système réservoir/couverture.

1.4.2. Suivi temporel

Au niveau de la subsurface, le suivi temporel des structures et des processus actifs qui s'y produisant devient d'une importance stratégique, que ce soit pour les pétroliers qui suivent dorénavant dans le temps les lieux de production, ou pour évaluer le confinement des expériences de séquestration stockage de CO₂, notamment avec l'imagerie sismique (Fig. 4.3). Cette approche sera également vitale pour les problèmes environnementaux en particulier ceux associés aux contaminants et de ressources en eau. De même, que ce soit pour la surveillance de différents aléas (glissements de terrain, chutes de blocs, glaciers), dont l'évolution peut-être amplifiée par des changements climatiques, un suivi discret temporellement sera sans doute une des missions des investigations futures. Une synthèse de différentes méthodes géophysiques prometteuses a été proposée par Snieder et al. (2007) pour des suivis de paramètres mécaniques, de transport de fluides et de processus biogéochimiques à grande échelle. Dans ce contexte, une prospective à moyen terme s'inscrivant en continuité des développements envisagés ci-avant en imagerie GPR ou sismique portera sur la quantification de l'évolution des paramètres par les méthodes de propagation d'ondes.

Sur cette problématique, un accord de collaboration a déjà été passé avec Total ce qui a permis la mise en place d'une thèse (Amir Asnaashari, [2010-2013]) dont le sujet porte sur l'inversion 2D différentielle du champ d'onde sismique complet, c'est-à-dire à partir d'une acquisition initiale (base). Classiquement, les images obtenues par traitement successif des

données, comme celles présentées figure 4.3, constituent une source importante d'informations sur l'évolution des caractéristiques du milieu. On pourrait donc envisager d'effectuer des inversions indépendantes pour chaque acquisition. Par contre, pour que l'information quantitative soit optimale, la chaîne de traitement doit être stable, que ce soit pour obtenir des images que pour l'inversion, pour limiter les incertitudes sur les résultats. Une autre approche que l'on va expérimenter par la suite consiste à tirer parti du fait que les changements temporels entre la base et les acquisitions successives sont d'amplitudes faibles et localisés spatialement.

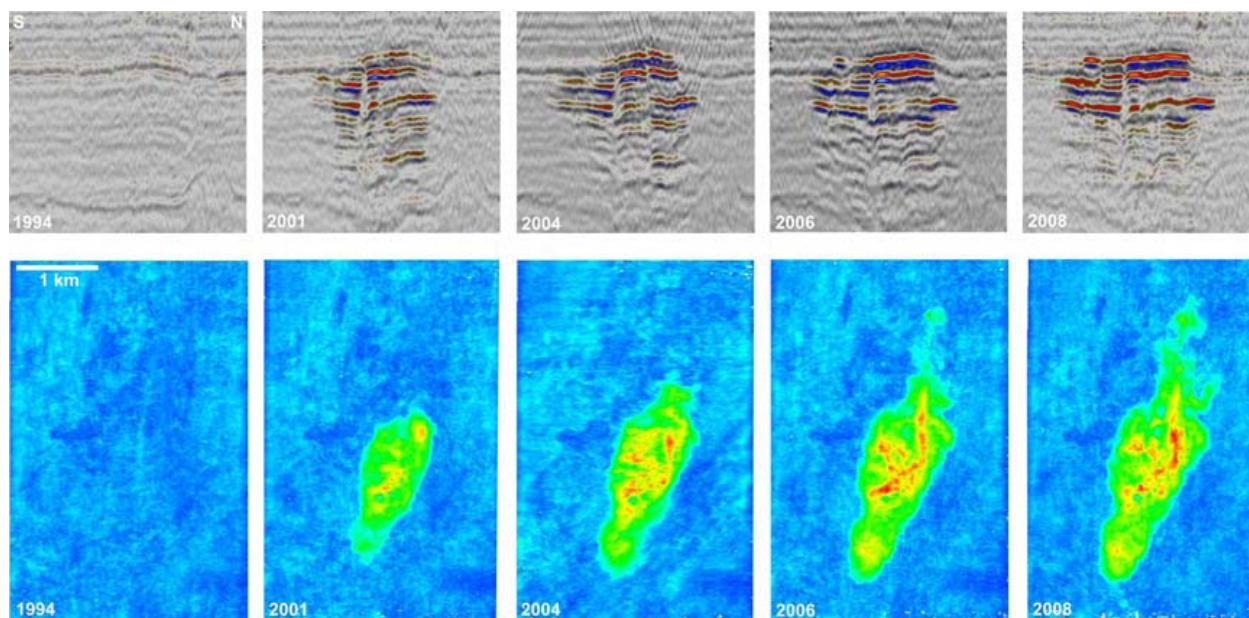


Fig. 4.3 Suivi temporel sismique d'un panache de CO₂ sur le site test de Sleipner (d'après Chadwick et al., 2009) : (haut) lignes transverses pré-injection (1994), puis à différentes dates (2001, 2004, 2006 et 2008) montrant l'augmentation de la réflectivité et la baisse des vitesses dues à la présence de CO₂. En bas, extensions latérales du panache à 850 m de profondeur.

Pour résoudre cette problématique différentielle, une possibilité que l'on va explorer est l'approche de Robertsson et Chapman (2000) qui focalisent les calculs sur une grille secondaire interne au milieu. Celle-ci est la zone où l'on suspecte des variations des parties solides ou fluides étendue à toute zone concernée par des perturbations du champ d'onde. Pour le modèle direct, après les calculs initiaux effectués sur l'ensemble de l'espace considéré, les calculs des champs d'ondes seront restreints au voisinage de ce volume (ou de la surface en 2D) perturbée, ce qui fait gagner un temps de calcul et une mémoire importante, avantages qui peuvent être décisifs pour l'inversion. Une seconde possibilité est l'approche de Wantanabe et al. (2004) qui ont analysé des données de suivi temporel acquises entre forages par une tomographie différentielle des champs d'ondes, ce qui leur a permis d'imager les altérations de vitesses causées par la simulation thermique d'hydrates de gaz.

1.3. Références (texte principal)

- Allègre V., Imagerie hydrogéophysique appliquées à l'étude d'une tourbière, MSc Thesis, Univ. J. Fourier, Grenoble.
- Archie E. 1942. The Electrical Resistivity Log as an Aid in Determining Some Reservoir Characteristics. Technical Publication 1422, Petroleum Technology, American Institute of Mining and Metallurgical Engineer, New York, USA; 8.
- Arcone S. A., Lawson D. E. and Delaney A. J. 1995. Short-pulse radar wavelet recovery and resolution of dielectric contrasts within englacial and basal ice of Matanuska Glacier, Alaska, U.S.A. *J. Glaciol.*, 41(137): 68–86.

- Barrett, B. E., T. Murray, R. Clark, and K. Matsuoka. 2008. Distribution and character of water in a surge-type glacier revealed by multifrequency and multipolarization ground-penetrating radar, *J. Geophys. Res.*, 113, F04011, doi:10.1029/2007JF000972.
- Binley, A., G. Cassiani, R. Middleton, and P. Winship, 2002, Vadose zone flow model parameterisation using cross-borehole radar and resistivity imaging: *Journal of Hydrology*, 267, 147–159.
- Binley, A., Winship, P., West, J.L., Pokar, M., Middleton, R., 2001. High-resolution characterization of vadose zone dynamics using cross-borehole radar. *Water Resource Research* 37, 2639–2652.
- Björnsson, H. 1974. Explanation of Jökulhlaups from Grimsvötn, Vatnajökull, Iceland, *Jökull*, 24, 1-26.
- Björnsson, H. 1998. Hydrological characteristics of the drainage system beneath a surging glacier. *Nature*, 395, 771-774.
- Björnsson, H. 2002. Subglacial lakes and jökulhlaups in Iceland. *Global and Planetary Change*, 35(3-4), 255-271.
- Bretaudeau F., Leparoux D., Brossier R., Abraham G., 2009, Small scale modeling, a tool to assess subsurface imaging methods - application to seismic full waveform inversion. Proc. of EAGE, Amsterdam.
- Brossier R., S. Operto and J. Virieux. Seismic imaging of complex onshore structures by two-dimensional elastic frequency-domain full-waveform inversion. *Geophysics*, 74 (6), WCC63-WCC76.
- Chadwick, R.A., Noy, D., Arts, R., and Eiken, O., 2009, Latest time-lapse seismic data from Sleipner yield new insights into CO₂ plume development, Proceedings of the 9th International Conference on Greenhouse Gas Control Technologies, Washington DC, 17-20 November 2008, ISSN: 1876 6102, Elsevier, published on CD.
- Chambers, J E, Kuras O, Meldrum P I, Ogilvy, R D, and Hollands J, 2006. Electrical resistivity tomography applied to hydrogeological and engineering investigations at a former waste disposal site. *Geophysics*, (Vol 71, 231-239).
- Dahlin, T., C. Bernstone, and M. H. Loke, 2002, A3-D resistivity investigation of a contaminated site at Lernacken, Sweden: *Geophysics*, 67, 1692–1700.
- De Barros, L. and M. Dietrich, 2008, Perturbations of the seismic reflectivity of a fluid-saturated depth-dependent poroelastic medium: *J. Acoust. Soc. Am.*, 123, 1409–1420.
- Deparis J., « Etude des éboulements rocheux par méthodes Géophysiques » *Thèse de doctorat*, Université Joseph Fourier, Grenoble 1, 2007.
- Descloitres, M., Guérin, R., Albouy, A., Tabbagh, A., Ritz, M., 2000. Improvement in TDEM sounding interpretation in presence of induced polarization. A case study in resistive rocks of Fogo volcano, Cape Verde Islands. *Journal of Applied Geophysics*, 45, pp 1-18.
- Descloitres, M., Ribolzi, O., Le Troquer, Y., Thiébaux, J. P., 2006. Spatializing Water Tension in Heterogeneous Sandy Soils with Surface ERT During Rain-Evaporation Cycles. 12th European Meeting of EAGE “Near Surface 2006”, Helsinki, Finland 4 - 6 September 2006. Extended abstract, Paper B039.
- Descloitres M., 2010, Aquifères, recharges et transferts d'eau en zone non-saturée: Caractérisation par spatialisation et suivi temporel géophysique, Hab . à Dir. Des rec., Univ J. Fourier, Grenoble.
- Dix, C. H., 1955, Seismic velocities from surface measurements: *Geophysics*, 20, 68–86.
- Dobson M.C. and Ulaby F.T. 1986. Active microwave soil moisture research. *IEEE Transactions on Geoscience and Remote Sensing* 24, 23–36.
- Dupuy B., de Barros L., Garambois S. & J. Virieux, 2010a, Discontinuous Galerkin method in frequency-space domain for wave propagation in 2D heterogeneous porous media, Proc. of Soc. of Expl. Geophysics, denver, 17-22 october.
- Dupuy B., de Barros L., Garambois S. & J. Virieux, 2010b, Wave propagation in heterogeneous porous media formulated in the frequency-space domain, to be submitted to *Geophysics*.
- Garambois, S., Sénéchal, P. & H. Perroud, 2002, « On the use of combined geophysical methods to assess water content and water conductivity of near-surface », *Journal of Hydrology*, 259, pp 32-48.
- Guéguen Y. And V. Palciaukas, 1997, Introduction à la physique des Roches, Hermann.
- Guérin R., Bégassat P., Benderitter Y., David J., Tabbagh A. & Thiry M.,(2004), Geophysical study of the industrial waste land in Mortagne-du-Nord (France) using electrical resistivity., *Near Surface Geophysics*, 2(3) :137-143.
- Grote K., Hubbard S., Rubin Y., 2003, *Field-scale estimation of volumetric water content using ground penetrating radar ground wave techniques*, *Water Resources Research*, vol. 39, no. 11, 1321.
- Gudmunsson, M.T., F. Sigmundsson and H. Björnsson. 1997. Ice-volcano interaction of the 1996 Gjalp subglacial eruption, Vatnajökull, Iceland, *Nature*, 389, 954-957.
- Haeberli, W. 1983. Frequency and characteristics of glacier floods in the Swiss Alps. *Ann. Glaciol.*, 4, 85-90.
- Haeberli, W., J.C. Alean, P. Müller and M. Funk. 1989. Assessing risks from glacier hazards in high mountain regions: some experiences in the Swiss Alps. *Ann. Glaciol.*, 13, 93-102.
- Hagrey S.A. al, Muller C., *GPR Study of pore water content and salinity sand*, Geo-phys. Pros. 48, 63-85, 2000.
- Hall, S. A., and J. M. Kendall, 2003, Fracture characterization at Valhall: Application of P-wave amplitude variation with offset and azimuth (AVOA) analysis to a 3D ocean-bottom data set: *Geophysics*, 68, 1150–1160.
- Hubbard, S.S., Peterson Jr., J.E., Majer, E.L., Zawislanski, P.T., Williams, K.H., Roberts, J., Wobber, F., 1997. Estimation of permeable pathways and water content using tomographic radar data. *The Leading Edge* 16, 1623–1630.
- Hubbard, S.S., Grote, K., Rubin, Y., 2002. Mapping the volumetric soil water content of a California vineyard using high-frequency GPR ground wave data. *The Leading Edge* 21, 552–559.
- Hubbard, S. and Y. Rubin, *Hydrogeophysics*, Chapter 1 in *Hydrogeophysics*, Y. Rubin and Susan Hubbard, eds., Springer, The Netherlands, Water and Science Technology Library, V. 50, p. 3-7, 2005.

- Huisman J. A., Snepvangers J. J. C., Bouten W., Heuvelink G. B. M., *Mapping spatial variation in surface soil water content: comparison of ground penetrating radar and time domain reflectometry*, *J. Hydrol.* 269, 194-207, 2002.
- Irvine-Fynn, T. D. L., B. J. Moorman, J. L. M. Williams and F. S. A. Walter. 2006. Seasonal changes in ground-penetrating radar signature observed at a polythermal glacier, Bylot Island, Canada, *Earth Surf. Processes Landforms*, 31, 892– 909.
- Jardani A., A. Revil, A. Bole`ve, and J.P. Dupont. 2008. 3D inversion of self-potential data used to constrain the pattern of ground water flow in geothermal fields. *Journal of Geophysical Research*. 113, B09204, doi: 10.1029/2007JB005302.
- Kemna, A., Vanderborght, J., Hardelauf, H., Vereecken, H., 2004. Quantitative imaging of 3-D solute transport using 2-D time-lapse ERT: A synthetic feasibility study. *Proc. Symp. Applications of Geophysics to Engineering and Environmental Problems*, *Environ. Eng. Geophys. Soc.*, 342-353.
- Kemna, A., Binley, A., and Slater, L., 2004. Crosshole IP imaging for engineering and environmental applications: *Geophysics*, 69, 97-107.
- Lailly, P., 1983, The seismic inverse problem as a sequence of before stack migrations: *Conference on Inverse Scattering, Theory and Application*, Society for Industrial and Applied Mathematics, Expanded Abstracts, 206–220.
- Laurent, J.-P. et al., 2005. Monitoring soil water content profiles with a TDR commercial system: Comparative field tests and laboratory calibration. *Vadose Zone Journal*, 4: 1030-1036.
- Lambot S., Slob E.C., Chavarro D., Lubczynski Maciek, Vereecken H., Measuring soil surface water content in irrigated areas of southern Tunisia using full-waveform inversion of proximal GPR data, *Near Surface Geophysics*, 6, 2008, p. 403-410.
- Legchenko, A., J.M. Baltassat, A. Beauce, and J. Bernard. 2002. Nuclear magnetic resonance as a geophysical tool for hydrogeologists. *Journal of Applied Geophysics* 50: 21-46.
- Legchenko, A., Clement, R., Garambois, S., Maury, M., Mic, L.-M., Laurent, J.-P., Desplanque C. & Guyard H., 2010, Locating water storage of Luitel lake peat bog using MRS, ERT and GPR, *Near Surface Geophysics*, accepted.
- Loke, M.H. and R.D. Barker, 1996, Rapid least-squares inversion of apparent resistivity pseudo-sections using quasi-Newton method: *Geophysical Prospecting*, 48, 181-152.
- Lunt I. A., Hubbard S. S., Rubin Y., Soil moisture estimation using ground penetrating radar reflection data, *J. Hydrol* 307, 254-269, 2005.
- Mahob, P., and J. Castagna, 2003, AVO polarization and hodograms: AVO strength and polarization product: *Geophysics*, 68, 849–862.
- Mathews, W. H. 1963. Discharge of a glacier stream. *IASH*. 63, 290-300.
- Massuel, S., Favreau, G., Descloitres, M., Le Troquer, Y., Albouy, Y., Cappelaere, B. Deep infiltration through a sandy alluvial fan in semiarid Niger inferred from electrical conductivity survey, vadose zone chemistry and hydrological modelling. 2006. *CATENA*, 67 (2), pp 105-118.
- Mavko G., Mukerji J. and J. Dvorkin, 2003, *The rock physics handbook: tools for seismic analysis in porous media*, Cambridge University Press.
- Masson Y. & Pride S., 2010, Finite-difference modeling of Biot's poroelastic equation across all frequencies, *Geophysics*, 75, N33.
- Moran, M. L., R. J. Greenfield and S.A. Arcone.. 2000. Delineation of a complexly dipping temperate glacier bed using short-pulse radar arrays. *J. Glaciol.*, 46, 274–286.
- Morency, C. and J. Tromp, 2008, Spectral-element simulations of wave propagation in porous media: *Geophy. J. Int.*, 175, 301–345.
- Murray, T., D.L. Gooch and Stuart, G.W., 1997. Structures within the surge front at Bakaninbreen Svalbard, using ground-penetrating radar. *Ann. Glaciol.* 24, pp. 122–129.
- Nye, J.F. 1976. Water flow in glaciers: jökulhlaups, tunnels and veins. *J. of Glaciol.*, 17 (76), 181-207.
- Pratt, R. G., 1999, Seismic waveform inversion in the frequency domain, Part I: Theory and verification in a physical scale model: *Geophysics*, 64, 888–901.
- Pride SR, Harris JM, Johnson DL, Mateeva A, Nihei KT, et al. 2003. Permeability dependence of seismic amplitudes. *Lead. Edge* 22:518–25.
- Pride S. & J. Berryman, 2003, Linear dynamics of double-porosity dual-permeability materials. I. Governing equations and acoustic attenuation, *Phys. Rev. E.*, 68, 036603.
- Pride, S., 2005, Relationships between seismic and hydrological properties, 253–284. *Water Science and Technology Library*, Springer.
- Rey, E., Jongmans D., Gotteland, P. & S. Garambois, 2006, Characterization of heterogeneous soils using geoelectrical measurements, *Journal of Applied Geophysics*, 58, pp 188-201.
- Robertsson, J. O. A., and Chapman, C. H., 2000, An efficient method for calculating finite-difference seismograms after model alterations: *Geophysics*, 65, 907–918.
- Robinson D.A., S.B. Jones, J.M. Wraith, D. Or and S.P. Friedman, 2003 "A review of advances in dielectric and electrical conductivity measurements in soils using time domain reflectometry". *Vadose Zone Journal* 2: 444–475.

- Sénéchal, P., Garambois S. & Bordes C., 2010, Feasibility of acoustic imaging for in-situ characterization of fresh concrete injected into soil subsurface", *Journal of Applied Geophysics*, accepted.
- Simmons, J., and M. Backus, 1994, AVO modeling and the locally converted shear wave: *Geophysics*, 59, 1237–1248.
- Singha, K., Gorelick, S. M. 2006. Effects of spatially variable resolution on field-scale estimates of tracer concentration from electrical inversions using Archie's law. *Geophysics*, Vol. 71, N°. 3, pp G83–G91.
- Slater, L., D. Ntarlagiannis, and D. Wishart. 2006. On the relationship between induced polarization and surface area in metal-sand and clay-sand mixtures. *Geophysics*: 71, 2, A1-A5.
- Snieder, R., S. Hubbard, M. Haney, G. Bawden, P. Hatchell, A. Revil, et al., 2007, *Advanced Noninvasive Geophysical Monitoring Techniques Annual Review of Earth and Planetary Sciences*.
- Stolt, R. H. 1978. Migration by Fourier transform. *Geophysics*, 43, no. 1, 23–48.
- Stovas, A., M. Landrø, and P. Avseth, 2006, AVO attribute inversion for finely layered reservoirs: *Geophysics*, 71, no. 3, C25–C36.
- Suski, B., A. Revil, K. Titov, P. Konosavsky, M. Voltz, C. Dages, and O. Huttel. 2006. Monitoring of an infiltration experiment using the self-potential method. *Water Resources Research* 42: W08418, doi: 10.10292005WR004840.
- Topp G.C, Davis J.L, Annan A. P., Electromagnetic determination of soil water content. Measurements in coaxial transmission lines, *Water Resources Research* 16, 574-582, 1980.
- Tarantola, A., 1984, Inversion of seismic reflection data in the acoustic approximation: *Geophysics*, **49**, 1259–1266.
- Velero H.P., Saracco G., Gibert D.- Three-dimensional seismic endoseopy - Part I: Design of apparatus and basic imaging algorithms. *IEEE Transactions on Geoscience and Remote Sensing*, vol 39, num 10, pp 2262-2274, 2001
- Van Overmeeren R. A., Sariowan S. V., J. C. Gehrels, 1997, Ground penetrating radar for determinig volumetric soil water content; results of comparative measurements at two test sites, *J. Hydrol.* 197, 316-338.
- Vincent C., Garambois, S., E. Thibert, E. Lefèbvre, E. Le Meur and D. Six, 2010, Origin of the outburst flood from Tete Rousse glacier in 1892 (Mont-Blanc area, France), *Journal of Glaciology*, accepted.
- Virieux J. and S. Operto, 2009, An overview of full waveform inversion in exploration geophysics, *Geophysics*, 74(6), 74, 6.
- Watanabe, T., S. Shimizu, E. Asakawa, and T. Matsuoka, 2004, Differential waveform tomography for time-lapse crosswell seismic data with application to gas hydrate production monitoring: 74th Annual International Meeting, SEG, Expanded Abstracts, 2323–2326.

CHAPITRE 2

ETUDES SUR LES CONVERSIONS D'ONDES SISMO-ELECTROMAGNETIQUES DANS LES MILIEUX POREUX

2.1 Introduction.

Le sujet de ma thèse de doctorat effectuée sous la direction de M. Dietrich (LGIT) portait principalement sur l'étude des phénomènes de couplages électrocinétiques entre ondes sismiques et électromagnétiques qui génèrent des conversions sismo-électromagnétiques dans les milieux poreux (Garambois, 1999). Les mécanismes microscopiques à l'origine de ces phénomènes macroscopiques sont dus à la présence d'une double couche électrique localisée à l'interface entre les grains solides et le fluide remplissant l'espace poreux, dont l'équilibre électrique sera modifié lorsque les fluides sont en mouvement. L'effet continu ou statique de ce phénomène donne lieu à de la polarisation spontanée, c'est-à-dire des courants d'électrofiltration microscopiques qui s'opposent aux courants de conduction pour générer un champ électrique macroscopique. La mesure de sa distribution spatiale est largement utilisée en hydrogéophysique ou en volcanologie pour détecter voir caractériser les mouvements de fluides (cf. les synthèses effectuées par Revil et al., 2006 ou par Jouniaux et al., 2009). En dynamique, c'est la propagation des ondes sismiques compressives qui va générer un mouvement différentiel entre les grains et le fluide (ou une accélération des grains dans le cas d'ondes S). Deux phénomènes principaux résultent de ce couplage en milieu poreux : i) des champs électriques (magnétiques) co-sismiques se propageant conjointement aux ondes P (S) et ii) des ondes électromagnétiques converties à des interfaces situées en profondeur. Ces effets ont été avancés pour tenter d'expliquer les anomalies électromagnétiques observées parfois avant ou pendant un séisme (Gokhberg et al., 1982) ou sur des volcans (Zlotnicki & Le Mouél, 1990), qui seraient ainsi générés par des grands mouvements de fluides associés ou précurseurs des ondes sismiques.

Un autre intérêt de ce phénomène dynamique réside dans la potentialité de ce phénomène à imager directement des contrastes de propriétés de l'espace poreux (porosité, perméabilité), de la nature du fluide saturant (viscosité) et/ou chimiques (salinité), tout en conservant la résolution des méthodes de sismique réflexion. Cette sensibilité n'existe que de manière indirecte via des relations pétrophysiques pour l'imagerie sismique ou pour des méthodes potentielles de types électrique ou électromagnétique (cf. Chapitre 1). Les applications potentielles de cette méthode originale de caractérisation se sont alors naturellement tournées vers les problèmes pétroliers et environnementaux très concernés par une caractérisation des propriétés de transport de l'espace poreux et de la partie fluide.

Durant le travail de thèse, deux axes de travail avaient été privilégiés : i) l'expérimentation in situ dans différents contextes avec les techniques de traitement du signal appropriées et ii) la modélisation numérique.

La partie expérimentale a nécessité de légères adaptations du matériel de sismique existant, et le développement de techniques de traitement du signal appropriées aux bruits électromagnétiques parasites et aux faibles amplitudes des champs électriques convertis. Ce

travail a notamment permis de confirmer l'existence de deux champs électriques convertis, un localement généré au passage d'une onde sismique (co-sismique) et un second, d'amplitude plus faible, associé à une onde électromagnétique diffusive convertie en profondeur à des interfaces de faible profondeur présentant des contrastes hydrologiques (Fig. 1.1). Le premier effet a pu être comparé quantitativement à la théorie développée par Pride (1994), que ce soit au niveau des formes d'ondes que des amplitudes (Garambois & Dietrich, 2001).

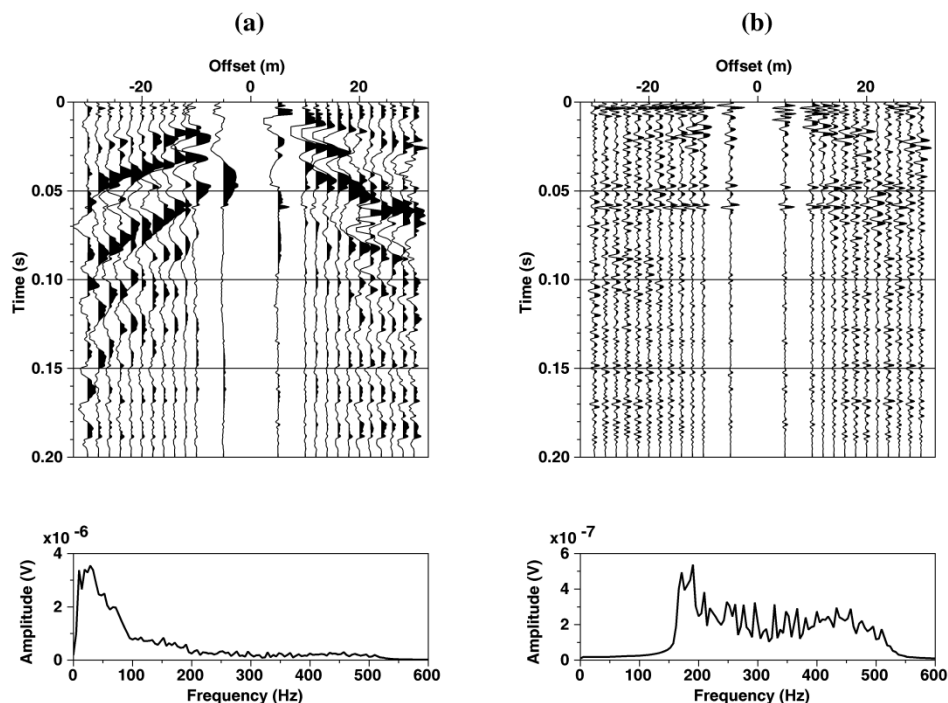


Fig.1.1 Données sismo-électriques générées par une explosion. (a) Champs électrique principalement co-sismiques et leur spectre après suppression des bruits harmoniques 50 Hz. (b) Données filtrées [160-600 Hz] faisant apparaître des arrivées converties en profondeur. D'après Garambois & Dietrich (2001).

En parallèle, nous avons développé un code de calcul permettant la modélisation de la propagation des ondes sismiques, électromagnétiques et sismo-électromagnétiques dans un milieu poreux saturé stratifié (Garambois & Dietrich, 2002). Pour ce faire, nous avons utilisé les équations macroscopiques développées par Pride (1994), qui couplent de manière dynamique la théorie de Biot en poroélastique avec les équations de Maxwell pour l'électromagnétisme via des équations de transport des fluides et des charges électriques. Les différents champs d'ondes en présence (sismiques, sismo-électriques, sismo-magnétiques) ont été calculés en étendant la méthode des matrices de réflexion/transmission généralisées proposée et synthétisée par Kennett (1983) couplée à la méthode d'intégration en nombres d'ondes discrets dans l'espace des fréquences et des nombres d'ondes (Bouchon, 1979). Ceci a permis d'analyser les deux phénomènes en jeu (co-sismiques et conversions à une profondeur) (Fig. 1.2).

Ces travaux de modélisation nous ont notamment permis de mettre en évidence que la zone qui contribue effectivement à la génération d'ondes EM à travers une interface plane coïncide avec la première zone de Fresnel associée à une conversion d'ondes sismo-EM, celle-ci étant située sous la source sismique en champ lointain. Nous avons également effectué une étude de sensibilité qui a montré que ces ondes converties en profondeur étaient particulièrement sensibles aux contrastes de porosité, de perméabilité, de salinité et de viscosité. Ceci a ouvert des potentialités d'applications nombreuses dans les domaines, pétroliers, hydrologiques et/ou environnementaux. Ceux-ci sont cependant restés limités en raison de la très faible amplitude de

ces ondes converties d'une part et de l'effet de masque des champs co-sismiques, particulièrement lorsque les enregistrements sont effectués depuis la surface avec la forte contribution des ondes de surface, d'autre part.

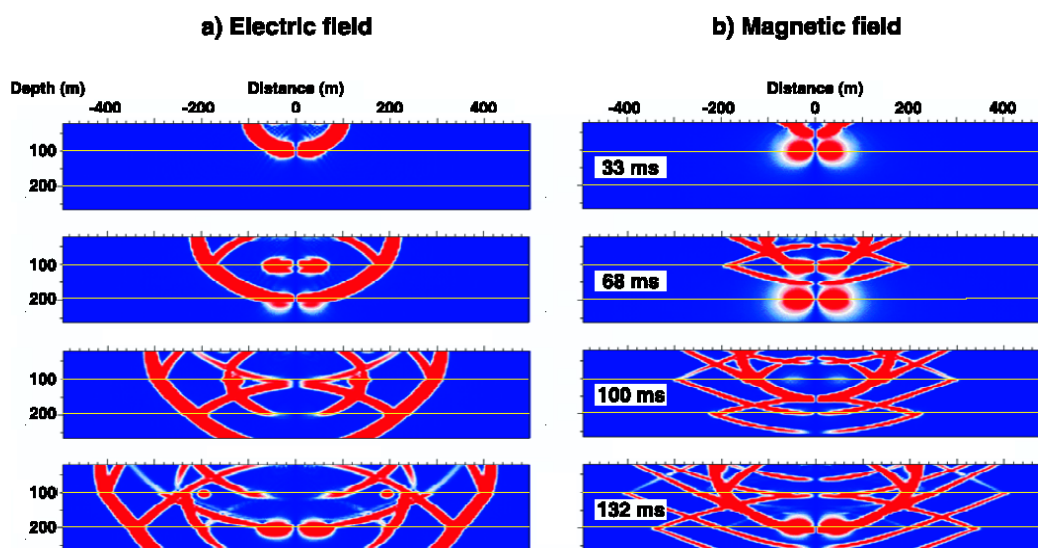


Fig.1.2. Instantanés de propagation des champs électriques et magnétiques synthétiques obtenus pour un modèle 3 couches présentant des contrastes de porosité et de perméabilité (Garambois & Dietrich, 2002). On observe les ondes co-sismiques (P pour le champ électrique, S pour le champ magnétique) ainsi que les ondes électromagnétiques converties aux interfaces.

Depuis ces travaux de thèse, de nombreuses études ont été menées par d'autres équipes internationales sur ce phénomène dynamique, que ce soit au niveau expérimental (à l'échelle du laboratoire et du terrain) qu'au niveau numérique. Sans présenter l'ensemble des études liées à ce sujet, un bref état des lieux des contributions importantes et des principaux points de blocage restant à lever est fourni ci-après. Il faut noter que l'étude de ces phénomènes bénéficie également des études menées en statique sur le couplage électrocinétique, notamment grâce à des mesures en laboratoire et des avancées théoriques, par exemple pour l'effet de la saturation (Guichet et al., 2003, 2006; Revil et al., 2007) sur la polarisation spontanée.

Au niveau des mesures de terrain, on pourra citer les contributions majeures de Haines et al. (2007) obtenues grâce à des expériences contrôlées en Californie. En effet, ceux-ci ont rempli des tranchées ce qui leur a permis de créer des interfaces contrôlées et de travailler en transmission, c'est-à-dire de profiter que la source sismique est située d'un côté de la tranchée et les récepteurs de l'autre. Cette configuration favorable leur a permis d'observer les ondes EM converties aux interfaces avec un très bon rapport signal sur bruit par rapport à des dispositifs de type réflexion pour lesquels la signature électrique des ondes de surface vient « polluer » les enregistrements. Strahser et al. (2007) ont étudié la polarisation des signaux sismo-électriques co-sismiques tandis que Dupuis et al. (2006, 2007, 2009) ont réussi à obtenir des données très convaincantes, que ce soit en forages que ou depuis la surface. Ce sont surtout les expériences depuis la surface qui ont retenu l'attention. En effet, une acquisition astucieuse de type sismique réflexion leur a permis de multiplier les traces disponibles (120 traces) et d'appliquer ainsi des techniques de traitements du signal particulièrement bien adaptées - le filtrage dans le plan fréquence - nombre d'onde. Ceci leur a permis de supprimer les arrivées co-sismiques qui masquent les arrivées EM. De plus, la sommation des traces pour chaque point de tir a permis d'améliorer le rapport signal sur bruit, très défavorable en général, et d'obtenir ainsi la première

image 2D sismo-électrique du toit d'une nappe phréatique, qui a pu être comparée à une image GPR classique (Fig. 1.3). Pour cela, ils ont parfaitement tiré avantage des propriétés des ondes converties, à savoir qu'elles arrivent quasi instantanément sur chaque récepteur, contrairement aux arrivées co-sismiques. Cette avancée majeure devrait relancer l'étude de ces phénomènes dont l'applicabilité pratique était fortement handicapée par les faibles niveaux d'amplitude.

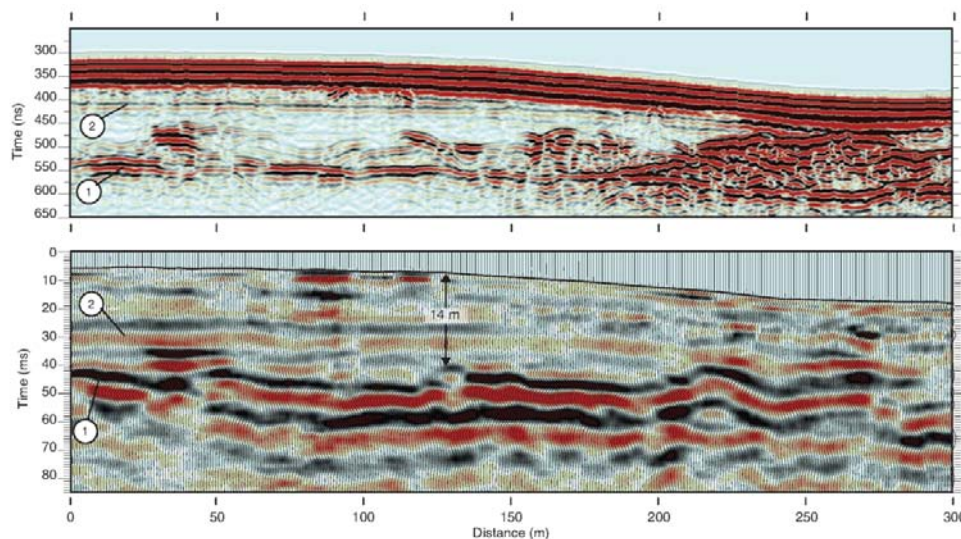


Fig.1.3. Comparaison entre une image GPR 50 MHz (haut) et une section sismo-électrique (bas) obtenue après traitements f-k pour supprimer les arrivées co-sismiques et sommation des traces d'un même point de tir entre elles. Cette image montre de manière très claire l'existence de ces conversions à une interface hydrologique. La résolution moindre en sismo-électrique par rapport au GPR est ici due à la source sismique utilisée.

Il convient également de citer les travaux précurseurs menés depuis 1993 par A. Thompson (Exxon). Il s'est réorienté depuis quelques années vers le phénomène réciproque, à savoir la conversion d'énergie électromagnétique en énergie mécanique, lui permettant d'imager des contrastes de fluides saturant dans les carbonates pour des applications pétrolières à grande profondeur (Thompson et al., 2007). Malheureusement, ces travaux sont restés peu publiés et peu explicités car ils se situent dans un contexte de concurrence pétrolière très forte. En forage, Mikhailov (1997, 2000) a réussi à enregistrer des champs électriques co-sismiques provenant des ondes de Stoneley tandis que Hunt et Worthington (2000) ont essayé de déplacer une sonde sismo-électrique en forage. Leur expérience montre des signaux basse fréquence assez inexplicables d'un point de vue de la théorie de Pride (1994), mais dont l'amplitude semble corrélée avec la présence de fractures au sein des formations. Nous proposons que les signaux enregistrés représentent la signature électrique de l'onde de Biot lente (cf. paragraphe suivant).

Si les travaux expérimentaux in situ ont souffert des faibles amplitudes enregistrées dans un contexte de bruit électromagnétique ambiant souvent défavorable, quelques études menées en laboratoire ont permis de confronter la théorie avec des données acquises à plus haute fréquence. Les premiers travaux en laboratoire ont été menés par Zhu et al. (1999) au MIT, qui ont acquis des signaux électriques aux fréquences ultrasonores dans des configurations de type forage sur des matériaux naturels et artificiels. Ils ont notamment conclu que l'amplitude et le contenu fréquentiel des signaux recueillis (dont l'origine est peu claire d'un point de vue extérieur) dépendait à la fois des propriétés de l'onde sismique mais également de la perméabilité et de la conductivité électrique des formations. Chen et Mu (2005) ont montré que les signaux co-sismiques semblaient avoir une forte sensibilité à la salinité et ont réussi à mesurer des signaux électriques provenant de conversions sismo-EM au travers de différentes interfaces présentant

des transitions de nature de fluide saturant (huile/eau salée). La sensibilité à la concentration de l'électrolyte a été revisitée par Block & Harris (2006) à des fréquences de l'ordre de la centaine de kHz. Ils ont pu montrer la bonne cohérence des amplitudes retrouvées avec le modèle proposé par Pride (1994) dans une large gamme de conductivités du fluide. La première expérience menée sur les effets sismo-magnétiques a été publiée par Zhu & Toksöz (2005). Cependant les différents choix instrumentaux effectués lors de cette expérience rendent probables des interactions électromagnétiques entre sources et récepteurs, ce qui pourrait expliquer les fortes amplitudes sismo-magnétiques observées, qui s'avèrent largement supérieures à celles attendues par la théorie. En parallèle à ces travaux, la thèse de C. Bordes (2005) a porté sur la mise au point d'une expérience originale menée dans le laboratoire à très bas Bruit de Rustrel. La conception d'une source adaptée lui a permis d'étudier la dépendance forte des signaux co-sismiques à la teneur en eau et également de faire des mesures convaincantes de signaux sismo-magnétiques co-sismiques. Une partie de ces travaux est résumée dans le paragraphe suivant.

Au niveau numérique, la non prise en compte des effets 2D constitue un point de blocage pour la compréhension des données acquises dans des milieux hétérogènes ou à géométrie plus réaliste que stratifiée. Ainsi, dans ces cas plus complexes, on ne sait prédire à l'heure actuelle l'origine spatiale des signaux sismo-EM convertis à une interface rugueuse ou 2D ou par un point diffractant, et encore moins leur diagramme de radiation et leurs attributs (propriétés spectrales, amplitude). Ce manque de codes de calculs 2D a également bloqué l'analyse réaliste d'acquisitions en configurations de transmission ou en forage. En effet, de part le caractère 1D de la géométrie des couches prise en compte dans le code disponible (Garambois & Dietrich, 2002), seuls des milieux homogènes peuvent être simulés pour ces configurations. Ceci freine non seulement la compréhension de données acquises, mais également l'avènement de techniques originales de traitement des signaux.

Pour contourner ce blocage, plusieurs auteurs ont tenté de modéliser ces effets en 2D. Haines & Pride (2006) ont utilisé un code de différences finies pour simuler ces effets dans des milieux hétérogènes non stratifiés. Pour cela, le champ sismique est modélisé par différences finies, tandis que la distribution de potentiel électrique est calculée à chaque pas de temps à partir des équations de couplage. Cette démarche ne prend donc pas en compte l'ensemble des équations couplées et ne permet pas de séparer les contributions co-sismiques de celles converties aux interfaces, ce qui rend difficile toute tentative d'étude de ces dernières, de part leur faible amplitude. Cette approche en temps, qui empêche également la prise en compte réaliste des effets dispersifs, leur a tout de même permis de mieux appréhender les causes et les effets des conversions sismo-EM dans certains cas 2D et en forage. Le traitement unifié des cas élastiques, acoustiques et électromagnétiques a été proposé par White & Zhou (2006) en utilisant la théorie des rais. Leur approche très mathématique s'est cependant bornée à montrer la relation linéaire reliant les magnitudes sismoélectriques ou électrosismiques et le coefficient de couplage électrocinétique, sans vraiment s'attaquer aux problèmes physiques générées par des milieux complexes. Zyserman et al. (2009) ont présenté un algorithme basé sur les éléments finis pour étudier les conversions électrosismiques dans un milieu 2D mais cette approche de numéricien n'apporte pas vraiment de réponse sur les phénomènes en jeu. Très récemment, Revil & Jardani (2010) ont développé une approche 2D à l'aide du logiciel COMSOL, qui utilise la technique des éléments finis. Ils réussissent ainsi à simuler la réponse sismo-électrique d'un matériau saturé par un fluide viscoélastique ou Newtonien, et prennent en compte les effets de relaxation. Prenant un cas d'application pétrolière, ils montrent qu'une nouvelle onde S résonne électriquement au niveau d'une structure enfouie, par couplage électrocinétique. Dans un article relativement concomitant, Jardani & Revil (2010) développent à partir de la modélisation directe présentée ci-avant un algorithme d'inversion stochastique. Celui-ci leur permet d'inverser conjointement des données synthétiques sismiques et sismo-électrique, en 2D, dans un cas relativement simple géométriquement. Si la porosité est mal contrainte, ils concluent que la perméabilité est assez

bien approchée par cette méthode, malheureusement relativement peu détaillée et validée. Enfin, Kröger et al. (2009) présentent une approche relativement semblable de modélisation par éléments finis dans le domaine temporel, toujours avec COMSOL et également en prenant une approximation basse-fréquence qui ne prend pas en compte les phénomènes dispersifs. Ils se focalisent sur l'étude des paramètres physiques influençant la réponse des ondes EM converties sur des structures 2D enfouies et montrent notamment leur capacité dans les applications pétrolières et environnementales.

2.2 Travaux effectués sur le sujet

Depuis le travail de thèse décrit en introduction, j'ai continué à m'intéresser à ces phénomènes, ce qui a donné lieu à quelques publications, dont certaines sont présentées ci-après, tandis que d'autres études sont actuellement en cours.

2.2.1 Influence de l'onde de Biot sur les amplitudes des ondes converties sismo-électromagnétiques et autres propriétés.

Dans un premier article (Pride & Garambois, 2002), nous avons numériquement modélisé les champs EM générés lorsqu'une onde sismique sphérique traverse une interface, en prenant en compte puis en négligeant l'onde de Biot lente. Cette omission a été possible en revisitant les équations poro-élastiques et notamment les équations constitutives dans lesquelles les termes de mouvement relatif fluide/solide on pu être supprimés. Nous avons ainsi montré le rôle essentiel de l'onde de Biot dans le calcul des amplitudes de champs sismo-EM convertis à une interface. La conclusion est qu'il n'est pas possible de modéliser correctement leurs attributs sans prendre en compte la génération de l'onde de Biot convertie à une interface, particulièrement lorsque l'onde sismique incidente est une onde de compression. C'est la seule manière de rendre compte des gradients de pression fluide au voisinage d'une interface, dont dépendent fortement les séparations de charges électriques générées de manière électrocinétique et qui vont contrôler les amplitudes sismo-EM. De manière intéressante, dans son dernier article concernant la théorie de l'acoustique linéaire, Biot (1962) conclut par une discussion sur le rôle de sa théorie dans la modélisation des phénomènes électrosismiques : « *un aspect intéressant de ce phénomène électrosismique est l'importance relative de l'onde lente par rapport à l'onde rapide. Nous avons montré que l'onde lente est associée à une plus forte vitesse relative du fluide dans les pores. Ceci doit avoir un effet important sur l'effet électrocinétique* ». Le papier présenté ci-après confirme quantitativement les prédictions qualitatives de Biot, 40 ans plus tard.

Dans un second article présenté ci-après, nous avons revisité quelque peu la théorie de Frenkel (1944) qu'il avait édifiée sur l'acoustique en milieu poroélastique en la comparant avec la théorie de Biot (1956a, 1956b) et déterminé les raisons des différences entre les deux approches (Pride & Garambois, 2005). Nous déterminons également si l'analyse de Frenkel portant sur les champs électriques co-sismiques est correcte. Comme il n'avait pas considéré d'ondes sismo-EM converties à des interfaces, nous en profitons pour présenter des propriétés de ces effets. A partir d'une étude paramétrique numérique, nous montrons notamment que la présence de couches fines dans le sous-sol peut amplifier la séparation des charges électriques lorsqu'une onde sismique la traverse, ce qui amplifie dans certains cas l'amplitude d'une onde sismo-EM converties à une interface. Cette observation devra à l'avenir être comparée avec des expériences contrôlées en laboratoire. De même nous avons étudié la réponse électrique dans générée dans une croûte poreuse uniforme par une dislocation en cisaillement d'une surface de glissement (modèle de faille). Ceci nous a permis de montrer que l'amplitude de ce signal électrique ainsi que sa dissipation étaient potentiellement observables par rapport au bruit. Cet effet pourrait ainsi expliquer les champs électriques co-sismiques enregistrés par endroits.

The role of Biot slow waves in electroseismic wave phenomena

Steven R. Pride^{a)}

Université de Rennes 1, Géosciences Rennes, Campus Beaulieu, Bât. 15, 35042 Rennes Cedex, France

Stéphane Garambois^{b)}

IGP, Université de Pau et des Pays de l'Adour, 64000 Pau Cedex, France

(Received 11 July 2001; revised 18 September 2001; accepted 22 November 2001)

The electromagnetic fields that are generated as a spherical seismic wave (either P or S) traverses an interface separating two porous materials are numerically modeled both with and without the generation of Biot slow waves at the interface. In the case of an incident fast- P wave, the predicted electric-field amplitudes when slow waves are neglected can easily be off by as much as an order of magnitude. In the case of an incident S wave, the error is much smaller (typically on the order of 10% or less) because not much S -wave energy gets converted into slow waves. In neglecting the slow waves, only six plane waves (reflected and transmitted fast- P , S , and EM waves) are available with which to match the eight continuity conditions that hold at each interface. This overdetermined problem is solved by placing weights on the eight continuity conditions so that those conditions that are most important for obtaining the proper response are emphasized. It is demonstrated that when slow waves are neglected, it is best to also neglect the continuity of the Darcy flow and fluid pressure across an interface. The principal conclusion of this work is that to properly model the electromagnetic (EM) fields generated at an interface by an incident seismic wave, the full Biot theory that allows for generation of slow waves must be employed. © 2002 Acoustical Society of America. [DOI: 10.1121/1.1436066]

PACS numbers: 43.20.Gp, 43.20.Bi, 43.30.Ky [JJM]

I. INTRODUCTION

Biot's (1956a, b, 1962a, b) theory of mechanical wave propagation in porous materials is the proper general framework for studying the effects of fluid movement into and out of each element of the porous material during the passage of a seismic wave (either P or S). The theory provides a set of differential equations for predicting the average displacement \mathbf{u} of the grains in each element as well as the average "fluid-filtration" displacement \mathbf{w} defined so that $\partial\mathbf{w}/\partial t$ corresponds to the Darcy filtration velocity in each element. By allowing for the dynamics controlling both the fluid and solid responses, the theory predicts the existence of two longitudinal modes, the so-called "fast" and "slow" P waves. For the problem of seismic wave propagation in the earth for which frequencies are generally below the kHz level, the slow- P wave is essentially a pure fluid-pressure diffusion through the pores of the material, while the fast- P wave is the compressional wave observed on seismograms.

As will be shown here, it is possible to completely eliminate slow waves from Biot's theory by requiring that the linear relation between $\nabla \cdot \mathbf{u}$ and $\nabla \cdot \mathbf{w}$ is everywhere that appropriate to fast- P waves. The price paid in neglecting slow waves is that the boundary conditions at isolated interfaces can never be exactly satisfied. Stated more generally, if slow waves are neglected, the response determined in heterogeneous porous continua can never be exact. However, since not much energy goes into slow-wave generation at isolated

interfaces one may ask whether the error made in neglecting slow waves is significant.

One known situation in which the neglect of slow waves leads to a significant error (White *et al.*, 1975; Norris, 1993; Gurevich and Lopatnikov, 1995; Gelinsky and Shapiro, 1997; Gelinsky *et al.*, 1998; Pride *et al.*, 2002) is when the porous material possesses fine layering relative to the fast- P wavelength. Since many layers are being compressed (or expanded) simultaneously by the fast- P wave and since each layer will have, in general, a different fluid-pressure response, there is a fluid-pressure-diffusion or "slow-wave-mediated" equilibration process set up between adjacent layers that can attenuate significant amounts of energy, especially at low frequencies. An analogous situation is Johnson's (2001) treatment of the patchy saturation problem. In both cases, the full Biot theory is required to properly model the fluid-pressure equilibration induced within an averaging volume. The Biot theory in these cases describes the local physics and upon averaging yields a macroscopic theory of viscoelasticity.

A central purpose of the present article is to give an example of a situation in which the macroscopic response itself requires a direct macroscopic modeling of the slow waves. When either P or S waves traverse interfaces in a porous material they generate electromagnetic (EM) fields through an electrokinetic mechanism (Thompson and Gist, 1993; Pride, 1994; Pride and Haartsen, 1996; Haartsen and Pride, 1997; Garambois and Dietrich, 2001; Garambois and Dietrich, 2002). Such seismic-to-EM coupling is called "electroseismic" phenomena. In the present article, we numerically model the EM field generated when a spherical seismic wave is incident at an interface. We perform the

^{a)}Electronic mail: spride@univ-rennes1.fr

^{b)}Electronic mail: Stephane.Garambois@ujf-grenoble.fr; present address LIRIGM, Université Joseph Fourier, BP 53, 38041, Grenoble Cedex 9, France.

simulations both with and without slow waves and demonstrate the essential role played by slow waves in fixing the amplitudes of such seismic-to-EM converted wave fields. The conclusion is that one cannot properly model the converted EM fields without allowing for slow waves.

Interestingly, the first paper that provided a quantitative theory for seismic waves in porous materials (Frenkel, 1944) had as its goal the explanation of electroseismic phenomena; however, Frenkel's formulation only allowed for the coseismic E-fields (those contained within the support of the seismic wave) and did not allow for any converted E-fields generated, for example, as a seismic wave traverses an interface. A further historical curiosity is that in Biot's final article concerning his linear theory of porous-media acoustics (Biot, 1962b), he concludes with a discussion of the role of his theory in modeling electroseismic phenomena. What follows are the final three sentences of Biot's (1962b) article:

An interesting aspect of this [electroseismic] phenomena is the relative importance assumed by the wave of the second kind [the slow wave] as compared to the wave of the first kind [the fast wave]. We have shown that the wave of the second kind is associated with a larger relative velocity of the fluid in the pores. This should have an important bearing on the electrokinetic effect.

The present article quantitatively confirms Biot's prediction.

II. DEFINING ELECTROSEISMIC RESPONSE

The governing equations controlling the complete electroseismic response when an $e^{-i\omega t}$ time dependence is assumed have been determined by Pride (1994)

$$\nabla \cdot \boldsymbol{\tau} = -\omega^2 \rho \mathbf{u} - \omega^2 \rho_f \mathbf{w}, \quad (1)$$

$$\boldsymbol{\tau} = -p_c \mathbf{I} + G[\nabla \mathbf{u} + (\nabla \mathbf{u})^T - \frac{2}{3} \nabla \cdot \mathbf{u} \mathbf{I}] \quad (2)$$

$$-\begin{bmatrix} p_c \\ p_f \end{bmatrix} = \begin{bmatrix} K_G & C \\ C & M \end{bmatrix} \cdot \begin{bmatrix} \nabla \cdot \mathbf{u} \\ \nabla \cdot \mathbf{w} \end{bmatrix} \quad (3)$$

$$-i\omega \mathbf{w} = \frac{k(\omega)}{\eta} [-\nabla p_f + \omega^2 \rho_f \mathbf{u}] + L \mathbf{E}, \quad (4)$$

$$\mathbf{J} = L[-\nabla p_f + \omega^2 \rho_f \mathbf{u}] + \sigma \mathbf{E}, \quad (5)$$

$$\nabla \times \mathbf{E} = i\omega \mu \mathbf{H}, \quad (6)$$

$$\nabla \times \mathbf{H} = -i\omega \varepsilon \mathbf{E} + \mathbf{J}. \quad (7)$$

Here, \mathbf{u} and \mathbf{w} are the displacements defined in the Introduction, while p_f is the average fluid pressure in the pores of an averaging element. The remaining response fields p_c , $\boldsymbol{\tau}$, \mathbf{E} , \mathbf{H} , and \mathbf{J} represent averages throughout both the fluid and solid phases of each averaging element and are, respectively, the bulk pressure, stress tensor, electric field, magnetic field, and electric-current density at each point in the porous continuum. Definition of the various coefficients is given by Pride (1994) and are modeled here in the Appendix. If the electrokinetic-coupling constant L is set to zero, these equations exactly separate into Biot's equations and Maxwell's equations. By integrating each of the above equations over a disk that straddles an initially uncharged interface, it is easy

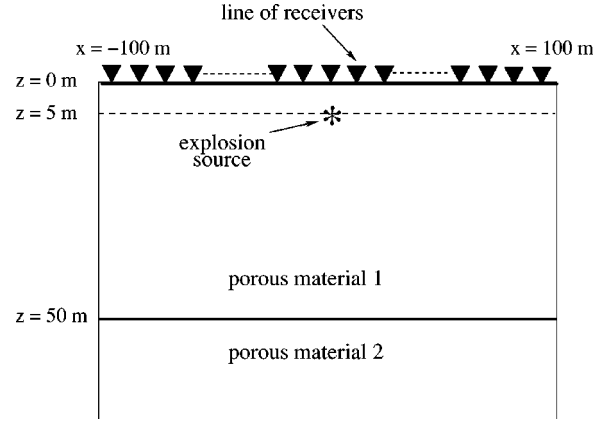


FIG. 1. The source, interface, and receiver locations used for all examples of this paper. There is no free surface at $z=0$ m.

to establish [Pride and Haartsen (1996)] that the quantities

$$\mathbf{n} \cdot \boldsymbol{\tau}, \quad \mathbf{u} \cdot \mathbf{n}, \quad \mathbf{n} \cdot \mathbf{w}, \quad -p_f, \quad \mathbf{n} \times \mathbf{E}, \quad \mathbf{n} \times \mathbf{H} \quad (8)$$

must all be continuous across an interface possessing a normal \mathbf{n} . Generalization to the case of an initially charged interface is given by Pride and Haartsen (1996).

Consider a spherical compressional wave propagating through a homogeneous porous material. A streaming electrical current $L(-\nabla p_f + \omega^2 \rho_f \mathbf{u})$ is set up from regions of compression toward regions of dilation that results in an accumulation of charge of one sign in the peaks of the wave and of the opposite sign in the troughs. The \mathbf{E} field associated with such half-wavelength scale charge separations then drives a conduction current $\sigma \mathbf{E}$ that exactly balances the streaming current so there is no net current inside the compressional wave. The charge density $\rho_e(\mathbf{r})$ within the support of the seismic wave is given by $\rho_e = \varepsilon \nabla \cdot \mathbf{E}$ so that from Eq. (5) we have $\rho_e = -(\varepsilon L / \sigma) \nabla \cdot (-\nabla p_f + \omega^2 \rho_f \mathbf{u})$. Volume integrating $\nabla \cdot \mathbf{E} = \rho_e / \varepsilon$ over a Gaussian box that straddles the wavefront and completely contains the support of the seismic pulse, and using the fact that the volume integral of the charge density is zero (the wave separates charge but does not create charge) demonstrates that no electric fields are present outside the support of the compressional wave.

However, when the spherical wave is incident at an interface separating two different porous materials, the charge density distributed within the transmitted wave will be different, in general, than the charge density distributed in the combined incident and reflected pulses. This breaks the symmetry of the charge distribution that held before the spherical wave encountered the interface. There is thus created an effective charge separation (having a strong dipolar component) across the interface as the first Fresnel zone of the pulse traverses the interface. The electric fields generated by this dipole can be recorded at large distances from the interface.

These effects are now demonstrated numerically for the situation depicted in Fig. 1, in which a single plane interface is located at $z=50$ m and a point explosion source is located at $z=5$ m. Geophones and electrical and magnetic antennas are placed every 4 meters along a receiver line at $z=0$ m. Details of the numerical reflectivity algorithm that solves

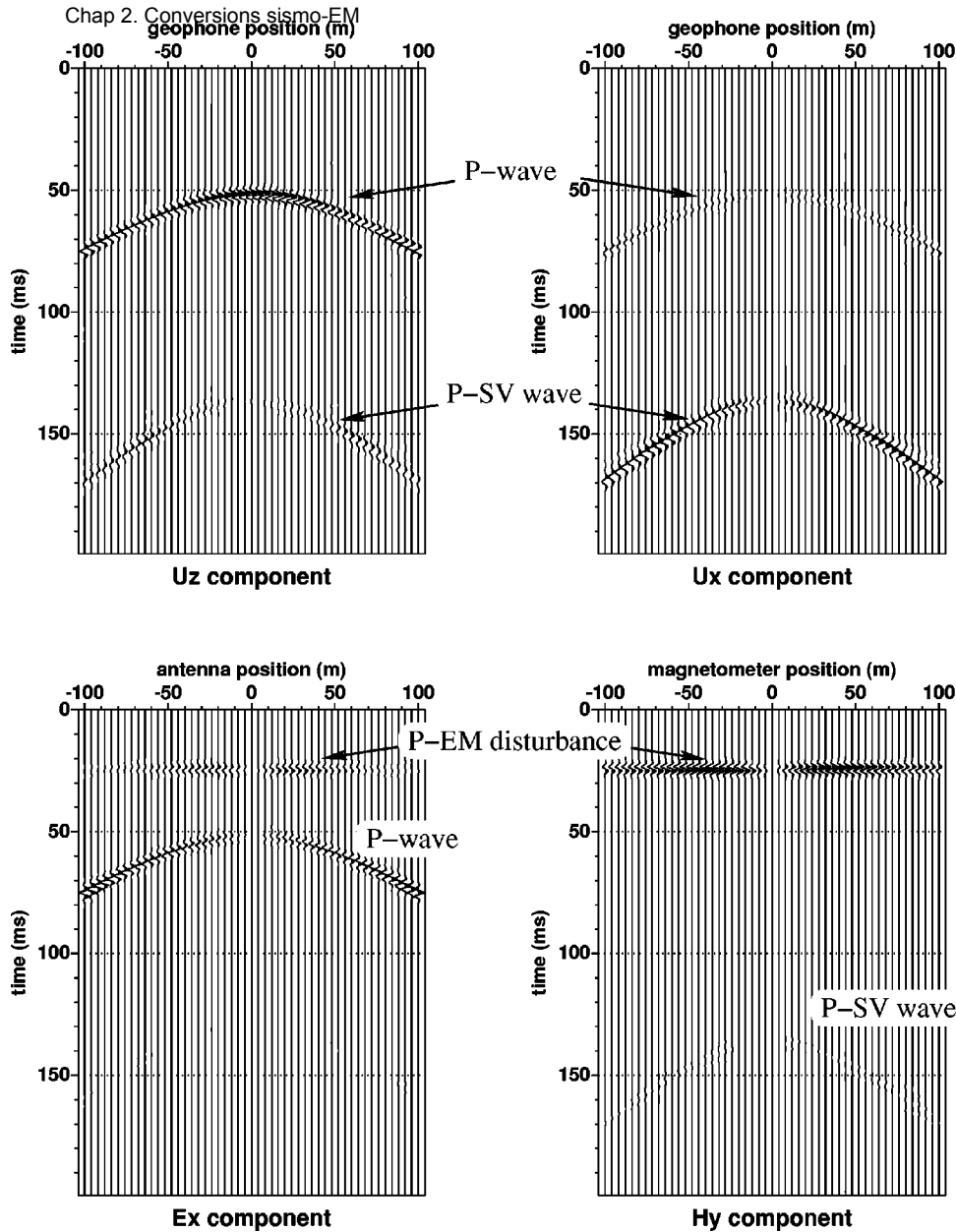


FIG. 2. An example of electroseismic response. The interface is located at a *P*-wave travel time of 21 ms. The no-moveout *P*-EM converted field generated as the *P* wave traverses the interface has been multiplied by 500 in both the electric and magnetic sections. The *P*-*SV* conversion is just barely discernible on the magnetic section (the hyperbola at 132 ms).

Eqs. (1)–(7) while respecting the continuity conditions at each interface will be given later. The upper half-space is modeled as a sand while the lower half-space is modeled as a sandstone. Details of how we fix the material properties will also be given later.

In Fig. 2 are shown the displacements and electric and magnetic fields that are recorded along the line at $z=0$ m. We do not show the response of the direct *P* wave that travels in straight-line trajectory from the source to the receivers. At a time of $t=21$ ms, the *P* wave is incident at the interface and generates the symmetry-breaking charge separation discussed above. The associated electric and magnetic fields have essentially no moveout on the seismic time scale, as seen in the figure. For display purposes, such *P*-EM converted fields have been multiplied by a factor of 500 in both the electric and magnetic sections. At the interface, the *P* wave is reflected both into another *P* wave and an *S* wave. We observe the electric and magnetic fields contained within these reflected waves when they arrive at the antennas.

The no-moveout electric fields generated at the interface by the *P* wave are the fields of predominant interest in an electroseismic study. In the present example, these fields have an amplitude of about $10 \mu\text{V/m}$ along the receiver line at $z=0$ and are quite detectable in the field (e.g., Thompson and Gist, 1993). These converted EM fields are highly sensitive to the precise details of the fluid-pressure gradients in the immediate vicinity of the interface. The goal of this paper is to study the role played by Biot slow waves in fixing the amplitude of such no-moveout converted electric fields.

III. ELECTROSEISMIC RESPONSE WITHOUT SLOW WAVES

A. Analytical considerations

If we place the transport equations for $-i\omega\mathbf{w}$ and \mathbf{J} [Eqs. (4) and (5)] into their respective dynamical equations

[Eqs. (1) and (6)] and if we use Faraday's law in Ampère's law, we can write without approximation the two dynamical equations

$$\nabla \cdot \boldsymbol{\tau} - i\omega \frac{\rho_f k(\omega)}{\eta} \nabla p_f + \omega^2 \rho \left(1 - i\omega \frac{\rho_f^2 k(\omega)}{\rho \eta} \right) \mathbf{u} = -i\omega \rho_f L \mathbf{E} \quad (9)$$

$$-\nabla \times \nabla \times \mathbf{E} + \omega^2 \varepsilon \left(1 + \frac{i\sigma}{\omega \varepsilon} \right) \mathbf{E} = -i\omega \mu L (-\nabla p_f + \omega^2 \rho_f \mathbf{u}) \quad (10)$$

that control the electroseismic response. The right-hand sides of these equations isolate the source terms responsible for cross coupling between the mechanical and electrical response.

Our approximation of neglecting slow- P waves amounts to writing a single additional relation

$$\nabla \cdot \mathbf{w} = \beta_L \nabla \cdot \mathbf{u}, \quad (11)$$

where an expression for β_L appropriate to fast- P waves will soon be derived. Note that the equivoluminal shear response also trivially satisfies this equation. The neglect of slow waves only affects the poroelastic constitutive laws, which are now given by

$$\boldsymbol{\tau} = (K_G + C\beta_L) \nabla \cdot \mathbf{u} \mathbf{I} + G[\nabla \mathbf{u} + (\nabla \mathbf{u})^T - \frac{2}{3} \nabla \cdot \mathbf{u} \mathbf{I}] \quad (12)$$

$$-p_f = (C + M\beta_L) \nabla \cdot \mathbf{u}. \quad (13)$$

Upon placing these "slow-wave-free" constitutive laws into the dynamical equations, we find that \mathbf{u} and \mathbf{E} are the only two independent fields to solve for. Simply by writing Eq. (11), \mathbf{w} has been completely eliminated from the theory. Note, however, that \mathbf{w} can still be determined from Eq. (4) if desired; i.e., our neglect of slow waves has not required that $\mathbf{w} = 0$.

In the special case of a uniform porous material, the governing equations reduce to

$$[K_E(\omega) + G/3] \nabla \nabla \cdot \mathbf{u} + G \nabla^2 \mathbf{u} + \omega^2 \rho_E(\omega) \mathbf{u} = -i\omega \rho_f L \mathbf{E} \quad (14)$$

$$-\nabla \times \nabla \times \mathbf{E} + \omega^2 \mu \varepsilon_E(\omega) \mathbf{E} = -i\omega \mu L [(C + M\beta_L) \nabla \nabla \cdot \mathbf{u} + \omega^2 \rho_f \mathbf{u}]. \quad (15)$$

When $L=0$, these are the usual elastodynamic and electromagnetic wave equations in a material having effective properties given by

$$K_E(\omega) = (K_G + C\beta_L) \left[1 + i\omega \frac{\rho_f k(\omega)}{\eta} \frac{C + M\beta_L}{K_G + C\beta_L} \right], \quad (16)$$

$$\rho_E(\omega) = \rho \left[1 - i\omega \frac{\rho_f^2 k(\omega)}{\rho \eta} \right], \quad (17)$$

$$\varepsilon_E(\omega) = \varepsilon \left[1 + \frac{i\sigma}{\omega \varepsilon} \right]. \quad (18)$$

Upon temporarily neglecting the electrokinetic coupling L , we obtain the complex compressional wave slowness s_p given by

$$s_p^2 = \frac{\rho_E(\omega)}{K_E(\omega) + 4G/3}. \quad (19)$$

The modification of this wave slowness due to the coupling coefficient L is, for all practical purposes, negligible [see Pride and Haartsen (1996) for both a discussion and exact expressions and numerical evaluations in the case where L is not neglected]. The coefficient β_L can be found by first taking the divergence of Eq. (1) to obtain

$$\nabla^2 \left[\left(K_G + \frac{4G}{3} \right) \nabla \cdot \mathbf{u} + C \nabla \cdot \mathbf{w} \right] = -\omega^2 \rho \nabla \cdot \mathbf{u} - \omega^2 \rho_f \nabla \cdot \mathbf{w}. \quad (20)$$

For a plane P wave with spatial dependence $\exp(i\omega s_p \hat{\mathbf{k}} \cdot \mathbf{r})$ where $\hat{\mathbf{k}}$ is the propagation direction, we thus obtain

$$\beta_L \equiv \frac{\nabla \cdot \mathbf{w}}{\nabla \cdot \mathbf{u}} = -\frac{H s_p^2(\omega) - \rho}{C s_p^2(\omega) - \rho_f}, \quad (21)$$

where for convenience we have introduced Biot's H modulus defined as

$$H = K_G + 4G/3. \quad (22)$$

Upon eliminating s_p^2 in Eq. (21) by introducing Eq. (19), we obtain the following quadratic equation for β_L :

$$a\beta_L^2 + b\beta_L + c = 0, \quad (23)$$

where the three coefficients are defined

$$a = C + i\omega \rho_f \frac{k}{\eta} M, \quad (24)$$

$$b = H + i\omega \rho_f \frac{k}{\eta} \left(2C + \frac{\rho}{\rho_f} M \right), \quad (25)$$

$$c = i\omega \rho_f \frac{k}{\eta} \left(H + \frac{\rho}{\rho_f} C \right). \quad (26)$$

The two roots correspond to the β_L for fast waves and slow waves. The fast-wave root of interest here is easily seen to be

$$\beta_L = -\frac{b}{2a} \left(1 - \sqrt{1 - \frac{4ac}{b^2}} \right). \quad (27)$$

For P waves in the seismic band of frequencies, we always have that $\omega \rho_f k / \eta \ll 1$, which allows us to write

$$\beta_L \rightarrow -i\omega \rho_f \frac{k}{\eta} \left(1 + \frac{\rho}{\rho_f} \frac{C}{H} \right) \quad (28)$$

to leading order in the small dimensionless quantity $\omega \rho_f k / \eta$.

We have thus shown that our approximation of neglecting slow- P waves amounts to working with Eqs. (14) and (15) in each piecewise homogeneous portion of the porous material. The fast- P and S waves that are retained in this approximation have all the properties they usually have in Biot theory. But, by taking the β_L to be everywhere appropriate to fast- P waves, no slow waves can ever come into existence. The equation $\nabla \cdot \mathbf{w} = \beta_L \nabla \cdot \mathbf{u}$ is an additional constraint placed on the exact governing equations Eqs. (1)–(7) and in no way alters the requirement that all of the components in Eq. (8) should be continuous at an interface. There-

fore, the question of what continuity conditions to take at an interface when slow waves are neglected may not, at first sight, be entirely clear-cut.

However, in order that both P - SV and EM disturbances properly propagate across interfaces, we need to take the standard requirement that all of

$$\mathbf{u}, \mathbf{n} \cdot \boldsymbol{\tau}, \mathbf{n} \times \mathbf{E}, \mathbf{n} \times \mathbf{H} \quad (29)$$

remain continuous when slow waves are neglected. This will be demonstrated numerically in the following subsection. Thus, when slow waves are neglected both p_f and $\mathbf{n} \cdot \mathbf{w}$ suffer jumps at interfaces.

Such an artificial jump in the fluid pressure at an interface created when slow waves are neglected has the effect of producing an effective electric dipole, as can be seen from the right-hand side of Eq. (10). Consider the extreme case of an interface in which only the permeability k changes with all other material properties held constant. In the exact treatment of the electroseismic response, the permeability contrast generates both transmitted and reflected slow waves. These slow waves alter the charge distribution that held in the spherically incident fast- P wave just prior to incidence and thus create an effective electric dipole (and higher-order multipoles) across the interface. The fast- P wave itself is not affected much by the permeability interface since never more than a few percent of the incident wave energy gets converted into slow waves (and typically much less). One might think, in this particular case, that the neglect of slow waves would lead to a large error in the predicted no-moveout electric field since it is the slow waves that have created the effective dipole.

However, as noted above, the jump in fluid pressure created when slow waves are neglected also produces an electric dipole. The fluid-pressure jump may be estimated from Eq. (13) using the fact that the permeability contrast has essentially no impact on the mechanical response of the fast- P and $-S$ waves so that $\nabla \cdot \mathbf{u}$ remains essentially continuous at the interface (indeed, exactly continuous in the limit of very small frequencies). Upon using the β_L given by Eq. (28), we predict that the fluid pressure in the immediate vicinity of an interface located at $z=z_0$ is, in the low-frequency limit, distributed as

$$p_f(z) = i\omega \frac{\rho_f}{\eta} M \left(1 + \frac{\rho}{\rho_f} \frac{C}{H} \right) \nabla \cdot \mathbf{u} [k_1 + (k_2 - k_1)H(z - z_0)], \quad (30)$$

where $H(z)$ is the Heaviside function, k_1 is the permeability of the overlying region, and k_2 that of the underlying region. We thus have that on the right-hand side of Eq. (10), there is an effective current dipole source \mathbf{J}_e given by

$$\mathbf{J}_e = \omega^2 \mu L \frac{\rho_f}{\eta} M \left(1 + \frac{\rho}{\rho_f} \frac{C}{H} \right) \nabla \cdot \mathbf{u} (k_2 - k_1) \delta(z - z_0) \hat{\mathbf{z}}. \quad (31)$$

We will see in a later numerical example that this effective electric dipole generated by the jump in fluid pressure when slow waves are neglected at a permeability contrast does a reasonable job at estimating the effects of the exact response involving slow waves. However, it will also be seen that

when jumps in the elastic properties are also allowed for, the neglect of slow waves can lead to huge errors in the amplitudes of the predicted no-moveout electric fields.

B. Numerical considerations

We now show how to neglect slow waves in the numerical modeling. Both Haartsen and Pride (1997) and Garambois and Dietrich (2002) have given algorithms for determining the exact point-source electroseismic response for waves in stratified materials. These codes are based on Kennett's (1983) scheme for modeling seismic waves in layered media and begin by decomposing the wave fields into their plane-wave (or, more precisely, cylindrical-wave) components. The various decomposed plane-wave amplitudes are then determined by requiring that the continuity conditions that hold at each interface in the layer stack are exactly satisfied. Thus, proper modeling of how plane waves reflect and transmit at an isolated interface is a key part of the analysis. In the following subsection, we outline how to obtain the reflection and transmission coefficients when slow waves are neglected.

1. The response at a plane interface

Working in an (x, y, z) Cartesian system, consider that a fast- P plane wave in porous-material 1 is incident at a plane interface that separates material 1 from a second porous-material 2. If this interface is uncharged prior to the arrival of the P wave, we then have that [cf. Eq. (8)]

$$\underline{\mathbf{b}} = [u_x, u_z, w_z, \tau_{xz}, \tau_{zz}, -p_f, H_y, E_x]^T \quad (32)$$

must be continuous across the interface (note that an underscore is used to denote an array while boldfaced symbols are used to denote vectorial and tensorial field quantities). Thus, at each interface we must satisfy the eight required equations $\underline{\mathbf{b}}_1 = \underline{\mathbf{b}}_2$. To exactly allow for all eight of these conditions, one must allow for the creation of eight distinct waves which are the reflected and transmitted fast- P , slow- P , S , and EM responses. This is what Haartsen and Pride (1997) and Garambois and Dietrich (2002) have done. Without the slow waves we cannot exactly satisfy all eight continuity conditions, and our goal is to quantify the amount of error this causes in the predicted no-moveout electric fields.

The full 8×8 eigenvector matrix $\underline{\underline{D}}$ appropriate to the electroseismic problem (e.g., Haartsen and Pride, 1997) has the form

$$\underline{\underline{D}} = [\mathbf{b}_{pf}^u, \mathbf{b}_{ps}^u, \mathbf{b}_s^u, \mathbf{b}_{em}^u, \mathbf{b}_{pf}^d, \mathbf{b}_{ps}^d, \mathbf{b}_s^d, \mathbf{b}_{em}^d], \quad (33)$$

where each column is the normalized plane-wave response of the stated wave type [e.g., \mathbf{b}_{ps}^d is the response of a unit-amplitude downgoing slow- P wave where the physical components of $\underline{\mathbf{b}}$ are those defined in Eq. (32)]. Analytical expressions for these various columns were initially worked out by Pride and Haartsen (1996) and are also given in Haartsen and Pride (1997). We now simply eliminate the two slow-wave columns and attempt to approximate the complete material response in each layer with only six wave types. In other words, with the definitions

$$\underline{\underline{D}}^{8 \times 6} = [\mathbf{b}_{pf}^u, \mathbf{b}_s^u, \mathbf{b}_{em}^u, \mathbf{b}_{pf}^d, \mathbf{b}_s^d, \mathbf{b}_{em}^d], \quad (34)$$

Chap 2. Conversions sjsmo-EM

$$\underline{w} = [w_{pf}^u, w_s^u, w_{em}^u, w_{pf}^d, w_s^d, w_{em}^d]^T, \quad (35)$$

where the components of \underline{w} are the (complex) amplitudes of the six wave types being allowed for in the approximation, we attempt to find the amplitudes \underline{w} that best satisfy

$$\underline{D}^{8 \times 6} \cdot \underline{w} = \underline{b} \quad (36)$$

in each layer where \underline{b} is the eight-component array defined in Eq. (32).

For the specific problem in which a unit-amplitude fast- P wave is incident from above at a plane interface, the eight continuity conditions $\underline{b}_1 = \underline{b}_2$ are written

$$\begin{pmatrix} \underline{M}_1^u & \underline{M}_1^d \\ \underline{N}_1^u & \underline{N}_1^d \end{pmatrix} \cdot \begin{pmatrix} R_{pf} \\ R_s \\ R_{em} \\ 1 \\ 0 \\ 0 \end{pmatrix} = \begin{pmatrix} \underline{M}_2^u & \underline{M}_2^d \\ \underline{N}_2^u & \underline{N}_2^d \end{pmatrix} \cdot \begin{pmatrix} 0 \\ 0 \\ 0 \\ T_{pf} \\ T_s \\ T_{em} \end{pmatrix}, \quad (37)$$

where the matrices $\underline{M}^{u,d}$ and $\underline{N}^{u,d}$ are the 4×3 partitions of the eigenvector matrix $\underline{D}^{8 \times 6}$. These equations can be rewritten as the overdetermined system

$$\underline{A} \cdot \underline{x} = \underline{y}, \quad (38)$$

where \underline{A} is the 8×6 matrix

$$\underline{A} = \begin{pmatrix} \underline{M}_1^u & -\underline{M}_2^u \\ \underline{M}_1^d & -\underline{M}_2^d \\ \underline{N}_1^u & -\underline{N}_2^u \\ \underline{N}_1^d & -\underline{N}_2^d \end{pmatrix}, \quad (39)$$

\underline{x} contains the six unknown reflection and transmission coefficients of interest

$$\underline{x} = [R_{pf}, R_s, R_{em}, T_{pf}, T_s, T_{em}]^T, \quad (40)$$

and $\underline{y} = -\underline{b}_{pf}^d$ is the negative of the response (eigenvector) of a unit-amplitude downgoing fast- P wave (the normalizations of the eigenvectors fix the physical interpretation of the reflection and transmission coefficients but otherwise play no role in obtaining the numerical results).

We solve for the reflection and transmission coefficients \underline{x} by first placing weights p_i on each of the eight continuity conditions. These weights simply emphasize the importance given to satisfying any one condition. The only restriction on these weights is that no more than two of them can be zero so that the system never becomes underdetermined. Thus, following the usual least-squares argument, we determine \underline{x} by minimizing the χ^2 error measure

$$\chi^2 = \sum_{i=1}^8 \sum_{j=1}^6 [p_i (y_i - A_{ij} x_j)]^2. \quad (41)$$

As is well-known and simply demonstrated, the \underline{x} that minimizes χ^2 is a solution of the following even (6×6) set of "normal equations"

$$(\underline{A}^T \cdot \underline{\Lambda} \cdot \underline{A}) \cdot \underline{x} = (\underline{A}^T \cdot \underline{\Lambda}) \cdot \underline{y}, \quad (42)$$

where the diagonal matrix $\underline{\Lambda}$ has the weights p_i^2 along the diagonal and zeros elsewhere; i.e.,

$$\underline{\Lambda} = \text{diag}\{p_i^2\}. \quad (43)$$

In the subsection that follows, we numerically investigate the question of which two of the p_i are best set to zero; i.e., which of the continuity equations can be neglected without creating considerable error.

2. Defining the weighting scheme

Although we anticipate from our earlier analytical considerations that the best approximation is to neglect the continuity of w_z and p_f (i.e., $p_3 = p_6 = 0$), we now numerically test this hypothesis.

A solution of the normal equations (42) for any given weighting of the eight continuity conditions determines the reflection and transmission coefficients at each isolated interface in a layer stack when no slow waves have been generated. The reflection and transmission coefficients at each interface are the fundamental material-property inputs for Kennett's (1983) reflectivity scheme. Garambois and Dietrich (2002) have generalized the reflectivity scheme to the electroseismic problem, and it is their code that is employed for the numerical simulations that follow and in the electroseismic response already shown in Fig. 2. Haartsen and Pride (1997) used the global-matrix approach, which is slightly different and will not be used here.

We again consider the simple geometry depicted in Fig. 1. Details of how to model a point-source explosion are given by Haartsen and Pride (1997) as well as by Garambois and Dietrich (2002). A Ricker wavelet with a center frequency of 200 Hz is chosen as the time signature of the source. Due to the rather large number of physical properties, we give a model in the Appendix that reduces the total number of free parameters down to just four: C (the salinity of the water in moles/liter), ϕ (the porosity), a (a dimensionless parameter defined in the Appendix that measures the degree of consolidation of the framework of grains), and k_0 (the dc permeability). This model is based on assuming the fluid is always water and the solid grains are always quartz. The properties of our two half-spaces are thus fixed by fixing these four parameters in each material.

Both in the present test and in the response of Fig. 2, we take the overlying material to be a sand characterized by $C_1 = 10^{-4}$ moles/liter, $\phi_1 = 0.35$, $a_1 = 100$, and $k_{01} = 10^{-11}$ m². The underlying material is a sandstone characterized by $C_2 = 10^{-4}$ moles per liter, $\phi_2 = 0.20$, $a_2 = 10$, and $k_{02} = 10^{-14}$ m². In Fig. 3, we give the amplitude of the reflected P wave when slow waves are neglected and when continuity of the pairs of components shown has been neglected at the interface. As anticipated, the exact result involving slow waves is indistinguishable from the case where slow waves are neglected and the continuity of w_z and p_f is neglected. Any other approximation of the exact continuity conditions leads to unacceptable error. In Fig. 4 the amplitude of the converted no-moveout electric field generated when the P wave traverses the interface is shown. Although, in the no-slow-wave approximation, neglecting the continuity of w_z and τ_{zz} provides a slightly better approximation than neglecting w_z and p_f , we have seen in Fig. 3 that it provides a much worse approximation of the reflected P wave.

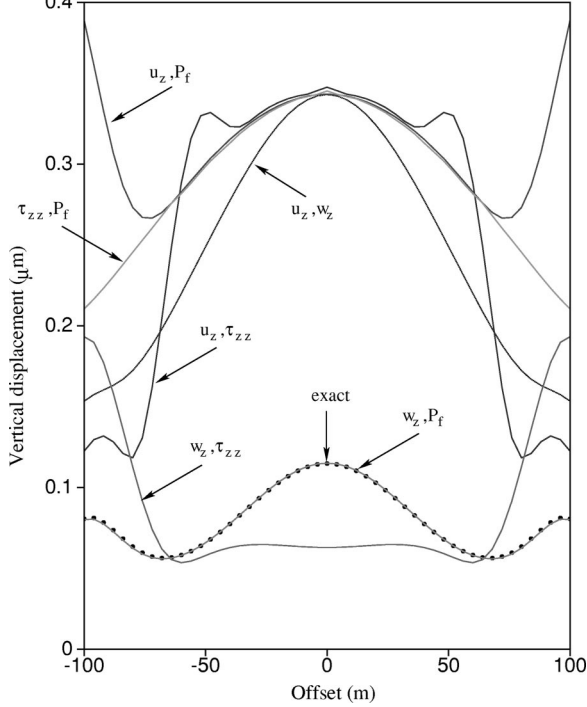


FIG. 3. The amplitude of the reflected P wave when slow waves are neglected and the continuity of the various shown displacement-stress components is neglected at the interface. The exact response with slow waves is shown both here and in all examples using dot symbols. This figure demonstrates that one must sacrifice the continuity of w_z and p_f when slow waves are neglected.

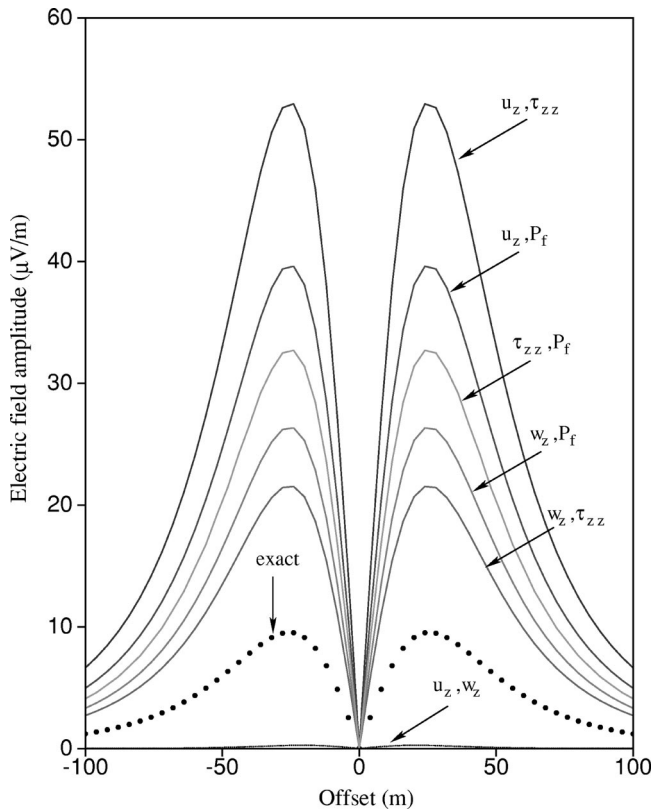


FIG. 4. The amplitude of the converted no-moveout electric field generated when the P wave is incident at the interface and recorded along the receiver line.

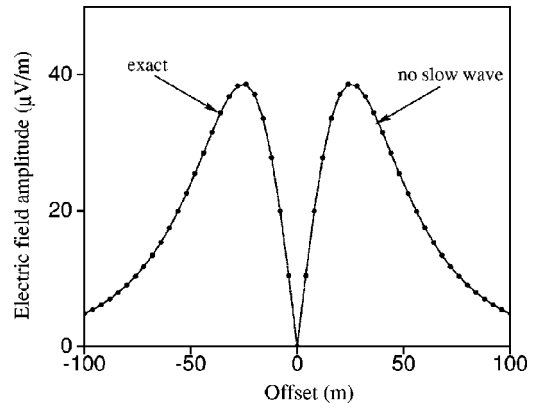


FIG. 5. The amplitude of the converted no-moveout electric field when the interface represents only a salinity jump.

The conclusion is that when slow waves are neglected, we must also neglect the continuity of w_z and p_f ; neglect of any other combination leads to unacceptably large error. We also see that for a realistically modeled sand/sandstone interface, the neglect of slow waves has led to a converted electric-field amplitude that is almost three times too big. Proper modeling of the converted electric field in this case requires the explicit generation of slow waves. We now go on to consider other examples.

IV. NUMERICAL EXAMPLES

Five examples will be given here that serve to further illustrate the role of slow waves in the generation of the electroseismic converted field. For all of these examples, the modeling without slow waves has neglected the continuity of w_z and p_f at the interface.

A. Salinity contrast

We begin with a test example in which the contrast is only in the salinity. In this case, there is no way for the fast- P wave to change properties as it traverses the interface, and so no slow waves are generated. Accordingly, we expect no slow-wave effect in the electroseismic response. The material properties are taken everywhere to be those of a sand: $\phi=0.35$, $a=100$, and $k_0=10^{-11} \text{ m}^2$. The salinity contrast is defined by $C_1=10^{-4}$ moles/liter and $C_2=10^{-1}$ moles/liter.

In Fig. 5, we see indeed that the modeling both with and without slow waves leads to virtually identical results. We take this to be a positive numerical check of our modeling.

B. Permeability contrast

This was the case considered earlier in our analytical discussion. For the numerical example, we take the material to have everywhere the same properties of $C=10^{-4}$ moles/liter, $\phi=0.35$, $a=100$, but we now take the overlying material to have a permeability of $k_{01}=10^{-11} \text{ m}^2$ and the underlying material to have a permeability of $k_{02}=10^{-14} \text{ m}^2$.

In Fig. 6 the somewhat surprising result that the result without slow waves is almost as good as the result with

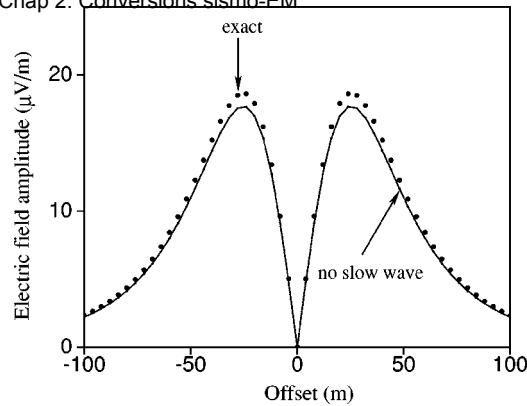


FIG. 6. The amplitude of the converted no-moveout electric field when the interface represents only a permeability jump.

slowwaves is seen. As discussed earlier, this is due to the artificial fluid-pressure jump in the modeling without slow waves acting as a current-dipole source in Ampère’s law. However, this result is rather particular and requires that the jump in permeability not be accompanied by a jump in the elastic properties, a situation that never holds true in the earth.

C. Elastic-property contrast

In this example, we keep both the permeability and salinity constant everywhere, given by $k_0 = 10^{-11} \text{ m}^2$ and $C = 10^{-4} \text{ moles/liter}$. The jump is only in the elastic properties with $\phi_1 = 0.35$, $a_1 = 100$ and $\phi_2 = 0.20$, $a_2 = 10$. See Fig. 7.

We see that there is now a rather large error of about a factor of 7 in the predicted converted electric-field amplitude.

D. Sandstone 1/sandstone 2 interface

In this example, we attempt to model a typical interface that might be found at depth in a sedimentary basin. The overlying material is taken to be a well-consolidated sandstone having $\phi_1 = 0.10$, $a_1 = 5$, and $k_{01} = 10^{-15} \text{ m}^2$, while the underlying material is taken to be a much cleaner sandstone having $\phi_2 = 0.25$, $a_2 = 50$, and $k_{02} = 10^{-13} \text{ m}^2$. The same salinity $C = 10^{-2} \text{ moles/liter}$ is present everywhere.

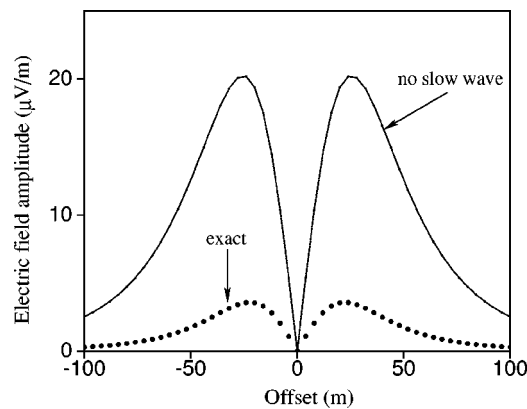


FIG. 7. The amplitude of the converted no-moveout electric field when the interface represents only a jump in elastic properties with permeability and salinity held constant.

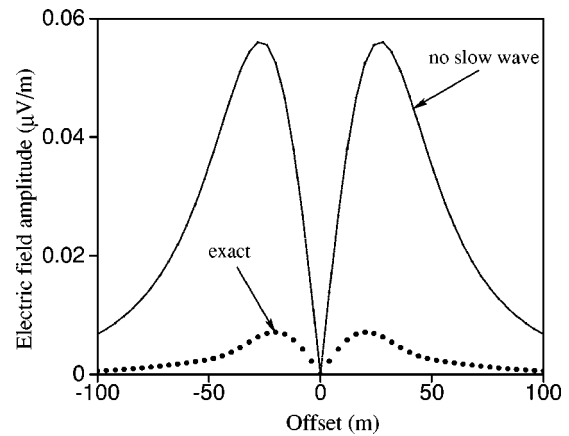


FIG. 8. The amplitude of the converted no-moveout electric field when the interface separates a well-consolidated sandstone from a relatively clean sandstone. This example is meant to represent a typical interface that might be found in a sedimentary basin.

In this case, the generation of both slow waves and the associated separation of charge is reduced compared to the previous examples due to both sides of the interface now having relatively stiff frameworks of grains. This is manifest in much smaller electric-field amplitudes. We again see in Fig. 8 that the full Biot theory is required in order to properly model the electroseismic response. The neglect of slow waves in this example has overestimated the converted electric field by more than a factor of 8. As compared to previous examples, the spatial distribution of the electric-field amplitudes with and without slow waves have different shapes. This is because the incident P -wave wavelength of roughly 17 m is much longer than in the previous examples and it now represents a significant fraction of the 45 m between the shot point and interface which changes the dimensions of the first Fresnel zone and the nature of the charge distribution relative to the antenna positions.

E. Incident shear wave

In this final example, a hammer source is now used that generates both compressional and shear waves. Our interest here is to study the EM conversion generated when the shear wave is incident at the interface. We consider the same sand/sandstone interface used in Figs. 2–4. With a shear wave incident at the interface, there is a discontinuity in the electrical-current sheets of the S waves. Such current sheets are entirely due to streaming current since there are no charge separations and, therefore, no electric fields inside a shear wave in a uniform material. The current-sheet discontinuity leads to charge separations across the interface and to converted no-moveout electric fields.

The slow waves converted from the incident shear wave act to further alter the amount of separated charge at the interface. However, in Fig. 9 we see that the effect is not very large. This is due to the fact that only a small amount of energy goes into slow waves when shear waves traverse an interface. In general, the seismic-EM converted wave fields are sensitive to the permeability contrast only through the generation of slow waves. Thus, the S -EM conversions are rather insensitive to the permeability contrast.

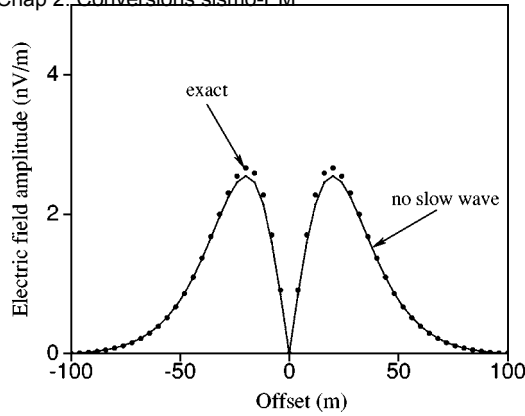


FIG. 9. The amplitude of the converted no-moveout electric field when the incident wave is a spherical shear wave coming from a shear-wave-generating “hammer” source again at $z=5$ m. The interface is the same sand/sandstone interface considered in Fig. 4.

V. CONCLUSIONS

We have numerically demonstrated that in order to properly model the generation of electric fields-when seismic waves traverse an interface, one must employ the full Biot theory in the modeling and take into account the generation of slow waves. This is the only way to properly model the details of the fluid-pressure gradients in the vicinity of the interface upon which the electrokinetically induced charge separations sensitively depend. The electroseismic problem may thus represent one of the most important applications of Biot’s theory of porous media acoustics.

ACKNOWLEDGMENTS

S.R.P. would like to thank the Geophysics Department at Stanford University and the Stanford Rock Physics and Borehole Consortium (S.R.B.) for providing support during his sabbatical there. S.G. thanks TotalFinaElf for the support they have provided him. The comments of both reviewers are appreciated.

APPENDIX: THE ELECTROSEISMIC MATERIAL PROPERTIES

For the poroelastic moduli, we use the results of Biot and Willis (1957) that hold whenever the grains consist of a single isotropic mineral. These expressions can be written

$$K_G = \frac{K_D + [1 - (1 + \phi)K_D/K_s]K_f/\phi}{1 + \Delta}, \quad (\text{A1})$$

$$C = \frac{(1 - K_D/K_s)K_f/\phi}{1 + \Delta}, \quad (\text{A2})$$

$$M = \frac{K_f/\phi}{1 + \Delta}, \quad (\text{A3})$$

where Δ is a small dimensionless parameter defined as

$$\Delta = \frac{1 - \phi}{\phi} \frac{K_f}{K_s} \left(1 - \frac{K_D}{(1 - \phi)K_s} \right). \quad (\text{A4})$$

Here, ϕ is the porosity, K_f is the fluid’s bulk modulus, and K_s is the solid’s bulk modulus. In the numerical examples,

we will always take the fluid to be water ($K_f=2.2$ GPa) and the solid to be quartz ($K_s=36$ GPa). The drained bulk modulus K_D and shear modulus G of the framework of grains are assumed to obey simple effective-medium laws of the form [pore-inclusion-based effective-medium theories such as Korrington *et al.* (1979) predict drained moduli of this form]

$$K_D = K_s \frac{1 - \phi}{1 + a\phi}, \quad (\text{A5})$$

$$G = G_s \frac{1 - \phi}{1 + b\phi}, \quad (\text{A6})$$

where a and b will vary with lithology and G_s is taken to be the shear modulus of pure quartz 44 GPa. In the numerical simulations, we somewhat arbitrarily take $b=2a$ in order to eliminate a model parameter. Thus, using the above expressions, the poroelastic moduli K_G , C , M , and G are fixed by specifying the two dimensionless numbers ϕ and a . Depending on the assumed consolidation of the framework of grains, we can expect a to have a rather large range from roughly 3 for a highly consolidated sandstone to as much as 300 for an unconsolidated sand.

Other parameters to be fixed in the model are the transport coefficients k (fluid-flow permeability), σ (conductivity of the porous material) and L (the coupling coefficient). For the permeability we use the result of Johnson *et al.* (1987)

$$\frac{k(\omega)}{k_0} = \left[\sqrt{1 - i \frac{\omega}{\omega_c} \frac{4}{n}} - i \frac{\omega}{\omega_c} \right]^{-1}, \quad (\text{A7})$$

where k_0 is the dc permeability and the frequency ω_c corresponds to when viscous-boundary layers begin to form in the pores. Johnson’s model predicts that

$$\omega_c = \frac{\eta}{\rho_f F k_0}, \quad (\text{A8})$$

where η is the water viscosity 10^{-3} Pa s, ρ_f the water density 10^3 kg/m³, and F the electrical formation factor. In this work, we assume Archie’s (1942) law to hold

$$\frac{1}{F} = \phi^m, \quad (\text{A9})$$

with a constant Archie exponent of $m=1.7$ for all materials. Depending on the permeability and porosity, one can expect that $\omega_c/2\pi > 1$ kHz (and usually dramatically so for rocks) so our assumed source puts us in the lower-frequency range where no viscous-boundary layers have yet developed in the pores. Because of this, we make no great effort to model the pore-geometry terms contained within n . Johnson’s model predicts that $n = \Lambda^2/(k_0 F)$, where Λ is a weighted pore-volume to pore-surface ratio; however, we simply take $n = 8$ for all materials.

The electrical conductivity of the porous material is

$$\sigma = \sigma_f/F, \quad (\text{A10})$$

where F is again the formation factor given by Archie’s law and σ_f is the conductivity of the water. We specify the water conductivity by fixing the molarity C (moles/liter) of NaCl in

the water and use the Einstein–Stokes estimate of the ionic mobilities to give the mks estimate

$$\sigma_f = \frac{e^2}{6\pi\eta} \left(\frac{1}{R_{Na}} + \frac{1}{R_{Cl}} \right) 6.022 \times 10^{26} C, \quad (A11)$$

where $R_{Na} = 1.83 \times 10^{-10}$ m, $R_{Cl} = 1.20 \times 10^{-10}$ m, and e is the fundamental charge.

The coupling coefficient L is given by

$$L = - \frac{\epsilon_0 \kappa_f}{F \eta} \zeta, \quad (A12)$$

where ϵ_0 is the vacuum permittivity, $\kappa_f = 80$ is the dielectric constant of water, and the ζ potential is a measure of the charge available for transport in the diffuse part of the electric double layer and is assumed to comply with the following empirical law that is roughly appropriate for quartz (this law holds strictly only for $pH=7$ but gives the right general trend for the pH dependence):

$$\zeta(\text{in volts}) = (0.01 + 0.025 \log_{10} C) \frac{(pH - 2)}{5}. \quad (A13)$$

In all examples we take $pH=7$. Because the frequency of our source is such that $\sigma \gg \omega \epsilon$, we will not attempt to model precisely the rock's dielectric properties and will simply take $\epsilon = \epsilon_0 \kappa_f / F$ as our estimate of the rock permittivity. The magnetic permeability is taken to be that of vacuum $\mu = \mu_0$.

Thus, despite the rather large number of parameters involved, by assuming the fluid to be water and the grains to be quartz we have reduced the material properties down to just the following four free parameters: C (molarity), ϕ (porosity), a (frame compliance factor), and k_0 (dc permeability).

- Archie, G. E. (1942). "The electrical resistivity log as an aid in determining some reservoir characteristics," *Trans. AIME* **146**, 54–62.
- Biot, M. A. (1956a). "Theory of propagation of elastic waves in a fluid-saturated porous solid. I. Low-frequency range," *J. Acoust. Soc. Am.* **28**, 168–178.
- Biot, M. A. (1956b). "Theory of propagation of elastic waves in a fluid-saturated porous solid. II. Higher frequency range," *J. Acoust. Soc. Am.* **28**, 179–191.

- Biot, M. A. (1962a). "Mechanics of deformation and acoustic propagation in porous media," *J. Appl. Phys.* **33**, 1482–1498.
- Biot, M. A. (1962b). "Generalized theory of acoustic propagation in porous dissipative media," *J. Acoust. Soc. Am.* **34**, 1254–1264.
- Biot, M. A., and Willis, D. G. (1957). "The elastic coefficients of the theory of consolidation," *J. Appl. Mech.* **24**, 594–601.
- Frenkel, J. (1944). "On the theory of seismic and seismoelectric phenomena in a moist soil," *J. Phys. (Soviet)* **8**, 230–241.
- Garambois, S., and Dietrich, M. (2001). "Seismo-electric wave conversions in porous media: Field measurements and transfer function analysis," *Geophysics* **66**, 1417–1430.
- Garambois, S., and Dietrich, M. (2002). "Full-waveform numerical simulations of seismo-electromagnetic wave conversions in fluid-saturated stratified porous media," *J. Geophys. Res.* (in press).
- Gelinsky, S., and Shapiro, S. A. (1997). "Dynamic-equivalent medium approach for thinly layered saturated sediments," *Geophys. J. Int.* **128**, F1–F4.
- Gelinsky, S., Shapiro, S. A., Müller, T., and Gurevich, B. (1998). "Dynamic poroelasticity of thinly layered structures," *Int. J. Solids Struct.* **35**, 4739–4751.
- Gurevich, B., and Lopatnikov, S. L. (1995). "Velocity and attenuation of elastic waves in finely layered porous rocks," *Geophys. J. Int.* **121**, 933–947.
- Haartsen, M. W., and Pride, S. R. (1997). "Electroseismic waves from point sources in layered media," *J. Geophys. Res.* **102**, 24745–24769.
- Johnson, D. L., Koplik, J., and Dashen, R. (1987). "Theory of dynamic permeability and tortuosity in fluid-saturated porous media," *J. Fluid Mech.* **176**, 379–402.
- Johnson, D. L. (2001). "Theory of frequency dependent acoustics in patchy-saturated porous media," *J. Acoust. Soc. Am.* **110**, 682–694.
- Kennett, B. L. N. (1983). *Seismic Wave Propagation in Stratified Media* (Cambridge University Press, Cambridge).
- Korringa, J., Brown, R. J. S., Thompson, D. D., and Runge, R. J. (1979). "Self-consistent imbedding and the ellipsoidal model for porous rocks," *J. Geophys. Res.* **84**, 5591–5598.
- Norris, A. N. (1993). "Low-frequency dispersion and attenuation in partially saturated rocks," *J. Acoust. Soc. Am.* **94**, 359–370.
- Pride, S. R. (1994). "Governing equations for the coupled electromagnetics and acoustics of porous media," *Phys. Rev. B* **50**, 15678–15696.
- Pride, S. R., and Haartsen, M. W. (1996). "Electroseismic wave properties," *J. Acoust. Soc. Am.* **100**, 1301–1315.
- Pride, S. R., Tromeur, E., and Berryman, J. G. (2002). "Biot slow-wave effects in stratified rocks," *Geophysics* **67**, 1–11.
- Thompson, A., and Gist, G. (1993). "Geophysical applications of electrokinetic conversion," *The Leading Edge* **12**, 1169–1173.
- White, J. E., Mikhaylova, N. G., and Lyakhovitsky, F. M. (1975). "Low-frequency seismic waves in fluid-saturated layered rocks," *Izv., Acad. Sci., USSR, Phys. Solid Earth* **11**, 654–659.

Electroseismic Wave Theory of Frenkel and More Recent Developments

Steven R. Pride¹ and Stephane Garambois²

Abstract: Frenkel's 1944 theory of porous media acoustics is carefully scrutinized. After some manipulation, Frenkel's equations are seen to have nearly identical form to Biot's 1962 equations. The only difference is that Frenkel includes an extraneous fluid-pressure gradient in his bulk force balance. Frenkel also makes a slight error in the development of his effective poroelastic moduli that prevents him from being the first to obtain the so-called "fluid-substitution" relations. Outside of these two small problems, Frenkel's analysis can be considered correct. He limits his treatment of electroseismic phenomena to explain the electric field that accompanies a compressional seismic wave in a homogeneous material. He predicts that the electric field in a compressional wave is directly proportional to the particle acceleration and this has been verified by the recent field measurements of Garambois and Dietrich. However, such electric fields are only a small part of the total electroseismic response of the earth. Accordingly, some of the additional phenomena not discussed by Frenkel are also presented and discussed.

DOI: 10.1061/(ASCE)0733-9399(2005)131:9(898)

CE Database subject headings: Poroelasticity; Electrokinetics; Porous media; Acoustics.

Introduction

Frenkel (1944) is the first writer to have developed a complete set of equations governing the acoustics of isotropic porous media. Kosten and Zwikker (1941) proposed two coupled force-balance equations for the average fluid and solid response of a porous material, and predicted the existence of two compressional-response modes (a "fast" and "slow" wave). However, Kosten and Zwikker (1941), unlike Frenkel (1944), proposed a purely scalar theory that failed to allow for shear and that did not define the effective compressibility moduli in terms of drained and undrained experiments. The coefficients in the Kosten and Zwikker (1941) theory are entirely phenomenological.

Frenkel only wrote one paper on poroelasticity. His principal motivation for developing a theory of porous-media acoustics is to quantitatively explain the so-called "E effect" (a nomenclature apparently no longer used in the literature) which is the phenomenon by which a pair of electrodes attached to the earth registers a voltage difference as a seismic wave traverses the electrode pair. Ivanov (1939) measured this phenomenon in the field and suggested that the explanation of the recorded electric field was electrokinetic in nature. The stated purpose of Frenkel's (1944) paper is to develop Ivanov's idea into a quantitative theory.

The purpose of the present paper is to: (1) carefully compare

Frenkel's porous-media acoustics equations to those of Biot (1956a and 1956b) and determine the reason for any discrepancies; (2) determine whether Frenkel's analysis of the electric field contained within a compressional wave is correct; and (3) present results for those effects not considered by Frenkel which include relaxation in the transport coefficients and an assortment of electrokinetic couplings between seismic waves (both compressional and shear) and electric and magnetic fields.

Frenkel's Theory of Porous-Media Acoustics

With some effort, the various macroscopic fields in Frenkel's theory can be identified and his governing equations rewritten in a form that is perhaps more familiar.

To achieve this, the response fields used in the present paper are slightly different from those in Frenkel's paper. The poroelastic displacements are taken to be \mathbf{u} and \mathbf{w} where \mathbf{u} is the average displacement in the solid phase of a porous sample, and \mathbf{w} is defined $\mathbf{w} = \phi(\mathbf{u}_f - \mathbf{u})$ where ϕ is porosity and \mathbf{u}_f is the average displacement of the fluid in the pores. The time derivative $\partial \mathbf{w} / \partial t$ thus represents the Darcy filtration velocity induced by the wave. The stress variables are the bulk stress tensor $\boldsymbol{\tau}$ and the average fluid pressure in the pores p_f . The bulk stress tensor represents the average stress throughout both the solid and fluid phases of a porous sample and can be identified as $\boldsymbol{\tau} = (1 - \phi)\boldsymbol{\tau}_s - \phi p_f \mathbf{I}$, where $\boldsymbol{\tau}_s$ is the average stress tensor of the solid phase. The confining pressure is defined as $P_c = -\text{tr}\{\boldsymbol{\tau}\} / 3 = (1 - \phi)p_s + \phi p_f$ and both P_c and p_f are used as the two independent pressure variables in the compressibility laws. In Table 1, Frenkel's (1944) variables are given in terms of these porous-continuum variables.

Frenkel is only concerned with developing a theory of linear acoustics. As such, we forego placing a small d or δ in front of the stress and displacement variables, it being understood that all stresses and displacements are increments induced by a passing wave.

¹Earth Sciences Division, Lawrence Berkeley National Laboratory, Berkeley, CA 94720 (corresponding author). E-mail: srpride@lbl.gov.

²LIRIGM, Maison des Geosciences, Univ. Joseph Fourier, 38041 Grenoble Cedex 9, France. E-mail: stephane.garambois@ujf-grenoble.fr

Note. Associate Editor: Alexander H.-D. Cheng. Discussion open until February 1, 2006. Separate discussions must be submitted for individual papers. To extend the closing date by one month, a written request must be filed with the ASCE Managing Editor. The manuscript for this paper was submitted for review and possible publication on November 11, 2003; approved on July 29, 2004. This paper is part of the *Journal of Engineering Mechanics*, Vol. 131, No. 9, September 1, 2005. ©ASCE, ISSN 0733-9399/2005/9-898-907/\$25.00.

Table 1. Identification of Frenkel Variables

Frenkel variable ^a	Equivalent definition ^b
T (partial stress tensor) (associated with solid)	$(1-\phi)\boldsymbol{\tau}_s = \boldsymbol{\tau} + \phi p_f \mathbf{I}$
f (porosity)	ϕ
p_2 (fluid pressure)	p_f
$p_1 = -\text{tr}\{\mathbf{T}\}/3$ (partial pressure) (associated with solid)	$(1-\phi)p_s = P_c - \phi p_f$
u (average displacement) (of solid phase)	u
$\theta = \Delta V/V = \nabla \cdot \mathbf{u}$ (dilatation) (of porous sample)	$\nabla \cdot \mathbf{u}$
$\varphi = -\Delta p_2/p_2$ (dilatation) (of fluid volume)	$-p_f/K_f$
v ₁ (average velocity) (of solid phase)	$\partial \mathbf{u} / \partial t$
v ₂ (average velocity) (of fluid phase)	$\phi^{-1} \partial \mathbf{w} / \partial t + \partial \mathbf{u} / \partial t$
Δf (porosity change)	$\Delta \phi = -\phi \nabla \cdot \mathbf{u} - \nabla \cdot \mathbf{w} - \phi p_f / K_f$

^aFrenkel (1944).

^bPresent paper.

Frenkel's Stress/Strain Relations

In short, Frenkel obtains the proper form of the stress/strain relations but, because of a small error to be described below, does not obtain the so-called Gassmann (1951) "fluid substitution relations" that give the poroelastic compressibility moduli in terms of the underlying fluid bulk modulus, solid bulk modulus, and drained bulk modulus.

Frenkel obtains his macroscopic compressibility laws by focusing on two thought experiments. Adding the results of the two thought experiments yields the functions $\nabla \cdot \mathbf{u}(P_c, p_f)$ and $\Delta \phi(P_c, p_f)$ that describe how sample volume and porosity are changed due to applied increments in confining pressure P_c and fluid pressure p_f . Frenkel makes the not so obvious identification that in a porous material

$$\nabla \cdot \mathbf{u} = \Delta V/V \quad (1)$$

where \mathbf{u} =average displacement in the solid phase and V =sample volume. Pride and Berryman (1998) demonstrate that only when the geometrical center of the grain space coincides with the geometrical center of the pore space in a porous sample does $\nabla \cdot \mathbf{u}$ become exactly the volumetric dilatation of the sample. However, most writers starting from Biot and Willis (1957) also invoke Frenkel's Eq. (1) and it can be considered a reasonable approximation.

In his first "drained" thought experiment, Frenkel applies a confining pressure to a sample with no change in the fluid pressure. Under such drained conditions, one has $P_c = (1-\phi)p_s = p_1$ (where p_1 is Frenkel's variable for the partial pressure in the solid). Frenkel introduces two poroelastic moduli K and α_F to describe the drained response [α_F is used here instead of Frenkel's original α so as to avoid later confusion with the Biot and Willis (1957) parameter]

$$\nabla \cdot \mathbf{u}(P_c, 0) = -\frac{P_c}{K} \quad (2)$$

$$\Delta \phi(P_c, 0) = -\left(\frac{1}{1+\alpha_F} - \phi\right) \frac{P_c}{K} \quad (3)$$

Here, K =so-called "drained" bulk modulus and α_F has no standard name ("Frenkel's alpha") but can either be defined from Eq. (3) or can be identified, as Frenkel properly does, as the ratio of the increment in solid volume ΔV_s to the increment of pore volume ΔV_ϕ under drained conditions; i.e., $\alpha_F = \Delta V_s / \Delta V_\phi|_{p_f=0}$.

In his second thought experiment, Frenkel applies a fluid pressure p_f everywhere throughout the pore space and, simultaneously, a confining pressure $P_c = p_f$ to the external surface of the sample. One way to realize this in practice is to immerse an unjacketed sample into a fluid reservoir and change the pressure of the reservoir by p_f . In this case, Frenkel notices that the effect of the applied-pressure increment is to simply scale down (or up) the grain pack without changing its relative geometry. Accordingly, the porosity remains unchanged in this experiment. This is only exactly correct when the grains are made of an isotropic material having a bulk modulus K_s that is spatially uniform. Under this isotropic monomineral assumption (that Frenkel does not discuss), he properly obtains

$$\nabla \cdot \mathbf{u}(p_f, p_f) = -\frac{p_f}{K_s} \quad (4)$$

$$\Delta \phi(p_f, p_f) = 0 \quad (5)$$

Up to this point, Frenkel has done everything correctly.

His error comes when he adds together the results of the two thought experiments. Because of the linear nature of the incremental response, the proper additions yield

$$\begin{aligned} \nabla \cdot \mathbf{u}(P_c, p_f) &= \nabla \cdot \mathbf{u}(P_c - p_f, 0) + \nabla \cdot \mathbf{u}(p_f, p_f) \\ &= -\frac{P_c}{K} + \left(1 - \frac{K}{K_s}\right) \frac{p_f}{K} \end{aligned} \quad (6)$$

$$\begin{aligned} \Delta \phi(P_c, p_f) &= \Delta \phi(P_c - p_f, 0) + \Delta \phi(p_f, p_f) \\ &= -\left(\frac{1}{1+\alpha_F} - \phi\right) \frac{(P_c - p_f)}{K} \end{aligned} \quad (7)$$

However, Frenkel performs the meaningless addition

$$\begin{aligned} \nabla \cdot \mathbf{u}(P_c - \phi p_f, 0) + \nabla \cdot \mathbf{u}(p_f, p_f) \\ = \nabla \cdot \mathbf{u}[P_c + (1-\phi)p_f, p_f] \neq \nabla \cdot \mathbf{u}(P_c, p_f) \end{aligned}$$

and similarly for $\Delta \phi$, which results in his Eqs. (13) and (24a) being incorrect. He thus makes the misidentifications

$$\nabla \cdot \mathbf{u}(P_c, p_f) = -\frac{P_c}{K} + \left(\phi - \frac{K}{K_s}\right) \frac{p_f}{K} \quad (8)$$

$$\Delta \phi(P_c, p_f) = -\left(\frac{1}{1+\alpha_F} - \phi\right) \frac{(P_c - \phi p_f)}{K} \quad (9)$$

It is this error that prevents Frenkel from properly identifying the poroelastic compressibility moduli.

The constitutive equation for $\Delta \phi$ can be translated into a constitutive equation for the increment in fluid content $\nabla \cdot \mathbf{w}$ by rewriting Frenkel's Eq. (20) for the conservation of fluid mass in terms of the variables of the present paper as

$$\Delta\phi + \frac{\phi}{K_f} p_f + \nabla \cdot \mathbf{w} + \phi \nabla \cdot \mathbf{u} = 0 \quad (10)$$

which is exact for linear response. If the proper results of Eqs. (6) and (7) are then employed, Frenkel's "corrected" compressibility laws can be written

$$\begin{bmatrix} \nabla \cdot \mathbf{u} \\ \nabla \cdot \mathbf{w} \end{bmatrix} = -\frac{1}{K} \begin{bmatrix} 1 & -1(1 - K/K_s) \\ -(1 + \alpha_f)^{-1} & \phi(K/K_f - K/K_s) + (1 + \alpha_f)^{-1} \end{bmatrix} \times \begin{bmatrix} P_c \\ p_f \end{bmatrix} \quad (11)$$

These equations can further be used to identify the nature of the parameter α_f , an issue not addressed by Frenkel. Since the compressibility laws can also be derived by taking derivatives of a strain-energy function, one has the Maxwell relation that

$$\frac{1}{1 + \alpha_f} = 1 - \frac{K}{K_s} \quad (12)$$

Frenkel does not state this result for α_f which can also be given as $1/(1 + \alpha_f) = \alpha$, where α is known as the Biot and Willis (1957) constant. As has been shown by Berge et al. (1993), α is always independent of the fluid's bulk modulus for any porous material and is only given exactly by $\alpha = 1 - K/K_s$ in the special case of isotropic monomineral grains.

In passing, we give the compressibility laws in perhaps their most useful form (applicable to porous media with anisotropy at either the grain or macroscales and with arbitrary heterogeneity in the mineral properties)

$$-\begin{bmatrix} P_c \\ p_f \end{bmatrix} = K_U \begin{bmatrix} 1 & B \\ B & B/\alpha \end{bmatrix} \begin{bmatrix} \nabla \cdot \mathbf{u} \\ \nabla \cdot \mathbf{w} \end{bmatrix} \quad (13)$$

where the coefficients K_U (undrained bulk modulus) and B [Skempton's (1954) coefficient] are defined as

$$K_U = -\left. \frac{P_c}{\nabla \cdot \mathbf{u}} \right|_{\nabla \cdot \mathbf{w} = 0} \quad (14)$$

$$B = \left. \frac{p_f}{P_c} \right|_{\nabla \cdot \mathbf{w} = 0} \quad (15)$$

Both K_U and B are measured on samples that have their exterior surface sealed ($\nabla \cdot \mathbf{w} = 0$). A generally valid definition of the Biot and Willis (1957) coefficient is

$$\alpha = (1 - K/K_U)/B \quad (16)$$

so that the three fundamental compressibility constants of poroelasticity can be taken to be K_U , K , and B . Under the restriction to isotropic monomineral grains, one obtains

$$\alpha = 1 - \frac{K}{K_s} \quad (17)$$

$$B = \frac{\alpha}{\alpha + \phi(K/K_f - K/K_s)} \quad (18)$$

$$K_U = \frac{K}{1 - B\alpha} \quad (19)$$

Gassmann (1951) only considers the undrained response ($\nabla \cdot \mathbf{w} = 0$) and, accordingly, only obtains results for K_U and B . It is Biot and Willis (1957) who first properly obtain the entirety of Eqs. (13)–(19). Frenkel also obtains poroelastic compressibility

laws of the form of Eq. (13). However, his error discussed earlier and his lack of use of the symmetry condition prevent him from obtaining the fluid-substitution relations of Eqs. (17)–(19).

Finally, like Gassmann (1951) and Biot and Willis (1957) who follow him, Frenkel makes the assumption that the fluid in the pores has no influence on the shear properties of an isotropic porous material. Frenkel thus assumes that the deviatoric stress tensor $\boldsymbol{\tau}^D = \boldsymbol{\tau} + P_c \mathbf{I}$ acting on the bulk material is related to the deviatoric shear by a fluid-independent constant G

$$\boldsymbol{\tau}^D = G(\nabla \mathbf{u} + \nabla \mathbf{u}^T - \frac{2}{3} \nabla \cdot \mathbf{u} \mathbf{I}) \quad (20)$$

At the low frequencies used in seismic exploration, Frenkel's assumption of fluid independent shear is usually appropriate.

Frenkel's Dynamics of Porous Media

Frenkel proposes force-balance equations for the fluid in relative motion to the solid [his Eq. (22)] and for the solid skeleton [his Eq. (23)] that, except for one slight problem discussed below, can be considered equivalent to those of Biot (1956a,b).

Frenkel states Darcy's law [his Eq. (18)] in a nonstandard form. The relative velocity $\mathbf{v}_2 - \mathbf{v}_1$ (his notation) that Frenkel uses in Darcy's law represents the average speed at which the fluid is moving relative to the solid and is not a filtration velocity like it should be. A filtration velocity is the volume of fluid traversing unit area of porous material in unit time and is the porosity ϕ times the relative fluid speed. In the notation of the present paper, the filtration velocity is denoted $\partial \mathbf{w} / \partial t$ where $\mathbf{w} = \phi(\mathbf{u}_f - \mathbf{u})$ is called the filtration displacement. Because of this, the steady-flow permeability k_0 used in the present paper (standard definition) is ϕ times the permeability used by Frenkel.

With this in mind, Frenkel's relative force balance [his Eq. (22a)] can be directly rewritten using the variables of the present paper as

$$\frac{\rho_f}{\phi} \frac{\partial^2 \mathbf{w}}{\partial t^2} + \frac{\eta_f}{k_0} \frac{\partial \mathbf{w}}{\partial t} = -\nabla p_f - p_f \frac{\partial^2 \mathbf{u}}{\partial t^2} \quad (21)$$

where η_f = fluid's shear viscosity. This force-balance can be considered equivalent to the one later developed by Biot. In modern retrospect, we now know (Brown 1980) that the effective fluid inertia in this force balance is more generally $\rho_f F$, where F is the electrical formation factor in the porous material when surface electrical conduction is not important. In models of the pore space where the current lines are straight, one has that $F = 1/\phi$, which then reduces to the Frenkel statement. Biot (1956b), and later Johnson et al. (1987) and others, have provided models that allow for the development of viscous-boundary layers in the pores at sufficiently high frequencies. However, for most earth materials of interest and across the entire frequency band of interest in seismic exploration, the flow in the pores is well modeled as being parabolic. As such, the inertial effect captured by the term $\rho F \partial^2 \mathbf{w} / \partial t^2$, as well as all viscous boundary layer effects, can normally be neglected in Eq. (21). This is particularly true for the seismic (as opposed to ultrasonic) applications of the theory that Frenkel has in mind.

The total force balance for all the material in an averaging volume is obtained by adding Frenkel's Eqs. (22) and (23) to directly obtain

$$\rho \frac{\partial^2 \mathbf{u}}{\partial t^2} + \rho_f \frac{\partial^2 \mathbf{w}}{\partial t^2} = \Phi^{(1)} - \phi \nabla p_f \quad (22)$$

where $\rho = (1 - \phi)\rho_s + \phi\rho_f$ = bulk density and where Frenkel defines $\Phi^{(1)}$ as the “elastic force acting on the solid skeleton.” Frenkel should therefore have identified this as $\Phi^{(1)} = (1 - \phi)\nabla \cdot \boldsymbol{\tau}_s = \nabla \cdot \boldsymbol{\tau} + \phi \nabla p_f$ so that the right-hand side of Eq. (22) becomes simply the total elastic force $\nabla \cdot \boldsymbol{\tau}$. Written in this way, Frenkel’s Eq. (22) is identical to the results of Biot (1956a,b).

However, Frenkel for some reason proposes that $\Phi^{(1)} = (1 - \phi)\nabla \cdot \boldsymbol{\tau}_s - (1 - \phi)\nabla p_f$ [his Eq. (16)]. He somehow pictures an additional fluid-pressure gradient acting directly on the solid frame which is erroneous. Because of this, his equation governing the total force balance has an extra fluid-pressure gradient term present that should not be there.

Frenkel’s Wave Properties

As seen above, the form of Frenkel’s equations, after some manipulation, are nearly identical to those of Biot (1956a,b). However, because his analysis misidentifies two of the three compressibility constants and adds an erroneous fluid-pressure gradient to the total force balance, his detailed results for the nature of compressional (longitudinal) slownesses are not correct. Since he correctly writes down the force balance governing the relative flow, he properly predicts the existence of two distinct longitudinal modes. Unfortunately, he gives little importance to the fluid-pressure-diffusion (or “slow-wave”) mode and even goes so far as to say it is “nonexistent.”

Something Frenkel gets entirely correct is the complex shear-wave slowness s_s

$$s_s = \sqrt{\frac{\rho + i\omega k_o \rho_f^2 / \eta}{G}} \quad (23)$$

This is because the shear-wave slowness is independent of the presence of fluid-pressure gradients and the compressibility moduli.

In the balance, Frenkel certainly deserves more recognition than he has received for his pioneering contribution to porous-media acoustics. He did many nonobvious things correctly, not the least of which is defining appropriate dependent and independent variables for a theory of porous-media acoustics.

Frenkel’s Electroseismic Theory

Ivanov (1939) measured an electric field as seismic waves passed electrode pairs on the earth’s surface. He proposes that such coupling is electrokinetic in nature. In soils, rocks, and other porous materials, the solid grains have an excess charge fixed to their surfaces that is balanced by free counter ions diffusely distributed in the fluid layers immediately adjacent to the grain surfaces. The bound charge on the grain surfaces is immobile while the free counter ions in the fluid are able to move in response to applied forces. The bound charge and diffuse counter charge together is called the “electric double layer.” Electrokinetic phenomena are, by definition, processes associated with the transport of the diffuse counter charge.

Frenkel states that his principal motivation for developing a theory of porous-media acoustics is to explain the electroseismic measurements of Ivanov. Both Ivanov and Frenkel envision that a compressional wave creates fluid-pressure gradients at the scale of the wavelength and that the associated flow from the compressions to dilatations transports the counter charge of the double

layer relative to the bound charge. In this way, counter charge accumulates in the regions of dilation and the bound charge becomes “exposed” in the regions of compression so that an electric field is created perpendicular to the wavefront at the scale of the wavelength. This electric field moves along with the seismic wave as part of the material response and can be recorded as the seismic wave traverses an electrode pair.

We have seen above that Frenkel produces a theory capable of predicting (properly so if he hadn’t made his small mistakes) the macroscopic fluid-pressure gradients ∇p_f associated with a compressional wave. It only remains to relate this seismic response to the associated electric field.

To do so, Frenkel simply quotes the famous result of von Smoluchowski (1903) for the electric field created by a static fluid-pressure gradient. In the present context in which a compressional wave is driving a relative fluid flow, the right-hand side of Eq. (21) identifies the applied force as $-\nabla p_f - \rho_f \partial^2 \mathbf{u} / \partial t^2$. von Smoluchowski’s result for the electric field \mathbf{E} created by this applied force is

$$\mathbf{E} = - \frac{\varepsilon_f \zeta}{\eta_f \sigma_f} \left(\nabla p_f + \rho_f \frac{\partial^2 \mathbf{u}}{\partial t^2} \right) \quad (24)$$

where ε_f = fluid’s dielectric permittivity; σ_f = fluid’s electrical conductivity; η_f = again the fluid’s viscosity; and ζ = property of the grain–fluid interface that quantifies the electric potential at the interface separating the bound charge from the diffuse-layer charge. The “zeta potential” ζ is thus a measure of the amount of charge separation present in the electric double layer.

For a plane P -wave having $e^{-i\omega t}$ time dependence and propagating in the x direction in a uniform porous material, Frenkel first calculates the $\partial p_f / \partial x$ associated with the wave and then determines E_x using Eq. (24). If the corrected variant of Frenkel’s equations are used, one obtains

$$\frac{E_x}{-\omega^2 u_x} = \frac{\rho_f \varepsilon_f \zeta}{\eta_f \sigma_f} \left(1 - \frac{\rho C}{\rho_f H} \right) \quad (25)$$

where u_x = amplitude of the particle displacement associated with the wave in the x direction; and where C and H = elastic moduli (as defined by Biot) related to the undrained bulk modulus K_U and Skempton’s coefficient B as

$$C = BK_U \quad (26)$$

$$H = K_U + 4G/3. \quad (27)$$

Eq. (25) for E_x , which corresponds to the low-frequency limit of an expression given by Pride and Haartsen (1996) and to an expression given by Garambois and Dietrich (2001), is the same as the culminating Eq. (46) of Frenkel’s paper except for a slightly different definition of the elastic moduli ratio C/H due to Frenkel’s errors associated with the longitudinal response as previously discussed.

The message of Frenkel’s result [Eq. (25)] is that the electric field E_x moving along with a P -wave as part of the material response is directly proportional (without phase adjustments) to the particle acceleration. This has been experimentally verified by Garambois and Dietrich (2001). In Fig. 1, the recorded particle accelerations (time derivatives of the geophone response which is proportional to the particle velocities) and associated electric fields are plotted together on the same time axis for receivers on the earth’s surface at different distances from the seismic source (a hammer). A horizontal geophone was at the center of each 50 cm electric-dipole antenna (two metal rods driven vertically

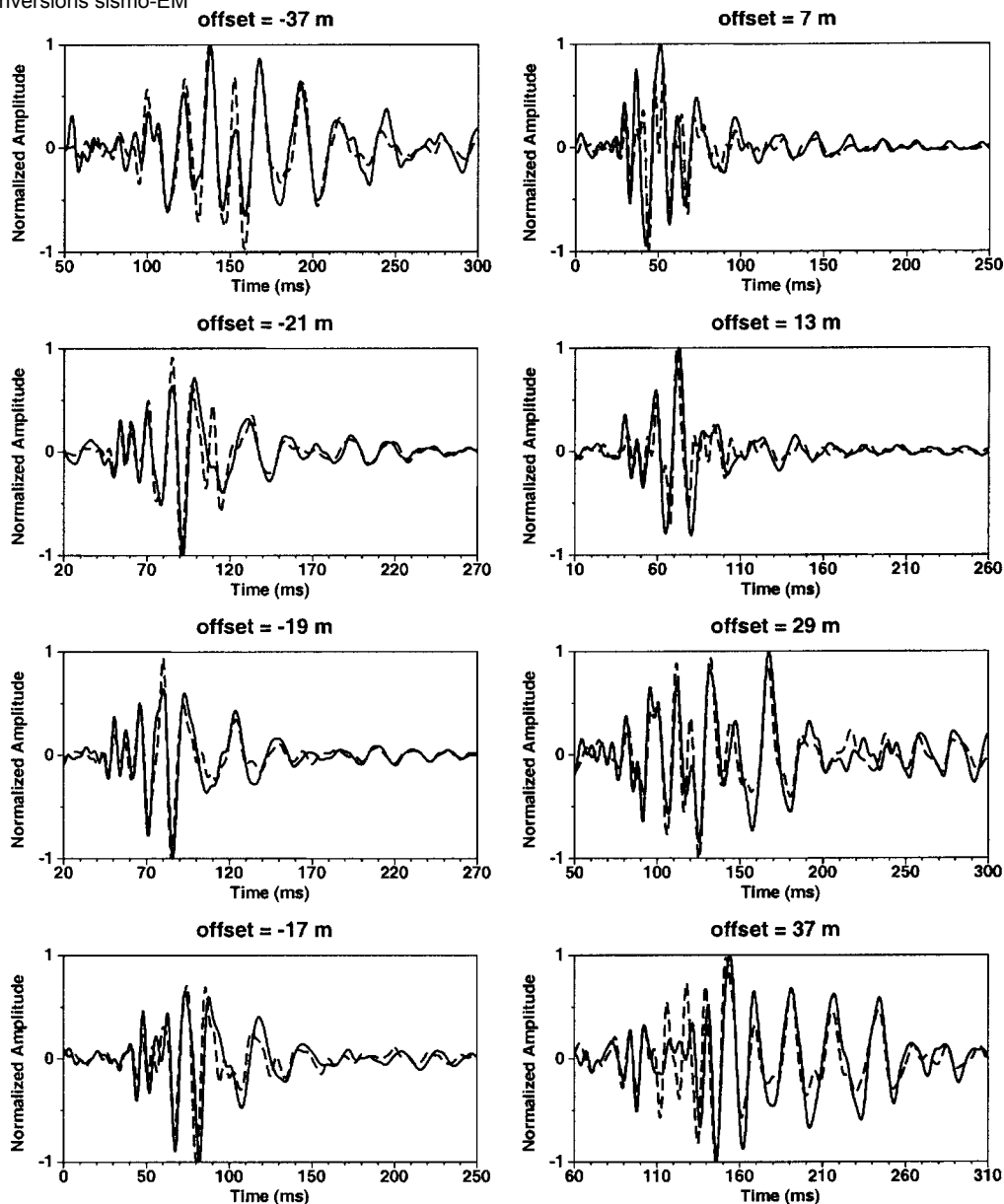


Fig. 1. Field data of Garambois and Dietrich (2001). Horizontal component of electric field (solid lines) along with horizontal component of particle acceleration (dashed lines) as recorded at earth’s surface at different offsets from seismic source which is hammer impacting a plate on earth’s surface.

into the earth, 50 cm apart) and the time difference between when the seismic wave arrives at the first electrode and when it arrives at a geophone have been allowed for (roughly 1 ms). The experimental field data of Fig. 1 provide the ultimate testimony to the lucidity and correctness of Frenkel’s pioneering work.

Modern Theory of Electrostatic Phenomena

Frenkel limited his electrostatic analysis to explaining the electric field that accompanies a propagating longitudinal wave. However, there are many other aspects to the electric and magnetic fields generated by both compressional and shear waves that Frenkel did not attempt to address as we now go on to discuss.

Governing Equations

In order to model these additional effects, equations of a more general character are required. Pride (1994) obtains the equations governing the coupled seismic and electromagnetic response of a porous material when electrokinetics is responsible for the coupling. Assuming an $e^{-i\omega t}$ time dependence, these equations are

$$-\omega^2 \rho \mathbf{u} = -\nabla P_c + \nabla \cdot \boldsymbol{\tau}^D + \omega^2 \rho_f \mathbf{w} \quad (28)$$

$$\boldsymbol{\tau}^D = G \left(\nabla \mathbf{u} + \nabla \mathbf{u}^T - \frac{2}{3} \nabla \cdot \mathbf{u} \mathbf{I} \right) \quad (29)$$

$$-\begin{bmatrix} P_c \\ p_f \end{bmatrix} = K_U \begin{bmatrix} 1 & B \\ B & B/\alpha \end{bmatrix} \begin{bmatrix} \nabla \cdot \mathbf{u} \\ \nabla \cdot \mathbf{w} \end{bmatrix} \quad (30)$$

Chap 2. Conversions sismo-EM

$$\begin{bmatrix} -i\omega\mathbf{w} \\ \mathbf{J} \end{bmatrix} = \begin{bmatrix} k(\omega)/\eta_f & L(\omega) \\ L(\omega) & \sigma(\omega) \end{bmatrix} \begin{bmatrix} -\nabla p_f + \omega^2\rho_f\mathbf{u} \\ \mathbf{E} \end{bmatrix} \quad (31)$$

$$\nabla \times \mathbf{H} = -i\omega\epsilon\mathbf{E} + \mathbf{J} \quad (32)$$

$$\nabla \times \mathbf{E} = i\omega\mu\mathbf{H} \quad (33)$$

and are simply the Frenkel/Biot equations for porous media acoustics along with the Maxwell equations for the electric and magnetic fields \mathbf{E} and \mathbf{H} . The electroseismic coupling occurs in the transport laws of Eq. (31) where \mathbf{J} is the electric-current density and $-i\omega\mathbf{w}$ the Darcy filtration velocity. If the coupling coefficient L were set to zero then there would be complete decoupling between the poroelastic and electromagnetic response fields.

Two types of electroseismic coupling are present in Eq. (31). Seismic waves generate a force $-\nabla p_f + \omega^2\rho_f\mathbf{u}$ that in addition to driving a Darcy fluid filtration $(k/\eta_f)(-\nabla p_f + \omega^2\rho_f\mathbf{u})$, also transports the diffuse charge of the double layer relative to the bound charge on the grain surfaces resulting in a “streaming” electric current $L(-\nabla p_f + \omega^2\rho_f\mathbf{u})$. Such generation of an electric current from an applied fluid-pressure gradient is known as “electro-filtration.” Conversely, when an applied electric field \mathbf{E} acts on a porous material, in addition to driving a conduction current given by $\sigma\mathbf{E}$, it also acts as a body force on the excess charge of the diffuse double layer resulting in a net fluid filtration given by $L\mathbf{E}$. Such generation of a fluid filtration from an electric field is known as “electro-osmosis.”

As stated, Frenkel (1944) only concerns himself with the electrofiltration (or “E”) effect. He makes the implicit assumption (correctly), that within a propagating compressional wave in a homogeneous material, there is no net electric current. The streaming electric current induced by the wave causes counter charge to accumulate in the troughs of the wave and the bound charge to become exposed in the peaks. The electric field associated with this wavelength-scale charge separation drives a conduction current that exactly balances the streaming current. Thus, for a P -wave propagating in a homogeneous material, $\mathbf{J}=0$ in Eq. (31) yielding $\mathbf{E} = -(L/\sigma)(-\nabla p_f + \omega^2\rho_f\mathbf{u})$, which, as will be seen next, is equivalent to Eq. (24).

Porous Media Transport Coefficients

The main purpose of this subsection is to address what is known about the frequency relaxation in the transport equations; an issue not addressed by Frenkel (1944).

Pride (1994) obtains analytic expression for the three porous-media transport coefficients: permeability $k(\omega)$, electrokinetic-coupling coefficient $L(\omega)$, and electric conductivity $\sigma(\omega)$. The results are valid to leading order in the dimensionless ratio d/Λ , where Λ is a characteristic pore-throat radius defined by Johnson et al. (1987) and d is a skindepth measure of the diffuse-charge-layer thickness known as the Debye length given by

$$d = \sqrt{\frac{\epsilon_f kT}{e^2 z^2 N}} \quad (34)$$

where kT =thermal energy; and ez =electric charge of each ion contributing to a symmetric electrolyte having ionic-number density N (number of ions having valence z per cubic meter). For most salinity conditions in the earth, d is on the order of nanometers and so the small d/Λ limit can be considered appropriate.

The results are

$$\frac{k(\omega)}{k_o} = \left[\left(1 - i \frac{4}{m} \frac{\omega}{\omega_t} \right)^{1/2} - i \frac{\omega}{\omega_t} \right]^{-1} \quad (35)$$

$$\frac{L(\omega)}{L_o} = \left[1 - i \frac{\omega}{\omega_t} \right]^{-1/2} \quad (36)$$

$$\frac{\sigma(\omega)}{\sigma_o} = 1 \quad (37)$$

where the following expressions for the viscous-to-inertial relative-flow transition frequency ω_t and the dimensionless number m have been used

$$\omega_t = \frac{\eta_f}{Fk_o\rho_f}$$

and

$$m = \frac{\Lambda^2}{Fk_o} \quad (38)$$

The effective pore-throat radius Λ and the electrical formation factor F both have precise mathematical definition given by Johnson et al. (1987) in terms of the dimensionless electric field $-\nabla\Phi$ in the pore space of an averaging volume of porous material of volume V

$$\frac{1}{F} = \frac{1}{V} \int_{\Omega_p} \nabla\Phi \cdot \nabla\Phi dV \quad (39)$$

$$\frac{2}{\Lambda F} = \frac{1}{V} \int_{\partial\Omega_{gp}} \nabla\Phi \cdot \nabla\Phi dS \quad (40)$$

Here, Ω_p =pore space and $\partial\Omega_{gp}$ =surface separating the grains from the pores. The electric potential Φ has units of length. Within a cylindrical disk of porous material having a thickness H , Φ satisfies the Laplace equation $\nabla^2\Phi=0$ throughout the pore space, and the boundary conditions that: (1) $\Phi=H$ on the flat surface $z=H$ of the disk; (2) $\Phi=0$ on $z=0$, and (3) $\mathbf{n} \cdot \nabla\Phi=0$ on both the circumferential surface of the disk as well as on the grain surfaces. In clean porous rocks where secondary clay on the grain surfaces has not created a large grain-surface area, Johnson et al. (1987) suggest that a good model for Λ is to take $m=8$ so that $\Lambda = \sqrt{8Fk_o}$.

The dynamic permeability of Eq. (35) was first obtained by Johnson et al. (1987) and allows for three distinct phenomena associated with the relative flow. At low enough frequencies $\omega \ll \omega_t m/4$, there is parabolic flow in the pores resulting in a permeability k_o that depends only on the topology and size of the pores. As frequencies increase and $\omega \approx \omega_t m/4$, viscous boundary layers develop in the pores. Finally, in the high-frequency limit where $\omega \gg \omega_t$, the viscous boundary layers have a thickness that diminishes with the square root of frequency, resulting in a relative motion dominated by inertial plug (ideal) flow. The real and imaginary parts of $k(\omega)$ in the high-frequency limit are

$$k(\omega) \sim \frac{\sqrt{2}}{F\Lambda} \left(\frac{\eta_f}{\rho_f\omega} \right)^{3/2} + \frac{i}{F} \frac{\eta_f}{\omega\rho_f} \text{ as } \omega \rightarrow \infty \quad (41)$$

So above the transition frequency ω_t , inertial forces dominate viscous forces, and the amplitude of the relative flow is reduced.

The relaxation in the dynamic coupling coefficient $L(\omega)$ of Eq. (36) is also due to the development of viscous boundary

layers in the pores. Pride (1994) allows for an additional relaxation in $L(\omega)$ as the viscous skin depth $\sqrt{\eta_f/(\rho_f\omega)}$ associated with the viscous boundary layers becomes smaller than the Debye length; however, over the range of frequencies and salinities normally encountered in the earth, this relaxation never takes place and as such has not been included in Eq. (36). The steady-state coupling coefficient L_0 is given by

$$L_0 = -\frac{\varepsilon_f \zeta}{\eta_f F} \quad (42)$$

to leading order in d/Λ where F is the same formation factor defined by Eq. (39).

There is no important relaxation in $\sigma(\omega)$ over frequencies where the viscous skin depth is greater than the Debye length; i.e., when $\sqrt{\eta_f/(\rho_f\omega)} > d$ which corresponds to the frequency range of all seismic applications (c.f., Pride 1994). To leading order in d/Λ , one simply has

$$\sigma(\omega) = \sigma_0 = \frac{\sigma_f}{F} \quad (43)$$

with the formation factor again defined by Eq. (39). Induced polarization effects associated with ion accumulations in the electric double layers surrounding the grains exist across the seismic band of frequencies, but manifest themselves as milliradian phase differences between the applied electric field and induced current that result in negligible changes in $\sigma(\omega)/\sigma_0$. Other polarization effects resulting in more significant variations in $\sigma(\omega)/\sigma_0$ due to interfaces between ionic and electronic conductors or due to clay membranes are not modeled here.

An immediate consequence of these results is that at frequencies where viscous boundary layers have not yet developed, one has that when there is no net current (e.g., in a longitudinal wave)

$$\left. \frac{E_x}{-\partial p_f / \partial x + \omega^2 \rho_f \mu_x} \right|_{J=0} = \frac{\varepsilon_f \zeta}{\eta_f \sigma_f} \quad (44)$$

to leading order in d/Λ which is the famous proposition of von Smoluchowski (1903). It is through Eq. (44) that the zeta potential is often measured. If the left-hand side is directly measured after applying a pressure drop across a porous sample, and if the fluid properties ε_f , η_f , and σ_f are known, ζ is determined. For quartz surfaces in contact with a saline solution having a given salinity C (moles/liter) and pH, ζ is observed to obey the empirical formula

$$\zeta(\text{Volts}) = (0.01 + 0.025 \log C) \frac{(\text{pH} - 2)}{5} \quad (45)$$

which gives the measured dependence on C when pH=7, and gives the appropriate general trend for the pH dependence.

In conclusion, the important relaxation in the porous-media transport coefficients is associated with the onset of viscous boundary layers in the pores. However, since the transition frequency $\omega_t = \eta_f/(\rho_f F k_o)$ normally lies above the frequency band of 10–10³ Hz used in seismic exploration, it is usually appropriate to ignore the frequency dependence in these coefficients (as did Frenkel 1944) and simply take $k(\omega) = k_o$, $L(\omega) = \varepsilon_f \zeta / (\eta_f F)$, and $\sigma(\omega) = \sigma_f / F$. In this case, only two porospace topology parameters k_o and F must be specified to model the electroseismic transport.

Diverse Electroseismic Wave Phenomena

Eqs. (28)–(33) allow for a wide range of electroseismic phenomena beyond the electric field contained in a compressional wave

that was the sole focus of Frenkel (1944). A few of the many possible phenomena/applications are now discussed.

Magnetic Field in Shear Wave

A shear wave in a homogeneous material does not cause the counter charge in the double layer to accumulate. Because of this, the grain accelerations produce a nonzero net current \mathbf{J} in the plane of the wavefront and such current sheets produce magnetic fields as part of the material response. There is a small electric field produced via induction but this is extremely small compared to the electric field in a compressional wave of similar amplitude and does not produce a conduction current that significantly opposes the streaming current. For a shear wave propagating in the x direction with a displacement amplitude u_y , Pride and Haartsen (1996) have determined the exact expression for the magnetic field which at low frequencies and to leading order in the dimensionless number $\omega k_o \rho_f^2 / (\rho \eta_f)$ reduces to

$$\frac{H_z}{-i\omega u_y} = \sqrt{\frac{G}{\rho}} \frac{\rho_f \varepsilon_f \zeta}{\eta_f F} \quad (46)$$

This result was also given by Garambois and Dietrich (2001) and states that the magnetic field in a seismic shear wave is directly proportional to the particle velocity which is the material response recorded by a geophone. The magnetic field measured by a magnetometer is $B_z = \mu H_z$, where μ is the magnetic susceptibility of the material (only different from that of vacuum when iron is significantly present in the soil). If the particle velocities of a shear wave are on the order of 10⁻³ m/s (a large amplitude but linear seismic response) and if characteristic values appropriate to water are used, one obtains that B_z is on the order of 10⁻² nT which is at the extreme limit of being measurable. Using magnetometers as shear-selective recording devices at seismic frequencies is, therefore, probably not a commercially interesting possibility.

Converted Seismic-to-Electromagnetic Fields at Interfaces

When a compressional (or shear) wave traverses an interface in which any of the transport properties or elastic moduli change, there is a dynamic imbalance of the streaming current that results in additional charge separation across the interface. Because this charge separation is concentrated in space and has a strong dipolar component, particularly so as the first Fresnel zone traverses the interface, there are electric (and magnetic) fields created that have extent outside the support of the seismic waves and that can be recorded at the earth's surface. Over the seismic band width of 10 Hz < f < 10³ Hz, the electromagnetic skin depth $\delta = 1/\sqrt{2\pi\mu_o\sigma f}$ varies as 10³ m > δ > 10² m. So if the interface of interest is less than 100 m from the electrical antennas, the recorded response is in the electrostatic and magnetostatic near field of the charge separation at the interface and induction effects may be neglected.

A numerical example of the electric and magnetic fields generated at an interface is now given for the situation depicted in Fig. 2. An isotropic explosion is located at $z=5$ m, a material-property interface is at $z=50$ m, and a line of geophones and electric-dipole antennas is at $z=0$ m. A numerical reflectivity algorithm (Haartsen and Pride 1997; Garambois and Dietrich 2002) is used to solve the complete set of governing equations [Eqs. (28)–(33) with no terms neglected] for this geometry. The interface separates a higher-porosity more compressible sandstone upper layer, from a lower-porosity stiffer lower layer. The results of the numerical simulation are displayed in Fig. 3.

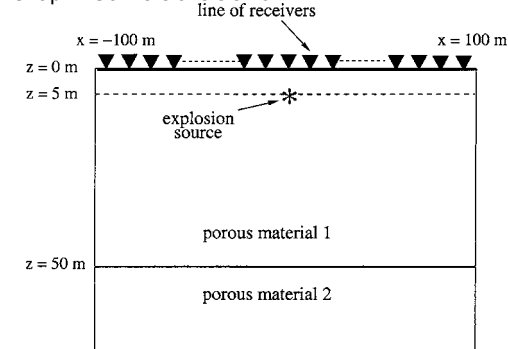


Fig. 2. Receiver, source, and interface geometry for numerical example given in Fig. 3

Of interest from an exploration perspective are the “flat” events shown on the electric and magnetic sections that are generated at $t=21$ ms as the P -wave traverses the interface. Such converted fields provide information about the interface that is distinct from the information in the seismic reflection (e.g., they are sensitive to fluid chemistry changes while seismic waves are not). Field data that have actually recorded such interface conversions (from P to EM) have been reported by Martner and Sparks (1959), Thompson and Gist (1993), and Garambois and Dietrich (2001). However, much further work is required before electrical

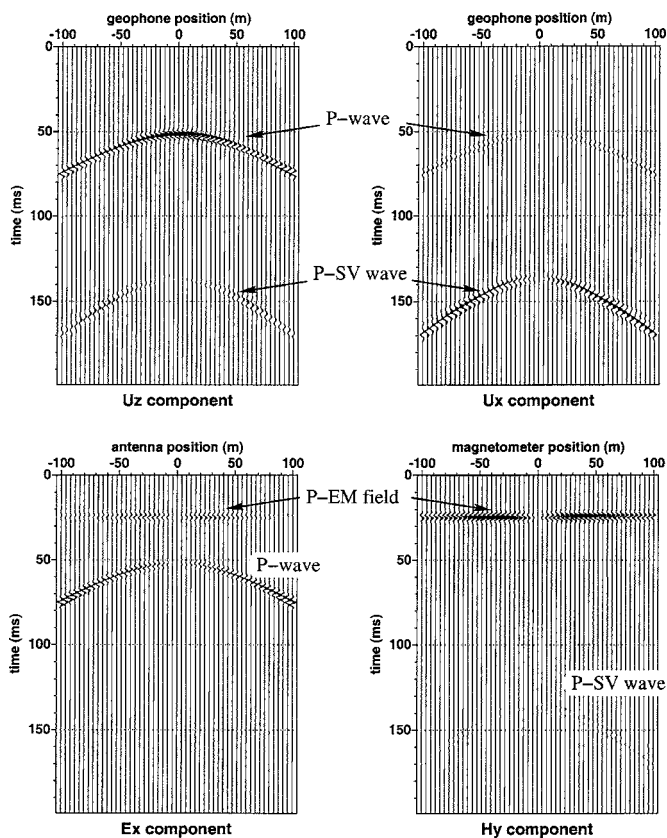


Fig. 3. Electro seismic example for geometry depicted in Fig. 2. Interface is located at P -wave travel time of 21 ms. The no-moveout P-EM converted fields have been multiplied by 500 in both electric and magnetic sections. P -SV conversion is just barely visible on magnetic section (the hyperbolic arrival at 130 ms). Direct P , wave from source to receivers is not shown.

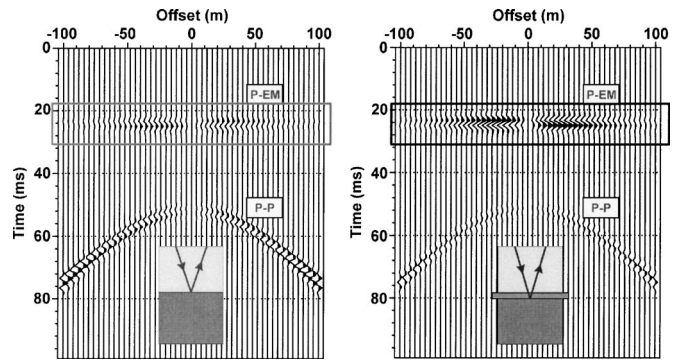


Fig. 4. Electrical section to left corresponds to same situation shown in Fig. 3 while electrical section to right corresponds to when a thin (1 cm) impermeable layer has been sandwiched between two half spaces. Converted electric field is roughly ten times larger in situation in which thin layer is present.

antenna data can be routinely processed to obtain the no-moveout interface fields. A principal challenge is that the electric fields created at an interface are far smaller than the fields contained within the seismic waves and so the electrical section has to be filtered to remove all events that move out as a function of time (since these are due to seismic waves traversing the antennae).

A particularly interesting aspect of the electro seismic conversion at an interface is that the amplitude of the converted electric field can be drastically increased if there is a thin layer of third material present at the interface. In Fig. 4, the same example as in Fig. 3 is considered but with the addition of a thin 1 cm layer of very low permeability material (a shale aquitard) sandwiched between the two half spaces. The amplitude of the converted electric field is increased by roughly a factor of 10 in the case where the thin shale layer is present, while the reflected seismic wave is essentially unaffected by the presence of the thin layer. This has the potential for being exploited as an aquitard detector in hydrological applications.

Applications to Electric Fields Created by Earthquakes

A fault that has undergone a shear dislocation creates lobes of compression and dilation in the crust surrounding the limits of the fault segment that slipped. Immediately after the earthquake, the poroelastic response is undrained (no fluid mass enters or leaves each mass element of the crust). However, the fluid pressure created by such undrained compression will subsequently equilibrate by diffusion (the slow wave) producing electric fields in the process by electrofiltration. Modeling the complete poroelastic and electric response as the fluid pressure equilibrates through time in a uniform crust after an earthquake has been the subject of a recent study (Pride et al. 2004).

An example is given in Fig. 5. The earthquake is modeled as 50 cm of uniform slip on a normal fault dipping at 45° . The slip surface is 5 km in the direction of slip and 20 km wide and is denoted in the top panel of Fig. 5 by the dashed-white line. This corresponds to a Magnitude 6 earthquake and the stress changes created immediately after the slip are numerically determined using the algorithm of Okada (1992). The subsequent fluid-pressure variations through time and space were numerically calculated using finite differences. The displayed vertical component of the electric field has an amplitude on the order of milliVolt/meter which is 100–1000 times larger than the telluric fields that are routinely measured (the telluric fields are electric

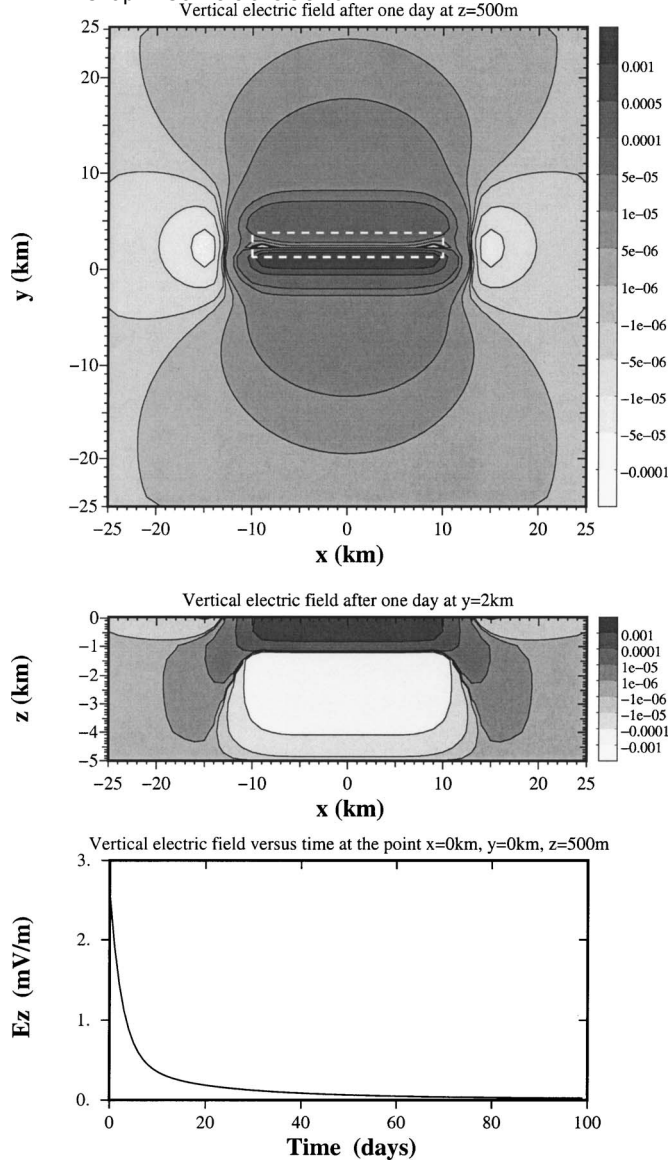


Fig. 5. Electrical field (V/m) generated in uniform crust after magnitude 6 earthquake on reverse fault dipping at 45° and positioned as shown in top panel with dashed-white line. Vertical-depth axis is z .

fields that enter the earth from the atmosphere each day as the ionosphere is heated by the sun). Direct measurement of the decay of the crust's electric field through time after an earthquake has not yet been attempted.

Electro-Osmotic Coupling

One of the greatest potential applications of Eqs. (28)–(33), concerns injecting time-varying current into the earth with the goal of generating seismic waves at interfaces at depth. The idea is that an applied electric field will drive an electro-osmotic flow of fluid LE . At interfaces where either L or $\mathbf{n} \cdot \mathbf{E}$ change (\mathbf{n} being the normal to the interface), there is an accumulation of fluid and an associated volumetric dilatation of the porous material that generates a compressional wave having the same time signature as the applied current.

Although this possibility has been discussed by Thompson and Gist (1993), no studies have ever been published in which such

electrically generated seismic waves have been measured. Numerical simulations indicate that for safe levels of injected current (say less than 10 A at the injection electrode), the generated seismic waves will have a very small amplitude (displacements less than angstroms). However, because the source is a nondestructive electric current that can be applied for long durations with a controlled time signature, it should be possible to extract even small-amplitude seismic waves from the ambient noise by cross-correlating the seismic data with the known time signature of the electric current. This is the subject of ongoing research.

Conclusions

Frenkel (1944) produced equations having nearly identical form to those of Biot (1956a,b). The only difference in the form of Frenkel's equations is an extra fluid pressure gradient term in the total conservation of momentum equation that should not be present. As was seen here, Frenkel also made a slight error in developing his effective poroelastic compressibility coefficients with the result that he did not obtain the fluid-substitution relations of Gassmann (1951) and Biot and Willis (1957). Frenkel's estimate of the electric field contained in a compressional wave (the focus of his electroseismic investigation) is correct if the proper compressibility constants are used and if the extra fluid-pressure gradient in the bulk-force balance is neglected. He did not attempt to analyze any of the other electroseismic phenomena that were discussed above.

Frenkel covered a lot of ground in his only paper on poroelastic phenomena, and the vast majority of his intuitive approach to obtaining the governing equations is correct. He certainly deserves a greater recognition for his pioneering contribution than he has so far been accorded. From the present writer's perspective, it seems entirely appropriate to refer to the equations governing the acoustics of isotropic porous materials as the "Frenkel/Biot equations" instead of just the "Biot equations" as is the current fashion.

References

- Berge, P. A., Wang, H. F., and Bonner, B. P. (1993). "Pore-pressure buildup coefficient in synthetic and natural sandstones." *Int. J. Rock Mech. Min. Sci. Geomech. Abstr.*, 30, 1135–1141.
- Biot, M. A. (1956a). "Theory of propagation of elastic waves in a fluid-saturated porous solid. I. Low-frequency range." *J. Acoust. Soc. Am.*, 28, 168–178.
- Biot, M. A. (1956b). "Theory of propagation of elastic waves in a fluid-saturated porous solid. II. Higher frequency range." *J. Acoust. Soc. Am.*, 28, 179–191.
- Biot, M. A., and Willis, D. G. (1957). "The elastic coefficients of the theory of consolidation." *J. Appl. Mech.*, 24, 594–601.
- Brown, R. J. S. (1980). "Connection between formation factor for electrical resistivity and fluid-solid coupling factor in Biot's equations for acoustic wave in fluid-filled porous media." *Geophysics*, 45, 1269–1275.
- Frenkel, J. (1944). "On the theory of seismic and seismoelectric phenomena in a moist soil." *J. Phys. (USSR)*, 8, 230–241.
- Garambois, S., and Dietrich, M. (2001). "Seismoelectric wave conversions in porous media: field measurements and transfer function analysis." *Geophysics*, 66, 1417–1430.
- Garambois, S., and Dietrich, M. (2002). "Full waveform numerical simulations of seismoelectromagnetic wave conversions in fluid-saturated stratified porous media." *J. Geophys. Res.*, 107, 40–58.

Chap 2. Conversions sismo-EM

- Gassmann, F. (1951). "Über die Elastizität poröser Medien." *Vierteljahrsschrift Naturforschenden Gesellschaft Zürich*, 96, 1–23.
- Haartsen, M. W., and Pride, S. R. (1997). "Electroseismic waves from point sources in layered media." *J. Geophys. Res.*, 102, 24745–24769.
- Ivanov, A. G. (1939). "Effect of electrization of earth layers by elastic waves passing through them." *Dokl. Akad. Nauk SSSR*, 24, 42–45.
- Johnson, D. L., Koplik, J., and Dashen, R. (1987). "Theory of dynamic permeability and tortuosity in fluid-saturated porous media." *J. Fluid Mech.*, 176, 379–402.
- Kosten, C. W., and Zwikker, C. (1941). "Extended theory of the absorption of sound by compressible wall coverings." *Physica (Amsterdam)*, 8, 968–978.
- Martner, S. T., and Sparks, N. R. (1959). "The electroseismic effect." *Geophysics*, 24, 297–308.
- Okada, Y. (1992). "Internal deformation due to shear and tensile faults in a half-space." *Bull. Seismol. Soc. Am.*, 82, 1018–1040.
- Pride, S. R. (1994). "Governing equations for the coupled electromagnetics and acoustics of porous media." *Phys. Rev. B*, 50, 15678–15696.
- Pride, S. R., and Berryman, J. G. (1998). "Connecting theory to experiment in poroelasticity." *J. Mech. Phys. Solids*, 46, 719–747.
- Pride, S. R., and Haartsen, M. W. (1996). "Electroseismic wave properties." *J. Acoust. Soc. Am.*, 100, 1301–1315.
- Pride, S. R., Moreau, F., and Gavrilenko, P. (2004). "Mechanical and electrical response due to fluid-pressure equilibration following an earthquake." *J. Geophys. Res.*, 109, B03302.
- Skempton, A. W. (1954). "The pore-pressure coefficients A and B." *Geotechnique*, 4, 143–147.
- Thompson, A. H., and Gist, G. A. (1993). "Geophysical applications of electrokinetic conversion." *The Leading Edge*, 12, 1160–1173.
- von Smoluchowski, M. (1903). "Contribution à la théorie de l'endosmose électrique et de quelques phénomènes corrélatifs." *Bull. Int. Acad. Sci. Cracovie*, 8, 182–200.

2.2.2. Expériences de laboratoire sur les effets sismo-magnétiques (et sismo-électriques)

J'ai également collaboré pour l'interprétation de données expérimentales obtenues dans une colonne de taille réduite et dans les conditions très favorables du laboratoire à très bas bruit électromagnétique et sismique de Rustrel. Ce travail expérimental, qui constitue le cœur de la thèse de C. Bordes (LGIT puis Univ. de Pau et des Pays de l'Adour), a permis l'acquisition de données sismo-électriques et sismo-magnétiques originales.

Pour confirmer l'origine électrocinétique des champs sismo-électriques et sismo-magnétiques, les données ont été acquises dans du sable sec et du sable saturé ce qui a permis d'éliminer d'autres origines potentielles, notamment celles potentielles dues à la vibration des magnétomètres. Dans ce cas, la composition du milieu n'influerait pas les propriétés des champs sismo-magnétiques enregistrés, qui seraient alors identiques d'une expérience à l'autre. Il faut préciser qu'au niveau expérimental, une attention particulière a été conduite pour assurer un découplage mécanique le plus efficace possible entre magnétomètres et la colonne de sable. Dans un des articles, non présenté ici, Bordes et al. (2006) décrivent l'appareillage expérimental et les premières données mesurées dans du sable homogène. Dans un deuxième article plus détaillé et quantitatif (Bordes et al., 2008), présenté ci-après, nous montrons notamment que les champs sismo-magnétiques co-sismiques sont mesurables bien que les amplitudes soient faibles. Les vitesses associées aux champs sismo-électrique et sismo-magnétique co-sismiques indiquent qu'ils sont associés à des modes de propagation différents. En se fondant sur la théorie poroélastique, nous avons notamment pu établir que le mode de propagation associé au champ sismo-magnétique mesuré est lié à la propagation de l'onde S, comme prédit par Pride (1994) ou Garambois & Dietrich (2002). Ce champ sismo-magnétique exhibe une amplitude de l'ordre de 0.035 nT lorsqu'une accélération sismique est de l'ordre de $1\text{m}\cdot\text{s}^{-2}$.

Evidence of the theoretically predicted seismo-magnetic conversion

Clarisse Bordes,^{1,2} Laurence Jouniaux,³ Stéphane Garambois,⁴ Michel Dietrich,⁴
Jean-Pierre Pozzi⁵ and Stéphane Gaffet⁶

¹Modélisation et Imagerie en Géosciences, Avenue de l'Université (UMR 5212), 64000 Pau, France

²Laboratoire de Géophysique Interne et Tectonophysique (UMR 5559), 1381 rue de la Piscine, 38041 Grenoble Cedex 9, France

³Institut de Physique du Globe de Strasbourg (UMR 7516), 5 rue R. Descartes, 67084 Strasbourg, France. E-mail: laurence.jouniaux@east.u-strasbg.fr

⁴Laboratoire de Géophysique Interne et Tectonophysique (UMR 5559), 1391 rue de la Piscine, 38041 Grenoble Cedex 9, France

⁵Ecole Normale Supérieure (UMR 8538), 24 Rue Lhomond, 75231 Paris Cedex 05, France

⁶Laboratoire Géosciences Azur (UMR 6526), 250 rue Albert Einstein, Sophia Antipolis 06560 Valbonne, France

Accepted 2008 April 21. Received 2008 April 18; in original form 2007 September 13

SUMMARY

Seismo-electromagnetic phenomena in porous media arise from seismic wave-induced fluid motion in the pore space, which perturbs the equilibrium of the electric double layer. This paper describes with details the original experimental apparatus built within the ultra-shielded chamber of the Low Noise Underground Laboratory of Rustrel (France). We measured seismo-magnetic conversions in moist sand using two induction magnetometers, and a pneumatic seismic source to generate the seismic wave propagation. We ensured to avoid the magnetometer vibrations, which could induce strong disturbances from induction origin. Interpretation of the data is improved by an analytical description of phase velocities for fast (P_f) and slow (P_s) longitudinal modes, transverse mode (S) as well as the extensional mode due to the cylindrical geometry of the sample.

The purpose of this paper is to provide elements to measure correctly coseismic seismo-magnetic fields and to specify their amplitude. The seismic arrivals recorded in the sample showing a 1200–1300 m s⁻¹ velocity have been associated to P and extensional waves. The measured seismo-magnetic arrivals show a velocity of about 800 m s⁻¹ close to the calculated phase velocity of S waves. Therefore, we show that the seismo-magnetic field is associated to the transverse part of the propagation, as theoretically predicted by Pride (1994), but never measured up to now. Moreover, the combined experimental and analytical approaches lead us to the conclusion that the measured seismo-magnetic field is probably about 0.035 nT for a 1 m s⁻² seismic source acceleration (0.1 g).

Key words: Magnetic and electrical properties; Hydrogeophysics; Acoustic properties.

1 INTRODUCTION

Seismic wave propagation in fluid-filled porous media generates electromagnetic phenomena due to electrokinetic couplings at the pore scale. These conversions are due to the relative motions of electrolyte ions with respect to the mineral surface (grains). Origin of these phenomena is generally attributed to an electrical double (Overbeek 1952) or triple-layer (Davis *et al.* 1978) at the rock/electrolyte interface. As a consequence, seismic wave propagation in the porous media can be accompanied by transient electric and magnetic fields created in the homogeneous porous medium. Existing investigations of the seismo-electromagnetic effects account for two main kinds of electrokinetic conversions.

(1) In a homogeneous media, the pore fluid dragging ions of the electrolyte causes an electrical convection current. This current is naturally balanced by an equal and opposite conduction current

that establishes an electrical potential gradient. Under an oscillating pressure source, the potential will linearly change in amplitude and sign with the pressure. This electrical potential will be seen as a wave travelling with the pressure, but since the total current is zero, no electric nor magnetic field will be observed outside the area of disturbances. This phenomena is the coseismic part of the seismo-electromagnetic phenomena.

(2) On the other hand, when the seismic wave crosses an interface, an electrical current imbalance can be induced by the contrast of porous media properties (Garambois *et al.* 2002). This acts as the source for an electromagnetic disturbance, travelling with high speed and spreading throughout the formation.

Seismo-electromagnetic effects are especially appealing for environmental or oil exploration as they open the possibility to characterize the fluids contained in the subsurface or in reservoir rocks with the resolution of seismic methods. The second kind of

seismo-electromagnetic conversion occurs at a contrast in electrical impedance, even if there is no contrast in seismic impedance. Interfaces between permeable or fractured zones may be detected by the measurement of either seismic to electric conversion (Thompson & Gist 1993) or electric to seismic conversion (Thompson *et al.* 2005). However, since the induced signals are low-amplitude signals, this method may not be efficient to characterize very deep formations, except in boreholes or using very high powerful seismic sources.

Over the past decades, field experiments were conducted to characterize these seismo-electromagnetic phenomena (Thompson 1936; Martner & Sparks 1959; Broding *et al.* 1963; Long & Rivers 1975). Successful field experiments performed in recent years (Butler & Russell 1993; Thompson & Gist 1993; Mikhailenko & Soboleva 1997; Russell *et al.* 1997; Beamish 1999; Hunt & Worthington 2000; Garambois & Dietrich 2001; Kepic & Rosid 2004; Thompson *et al.* 2005; Dupuis & Butler 2006; Dupuis *et al.* 2007; Haines *et al.* 2007a,b; Strahser *et al.* 2007) have stimulated new interest in this particular mechanism. As described by Pride (1994), analytical interpretation of these phenomena needs to connect the theory of Biot (1956) for the seismic wave propagation in a two phases medium with the Maxwell's equations, using dynamic electrokinetic couplings. These analytical developments opened the possibility to numerically simulate the electrokinetic coupling phenomena in homogeneous or layered saturated media (Haartsen & Pride 1997; Haartsen *et al.* 1998; Singer & Fainberg 1999; Garambois & Dietrich 2001, 2002) with applications to reservoir geophysics (Hu & Wang 2000; Jackson *et al.* 2005; Singer *et al.* 2005; Saunders *et al.* 2006).

Some laboratory studies exist on the zero-frequency limit, often referred to as the streaming potential (Ishido & Mizutani 1981; Pozzi & Jouniaux 1994; Jouniaux & Pozzi 1995a,b, 1997; Pengra *et al.* 1999; Lorne *et al.* 1999a,b; Jouniaux *et al.* 2000; Doussan *et al.* 2002; Hase *et al.* 2003; Guichet *et al.* 2003, 2006). Applying a sinusoidal fluid pressure, some authors studied the frequency-dependence of the streaming potential (Packard 1953; Cooke 1955; Reppert *et al.* 2001). These measurements on sand or core samples showed that the electrokinetic effect is particularly sensitive to the fluid conductivity, to the fluid- pH and to the water-saturation state. However, few laboratory experiments have been performed on dynamic seismo-electric conversions (Parkhomenko & Tsze-San 1964; Gaskarov & Parkhomenko 1974; Chandler 1981; Mironov *et al.* 1994; Jiang *et al.* 1998; Ageeva *et al.* 1999; Zhu *et al.* 2000) some of them focusing on laboratory borehole measurements (Zhu *et al.* 1999; Zhu & Toksöz 2003, 2005). Recently, Chen & Mu (2005) as well as Block & Harris (2006) confirmed that a seismic wave crossing an interface induces an electromagnetic field, with electrokinetic origin, by measuring the associated electric field.

Most of these field and laboratory studies have concentrated on measurements of electrical fields as they require simple and cheap instrumentation. The investigation of seismo-magnetic fields has received much less attention, mainly because of the complex apparatus for measuring low magnetic fluxes. As suggested by Pride & Haartsen (1996), the seismo-electric field E has to be associated to the whole seismic field whereas the seismo-magnetic field B is coupled to transverse modes (S waves). To our knowledge, no study succeeded to confirm the theoretically predicted seismo-magnetic field: neither its existence nor its magnitude. In a recent short paper Bordes *et al.* (2006) announced that seismo-magnetic couplings were measurable at least in low magnetic noise environment and consistent with these theoretical predictions. In this paper, the seismic, seismo-electric and seismo-magnetic field were com-

pared, but these preliminary results were not fully interpreted and seismo-magnetic amplitudes were not given.

To go further, this paper describes with details the original experimental apparatus and presents arguments to give seismo-magnetic amplitudes. This experiment was built in the ultra-shielded chamber of the Low Noise Underground Laboratory of Rustrel (France) to measure seismo-electromagnetics of the coseismic type. It is shown that very weak residual vibrations can generate strong disturbing coseismic signals that could be misinterpreted. We point out that devices for seismo-magnetic couplings measurements have to be very carefully designed for experimental measurements as well as for field investigations.

The major difficulty blocking access to seismomagnetic amplitudes is due to magnetometers, which are sensitive both to radial and azimuthal components of the magnetic field. As this dependence differs strongly according to the component (10 V nT^{-1} for radial and 10 mV nT^{-1} for azimuthal component), the access to real amplitudes can be a difficult task. However, analytical developments adapted to our experiment configuration showed that the radial component is negligible. It allowed to provide an estimation of the measured seismomagnetic field amplitude around 0.035 nT for a 1 m s^{-2} seismic source.

2 SEISMIC TO ELECTROMAGNETIC FIELD CONVERSION: THEORETICAL BACKGROUND

The equations governing the coupled seismic and electromagnetic wave propagation in a fluid-saturated porous medium have been developed by Pride (1994). In his work, this author derived a complete set of nine macroscopic equations, grouping into four Maxwell's and three poroelastic equations which are connected by two transport relations (Pride 1994) eqs 250 and 251:

$$\mathbf{J} = \sigma(\omega)\mathbf{E} + L(\omega) (-\nabla p + \omega^2 \rho_f \mathbf{u}_s). \quad (1)$$

$$-i\omega \mathbf{w} = L(\omega)\mathbf{E} + \frac{k(\omega)}{\eta} (-\nabla p + \omega^2 \rho_f \mathbf{u}_s). \quad (2)$$

In eq. (1), the macroscopic electrical current density \mathbf{J} is written as the sum of the average conduction and streaming current densities. Similarly, the fluid flux \mathbf{w} of eq. (2) is separated into electrically and mechanically induced contributions. The electrical fields and mechanical forces that generate the current density \mathbf{J} and fluid flux \mathbf{w} are, respectively, \mathbf{E} and $(-\nabla p + i\omega^2 \rho_f \mathbf{u}_s)$, where p is the pore-fluid pressure, \mathbf{u}_s is the solid displacement, and \mathbf{E} is the electric field. In the above relationships, ρ_f is the pore-fluid density, η is the fluid's shear viscosity, and ω is the angular frequency. The most important parameter in eqs (1) and (2) is the complex and frequency-dependent electrokinetic coupling coefficient $L(\omega)$, which describes the coupling between the seismic and electromagnetic fields (Pride 1994; Reppert *et al.* 2001):

$$L(\omega) = L_0 \left[1 - i \frac{\omega}{\omega_c} \frac{m}{4} \left(1 - 2 \frac{d}{\Lambda} \right)^2 \left(1 - i^{3/2} d \sqrt{\frac{\omega \rho_f}{\eta}} \right)^2 \right]^{-1/2}, \quad (3)$$

where the static electrokinetic coupling is given by:

$$L_0 = -\frac{\phi}{\alpha_\infty} \frac{\varepsilon_{rf} \zeta}{\eta} \left(1 - 2 \frac{d}{\Lambda} \right), \quad (4)$$

where m and Λ are geometrical parameters of the pores given in Table C1, ϕ is the porosity, α_∞ the tortuosity, d the Debye length and ε_{rf} the dielectric constant of the fluid. The critical angular

frequency ω_c defined in the Biot's theory separates the viscous and inertial flow domains. Its value depends on the permeability k_0 :

$$\omega_c = \frac{\phi}{\alpha_\infty k_0} \frac{\eta}{\rho_f}. \quad (5)$$

The remaining two coefficients $\sigma(\omega)$ and $k(\omega)$ of eqs (1) and (2), represent the electric conductivity and dynamic permeability of the porous material, respectively. These coefficients are detailed in Appendix Section A1. The most influencing parameter on the electrokinetic coupling coefficient (eqs 3 and 4) is the electrical potential at the rock/fluid interface (called zeta potential), (itself depending on fluid composition, pH) and formation factor (Davis *et al.* 1978; Ishido & Mizutani 1981; Jouniaux & Pozzi 1995a; Lorne *et al.* 1999a; Jouniaux *et al.* 2000; Guichet *et al.* 2006).

In light of Pride's theory, Garambois & Dietrich (2001) expressed the electric and magnetic fields \mathbf{E} and \mathbf{H} as a function of the seismic displacement \mathbf{u} . In case of plane waves propagating in the homogeneous medium at seismic frequencies ($\omega < \omega_c$), they found:

$$\mathbf{E} \simeq \frac{1}{\sigma_f} \frac{\varepsilon_0 \rho_f \kappa_f \zeta}{\eta} \left(1 - \frac{\rho}{\rho_f} \frac{C}{H} \right) \ddot{\mathbf{u}} \quad (6)$$

for displacements associated to the longitudinal fast (type I) P -waves (Biot 1956, 1962), and

$$|\mathbf{H}| \simeq \frac{\phi}{\alpha_\infty} \frac{\varepsilon_0 \rho_f \kappa_f |\zeta|}{\eta} \sqrt{\frac{G}{\rho}} |\dot{\mathbf{u}}| \quad (7)$$

for displacements associated to transverse SH and SV waves.

Note that the seismo-magnetic field is coupled to the transverse propagation mode. The in-line component E of the electric field accompanying the compressional waves is, therefore, approximately proportional to the grain acceleration. In expressions 6 and 7, ε_0 is the vacuum's dielectric constant and σ_f represents the fluid's electric conductivity, G is the shear modulus of the framework, ϕ is the porosity, and ρ is the bulk density. The tortuosity α_∞ represents a geometrical factor depending on the pore structure and orientation, and is usually taken equal to the product of the porosity by the formation factor. The definitions of the C and H moduli are those of Biot (1962) (Appendix Section A1).

However, boundary conditions can produce significant effects on the seismic propagation and have to be taken into account for the seismo-electromagnetic interpretations. In the experiment described afterwards, the sand is placed in a cylindrical column. Therefore, extensional modes have to be taken into account. As an illustration, analytical solutions of the seismo-electromagnetic fields are developed in Appendix B. Moreover, we will show in Section 5 that the vertical seismic excitation should induce an azimuthal magnetic field in such a configuration.

3 EXPERIMENTAL SETUP

3.1 Underground low magnetic noise laboratory

Since the decommissioning of the ground-based component of the French nuclear missile system, the underground control chamber has been turned into an underground low magnetic noise laboratory. The Laboratoire Souterrain à Bas Bruit (LSBB, Rustrel France) presents very low electromagnetic noise conditions which give the possibility to perform very sensitive electromagnetic measurements. At the deepest point (500 m below the surface), a non-conventional shielded cylindrical capsule is embedded without any

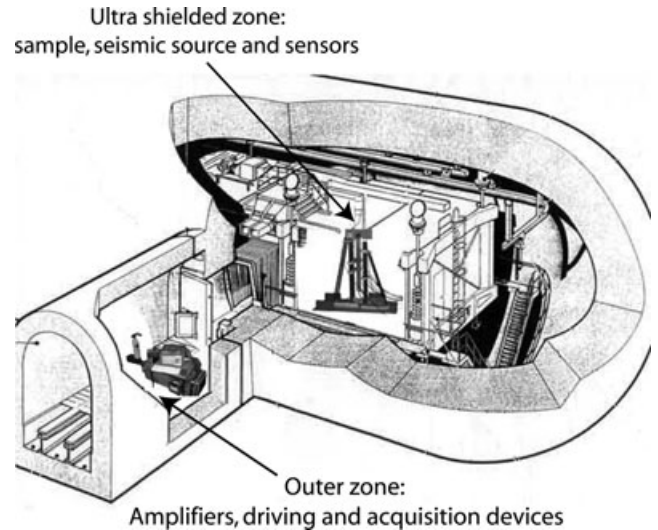


Figure 1. Sensitive part of the experiment (sample and magnetometers) is located within the ultra-shielded chamber of the laboratory whereas devices generating electromagnetic disturbances are located outside. The ambient magnetic noise is lower than $2 fT/\sqrt{\text{Hz}}$ above 10 Hz within the chamber (adapted from <http://lsbb.unice.fr>).

μ -metal. The chamber is suspended on massive springs cutting off low frequency ground motions with a residual electromagnetic noise lower than $2 fT/\sqrt{\text{Hz}}$ above 10 Hz (Waysand *et al.* 1999; Gaffet *et al.* 2003). To preserve these outstanding conditions, sensitive parts of the experiment including sample, seismic source and sensors, are located within the ultra-shielded chamber. On the contrary, the instruments generating electromagnetic disturbances (electronic devices) are placed outside the chamber, within the corridor (Fig. 1).

3.2 Characteristics of the porous medium

Physico-chemical properties of the mineral grains are of the highest importance on seismo-electromagnetic couplings. Especially, the grains have to be poorly soluble to avoid increasing of the fluid conductivity and decreasing of the electrokinetic coupling (see eq. 6). Consequently, we chose a highly referenced medium for mechanical, electrical and chemical properties composed with 99 per cent of silica. A Plexyglas column 104 cm long and 8 cm diameter (Fig. 2, part A) is filled with Fontainebleau sand that can be imbibed from below with demineralized water to obtain high electrokinetic couplings (Guichet *et al.* 2003; Lorne *et al.* 1999a). The sand was highly compacted by about 1500 hammer shots during the filling in order to limit the high frequency attenuation. The measured permeability of the sand is $5.8 \times 10^{-12} \text{ m}^2$, its electrical resistivity is 22 k Ω m, and the water conductivity is 3.1 mS m^{-1} with a pH of 6.55 at 20.5°C.

The bulk density of the sand ($1.77 \times 10^3 \text{ kg m}^{-3}$) has been measured by weighing during the filling. By comparing to the bulk density of silica ($2.65 \times 10^3 \text{ kg m}^{-3}$), we obtain the total porosity of the sand (33 per cent) which is constant along the sample. On the other hand, the volume of water imbibed in the sand does not exceed 1.9 L. The sand has been fluid filled by imbibition from a water tank connected to the lower extremity. This procedure does not allow to acquire a fully saturated sample, but rather in the range of 80–95 per cent.

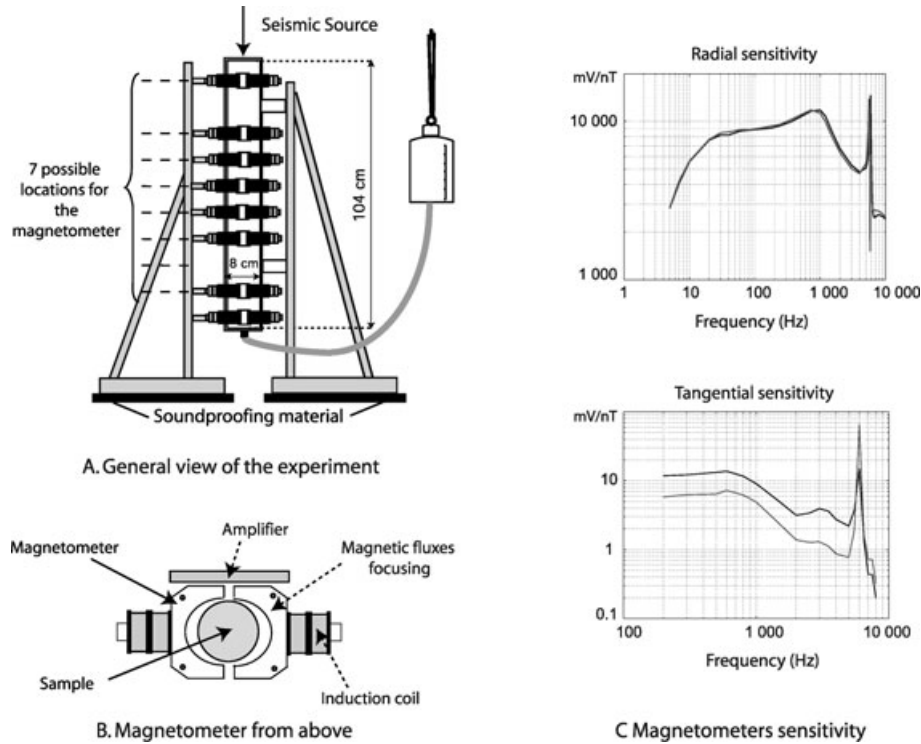


Figure 2. (A) The magnetometers and the Plexyglas column are fixed on two different stands; (B) the induction magnetometers consist in two focusing cores and induction coils and (C) radial sensitivity of magnetometers is around 10 V nT^{-1} and azimuthal sensitivity is around 10 mV nT^{-1} (grey and black lines are, respectively, attributed to lower and upper magnetometer).

3.3 Experimental setup within the ultra-shielded chamber

Seismic wave propagation is generated by a pneumatic seismic source (Bordes *et al.* 2006) able to reproduce a large number of identical impacts within a few minutes. This system was carefully designed to be free of electromagnetic noise and to allow stacking in order to improve the signal-to-noise ratio. The impact is obtained by launching a ruby ball on a granite plate. The time source function is recorded by an accelerometer fixed on the plate and exhibits a broad band spectra from 150 Hz to 10 kHz (Bordes *et al.* 2006). Seismic excitation is vertically polarized and the seismic propagation contains longitudinal (compressive), transverse (shear) and extensional modes.

Seismo-magnetic couplings associated to the seismic propagation can be measured with two induction magnetometers. The first one, in the upper position, can be placed in seven different locations whereas the second one is fixed as a reference position (Fig. 2, part A). Each magnetometer is divided into two elements (Fig. 2, part B) which can be splitted to be placed around the column without any contact with the sample. Each element consists in a magnetic core focussing magnetic fluxes. These fluxes generate induction currents in the coils that are finally amplified and recorded.

These magnetometers are sensitive both to radial and azimuthal components of the magnetic field and the output consists in one channel. As a consequence, getting real amplitudes needs to expect or at least to assume a field polarization. Sensitivities are given in Fig. 2(part C), where grey and black lines represent, respectively, lower and upper magnetometer. The radial sensitivity was calibrated by measuring magnetic fluxes generated by a calibration coil placed in the symmetry axis of the magnetometers. It is almost constant, nearly 10 V nT^{-1} , in the 100–1000 Hz range. The azimuthal sensitivity was calibrated by measuring fluxes generated by a vertical wire

in the magnetometer’s symmetry axis and is rounded to 10 mV nT^{-1} in order to give an order of magnitude of azimuthal fields.

3.4 Remote control of the experimental setup

To avoid strong electromagnetic disturbances from electronic devices, the whole experiment was remote controlled from the corridor of the laboratory (Fig. 3). It includes the seismic source driving, the charge amplifier of the accelerometer, and the acquisition system. All measurements were performed using a 24 bit seismic recorder (Geometrics StrataVisor NZ) using a $21 \mu\text{s}$ time sampling rate. The source driving system consists in an electrovalve supplied by a pulse generator ($24 \text{ V}/256 \text{ ms}$) whose input is protected from a possible discharge of the coil by a freewheel diode. This driving system is enclosed in a ground connected shielding box to avoid the transmission of electromagnetic disturbances from the electrovalve to the acquisition wires.

4 SEISMO-MAGNETIC MEASUREMENTS

4.1 Necessity of exceptional care for seismo-magnetic measurements

Seismo-magnetic measurements need carefully designed experimental apparatus to avoid electromagnetic disturbances. Especially, it is essential to avoid those due to the seismic triggering. All disturbances occurring using the seismic source trigger would be stacked and could distort or mask real signals. Indeed as the permanent magnetic field is 10 times smaller than in usual conditions, the moving of conductive or magnetic material can generate some strong disturbances from induction origin. Thus, the stainless steel ball and

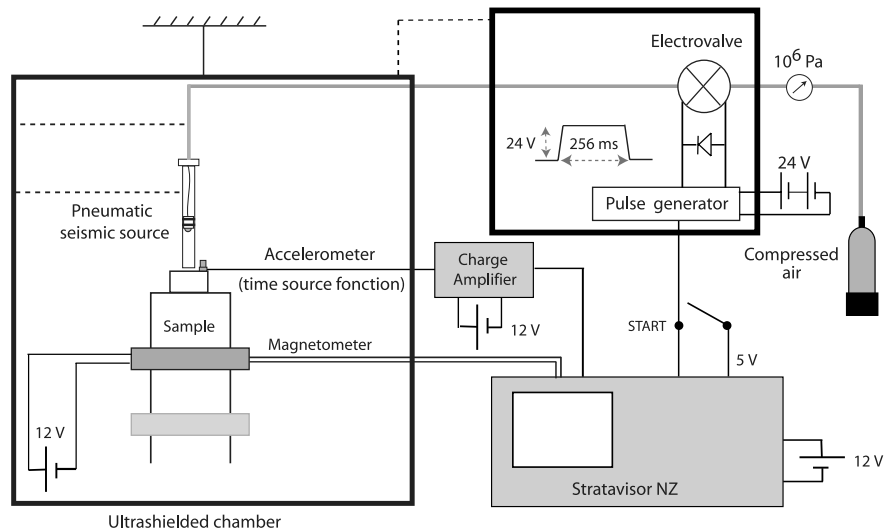


Figure 3. General scheme of the experiment showing devices located within and outside the underground shielded chamber.

the metallic spring we choose at the beginning of the experiment was replaced by a ruby ball and a rubber band in the final free noise seismic source. Moreover, all metallic screws of the experimental apparatus were replaced by nylon screws. Only the copper tube of the seismic source, poorly moving and non-magnetic, was preserved to be ground-connected and avoid an electrostatic charge accumulation.

Once this simple care taken, most serious disturbances occur when the magnetometer standing have mechanical contacts with the sample. Indeed, if vibrations due to the seismic propagation are transmitted to the magnetometers, a transient magnetic field is measured but is not related to any electrokinetic origin. These signals, due to the transient moving of the magnetometer in the permanent magnetic field, cannot be distinguished from electrokinetically generated seismo-magnetic field.

The experimental apparatus was anticipated to avoid these disturbances: the magnetometers and the sample were fixed on two different stands (Fig. 2, part A). Thereby, there is no contact between the sample and the magnetometers (Fig. 2, part B). However, residual seismic waves can be transmitted to the floor and then to the magnetometer stand. To illustrate this phenomena, we recorded the horizontal and vertical residual vibrations of the upper magnetometer occurring after one shot (Fig. 4). This simple test clearly shows that the magnetometer's vibrations are very weak and measurable by accelerometers ($< 2 \times 10^{-3} \text{ m s}^{-2}$ on the horizontal but negligible on the vertical accelerometer, part A). In this case, corresponding magnetic signals show a strong 80 Hz/8 mV signal probably corresponding to the resonant frequency of the magnetometers stands. This phenomena can be strongly attenuated by introducing a sound-proofing protection on the floor (Fig. 4 part B) but cannot be totally cancelled (in the range of 2 mV). In the next section, it will be shown that these disturbances are delayed with respect to the seismic propagation in the sample and are out of the time window of interest (0–2 ms).

4.2 Results

The existence of the theoretically predicted seismo-magnetic conversions can be studied by comparing seismic and magnetic signals in dry and moist sand. Such a comparison allows to separate as an evidence coherent magnetic signals identified as disturbances from

those generated by electrokinetic effects. Indeed, the electrokinetic effects occur only when water is present (Guichet *et al.* 2003), as shown in the Fig. 5. Seismo-magnetic sections presented were obtained by stacking 100 records of the upper magnetometer at the seven possible locations. Corresponding seismic records obtained on an identical apparatus are given to show the comparison of seismic and seismo-magnetic propagations. The grey zone is jointly defined for seismic and magnetic sections only to highlight the location of first arrivals.

All sections are trace by trace normalized to emphasize the propagation phenomena. This figure clearly shows that coherent magnetic arrivals appear when the sand is fluid-filled. This comparison of measurements in dry and moist sand gives arguments to show the electrokinetic origin of the transient magnetic field. These seismo-magnetic signals are the first kind of the seismo-magnetic conversion, and are travelling with the seismic wave within the moist sand.

4.2.1 Comments on amplitudes

In order to find a representative event in the seismic and magnetic sections, we picked the negative polarity of first arrival as it is the cleanest in the seismo-magnetic records. The maximum negative amplitudes were measured within the grey area and plotted on the right of each section. Furthermore, the occurrence of seismomagnetic phenomena in fluid-filling sand is highlighted by the comparison of the first arrival amplitude (black line) with the average noise level recorded before the impact (grey line). In order to respect a meticulous interpretation of the data, the maximum amplitude values correspond to the output of the magnetometer (mV). Indeed, the discussion on real magnetic amplitudes needs a complete analytical discussion given in Section 5.

As evoked above, Garambois & Dietrich (2001) showed that seismo-magnetic signals are proportional to the *S*-waves grain velocity in the low frequency approximation. Using the same procedure, we show in Appendix B that the azimuthal seismo-magnetic field should be proportional to the radial grain velocity associated to transverse waves. In the moist sand the amplitude of the seismo-magnetic signal decreases from the top to the bottom of the column, mainly because the seismic energy decreases from the impact seismic source. Full waveform of seismic and seismo-magnetic signals

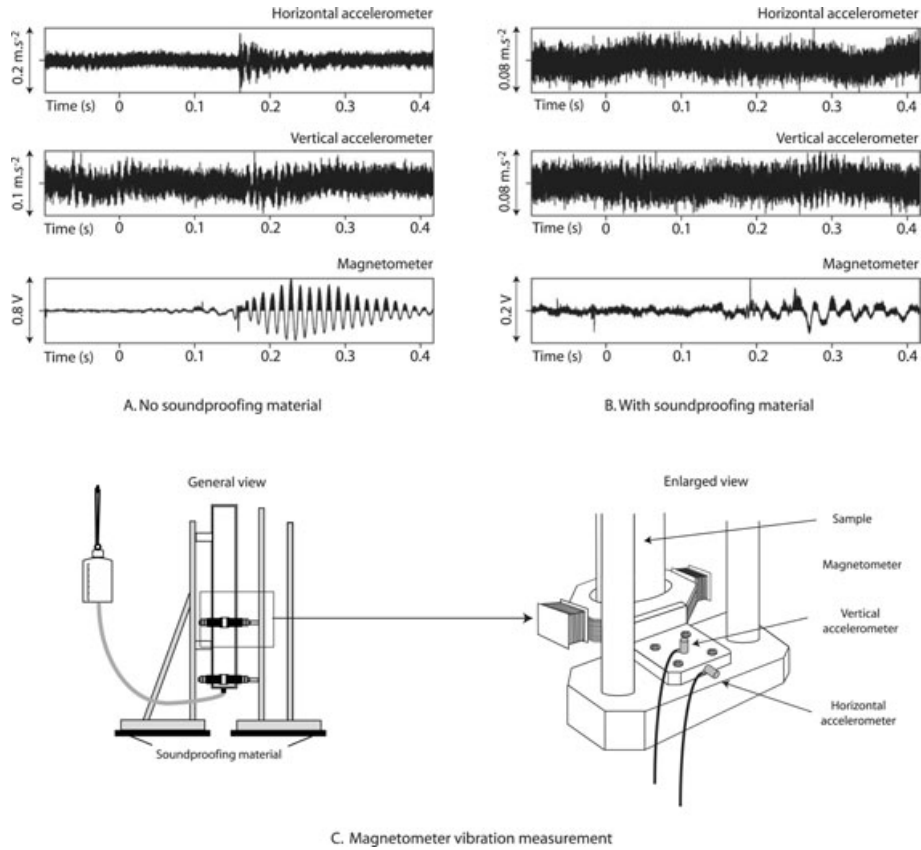


Figure 4. Disturbances due to weak vibrations of the magnetometers occurring after one shot, normalized for a 1 m s^{-2} seismic source. This simple test clearly shows that the magnetometer’s vibrations are very weak and barely measurable but generate some strong transient magnetic signals (part A). This phenomena can be strongly attenuated by introducing a soundproofing protection on the floor (part B).

are similar, however, a complete comparison of magnetic and seismic fields would be not appropriate in this case. Indeed, the seismic source generates *P*, *S* and extensional waves, but the different seismic modes can not be separated because of the too small sample length and because accelerometers measure the axial component of the grain acceleration. Thus, it is impossible to choose an event in the seismic signals that could be directly associated to *S* waves and compared to the seismo-magnetic field.

The comparison of the magnetic amplitudes in dry and moist sand shows as an evidence that the seismo-magnetic conversions are very weak. A comparison of maximum amplitudes of the grey zones in magnetic signals show that signals in moist sand (0.3 mV at 10 cm) are only 6 times larger than in dry sand (0.05 mV at 10 cm). It is interesting to note that the signal to noise ratio is better in moist sand, partly due to a lower noise level in moist sand. Indeed, real noise amplitudes measured before the triggering are significantly lower in moist (0.02 mV) than in dry sand (0.05 mV).

The conversion to real magnetic amplitude values needs the assumption of a purely azimuthal or radial field. According to the major polarization of the magnetic field, this amplitude could vary from 0.035 pT to 0.035 nT for a 1 m s^{-2} seismic source. This topic will be discussed in the light of the analytical approach of seismo-electromagnetic fields of the Section 5.

4.2.2 Comments on propagation velocities

One of the most significant results is obtained by comparing seismic and seismo-magnetic propagation velocities by picking first breaks

on enlarged views of the seismic and magnetic sections (Fig. 6). A careful analysis in the [0–1.5 ms] window of the magnetic records on dry and moist sand shows a residual disturbance arising at $t = 0 \text{ s}$. This phenomenon exhibits amplitude of the same order as the signal. Then, it is invisible on the one shot record but appears after the stacking procedure. It is due to the seismic triggering and can be due to cross-talk (from time source function recording) or to electromagnetic disturbances by the impact. This disturbance has to be eliminated, or at least attenuated, to enable the computing of the apparent velocity of the seismo-magnetic wave within the compacted sand. In order to minimize this phenomenon, the lower magnetometer was used as a reference. The subtraction of the reference from each point of measurement improves the data by minimizing the disturbance and unmasking the first breaks of interest (Fig. 6).

This subtraction enables us to deduce the apparent velocity of the seismo-magnetic field ($791 \pm 80 \text{ m s}^{-1}$) with a better signal-to-noise ratio. This velocity can be compared to the significantly faster seismic velocities. The measured seismic velocities are almost the same in dry ($1201 \pm 85 \text{ m s}^{-1}$) and moist sand ($1328 \pm 94 \text{ m s}^{-1}$). These values are consistent with *P*-waves velocities measured by Elliott & Wiley (1975) in partially saturated compacted sample (Ottawa sand, porosity 30 per cent).

The fact that any significative increase in seismic velocity with fluid filling is not observed is consistent with laboratory measurements of Knight & Nolen-Hoeksema (1990). They showed that the behaviour of the *P*-wave velocity with increasing water-saturation within sandstones strongly depends on the means used to saturate the porous medium. In the imbibition case, the *P*-wave velocity is

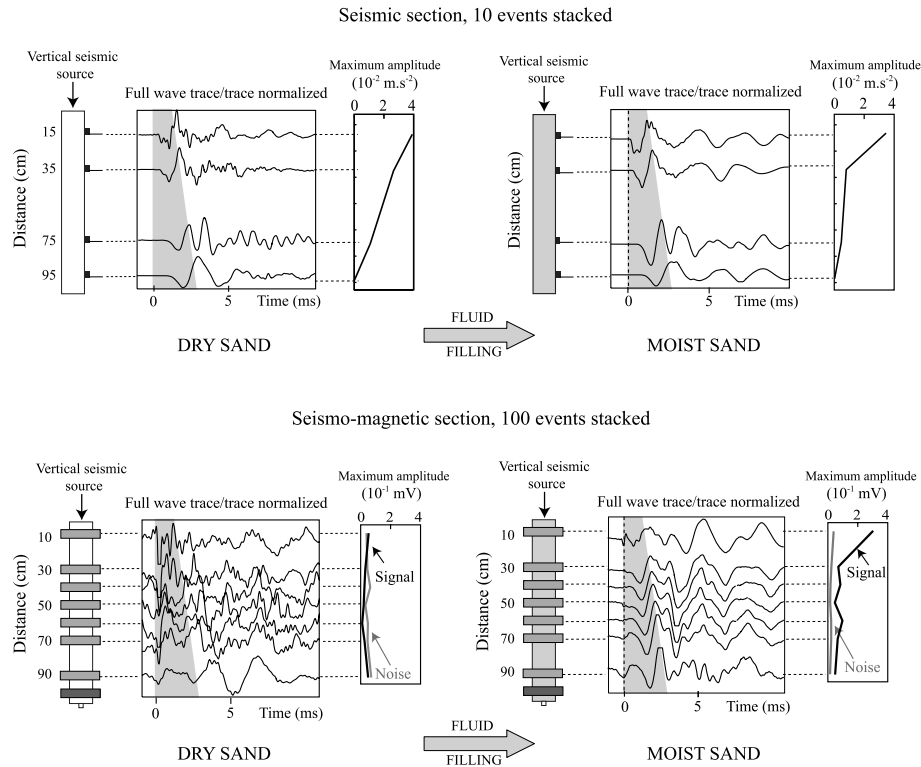


Figure 5. Comparison of seismic and seismo-magnetic measurements on dry and moist compacted sand showing the evidence of coherent magnetic arrival in the moist sand. The seismo-magnetic signal is referenced to the lower magnetometer.

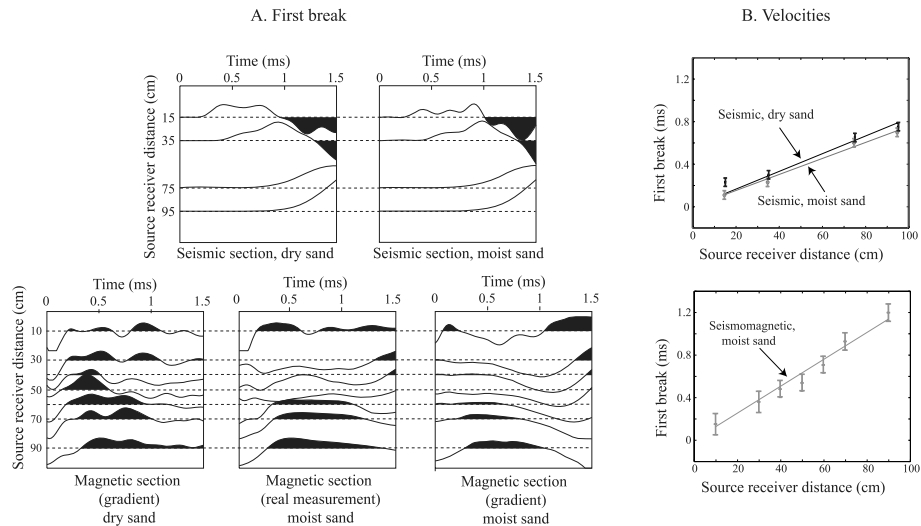


Figure 6. Zoom on first break of the seismic and seismo-magnetic measurements (trace/trace normalized). The seismo-magnetic gradient representation improves the velocity resolution by partly subtracting the disturbance occurring around $t = 0$ s. Apparent velocities in moist sand are measured to be $1328 \pm 94 \text{ m s}^{-1}$ for seismic wave and $791 \pm 80 \text{ m s}^{-1}$ for the seismo-magnetic wave.

increased only after 80 per cent of water-saturation (and is constant below), whereas in drainage conditions the P -wave velocity is increased with water-content as soon as 45 per cent of water saturation (see also Gist 1994). Since the seismic velocities in our dry and moist sand are the same (given the associated errors), and because we are in imbibition conditions, we can deduce that the sand is partly saturated, probably with a maximum of 80–85 per cent of water saturation.

In this section, we proved that seismo-magnetic phenomena in partly saturated sand have an electrokinetic origin. The velocity

of the seismo-magnetic field is measured to be lower than the seismic velocity. In order to improve interpretations of velocities and to better understand seismomagnetic amplitudes, an analytical approach of the seismo-electromagnetic couplings including the geometrical characteristics of our experimental setup is proposed. Indeed, under a vertical seismic excitation in a cylindrical porous medium, specific modes can be generated due to the presence of the free cylindrical surface. In the next section we calculate the extensional phase velocity and deduce that the fast seismic arrivals are associated to the P and extensional waves,

and that the slower seismo-magnetic arrivals are associated to S wave.

5 ANALYTICAL APPROACH FOR SEISMO-ELECTROMAGNETIC FIELDS INTERPRETATIONS

The description of the complete seismic propagation needs to take into account the fast (P_f) and slow (P_s) longitudinal modes, the transverse modes (S) as well as the specific modes due to the cylindrical free surface. Considering the axial seismic excitation, we assume that these specific modes are only extension and we neglect flexion and torsion (Dunn 1986). The goal of this analytical approach is to evaluate expected phase velocities of the different waves, in order to identify which waves are converted into seismo-electromagnetic fields. We show that V_{ext} and V_{P_f} are very close unless the sand is not totally fluid-filled. Moreover, we show that in a cylindrical porous medium under a vertical excitation, the induced seismo-magnetic field should be azimuthal.

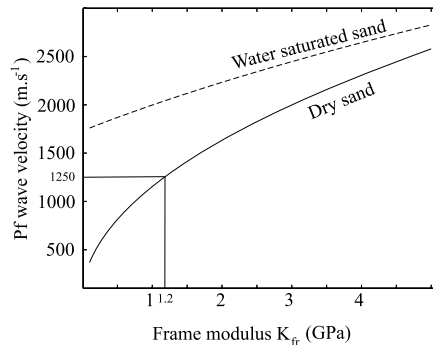
5.1 Seismic velocities of body waves

In order to compute the phase velocity of the extensional mode, the bulk (K_{fr}) and shear (G) frame moduli of the sand have to be estimated. Then, K_{fr} can be deduced from inversion of the measured P_f wave velocity. Indeed, suitable moduli can be calculated from observations using expressions of phase velocities:

$$V_{P_f} = \frac{1}{Re(s_{P_f})} \quad V_{P_s} = \frac{1}{Re(s_{P_s})} \quad V_S = \frac{1}{Re(s_S)} \quad (8)$$

where s_{P_f} , s_{P_s} and s_S are slownesses of P_f , P_s and S waves from Pride & Haartsen (1996) (eqs A14, A15 and A16 of Appendix A.2).

As it was evoked above, our fluid-filling method (imbibition) does not enable us to obtain a fully saturated sample and the seismic velocities in dry and moist sand are very close. Indeed, Knight & Nolen-Hoeksema (1990) showed that during the imbibition procedure, the P_f wave velocity is quite constant until the saturation coefficient exceeds 85 per cent. A computation of phase velocities needs to take into account the partial saturation. Since the velocity change is negligible in the 0–80 per cent saturation range, a first order approximation of the frame modulus can be obtained by considering that the fluid is totally replaced by air. In this case, the computation of the P_f -wave velocity from expressions 8 versus frame modulus shows that the measured 1250 m s^{-1} velocity corresponds to a unique value of the frame modulus $K_{fr} = 1.2 \times$



10^9 Pa (Fig. 7). This value is larger than the usually assumed values for sand, which are around $[0.1\text{--}0.5 \text{ GPa}]$ (Garambois & Dietrich 2001; Block & Harris 2003, 2006; Karner *et al.* 2003). However this value is within the range $[0\text{--}4.2 \text{ GPa}]$ proposed by Hickey & Sabatier (1997) for modelling water-saturated sand.

On the other hand, the shear modulus $G \simeq 1.32 \times 10^9 \text{ Pa}$ can be inferred considering the ratio $K_{fr}/G = 0.9$ from Murphy *et al.* (1993) for quartzic granular media. This computation shows that the S -wave velocity can be estimated to 860 m s^{-1} from these deduced moduli in the dry sand (Fig. 7). Assuming that this first order inversion in dry sand can not introduce strong errors, the calculated frame bulk and shear moduli values will be used in the next section to compute the phase velocity of the extensional mode.

5.2 Extensional modes

Considering the vertical seismic source, some specific modes can be generated on the free cylindrical surface of the sample from interferences of P and S waves. Extensional modes occurring in water saturated porous media have been early studied by Gardner (1962) for quantitative interpretation of seismic velocities in resonant bars. Using this approach, numerical computation of Dunn (1986) show specific dispersion and attenuation effects in cylindrical samples of sandstones. In this case, the phase velocity of extensional modes is smaller than P_f but larger than S wave phase velocity. A first order approximation of the extensional phase velocity can be obtained from the *bar velocity* given by:

$$V_{ext} = \sqrt{\frac{E}{\rho}}, \quad (9)$$

where E is the Young's modulus usually defined in elastic media, and can be measured for rock samples as the slope of an axial stress versus axial strain curve from a deformation test. We can use this expression for the porous media by substituting the elastic moduli K by the equivalent Gassman moduli K_G :

$$E = \frac{9 K_G G}{3 K_G + G}, \quad (10)$$

where K_G , the Gassman's modulus defined in Appendix C and A1, represents the equivalent K modulus for the porous media. A prediction of the phase velocities in the partially saturated sand can be obtained by using an average on the density ρ_f and the bulk modulus K_f versus the saturation coefficient S_w :

$$\rho_f(S_w) = S_w \rho_{water} + (1 - S_w) \rho_{air} \quad (11)$$

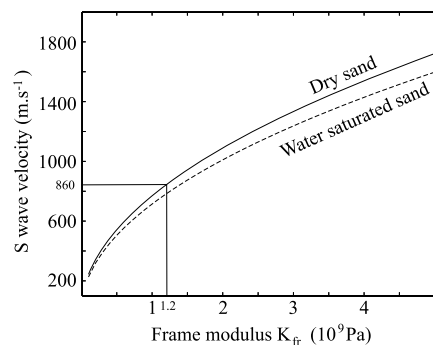


Figure 7. Computation of the seismic velocities from versus frame modulus K_{fr} in the dry and water saturated cases (Pride & Haartsen 1996). Considering the measured P_f velocity (1250 m s^{-1}), the corresponding frame modulus of the sand can be estimated to 1.2 GPa . The calculated S wave velocity, deduced from this K_{fr} value, is near 860 m s^{-1} .



Figure 8. Comparison of the phase velocities of P_f , extension and S waves versus saturation coefficient. The P and extensional waves can not be distinguished by velocity measurements.

$$K_f(S_w) = \left[\frac{S_w}{K_{\text{water}}} + \frac{1 - S_w}{K_{\text{air}}} \right]^{-1}. \quad (12)$$

In the following expressions, we will take into account the partial saturation by substituting K_f and ρ_f by their average values. Finally, an estimation of the extension's phase velocity in the partially saturated sample can be computed from:

$$V_{\text{ext}}(S_w) = \sqrt{\frac{9 K_G(S_w) G}{\rho(S_w) [3 K_G(S_w) + G]}}. \quad (13)$$

A computation of eqs (11), (12), (13) and (8), respectively, predicts 1250 and 1260 m s^{-1} phase velocities for extensional and P waves in dry sand (Fig. 8). These velocities, respectively, increase to 1315 and 2050 m s^{-1} for the water-saturated sand. This result is consistent with the work of Dunn (1986) showing a $V_{\text{ext}}/V_S = 1.6$ ratio. The P -wave velocity is strongly increased by water only when approaching the water-saturation state. Since the extensional waves are induced by interferences of S and P waves, the extensional wave is also fastened. Finally, this computation clearly shows that the P_f and extension modes are very difficult to distinguish in partial saturation conditions, at least by considering the first break of seismic arrival. Thus, the seismic arrivals recorded in the sample showing a 1200/1300 m s^{-1} velocity will be associated to P and extensional waves. Slow events with 800/900 m s^{-1} velocities will be associated to S -waves.

5.3 Seismo-magnetic field polarization

As a complement of the seismic velocities analysis, a complete formulation of seismo-electromagnetic fields is required to propose a correct interpretation of the measurements, especially for the seismo-magnetic field polarization and magnitude. Seismo-electromagnetic fields can be expressed from seismic displacements via appropriate coefficients for each propagation mode (Pride & Haartsen 1996). As reminded in Appendix B, displacements associated to P_f and P_s waves are described by the scalar potentials ϕ_f and ϕ_s whereas S waves displacements can be represented by the vector potential Γ_S .

The seismo-magnetic field is derived from the Maxwell equation:

$$\mathbf{H} = -\frac{i}{\omega \mu} (\nabla \times \mathbf{E}), \quad (14)$$

where μ is the magnetic permeability of the free space, and H and E are, respectively, the seismo-magnetic and seismo-electric fields. Indeed, the purely longitudinal part of the seismic propagation (P waves) does not contribute to the seismo-magnetic field and only S and extensional waves can produce coseismic magnetic effects. In appendix B, we showed that the seismo-magnetic field generated from S waves (H_S) and from extensional waves (H_{ext}) are expressed by:

$$H_{S,\theta} = -\frac{\phi}{\alpha_\infty} \frac{\epsilon_0 \kappa_f \zeta}{\eta} \rho_f \sqrt{\frac{G}{\rho}} \frac{du_{s,r}}{dt} \quad (15)$$

and

$$H_{e,\theta} = -\frac{\phi}{\alpha_\infty} \frac{\epsilon_0 \kappa_f \zeta}{\eta} \rho_f \sqrt{\frac{E}{\rho}} \frac{du_{s,r}}{dt}. \quad (16)$$

Whatever the origin of the seismo-magnetic field is, the only non-zero component is the azimuthal one and the analytical prediction shows that the measured magnetic field should be azimuthal. Even if it is not possible to rule out very weak radial perturbations, it is reasonable to assume that they are negligible. These results are consistent with the study of Hu & Wang (2000) for a fluid-filled borehole and give fundamental arguments for the interpretation of the seismo-magnetic measurements. Indeed, it is possible to assume that the quantification of amplitudes needs to take into account the azimuthal sensitivity of the magnetometers.

6 DISCUSSION AND CONCLUSION

The exceptional environment and facilities of the Low Noise Underground Laboratory of Rustrel gave us the possibility to build a carefully designed experimental setup for seismo-magnetic measurements in moist sand. The seismic arrivals recorded in the sample shows a $1328 \pm 94 \text{ m s}^{-1}$ velocity and have been associated to P and extensional waves in the partially saturated sand. We calculated a S -wave velocity of 800–900 m s^{-1} . The measured seismo-magnetic arrivals shows a velocity of about $791 \pm 80 \text{ m s}^{-1}$. Therefore, we propose that the seismo-magnetic field is electrokinetically induced and is associated to S -wave propagation. This was theoretically predicted by Pride (1994), but never measured up to now.

Magnetic measurements were performed with two induction magnetometers whose radial and azimuthal resolution are, respectively, around 10 V nT^{-1} and 10 mV nT^{-1} for a maximal amplitude of 0.3 mV in output of the magnetometers. Applying the Pride's theory for seismo-electromagnetic couplings, we show that the seismo-magnetic field is purely azimuthal. Even if it is very difficult to rule out the possibility of very weak non-axial vibrations, generating radial magnetic field, it is reasonable to conclude that the measured amplitudes are in the order of 0.035 nT for a 1 m s^{-2} seismic source. Further studies, implying the measurement of the three components of the magnetic field, are necessary to definitely conclude on the seismo-magnetic amplitudes. In order to better understand the seismo-magnetic conversions, further numerical, field and laboratory investigations are needed. To this end, the LSBB facilities give exceptional possibility to measure seismo-electromagnetic couplings in porous media.

Usual field seismic sources are explosives, vibroseis or sledgehammer blows which induce accelerations values in the range of 0.05–100 m s^{-2} (Table 2). In the assumption of amplitudes about 0.03 nT for a 1 m s^{-2} seismic source, field seismo-magnetic measurements could be performed out of the low noise environment. Nevertheless, extra care has to be taken to ensure the electrokinetic

Table 1. Values of the parameters used for computations. Electrokinetic coupling measured by Guichet *et al.* (2003) on Fontainebleau sand was converted to the measured fluid conductivity. α is assumed = 3.

Measured parameters					
ϕ	k_0	σ_f	C_{ek} from Guichet <i>et al.</i> (2003)		
	(m ²)	(S m ⁻¹)	(V Pa ⁻¹)		
0.3	5.8×10^{-12}	3.1×10^{-3}	-6545×10^{-9}		
Assumed parameters					
	ρ_f (kg m ⁻³)	ρ_s (silica) (kg m ⁻³)	η (Pa s)	K_s (Pa)	K_f (Pa)
Water	1000	2650	0.001	36×10^9	2.22×10^9
Air	1.2		18×10^{-6}		0.15×10^6

Table 2. Measured acceleration versus source–receiver distance for different seismic sources (personal data). The terrestrial air gun (Vesdun en Berry, France) consists in an air gun placed in an artificial basin.

Source type	Source–receiver distance (m)	Measured acceleration (g) (m s ⁻²)
Terrestrial Air Gun	15	0.5
Explosives (200 g)	7.5	96
Sledgehammer blow	10	0.05
Vibroseis (<i>P</i> -waves)	5	3 (vertical)
Vibroseis (<i>S</i> -waves)	5	4 (horizontal)

origin of the measurements. Especially, magnetometers have to be isolated from ground motions as well as from coherent electromagnetic noise. Thus, borehole measurements would be very difficult, because of unavoidable contacts between the tool and the mud transmitting ground vibrations. Nevertheless, subsurface measurements could be performed with ingenious experimental apparatus including a strong stacking procedure to improve the signal-to-noise ratio.

ACKNOWLEDGMENTS

This work was supported by the French National Scientific Research Center (CNRS), and ‘ACI Eau et Environnement’ of the French Ministry of Research. We are grateful to G. Waysand for helpful discussions and authorization to perform this experiment in the LSBB laboratory. We thank M. Auguste, D. Boyer, A. Cavailleu, G. Clerc, R. Guiguet and Y. Orenge for their technical help.

REFERENCES

Ageeva, O.A., Svetov, B.S., Sherman, G.K. & Shipulin, V., 1999. E-effect in rocks, *Russ. Geol. Geophys.*, **64**, 1349–1356.
 Beamish, D., 1999. Characteristics of near surface electrokinetic coupling, *Geophys. J. Int.*, **137**, 231–242.
 Biot, M.A., 1956. Theory of propagation of elastic waves in a fluid-saturated porous solid: I. low frequency range, *J. acoust. Soc. Am.*, **28**(2), 168–178.
 Biot, M.A., 1962. Mechanics of deformation and acoustic propagation in porous media, *J. Appl. Phys.*, **34**(1), 36–40.
 Block, G. & Harris, J.G., 2003. Coupled electrokinetic-biot theory and measurement techniques in sediment acoustics, in *Proceedings of the 16th ASCE Engineering Mechanics Conference*, University of Washington, Seattle.
 Block, G.I. & Harris, J.G., 2006. Conductivity dependence of seismoelectric wave phenomena in fluid-saturated sediments, *J. geophys. Res.*, **111**, B01304.

Bordes, C., Jouniaux, L., Dietrich, M., Pozzi, J.-P. & Garambois, S., 2006. First laboratory measurements of seismo-magnetic conversions in fluid-filled fontainebleau sand, *Geophys. Res. Lett.*, **33**, L01302.
 Broding, R.A., Buchanan, D. & Hearn, P.D., 1963. Field experiments on the electroseismic effect, *IEEE Trans. Geosci. Electron.*, GE-1, 23–31.
 Butler, K.E. & Russell, R.D., 1993. Subtraction of powerline harmonics from geophysical records, *Geophysics*, **58**, 898–903.
 Chandler, R., 1981. Transient streaming potential measurements on fluid-saturated porous structures: an experimental verification of biot’s slow wave in the quasi-static limit, *J. acoust. Soc. Am.*, **70**, 116–121.
 Chen, B. & Mu, Y., 2005. Experimental studies of seismoelectric effects in fluid-saturated porous media, *J. Geophys. Eng.*, **2**, 222–230.
 Cooke, C.E., 1955. Study of electrokinetic effects using sinusoidal pressure and voltage, *J. Chem. Phys.*, (23), 2299–2303.
 Davis, J.A., James, R.O. & Leckie, J., 1978. Surface ionization and complexation at the oxide/water interface, *J. Coll. Inter. Sci.*, **63**, 480–499.
 Doussan, C., Jouniaux, L. & Thony, J.-L., 2002. Variations of self-potential and unsaturated flow with time in sandy loam and clay loam soils, *J. Hydrol.*, **267**, 173–185.
 Dunn, K.-J., 1986. Acoustic attenuation in fluid-saturated porous cylinders at low frequencies, *J. acoust. Soc. Am.*, **79**(6), 1709.
 Dupuis, J.C. & Butler, K.E., 2006. Vertical seismoelectric profiling in a borehole penetrating glaciofluvial sediments, *Geophys. Res. Lett.*, **33**, L16301.
 Dupuis, J.C., Butler, K.E. & Kepic, A.W., 2007. Seismoelectric imaging of the vadose zone of a sand aquifer, *Geophysics*, **72**, A81–A85.
 Elliott, S.E. & Wiley, B.F., 1975. Compressional velocities of partially saturated, unconsolidated sands, *Geophysics*, **40**(6), 949–954.
 Gaffet, S. et al., 2003. Simultaneous seismic and magnetic measurements in the low-noise underground laboratory (LSBB) of Rustrel, France, during the 2001 January 26 Indian earthquake, *Geophys. J. Int.*, **155**, 981–990.
 Garambois, S. & Dietrich, M., 2001. Seismoelectric wave conversions in porous media: field measurements and transfer function analysis, *Geophysics*, **66**, 1417–1430.
 Garambois, S. & Dietrich, M., 2002. Full waveform numerical simulations of seismoelectromagnetic wave conversions in fluid-saturated stratified porous media, *J. geophys. Res.*, **107**(B7), ESE5-1–ESE5-11.
 Garambois, S., Senechal, P. & Perroud, H., 2002. On the use of combined geophysical methods to access water content and water conductivity of near surface formations, *J. Hydrol.*, (259), 32–48.
 Gardner, G.H.F., 1962. Extensional waves in fluid-saturated porous cylinders, *J. acoust. Soc. Am.*, **34**(1), 36–40.
 Gaskarov, I. & Parkhomenko, E., 1974. The seismoelectric effect in rocks and the preconditions for its application in geological prospecting work, *Izv. Akad. Sci. USSR, Phys. Solid Earth*, **1**, 71–74.
 Gist, G.A., 1994. Interpreting laboratory velocity measurements in partially gas-saturated rocks, *Geophysics*, **59**(7), 1100–1109.
 Guichet, X., Jouniaux, L. & Pozzi, J.-P., 2003. Streaming potential of a sand column in partial saturation conditions, *J. Geophys. Res.*, **108**(B3), ECV2-1–ECV2-12.
 Guichet, X., Jouniaux, L. & Catel, N., 2006. Modification of streaming potential by precipitation of calcite in a sandwater system: laboratory measurements in the ph range from 4 to 12, *Geophys. J. Int.*, **166**, 445–460.
 Haartsen, M.W. & Pride, S., 1997. Electrostatic waves from point sources in layered media, *J. geophys. Res.*, **102**, 24 745–24 769.
 Haartsen, M.W., Dong, W. & Toksöz, M.N., 1998. Dynamic streaming currents from seismic point sources in homogeneous poroelastic media, *Geophys. J. Int.*, **132**, 256–274.
 Haines, S.S., Guitton, A. & Biondi, B., 2007a. Seismoelectric data processing for surface surveys of shallow targets, *Geophysics*, **72**, G1–G8.
 Haines, S.S., Pride, S.R., Klemperer, S.L. & Biondi, B., 2007b. Seismoelectric imaging of shallow targets, *Geophysics*, **72**, G9–G20.
 Hart, D.J. & Wang, H.F., 1995. Laboratory measurements of a complete set of poroelastic moduli of berea sandstone and Indiana limestone, *J. geophys. Res.*, **100**(B9), 17 741–17 751.

- Hase, H., Ishido, T., Takakura, S., Hashimoto, T., Sato, K. & Tanaka, Y., 2003. Zeta potential measurement of volcanic rocks from aso caldera, *Geophys. Res. Lett.*, **23**(30), 2210.
- Hickey, C.J. & Sabatier, J.M., 1997. Choosing biot parameters for modeling water-saturated sand, *J. acoust. Soc. Am.*, **102**, 1480–1484.
- Hu, H. & Wang, K., 2000. Simulation of an acoustically induced electromagnetic field in a borehole embedded in a porous formation, *Borehole Acoustics and Logging Reservoir Delineation consortis, Annual Report*, pp. 13-1–13-20.
- Hunt, C.W. & Worthington, M.H., 2000. Borehole elektrokinetic responses in fracture dominated hydraulically conductive zones, *Geophys. Res. Lett.*, **27**(9), 1315–1318.
- Ishido, T. & Mizutani, H., 1981. Experimental and theoretical basis of electrokinetic phenomena in rock water systems and its applications to geophysics, *J. geophys. Res.*, **86**, 1763–1775.
- Jackson, M.D., Saunders, J.H. & Addiego-Guevara, E.A., 2005. Development and application of new downhole technology to detect water encroachment toward intelligent wells, in *Proceedings of the Society of Petroleum Engineers, Annual Technical Conference*.
- Jiang, Y.G., Shan, F.K., Jin, H.M. & Zhou, L.W., 1998. A method for measuring electrokinetic coefficients of porous media and its potential application in hydrocarbon exploration, *Geophys. Res. Lett.*, **25**(10), 1581–1584.
- Johnson, D.L., Koplik, J. & Dashen, R., 1987. Theory of dynamic permeability in fluid saturated porous media, *J. Fluid. Mech.*, **176**, 379–402.
- Jouniaux, L. & Pozzi, J.-P., 1995. Permeability dependance of streaming potential in rocks for various fluid conductivity, *Geophys. Res. Lett.*, **22**, 485–488.
- Jouniaux, L. & Pozzi, J.-P., 1995. Streaming potential and permeability of saturated sandstones under triaxial stress: consequences for electrotelluric anomalies prior to earthquakes, *J. geophys. Res.*, **100**, 10 197–10 209.
- Jouniaux, L. & Pozzi, J.-P., 1997. Laboratory measurements anomalous 0.1–0.5 hz streaming potential under geochemical changes: implications for electrotelluric precursors to earthquakes, *J. geophys. Res.*, **102**, 15 335–15 343.
- Jouniaux, L., Bernard, M.-L., Zamora, M. & Pozzi, J.-P., 2000. Streaming potential in volcanic rocks from mount peleé, *J. geophys. Res.*, **105**, 8391–8401.
- Karner, S.L., Chester, F.M., Kronenberg, A.K. & Chester, J.S., 2003. Sub-critical compaction and yielding of granular quartz sand, *Tectonophysics*, **377**, 357–381.
- Kepic, A. & Rosid, M., 2004. Enhancing the seismoelectric method via a virtual shot gather, *SEG Technical Program Expanded Abstracts*.
- Knight, R. & Nolen-Hoeksema, R., 1990. A laboratory study of the dependence of elastic wave velocities on pore scale fluid distribution, *Geophys. Res. Lett.*, **17**, 1529–1532.
- Long, L.T. & Rivers, W.K., 1975. Field measurement of the electroseismic response, *Geophysics*, **40**, 233–245.
- Lorne, B., Perrier, F. & Avouac, J.-P., 1999a. Streaming potential measurements: 1. Properties of the electrical double layer from crushed rock samples, *J. geophys. Res.*, **104**(B8), 17 857–17 877.
- Lorne, B., Perrier, F. & Avouac, J.-P., 1999b. Streaming potential measurements. 2. relationship between electrical and hydraulic flow patterns from rocks samples during deformations, *J. geophys. Res.*, **104**(B8), 17 857–17 877.
- Martner, S.T. & Sparks, N.R., 1959. The electroseismic effect, *Geophysics*, **24**(2), 297–308.
- Masson, Y.J., Pride, S.R. & Nihei, K.T., 2006. Finite difference modeling of biot's poroelastic equations at seismic frequencies, *J. geophys. Res.*, **111**, B1035.
- Mikhailenko, B.G. & Soboleva, O.N., 1997. Mathematical modeling of seismomagnetic effects arising in the seismic wave motion in the earth's constant magnetic field., *Appl. Math. Lett.*, **10**, 47–51.
- Mironov, S.A., Parkhomenko, E.I. & Chernyak, G.Y., 1994. Seismoelectric effect in rocks containing gas or fluid hydrocarbon (English translation), *Phys. Solid Earth*, **29**(11), 1000–1006.
- Murphy, W., Reischer, A. & Hsu, K., 1993. Modulus decomposition of compressionnal and shear velocities in sand bodies, *Geophysics*, **58**, 227–239.
- Overbeek, J.T.G., 1952. Electrochemistry of the double layer, *Colloid Science, Irreversible Systems*, Vol. 1, pp. 115–193, ed. Kruyt, H.R., Elsevier, New York.
- Packard, R.G., 1953. Streaming potentials across capillaries for sinusoidal pressure, *J. Chem. Phys.*, **1**(21), 303–307.
- Pain, C., Saunders, J.H., Worthington, M.H., Singer, J.M., Stuart-Bruges, C.W., Mason, G. & Goddard, A., 2005. A mixed finite-element method for solving the poroelastic biot equations with electrokinetic coupling, *Geophys. J. Int.*, **160**, 592–608.
- Parkhomenko, I. & Tsze-San, C., 1964. A study of the influence of moisture on the magnitude of the seismoelectric effect in sedimentary rocks by a laboratory method, *Bull. (Zv.) Acad. Sci., USSR, Geophys. Ser.*, pp. 115–118.
- Pengra, D.B., Li, S.X. & Wong, P.-Z., 1999. Determination of rock properties by low frequency ac electrokinetics, *J. geophys. Res.*, **104**(B12), 29 485–29 508.
- Pozzi, J.-P. & Jouniaux, L., 1994. Electrical effects of fluid circulation in sediments and seismic prediction, *C.R. Acad. Sci. Paris, serie II*, **318**(1), 73–77.
- Pride, S., 1994. Governing equations for the coupled electromagnetics and acoustics of porous media, *Phys. Rev. B*, **50**, 15 678–15 695.
- Pride, S.R. & Berryman, J.G., 1998. Connecting theory to experiment in poroelasticity, *J. Mech. Phys. Solids*, **46**, 719–747.
- Pride, S. & Haartsen, M.W., 1996. Electrostatic wave properties, *J. acoust. Soc. Am.*, **100**, 1301–1315.
- Reppert, P.M., Morgan, F.D., Lesmes, D.P. & Jouniaux, L., 2001. Frequency-dependent streaming potentials, *J. Coll. Inter. Sci.*, (234), 194–203.
- Russell, R.D., Butler, K.E., Kepic, A.W. & Maxwell, M., 1997. Seismoelectric exploration, *Leading Edge*, pp. 1611–1615.
- Saunders, J.H., Jackson, M.D. & Pain, C.C., 2006. A new numerical model of electrokinetic potential response during hydrocarbon recovery, *Geophys. Res. Lett.*, **33**, L15316.
- Singer, B.S. & Fainberg, E.B., 1999. Modelling of electromagnetic fields in thin heterogeneous layers with application to field generation by volcanoes—theory and example, *Geophys. J. Int.*, **138**, 125–145.
- Singer, J., Saunders, J., Holloway, L., Stoll, J., Pain, C., Stuart-Bruges, W. & Mason, G., 2005. Electrokinetic logging has the potential to measure the permeability, *Society of Petrophysicists and Well Log Analysts, 46th Annual Logging Symposium*.
- Strahser, M.H., Rabbel, W. & Schildknecht, F., 2007. Polarisation and slowness of seismoelectric signals: a case study, *Near Surf. Geophys.*, **5**, 97–114.
- Thompson, R.R., 1936. The seismic-electric effect, *Geophysics*, **1**(3), 327–335.
- Thompson, A.H. & Gist, G.A., 1993. Geophysical applications of electrokinetic conversion, *Leading Edge*, **12**, 1169–1173.
- Thompson, A. et al., 2005. Field tests of electroseismic hydrocarbon detection, *SEG Technical Program Expanded Abstracts*.
- Waysand, G., Bloyet, D., Bongirax, J.-P., Collar, J.-I., Dolabdjian, C. & Thiec, P.L., 1999. First characterization of the ultra-shielded chamber in the low-noise underground laboratory (LSBB) of Rustrel pays D'apt, in *Workshop on Low Temperature Devices (LDT8), August 1999-Nuclear instrumentation and Methods in Physics Research*, (A444), 336–339.
- Zhu, Z. & Toksöz, M.N., 2003. Crosshole seismoelectric measurements in borehole models with fractures, *Geophysics*, **68**(5), 1519–1524.
- Zhu, Z. & Toksöz, M.N., 2005. Seismoelectric and seismomagnetic measurements in fractured borehole models, *Geophysics*, **70**(4), F45–F51.
- Zhu, Z., Haartsen, M.W. & Toksöz, M.N., 1999. Experimental studies of electrokinetic conversions in fluid-saturated borehole models, *Geophysics*, **64**, 1349–1356.
- Zhu, Z., Haartsen, M.W. & Toksöz, M.N., 2000. Experimental studies of seismoelectric conversions in fluid-saturated porous media, *J. geophys. Res.*, **105**, 28 055–28 064.

APPENDIX A: PRIDE'S THEORY FOR SEISMO-ELECTROMAGNETIC COUPLINGS

A1 Mechanical and transport macroscopic equations

The Biot's theory is the correct general model governing poroelastic response (Pride & Berryman 1998; Pain *et al.* 2005; Masson *et al.* 2006). Poroelastic response allows for the coupled interactions between the elastic deformation of a porous solid and the fluid flow and fluid accumulation in the same material. The Pride's theory for the seismo-electromagnetic couplings is based on the connexion of the Biot's and Maxwell's equations via electrokinetic couplings. This theory is, therefore, suitable for the fluid flow induced by seismic wave. Pride (1994) obtained macroscopic equations governing mechanical motion, charge transport and electromagnetism laws characterizing the full wave propagation field. All notations used in this section are explicited in Appendix C. The mechanical equations are obtained *via* a generalized Biot's law taking into account the boundary conditions at the pore scale:

$$\nabla \cdot \boldsymbol{\tau}_B = -\omega^2 (\rho \mathbf{u}_s + \rho_f \mathbf{w}) \quad (\text{A1})$$

$$\boldsymbol{\tau}_B = (K_G \nabla \cdot \mathbf{u}_s + C \nabla \cdot \mathbf{w}) \mathbf{I} + G \left(\nabla \mathbf{u}_s + \nabla \mathbf{u}_s^T - \frac{2}{3} \nabla \cdot \mathbf{u}_s \mathbf{I} \right) \quad (\text{A2})$$

$$-p = C \nabla \cdot \mathbf{u}_s + M \nabla \cdot \mathbf{w}, \quad (\text{A3})$$

where $\boldsymbol{\tau}_B$ is the stress tensor, \mathbf{I} is the identity matrix, \mathbf{u}_s is the displacement of the solid and \mathbf{w} is the average volume filtration. And K_G , C , M and Δ are poroelastic constants defined by:

$$K_G = \frac{K_{fr} + \phi K_f + (1 + \phi) K_s \Delta}{1 + \Delta} \quad (\text{A4})$$

$$C = \frac{K_f + K_s \Delta}{1 + \Delta} \quad (\text{A5})$$

$$M = \frac{K_f}{\phi(1 + \Delta)} \quad (\text{A6})$$

$$\Delta = \frac{K_f}{\phi K_s^2} [(1 - \phi) K_s - K_{fr}]. \quad (\text{A7})$$

The frame bulk modulus K_{fr} is the reverse of the compressibility, itself being a measure of the volumetric strain resulting from an applied change in pressure (Hart & Wang 1995).

In Section 2 the eqs (1) and (2) refer to complex dynamic parameters such as electrokinetic coupling $L(\omega)$, permeability $k(\omega)$ and effective conductivity $\sigma(\omega)$:

$$L(\omega) = L_0 \left[1 - i \frac{\omega}{\omega_c} \frac{m}{4} \left(1 - 2 \frac{d}{\Lambda} \right)^2 \left(1 - i^{3/2} d \sqrt{\frac{\omega \rho_f}{\eta}} \right)^2 \right]^{-\frac{1}{2}}, \quad (\text{A8})$$

where the static electrokinetic coupling is given by:

$$L_0 = -\frac{\phi}{\alpha_\infty} \frac{\varepsilon_{rf} \zeta}{\eta} \left(1 - 2 \frac{d}{\Lambda} \right), \quad (\text{A9})$$

where m and Λ are geometrical parameters of the pores given in Table C1. The critical angular frequency ω_c separates the viscous and inertial flow domains and is defined by:

$$\omega_c = \frac{\phi}{\alpha_\infty k_0} \frac{\eta}{\rho_f}. \quad (\text{A10})$$

Assuming that the d/Λ term is negligible, L_0 parameter can be expressed versus electrokinetic coupling C_{ek} from electrofiltration measurements (Guichet *et al.* 2003). Then:

$$L_0 = -\frac{\phi}{\alpha_\infty} C_{ek} \sigma_f = -C_{ek} \sigma_r. \quad (\text{A11})$$

Expression of the effective conductivity of the material introduces surface conduction effects due to electrofiltration (C_{em}) and electro-osmotic (C_{os}) effects:

$$\sigma(\omega) = \frac{\phi \sigma_f}{\alpha_\infty} \left[1 + 2 \frac{C_{em} + C_{os}(\omega)}{\sigma_f \Lambda} \right]. \quad (\text{A12})$$

At last, the dynamic permeability of the porous media (Johnson *et al.* 1987) depends on the observed frequency, especially for very high frequencies:

$$k(\omega) = k_0 \left[\sqrt{1 - i \frac{\omega}{\omega_c} \frac{4}{m}} - i \frac{\omega}{\omega_c} \right]^{-1}. \quad (\text{A13})$$

A2 Phase velocities of body waves

The phase velocities analysis used in this paper is based on the formulation of Pride & Haartsen (1996) in the low frequency domain. This approach has been developed for seismoelectric studies, but in the case $L(\omega) = 0$ the phase velocities are equivalent to the Biot's results (1956). Slowness are expressed in the case of plane longitudinal and transverse waves:

For the fast P waves:

$$2s_{P_f}^2 = \gamma - \sqrt{\gamma^2 - \frac{4\tilde{\rho}\rho}{MH - C^2} \left[\frac{\rho_t}{\rho} + \frac{\tilde{\rho}L(\omega)^2}{\tilde{\varepsilon}} \right]}. \quad (\text{A14})$$

For the slow P waves:

$$2s_{P_s}^2 = \gamma + \sqrt{\gamma^2 - \frac{4\tilde{\rho}\rho}{MH - C^2} \left[\frac{\rho_t}{\rho} + \frac{\tilde{\rho}L(\omega)^2}{\tilde{\varepsilon}} \right]}. \quad (\text{A15})$$

where

$$\gamma = \frac{\rho M + \tilde{\rho} H [1 + \rho \frac{L(\omega)^2}{\tilde{\varepsilon}}] - 2\rho_f C}{MH - C^2}. \quad (\text{A16})$$

For the S waves:

$$2s_S^2 = \frac{\rho_t}{G} + \mu_0 \tilde{\varepsilon} \left[1 + \frac{\tilde{\rho}L(\omega)^2}{\tilde{\varepsilon}} \right] + \sqrt{\left\{ \frac{\rho_t}{G} - \mu_0 \tilde{\varepsilon} \left[1 + \frac{\tilde{\rho}L(\omega)^2}{\tilde{\varepsilon}} \right] \right\}^2 - 4\mu_0 \frac{\rho_f^2 L(\omega)^2}{G}}, \quad (\text{A17})$$

where $H = K_G + 4G$ is an elastic modulus, ρ_t the complex density and $\tilde{\rho}$ the effective density given by:

$$\rho_t = \rho - \frac{\rho_f^2}{\tilde{\rho}} \quad (\text{A18})$$

$$\tilde{\rho} = \frac{i}{\omega} \frac{\eta}{k(\omega)}. \quad (\text{A19})$$

Attenuation effects of the Biot's theory are described by the imaginary part of the effective density $\tilde{\rho}$. In this expression $\tilde{\varepsilon}$ corresponds to the effective permittivity introducing conduction and electro-osmotic dissipation:

$$\tilde{\varepsilon} = \varepsilon_0 \varepsilon_{rT} + \frac{i}{\omega} \sigma(\omega) - \tilde{\rho}(\omega) L^2(\omega). \quad (\text{A20})$$

APPENDIX B: SEISMO-ELECTROMAGNETIC FIELDS IN THE POROUS CYLINDRICAL SAMPLE

Similarly to Hu & Wang (2000) study for a fluid-filled borehole, we consider an axisymmetric porous system under vertical seismic excitation generating P -SV waves. According to Pride & Haartsen (1996), four different propagation modes should be taken into account: fast and slow P waves (P_f and P_s) as longitudinal modes and S and electromagnetic (em) waves as transverse modes. Nevertheless, we neglect electromagnetic modes generating electroosmotic displacements in the absence of significant source.

B1 Seismomagnetic coupling from extensional modes

The total displacement \mathbf{u} can be expressed in the (i_r, i_θ, i_z) coordinate system by:

$$\mathbf{u}_e = A_{P_f} \nabla \Phi_{P_f} + A_{P_s} \nabla \Phi_{P_s} + A_S \nabla \times (\Gamma_S i_\theta), \quad (\text{B1})$$

where Φ_{P_f} and Φ_{P_s} are scalar potentials and Γ_S a vector potential satisfying the Helmholtz decomposition with wavenumbers $l_j = \omega s_j$. In the case of the vertical seismic source, the potentials can be expressed by:

$$\begin{cases} \Phi_{P_f} = I_0(\eta_{P_f} r) e^{ik_e z} & \text{and} & \Phi_{P_s} = I_0(\eta_{P_s} r) e^{ik_e z} \\ \Gamma_S = I_1(\eta_S r) e^{ik_e z}, \end{cases} \quad (\text{B2})$$

where I_i are the modified Bessel's function of order i and η_j ($j = P_f, P_s$ or S) are related to the axial wavenumber k_e of extensional waves (in the vertical direction z) by the relation:

$$\eta_j = \sqrt{k_e^2 - l_j^2}, \quad (\text{B3})$$

where $l_j = \omega s_j$ are the radial wavenumbers of each mode. Then, components of the displacement \mathbf{u} can be calculated:

$$\mathbf{u}_e = \begin{bmatrix} A_{P_f} \eta_{P_f} I_1(\eta_{P_f} r) + A_{P_s} \eta_{P_s} I_1(\eta_{P_s} r) - i k_e A_s I_1(\eta_S r) \\ 0 \\ i k_e A_{P_f} I_0(\eta_{P_f} r) + i k_e A_{P_s} I_0(\eta_{P_s} r) + A_s \eta_s I_0(\eta_S r) \end{bmatrix}_{(r, \theta, z)} e^{i k_e z}. \quad (\text{B4})$$

According to Pride & Haartsen (1996), the seismoelectric field can be deduced *via* appropriate coefficients β_j for each propagation mode:

$$\mathbf{E}_e = \begin{bmatrix} \beta_{P_f} A_{P_f} \eta_{P_f} I_1(\eta_{P_f} r) + \beta_{P_s} A_{P_s} \eta_{P_s} I_1(\eta_{P_s} r) - i k_e \beta_s A_s I_1(\eta_S r) \\ 0 \\ i k_e \beta_{P_f} A_{P_f} I_0(\eta_{P_f} r) + i k_e \beta_{P_s} A_{P_s} I_0(\eta_{P_s} r) + \beta_s A_s \eta_s I_0(\eta_S r) \end{bmatrix}_{(r, \theta, z)} e^{i k_e z}, \quad (\text{B5})$$

where coefficients β_j are given by:

$$\beta_j = \begin{cases} \frac{i \omega L \tilde{\rho}}{\tilde{\epsilon}} \left(\frac{H s_j^2 - \rho}{C s_j^2 - \rho_f} \right) & \text{for } j = P_f \text{ or } P_s \\ -i \omega \mu \tilde{\rho} L \frac{G}{\rho_f} \left(\frac{s_j^2 - \frac{\rho}{G}}{s_j^2 - \mu \tilde{\epsilon}} \right) & \text{for } j = S, \end{cases} \quad (\text{B6})$$

where ρ , C and M formation parameters are given by eqs (A5) and (A6). Then, the seismomagnetic field \mathbf{H} can be deduced from classical Maxwell's equation:

$$\mathbf{H} = -\frac{i}{\omega \mu} (\nabla \times \mathbf{E}), \quad (\text{B7})$$

where μ is the magnetic permeability of the free space. Combined with eq. (6), this equation leads to:

$$\mathbf{H}_e = \begin{bmatrix} 0 \\ \frac{1}{i \mu} \omega s_S^2 A_s \beta_s I_1(\eta_S r) \\ 0 \end{bmatrix}_{(r, \theta, z)} e^{i k_e z}. \quad (\text{B8})$$

By comparison with eq. (B4) we get:

$$H_{e,\theta} = \frac{1}{i \mu} \frac{\beta_s s_S^2}{k_e} \frac{d u_{s,r}}{dt}. \quad (\text{B9})$$

This equation shows that the seismomagnetic field associated to extensional waves is proportional to the grain velocity of S waves *via* the dynamic variables β_s , s_S^2 and k_e .

B2 Seismomagnetic coupling from S waves

On the other hand, seismomagnetic coupling can be generated by pure S waves. Using the same procedure, we can obtain the expressions of seismoelectric and magnetic fields

$$\mathbf{E}_s = \begin{bmatrix} -i k_s I_1(\eta_S r) \\ 0 \\ \eta_s I_0(\eta_S r) \end{bmatrix}_{(r, \theta, z)} A_s \beta_s e^{i k_s z} \quad (\text{B10})$$

and

$$\mathbf{H}_s = \begin{bmatrix} 0 \\ \frac{1}{i \mu} \omega s_S^2 A_s \beta_s I_1(\eta_S r) \\ 0 \end{bmatrix}_{(r, \theta, z)} e^{i k_s z} \quad (\text{B11})$$

leading to

$$H_{s,\theta} = \frac{1}{i \mu} \frac{\beta_s s_S^2}{k_s} \frac{d u_{s,r}}{dt}. \quad (\text{B12})$$

This expression shows that the seismomagnetic field is proportional to the grain velocity of s waves similarly to extensional mode (note the difference of coefficient with k_s instead of k_e).

B3 Low frequency approximation

As suggested by Garambois & Dietrich (2001), the low frequency approximation leads to a significantly simpler form of eq. (B12). Using the same procedure (not detailed here) we use the zero frequency value of the S wave slowness:

$$s_S^2 = \frac{\rho_t}{G}. \quad (\text{B13})$$

Using the zero frequency electrokinetic coupling L_0 , the β_S coefficient can be expressed by:

$$\beta_S = i\omega\mu L_0 \frac{G \rho_f}{\rho_t}. \quad (\text{B14})$$

Leading to the relation:

$$H_{s,\theta} = \omega L_0 \frac{\rho_f}{k_s} \frac{du_{s,r}}{dt} = H_\theta = L_0 \rho_f \sqrt{\frac{G}{\rho}} \frac{du_{s,r}}{dt}. \quad (\text{B15})$$

Using the definition of the electrokinetic coupling:

$$L_0 = -\frac{\phi}{\alpha_\infty} \frac{\epsilon_0 \kappa_f \zeta}{\eta} \quad (\text{B16})$$

we get:

$$H_{s,\theta} = -\frac{\phi}{\alpha_\infty} \frac{\epsilon_0 \kappa_f \zeta}{\eta} \rho_f \sqrt{\frac{G}{\rho}} \frac{du_{s,r}}{dt}. \quad (\text{B17})$$

Using the same procedure, we get the expression of the seismomagnetic field associated to extensional modes:

$$H_{e,\theta} = -\frac{\phi}{\alpha_\infty} \frac{\epsilon_0 \kappa_f \zeta}{\eta} \rho_f \sqrt{\frac{E}{\rho}} \frac{du_{s,r}}{dt}, \quad (\text{B18})$$

where E is the Young's modulus of the sample defined by eq. (10). The low frequency approximation shows that the seismomagnetic field is proportional to the radial grain velocity associated to S waves. The transfert function depends on the origin of the seismic propagation (S or extensional waves), *via* the phase velocities $\sqrt{E/\rho}$ and $\sqrt{G/\rho}$. A simple comparison of the transfert functions from eqs (B12) and (B17) leads to the conclusion that the error from low frequency approximation is lower than 2 per cent in the range of 100–3000 Hz.

APPENDIX C: NOTATIONS

Table C1. List of Notations.

α_∞	Tortuosity	
ε_0	Dielectric constant of the free space	$\varepsilon_0 = 885\,418\,782 \times 10^{-12}$
$\varepsilon_{rT}, \varepsilon_{rf}, \varepsilon_{rs}$	Dielectric constants (total, fluid and solid)	
$\tilde{\varepsilon}$	Effective permittivity	cf. eq. (A20)
η	Fluid viscosity	
k_0	Measured permeability	$5.8 \times 10^{-12} \text{ m}^2$
$k(\omega)$	Dynamic permeability	cf. eq. (A13)
Λ	Pore geometry parameter	$\Lambda = \sqrt{\frac{\kappa_0 m \alpha_\infty}{\phi}}$
ρ_f, ρ_s and ρ	Fluid, solid and total bulk density	$\rho = \phi \rho_f + (1 - \phi) \rho_s$
ρ_t	Complex density	cf. eq. (A18)
$\tilde{\rho}$	Effective density	cf. eq. (A19)
σ_f	Electrical conductivity of the fluid	3.1 S m^{-1}
σ_s	Electrical conductivity of the grains	
$\sigma(\omega)$	Effective conductivity	cf. eq. (A12)
τ_B	General stress tensor	$\tau_B = \phi \tau_f + (1 - \phi) \tau_s$
τ_f and τ_s	Fluid and solid stress tensor	
ϕ	Porosity	
ω	Pulsation	
ω_c	Critical frequency	$\omega_c = \frac{\phi}{\alpha_\infty \kappa_0} \frac{\eta}{\rho_f}$
ζ	Zeta potential	
C_{ek}	Electrofiltration coupling	
d	Debye length	$d = \frac{3 \cdot 10^{-10}}{\sqrt{C_0}}$
G	Frame shear modulus	
E and H	Seismo-electric and seismo-magnetic fields	
H	Elastic constant	$H = K_G + 4G$
K_G	Gassman's modulus	$K_G = \frac{K_{fr} + \phi K_f + (1 + \phi) K_s \Delta}{1 + \Delta}$
K_{fr}, K_f and K_s	Frame, fluid and grain bulk moduli	
$L(\omega)$	Dynamic electrokinetic coupling	cf. eq. (3)
L_0	Static electrokinetic coupling	cf. eq. (4)
m	Geometrical parameter of the pores	$2 \leq m \leq 8$
p	Pore pressure	
S_w	Saturation coefficient	
$\mathbf{u}_s, \mathbf{u}_f$	Displacement of the solid and the fluid	
\mathbf{u}	Total displacement	
\mathbf{w}	Volume average filtration (fluid flow)	$\mathbf{w} = \phi (\mathbf{u}_s - \mathbf{u}_f)$

2.2.3. Travaux en cours

Nous avons montré de manière numérique que dans un milieu saturé, il existe une « plage » de propriétés constitutives de l'espace poreux pour laquelle l'onde de Biot lente est observable dans sa partie diffuse, via sa signature électrique. La figure 1.4 montre un exemple de sismogrammes et un sismo-électrogramme pour lesquels on voit que l'onde de Biot est visible uniquement au niveau du champ sismo-électrique et donc mesurable via des électrodes, alors qu'elle reste très difficile (impossible ici) à mesurer via sa composante sismique. On notera d'ailleurs la forte atténuation de l'onde de Biot à grand offset par rapport à celle de l'onde P, alors qu'elle domine le signal à offset court. Les propriétés constitutives de ce milieu ressemblent à celles d'un sable de porosité 30 %, de perméabilité $5 \cdot 10^{-12} \text{ Pa}\cdot\text{s}$ et de vitesses 2220 m/s pour les ondes P et 59 m/s pour les ondes de Biot lentes (à 100 Hz).

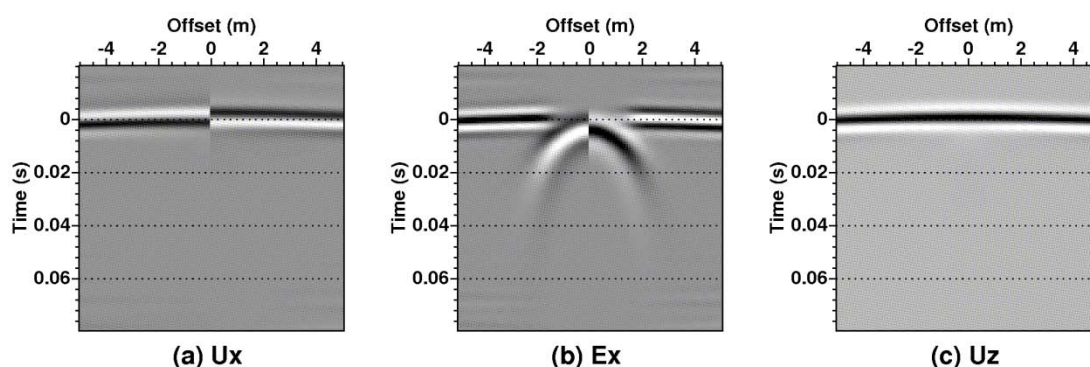


Fig.1.4. Modélisation numérique des ondes directes sismiques (a) et (c) et sismo-électriques (b) obtenues du sable après une explosion, en champ proche. La signature électrique de l'onde de Biot est visible tandis qu'elle génère des amplitudes sismiques trop faibles par rapport à l'onde P rapide pour être observable.

Ces données ont été modélisées entre -5 et +5 m par rapport à une source explosive centrée sur 100 Hz. Ici, la fréquence de transition « de Biot » est égale à 3.2 kHz. C'est la fréquence qui sépare les différents régimes contrôlant l'écoulement du fluide engendré par le passage des ondes sismiques. Celui-ci passe d'un régime dominé par la viscosité (basse fréquence, l'onde de Biot est donc diffuse et très dispersive) à un régime dominé par l'inertie (l'onde de Biot est propagative et peu dispersive). Si ces modélisations numériques sont correctes, cette observation obtenue dans le régime dispersif est importante. D'une part, l'onde de Biot lente prédite par la théorie de Biot et responsable d'atténuation importante au passage d'interfaces n'a été observée que dans un nombre très limité d'expériences de laboratoire spécifiquement conçues pour ce but, et uniquement à haute fréquence, c'est à dire dans sa partie de propagation. Son enregistrement dans le régime diffusif permettrait une confrontation entre données expérimentales (vitesse, atténuation, dispersion) et modèles théoriques dynamiques, très importante pour l'étude du modèle poroélastique.

D'autre part, l'amplitude observable de sa signature électrique lorsque les distances de propagation sont faibles, fait que celle-ci, très sensible à la diffusion fluide et aux propriétés de perméabilité du milieu, permettrait d'entrevoir la construction de sondes prototypes, non pas basées sur la mesure de sa signature sismique, mais plutôt sur celle de sa signature électrique. Ce type d'application est l'objet du projet ANR HPPP-CO2 (coordinateur Y. Guglielmi) qui vise à enregistrer les signaux sismiques et la déformation générés par un signal de haute pression, ceci pour remonter aux paramètres des milieux traversés (perméabilité, porosité, fracturation).

Enfin, cet effet électrocinétique pourrait expliquer les signaux électriques basse-fréquence mesurés par Hunt & Worthington (2000) dans un forage avec un appareillage à faible offset constant (1 m) entre source sismique et récepteur électrique. Dans cette expérience, l'amplitude de ces signaux était fortement corrélée avec le degré de fracturation du milieu, c'est-à-dire avec la perméabilité, sans que leur origine soit alors identifiée.

A l'heure actuelle, beaucoup d'études (numériques, expérimentales) tendent à considérer une approximation basse-fréquence, qui s'avère commode car elle permet plus facilement de comparer les signaux co-sismiques avec la théorie en s'affranchissant des aspects fréquentiels, difficiles à modéliser avec les codes de modélisation conçus en temps. Dans le cadre d'une collaboration avec C. Bordes (Univ. de Pau), nous voulons comparer les signaux sismiques et sismo-électriques en analysant leurs propriétés dispersives. Ceci est illustré Figure 1.5 sur des données expérimentales obtenues dans du sable présentant des saturations différentes (Bordes et al., 2009).

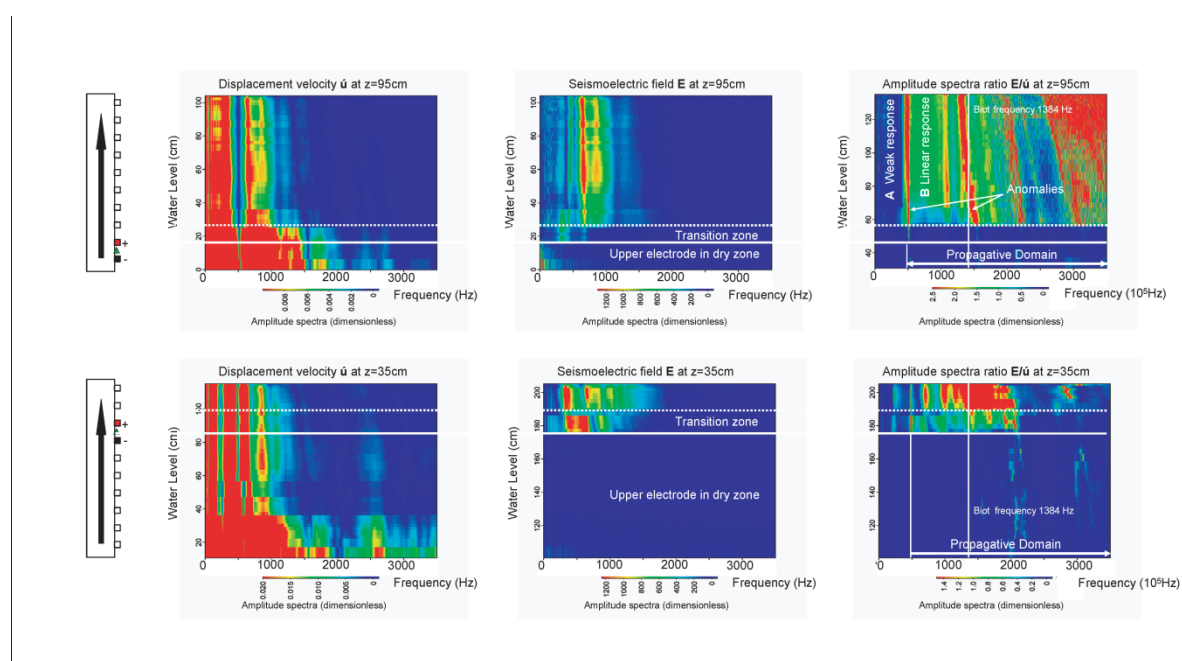


Fig.5. Suivi temporel des spectres sismiques (gauche) sismo-électriques (milieu) et de leur rapport spectral obtenus pendant le remplissage en eau d'une colonne de sable à 95 cm (haut) et 35 cm (bas) de la source. D'après Bordes et al. (2009).

Les saturations différentes ont été obtenues lors du remplissage discret d'une colonne de sable. Les spectres représentés figure 1.5 montrent l'absence (ou du moins le très faible niveau d'amplitude) du champ sismo-électrique co-sismique tant qu'une des électrodes de mesure se situe dans la partie sèche de la colonne. Ils montrent également que les effets sismo-électriques apparaissent dès que de très faibles taux de saturation atteignent l'électrode positionnée en haut de la colonne. On observe également de très forts effets dispersifs au niveau sismique mais surtout au niveau du champ sismo-électrique. Si les effets dispersifs sismiques peuvent être globalement expliqués par l'atténuation (atténuation des hautes fréquences), on voit que la partie basse-fréquence (régime quasi-statique si l'on se réfère aux dimensions de la colonne) est beaucoup plus faible en électrique. Les rapports spectraux effectués entre ces deux champs sont proposés à droite de la figure et montrent une forte variabilité fréquentielle, ce qui prouve que les effets électrocinétiques sont très dispersifs notamment aux alentours de la fréquence de Biot. Des études complémentaires devront être menées pour mieux comprendre ces observations, sans doute en passant par la modélisation numérique de ces effets en milieu cylindrique, code qui n'a

pas été développé jusqu'à présent et également pourra servir à mieux comprendre les données acquises en forage.

2.3 Perspectives

Afin de mieux comprendre ces phénomènes et rendre réellement opérationnelle une méthode de caractérisation de la subsurface et de l'espace poreux basée sur les phénomènes de conversion sismo-électromagnétique, plusieurs pistes de recherche peuvent être avancées, dans lesquelles j'espère pouvoir jouer un rôle actif.

2.3.1. Développements numériques.

Les travaux numériques récents menés en parallèle par plusieurs groupes de recherche ont principalement porté sur la modélisation des phénomènes dans les milieux 2D. Une des difficultés rencontrées réside dans la non prise en compte de l'ensemble des équations couplées, c'est-à-dire que la propagation des ondes sismiques est généralement « convoluée » aux couplages électrocinétiques, ce qui permet de fournir les champs électromagnétiques correspondants. Cette approche reste très approximative et sans doute peu applicable aux objets hétérogènes et complexes géométriquement. De même, d'autres approches s'appuyant sur des logiciels de résolution d'équations couplées de type COMSOL, restent à l'heure actuelle limitées à une résolution en temps nécessitant un certain nombre d'hypothèses simplificatrices (approximations basses fréquences). Celles-ci posent problème car elles ne rendent compte des phénomènes en jeu que de manière partielle et non dynamique. En effet, les phénomènes de dispersion (sismiques, électromagnétiques, couplages) modifient les formes d'ondes et les amplitudes.

Pour ces raisons, il convient à l'avenir de modéliser ces phénomènes en 2D en privilégiant une approche fréquentielle pour le modèle direct, qui permette la description complète des relations constitutives et des équations directement en fréquence. Pour cela, les techniques de modélisation proposées au sein du groupe Imagerie du LGIT (cf. chapitre 1) semblent particulièrement adaptées à cette problématique. Les enjeux d'une telle modélisation 2D sont nombreux. D'une part, ils permettront d'établir l'impact de structures 2D sur le diagramme d'amplitude des ondes sismo-électromagnétique converties, qui reste encore inconnu à l'heure actuelle. Ceci est également vrai pour la réponse sismo-EM de points diffractant. Ces avancées numériques permettront également d'être plus réalistes pour la confrontation nécessaire entre la théorie et des données de terrain ou expérimentales. La modélisation en milieu non saturé (qui nécessite un modèle théorique unifié et dynamique du coefficient de couplage électrocinétique) permettra d'évaluer l'impact de la saturation sur ces phénomènes et de comparer les résultats numériques avec des expériences contrôlées en laboratoire, qui seront menées par ailleurs. Enfin, toujours au niveau numérique, les récents travaux en forage menés par Dupuis et al. (2009) et dans des colonnes de sables en laboratoire (Bordes et al., 2008) font qu'il devient nécessaire de développer un code de modélisation adapté aux configurations d'acquisitions cylindriques.

Dans un second temps, une tentative d'inversion par rapport à certaines propriétés pourra être menée lorsque le modèle direct sera considéré comme robuste. Ceci pourra découler des travaux effectués en imagerie sur la propagation des ondes sismiques en milieu poreux et électromagnétiques pour le GPR (cf. chapitres 1 et 4). Pour cela, des traitements des signaux adaptés devront être testés sur des données synthétiques afin de mieux évaluer le pré-conditionnement optimal des données pré-inversion, qui sera effectuée en fréquence.

2.3.2. Expériences de laboratoire envisagées

En France, l'ANR TRANSEK (coordinatrice L. Jouniaux) tente de regrouper plusieurs équipes françaises (Strasbourg, Pau, Grenoble) sur cette thématique. Elle vise d'une part à l'élaboration d'expériences contrôlées en laboratoire, et d'autre part à améliorer les systèmes d'enregistrements in-situ via le développement de filtres analogiques. Les expériences de laboratoire devront permettre l'étude de la réponse co-sismique en fonction des propriétés du fluide saturant (saturation, nature, salinité) et de l'espace poreux (porosité et perméabilité), ceci afin de proposer des applications en forage. Un effort doit être conjointement mené sur l'étude des conversions sismo-EM à une interface, et ceci pour différentes problématiques : hydrologiques (nappe saturée), géochimiques (pollution, salinité), saturation (transition eau-gaz) et pétrolières (transition eau-huile). Egalement, des structures complexes avec variations latérales des géométries des interfaces, puis des propriétés constitutives des milieux devront être mises en place afin d'étudier le diagramme de rayonnement des champs électriques et magnétiques associés aux conversions à ces contrastes de propriétés. Ce sont ces allers-retours entre expériences contrôlées et développements théoriques et numériques qui permettront de mieux comprendre et décrire ces phénomènes avant applications éventuelles. Enfin, la réponse à des structures fortement anisotropes (fractures) devra également être mieux cernée, celles-ci jouant sans doute un rôle majeur au niveau des champs attendus, en raison de leur forte perméabilité et donc des forts gradients de pression fluide qu'elles peuvent engendrer. Enfin, l'étude de la signature électrique de l'onde de Biot devra être confirmée (ou infirmée) par des études en champs proche dans des situations favorables.

2.3.3. Traitement du signal

En parallèle à ces travaux, il conviendra également d'effectuer à nouveau des acquisitions in-situ à des échelles intermédiaires (premières dizaines de mètres de profondeur). En effet, des progrès significatifs ont été accomplis par plusieurs groupes, notamment grâce aux techniques de traitement dans le plan f-k et de sommation. Outre le faible niveau d'amplitude d'éventuelles ondes converties à une interface, le principal problème concerne les arrivées co-sismiques qui masquent les ondes électromagnétiques. En surface, c'est la signature électrique des ondes de surface qui pollue principalement les enregistrements. Outre les techniques f-k ou transformées en ondelettes, il faudra sans doute utiliser les enregistrements sismiques pour déconvoluer les données sismo-électriques via les fonctions de transferts dispersives. Pour cela, une approche numérique permettra de tester les différentes stratégies possibles. Il conviendra également d'évaluer sur des synthétiques quelle stratégie adopter en termes de traitements des signaux afin de mettre en forme au mieux les données avant une tentative d'inversion, sans doute en tentant d'atténuer au mieux les champs co-sismiques.

2.4. Références citées dans le texte principal

- Biot, M. A., 1956a, Theory of propagation of elastic waves in a fluidsaturated porous solid. I. Low-frequency range, *J. Acoust. Soc. Am.*, 28, 168–178.
- Biot, M. A., 1956b, Theory of propagation of elastic waves in a fluid saturated porous solid. II. Higher frequency range, *J. Acoust. Soc. Am.*, 28, 179–191.
- Biot, M.A., 1962. Mechanics of deformation and acoustic propagation in porous media, *J. Appl. Phys.*, **34**(1), 36–40.
- Block, G.I. & Harris, J.G., 2006. Conductivity dependence of seismoelectric wave phenomena in fluid-saturated sediments, *J. geophys. Res.*, **111**, B01304.

- Bordes C., 2005, etude des couplages sismo-électriques et sismo-magnétiques en milieu poreux, PhD thesis, univ. J. Fourier, Grenoble.
- Bordes, C., Jouniaux, L., Dietrich, M., Pozzi, J.-P. & Garambois, S., 2006. First laboratory measurements of seismo-magnetic conversions in fluidfilled fontainebleau sand, *Geophys. Res. Lett.*, **33**, L01302.
- Bordes C., Jouniaux L., Garambois S., Dietrich M., Pozzi J.-P. & S. Gaffet, 2008, Evidence of the theoretically predicted seismo-magnetic conversion, *Geophysical Journal International*, doi: 10.1111/j.1365-246X.2008.03828.x.
- Bordes C., Garambois S., Jouniaux L. & P. Sénéchal, 2009, Seismoelectric measurements for the characterisation of partially saturated porous media, AGU Fall meeting, 14-18 December, San Francisco, USA.
- Bouchon, M., Discrete wave number representation of elastic wave fields in three-space dimensions, *J. Geophys. Res.*, **84**, 3609–3614, 1979.
- Chen, B. & Mu, Y., 2005. Experimental studies of seismoelectric effects in fluid-saturated porous media, *J. Geophys. Eng.*, **2**, 222–230.
- Dupuis, J.C. & Butler, K.E., 2006. Vertical seismoelectric profiling in a borehole penetrating glaciofluvial sediments, *Geophys. Res. Lett.*, **33**, L16301.
- Dupuis, J.C., Butler, K.E. & Kopic, A.W., 2007. Seismoelectric imaging of the vadose zone of a sand aquifer, *Geophysics*, **72**, A81–A85.
- Dupuis, J. C., K. E. Butler, A. W. Kopic, and B. D. Harris (2009), Anatomy of a seismoelectric conversion: Measurements and conceptual modeling in boreholes penetrating a sandy aquifer, *J. Geophys. Res.*, **114**, B10306, doi:10.1029/2008JB005939.
- Frenkel, J. _1944_. “On the theory of seismic and seismoelectric phenomena in a moist soil.” *J. Phys. (USSR)*, **8**, 230–241.
- Garambois S., 1999, Etudes expérimentales et théoriques des conversions d’ondes sismo-électriques dans les milieux poreux, PhD theis, Univ. J. Fourier, Grenoble, 259 p.
- Garambois, S., and Dietrich, M. _2001_. “Seismoelectric wave conversions in porous media: field measurements and transfer function analysis.” *Geophysics*, **66**, 1417–1430.
- Garambois, S., and Dietrich, M. _2002_. “Full waveform numerical simulations of seismoelectromagnetic wave conversions in fluid saturated stratified porous media.” *J. Geophys. Res.*, **107**, 40–58.
- Gokhberg, M. B., Morgunov, V. A., Yoshino, T., & Tomizawa, I. (1982). Experimental measurement of electromagnetic emissions possibly related to earthquakes in Japan. *J. Geophys. Res.*, **87**, 7824–7828.
- Guichet, X., L. Jouniaux, and J.-P. Pozzi (2003), Streaming potential of a sand column in partial saturation conditions, *J. Geophys. Res.*, **108**(B3),
- Guichet, X., Jouniaux, L. & Catel, N., 2006. Modification of streaming potential by precipitation of calcite in a sandwater system: laboratory measurements in the ph range from 4 to 12, *Geophys. J. Int.*, **166**, 445– 460. 2141, doi:10.1029/2001JB001517.
- Jouniaux, L., A. Mainault, V. Naudet, M. Pessel, and P. Sailhac, Review of self-potential methods in hydrogeophysics, *C. R. Geoscience*, doi:10.1016/j.crte.2009.08.008, 2009
- Kröger, B., Yaramanci, U., and Kemna, A., 2009, Modeling of seismoelectric effects. European COMSOL Conference 2008 Hannover. Proceedings on CD-ROM, ISBN 978-0-9766792-3-3.
- Mikhailov, O. V., J. Queen, and M. N. Toksöz (2000), Using borehole electroseismic measurements to detect and characterize fractured (permeable) zones, *Geophysics*, **65**, 1098– 1112.
- Mikhailov, O. V., J. Queen, and M. N. Toksöz (2000), Using borehole electroseismic measurements to detect and characterize fractured (permeable) zones, *Geophysics*, **65**, 1098– 1112.
- Haines, S., and S. Pride, 2006, Seismoelectric numerical modeling on a grid: *Geophysics*, **71**, no. 6, N57–N65.
- Haines, S.S., Pride, S.R., Klemperer, S.L. & Biondi, B., 2007. Seismoelectric imaging of shallow targets, *Geophysics*, **72**, G9–G20.
- Hunt, C.W. & Worthington, M.H., 2000. Borehole elektrokinetic responses in fracture dominated hydraulically conductive zones, *Geophys. Res. Lett.*, **27**(9), 1315–1318.
- Jardani, A., Revil, A., Slob, E. & Sollner, W., 2010. Stochastic joint inversion of 2D seismic and seismoelectric signals in linear poroelastic materials, 2010, *Geophysics*, **75**, *1*, 10.1190/1.3279833
- Kennett, B. L. N. ,**1983**, *Seismic Wave Propagation in Stratified Media*, Cambridge University Press, Cambridge.
- Mikhailov, O. V., J. Queen, and M. N. Toksöz (2000), Using borehole electroseismic measurements to detect and characterize fractured (permeable) zones, *Geophysics*, **65**, 1098– 1112.
- Mikhailov, O. V., J. Queen, and M. N. Toksöz (2000), Using borehole electroseismic measurements to detect and characterize fractured (permeable) zones, *Geophysics*, **65**, 1098– 1112.
- Pride, S, 1994, Governing equations for the coupled electromagnetic and acoustics of porous media, *Phys. Rev. B*, **50**, 15678–15696.

- Pride, S., Garambois, S., 2002, «The role of Biot slow waves in electroseismic wave phenomena », *Journal of Acoustical Society of America*, 111, 697-706.
- Pride, S. & S. Garambois, 2005, Electroseismic wave theory of Frenkel and more recent developments, *Journal of Engineering Mechanics*, pp 898-907.
- Revil, A., Naudet, V., Nouzaret J., and M. Pessel, 2003, Principles of electrography applied to self-potential electrokinetic sources and hydrogeological applications: *Water Resources Research*, **39**, 1114, doi: 10.1029/2001WR000916.
- Revil, A., Linde, N., Cerepi, A., Jougnot, D., Matthäi, S. & Finsterle, S., 2007. Electrokinetic coupling in unsaturated porous media, *J. Coll. Interf. Sci.*, **313**(1), 315–327.
- Revil, A. and A. Jardani, 2010, Seismoelectric response of heavy oil reservoirs: theory and numerical Modeling, *Geophys. J. Int.* (2010) 180, 781–797.
- Strahser, M.H., Rabbel, W. & Schildknecht, F., 2007. Polarisation and slowness of seismoelectric signals: a case study, *Near Surf. Geophys.*, **5**, 97–114.
- Thompson, A. H., S. Hornbostel, J. Burns, T. Murray, R. Raschke, J. Wride, P. McCammon, J. Sumner, G. Haake, M. Bixby, W. Ross, B. White, M. Zhou, and P. Peczak, 2007, Field tests of electroseismic hydrocarbon detection: *Geophysics*, **72**, no. 1, N1–N9.
- White, B.S., & Zhou, M.Y., 2006, Electroseismic prospecting in layered media, *Society for Industrial and Applied Mathematics*, 67(1), 69-98
- Zhu, Z., Haartsen, M.W. & Toksoz, M.N., 1999. Experimental studies of electrokinetic conversions in fluid-saturated borehole models, *Geophysics*, **64**, 1349–1356.
- Zhu, Z. & Toksoz, M.N., 2005. Seismoelectric and seismomagnetic measurements in fractured borehole models, *Geophysics*, **70**(4), F45–F51.
- Zlotnicki J. and J.L. Le Mouél, 1990. Possible electrokinetic origin of large magnetic variations at la Fournaise volcano, *Nature*, 343, 633-636.
- Zysermana, F., Gauzellinob P. & J. E. Santosa, c, 2009, Finite element modeling of SHTE and PSVTM Electroseismics, *Journal of Applied Geophysics*, accepted.

CHAPITRE 3

Investigations et suivi temporel géophysiques des glissements de terrain

3.1 Introduction.

Les mouvements de terrain constituent un aléa majeur dans les zones montagneuses et ont un impact socio-économique qui peut s'avérer dramatique de par le monde. Ils sont caractérisés par une grande variété de taille, de forme, de matériaux en jeu et de vitesse de déplacement. Pour ceux qui présentent de faibles volumes, ils provoquent chaque année des dégâts géotechniques directs de par la propagation de matériaux en mouvement. Pour les instabilités gravitaires de plus grande ampleur, la propagation des matériaux peut enfouir des villages au pied ou en aval de la zone instable ou constituer des barrages naturels dans les vallées étroites. Ceci pour générer un lac en amont (Fig. 3.1), qui peut provoquer une vague de crue dévastatrice en aval en cas de rupture du barrage. Certaines instabilités qui se sont écoulées dans des fjords norvégiens ont également généré un tsunami dévastateur.

Pour l'Europe seule, les dommages créés par les mouvements de terrain s'élèvent à 1.7 milliards de dollars et 16158 tués pour 75 gros événements se produisant entre 1903 et 2004 (International Disaster database). De plus en cas de séisme, un grand nombre de glissements co-sismiques rajoutent aux dégâts humains et aux infrastructures routières, ce qui bloque l'accès aux secours (Keefer, 1984).



Fig. 3.1. Photographies du mouvement de terrain de Randa (Suisse, 18 avril et 9 mai 1991), environ 30 millions de m³ (droite), qui a provoqué la formation d'un lac, et de celui, visqueux, de Monestier du Percy (Trièves, 9 avril 1978).

Les nombreux mécanismes complexes à l'origine de ces instabilités gravitaires ainsi que l'influence de facteurs externes entraînent une forte incertitude dans la compréhension quantitative de leur fonctionnement.

Plusieurs types de ruptures peuvent se produire lors de mouvements gravitationnels de forte ampleur, fréquents dans les formations cristallines (Hutchinson, 1988). Dans certains cas, un de ces mécanismes peut évoluer vers une rupture catastrophique et une avalanche rocheuse (Valpola, Italie, 1987; Randa, Suisse, 1991, Fig. 3.1; Köfels, Autriche, préhistorique ; Langtang, Népal, préhistorique). Les processus de rupture sont souvent très complexes et comprennent souvent différents mécanismes de déformation reliés aux conditions géologiques, à l'érosion, à l'influence des conditions hydrogéologiques, aux discontinuités et aux conditions externes. Pour les instabilités rocheuses, ils sont principalement gouvernés par les propriétés des roches concernées et par les caractéristiques des discontinuités présentes (foliation, schistosité, failles et fractures) qui affectent la masse rocheuse (Antoine et al., 1994; Glastonbury and Douglas, 2000). Les glissements de terrain de type « sols » sont en général plus lents mais peuvent subir des accélérations brutales en présence de forçages externes (pluviométrie, sismicité) et d'augmentation brutale de la pression interstitielle. Ils peuvent également se transformer en coulées boueuses ou en laves torrentielles qui vont alors se propager de manière très rapide.

Malgré les progrès spectaculaires réalisés au niveau de la modélisation numérique, la forte incertitude liée aux paramètres d'entrée à ces modèles se répercute sur les résultats. Ceci est particulièrement vrai au niveau de la compréhension de la dynamique du phénomène et donc sur la prévision que ce soit dans le domaine spatial (volume mis en jeu, localisation) que temporel (occurrence, dynamique). Ceci provoque un important décalage entre la communauté scientifique, les gestionnaires du risque et les acteurs de la société civile, la gestion des incertitudes étant abordée selon des protocoles très divers, propres aux acteurs impliqués et à leur responsabilité. C'est pourquoi l'estimation quantitative du risque associé à cet aléa ainsi que son évolution temporelle restent problématiques et incertaines à l'heure actuelle, au moins sur le moyen terme.

Contrairement à d'autres aléas naturels (séismes, volcans, inondations), les mouvements de terrains sont finalement restés assez peu instrumentés, et il existe peu de bases de données accessibles à la communauté scientifique. De manière assez surprenante, cette problématique est restée assez peu présente en sciences de la Terre. Cette situation semble évoluer si l'on prend en compte le nombre croissant de publications ayant trait aux mouvements de terrain à l'échelle internationale dans les revues et congrès « sciences de la Terre ».

Les zones réelles affectées par un possible mouvement soudain ne sont pas toujours évidentes à évaluer correctement du point de vue de leur extension et de leur épaisseur. Les mesures de déformation (géodésiques ou extensométriques) et maintenant par fibres optiques, bien que très performantes, montrent à ce titre des limites fortes, car l'information sur les déformations est uniquement superficielle et ne contraint pas le glissement en profondeur. D'autres problèmes subsistent également quant à une meilleure connaissance des propriétés mécaniques des formations au sein du mouvement, des circulations de fluides qui semblent jouer un rôle moteur dans l'accélération du mouvement vers sa rupture brutale et du couplage hydro-mécanique. Les mesures en forage (inclinomètres, mesures de pression, essais en laboratoire) sont extrêmement précieuses pour à la fois délimiter les zones de cisaillement et évaluer certaines propriétés hydrologiques ou mécaniques. Néanmoins, celles-ci peuvent s'avérer difficiles à mettre en place dans des zones souvent escarpées et difficiles d'accès, et restent localisées (représentativité limitée et extrapolation des résultats périlleuse).

Pour ces raisons, un nombre croissant d'investigations géophysiques a été mené sur les mouvements de terrain. Celles-ci visent à évaluer le potentiel des différentes méthodes

géophysiques à disposition et l'intérêt de leur couplage, pour permettre une meilleure caractérisation de la géométrie des matériaux en jeu et éventuellement pour imager la distribution de certaines propriétés hydrologiques et mécaniques, souvent de manière qualitative. En fait, la très forte hétérogénéité de certains mouvements, que ce soit au niveau des géométries 3D que de la très forte variabilité des propriétés mécaniques (déformation hétérogène), hydrologiques et du caractère multi-échelle des discontinuités, en fait un des objets les plus complexes de la subsurface d'un point de vue géophysique. Les méthodes d'investigation potentielles sont très diverses de par leur sensibilité à différents paramètres, de part leur résolution (horizontale et/ou verticale) et de par leur facilité à être mises en œuvre. L'utilisation combinée de différentes méthodes géophysiques est une évolution souhaitable pour mieux contraindre les interprétations proposées, ce qui est primordial pour l'estimation du volume affecté par les mouvements, et pour la quantification des propriétés géotechniques des formations en mouvement. En effet, la connaissance de différentes observables géophysiques permet de mieux caractériser certaines propriétés mécaniques et hydrologiques des formations en mouvement, grâce à des relations pétrophysiques et d'homogénéisation (par exemple Mavko et al., 2003).

A la base, c'est ce challenge de la reconnaissance géophysique de ces objets complexes et importants au niveau socio-économique qui m'a attiré, en plus du caractère souvent multi-disciplinaire des approches (géologues, mécaniciens, géodésiens). De plus, les mouvements présentant une vulnérabilité potentielle bénéficient d'un minimum de reconnaissance géotechnique voir de forages (inclinomètres) et de surveillance (mesures de déplacements, stations météorologiques), ce qui en fait des objets très intéressants pour des développements géophysiques potentiels et leur validation. Enfin, leurs propriétés mécaniques et hydrologiques évoluent dans le temps.

Dans un premier temps, nous avons ainsi tenté d'évaluer le potentiel de nombreuses méthodes géophysiques pour déterminer la géométrie des masses en mouvement dans un contexte rocheux (donc fracturé) et un contexte plus visqueux (sols). La thèse d'O. Méric (2006) a notamment porté sur cette problématique, en essayant d'apporter des informations, mécaniques, géologiques ou hydrologiques mais de manière assez qualitative. Le paragraphe 3.2 présentera tout d'abord une synthèse sur les observables géophysiques classiquement utilisées dans le cadre de la reconnaissance des mouvements de terrain (Jongmans et Garambois, 2007). Nous soulignerons notamment la sensibilité des différentes méthodes géophysiques, leurs limites et avantages que ce soit en termes de résolution que de profondeur de pénétration. Après ces rappels, deux études seront présentées portant sur

- i) la reconnaissance géophysique multi-méthodes du glissement rocheux de grande ampleur (et emblématique) de Séchilienne (Méric et al., 2005), dont la problématique sera introduite, et
- ii) l'intérêt de la reconnaissance par les vitesses sismiques de cisaillement de deux glissements visqueux (Méric et al., 2007).

Cette seconde étude comparera notamment l'efficacité des méthodes géophysiques classiques (tomographies électriques, ondes de surfaces SASW) avec des techniques plus originales pour retrouver la géométrie des surfaces de ruptures, qui génèrent un contraste important de la vitesse des ondes S entre matériaux déformés et sains. En particulier, nous comparerons les techniques de détermination de la fréquence de résonance sismique des couches (techniques H/V, Bonnefoy-Claudet, 2006) et celles accédant aux courbes de dispersion des ondes de surface par analyse du bruit de fond sismique en réseau (Wathelet et al., 2004). Celles-ci ont été comparées et complétées avec les courbes de dispersion (DC) déduites à plus haute fréquence des mesures SASW. Dans un second temps, nous montrerons que leur inversion permet de déterminer la distribution verticale des vitesses d'ondes S, paramètre très sensible à la déformation dans ce

type de mouvement (Socco et Jongmans, 2004), et de retrouver les profondeurs des surfaces de rupture.

Outre les problèmes de reconnaissance, la compréhension des mécanismes qui dirigent les instabilités gravitaires est actuellement bloquée par le manque de données de suivi temporel sur une période représentative. Cet état de fait prédomine malgré le développement de codes numériques 2D et 3D qui permettent de mieux simuler la complexité des mécanismes contrôlant la dynamique des mouvements. Pour palier à ce manque, j'ai participé à la création d'un observatoire National multi-paramètres sur les glissements de terrain (OMIV), qui a été labellisé par l'INSU. Celui-ci concerne 4 sites dans les Alpes, marqués par des différences en termes de géologique, de vitesses de déplacement, de maturité. Cette approche pérenne doit être également complétée par des expériences de suivi temporel à plus court terme sur d'autres sites présentant des forçages plus extrêmes. Parmi les observables disponibles, notre groupe s'est plus particulièrement focalisé sur l'écoute sismologique à long et moyens termes des ces mouvements, qui sont surveillés par ailleurs. Dans ce contexte, deux travaux seront présentés qui illustrent quelques résultats de l'approche d'écoute sismologique.

La première a été conduite dans le cadre de l'observatoire OMIV sur le site de Séchilienne, fortement instrumenté par ailleurs pour des besoins de surveillance et d'alerte. La question centrale était d'établir l'intérêt de la surveillance sismologique pour la surveillance des glissements de terrain. Ce travail, largement mené par A. Helmstetter (LGIT), a permis de montrer différentes classes de signaux sismiques enregistrés durant deux ans, que nous avons identifié comme des événements liés à de l'activité micro-sismiques interne, à des chutes de blocs et à des séismes externes. Leur activité en fonction du temps a pu être corrélée avec les mesures de pluviométrie et de déplacement, et montré des relaxations différentes entre les phénomènes.

Le faible nombre de séismes de magnitude modérée [3-5.5] au niveau des mouvements de terrain instrumentés constitue un point de blocage qui empêche de répondre à l'ensemble des questions scientifiques soulevées sur le rôle des séismes dans les variations de la dynamique des mouvements, et comment les prendre en compte dans les modèles de prédiction. Pour contourner ce problème, il est indispensable d'étudier des régions caractérisées par une sismicité plus forte et plus dense, puis de tenter d'extrapoler les résultats expérimentaux en terme de lois ou de modèles numériques de déclenchement aux Alpes françaises. Ainsi, j'ai conduit une campagne d'instrumentation sismologique qui a duré 14 mois (décembre 2008-janvier 2010), localisée sur le mouvement de terrain d'Utiku (île du nord, Nouvelle-Zélande). Ceci a été effectué en collaboration avec des partenaires de la GNS (Geological and Nuclear Sciences) qui suivent ce glissement avec des données GPS continues et des mesures de pression fluide. Ces travaux étant en cours, nous présenterons les résultats préliminaires qui se sont focalisés sur la variabilité spatiale et l'anisotrope des effets de site au sein du glissement. Ceux-ci ont été déduits à la fois de méthodes de bruit sismique et de rapport spectraux liés aux événements sismiques séismes. Il faudra comprendre ces résultats, notamment d'anisotropie de la réponse sismique, par des modélisations numériques. Ce travail fait l'objet d'une publication en préparation (Garambois et al., 2010) et sera présenté de manière synthétique, en anglais.

Dans une dernière partie, les perspectives seront présentées, notamment dans le cadre d'une ANR interdisciplinaire [2010-2013] sur Séchilienne, que je coordonne.

3.2 Investigations géophysiques multi-méthodes dans différents contextes

3.2.1. Synthèse sur les techniques géophysiques de reconnaissance

Geophysical investigation of landslides : a review

DENIS JONGMANS and STÉPHANE GARAMBOIS

Key words. – Landslides, Geophysical techniques, State-of-the-art

Abstract. – In the last two decades, shallow geophysics has considerably evolved with the emergence of 2D spatial imaging, then 3D spatial imaging and now 4D time and space imaging. These techniques allow the study of the spatial and temporal variations of geological structures. This paper aims at presenting a current state-of-the-art on the application of surface geophysical methods to landslide characterization and focuses on recent papers (after 1990) published in peer-reviewed international journals. Until recently, geophysical techniques have been relatively little used for the reconnaissance of landslides for at least two main reasons. The first one is that geophysical methods provide images in terms of physical parameters, which are not directly linked to the geological and mechanical properties required by geologists and engineers. The second reason shown through this study probably comes from a tendency among a part of the geophysicists to overestimate the quality and reliability of the results. This paper gave the opportunity to review recent applications of the main geophysical techniques to landslide characterisation, showing both their interest and their limits. We also emphasized the geophysical image characteristics (resolution, penetration depth), which have to be provided for assessing their reliability, as well as the absolute requirements to combine geophysical methods and to calibrate them with existing geological and geotechnical data. We hope that this paper will contribute to fill the gaps between communities and to strength of using appropriate geophysical methods for landslide investigation.

Reconnaissance géophysique des glissements de terrain : état de l'art

Mots clés. – Glissements de terrain, Investigations géophysiques, Etat de l'art

Résumé. – Depuis 20 ans, la prospection géophysique à faible profondeur a considérablement évolué avec l'apparition de techniques d'imagerie 2D (x,z), puis 3D (x,y,z) et maintenant 4D (x,y,z,t), qui permettent de considérer les variations spatiales et temporelles des objets géologiques étudiés. A partir de la littérature internationale, nous tentons de faire une synthèse sur l'application des méthodes géophysiques à l'étude et au suivi des mouvements de terrain qui sont des structures complexes et évolutives. Paradoxalement, il apparaît que l'utilisation des techniques géophysiques pour la reconnaissance des mouvements de terrain est restée jusque récemment relativement limitée pour deux raisons principales. La première vient de la réticence d'une partie des ingénieurs et des géologues d'appliquer des techniques complexes qui ne fournissent pas des données géologiques, hydrogéologiques ou mécaniques directement utilisables. La seconde raison, apparue lors de cette étude, résulte de la tendance d'une partie de la communauté géophysique de surestimer la qualité et la fiabilité des résultats obtenus. A travers cette synthèse des publications, nous passons en revue les applications récentes des principales méthodes géophysiques aux mouvements de terrain en illustrant leur intérêt mais en insistant également sur leurs limites et sur les caractéristiques à fournir pour évaluer la fiabilité des images obtenues. Pour atteindre un certain degré de fiabilité, il apparaît clairement que les techniques géophysiques doivent être systématiquement combinées et calibrées par rapport aux données géologiques et géotechniques disponibles. Ce manuscrit a pour objectif d'améliorer la compréhension entre les deux communautés et à promouvoir une utilisation adaptée et combinée des techniques géophysiques modernes pour l'étude des mouvements de terrain.

INTRODUCTION

The term landslide refers to a large variety of mass movements ranging from very slow slides in soils to rock avalanches. Several landslide classifications were proposed and the most widely used at the present time is probably the one of Cruden and Varnes [1996], which mainly considers the activity (state, distribution, style) and the description of movement (rate, water content, material type). Landslides affect all geological materials and exhibit a large variety of

shapes and volumes. The characterisation of these phenomena is not a straightforward problem and may require a large volume of investigation. Reconnaissance methods, which mainly include remote-sensing and aerial techniques, geological and geomorphological mapping, geophysical and geotechnical techniques, have to be adapted to the characteristics of the landslide. According to M^c Cann and Foster [1990], a geotechnical appraisal of landslide's stability has to consider three following issues : (1) the definition of the 3D geometry of the landslide with particular reference to

'Laboratoire Interdisciplinaire de Recherche impliquant la géologie et la mécanique' (LIRIGM), EA 3111 UJF, Maison des Géosciences, BP 53, F-38041 Grenoble cedex 9, France. Tel. +33 (0)476 828 046 / Fax. +33 (0)476 828 070 / E-mail : stephane.garambois@ujf-grenoble.fr
Manuscrit déposé le 27 janvier 2006 ; accepté après révision le 5 juillet 2006.

failure surfaces, (2) the definition of the hydrogeological regime, (3) the detection and characterisation of the movement. Except in very peculiar cases, a landslide generally results in a modification of the morphology and of the internal structure of the affected ground mass, both in terms of hydrogeological and mechanical properties. Mapping the surface area affected by the landslide is usually done by observation of aerial photographs or remote-sensing images [Van Westen, 2004], which indicate the topographical expression of the landslide. However, if the landslide is ancient or little active, its morphologic features and boundaries may have been degraded by erosion and surface observations and measurements have to be supported by reconnaissance at depth [Dikau *et al.*, 1996]. Also, the definition of the 3D shape of the unstable body requires the investigation of the slide mass down to the undisturbed rock or soil. Conventional geotechnical techniques, which mainly include boreholes, penetration tests (when possible) and trenching [Fell *et al.*, 2000], allow a detailed geological description and mechanical characterisation (eventually through laboratory tests) of the material, defining the vertical boundary of the slide and the parameters required for slope stability analysis. These techniques only give punctual information and their use is limited by the difficulty of drilling onto steep and unstable slopes.

Ground modifications due to a landslide are likely to generate changes of the geophysical parameters characterizing the ground, which can be used to map the landslide body and to monitor its motion. Since the pioneering work of Bogoslovsky and Ogilvy [1977], geophysical techniques have been increasingly used but relatively little referenced for landslide investigation purposes, with a growth of interest during these last few years. Among the reasons explaining the reluctance to employ geophysical techniques, one can mention the relative difficulty of deploying geophysical layouts (although the expense is far less than the one required for drilling), the limitations of most ancient geophysical methods to adequately investigate a 3D structure, and the problem of linking the measured geophysical parameters to geotechnical properties. This last aspect made probably many geotechnical engineers reluctant to use geophysical methods. In a recent review of the state-of-the-art of geotechnical engineering of natural slopes, cuts and fills in soil, Fell *et al.* [2000] evaluated that there are few landslide situations where geophysical techniques are a great deal of value. The recent emergence of 2D and 3D geophysical imaging techniques and the efforts of manufacturers to provide reliable and portable equipments have dramatically increased the attractiveness of geophysical techniques for landslide applications and, even if the relation between geophysical parameters and geological/geotechnical properties is still posed, these methods now appear as major tools for investigating and monitoring landslides.

This paper aims at presenting a current state-of-the-art on the application of surface geophysical methods to landslide characterization. Our work is focused on recent papers (after 1990) published in peer-reviewed international journals, the authors of which are mainly scientists. In order to consider the engineering expertise in this field, we also included a limited number of proceedings of international conferences, written by scientists and/or engineers. This paper will contribute to improve the exchange of expertise

between geophysicists, geologists, geomorphologists and geotechnical engineers.

GEOPHYSICAL METHODS: AN OVERVIEW

Geophysics is based on the acquisition of physical measurements from which physical parameters can be deduced. It is beyond the scope of this paper to detail the different methods used for landslide investigation and their characteristics. The principle of most of these methods can be found in general books [Reynolds, 1997; Telford *et al.*, 1990; Sharma, 1997; Kearey *et al.*, 2002]. A review of the geophysical methods applied at the reconnaissance stage in a landslide investigation was made by M^c Cann and Forster [1990], who illustrated with several case studies from different geological settings. Recently, Hack [2000] presented in a general way and discussed various geophysical techniques for slope stability analyses, quickly examining their merits and illustrating them.

The main characteristics of geophysical methods are pointed out in the above mentioned publications and are summarized here. On the one hand, advantages of geophysical techniques are that (1) they are flexible, relatively quick and deployable on slopes, (2) they are non-invasive and give information on the internal structure of the soil or rock mass, and (3) they allow a large volume to be investigated. On the other hand, their main drawbacks are: (1) the decreasing resolution with depth, (2) the non-uniqueness of the solution for a set of data and the resulting need for calibration and (3) the indirect information they yield (physical parameters instead of geological or geotechnical properties). It is worth noting that almost all the advantages of geophysical methods correspond to disadvantages of the geotechnical techniques and vice-versa, outlining the complementarities between the two investigation techniques. A reconnaissance campaign implying geophysical techniques has to be properly designed. The method to apply depends on its adequacy to the problem to solve and on four controlling factors, which have to be thoroughly considered before any field experiment [M^c Cann and Foster, 1990]. The first and obvious one is the existence of a geophysical contrast. The presence of a geological, hydrological or mechanical boundary (e.g., the limit of the sliding mass) does not necessarily imply a variation in terms of geophysical properties. The second issue is the characteristics of the geophysical method itself, namely the penetration depth and the resolution (ability of the method to detect a body of a given size). As mentioned above, there is usually a trade-off between resolution and penetration: the deeper-the penetration, the poorer-the resolution. These limits have to be accounted for during the design of a geophysical survey. Due to the indirect information they provide, geophysical techniques have always to be calibrated by geological or geotechnical data to obtain a reliable interpretation. Finally, the performance of geophysical techniques is strongly dependent on the signal-to-noise ratio. Landslide material can be highly disturbed and consequently lead to electrical current injection difficulties or strong seismic wave attenuation. Preliminary tests are always required before designing a survey.

After processing, geophysical methods provide the variation of a physical parameter with one, two or three spatial coordinates, corresponding to 1D, 2D and 3D information,

respectively. 1D information corresponds to a profile (horizontal or vertical) while 2D and 3D information are geophysical images usually obtained through an inversion process [Sharma, 1997]. Geophysical imaging (tomography) has dramatically developed during the last twenty years and has the major advantage to give continuous information of the studied body. Geophysical inversion is a complex and nonlinear problem [Zhdanov, 2002] and image interpretation has to be done with a critical mind, considering the already mentioned drawbacks of geophysical techniques and additional limits linked to the inversion process. It is beyond the scope of this paper to detail the geophysical imaging characteristics and only the main issues will be outlined. The obvious and necessary condition an image (model) has to fulfil is that it explains the data, i.e. the forward modelling of the derived image give results close enough to the data. This is usually assessed by a misfit error (RMS), which has to be systematically provided with the image. Even if the RMS value is low (a limit of 5% is usually considered), due to the limited measurement coverage and to errors on the data, the obtained image may only be one of the solutions explaining the data. Depending on the inversion technique, different strategies exist to address this problem of non-uniqueness: tests of inversions considering different starting models, introduction of a priori information in the inversion to constrain the solution, joint inversion of several geophysical data sets. The second issue is the image smoothness caused by most of the inversion techniques used in geophysical tomography, resulting in an inability to determine sharp layer interfaces [Wisén *et al.*, 2003]. Also, new techniques for solving this problem are emerging, using a priori information [Wisén *et al.*, 2005], regularization for favouring sharp boundaries in the inversion process [Zhdanov, 2002] or image processing tools such as crest lines extraction process in gradient images [Nguyen *et al.*, 2005]. Finally, most of the existing images are 2D, while a landslide is a 3D phenomenon. 2D images of 3D structures may be affected by strong artefacts, which are very hard to detect [Wisén, 2005]. A judicious strategy to tackle this problem is to perform 2D and 3D forward modelling to evaluate the robustness and reliability of the obtained image. In any case, the geological or geotechnical interpretation of geophysical images has to be done by considering all the data available on the site, after a discussion between geologists, geophysicists and geotechnical engineers, and has to be clearly argued and shown.

APPLICATION OF GEOPHYSICAL METHODS TO SUBSURFACE MAPPING OF LANDSLIDES

Table I shows a synthesis of the main geophysical methods used for landslide investigation, with the measured geophysical parameter and the information type, the geological context, the landslide classification following Cruden and Varnes [1996], the geomorphology and the application (target). When available, the landslide volume is indicated. Examination of Table I illustrates the wide range of both geophysical techniques and geological settings in landslide applications. Geophysical prospecting was applied on various types of landslides for slope varying from a few degrees (earth slide) to vertical (rock fall). The penetration depth of the surveys ranges from 3 m to 400 m and the

targets of the surveys were mainly two. By far, the major one was the location of the vertical and lateral boundaries of the slip mass or, equivalently, of the failure surface. An additional and implicit target is the mapping of the internal structure of the landslide. All geophysical methods were used with this purpose. Four main different situations can occur. In the first case, geophysical contrasts are due to the lithological changes (layering, tectonic contact or pre-slide weathering) and the failure surface mainly coincides with a geological interface or layer [Batayneh and al Diabat, 2002; Glade *et al.*, 2005; Jongmans *et al.*, 2000; Agnesi *et al.*, 2005; Havenith *et al.*, 2000; Wisén *et al.*, 2003]. In the second case, geophysical contrasts are also controlled by lithological variations but the failure surface cuts the structure in a more complex way and may be or not deduced from the geophysical image [Bichler *et al.*, 2004; Ferrucci *et al.*, 2000; Mauritsch *et al.*, 2000; Demoulin *et al.*, 2003], depending on the landslide velocity, the heterogeneity of the material and the resolution of the technique. Exceptionally (third situation), the failure surface (or potential failure) is directly detected, mainly by propagation methods [Bichler *et al.*, 2004; Jeannin *et al.*, 2006; Petinelli *et al.*, 1996; Willenberg *et al.*, 2004]. In the fourth case, the landslide develops in a globally homogeneous layer and alters its characteristics. The geophysical contrast then arises between the slide and the unaffected mass [Caris and van Asch, 1991; Méric *et al.*, 2005; Lapenna *et al.*, 2005; Schmutz *et al.*, 2000; Lebourg *et al.*, 2005; Bruno and Marillier, 2000], from the cumulative or separate action of the mechanical dislocation, the weathering and an increase of water content. The second target of geophysical prospecting is the detection of water within the slip mass, for which electrical [Lebourg *et al.*, 2005; Bruno and Marillier, 2000; Lapenna *et al.*, 2005] and electromagnetic [Caris and van Asch, 1991; Mauritsch *et al.*, 2000] methods were most applied.

Critical analysis of geophysical methods in landslide investigation

Seismic methods

Seismic reflection

High resolution seismic reflection has been seldom used for landslide investigation [Bruno and Marillier, 2000; Bichler *et al.*, 2004; Ferrucci *et al.*, 2000]. Compared to other geophysical techniques, this method requires a bigger effort to deploy the geophone layouts, particularly in the conditions of rugged topography, making the technique time consuming and costly. Also, the success of shallow seismic reflection requires a good signal to noise ratio and the recording of high frequency waves to reach the desired resolution. These two conditions may be difficult to fulfil on landslides where the ground is strongly disturbed and heterogeneous, affecting the geophone-soil coupling, attenuating the seismic waves and generating scattered waves. The major interest of seismic reflection profiling is its potential for imaging the geometry of the landslide structure, such as the internal bedding or the rupture surface(s) and the robustness of processing tools compared to tomography.

All the authors carried out traditional P-wave seismic surveys, with the exception of Bichler *et al.* [2004], who also

TABLE I. – Synthesis of the geophysical methods used for landslide investigation. Vp and Vs: P-wave and S-wave seismic velocity; ρ : electrical resistivity; V: electrical potential; ϵ : electrical permittivity; γ : density; α : average slope gradient. The maximum penetration depth is indicated in brackets.
 TABLE I. – Synthèse des méthodes géophysiques utilisées pour les investigations de glissements de terrain. Vp et Vs : vitesses sismiques des ondes P et S ; ρ : résistivité électrique ; V : potentiel électrique ; ϵ : permittivité diélectrique ; γ : densité ; α : pente moyenne du versant instable. La profondeur maximale de pénétration est indiquée entre parenthèses.

Method	Parameter-information	Geological context	Landslide type	Application	Authors
Seismic reflection	Vp, Vs, 2D vertical sections	Soft sediments (sand to clay)	Earth slide-debris flow ($\alpha=25^\circ$)	Geological boundary (80 m)	Bichler <i>et al.</i> [2004]
	Vp, Vs, 2D vertical sections	Gypsum, shale and sandstone	Complex active slide ($\alpha=10^\circ$)	Slip surface (50 m) within a gypsum layer	Bruno and Marillier [2000]
Seismic refraction	Vp, Vs, 2D vertical sections	Phyllitic rocks, gneiss	Rockslide ($\alpha=26^\circ$)	Internal geometry (layering, faults)	Ferrucci <i>et al.</i> [2000]
	Vp, Vs	Weathered marl and limestone	Active complex slide ($\alpha=7^\circ$)	Slip surface (3 m)	Glade <i>et al.</i> [2005]
	Vp, Vs	Limestone, shale and debris	Active rock fall-debris slides	Relief of the bedrock (30 m) and internal structure	Mauritsch <i>et al.</i> [2000]
Seismic tomography	Vp, Vs	Black marl	Complex mudslide ($\alpha=26^\circ$)	Basal slip surface (9 m)	Caris and Van Asch [1991]
	Vp, 2D vertical sections	Shale	Translational rockslide (vertical cliff)	Geometry of the slide (5-10 m)	Jongmans <i>et al.</i> [2000]
	Vp, 2D vertical sections	Micaschist	Rock slide ($\alpha=32^\circ$)	Geometry and internal structure	Méric <i>et al.</i> [2005]
	Vs, 1D vertical profile	Varicoloured clay	Complex earth slide- flow ($\alpha=9^\circ-10^\circ$)	Geometry and thickness (30 m)	Lapenna <i>et al.</i> [2005]
Seismic noise measurements (H/V method)	Vs, 1D vertical profile	Black marl	Complex mudslide ($\alpha=25^\circ$)	Failure surface (35 m)	Méric <i>et al.</i> [2006]
	Vs, 1D vertical profile	Varved clay	Translational slide ($\alpha=10^\circ$)	Slip surface (27-37 m) and bedrock depths (33-62 m)	Méric <i>et al.</i> [2006]
Vertical electrical sounding (VES)	ρ , 1D vertical profile	Clayey arenitic rock	Composite soil-rock slump ($\alpha=6^\circ$)	Slip surface (100 m)	Agnesi [2005]
	ρ , 1D vertical profile	Black marl	Complex mudslide ($\alpha=25^\circ$)	Slip surface and bedrock depths (15 m)	Schmutz <i>et al.</i> [2000]
Electrical tomography	ρ , 1D vertical profile	Black marl	Complex mudslide ($\alpha=25^\circ$)	Bedrock depth (7.5 m)	Caris and Van Asch [1991]
	ρ , 2D vertical section	Limestone to shale	Rock slide ($\alpha=22^\circ$)	Slip surface depth (10 m)	Batayneh and Al-Diabat [2002]
	ρ , 2D vertical section	Soft sediments (sand to clay)	Earth slide-debris flow ($\alpha=25^\circ$)	Geological boundary and slip surface depth	Bichler <i>et al.</i> [2004]
	ρ , 2D vertical section	Alluvial debris on gneissic rock	Large rockslide ($\alpha=40^\circ$)	3D slip surface geometry and water flows	Lebourg <i>et al.</i> [2005]
	ρ , 2D vertical section	Clay and sand	Multiple earth slide ($\alpha=8^\circ$)	Geological boundary and slip surface depth	Demoulin <i>et al.</i> [2003]
	ρ , 2D vertical section	Varicoloured clay	Complex earth slide-flow ($\alpha=9^\circ-10^\circ$)	Slip surface depth (30 m)	Lapenna <i>et al.</i> [2005]
	ρ , 2D vertical section	Arenite and clay	Large rockslide	Slip surface depth (20 m)	Havenith <i>et al.</i> [2000]
	ρ , 2D vertical section	Micaschist	Large rockslide	Geometry and thickness (100 m)	Méric <i>et al.</i> [2005]
	ρ , 2D vertical section	Clayey sand on crystalline rock	Complex active slide ($\alpha=10^\circ$)	Slip surface depth	Wisén <i>et al.</i> [2003]
	ρ , 1D horiz. profile and 2D map	Gypsum, shale and sandstone	Complex active slide ($\alpha=10^\circ$)	Upward flow of water on the landslide	Bruno [2000]
Spontaneous Potential (SP)	V, 1D horiz. profile and 2D map	Varicoloured clay	Complex earth slide- flow ($\alpha=9^\circ-10^\circ$)	Landslide boundary, and water flows	Lapenna <i>et al.</i> [2005]
	ρ , 1D horiz. profile and 2D map	Gypsum, shale and sandstone	Complex active slide ($\alpha=10^\circ$)	Lateral boundary of the slide	Bruno and Marillier [2000]
Electro-magnetism (EM34 or TEM)	ρ , 1D horiz. profile and 2D map	Micaschist	Large rockslide	Lateral boundary of the slide	Méric <i>et al.</i> [2005]
	ρ , 1D horiz. profile and 2D map	Black marl	Complex mudslide ($\alpha=25^\circ$)	Slip surface and bedrock depths (15 m)	Schmutz <i>et al.</i> [2000]
Ground penetrating Radar (GPR)	ρ , 1D horiz. profile and 2D map	Limestone and shale, debris	Active rock fall-debris slides	Location of saturated areas	Mauritsch <i>et al.</i> [2000]
	ρ , 1D horiz. profile and 2D map	Black marl	Complex mudslide ($\alpha=26^\circ$)	Differences in water content	Caris and Van Asch [1991]
Borehole radar	ϵ , 2D vertical sections	Soft sediments (sand to clay)	Earth slide-debris flow ($\alpha=25^\circ$)	Geological boundary and slip surface depth	Bichler <i>et al.</i> [2004]
	ϵ , 2D vertical sections	Limestone	Rock slide	Geometry of the moving mass (5m)	Petinelli <i>et al.</i> [1996]
Gravimetry	γ , 1D horiz. profile and 2D map	Limestone	Rock slide	Location of fractures (15 m)	Jeannin <i>et al.</i> [2006]
	γ , 1D horiz. profile and 2D map	Gneiss	Rock slide	Location of fractures (49 m)	Willenberg <i>et al.</i> [2004]
		Flysch	Hollow in bedrock near headscarp		Del Gaudio <i>et al.</i> [2000]

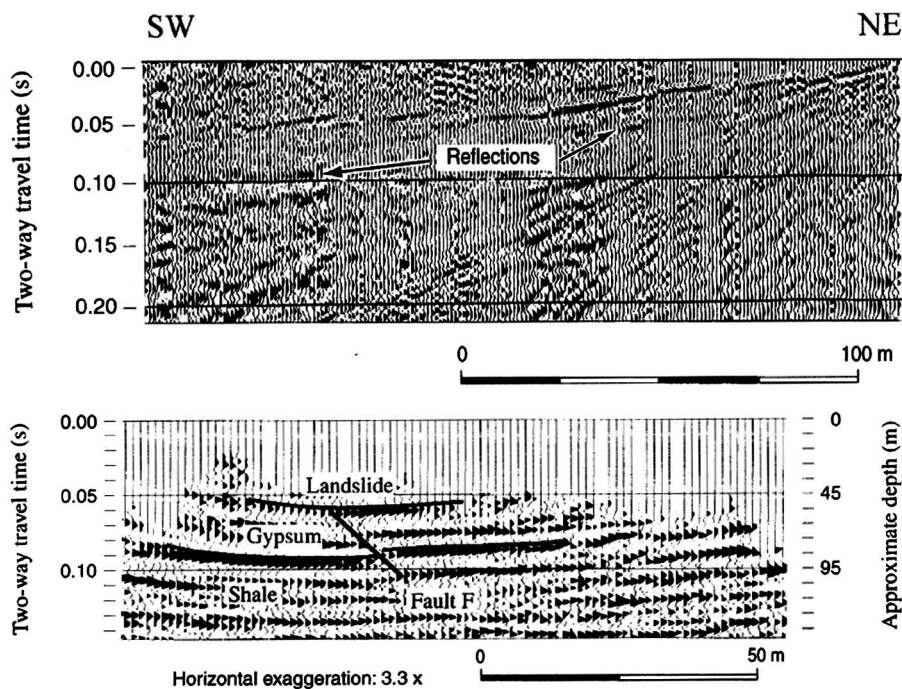


FIG. 1. – Seismic reflection data obtained at the “Boup” landslide (Swiss Alps) by Bruno and Marillier [2000]. An acquisition test shotpoint section (top) shows the presence of two seismic reflections hyperbolae around 90 and 50 ms, presenting a poor signal-to-noise ratio. According to authors, they correspond to the gypsum-shale interface and to the sliding surface within gypsum, respectively. After classical seismic reflection processing, the bottom image shows poststack section after FK migration (constant velocity of 2000 m.s⁻¹) together with geological interpretation. The reflection on the landslide sliding surface appears near the limit of resolution of the image (no data in the first 50 ms TWT) (With kind permission of Springer Science and Business Media).

FIG. 1. – Données de sismique réflexion obtenues sur le glissement de terrain de “Boup” (Alpes Suisses) par Bruno et Marillier [2000]. Un point de tir test (haut) montre la présence de deux hyperboles de réflexion autour de 90 et 50 ms qui présentent un faible rapport signal sur bruit. Selon les auteurs, celles-ci correspondent respectivement à l’interface gypse-schiste et à la surface de glissement. Après un traitement des données classiques l’image du bas montre la section sismique après sommation migrée par FK (vitesse constante de 2000 m.s⁻¹) ainsi que l’interprétation géologique. La réflexion sur la surface de glissement apparaît proche de la limite de résolution de l’image (aucune donnée dans les 50 premiers ms) (Avec l’autorisation de Springer Science and Business Media).

performed S-wave reflection profiles. The main acquisition parameters are presented in table II. The survey of Ferrucci *et al.* [2000] in a complex geological context of tectonised metamorphic rocks depicted the geological structure from 100 m to 400 m depth but failed in detecting the rupture surface, due to the too low resolution at shallow depth. Closer geophone spacing and higher fold coverage should have been adopted to reach this goal. Bruno and Marillier [2000] claimed to locate the surface of rupture for the “Boup” landslide at a depth of about 50 m (50 ms TWT) within a gypsum layer. The reflection (fig. 1) is interpreted as the contact between landslide material (disturbed gypsum) and undisturbed gypsum. A top mute was applied above 50 ms

to suppress refracted waves. As shown in figure 1, the surface rupture was at the upper detection limit of the method and the resolution can be estimated to about 5 m (a quarter of the wavelength). Bichler *et al.* [2004] studied the “Quesnel Forks” landslide which affected a 75 m high terrace composed of sediments deposited during the last glaciation and underlain by volcanic bedrock. The reflection surveys (both P-wave and S-wave) were made parallel to the slide motion, due to the presence of a 40° deep escarpment separating a lower block from an upper block. The method mainly succeeded in obtaining the layering boundaries within each block but had little contribution in locating the surface rupture.

TABLE II. – Acquisition parameters used for seismic reflection profiles.
 TABL. II. – Paramètres d’acquisition utilisés pour les profils de sismique réflexion.

Authors	Channels [maximum fold]	Geophone type and spacing	Reflectors (shallow/deep)	Source type	Profile length
Bruno and Marillier [2000]	24 – 48 [12 – 24]	30 Hz 3 m – 1 m	50 m–120 m	Sledge hammer Buffalo gun	110 m
Ferrucci <i>et al.</i> [2000]	24 [6]	- 10 m	100 m–400 m	0.1-0.2 kg of dynamite	1180 m
Bichler <i>et al.</i> [2004]	36 [18]	100 Hz (P-W) 8 Hz (S-W) 3 m	15 m–80 m 20 m–30 m	Sledge hammer (I beam for S-W)	130 m (P-W) 50 m (S-W)

Seismic refraction

This method is based on the interpretation of the first arrivals in the seismic signals and assumes that the velocity increases with depth [Kearey *et al.*, 2002]. It is widely used in engineering geology for determining the depth to bedrock. For landslide investigation, the method has proved to be applicable, as both shear and compressional wave velocities are generally lower in the landslide body than in the unaffected ground. M^c Cann and Forster [1990] documented several case histories showing the use of seismic refraction for locating the undisturbed bedrock below landslides. In recent studies, the travel time data have been interpreted using delay methods [Kearey *et al.*, 2002] like the plus-minus technique or the Generalized Reciprocal Method (GRM), which allow the mapping of an undulating refractor.

The GRM method was used by Glade *et al.* [2005] for positioning the failure surface of a very shallow landslide (1 to 3 m depth), which coincides with the interface between the colluvium (370 m.s⁻¹) and marly and calcareous sediments (1100 m.s⁻¹) of the Upper-Oligocene in the region of Rheinhessen (Germany). No signals or travel-time curves are shown to support the interpretation. Caris and Van Asch [1991] applied the plus-minus technique on a small landslide in black marl landslide (French Alps). They found a strong velocity contrast between the landslide body (350 m.s⁻¹) and the bedrock (2800 m.s⁻¹), which varies in depth between 4 and 9 m. Mauritsch *et al.* [2000] applied the GRM technique for the investigation of large landslides in the Carnic Region of southern Austria, affecting slopes with a complex geological structure made of limestone, dolomitic conglomerates, sandstones and shales. The survey pointed out a strong increase of P-wave velocity with depth (from 400 m.s⁻¹ to 3600-4000 m.s⁻¹) down to 30 m, with lateral velocity variations which were interpreted as lithology changes. In this context, the method was unable to identify a slip surface and mainly helped in determining the internal composition of the sliding masses and the relief of the bedrock surface. In these case histories, the refraction method was limited to a depth between a few meters to 30 meters. This shallow penetration depth results from the method itself, which requires a relatively long profile (3 to 5 times the penetration depth as a rule of the thumb) and from the wave attenuation in the highly disturbed landslide material. In their survey, Mauritsch *et al.* [2000] had to switch from a sledgehammer to explosives in order to impart enough energy in the ground.

Seismic tomography

The seismic tomography technique consists of inverting first-arrival times to get an image of P-wave velocity distribution in the ground. Compared to classical seismic refraction, the technique requires much more travel-time data and field effort, but allows lateral P-wave velocity variations to be determined. For landslide investigation, the technique was used in rock conditions [Méric *et al.*, 2005; Jongmans *et al.*, 2000] and showed a significant decrease of P-wave velocity values (division by at least a factor 2) in the slide-prone or unstable mass. Méric *et al.* [2005] performed a 300 m long seismic profile across the western limit of the large "Séchilienne" landslide (French Alps) affecting micaschists. Out of the unstable mass, the image (fig. 2) showed a strong vertical velocity, with V_p values ranging from

500 m.s⁻¹ at the surface to 4000 m.s⁻¹ at 25 m depth (sound bedrock). The same profile also pinpointed a significant lateral velocity eastward decrease (from 4000 m.s⁻¹ to 2000 m.s⁻¹) delineating the landslide limit. The correlation with the electrical image performed at the same place will be discussed further.

Seismic noise measurements (H/V method)

Seismic noise measurements have been increasingly used during these last ten years in earthquake engineering for determining the geometry and shear wave velocity values of the soil layers overlying the bedrock [Bard, 1999]. The single station method (also called the H/V technique) consists in calculating the horizontal to vertical spectral ratio of the noise records and allows the resonance frequency of the soft layer to be determined [Nakamura, 1989]. For a single homogeneous soft layer, this fundamental frequency is given by $f = V_s/4h$ where V_s is the soft layer shear wave velocity and h is the layer thickness. Knowing an estimate of V_s allows the thickness of the soft layer to be calculated. The three main assumptions behind the method are that : 1) seismic noise is composed of surface waves; 2) the structure of the soil is 1D and; 3) the V_s contrast is large enough to generate a clear frequency peak. Difficulties also appear in heterogeneous soils (diffraction and diffusion effects) and if various frequencies can be picked (due to the presence of unexpected layers or harmonic noise [Bonney-Claudet, 2004]). As slip surfaces may generate shear wave velocity

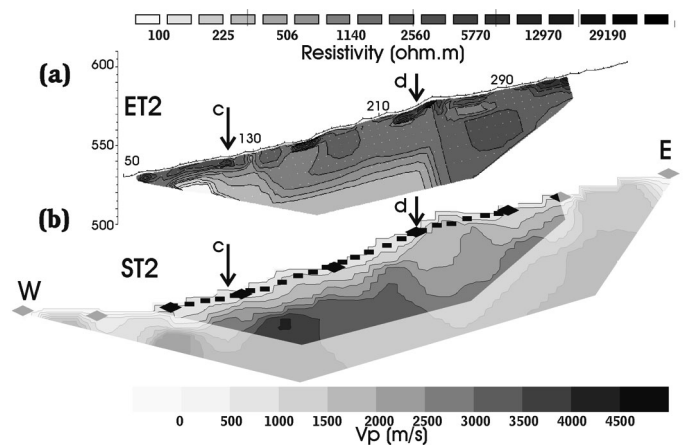


FIG. 2. – Comparison between electrical (a) and seismic (b) tomography sections acquired at across the western limit of the large rocky landslide of "Séchilienne" (French Alps) affecting micaschists [Méric *et al.*, 2005]. RMS values after inversion are 5% (a) and 2% (b). Out of the unstable mass, the image shows a strong vertical velocity, with V_p values ranging from 500 m/s at the surface to 4000 m/s at 25 m depth (sound bedrock) and a significant lateral velocity eastward decrease (from 4000 m/s to 2000 m/s) delineating the landslide limit. The electrical image (Wenner array configuration, RES2DINV inversion software) shows an eastward resistivity increase, from 200 Ω.m to 1 kΩ.m, correlated to the previously described V_p decrease. (With kind permission of NRC Research Press). FIG. 2. – Comparaison entre tomographies (a) électrique et (b) sismiques acquises à travers la limite ouest du grand éboulement rocheux de "Séchilienne" (Alpes françaises) affectant des micaschists [Méric *et al.*, 2005]. Les valeurs de RMS après inversion atteignent 5 % (a) et 2 % (b). Hors de la masse instable, l'image montre une vitesse verticale forte, avec V_p variant de 500 m/s vers la surface à 4000 m/s à la profondeur de 25 m (roche en place saine), ainsi qu'une diminution de vitesse latérale significative (de 4000 m.s⁻¹ à 2000 m.s⁻¹) vers l'est, séparant la limite d'éboulement. L'image électrique (configuration de Wenner, logiciel d'inversion RES2DINV) montre également une augmentation de la résistivité vers l'est, de 200 Ω.m à 1 kΩ.m, corrélée avec la diminution de V_p (Avec l'autorisation de NRC Research Press).

contrasts, the method can theoretically directly detect these surfaces. It was used on three landslides affecting clayey or marly terrains in the southern Apennines [Gallipoli *et al.*, 2000] and in the French Alps [Méric *et al.*, 2007]. The fundamental frequency was derived from the H/V curves and used for deriving an estimate of the rupture surface depth. Depending on the studied case, these estimations were successfully compared with electrical measurements [Lapenna *et al.*, 2003] or with geotechnical soundings or borehole measurements [Méric *et al.*, 2007]. This easy to perform survey opens interesting perspectives for 3D investigation, with the limit of strong 2D or 3D effects which can disturb the propagation of surface waves. More complex techniques using seismic noise arrays were successfully applied by Méric *et al.* [2007] to derive consistent shear-waves velocity profiles versus depth on two soil landslides.

Inversion of surface waves

As slip surfaces may generate shear wave velocity contrasts due to a decrease of shear strength in the unstable zone, all methods able to show Vs variations with depth are of great interest. Beside seismic noise and SH refraction or reflection methods, the analysis of surface waves (SW) is now increasingly used to derive shear wave velocity versus depth in subsurface investigation [Socco and Jongmans, 2004]. The advantage of SW is that they are recorded together with P-wave refraction or reflection data, if a sufficient time length recording was considered during the acquisition. Until now, only a few 1D analyses were performed on landslides. Méric *et al.* [2007] derived the dispersion curves of surface waves recorded on two landslides using the GEOPSY software developed by Wathelet *et al.* [2004]. In both cases, the results were consistent with other geophysical data and borehole measurements and detected quantitatively a large contrast of Vs between the sliding (250-300 m.s⁻¹) and the stable mass (550-800 m.s⁻¹) at depths between 20 and 35 m. For this, the frequency range

of surface waves must be large band and contain information within the stable mass, e.g. at low frequencies (the investigation depth roughly corresponds to Vs/3f).

Electrical methods (resistivity and spontaneous-potential)

Electrical resistivity method

The electrical resistivity method is one of the most used geophysical methods in shallow investigation [Telford *et al.*, 1990; Reynolds, 1997]. It is based on measuring the electrical potentials between one electrode pair while transmitting a direct current between another electrode pair. The technique can be used in three ways : 1) vertical electrical sounding (VES) where electrodes are moved from a mid-point; 2) profiling where the array is moved along a direction with constant electrode spacing, and; 3) electrical tomography where a large number of electrodes and combinations of electrode pairs are used. VES is quick and easy to perform and interpret. It however suffers two major drawbacks: first only vertical variations of resistivity can be considered (1D hypothesis) although measurements must be acquired over a large distance to reach large depth and second the data are likely to be explained by infinity of solutions (non-uniqueness problem). Landslides usually exhibit heterogeneous material and lateral variations of physical parameters, which make difficult the interpretation of VES. Electrical tomography, which provides a 2D (or 3D) image of electrical resistivity, has progressively taken over from the first two methods (tabl. I) in the last decade and has emerged as a standard geophysical imaging technique known for its simplicity. However, the choice of array configuration prior to acquisition must be carefully designed, depending on the desired penetration depth, vertical and lateral resolution and ambient electrical noise. Also, as discussed before, interpretation of obtained images may be

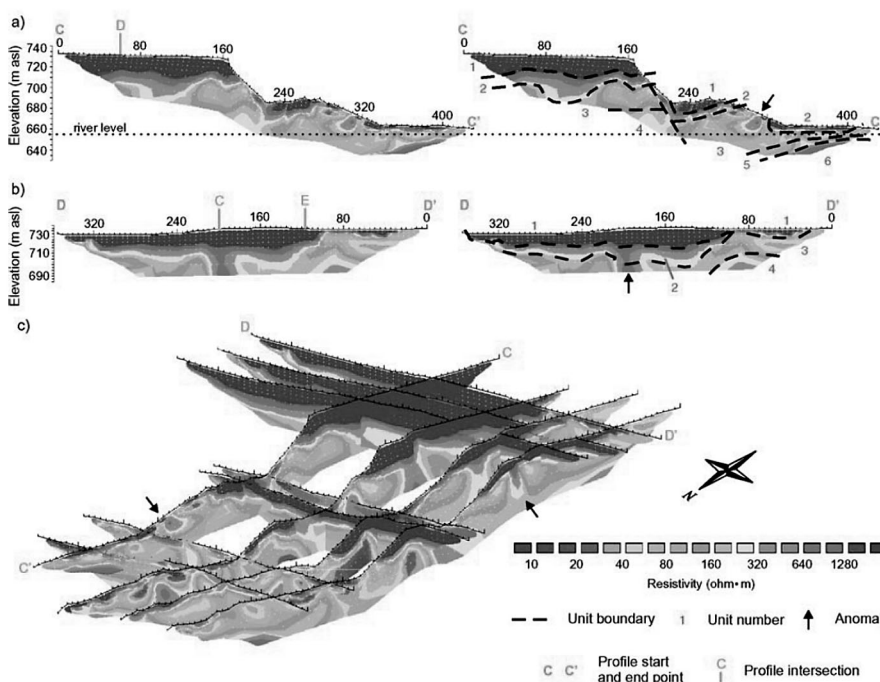


FIG. 3. – DC electrical resistivity profiles (both interpreted and uninterpreted) acquired on the “Quesnel Forks” retrogressive, dry earth slide debris flow (British Columbia, Canada) by Bichler *et al.* [2004]. Profiles C-C’ (located perpendicular to head scarp), D-D’ (parallel to head scarp) and 3D fence diagram were all acquired considering a leapfrog approach with Wenner array configuration. Six different units were identified from the data as authors noted that resistivity values exhibited the largest range of any geophysical parameter tested on this landslide (With kind permission of Springer Science and Business Media). FIG. 3. – Tomographies de résistivité électrique (interprétées et non-interprétées) acquises sur la coulée de “Quesnel Forks” (Colombie Britannique, Canada) par Bichler *et al.* [2004]. Les profils C-C’ (perpendiculaire à l’escarpement) ainsi que le diagramme 3D ont tous été acquis en considérant une configuration Wenner. Six unités stratigraphiques différentes ont été identifiées à partir des données de résistivité, qui présente les plus grandes variations de tous les paramètres géophysiques testés (Avec l’autorisation de Springer Science and Business Media).

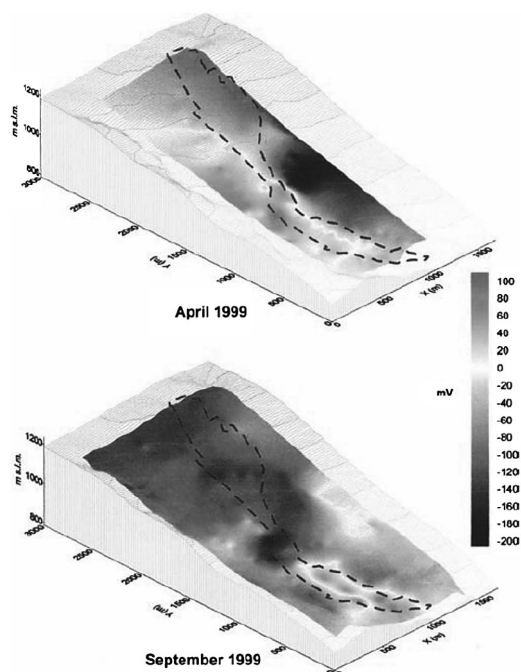


FIG. 4. – Self-potential maps presented by Lapenna *et al.* [2003] on the “Giarossa” landslide (Apennines, southern Italy) in different climatic conditions. Spatial SP variations (negative to positive SP anomalies) are qualitatively interpreted in term of groundwater movements within the landslide from the source zone (negative) to the accumulation zone (positive). Temporal variations could be due to the lowering of the water level within the landslide after the dry period (With kind permission of Springer Science and Business Media).

FIG. 4. – Cartes de potentiel spontané acquis par Lapenna *et al.* [2003] sur le glissement de “Giarossa” (Apenins, Italie du sud) dans des conditions climatiques différentes. Les variations spatiales d’anomalies positives et négatives sont interprétées qualitativement en terme d’infiltrations d’eau (négatives) et d’accumulations de charges (positives). Les variations temporelles seraient dues à une baisse du niveau d’eau dans le mouvement après la période sèche (Avec l’autorisation de Springer Science and Business Media).

complex and should be sometimes checked using numerical modelling (e.g., anisotropy effects).

Electrical resistivity is a parameter exhibiting a large range of values [Telford *et al.*, 1990] sensitive to various factors like the nature of material (particularly clay percentage), the water content and its conductivity, as well as the rock weathering and fracturing. This explains why this method has been the most applied for landslide investigation purposes (tabl. I). The main target of resistivity methods prospecting for landslide investigation is the location of the rupture surface and almost all the authors having used electrical tomography claimed to have detected it in a way or another. The first case is when the surface rupture coincides with an electrically and strength contrasting geological boundary, like shale over limestone [Batayneh and al Diabat, 2002], arenite over consolidated clay [Havenith *et al.*, 2000] or clay over sand [Wisén *et al.*, 2003; Demoulin *et al.*, 2003]. Another situation is when the rupture surface is imaged by the juxtaposition of electrically contrasting units. Bichler *et al.* [2004] performed 4,100 m of resistivity profiles on the “Quesnel Forks” landslide. Figure 3 shows two of the electrical resistivity profiles and a 3D fence diagram of all resistivity data. Six resistivity units were identified, allowing the mapping of the rupture surface (fig. 3a).

Finally, landslides affecting homogeneous terrains can lead to a resistivity variation within the moving mass both in clayey material [Caris and van Asch, 1991; Schmutz *et al.*, 2000; Lapenna *et al.*, 2005] and in metamorphic rock conditions [Méric *et al.*, 2005; Lebourg *et al.*, 2005]. In clayey materials, the landslide body is usually associated with low resistivity values (generally between 10 and 30 $\Omega.m$) which characterizes a high content of clay and/or water. It must be stressed out that in all the listed cases the unaffected clayey material is a compact clay or marl characterized by a resistivity over 60-75 $\Omega.m$. The dislocation of this material by the slide allows the weathering of the minerals and the water content to be increased. Guéguen *et al.* [2004] were not able to detect sliding surfaces from electrical images derived on a slow clayey landslide, where slow deformation did not created observable resistivity contrast. In metamorphic rock conditions, the effect of gravitational deformation can lead to an increase [Méric *et al.*, 2005] or decrease [Lebourg *et al.*, 2005] of resistivity, according to the absence or presence of a water table in the involved mass. Figure 2 shows the comparison of two seismic and electrical profiles across the “Séchilienne” landslide boundary [Méric, 2005]. The electrical image shows an eastward resistivity decrease, from 200 $\Omega.m$ to 1 k $\Omega.m$, correlated to the previously described Vp decrease. These results provide evidence the resistivity and seismic velocity variations are caused by a higher degree of fracturing in dry conditions.

Induced polarization methods were not used on landslides to our knowledge, although it has the property to distinguish clayey zones from water-saturated zones, which exhibit almost same resistivities.

Spontaneous potential

It is well known that groundwater and associated flows contained in any landslide body play a major role in slope stability. The level of groundwater determines the supporting hydrostatic pressure, which, together with hydrodynamic pressure of seepage, are factors decreasing the landslide stability. Imaging water level and water flows within the subsurface at a large scale, as well as their fluctuations over time is a challenging problem, which resulted in specific research purposes on hydrogeophysics [Rubin and Hubbard, 2005]. Only few hydrogeophysical methods were applied on landslides, except those conducted with the self-potential method (SP), which is the easier to deploy and monitor.

Self-potential surveys are conducted by measuring natural electrical potential difference between pairs of electrodes connected to a high impedance voltmeter. These natural fields represent the ground surface electric field signature of various charging mechanisms (electrokinetic, thermoelectric, electrochemical, cultural activity) occurring at depth [Patella, 1997; Révil *et al.*, 1999]. In absence of electrochemical processes and large telluric current, electrokinetic phenomena, describing the generation of electric fields by fluid flows, is the main source of the recorded electric field. The SP source ambiguity and the lack of quantitative interpretation on the fluid source (depth, extension) are the main limitations of the method, which was poorly used on landslides.

Bruno and Marillier [2000] measured an SP profile on the “Boup” landslide and observed that high positive SP

values (40 to 120 mV) coincide with the boundary between the stable ground and the landslide material and interpret them as the electrical signature of resurgent groundwater flow. Comparable large and stable over time positive SP anomalies (up to 350 mV) were acquired by Méric *et al.* [2005] across the “Séchilienne” landslide. Although they noted that the shape of the SP data was highly correlated with displacement rate curve, authors did not conclude whether the source of this anomaly was electrokinetically due to a deep main water flow nearly parallel to the surface or electrochemically due to the geological structure of the movement (fractures, lead-zinc and quartz veins). However, large time-varying negative anomalies on the edge of the landslide were attributed to fluid flow variations within major faults and fractures.

Lapenna *et al.* [2003] presented two SP maps carried out at different climatic conditions on the “Giarossa” landslide (fig. 5). They assume the positive and negative anomalies within the landslide are due to movements of underground water from the source zone to the accumulation zone within the landslide body. Further, SP changes over time were explained by the lowering of the water level inside the landslide body after the dry summer period. To be more quantitative, they also present SP tomographies [Patella, 1997] showing lateral boundaries of the landslide as well as geological heterogeneities. Lapenna *et al.* [2005] also presented an SP map of the “Varco d’Izzo” landslide that they interpreted qualitatively in term of water infiltration and charge accumulation in different zones of the landslide.

In future, increasing number of SP monitoring experiments using networks as well as improvements in numerical simulations and specific signal processing techniques [Gibert and Pessel, 2001; Sailhac and Marquis, 2001] should help the understanding of acquired data and improve hydrological information within landslides.

Electromagnetic methods

As shown in table I, electromagnetic (EM) methods were recently used by several authors for landslide investigation, mainly for determining the geometrical limits of the unstable mass. Except the work of Schmutz *et al.* [2000] who used TEM (Transient Electromagnetic Method) jointly with

VES, EM measurements [Méric *et al.*, 2005; Bruno and Marillier, 2000; Mauritsch *et al.*, 2000] were usually performed in the frequency domain with two horizontal loops and a ground conductivity meter (Geonics EM 34 or EM31). The method, which yields a single apparent electrical resistivity value, allows quick profiling or mapping [Reynolds, 1997]. Penetration depth depends on the coil separation (10 m, 20 m or 40 m for the EM34) and ranges from a few meters to a few tens of meters. Méric *et al.* [2005] and Bruno and Marillier [2000] pointed out a significant variation of apparent resistivity (between 2 and 10) at the limit between the landslide and the stable ground. In rock landslides, Bruno and Marillier [2000] and Mauritsch *et al.* [2000] interpreted electromagnetic data acquired with different modes and coil separations, assuming a two layer model (moving mass above stable ground). They found a relatively good agreement between the bedrock depths derived from electromagnetic interpretation and seismic results, without discussing the vertical or lateral resolution. All the authors stressed out that electromagnetic methods have to be combined with other geophysical techniques for landslide investigation.

Ground penetrating radar (GPR)

The number of published case studies using GPR data has dramatically increased during the last tens years. This success is due to : 1) its high resolution, which moreover presents a large range depending on the chosen antenna, going from a few cm to a few m; 2) its wide range of penetration depth in resistive materials; 3) its sensitivity to dielectric, electric and magnetic contrast and particularly to water content, and; 4) its light instrumentation. All of these properties make it potentially appropriate for investigations in various fields (geological, geomorphological, glaciological, environmental, geotechnical, hydrological). However, severe limitations decrease this potential for landslide investigations, as attested by the very low number of applications in this field (tabl. I). First, GPR signals are highly attenuated in high conductive formations, thus preventing any application in soil landslides or when water saturation is higher than the target. Second, heterogeneities like fractures and blocks create diffractions decreasing dramatically the penetration depth.

Bichler *et al.* [2004] presented GPR reflection profiles acquired on the “Quesnel Forks” landslide using low-

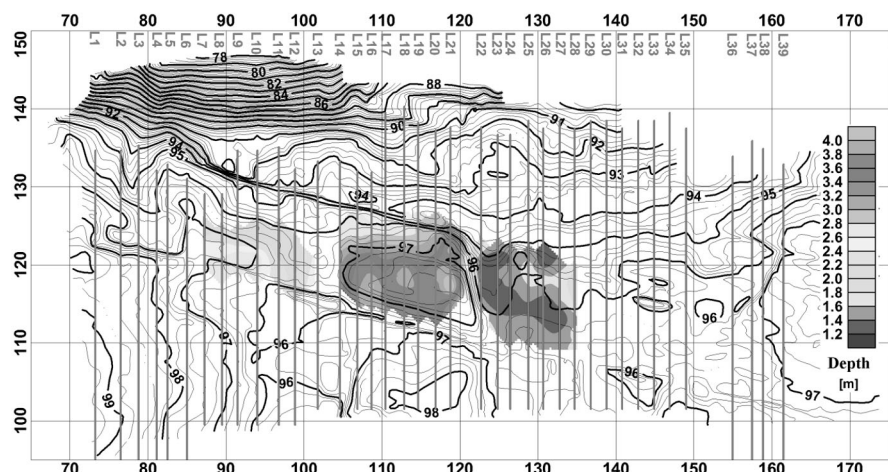


FIG. 5. – Map of the amplitude reflectivity of GPR signals as a function of depth with the relief of the rock fall surface [Roch *et al.*, 2006]. This map was obtained from a dense 3D GPR surveying composed of closely spaced parallel profiles deployed on the cliff face with 100 MHz antennas. The major discontinuity exhibited an extent of 350 m² (With kind permission of Springer Science and Business Media).

FIG. 5. – Carte de l’amplitude de la réflectivité de signaux GPR en fonction de la profondeur représentée avec le relief de la face de la falaise [Roch *et al.*, 2006]. Cette carte a été obtenue à partir d’une investigation 3D par des antennes GPR à 100 MHz, constituée de profils parallèles peu espacés déployés le long de la face de la falaise. La discontinuité majeure a une extension de 350 m² (Avec l’autorisation de Springer Science and Business Media).

frequencies 50 MHz antennas, which allowed identifying seven radar facies until 25 m depth and a possible slip surface. Barnhardt and Kayen [2000] used GPR to investigate the internal structure of two large seismically-induced landslides in Anchorage (Alaska). Their surveys accurately reproduced the subsurface geometry of horst and graben structures down to a depth of 10 m and imaged finer scale features such as cracks. At greater depth, the presence of electrically conductive clay deposits made impossible the imaging of the failure surface. Applications of heavy field GPR investigations for rock fall stability assessment have recently emerged, favoured by the high resolution properties and penetration depth in resistive formation. Recently, Jeannin *et al.* [2006] performed GPR measurements with different configurations (reflection, CMP, tomography) on a limestone cliff, to evaluate their imaging potential of discontinuities inside the rock mass. GPR reflection profiles were carried out on the vertical cliff face and reached a maximum penetration of 20 m with 100 MHz antenna which gave a satisfactory resolution (approximately 25 cm) and detection power (approximately 1.5 cm). They showed that location and orientation of several reflectors coincide with the fractures observed at the surface. Roch *et al.* [2006] explored the potential of GPR to monitor rock walls. They acquired 3D GPR and photogrammetric data, which allowed 3D interpretation of discontinuities. Figure 5 shows the amplitude reflectivity as a function of depth with the relief of the rock fall surface. The survey pointed out a major discontinuity presenting an extent of 350 m², which poses a problem in term of slope stability. On the contrary, the monitoring experiment did not detect any changes but yielded reproducible results under such complex conditions. All the data acquired during these two studies [Jeannin *et al.*, 2006; Roch *et al.*, 2006] exhibited reflectivity variations both with distance along the same fracture and with frequency, which suggest that GPR measurements are sensitive to fracture properties (filling, aperture).

Gravimetric studies

The light instrumentation and high sensitivity to density contrasts should be an advantage of gravimetric surveys for landslide investigations, compared to other classical geophysical methods. Indeed, they allow a dense coverage and are able to detect gravimetric anomalies generated by sufficient density contrast (at least a few tenths of a g.cm⁻³). This condition is fulfilled when the surface failure coincides with the bedrock top or when the landslide develops generates loss of coherence and compactness in the moving mass. Del Gaudio *et al.* [2000] underlined that together with the support of limited other subsurface data (mechanical, geophysical, DTM), gravimetric surveys are able to provide useful information for slope stability analysis: 1) estimation of landslide body thickness and density contrasts between the moving and stable mass and, 2) location and geometry of heterogeneities within the moving mass. Blaha *et al.* [1998] also claimed that gravimetric surveys provided an effective contribution to the description of the structures (deformation, particular blocks, zones under tensile stress) and their dynamic control over time (by gravimetric monitoring).

However, as noted by del Gaudio *et al.* [2000], the use of gravimetric surveys in slope stability investigations is rather uncommon, mainly due to the long and difficult data

processing and to the strong non-uniqueness of interpretation [Reynolds, 1997]. The major problem is separating anomalies of interest from the overlapping effects of other features. In the example of the "Senerchia" slump-earthflow (southern Apennines), del Gaudio *et al.* [2000] performed two micro-gravimetric surveys in order to evaluate the potential of gravimetry to detect possible spatial-temporal density variations observed at surface. They showed that this method was able to provide information on lithological heterogeneities that may control the dynamic of landslide enlargement, if bore-hole measurements are available. The surveys did not show enough sensitivity to detect any temporal density changes.

DISCUSSION

Landslides are complex structures exhibiting a wide variety of geological, geomorphological and hydrogeological properties. Investigation of such heterogeneous structures is one of the more challenging themes for near surface geophysics. The development of 2D and 3D geophysical techniques has aroused a growing interest for assessing the landslide volume, characterising the physical properties of the landslide material and locating the groundwater flows within and around the slide. The design of a geophysical survey for landslide recognition is still a much debated question and no unique strategy came out from this review. In such heterogeneous structures, the combination of different geophysical techniques however appeared as a necessary condition for obtaining reliable results. The choice of the techniques is clearly guided by the expected contrasts in physical parameters. Other parameters, like the required penetration depth, as well as the volume and the morphology of the landslide, may also have a significant effect on the survey strategy, including for economical reasons. This review has tentatively pointed out the potentials and the limitations of geophysical methods for landslide investigation. Among these latter ones, the major difficulty of applying geophysical techniques to landslides is probably the complex relationship between the measured geophysical parameters and the desired geotechnical and hydrogeological properties, which prevents from giving a straightforward interpretation in terms of engineering properties. Outside the landslide areas, several attempts were made in engineering geology to derive soil or rock properties from geophysical measurements, using experimental relationships. In soils, correlations were developed between the small-strain shear wave velocity (V_s) and penetration resistance from the CPT test [Hegazy and Mayne, 1995; Mayne and Rix, 1995; Andrus and Stokoe, 2000], mainly in geotechnical earthquake engineering. Recently, Ghose [2004] proposed a model-based integration of seismic and CPT data to derive soil parameters for sandy material. In rocks, most of the geophysical studies were aimed at characterizing the rock quality or fracturing. The application of GPR techniques for determining the fracture geometry is detailed in this paper. Apart from radar imaging, seismic methods play a more and more important role in characterizing rock sites for geotechnical purpose. As an example, a relationship between shear wave velocity and the Rock Mass Rating, which is a geotechnical factor used for tunnel design, was recently proposed by Cha *et al.* [2006]. In landslide investigation, similar relationships, linking for instance geophysical parameters to the displacement rate [Méric *et al.*, 2005] should be studied

more deeply. About assessing hydrogeological properties from geophysical data, outstanding results have been obtained in recent years in a new interdisciplinary field (hydrogeophysics), combining the integration of multiple sources of data and the development of comprehensive petrophysical models. The application of these methods allows hydrogeological parameters of the subsurface, like the porosity, the water content, the hydraulic conductivity to be estimated from high-resolution fluid-sensitive geophysical data (seismic, electrical, electromagnetic) : a recent state-of-the-art can be found in Rubin and Hubbard [2005]. After this review, our feeling is that both experimental relationships and quantitative approaches should be developed in the future for landslide investigations, incorporating under-used techniques, such as spontaneous potential and induced polarization [Kemna *et al.*, 2004] and including numerical modelling, data inversion and fusion.

CONCLUSIONS

Areas affected by landslides usually exhibit spatial and temporal variations of lithological and hydrogeological conditions. This review of the geophysical techniques applied to landslide reconnaissance has pointed out the large number of available methods, some of them having recently emerged. The development of 2D, and very recently 3D, geophysical imaging techniques has been a first major advance forward for investigating the complex structure of landslide areas. A second one will be the installation of permanent arrays of geophysical sensors as a part of the monitoring system of landslides. Such geophysical time-lapse surveys have recently been initiated on some landslides [Supper and Romer, 2003; Lebourg *et al.*, 2005], mainly with multi-

electrode electrical arrays. Coupled with high resolution remote-sensing techniques [Van Westen, 2004] and self-potential monitoring systems for hydrological purposes [Méric *et al.*, 2006], these permanent geophysical imaging systems give a new insight into the 4D mechanisms of landslides. However, geophysical techniques may suffer severe drawbacks, which are listed in the introduction of this paper, and they need to be combined and calibrated against geological and geotechnical data to give reliable information. Also, the complexity of landslides requires using a combination of different geophysical techniques. After this review on the application of geophysics to landslide investigation, we have the feeling that geophysicists have to make an effort in the presentation of their results. Resolution and penetration are not systematically discussed in an understandable way and the geological interpretation of the geophysical data should be more clearly and critically explained. This attitude probably partly explains the reluctance of the engineering community to use geophysical techniques, in addition to the reasons already mentioned in the introduction. It is now a challenge in the following years for geophysicists to convince geologists and engineers that the 3D and 4D geophysical imaging techniques can be valuable tools for investigating and monitoring landslides. Finally, efforts should also be done towards quantitative information from geophysics in term of geotechnical parameters and hydrological properties.

Acknowledgements. – Support of this work was partially provided by the French National Institute of Universe (INSU) in the framework of the 'ACI – Prévention des Catastrophes Naturelles' Program (Project SAMOA). The authors are grateful to two anonymous reviewers for their improvements of the manuscript.

References

- AGNESI V., CAMARDAB M., CONOSCIENTIA C., DI MAGGIO A., DILIBERTO I., MADONIA P. & ROTIGLIANO E. (2005). – A multidisciplinary approach to the evaluation of the mechanism that triggered the Cerda landslide (Sicily, Italy). – *Geomorphology*, **65**, 101-116.
- ANDRUS R.D. & STOKOE K.H. (2000). – Liquefaction resistance of soils from shear-wave velocity. – *J. Geotech. Geoenv. Eng.*, ASCE, **126**, 1015-1025.
- BARD P.-Y. (1999). – Microtremor measurements : a tool for site effect estimation? In: *Proc. 2nd Int. Symp. on the Effects of Surface Geology on Seismic Motion*, Yokohama, Japan. – Balkema, Rotterdam, vol. 3, 1251-1279.
- BARNHARDT W. A. & KAYEN R. E. (2000) – Radar structure of earthquake-induced coastal landslides in Anchorage, Alaska. – *Environ. Geosciences*, **7**, 38-45.
- BATAYNEH A.T. & AL-DIABAT A.A. (2002) – Application of a two-dimensional electrical tomography technique for investigating landslides along the Amman-Dead Sera Highway, Jordan. – *Env. Geol.*, **42**, 399-403.
- BICHLER A., BOBROWSKY P., BEST M., DOUMA M., HUNTER J., CALVERT T. & BURNS R. (2004). – Three-dimensional mapping of a landslide using a multi-geophysical approach : the Quesnel Forks landslide. – *Landslides*, **1** (1), 29-40.
- BLÁHA P., MRLINA J. & NEŠVARA J. (1998). – Gravimetric investigation of slope deformations. – *Expl. Geophys. Remote-Sens. and Env. J.*, **1**, 21-24.
- BOGOSLOVSKY V.A. & OGILVY A.A. (1977). – Geophysical methods for the investigation of landslides. – *Geophysics*, **42**, 562-571.
- BONNEFOY-CLAUDET S. (2004). – Nature du bruit de fond sismique : implications pour les études des effets de site. – Thèse de Doctorat, Univ. J. Fourier, Grenoble, France, 241 p.
- BRUNO F. & MARILLIER F. (2000). – Test of high-resolution seismic reflection and other geophysical techniques on the Boup landslide in the Swiss Alps. – *Surv. Geophys.*, **21**, 333-348.
- CARIS J.P.T. & VAN ASCH TH.W.J. (1991). – Geophysical, geotechnical and hydrological investigations of a small landslide in the French Alps. – *Eng. Geol.*, **31**, 249-276.
- CHA Y., KANG J. & JO C.H. (2006). – Application of linear-array microtremor surveys for rock mass classification in urban tunnel design. – *Expl. Geophys.*, **37**, 108-113.
- CRUDEN D.M. & VARNES D.J. (1996). – Landslide types and processes. In: *Landslides investigation and mitigation*, Transportation Research Board, Special Report **247**. – National Academy of Sciences, Washington DC., USA, 36-75.
- DEL GAUDIO V., WASOWSKI J., PIERRI P., MASCIA U. & CALCAGNILE G. (2000). – Gravimetric study of a retrogressive landslide in southern Italy. – *Surv. Geophys.*, **21**, 391-399.
- DEMOULIN A., PISSART A. & SCHROEDER C. (2003). – On the origin of late Quaternary palaeolandslides in the Liège (E Belgium) area. – *Int. J. Earth Sci. (Geol Rundsch)*, **92**, 795-805.

- DIKAU R., BRUNDSSEN D., SCHROTT L. & IBSEN M.-L. (1996). – Landslide recognition: identification, movement and causes. – Wiley, Chichester, UK, 274 p.
- FELL R., HUNGR O., LEROUÉIL S. & RIEMER W. (2000). – Keynote paper – Geotechnical engineering of the stability of natural slopes and cuts and fills in soil. *In: Proc. GeoEng2000, Int. Conf. on Geotechnical and Geol. Eng.*, Melbourne, Australia. – Technomic Publishing, Lancaster Vol 1, 21-120.
- FERRUCCI F., AMELIO M., SORRISO-VALVO M. & TANSI C. (2000). – Seismic prospecting of a slope affected by deep-seated gravitational slope deformation : the Lago Sackung, Calabria, Italy. – *Eng. Geol.*, **57**, 53-64.
- GALLIPOLI M., LAPENNA V., LORENZO P., MUCCIARELLI M., PERRONE A., PISCITELLI S. & SDAO F. (2000). – Comparison of geological and geophysical prospecting techniques in the study of a landslide in southern Italy. – *Eur. J. Env. Eng. Geophys.*, **4**, 117-128.
- GIBERT D. & PESSEL M. (2001). – Identification of sources of potential fields with the continuous wavelet transform: Application to self-potential profiles. – *Geophys. Res. Lett.*, **28**, 1863-1866.
- GHOSE R. (2004). – Model-based integration of seismic and CPT data to derive soil parameters. *In: (Ed.) Proc. 10th European Meeting of Environmental and Engineering Geophysics*, Utrecht, The Netherlands. – EAGE Publications, Houten, Paper B019, 4 p.
- GLADE T., STARK P. & DIKAU R. (2005). – Determination of potential landslide shear plane depth using seismic refraction. A case study in rheinessen, Germany. – *Bull. Eng. Geol. Environ.*, **64**, 151-158.
- GUEGUEN P., GARAMBOIS S., CRAVOISIER S. & JONGMANS D. (2004). – Geotechnical, geophysical and seismological methods for surface sedimentary layers analysis. – *Proc. 13th World Conf. Earth. Eng.* Vancouver, Canada. – IAEE., Tokyo, Paper 1777, 6 p.
- HACK R. (2000). – Geophysics for slope stability. – *Surv. Geophys.*, **21**, 423-448.
- HAVENITH H.B., JONGMANS D., ABDRAKMATOV K., TREFOIS P., DELVAUX D. & TORGUEV A. (2000). – Geophysical investigations on seismically induced surface effects, case study of a landslide in the Suusamyr valley, Kyrgyzstan. – *Surv. Geophys.*, **21**, 349-369.
- HEGAZY Y.A. & MAYNE P.W. (1995). – Statistical correlations between Vs and CPT data for different soil types. *In: Proc. Cone Penetration Testing (CPT'95)*, Linköping, Sweden. – Swedish Geotechnical Society, Göteborg, Vol. **2**, 173-178.
- JEANNIN M., GARAMBOIS S., GREGOIRE S. & JONGMANS D. (2006). – Multi-configuration GPR measurements for geometrical fracture characterization in limestone cliffs (Alps). – *Geophysics*, **71**, 885-892.
- JONGMANS D., HEMROULLE P., DEMANET D., RENARDY F. & VANBRABANT Y. (2000). – Application of 2D electrical and seismic tomography techniques for investigating landslides. – *European J. Env. Eng. Geophys.*, **5**, 75-89.
- KEAREY P., BROOKS M. & HILL I. (2002). – An introduction to geophysical exploration, 3rd Edition. – Blackwell, Oxford, 262 p.
- KEMNA A., BINLEY A. & SLATER L. (2004). – Cross-borehole IP imaging for engineering and environmental applications. – *Geophysics*, **69**, 97-105.
- LAPENNA V., LORENZO P., PERRONE A., PISCITELLI S., RIZZO E. & SDAO F. (2003). – High-resolution geoelectrical tomographies in the study of the Giarossa landslide (Potenza, Basilicata). – *Bull. Eng. Geol. Env.*, **62**, 259-68.
- LAPENNA V., LORENZO P., PERRONE A., PISCITELLI S., RIZZO E. & SDAO F. (2005). – 2D electrical resistivity imaging of some complex landslides in Lucanian Apennine chain, southern Italy. – *Geophysics*, **70**, B11-B18.
- LEBOURG T., BINET S., TRIC E., JOMARD H. & EL BEDOUI S. (2005). – Geophysical survey to estimate the 3D sliding surface and the 4D evolution of the water pressure on part of a deep-seated landslide. – *Terra Nova*, **17**, 399-406.
- MAURITSCH H.J., SEIBERL W., ARNDT R., ROMER A., SCHNEIDERBAUER K. & SENDLHOFER G.P. (2000). – Geophysical investigations of large landslides in the Carnic region of southern Austria. – *Eng. Geol.*, **56**, 373-388.
- MAYNE P.W. & RIX G.J. (1995). – Correlations between shear wave velocity and cone tip resistance in clays. – *Soils and Found.*, **35**, 107-110.
- Mc CANN D.M. & FORSTER A. (1990). – Reconnaissance geophysical methods in landslide investigations. – *Eng. Geol.*, **29**, 59-78.
- MERIC O., GARAMBOIS S., JONGMANS D., WATHELET M., CHATELAIN J.-L. & VENGEON J.-M. (2005). – Application of geophysical methods for the investigation of the large gravitational mass movement of Séchilienne, France. – *Can. Geotech. J.*, **42**, 1105-1115.
- MÉRIC O., GARAMBOIS S. & ORENGO Y. (2006). – Large gravitational movement monitoring using a spontaneous potential network. *In: Proc. 19th Annual meeting of SAGEEP*, Seattle, USA. – EEGS, Denver, USA, 6 p.
- MÉRIC O., GARAMBOIS S., MALET J.-P., CADET H., GUÉGUEN P. & JONGMANS D. (2007). – Seismic noise-based methods for soft-rock landslide characterization. – *Bull. Soc. géol. Fr.*, **178**, 2, 137-148.
- NAKAMURA Y. (1989). – A method for dynamic characteristics estimation of subsurface using microtremor on ground surface. – *Quar. Report. Railway. Tech. Res. Institute*, **30**, 25-33.
- NGUYEN F., GARAMBOIS S., JONGMANS D., PIRARD E. & LOCKE M. (2005). – Image processing of 2D resistivity data to locate precisely faults. – *J. App. Geophys.*, **57**, 260-277.
- PATELLA D. (1997). – Introduction to ground surface self-potential tomography. – *Geophys. Prospect.*, **45**, 653-681.
- PETTINELLI E., BEAUBIEN S. & TOMMASI P. (1996). – GPR investigations to evaluate the geometry of rock slides and bulking in a limestone formation in northern Italy. – *European J. Env. Eng. Geophys.*, **1**, 271-286.
- REVLIL A., PEZARD P. & GLOVER E.W.J. (1999). – Streaming potential in porous media. 1, Theory of the zeta potential. – *J. Geophys. Res.*, **104**, 20,021-20,031.
- REYNOLDS J.M. (1997). – An introduction to applied and environmental geophysics. – Wiley & Sons, Chichester, 806 p.
- ROCH K.H., SCHWATAL, B. & BRUCKL E. (2006). – Potentials of monitoring rock fall hazards by GPR: considering as example the results of Salzburg. – *Landslides*, **3**, 87-94.
- RUBIN Y. & HUBBARD S. (Eds) (2005). – Hydrogeophysics. – Springer, Heidelberg, 530 p.
- SAILHAC P. & MARQUIS G. (2001). – Analytic potentials for the forward and inverse modeling of SP anomalies caused by subsurface fluid flow. – *Geophys. Res. Lett.*, **28**, 1851-1854.
- SCHMUTZ M., ALBOUY Y., GUÉRIN R., MAQUAIRE O., VASSAL J., SCHOTT J.-J. & DESCLÔTRES M. (2000). – Joint electrical and time domain electromagnetism (TDEM) data inversion applied to the Super Sauze earthflow (France). – *Surveys in Geophys.*, **21**, 371-390.
- SHARMA P.V. (1997). – Environmental and engineering geophysics. – Cambridge Univ. Press, New York, 475 p.
- SOCCO V. & JONGMANS D. (2004). – Special issue on seismic surface waves. – *Near Surf. Geophys.*, **2**, 163-258.
- SUPPER R. & RÖMER A. (2003). – New achievements in developing a high-speed geoelectrical monitoring system for landslide monitoring. *In: Proc. 9th Meeting Env. Eng. Geophys.*, Prague, Czech Republic. – EAGE Publications, EEGS, Houten, Paper O-004, 6 p.
- TELFORD W.M., GELDART L.P., SHERIF R.E. & KEYS D.A. (1990). – Applied geophysics. – Cambridge Univ. Press, Cambridge, 770 p.
- VAN WESTEN C.J. (2004). – Geo-Information tools for landslide risk assessment: an overview of recent developments. – *In: Proc. 9th Int. Symp. Landslides*, Rio de Janeiro, Brazil, Balkema, Rotterdam, 39-56.
- WATHELET M., JONGMANS D. & OHRNBERGER M. (2004). – Surface wave inversion using a direct search algorithm and its application to ambient vibration measurements. – *Near Surf. Geophys.*, **2**, 221-231.
- WILLENBERG H., EVANS K.F., EBERHARDT E., LOEW S., SPILLMANN T. & MAURER H.R. (2004). – Geological, geophysical and geotechnical investigations into the internal structure and kinematics of an unstable, complex sliding mass in crystalline rock. *In: Proc. 9th Int. Symp. Landslides*, Rio de Janeiro, Brazil. – Balkema, Rotterdam, 489-494.
- WISEN R., CHRISTIANSEN A.V., AUKEN E. & DAHLIN T. (2003). – Application of 2D laterally constrained inversion and 2D smooth inversion of CVES resistivity data in a slope stability investigation. *In: Proc. 9th Meeting Env. Eng. Geophys.*, Prague, Czech Republic. – EAGE Publications, EEGS, Houten, Paper O-002, 6 p.
- WISEN R., AUKEN E. & DAHLIN T. (2005). – Combination of 1D laterally constrained inversion and 2D smooth inversion of resistivity data with a priori data from boreholes. – *Near Surf. Geophys.*, **3**, 71-79
- ZHDANOV M.S. (2002). – Geophysical inverse theory and regularization problems. – Elsevier, Amsterdam, 628 p.

3.2.2. Applications de différentes méthodes géophysiques pour l'investigation du mouvement rocheux de terrain de Séchilienne

Introduction: le mouvement de terrain de Séchilienne

Ce mouvement gravitaire affecte la rive droite de la Romanche constitué de micaschistes avec un escarpement sommital (Mont-Sec) surmontant la vallée de plus de 800 m (Figure 3.2).

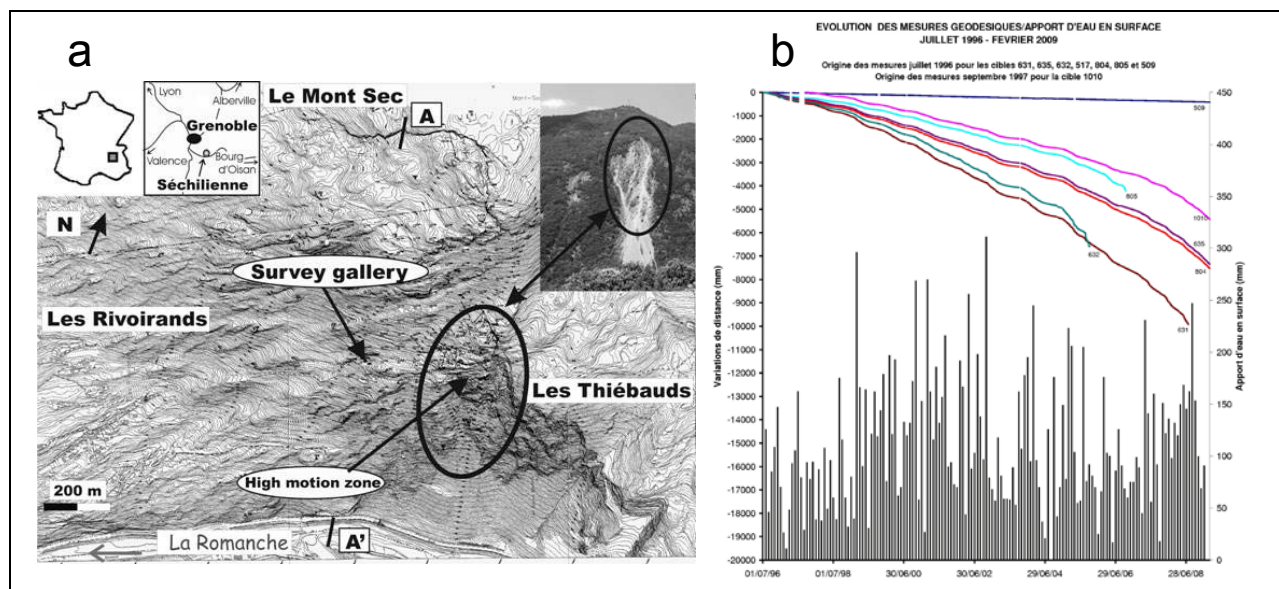


Figure 3.2. Localisation du Mouvement de Séchilienne et de la zone active (a). Variations de distance entre la station de contrôle et des points cibles au cours du temps, ainsi que de la pluviométrie (b).

Depuis la fin des années 80, le site a fait l'objet de nombreuses reconnaissances géologiques, géodésiques, géotechniques, géophysiques et hydrogéologiques (Vengeon, 1998; Guglielmi et al., 2002; Durville et al. 2004; Meric et al., 2005; Kasperski, 2008; Leroux et al., 2009). Un système de surveillance a progressivement été mis en place (Evrard et al. 1990; Duranthon et al. 2003). Les roches composant le site instable appartiennent à la « Série Satinée », une ancienne formation faite de lits de pélites et de grès métamorphisés dans le faciès schistes verts, affectée par les orogénèses calédoniennes à alpines et parcourues par plusieurs familles de fractures délimitant les blocs en mouvement (Pothérat and Alfonsi, 2001).

La déformation gravitaire observée est complexe et implique l'ensemble du versant, de 600 m d'altitude au niveau du couloir des « Ruines », jusqu'à l'escarpement sommital du Mont Sec (1100 m). Différentes études ont permis de mettre en évidence une zone particulièrement active d'un volume de $3 \cdot 10^6 \text{ m}^3$ (zone frontale, Fig. 3.3), caractérisée par une vitesse de déplacement comprise entre 0.15 m/an et 1 m/an (Fig. 3.2). La déformation du versant de Séchilienne n'est pas un phénomène de glissement au sens propre du terme mais implique une déformation située à grande profondeur. Elle peut être décrite comme le basculement de lits verticaux recoupés par des discontinuités héritées de l'histoire structurale du site. Le secteur le plus actif est affecté par des fractures qui s'ouvrent graduellement et provoquent des chutes de blocs ou de petits éboulements tandis que des entonnoirs d'effondrement apparaissent dans la zone de subsidence du Mont Sec. Des datations récentes (le Roux et al., 2009) ont montré que l'escarpement du

Mont Sec avait été initié il y a environ 6500 ans et qu'il avait régulièrement progressé avec un taux de déplacement de 0.6 cm/an à 1.3 cm/an. La déformation du versant semble avoir accéléré dans le dernier quart du 20^{ème} siècle, sans qu'aucune raison spécifique n'ait été mise en évidence.



Figure 3.3 Vue oblique plongeante vers la vallée de la partie sommitale de la zone très active, prise par hélicoptère (Kasperski, 2008).

La gestion actuelle du risque à Séchilienne est principalement axée sur le système de surveillance géré par le CETE de Lyon pour le compte de la DDE. L'instrumentation comporte une trentaine de mesures extensométriques automatiques de fractures actives et environ 80 mesures de distance par visées d'ondes infrarouges et radar réalisées depuis le versant opposé. Les ingénieurs responsables du site sont automatiquement alertés en cas de dépassement des seuils fixés à l'avance, en accord avec le collège d'experts. Les mesures réalisées (Figure 3.2b) montrent des variations saisonnières partiellement corrélées avec les chutes de pluie et les périodes de fonte de neige. La tendance à long terme est une croissance régulière des taux de déplacement mais le processus de contrôle hydraulique n'est pas encore bien compris.

Les premières mesures de gestion du risque, prises il y a près de 25 ans, ont comporté la construction d'une route sur l'autre rive de la Romanche, la construction d'un merlon de protection dans l'axe de la zone frontale pour arrêter les blocs et la construction d'un chenal de dérivation de la Romanche. En 1997, en application de la loi Barnier, la population résidant sur l'île Falcon (300 personnes) a été déplacée et 90 maisons ont été détruites. Pour garantir la protection de la route RD 1091, deux solutions ont été proposées : la création d'un tunnel de dérivation de la Romanche ou la surélévation de la route à une hauteur la mettant hors de portée d'un éboulement de 3 millions de m³. La première option a été rejetée pour des raisons financières. Pour diminuer le risque hydraulique en cas de barrage de la vallée, la construction de digues et de casiers de rétention d'eau est envisagée sur le site de l'île Falcon pour réduire l'intensité de la vague créée par la rupture potentielle du barrage.

Malgré les reconnaissances réalisées et le système de surveillance mis en place, le mécanisme de déformation du versant de Séchilienne n'est toujours pas bien comprise et les scénarios de risque doivent être régulièrement revus, en fonction des nouvelles données et observations. Plusieurs questions posées par les décideurs restent ouvertes, comme l'évaluation des volumes affectés par la déformation gravitaire et la prédiction de l'évolution du versant, particulièrement à moyen et long termes. La réalisation de 3 forages profonds en 2009, puis leur interprétation en 2010 vont contribuer à une meilleure compréhension du comportement mécanique et hydrogéologique du versant, qui fait en outre l'objet d'un projet de recherche multi-disciplinaire (ANR SLAMS, 2010-2013), que je coordonne.

Application of geophysical methods for the investigation of the large gravitational mass movement of S chilienne, France

O. Meric, S. Garambois, D. Jongmans, M. Wathelet, J.L. Chatelain, and J.M. Vengeon

Abstract: Several geophysical techniques (electromagnetic profiling, electrical tomography, seismic refraction tomography, and spontaneous potential and seismic noise measurement) were applied in the investigation of the large gravitational mass movement of S chilienne, France. The aim of this study was to test the ability of these methods to characterize and delineate the rock mass affected by this complex movement in mica schists, whose lateral and vertical limits are still uncertain. A major observation of this study is that all the zones strongly deformed (previously and at present) by the movement are characterized by high electrical resistivity values ($>3 \text{ k}\Omega\text{-m}$), in contrast to the undisturbed mass, which exhibits resistivity values between a few hundred and $1 \text{ k}\Omega\text{-m}$. As shown by the surface observations and the seismic results, this resistivity increase is due to a high degree of fracturing associated with the creation of air-filled voids inside the mass. Other geophysical techniques were tested along a horizontal transect through the movement, and an outstanding coherency appeared between the geophysical anomalies and the displacement rate curve. These preliminary results illustrate the benefits of combined geophysical techniques for characterizing the rock mass involved in the movement. Results also suggest that monitoring the evolution of the rock mass movement with time-lapse geophysical surveys could be beneficial.

Key words: gravitational movement, geophysical methods, S chilienne.

R sum : Plusieurs techniques géophysiques (profil électromagnétique, tomographie électrique, tomographie sismique et potentiel spontané et bruit de fond sismique) ont été appliquées pour la reconnaissance du grand mouvement de terrain de S chilienne (France) situés dans des micaschistes. L'objectif de cette étude était de tester ces méthodes géophysiques afin de caractériser et de délimiter la masse de roche affectée par ce mouvement complexe dont la limite latérale reste incertaine. L'étude a montré que toutes les zones transformées (encore actuellement et dans le passé) par le mouvement sont caractérisées par de fortes valeurs de résistivité électrique (supérieure à $3 \text{ k}\Omega\text{-m}$), tandis que dans la zone non perturbée les valeurs de résistivité sont de quelques centaines de $\Omega\text{-m}$ à $1 \text{ k}\Omega\text{-m}$. Comme le montrent les observations de surface et les profils de tomographie sismique, cette augmentation de résistivité est due à une fracturation importante associée à la création de vides remplis d'air au sein du massif. Les techniques électromagnétiques, PS et de mesure de bruit ont été testées le long d'un profil transversal recoupant le mouvement. Une corrélation remarquable est obtenue entre les anomalies géophysiques et le taux de déplacement. Ces résultats préliminaires soulignent l'intérêt de combiner les méthodes géophysiques pour caractériser la masse de roche impliquée dans le mouvement et pour déterminer l'évolution du mouvement par un suivi temporel des paramètres géophysiques.

Mots clés : mouvement gravitaire, méthodes géophysiques, S chilienne.

Introduction

Various types of failure, such as toppling, sagging, and translational or rotational sliding (Hutchinson 1988), may occur during large gravitational movements, which are common in the crystalline formations of mountain ranges. In

some cases, one of these mechanisms can evolve into a catastrophic failure and into a long-runout avalanche, such as the recent rockslides of Valpola, Italy, in 1987 (Azzoni et al. 1992) and Randa, Switzerland, in 1991 (Noverraz and Bonnard 1991) or the prehistoric events of K fels, Austria, and Langtang, Nepal (Erismann and Abele 2001). In con-

Received 30 March 2004. Accepted 1 March 2005. Published on the NRC Research Press Web site at <http://cgj.nrc.ca> on 30 August 2005.

O. Meric¹. Laboratoire interdisciplinaire de recherche impliquant la géologie et la mécanique, B.P. 53-38041 Grenoble CEDEX 9, France; and Societ Alpine de géotechnique Z.I. de Mayencin, B.P. 17-38610 Gi res, France.

S. Garambois, D. Jongmans, M. Wathelet, and J.M. Vengeon. Laboratoire interdisciplinaire de recherche impliquant la géologie et la mécanique, B.P. 53-38041 Grenoble CEDEX 9, France.

J.L. Chatelain. Laboratoire de géophysique interne et tectonophysique; and Institut de recherche et de développement Grenoble, B.P. 53-38041 Grenoble CEDEX 9, France.

¹Corresponding author (e-mail: Ombeline.Meric@ujf-grenoble.fr).

trast, large, slow rockslides with signs of self-stabilizing movement have also been observed; an example is the La Clapi re rockslide in gneiss (Follacci et al. 1988). The different failure processes are mainly governed by the rock properties and the characteristics of the discontinuities (foliation, schistosity, faults, and fractures) affecting the rock mass (Antoine et al. 1994; Glastonbury and Douglas 2000). From the study of two large-scale field examples and numerical modelling, Nichol et al. (2002) recently distinguished two alternative modes of toppling in rock slopes: ductile flexural toppling in weak rocks (schist and phyllite) with a single dominant joint; and brittle block toppling in strong rocks (granite) with well-developed cross-joints. These researchers concluded that the brittle process can lead to rock avalanches, whereas the other one exhibits slow deformations without a catastrophic event. Rockslide failures can, however, be highly complex and involve several deformation mechanisms relating to geological variations, weathering, influence of groundwater conditions, and the presence of faults and several fracture sets.

In the Alps, most of the large gravitational movements were probably initiated or reactivated after the retreat of glaciers (Noverraz 1996) some 10 000 – 15 000 years ago. The movements have evolved at very different rates, depending on the initial geological and topographic characteristics, as well as on the other factors contributing to lower stability (influence of water, toe erosion, earthquake ground motions, and climatic cycles). The instability process progresses through periods of stabilization and reactivation and leads to slope failure after decades or centuries.

Forecasting the failure characteristics of a rockslide remains a difficult problem, mainly because of the difficulty of obtaining reliable and representative information on the geometry, rheology, and kinematics of the unstable slope (Crosta and Agliardi 2003; Moser 2002; Noverraz 1996). This lack of information can only be mitigated by the observation, investigation, and monitoring of numerous sites over long periods. In the last 10 years, innovative techniques have emerged in geodesy for measuring ground displacements on the surface (global positioning systems; synthetic aperture radar interferometry) and in applied geophysics for imaging the subsurface. In parallel, 2D and 3D numerical modelling methods have been developed that can better simulate the complexity of the mechanisms. However, because of the large uncertainties in input parameters, the use of numerical modelling is mainly limited to back analysis and to the understanding of the significant factors leading to failure. In combination, all these investigative techniques and computational methods offer researchers the opportunity to get a better insight into the deformation mechanisms of rock slopes (Br ckl 2001; Havenith et al. 2003).

In this study, we used geophysical prospecting methods to investigate the large gravitational mass movement of S chilienne (the French Alps). In the past, except for some seismic reflection or refraction experiments (e.g., Bogoslovsky and Ogilvy 1977; McCann and Forster 1989), geophysical methods were rarely applied to such slides, particularly in rocky conditions. This is probably partly due to the difficulties of deploying geophysical sensors in rocky ground and taking measurements on steep slopes. Recently, several studies using different geophysical techniques were performed in

mountainous areas on large slides (Bruno and Marillier 2000; Br ckl 2001; Havenith et al. 2002; Supper and R mer 2003; Lapenna et al. 2003). Advantages of geophysical methods are that they are fairly flexible, they give information on the inside of the mass, and they can investigate a large volume of rock. The main drawbacks are the decreasing resolution with depth, the need for calibration, and the indirect information (geophysical parameters) they yield. Some of the measured parameters (seismic velocity, for instance) can, however, be correlated with mechanical properties, such as the degree of fracturing (Sharma 1997). Recent developments in geophysical prospecting make it possible to generate images of the subsurface distribution of geophysical properties by inverting the acquired data (Reynolds 1997). In particular, electrical tomography (ET) and seismic tomography (ST) are now standard methods (Jongmans et al. 2000; Havenith et al. 2002; Lapenna et al. 2003) that can contribute useful information, in addition to high-resolution seismic reflection surveys (Bruno and Marillier 2000). However, Musil et al. (2002) recently showed that in shallow low-velocity and heterogeneous layers (rock glaciers), seismic reflection failed to map the bedrock surface. The main factor contributing to this failure was the unexpected low-frequency signals returned by the subsurface as a result of the anelastic attenuation, scattering, and low-pass filter effect of the heterogeneous shallow layer. In contrast, the *P*-wave refraction tomography technique provided reliable information on the structure of the rock glacier.

The aim of this study was to test the applicability of a variety of geophysical techniques (electromagnetic (EM) profiling, ET, ST, and spontaneous potential (SP) and seismic noise (SN) measurements) in the investigation of a large movement in crystalline formations. The seismic reflection technique was discarded in the first stage, because of the high heterogeneity of the slope and the difficulty of continuously deploying geophones in such an environment.

The S chilienne mass movement

The S chilienne movement, located in the French Alps, near Grenoble, is affecting the right south-facing bank of the Romanche River (Fig. 1). The slope consists mainly of mica schists with interbedded quartz–feldspar-rich layers, whose thickness can reach a few metres. These rocks were affected by the Hercynian and Alpine orogenies, resulting in a near-vertical foliation that is at right angles to the valley, except in the upper part of the slope, where it is folded with an axis inclined 30° northward (see Fig. 3). In the lower part of the hill, at an elevation of 330–950 m above sea level (a.s.l.), the slope is about 40°–50° (Fig. 2), but it decreases to 20° between 950 and 1100 m a.s.l. (Mont Sec area). Near the crest, a scarp that is a >20 m high and several hundred metres long (Fig. 3) reveals an upper subsidence. The nonfreshness of the scarp shows that this movement is old; it was probably initiated or reactivated after the retreat of glaciers. Because of the tectonic history, the mass is cut by several faults (F1–F4, Fig. 3) and three sets of near-vertical fractures (Poth rat and Alfonsi 2001). The main fracture family, running N70°E, delimits vertical slices in the rock mass and is clearly distinguished by depressions, several hundred metres long, in the morphology; these depressions are associated

Fig. 1. Location and topographical map of the S chilienne movement. Ellipse delineates the most active zone. Circle indicates the location of the survey gallery.

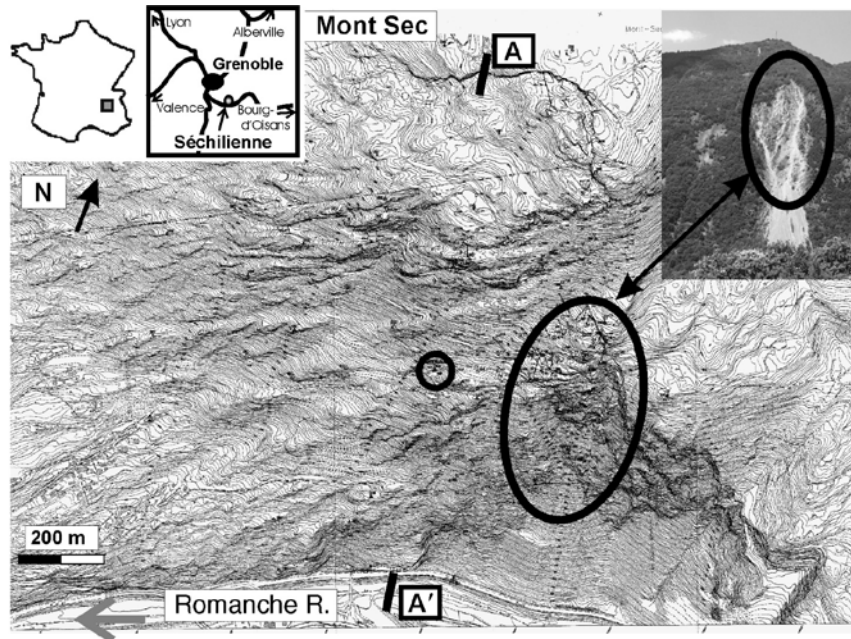
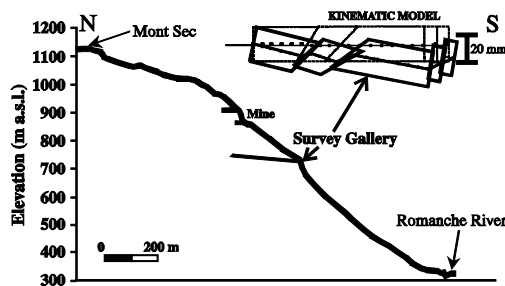


Fig. 2. Cross section (labelled A–A' in Fig. 1) through the S chilienne movement, with the location of the survey gallery and the kinematic model deduced from the displacement measurements within the gallery (after Vengeon 1998).



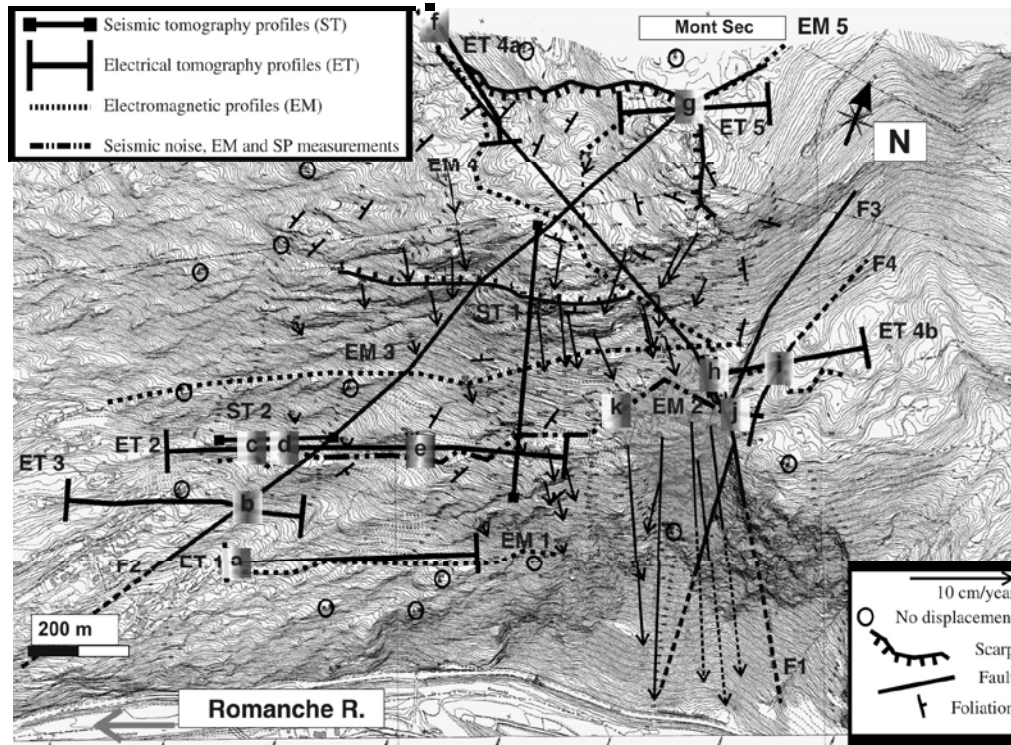
with north-facing scarps several metres high (Figs. 1 and 3) (Vengeon 1998). Some of the depressions are 20 m wide, attesting to the lengthy duration of the gravity-induced processes. At a late tectonic stage, the rock mass was cut by metallic sulphur veins, which were worked at different levels during the 19th and 20th centuries (Durville et al. 2004).

The part of the slope that exhibits more signs of current instability (high-motion zone, Fig. 1) is in the middle of the hill, at an elevation of 600–900 m a.s.l., and involves a rock volume estimated from geometric constraints to be about $3 \times 10^6 \text{ m}^3$ (Giraud et al. 1990). This area has been extensively

instrumented since 1988 (Evrard et al. 1990; Duranthon et al. 2003); the measured displacements are globally oriented in a south-southeast direction (Fig. 3), perpendicular to the strike of the main fractures, and dip downhill between 10° and 20° . The displacement rate in the high-motion zone varies from 15 cm/year to 1 m/year and regularly decreases to the north and to the west. In 1993–1994, a 240 m long gallery was excavated at 710 m in a zone to the west of the high-motion zone and characterized by a displacement rate of about 5 cm/year (see Figs. 1 and 2). Displacement measurements and observations inside the gallery showed a succession of rigid moving blocks delimited by highly fractured zones parallel to the main fracture set. These blocks exhibit differential normal faulting movement, as shown by the kinematic model presented in Fig. 2. Unfortunately, the gallery did not reach the sound rock, and the existence of a sliding surface is still an open question. On the basis of structural data, numerical modelling of the rock mass was performed with the discrete element method (Vengeon 1998; Poth rat and Alfonsi 2001), which modelled the main field observations. These results suggest that the movement at S chilienne is controlled by the principal discontinuities, where the mass breaks into blocks, and includes toppling and local sliding, evolving from progressive damage to a potential large slide of unknown characteristics.

Isotopic and hydrochemical methods were used to investigate groundwater movement inside the S chilienne slope (Vengeon 1998; Guglielmi et al. 2002). This analysis showed the existence of a deep saturated zone, which extends into

Fig. 3. Topographical map with the main geological structures and displacement rate affecting the S chilienne hill. The high-motion zone is shaded in grey. This map also shows the location of the geophysical profiles: electromagnetic (EM), electrical tomography (ET), and seismic tomography (ST). Three geophysical measurement methods, EM, seismic noise (SN), and spontaneous potential (SP), were used along the EM2 profile. Finally, this map outlines the main electrical contrasts found by the survey and their relation to morphological features. Electrical contrasts are represented by boxes, the resistive part of which is darker: points f and g are on the Mont Sec scarp; points h and j are on the eastern limits of the movement; point k marks a limit inside the movement that delineates the most active part; points b and i are located on faults F2 and F4, respectively; and points a, c, d, and e are deduced from geophysical prospecting.



the fractured metamorphic bedrock, with a probable 100 m thick vadose zone above. With intensive rainfall and long-time water recharge, this vadose zone could be saturated for a short time, increasing the displacement rate.

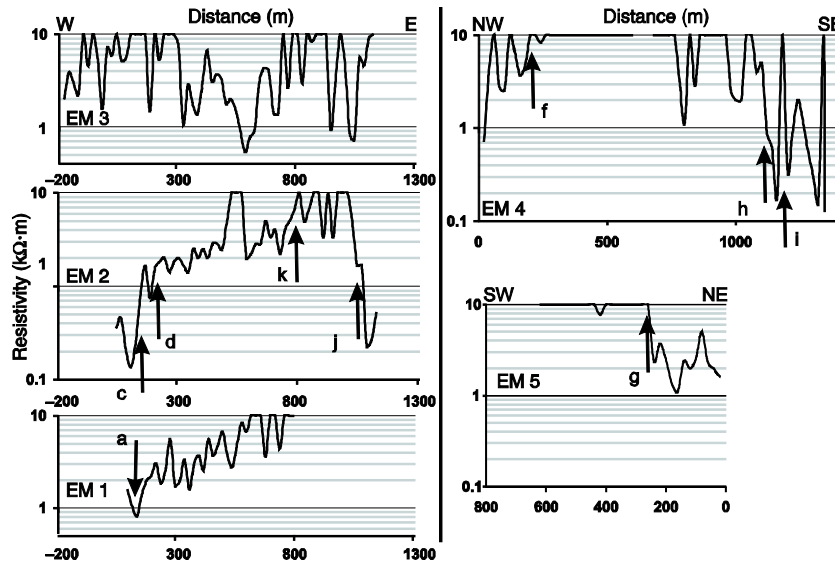
The data available at S chilienne have led some authors to propose that the hill could be affected by a massive movement, delineated to the east by the high-motion zone and to the north by the Mont Sec scarp. No western limit is clearly visible in the topography, and the thickness of this potentially moving mass is unknown. Consequently, the volume estimations for a rock avalanche scenario are highly variable and poorly constrained, ranging from 3×10^6 to 20×10^6 m³ (Giraud et al. 1990; Antoine et al. 1994) inside a total, slowly moving mass of $(50-100) \times 10^6$ m³. It is noticeable that a rockfall of more than 3×10^6 m³ can generate a secondary hazard, flooding, by damming the valley (upstream, during filling of the reservoir created by the dam; downstream, in case of dam failure). Furthermore, the presence of

an active seismic strike-slip fault (Thouvenot et al. 2003) has recently been pointed out in the vicinity of the landslide, indicating the possibility of an earthquake trigger for a rockfall.

Geophysical investigation

Five geophysical methods (EM profiling, ET, ST, and SP and SN measurements) were applied to delineate the mass affected by the movement and to find possible relations between geophysical parameters and zones of rock deformation. The principles of the first four methods can be found in Reynolds (1997). Geophysical tests are being used more often now for engineering site characterization (Foti and Butcher 2004). In a rock mass, geophysical properties (primarily electrical resistivity and seismic velocity in our study) can vary with the nature of the geologic formation and the degree of fracturing and weathering, as well as with the presence of water. For example, an increase in the degree

Fig. 4. Electromagnetic profiles EM1–EM5: points f and g are on the Mont Sec scarp; points h and j are on the eastern limits of the movement; point k marks a limit inside the movement that delineates the most active part; point i is located on fault F4; and points a, c, and d are deduced from geophysical prospecting.



of fracturing leads to a decrease in *P*-wave velocity and variations in electrical resistivity, depending on the water content. In a dry context, increased fracturing will lead to increased electrical resistivity.

Electromagnetic profiling

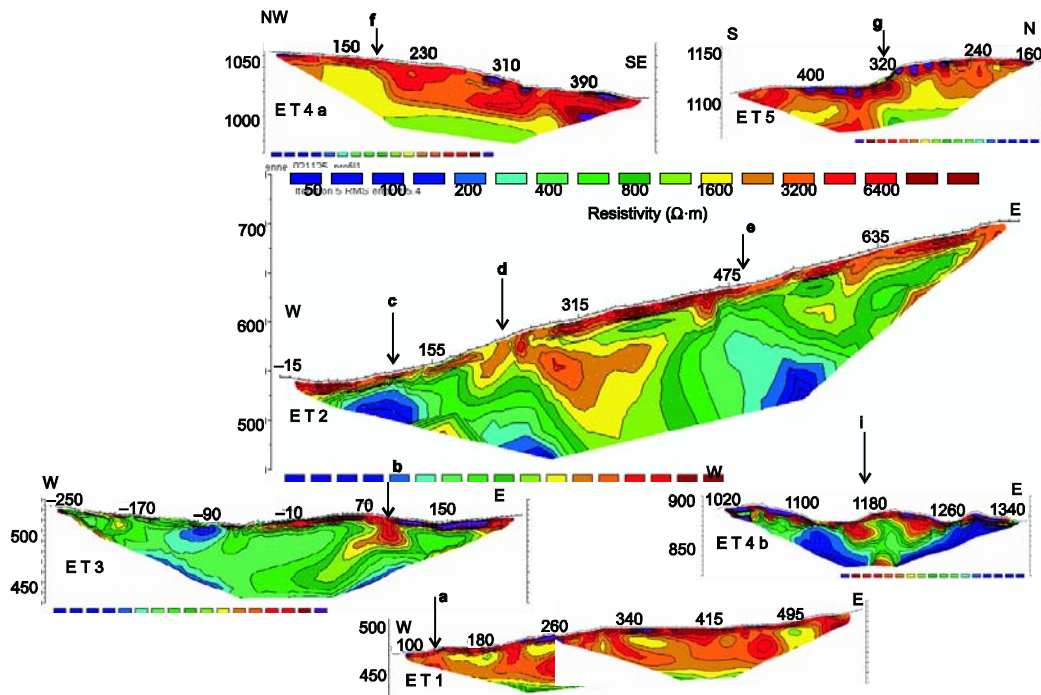
As a first step, EM profiles were recorded with a ground conductivity meter (EM34, Geonics Ltd., Mississauga, Ont.) at different locations on the hill. This method, which yields a single apparent electrical resistivity value at each measurement location, was favoured because it does not require that electrodes be driven into the ground. The EM measurements were performed with horizontal loops, an intercoil separation of 20 m, and a measurement interval of 20 m. Penetration depth ranged from 4 to 30 m with this configuration, with a maximum contribution from approximately 8 m. EM measurements were taken along five transects (labelled EM1–EM5 in Fig. 3) across the movement zone; the resulting curves are displayed in Fig. 4. Vertical dipole measurements show that the apparent resistivity values range from 0.2 to >10 k Ω ·m, which is the limit of the device. Profile EM5 crosses the Mont Sec scarp, the location of which is shown by a resistivity increase from about 2 k Ω ·m to >10 k Ω ·m in the subsiding zone (at point g, Fig. 4). Profile EM4 also starts above the Mont Sec scarp, crosses the area of rock movement, and ends in the undisturbed zone, east of fault F4 (Figs. 3 and 4). Apparent resistivity values, which are between 0.5 k Ω ·m and a few k Ω ·m at both ends of the profile, dramatically increase (>10 k Ω ·m) in the deformed zone defined between the Mont Sec scarp and fault F1 (at points f and h, Fig. 4). A local resistivity increase (at point i, Fig. 4) was also observed where fault F4 crosses the profile.

The three other profiles, EM1, EM2, and EM3, orientated approximately west-southwest–east-northeast (Fig. 3), were recorded at elevations of 460–560, 540–840, and 590–870 m a.s.l., respectively. To the west, the resistivity measured along profile EM2 regularly increases from <1 k Ω ·m (at points c and d, Fig. 4) to >10 k Ω ·m in the high-motion zone, whose limits are at points k and j. At the limit with the undisturbed rock, the resistivity strongly decreases to <1 k Ω ·m (at point j, Fig. 4). Profile EM1, which is shorter, exhibits a similar increase from the west to the western limit of the high-motion zone, which is impossible to cross. In contrast, resistivity values at the western end of profile EM3 do not show a clear decrease. The transect was made along a major depression corresponding to a fracture zone, which probably influences the resistivity values. Resistivity values of <1 k Ω ·m are locally observed in the middle of the profile. The results from the EM transects suggest that the strongly fractured zones are well correlated with high resistivity values and can be distinguished from the undisturbed mass, which is characterized by apparent resistivity values of <1 k Ω ·m close to the surface.

Electrical tomography

We tried to understand the observed variations in apparent resistivity more quantitatively and at greater depths by recording six ET profiles along specific lines, whose length varied from 320 to 750 m. The electrical data were processed with the algorithm developed by Loke and Barker (1996). Unlike EM profiling, ET involve inversion of direct-current resistivity field data to produce models of the distribution of the ground's electrical resistivity directly under the survey line. Resulting images show real electrical resistivity

Fig. 5. Electrical images ET1–ET5. Vertical arrows and labels are the same as in Fig. 4. The RMS values after inversion are 5% for ET1, 5% for ET2, 7.5% for ET3, 3% for ET4a, 5% for ET4b, and 2% (ET5).

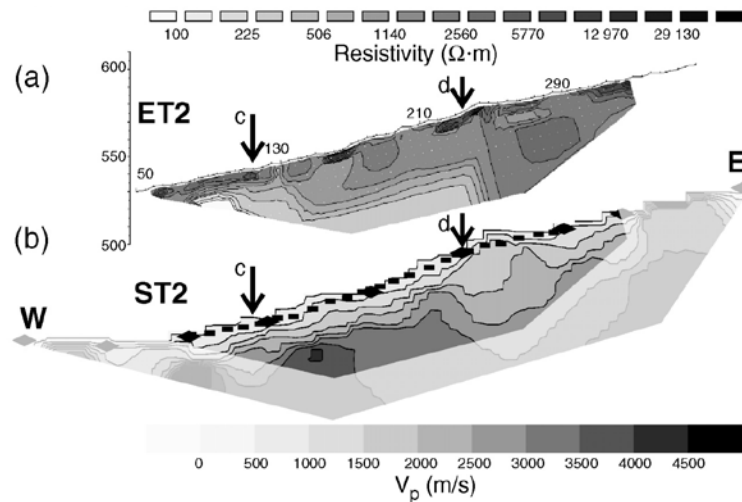


values, and the vertical axis represents the true depth under the profile line. The derived models are smoothed, owing to the methodology, and the final deduced solution must not be considered as unique, because of the sparsity of field data. Nevertheless, the inversion reliably provides estimates of the broader scale variations within the ground. Figure 5 presents six ET sections (ET1–ET4a, ET4b, and ET5; see Fig. 3). Models shown in Fig. 5 were obtained by inversion, which yielded root mean square (RMS) values of 5%, implying that each model was reliably able to reproduce its corresponding dataset. Profile ET4b was recorded in the eastern unaffected zone, where mica schists outcrop. Below a resistive layer of rock debris a few metres thick, the bedrock exhibits a resistivity of 50–800 Ω-m, with a vertical resistive zone (at point i) already shown on EM4 and corresponding to the presence of a fault (F4 in Fig. 3). Profile ET5 was recorded at the top of the movement across the Mont Sec scarp (Fig. 3; point g in Fig. 5), where the transect EM5 was carried out. Below a highly resistive surficial layer of debris and glacial deposits, a few metres thick, the resistivity values are globally higher than in ET4b, with a lateral resistivity increase below the Mont Sec scarp, from about 800 Ω-m to 3 kΩ-m in the settled zone (at point g). This latter zone is also characterized by its thicker surficial resistive layer. These results explain the lateral variation of the EM data across the scarp. Another electrical profile (ET4a) was re-

corded along EM4 at the western end of the Mont Sec scarp. This electrical profile also shows a lateral resistivity contrast (at point f), with increased thickness of the resistive layer to the south. Three other ET profiles (ET1–ET3) were recorded to the west, parallel to profiles EM1 and EM2 (Fig. 3). The first one (ET2), which is 750 m long and reaches a penetration depth of >100 m, exhibits strong lateral resistivity contrasts (at points c, d, and e). The first two of these (points c and d) correspond to an eastward resistivity increase, which is consistent with the results of the EM2 profile. In particular, the first contrast (at point c), from 200 to >1 kΩ-m, fits with the strong resistivity rise noticed along the EM2 profile, whereas the second one corresponds to the trace of fault F2. The third electrical contrast corresponds to the presence of a more conductive zone at depth. Profile ET3 is located farther west than the other profiles. Below a surficial resistive layer, the corresponding image exhibits resistivity values of <750 Ω-m in the western part of the profile, with a lateral resistivity increase (at point b) that is consistent with the location of fault F2.

Finally, the ET1 profile shows relatively high resistivity values (usually >1 kΩ-m in the upper 30 m), with a general increase of the average resistivity of the surficial layers to the east, consistent with the data from EM1. An important feature of this image is the vertical decrease in resistivity with depth below 30 m, where values as low as 800 Ω-m are

Fig. 6. Comparison between the electrical (a) and seismic (b) tomography sections ET2 and ST2: points c and d are at the limits deduced from geophysical prospecting. The RMS values after inversion are 5% for ET2 and 2% for ST2.



reached. This result, which suggests the presence of sound bedrock at that depth, was checked by using another inversion technique, DCIP2D (UBC-GIF 2001), which is based on subspace methods (Oldenburg et al. 1993). The obtained image (not shown here) also exhibits a low-resistivity zone (about $800 \Omega \cdot m$) below 35 m depth. When the technique proposed by Oldenburg and Li (1999) was applied, the depth of investigation was estimated to be about 45 m, supporting the presence of sound bedrock below 30 or 35 m.

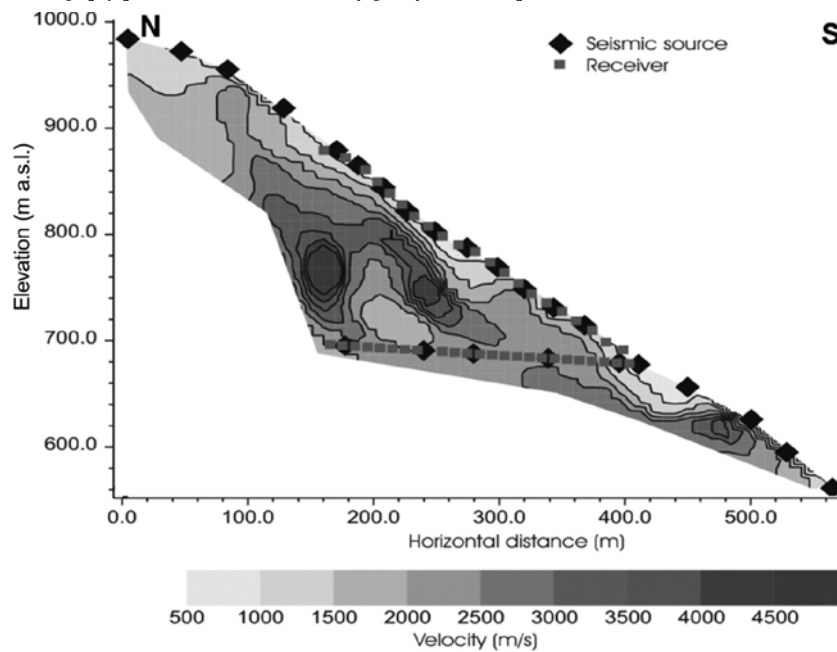
The EM and electrical profiles show a significant increase in electrical resistivity values when entering the zone affected by the gravitational movement, both at the two limits of the high-motion zone (at points k and j, Fig. 5) and across the Mont Sec scarp. This global electrical resistivity rise probably results from the presence of air-filled voids induced by the deformation. Some local lateral resistivity variations have, however, been observed within the movement area, which probably result from differences in the fracturing degree and (or) in the rock types. Also, the measurements in the supposedly undisturbed zone show a large resistivity range, from $100 \Omega \cdot m$ to the east of the movement to $>1 \text{ k}\Omega \cdot m$ in the Mont Sec area, which might, however, be affected by fracturing above the upper main scarp. Finally, the vertical resistivity variations seem to indicate the presence of undisturbed bedrock approximately 30 m below ET1 and $>100 \text{ m}$ below the central part of ET2.

Seismic tomography

The ST technique, which consists of inverting first-arrival times to get an image of P-wave velocity distribution in the ground, is applied, in engineering geology, between boreholes and at the surface (e.g., Lanz et al. 1998; Jongmans et al. 2000). For this study two long seismic profiles (300 and 650 m) were recorded, and the first-arrival times were inverted by the simultaneous iterative reconstruction technique

(Dines and Lytle 1979). The strong eastward resistivity increase (at points c and d, Fig. 5), observed on both the EM2 and the ET2 profiles, was investigated with a 300 m long seismic refraction profile. Ten shots were recorded by 24 geophones 10 m apart, and the P-wave first-arrival times were inverted. The resulting seismic image is compared with the electrical one in Fig. 6. The measured seismic velocities, V_p , range from 500 m/s at the surface (weathered layer, rock debris) to 4000 m/s (sound bedrock) at depth. The seismic image also shows lateral variations, and the previously described eastward resistivity increase, from $200 \Omega \cdot m$ to $1 \text{ k}\Omega \cdot m$, is clearly correlated with a seismic velocity decrease, from 3500 m/s to about 2000 m/s (at point d). These results provide strong evidence that the resistivity decrease is caused by a higher degree of fracturing, which also lowered the seismic velocity values. For the 650 m long seismic profile, we made use of the 240 m long survey gallery to perform ST between the slope surface and the gallery. Forty-eight geophones, 10–15 m apart, recorded the signals generated by 24 explosions (see Figs. 4 and 8). The seismic image obtained after inversion of the travel-time values (with RMS error of 1%) is presented in Fig. 7. The robustness of the image was tested with different initial models. As in the 300 m profile, the major features are the large range of P-wave seismic velocities, whose values range between 500 and 5000 m/s, and the presence of strong lateral velocity gradients. Considering that the volume investigated is fairly homogeneous rock (mica schists), these two features highlight the strong fracturing and weathering, whose intensity not only is depth dependent but also varies laterally. No systematic surficially damaged zone overlying the sound bedrock has been detected, at least not down to 100 m depth. These results, showing the juxtaposition of near-vertical highly fractured zones and little deformed blocks, are consistent with geological field observations and motion measurements

Fig. 7. Seismic tomography profile ST1 between the survey gallery and the slope. RMS = 1%.



at the surface and in the gallery, as well as with the geological model used for discrete numerical simulations (Vengeon 1998; Poth rat and Alfonsi 2001). This seismic image suggests that the survey gallery was driven into a lower velocity zone that is too wide to have resulted from the decompression around the gallery. This survey, which involved measurements between the surface and the underground gallery, used an unusual configuration that provided high-quality, continuous information on the rock mass inside the moving massif.

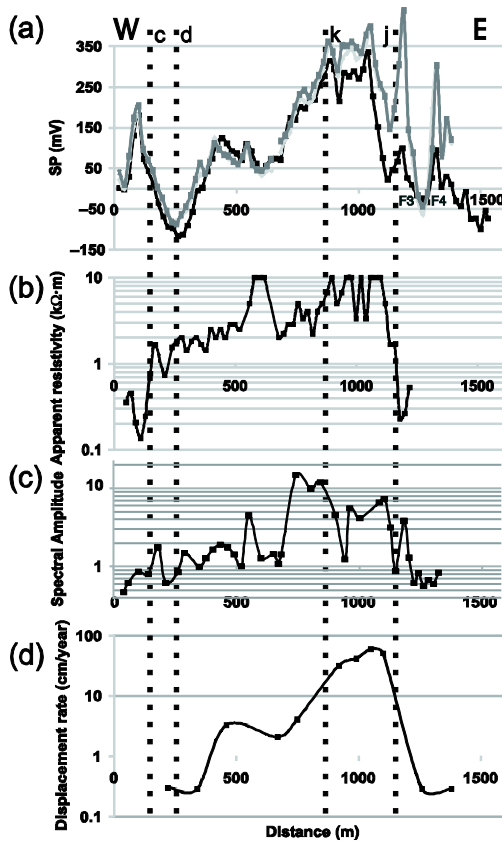
Spontaneous potential and seismic noise measurements

Finally, two other techniques, SP and SN measurements, were tested. The SP method measures differences in natural electrical potentials, which can be produced by electrochemical, mineral, and electrokinetic effects (Reynolds 1997). In recent decades, SP measurements have been regularly used for detecting groundwater flow in landslides (Bogoslovsky and Ogilvy 1977; Giano et al. 2000; Bruno and Marillier 2000). In our study, SP data, as well as SN data, were acquired along the EM2 profile, which crosses the movement zone. In Fig. 8 are plotted the SP values (Fig. 8a), profile EM2 (Fig. 8b), the noise measurements (Fig. 8c), and the mean displacement rate during the last 2 years. The measured SP values (Fig. 8a) range from -100 to 350 mV. The SP anomaly is positive across the movement and becomes negative at both ends. The shapes of the SP and displacement rate curves are similar, showing two maxima at the same location. The stronger SP positive anomaly is observed over the high-motion zone. Similar results were also ob-

tained on the Boup landslide (Bruno and Marillier 2000), where SP data showed a positive anomaly over the landslide body, particularly in the vicinity of the boundary between the landslide and the stable ground. At this stage, it is difficult to determine which SP source produces these large anomalies. Repeated measurements were made along the same profile at three different dates over a period of 7 months. They show very stable behaviour with time across the movement (Fig. 8a). These large, stable positive and negative anomalies could be generated by the geological structure of the movement (fracturing, lead-zinc and quartz veins) and (or) a permanent, deep main water flow nearly parallel to the surface. However, Fig. 8a also displays local SP variations with time, particularly outside the mass movement, where the profile crosses faults F3 at 1220 m a.s.l. and F4 at 1360 m a.s.l. (see Fig. 3). These variations could be electrokinetically generated by fluid flow changes inside these major discontinuities.

SN measurements are used in earthquake engineering for estimating site effects (Bard 1998) or in exploration for mapping soft deposits (e.g., Delgado et al. 2000). In our study, measurements of ambient vibration were made every 50 m along the same profile (EM2) with a 5 s sensor. Figure 8c displays the behaviour of the mean spectral amplitude computed between 0.25 and 35 Hz along this line. As the vibrations were measured at different periods, they were all normalized with a reference station. Dramatic variations (from 1 to 10) of the noise energy were observed. The striking feature is that the spectral amplitude values are higher in the same zone as the SP and apparent resistivity curves, and

Fig. 8. Geophysical anomalies along electromagnetic profile EM2. (a) Spontaneous potential data measured on three dates (black curve, December 2003; light grey curve, March 2004; dark grey curve, June 2004). (b) Electromagnetic profile EM2. (c) Spectral amplitude of the seismic noise computed between 0.5 and 30 Hz. (d) Displacement rate. Points c and d are at the limits deduced from geophysical measurements; points k and j are morphological limits (k marks a limit inside the movement that delineates the most active part; and j is at the eastern limit of the movement).



they significantly decrease at both ends of the profile. A possible explanation for these results is the decrease in *P*-wave and *S*-wave velocities with rock deformation. This phenomenon generates a ground motion amplification effect, whose magnitude increases with the seismic impedance contrast between the deformed zone and the underlying bedrock (Bard and Bouchon 1990).

Discussion and conclusions

Five geophysical techniques (EM profiling, ET, ST, and SP and SN measurements) were applied on the large gravita-

tional movement of S chilienne, with the aim of characterizing and delineating the mass affected by the movement. Because of the difficulty of performing tests on steep slopes, the number of geophysical profiles is limited, and the results presented here allow only preliminary conclusions to be drawn. A major outcome of this study is that all zones exhibiting signs of present-time or previous movements (collapse, toppling, sliding) are characterized by high electrical resistivity values (>3 kΩ·m), compared with the undisturbed zones (between a few hundred and 800 Ω·m). Figure 3 shows the location of the main electrical contrasts pointed out by the survey. This relation between electrical resistivity and gravitational deformation was particularly well demonstrated in the Mont Sec subsiding area (at points f and g, Fig. 3) and at the two limits of the present-time high-motion zone (at points k and j). The consistency between the geophysical parameters and the displacement rates was also shown along east-west-oriented profile EM2. It is reasonable to assume that the present relative rates of movement at S chilienne reflect the total relative movement that has occurred since movement began along this profile. The very good agreement between the two curves (Figs. 8c and 8b) and the inverse relation between electrical resistivity and *P*-wave velocity (Fig. 6) support the interpretation that resistivity variations along the profile are mainly related to the degree of fracturing. The resistivity increase corresponds to a *P*-wave velocity decrease, both of which can result from fracturing and the creation of voids that are not filled with water over a depth of a several tens of metres. Most remarkable is the similarity in the overall shape of the four curves of Fig. 8: all exhibit an asymmetric bell shape with a maximum across the high-motion zone. Our interpretation is that this area, which now experiences the highest displacement rates, exhibits the highest resistivity values because of the presence of voids, is probably the place of deep preferential groundwater flow (SP data), and has the lowest *V_s* and *V_p* values (highest noise spectral amplitudes). The eastern limit of the movement is clearly indicated by a sharp geophysical contrast (at points h and j, Fig. 3), as all the curves show a regular decrease to the west. However, the negative-positive SP anomaly, the local resistivity and seismic gradients, and to a lesser extent, the noise amplitude all suggest that the western limit of the zone affected by the movement could be between points c and d along ET2 and around point a along ET1 (Figs. 3 and 8). At these sites all the measured geophysical data have approximately the same values as those from the eastern unaffected zone. As observed on the curves of Fig. 8 and in other data presented above, strong lateral variations are present along the geophysical profiles. These variations in geophysical parameters probably result from the numerous fractures and faults of tectonic origin that affected the massif before the movement. However, these low-strength discontinuities have without doubt controlled the action of the forces of gravity, resulting in a heterogeneous deformation pattern juxtaposing near-vertical, highly fractured zones and little deformed blocks, as observed in the gallery and as shown by the seismic and electrical images.

The limit of the movement at depth was a major focus of this study. Although most of the geophysical images show prominent horizontal variations, which probably mask the vertical ones, some indications of characteristics at depth

were given. At its western limit, electrical image ET2 (Fig. 5) nicely shows the deepening of the sound bedrock top, which is located at a minimum of 40 m depth across point d, if we consider the 800 Ω -m isoline as this boundary. Similarly, the depth to bedrock can be estimated as being at about 30 m below ET1, which is the only electrical image showing a clear resistivity decrease with depth. Below the Mont Sec scarp, section ET5 gives a depth of >40 m for the sound bedrock. Finally, image ST1 and profile ET2 apparently did not detect the sound bedrock within 100 m. All these results indicate that the S chilienne movement is deep seated, with heterogeneous deformation, as locally shown by the investigation gallery.

The geophysical campaign on the S chilienne movement tested different techniques and has brought new information on the characteristics of the deformed zone. In future, the first objective will be to delineate the zone affected by the movement to the northwest, where the boundary is quite uncertain. An effort will also be made to more quantitatively interpret the results of SP and SN measurements. Other fast and innovative techniques, such as the transient electromagnetic method (Reynolds 1997) and noise array measurements (Wathelet et al. 2004), will also be tested in an effort to detect the undisturbed bedrock top. Finally, the outstanding coherence between geophysical anomalies and displacement rate data highlights the potential for using time-lapse geophysical techniques as a component of a monitoring system; this has been initiated on other movements (Supper and R mer 2003).

Acknowledgements

This work was partially supported by the P le grenoblois des risques naturels through funding from the General Council of Is re (France). We thank all the numerous and enthusiastic participants in the field campaigns, the Centre d' tudes techniques de l' quipement de Lyon for providing the displacement measurements, and P. Desvarreux (SAGE Co.) for fruitful discussions. Our special thanks go to Frederic Nguyen for his help with estimating the depth of investigation along ET profiles. The Laboratoire interdisciplinaire de recherche impliquant la g ologie et la m canique is part of the French Risques naturels et vuln rabilit des ouvrages network.

References

- Antoine, P., Giraud, A., Evrard, H., and Rochet, L. 1994. A huge slope movement at S chilienne, Is re, France. *Landslide News*, 8: 15–18.
- Azzoni, A., Chiesa, S., Frassoni, A., and Govi, M. 1992. The Valpola landslide. *Engineering Geology*, 33: 59–70.
- Bard, P.-Y. 1998. Microtremor measurements: a tool for site effect estimation? *In Proceedings of the 2nd International Symposium on the Effects of Surface Geology on Seismic Motion*, Yokohama, Japan, 1–3 December 1998. *Edited by* K. Iribura, K. Kudo, H. Okada, and T. Sasatani. A.A. Balkema, Rotterdam, The Netherlands, pp. 1251–1279.
- Bard, P.-Y., and Bouchon, M. 1980. The seismic response of sediment-filled valleys. Part 1. The case of incident SH waves. *Bulletin of the Seismological Society of America*, 70: 1263–1286.
- Bogoslovsky, V.A., and Ogilvy, A.A. 1977. Geophysical methods for the investigation of landslides. *Geophysics*, 42: 562–571.
- Br ckl, E.P. 2001. Cause-effect models of large landslides. *Natural Hazards*, 23: 291–314.
- Bruno, F., and Marillier, F. 2000. Test of high-resolution seismic reflection and other geophysical techniques on the Boup landslide in the Swiss Alps. *Surveys in Geophysics*, 21: 333–348.
- Crosta, G.B., and Agliardi, F. 2003. Failure forecast for large rock slides by surface displacement measurements. *Canadian Geotechnical Journal*, 40: 176–191.
- Delgado, J., Lopez Casado, C., Estevez, A., Giner, J., Cuenca, A., and Molina, S. 2000. Mapping soft soils in the Segura River valley (SE Spain): a case of study of microtremors as an exploration tool. *Journal of Applied Geophysics*, 45: 19–32.
- Dines, K., and Lyttle, J. 1979. Computerized geophysical tomography. *Proceedings of the Institute of Electrical and Electronics Engineers*, 67: 1065–1073.
- Duranthon, J.-P., Effendiantz, L., M mier, M., and Pr vitali, I. 2003. Apport des m thodes topographiques et topom triques au suivi du versant rocheux instable des ruines de S chilienne. *XYZ revue de l'AFT*, 94: 31–38.
- Durville, J.L., Effendiantz, L., and Potherat, P. 2004. The S chilienne landslide. *In Identification and mitigation of large landslide risks in Europe*. A.A. Balkema, Rotterdam, The Netherlands. p. 317.
- Erisman, T.H., and Abele, G. 2001. *Dynamics of rockslides and rockfalls*, Springer-Verlag, New York.
- Evrard, H., Gouin, T., Benoit, A., and Duranthon, J.-P. 1990. Risques majeurs d' boulements en masse : point de surveillance du site. *Bulletin de liaison des laboratoires des ponts et chauss es*, 165: 7–16.
- Follacci, J.-P., Guardia, P., and Ivaldi, J.-P. 1988. Le glissement de La Clapi re dans son cadre g odyamique. *In Proceedings of the 5th International Symposium on Landslides*, Lausanne, Switzerland. pp. 1323–1327.
- Foti, S., and Butcher, A.P. 2004. General report: geophysical methods applied to geotechnical engineering. *In Geotechnical and Geophysical Site Characterization: Proceedings of the 2nd International Conference on Site Characterization, ISC-2*, Porto, Portugal, 19–22 September 2004. *Edited by* A. Viana da Fonseca and P.W. Mayne. Millpress Science Publishers. Vol. 1, pp. 409–418.
- Giano, S.I., Lapenna, V., Piscitelli, S., and Schiatarella, M. 2000. Electrical imaging and self-potential surveys to study the geological setting of the Quaternary slope deposits in the Agri high valley (southern Italy). *Annali di Geofisica*, 43: 409–419.
- Giraud, A., Rochet, L., and Antoine, P. 1990. Processes of slope failure in crystallophyllian formations. *Engineering Geology*, 29: 241–253.
- Glastonbury, J., and Douglas, K. 2000. Catastrophic rock slope failures: observed characteristics and behaviour. *In GeoEng2000: An International Conference on Geotechnical and Geological Engineering*, Melbourne, Australia, 19–24 November 2000. Technomic Publishing, Lancaster, Pa. Vol. 2.
- Guglielmi, Y., Vengeon, J.M., Bertrand, C., Mudry, J., Follacci, J.-P., and Giraud, A. 2002. Hydrogeochemistry: an investigation tool to evaluate infiltration into large moving rock masses (case study of La Clapi re and S chilienne alpine landslides). *Bulletin of Engineering Geology and the Environment*, 61: 311–324.
- Havenith, H.B., Jongmans, D., Faccioli, E., Abdrakhmatov, K., and Bard, P.-Y. 2002. Site effects analysis around the seismically induced Ananevo rockslide, Kyrgyzstan. *Bulletin of the Seismological Society of America*, 92: 3190–3209.

- Havenith, H.B., Strom, A., Calvetti, F., and Jongmans, D. 2003. Seismic triggering of landslides. Part B: Simulation of dynamic failure processes. *Natural Hazards and Earth System Sciences*, **3**: 663–682.
- Hutchinson, J.N. 1988. General report: morphological and geotechnical parameters of landslides in relation to geology and hydrogeology. *In Proceedings of the 5th International Symposium on Landslides, Lausanne, Switzerland. Edited by C. Bonnard. A.A. Balkema, Rotterdam, The Netherlands, Vol. 1, pp. 3–35.*
- Jongmans, D., Hemroulle, P., Demanet, D., Renardy, F., and Vanbrabant, Y. 2000. Application of 2D electrical and seismic tomography techniques for investigating landslides. *European Journal of Environmental and Engineering Geophysics*, **5**: 75–89.
- Lanz, E., Maurer, H., and Green, A.G. 1998. Refraction tomography over a buried waste disposal site. *Geophysics*, **63**: 1414–1433.
- Lapenna, V., Lorenzo, P., Perrone, A., Piscitelli, S., Sdao, F., and Rizzo, E. 2003. High-resolution geoelectrical tomographies in the study of Giarossa landslide (southern Italy). *Bulletin of Engineering Geology and the Environment*, **62**: 259–268.
- Loke, M.H., and Barker, R.D. 1996. Rapid least-squares inversion of apparent resistivity pseudosections by a quasi-Newton method. *Geophysical Prospecting*, **44**: 131–152.
- McCann, D.M., and Forster, A. 1989. Reconnaissance geophysical methods in landslide investigations. *Engineering Geology*, **29**: 59–78.
- Moser, M. 2002. Geotechnical aspects of landslides in the Alps. *In Proceedings of the 1st European Conference on Landslides, Prague, Czech Republic, 25–28 November 2002. Edited by J. Rybar, J. Stemberk, and P. Wagner. A.A. Balkema, Lisse, The Netherlands, pp. 355–361.*
- Musil, M., Maurer, H., Green, A.G., Horstmeyer, H., Nitsche, F.O., Vonder Muhl, D., and Springman, S. 2002. Shallow seismic surveying of an alpine rock glacier. *Geophysics*, **67**: 1701–1710.
- Nichol, S.L., Hung, O., and Evans, S.G. 2002. Large-scale brittle and ductile toppling of rock slopes. *Canadian Geotechnical Journal*, **39**: 773–788.
- Noverraz, F. 1996. Sagging or deep-seated creep: fiction or reality? *In Proceedings of the 7th Symposium on Landslides, Trondheim, Norway, 17–21 June 1996. Edited by K. Senneset. A.A. Balkema, Rotterdam, The Netherlands, pp. 821–828.*
- Noverraz, F., and Bonnard, C. 1991. L'écroulement rocheux de Randa, près de Zermatt. *In Landslides: Proceedings of the 6th International Symposium on Landslides, Christchurch, N.Z.. Ashgate, pp.165–170.*
- Oldenburg, D.W., and Li, Y. 1999. Estimating depth of investigation in DC resistivity and IP surveys. *Geophysics*, **64**: 403–416.
- Oldenburg, D.W., McGillivray, P.R., and Ellis, R.G. 1993. Generalized subspace methods for large-scale inverse problems. *Geophysical Journal International*, **114**: 12–20.
- Pothrat, P., and Alfonsi, P. 2001. Les mouvements de versant de S chilienne (Is re). *Revue française de géotechnique*, **95–96**: 117–131.
- Reynolds, J.M. 1997. *An introduction to applied and environmental geophysics.* John Wiley & Sons, New York.
- Sharma, P.V. 1997. *Environmental and engineering geophysics.* Cambridge University Press, Cambridge, U.K.
- Supper, R., and R mer, A. 2003. New achievements in developing a high speed geoelectrical monitoring system for landslide monitoring. *In Proceedings of the 9th Meeting of Environmental and Engineering Geophysics, Prague, Czech Republic. O-004.*
- Thouvenot, F., Fréchet, J., Jenatton, L., and Gamond, J.-F. 2003. The Belledonne border fault: identification of an active seismic strike-slip fault in the western Alps. *Geophysical Journal International*, **155**: 174–192.
- UBC-GIF. 2001. DCIP2D: a program library for forward modeling and inversion of DC resistivity and induced polarization data over 2D structures. Version 3.2. Developed under the consortium research project Joint/Cooperative Inversion of Geophysical and Geological Data, The University of British Columbia's Geophysical Inversion Facility, Department of Earth and Ocean Sciences, Vancouver, B.C.
- Vengeon, J.-M. 1998. D formation et rupture des versants en terrain métamorphique anisotrope : apport de l'étude des ruines de S chilienne. Ph.D. thesis, Université Joseph Fourier, Grenoble.
- Wathelet, M., Jongmans, D., and Ohrnberger, M. 2004. Surface wave inversion using a direct search algorithm and its application to ambient vibration measurements. *Near Surface Geophysics*, **2**: 211–221.

3.2.3. Utilisation des méthodes de bruit de fond sismique pour l'auscultation des glissements de terrain de type argileux

Les méthodes de caractérisation de structures géologiques et/ou anthropiques par l'enregistrement du bruit de fond sismique ont été très développées depuis le début des années 1990, notamment depuis que la méthode dite H/V a été diffusée par Nakamura (1989). Celle-ci consiste à calculer le rapport spectral entre composantes horizontales et verticales du bruit sismique, ce qui permet d'accéder à la réponse spectrale d'un site et ceci notamment dans le cas de couches molles surmontant des couches plus rigides (Bard, 1997; Nakamura, 2000). Sa popularité pour les études de zonage sismique, vient du fait qu'elle est rapide et légère, ce qui permet d'envisager des micro-zonages à l'échelle d'une vallée et d'en retrouver sa fréquence fondamentale de résonance et son épaisseur si la vitesse des ondes S est connue. L'efficacité et les limites de cette méthode ont été largement étudiées expérimentalement (Lermo et Chavez-Garcia, 1995; Lebrun et al., 2001) et numériquement (Field et Jacob, 1993; Lachet et Bard, 1994, Cornou et al., 2004 ; Bonnefoy-Claudet, 2004, Gueguen et al., 2007). Les trois hypothèses inhérentes à cette méthode (SESAME, 2004) sont que i) le bruit sismique est majoritairement composé d'ondes de surface, ii) la structure du sous-sol est 1D et iii) le contraste de vitesse de cisaillement est relativement élevé. Des difficultés existent également dans les milieux hétérogènes, dans lesquelles des effets de diffraction et de diffusion des ondes de surface se produisent. C'est sans doute le cas sur Séchilienne (Méric et al., 2005), où aucun pic cohérent n'a pu être mis en évidence, malgré la présence d'une zone fortement remaniée surplombant une zone plus saine. Il faut également noter que la mesure du bruit de fond sismique à l'aide d'un réseau de capteurs sismologiques permet de retrouver la courbe de dispersion des ondes de Rayleigh dans une gamme de fréquences complémentaire de celle déduite d'acquisitions sismiques actives (Tokimatsu, 1997; Satoh *et al.*, 2001; Scherbaum *et al.*, 2003). Celle-ci peut ensuite être inversée pour retrouver la distribution verticale des vitesses d'ondes S.

Dans l'article présenté ci-après, une comparaison entre les méthodes de tomographies électriques et de bruit de fond sismique (H/V et réseau) a été effectuée sur deux glissements présentant des caractéristiques différentes : le glissement-coulée de Super-Sauze (site d'OMIV) caractérise par des variations géométriques 3D brutales et un glissement lent dans les argiles du Trièves (St-Guillaume, Isère) où les variations sont plus lisses. Cette étude montre notamment la nécessité d'acquérir des profils H/V selon des profils, et non pas de façon aléatoire, pour pouvoir suivre la forte variabilité des pics s'amplification. Il montre également que les distributions d'ondes S déduites des enregistrements en réseau sont cohérentes avec les données existantes, mais que sur le site plus 3D, les réseaux de rayon large sont moins efficaces.

Un des problèmes inhérent à ces méthodes réside dans le fait que les milieux sont supposés être 1D. Pour contourner ce problème, les propriétés de propagation des ondes sismiques entre deux points peuvent être retrouvées en utilisant les ondes de coda (diffusion) ou de longs enregistrements de bruit ambiant (Campillo et Paul, 2003 ; Shapiro et Campillo, 2004). Ces techniques d'inter-corrélation des composantes verticales du bruit sismique ont été appliquées avec succès sur le glissement de terrain d'Avignonet (site OMIV) par Renalier et al. (2010). Ceci leur a permis de retrouver les fonctions de Green des ondes de Rayleigh entre 2 capteurs et d'estimer la dispersion de leur vitesse de groupe entre 1.5 et 5 Hz, fréquences difficilement accessibles par des enregistrements actifs. L'ensemble des résultats présenté ci-avant laisse penser que la reconnaissance et le suivi temporel par les méthodes basées sur le bruit sismique vont connaître un fort développement dans les années à venir, et il sera important de mieux comprendre l'ensemble des phénomènes via des simulations numériques (anisotropie, effets 2D-3D).

Seismic noise-based methods for soft-rock landslide characterization

OMBELINE MÉRIC^{1,2}, STÉPHANE GARAMBOIS^{1,4}, JEAN-PHILIPPE MALET³, HÉLOÏSE CADET^{4, 5},
PHILIPPE GUÉGUEN⁴ and DENIS JONGMANS^{1,4}

Key words. – Seismic noise, Soft-rock landslide, *In-situ* characterization, 3D geometry

Abstract. – In order to better understand the mechanics and dynamic of landslides, it is of primary interest to image correctly their internal structure and their slip surface. Several active geophysical methods are able to provide the geometry of a given landslide, but were rarely applied in 3 dimensions in the past. The main disadvantages of methods like seismic reflection and electrical tomography are that there are heavy to set up and/or to process, and they consequently are expensive and time consuming. Moreover, in the particular case of soft-rock landslides, their respective sensitivity and resolution are not always adequate to locate the potential slip surfaces. Passive methods may represent an interesting alternative particularly for landslides difficult to access, as they require lighter instrumentation and easier processing tools. Among them, the seismic noise based methods have shown increasing applications and developments, in particular for seismic hazard mapping in urban environment. In this paper, we present seismic noise investigations carried out on two different sites, the “Super Sauze” mudslide and the “Saint Guillaume” translational clayey landslide (France), where independent measurements (geotechnical and geophysical tests) were performed earlier. Our investigations were composed of electrical tomography profiles, seismic profiles for surface-wave inversions, H/V measurements, which are fast and easy to perform in the field, in order to image shear wave contrasts (slip surfaces), and seismic noise array method, which is heavier to apply and interpret, but provides (S)-waves velocity profile versus depth. For both sites, landslide bodies are characterized by lower S wave velocity ($V_s < 300 \text{ m.s}^{-1}$) and lower resistivity ($\rho < 60 \text{ Ohm.m}$) than in the stable part ($V_s > 550 \text{ m.s}^{-1}$; $\rho > 150 \text{ ohm.m}$). Their thickness vary from a few m to 50 m. Comparison between geophysical investigations and geotechnical data proved the applicability of such passive methods in 3D complex structures, with however some limitations.

Caractérisation de glissements de terrain argileux par des méthodes de bruit de fond sismique

Mots clés. – Bruit de fond sismique, Glissement de terrain argileux, Caractérisation *in-situ*, Géométrie 3D

Résumé. – Afin d’identifier les mécanismes de contrôle et de caractériser la dynamique de glissements de terrain, il est impératif d’imager correctement leur structure interne et leur surface de glissement. Plusieurs méthodes de prospection géophysique de proche surface sont utilisables pour identifier la géométrie d’un glissement de terrain, mais leurs potentialités ont été rarement testées en 3D. Les principaux inconvénients de méthodes géophysiques telles que la sismique réflexion ou la tomographie électrique sont la difficulté de mise en œuvre et/ou la complexité des traitements de données, ce qui les rend chères et consommatrices en temps. De plus, pour le cas particulier de glissements argileux, leur sensibilité et résolution ne sont pas toujours adaptées à la détection des surfaces de glissement. Les méthodes géophysiques passives, qui offrent l’avantage d’une instrumentation légère et d’un traitement des données plus simple, représentent ainsi une alternative intéressante, particulièrement pour les mouvements de terrain difficiles d’accès. Parmi celles-ci, les méthodes de bruit sismique ambiant connaissent depuis quelques années des développements et applications intéressants, notamment pour le zonage de l’aléa sismique en milieu urbain. Nous présentons dans ce papier des investigations par bruit de fond sismique effectuées sur deux sites instables, le glissement-coulée de “Super Sauze” et le glissement translationnel de “Saint Guillaume” (France), où des investigations géotechniques et géophysiques indépendantes étaient disponibles.

Nos investigations se composent (1) de tomographies électriques, de profils sismiques pour l’analyse des ondes de surface et de mesures H/V, simples, légères et rapides à installer sur site, afin de cartographier des contrastes de vitesse d’onde S (surface de glissement) et (2) de mesures de bruit de fond réseau, plus délicates et complexes à déployer sur site et à interpréter, mais qui permettent d’accéder à des profils de vitesses d’ondes S en fonction de la profondeur. Les deux glissements sont caractérisés par de plus faibles vitesses d’onde de cisaillement ($V_s < 300 \text{ m.s}^{-1}$) et de plus faibles résistivités ($\rho < 60 \text{ ohm.m}$) dans le corps du glissement que dans la partie stable ($V_s > 550 \text{ m.s}^{-1}$; $\rho > 150 \text{ ohm.m}$). Leurs épaisseurs varient de quelques mètres à 50 m. Les comparaisons entre nos investigations géophysiques et les sondages géotechniques prouvent l’applicabilité des méthodes géophysiques passives dans des environnements 3D, mais indiquent également certaines limites.

1. ‘Laboratoire Interdisciplinaire de Recherche Impliquant la Géologie et la Mécanique’ (LIRIGM), EA 3111 UJF, Maison des Géosciences, BP 53, F-38041 Grenoble cedex 9, France. Tel. +33 (0)476 828 046 / Fax. +33 (0)476 828 070 / E-mail : ombeline.meric@ujf-grenoble.fr

2. ‘Société Alpine de Géotechnique’ (SAGE), ZI de Mayencin, BP 17, F-38610 Gières, France.

3. ‘Faculty of Geosciences’, UCEL, Utrecht University, Po Box 80.115, NL-3508 TC Utrecht, Netherlands.

4. ‘Laboratoire de Géophysique Interne et Tectonophysique’ (LGIT), UMR 5559 CNRS-UJF-US, Maison des Géosciences, BP 53, F-38041 Grenoble cedex 9, France.

5. ‘Centre d’Etude Technique de l’Équipement’ (CETE), Antenne Méditerranée, Laboratoire Régional de Nice, 56 Boulevard Stalingrad, F-06359 Nice cedex 4, France.

Manuscrit déposé le 27 janvier 2006 ; accepté après révision le 27 juin 2006.

INTRODUCTION: STATE OF THE ART AND SCIENTIFIC ISSUES

Authorities responsible for protecting human lives as well as infrastructures from the threat of landslide hazard are particularly concerned with three critical aspects: (1) the spatial distribution of the processes, (2) the understanding of their mechanisms, (3) their magnitude and temporal frequency. These concerns imply accurately assessing landslide characteristics and evaluating their controlling factors (climate or seismic triggers) in a dynamic dimension. For these reasons, 2D and 3D mathematical models have been developed during the last decade in order to simulate the complexity of landslide mechanisms [Commend *et al.*, 2004; Malet *et al.*, 2005; Tacher *et al.*, 2005]. Presently, one of their main weaknesses lies in the large uncertainty of parameters describing the unstable area. For example, critical information such as the 3D geometry of a landslide, its geo-mechanical and hydrological properties, or its internal discontinuities, as well as the uncertainties associated to these parameters, are rarely available.

Landslides are generally studied using geotechnical investigations (boreholes, penetrometric tests, etc), local instrumentation placed in boreholes (piezometers, inclinometers), as well as detailed geomorphological observations [Giraud *et al.*, 1991; Flageollet *et al.*, 2004]. Even though these studies provide direct information on the landslide material, their cost and limited spatial representativeness hinder their use for 3D studies. In particular, except by multiplying the number of tests, these methods are not able to image the lateral variability of landslide characteristics. To address this problem, a large selection of geophysical methods is available on a broad spatial scale. An increasing trend to apply geophysical studies for landslide characterization has been recently observed, mainly thanks to the improvement of data-acquisition systems and of data-inversion softwares. A critical review of these methods is discussed by Jongmans and Garambois [2007], who point out the need of combining geophysical methods [Israil and Pachauri, 2003] and of validating geophysical data with geotechnical information [Maquaire *et al.*, 2001; Flageollet *et al.*, 2004]. In practice, 3D geophysical investigations of large active landslides can be time consuming and expensive. Consequently, fast and low costs methods, with instruments easy to deploy have to be developed in the future, at least to locate the slip surfaces and to characterize bedrock geometries in 3D. Methods based on seismic noise measurements, which were extensively applied for seismic hazard mapping in the recent years [Asten, 2004], fill part of those criteria.

In this paper, we present two examples of seismic noise investigations carried out on two soft-rock landslides of the South French Alps (fig. 1), *e.g.* the “Super-Sauze” mudslide in the black marls of the Ubaye valley and the “Saint-Guillaume” translational landslide in the varved clays of the Trièves Plateau. At both sites, the slip surfaces are located within a homogeneous clay formation. The purposes of our studies are to evaluate the potential of seismic noise data, first to detect the slip surfaces using the H/V spectral ratio and second, to derive (S)-wave velocity profiles using networks. Very few seismic noise investigations were performed on landslides so far. Gallipoli *et al.* [2000] briefly mentioned the use of H/V methods on the large “Giarossa” landslide (southern Italy), which helped to interpret electrical tomography images.

Recently, Méric *et al.* [2005] failed to identify the slip surface of the “Séchilienne” large rocky landslide using H/V measurements. They however noted a clear correlation between amplitude of the seismic noise and the landslide displacement rate explained by fracture density. As both “Super-Sauze” and “Saint-Guillaume” landslides were characterized and monitored using geotechnical and geophysical measurements, a critical discussion of the results provided by seismic noise methods is possible.

SEISMIC NOISE THEORY

The H/V method involves computing the spectral ratio between the horizontal and vertical components of the seismic noise recorded simultaneously at a given location with a 3D seismometer placed at the ground surface. Nogoshi and Igarashi [1971] first proposed the use of the H/V method as a tool for the estimate of the seismic response of the surface layers. This method has since been widely diffused around the world by Nakamura [1989]. Since 1989, because of its low-cost and its fast deployment, H/V method has become widespread used, mainly with the objective of detecting the sedimentary zones that could amplify seismic ground

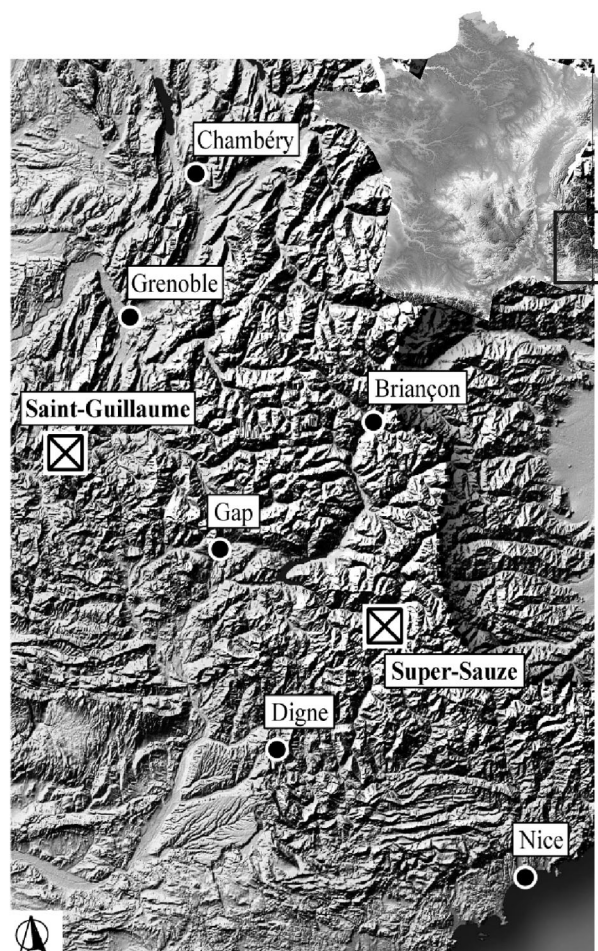


FIG. 1. – Location of the two test sites in the South French Alps: mudslide of “Super-Sauze” and translational landslide of “Saint-Guillaume”.
 FIG. 1. – Localisation des deux sites tests dans les Alpes du Sud de la France : glissement-coulée de “Super-Sauze” et glissement translational de “Saint-Guillaume”.

motion. The validation of the H/V method has been since confirmed both experimentally [Lermo and Chávez-García, 1993; Field and Jacob, 1995; Guéguen *et al.*, 2000; Lebrun *et al.*, 2001] and from theoretical and numerical studies [Field and Jacob, 1993; Lachet and Bard, 1994; Cornou *et al.*, 2004; Bonnefoy-Claudet, 2004]. In the case of a stratified soil profile composed of a soft layer on top of a stiffer bedrock, the amplified frequency f_0 may be estimated using the equation $f_0 = V_s / 4H_s$ [Haskell, 1960], where H_s is the thickness and V_s the shear wave velocity of the topmost layer, respectively, provided that the (S)-wave contrast is sufficiently large [Bonnefoy-Claudet, 2004]. As outlined by the equation linking f_0 to H_s , knowing the shear wave velocity V_s of the upper layer is fundamental to deduce the thickness of this layer. This information can be derived from (S)-wave refraction or surface wave analyses. Nevertheless, the simple relation linking fundamental frequency, shear wave velocity and depth is valid for a 1D model, which is not the geometry of most valleys. For instance, Steimen *et al.* [2003] and Roten *et al.* [2004] recently showed experimentally the strong 2D effect of valley shape on the resonance frequency deduced from ambient seismic noise. However, according to the concept of critical shape ratio proposed by Bard and Bouchon [1985], who numerically studied the dynamic response of various 2D structures shapes, the seismic behaviour of both landslides should be mainly characterized by one-dimensional resonance and surface wave propagation. A shear-wave velocity depth-profile can also be obtained from seismic noise measurements recorded by an array of seismometers, which allow the dispersion curve of Rayleigh-wave phase velocity to be computed [Tokimatsu, 1997; Satoh *et al.*, 2001; Scherbaum *et al.*, 2003].

In the following, all dispersion curves deduced from active surface-wave (e.g. surface waves recorded during seismic refraction acquisitions) or from seismic noise network analyses, were computed using the conventional semblance-based frequency-wavenumber method [Lacoss *et al.*, 1969; Kvaerna and Ringdahl, 1986; Ohrnberger, 2001], which provides a semblance map of the velocity (or slowness) and frequency of the waves travelling with the highest energy. The obtained dispersion curves have been inverted to obtain a (S)-wave vertical velocity depth-profile. We used a neighbourhood algorithm inversion method for which computation time was optimized [Wathelet *et al.*, 2004]. This method is a stochastic direct search method for finding models of acceptable data fit within a multidimensional parameter space [Sambridge, 1999a; 1999b]. Four parameters were investigated, *i.e.* thickness, density, (P)-wave velocities and (above all) (S)-wave velocities of each layer. Thousands of direct models were tested and only those exhibiting lower RMS errors were kept. To reduce the number of good fitting models, the H/V resonance frequency of the central station was added as an additional constraint during the inversion process.

INVESTIGATION OF THE “SUPER-SAUZE” MUDSLIDE

Geological, geomorphological and geotechnical setting of the mudslide

The “Super-Sauze” mudslide (Ubaye valley) is one of the persistently active slides (since the 1970’s) occurring in

black marls [Malet and Maquaire, 2003]. Its geological environment is very complex and is the consequence of the geological history of this alpine zone characterized by an overthrust of allochthonous sandstone and limestone formations over the autochthonous black marl bedrock. From the highest to the lowest elevations, geology consists of: (1) the calcareous Klippe of Lan which overhangs the mudslide, (2) a moraine deposited by the Ubaye glacier during the Quaternary, (3) a bedrock consisting of Callovo-Oxfordian black marls with a grey clayey schist facies, very finely laminated and highly tectonized.

The “Super-Sauze” mudslide is a clayey flow-like landslide characterized by a complex vertical structure associating a slip surface and a viscoplastic plug. Multidisciplinary observations (geology, geomorphology, geotechnics, hydrology) carried out since 1991 [Weber and Hermann, 2000; Flageollet *et al.*, 2004] provide substantial information about its geology and geometry. The mudslide material consists of a silty-sand matrix mixed with moraine debris. It extends over a horizontal distance of 850 m and occurs between an elevation of 2105 m at the crown and 1740 m at the toe with an average 25° slope. Its total volume is estimated at 750,000 m³ and creeping velocities range from 0.01 to 0.4 m.day⁻¹ [Malet and Maquaire, 2003]. A detailed morphological description of the mudslide since its genesis can be found in Weber and Herrmann [2000]. The bedrock topography corresponds in the upper part to a succession of more or less parallel crests and gullies and, in the medium and lower parts, to a narrow and deeply incised channel. Consequently, its thickness is highly variable and varies between 0 and approximately 20 m. This geometrical scheme plays an essential role in the dynamics of the landslide by delimiting preferential water and material pathways and creating sections with differing kinematical, mechanical and hydrological characteristics. Its geotechnical structure consists in two superimposed units [Flageollet *et al.*, 2004; Malet and Maquaire, 2003]. The topmost unit, 5 to 9 m thick, is a very wet muddy formation, whereas the lowermost unit, with a maximum thickness of 10 m, is a stiff compact, relatively impervious and apparently stable formation. The hillslopes delimitating the lateral extension of the mudslide are characterized by moraine deposits, 3 to 15 m thick, especially on the eastern flank.

Electrical tomography

Six electrical tomography profiles were carried out on the mudslide allowing a pseudo-3D view of its internal structure (fig. 2, white lines). The tomography profiles were acquired using a Wenner configuration selected for its high signal to noise ratio property and its sensitivity to horizontal contrasts. This configuration is less adapted to accurately image lateral contrasts [Dahlin and Zhou, 2004]. Three transverse profiles A1, A2 and A3 were acquired using 64 electrodes spaced at 4 m in the upper part of the mudslide. Two transverse profiles C1 (80 electrodes, 4 m spacing) and C2 (48 electrodes, 5 m spacing) were acquired in the middle part of the mudslide. Finally, longitudinal profile CA (64 electrodes, 5 m spacing) was performed between transects C1 and A1. The raw data were inverted independently in 2D using the RES2DINV inversion software [Loke and Barker, 1996], considering a L2-norm for optimisation. The

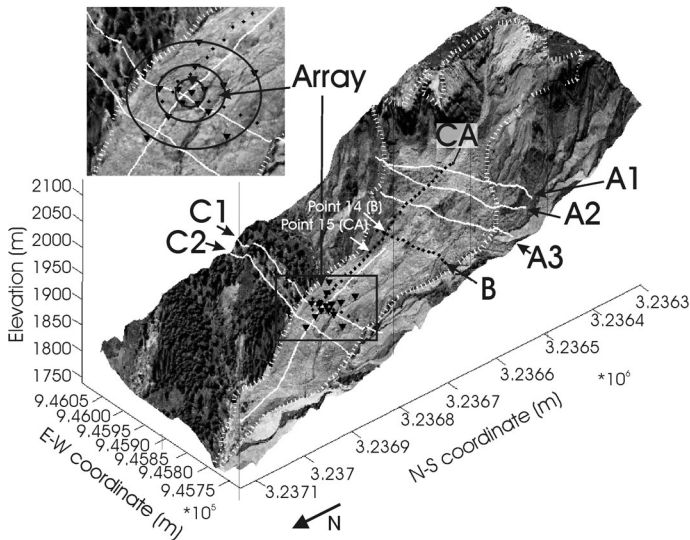


FIG. 2. – 3D topography image of the “Super-Sauze” mudslide and locations of the geophysical measurements. White lines: electrical tomography profiles; black dots: seismic noise measurements (H/V); black triangles: seismic noise network.

FIG. 2. – Image 3D de la topographie du glissement-coulée de “Super-Sauze” et positionnement des mesures géophysiques et de bruit de fond sismique. Lignes blanches : tomographies électriques ; points noirs : points de mesures du bruit de fond sismique (H/V) ; triangles noirs : capteurs du bruit de fond réseau.

derived resistivity sections have RMS errors lower than 3% after 5 iterations.

The electrical sections (fig. 3) show a contrast between the mudslide material with low resistivity values (lower than $60 \pm 24 \Omega.m$) and the stable bedrock with higher resistivity values (higher than $150 \pm 60 \Omega.m$). These resistivity values are comparable with those obtained by Schmutz *et al.* [2000] from joint-inversion of VES and TDEM data, who found resistivities ranging from 2 to 50 $\Omega.m$ for the active unit and more than 400 $\Omega.m$ for the bedrock. The increase of resistivity values with depth observed in the mudslide material can be explained by a decrease of the hydraulic conductivity with depth due to both the presence of water-saturated cracks in the topmost layer and compaction of the lowermost layer. On the eastern part of profiles C1 and C2, higher resistivity values (more than 700 $\Omega.m$) are observed; they correspond to stable hillslopes made of moraine deposits. Below the eastern part of the landslide body on profile C1, a high resistivity anomaly is imaged, which probably corresponds to a former coarse landslide mainly composed by moraine deposits. These results agree with geotechnical investigations, which outline the transverse and the longitudinal thickness changes of the mudslide, underlying its complex bedrock topography.

In the middle part of the mudslide, the electrical sections indicate a total thickness ranging from 24 m to less than 5 m along profiles C1 and C2; this geometry is consistent with the depth variations proposed by Malet and Maquaire [2003] for this section on the basis of geotechnical tests. In the upper part of the mudslide, a more or less constant thickness of 18 m is found along profile A1, while profiles A2 and A3 indicate strong lateral changes due to the presence of bedrock crests. These profiles point out a deeper bedrock (more than 30 m) than in the middle part.

Although geotechnical data are more scarce in this part of the mudslide, the resistivity variations agree with the combined geomorphological-geotechnical interpretation suggested by Malet [2003]. The surface formations show larger resistivity values probably due to dryer hydrological conditions in autumn. Finally, the longitudinal electrical image indicates smooth vertical variations of the mudslide thickness, with a maximum value of 18 m at the intersection with profile C1.

These electrical data will be used in zones lacking of geotechnical measurements for interpreting the seismic noise measurements, assuming that the slip surface is localized at the 60-150 ohm.m contrast.

H/V method

Three H/V seismic noise profiles were performed on the mudslide (fig. 2). Two of them (C and B) were carried out in the transverse direction along geotechnical cross-sections, with a seismometer spacing of respectively 15 m and 10 m. A longitudinal profile (CA) was acquired between geotechnical cross-sections A and C with a 10 m spacing. The experimental device included six 3D Lennartz sensors (5 seconds), which have a flat response in the [0.2-50 Hz] frequency range, connected to a CitySharkTM II acquisition system developed for seismic noise measurements [Chatelain *et al.*, 2000]. Ambient vibration data were sampled at 200 Hz and recorded for 30 minutes (fig. 4a). From this dataset, as many as possible short time-windows (about 40 seconds in duration) were selected using an anti-trigger process in order to select signals presenting the most uniform noise ratio, *i.e.* without transient high-frequency waves (grey selections on figure 4a). The procedure to detect transients is based on a comparison between the short term average “STA”, *e.g.*, the average level of signal amplitude over a short period of time (1 s) and the long term average “LTA”, *e.g.*, the average level of signal amplitude over a much longer period of time (30 seconds). For this application the STA/LTA ratio must remain below a small threshold value (typically around 1.5-2) over a sufficient duration. Finally each of the three components time signals were fast Fourier transformed and the spectral ratio was computed for each horizontal component (*e.g.*, H_1/V and H_2/V) as well as for the root mean square of the spectral ratio (H/V). To investigate complex and irregular structures, Uebayashi [2003] suggested orientating one component of the seismometer parallel to the main structure as the frequency peak amplitude is sensitive to the orientation of the horizontal component. Figures 4b and 4c show spectral ratio computed using the E-W component, the N-S component and the H component (square root of E-W and N-S components) for point 15 of profile CA and for point 14 of profile B respectively (fig. 2). Both points are located in the area where 2D effects were detected on the H/V data. Figure 4b shows a similar frequency peak around 11 Hz obtained from both E/V and N/V ratios. However, the amplitude of these peaks range from 1.8 for the N/V ratio to 2.8 for the E/V ratio. On contrary, figure 4c exhibits different frequency peaks (9 Hz on N/V ratio, 11 Hz on E/V ratio) with similar amplitudes. These variations of spectral ratio amplitude (fig. 4b) and of the value of the amplified frequency f_0 are probably caused by 2D or 3D effects. In order to take this effect into account, the spectral ratio was computed using the E-W

component on profiles CA and C, as the most important structure change is expected to occur along the longitudinal axis of the mudslide. On profile B, the spectral ratio was computed using the N-S components because the geotechnical investigations indicate large lateral variations in the bedrock depth.

Figures 5a, 5b and 5c present H/V spectral ratios calculated in the [0.2-20 Hz] frequency range for the profiles B, C1 and CA as a function of frequency and location along each profile. Colours represent the neperian logarithm of the horizontal to vertical spectral ratio. The black dotted points show the picked frequency peaks and the white dot lines locate the intersections with other profiles. Figure 5d maps the spatial variation of the picked frequency (colour scale) including those acquired during the seismic noise network experiment.

On profile CA, a clearly distinguishable dominant frequency can be easily picked on most point measurements; this dominant frequency varies smoothly from 4 to 11 Hz along the profile. For some points, higher frequencies exhibiting stronger H/V amplitudes could have been wrongly picked (eg., like for point 7, with two major frequencies around 10 Hz and 15 Hz) but also lower frequencies at some other points. Even if the landslide structure is 3D, the dominant frequency varies continuously, resulting from the smooth variations of the thickness along the profile and by a well-adapted spatial sampling (10 m). In this case, no 3D effect significantly disturbed data acquisition and data processing, implying that surface wave propagation can be considered as 1D [Bonnefoy-Claudet, 2004]. On profile B several resonance frequencies can be picked at single point measurements, probably generated by interferences from several layers. A blind frequency picking carried out by looking for the maximum of H/V amplitudes resulted in too strong heterogeneities. Consequently, we decided to pick two frequencies at some points, where we propose a non-unique interpretation (fig. 6), considering the presence

of several layers. Because of large lateral thickness variations over short distances, the selected spatial sampling (every 10 m) is probably too large to identify continuous variations of the correct frequency. To overcome this problem, a denser sampling scheme may improve the interpretation. As the low-frequency (2-3 Hz) mainly appears on the flanks of the mudslide, it may be related to a deeper interface linked to the presence of a former coarse mudslide. Other points (11 on profile B, for example) exhibited amplification at low frequencies, probably due to acquisition problems such as soil/seismometer coupling effects or local subsurface heterogeneities, which disturbed surface-wave propagation. Profile C1 is a mix between profiles CA and B. The observed frequency variations are smoother (fig. 5b), and the calculated thickness appear consistent with the geotechnical data except in the eastern part of the profile (from points 1 to 5, points 1 to 3 being located outside of the mudslide). In this area, the discrepancy between our results and geotechnical tests must come from the presence of a former coarse mudslide. Finally, the seismic noise measurements recorded for the network experiment (fig. 5d) exhibit frequencies consistent with those derived from the H/V profiles, underlying a smooth geometry of the sliding surface in this part of the mudslide.

Figure 6 presents the interpretation of the picked frequencies in term of thickness (grey points). The thickness was computed using the formula $Hs = Vs/4f_0$ with a constant shear velocity $Vs = 260 \text{ m.s}^{-1}$ in the mudslide. This velocity was obtained from surface wave interpretation and seismic noise network analyses (fig. 7; fig. 8). The bedrock geometry was derived from geotechnical data (black dots), photogrammetric stereo-restitution of the topography before and after the mudslide [Weber and Herrman, 2000] and H/V interpretation. The surface topography changes between 1996 (when the geotechnical tests were performed) and 2005 (when the geophysical acquisition was carried out) were taken into account. Finally, the blue dashed line corresponds

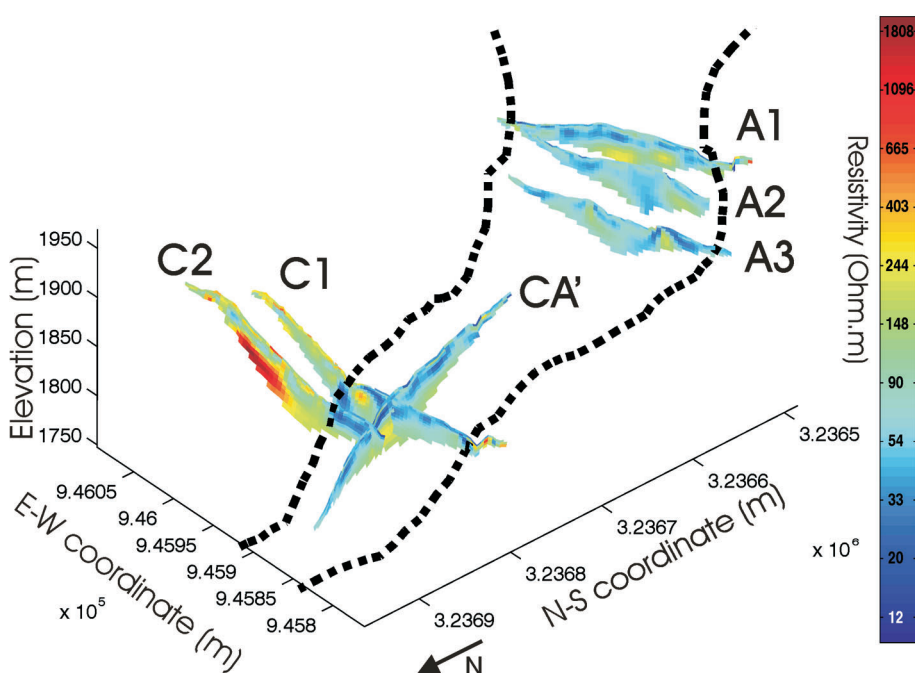


FIG. 3. – Electrical tomography images derived after inversion of data acquired using a Wenner acquisition at the “Super-Sauze” mudslide.
 FIG. 3. – Image de tomographies électriques déduites après inversion de données acquises en mode Wenner sur le glissement-coulée de “Super-Sauze”.

to the interpretation of electrical tomography sections (fig. 3). The slip surface was adjusted using geotechnical measurements. These results show that the interpretation of the picked frequency in term of thickness is particularly consistent with other measurements, even if the structure is 3D. However, it is clear that when H/V spectral ratios exhibit more than one peak in the interesting frequency range, interpretation could be ambiguous and a dense spatial sampling is needed. Variability of the mudslide shear-wave velocity can also explain the small differences between the geotechnical results and the thicknesses derived from the seismic noise data. Electrical results are consistent with the H/V data along profile CA, but less with profile C. This difference results from the lack of accuracy of the electrical tomography (smoothing effect), in particular when carried out with the Wenner configuration.

Seismic noise network

Seismic noise experiment using an array was carried out in the middle part of cross-section C (fig. 2). The array consists of three circles (radius of 10, 25 and 50 m) each composed of 6 seismic stations. To validate the dispersion curves derived from these measurements, a longitudinal active seismic profile was also recorded along profile CA (fig. 2) using 24 4.5 Hz-vertical geophones placed every 10 m apart.

Figure 7 displays the dispersion curves, the derived (S)-wave velocity models, with associated errors for the passive (fig. 7c and d) and active (fig. 7a and b) and the energy map of the surface waves. Only two seismic noise arrays (radius of 10 and 25 m) were used (transition frequency around 7 Hz on the dispersion curve), the larger one (50 m radius) presenting no dispersion effect (probably due to 3D effects for wavelengths ranging from 16 to 38 m). The two dispersion curves are consistent and display the same variations except at low frequencies (fig. 7e). This

corroborates that the seismic noise is mainly composed of surface waves, which is one of the major assumptions for 1D seismic noise interpretation.

During the inversion of the dispersion curves derived from seismic noise processing, the H/V peak frequency was added as *a priori* information. All models, which did not satisfy the resonance frequency at the central station of the array were rejected. For both the surface-wave profile and the seismic noise data, models with the lowest misfit values show (S)-waves velocity ranging between 260 and 300 m.s⁻¹ in the topmost layer, with a well-defined thickness between 19-22 m for the noise data. For the surface wave profiles, the thickness is not well constrained between 14 and 24 m. These results are consistent with electrical measurements and H/V data. Within the mudslide, both inversion results showed weak Vs contrasts, which could be related to the observed superimposed units discussed before. On the contrary, the shear-wave velocity in the bedrock is not well constrained. It varies from 600 to 700 m.s⁻¹ for the surface wave profiles and from 1100 to 1300 m.s⁻¹ for the seismic noise data. Because of the large uncertainty on the dispersion curves of the seismic noise data at low frequencies, we only retained the velocity derived from the surface wave profile.

INVESTIGATION OF THE “SAINT-GUILLAUME” LANDSLIDE

Geological, geomorphological and geotechnical setting of the translational landslide

The “Saint-Guillaume” landslide is located in the Trièves Plateau (fig. 1) where many clayey landslides occurred in the past in the so-called varved clays; these clays are finely laminated glacio-lacustrine deposits dating from the Pleistocene

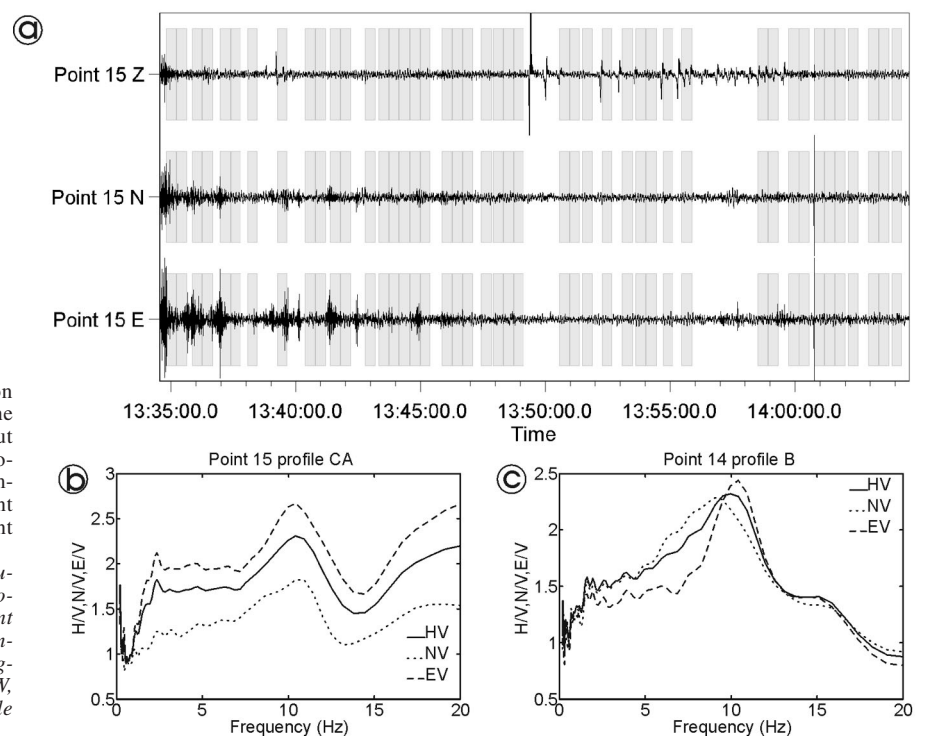


FIG. 4. – Ambient vibration data: a) ambient vibration data sampled at 200 Hz and recorded for 30 min. The grey shade indicates the short time-windows (about 40 s. in duration) selected with an anti-trigger process; b) spectral ratio computed using the E-W component, the N-S component and the H component (square root of E-W and N-S components) for point 15 of profile CA; c) for point 14 of profile B.

FIG. 4. – Mesures de bruit de fond sismique : a) mesures de bruit de fond sismique dans le domaine temporel, échantillonné à 200 Hz et enregistré pendant 30 minutes. Le grisé indique les courtes fenêtres temporelles sélectionnées avec un processus d'anti-trigger ; b) rapports spectraux des composantes E-W, N-S et H pour le point 15 du profil CA ; c) pour le point 14 du profil B.

(Wurmian) period [Antoine *et al.*, 1981; van Asch *et al.*, 1996]. The observed landslides present slip surfaces at different depths [Antoine *et al.*, 1981; Nieuvenhuis, 1991] from shallow ones (4 to 8 m) to more deeper ones (20 to 40 m).

The investigated landslide is a slow (1-5 cm.year⁻¹) translational landslide affecting the small village of “Saint-Guillaume”. The geological basement is composed of Oxfordian marly limestone covered with 40 to 60 m of varved clays. The landslide is limited to the south by a limestone cliff overhanging a scree hillslope (fig. 8). A umbilical zone of limestone is also visible to the east sub-dividing the clay formation into two parts. To the north, the landslide is limited by the Gresse torrent, which incised a narrow channel in the varved clays. In the western part of the landslide, a geomorphological survey (geomorphological map, topographic control points) and a geotechnical investigation (with three inclinometers and one piezometer) were carried out from the late nineties [Guéguen *et al.*, 2004; Cravoisier *et al.*, 2004]. The results from the boreholes indicated the existence of an interface between the

uppermost varved clay and the marly limestone bedrock at depths of 38.5 m, 61.7 m and 33.1 m for boreholes I1, I3 and I4 respectively (fig. 8). The inclinometers detected several slip surfaces inside the clay formation, with the main one and deeper located at 34.5 m, 37.0 m, and 27.0 m depth, respectively. This monitoring system has been complemented since 2003 by geophysical investigations. As a consequence, only a sum up of the main characteristics of the landslide is developed hereafter. Similarly to the “Super-Sauze” mudslide, seismic noise measurements (H/V and seismic noise network) were tested (fig. 8). The comparison with the “Super-Sauze” results is interesting because the “Saint-Guillaume” situation presents a smoother bedrock geometry and weaker (S)-wave contrasts.

H/V method

The H/V profile was carried out along an east-west direction perpendicular to the main displacement direction of the landslide (fig. 8). Measurements were made every 20 m, all along the profile, including in the village and on the marly

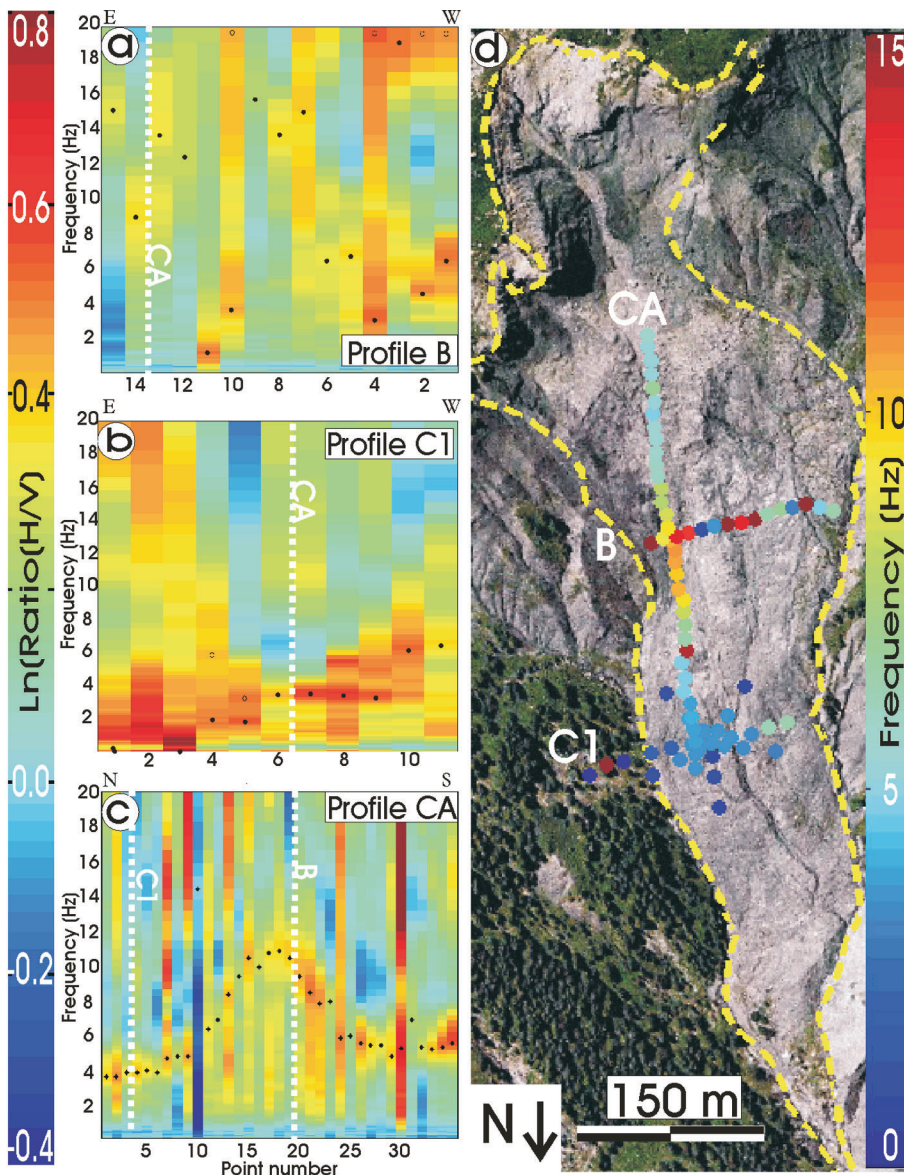


FIG. 5. – Ratio of the vertical and horizontal component (H/V) of seismic noise analysis and seismic noise network results obtained at the “Super-Sauze” mudslide: a) along profile B; b) along profile C1; c) along longitudinal profile CA; d) spatial representation of the picked frequency (displayed in colour).
 FIG. 5. – Résultats des mesures H/V obtenues sur le glissement-coulée de “Super-Sauze” : a) sur le profil B; b) sur le profil C1 ; c) sur le profil longitudinal CA ; d) représentation spatiale des pics de fréquence (représenté par un code de couleur).

limestone bedrock outcropping at the surface (points 70 to 80). As no clear differences appear on the two horizontal spectra components, only the square root of E-W and N-S components (H) is plotted (fig. 9a). Two frequency peaks can be observed around 1.3 Hz (black dots on fig. 9a, denoted f_0) and ranging from 2 Hz to 12 Hz (circle and black dots on figure 9a, denoted f_1). The lower frequency f_0 vanishes from points 55 to 76 (high single frequency) and at the edges of the profiles (low single frequency). In the area where the bedrock outcrops (from point 71 to point 74), maximum values of the H/V ratio are irregular.

(S)-wave refraction [Guéguen *et al.*, 2004] and surface-wave analysis (fig. 10) showed that the (S)-wave velocity of the upper layer $V_{\text{disturbed clays}}$ is around 260 m.s^{-1} . We consequently used this velocity to calculate the landslide thickness from the highest peak frequency (fig. 9b). Black circles located below point 32 represent the known slip surface and bedrock depth derived from I3 inclinometer data. The interface lies between 0 m (where the bedrock reaches the surface) and 50 m deep. Below I3 the landslide bottom

deduced from H/V data fits very well with the surface rupture evinced by the inclinometer data. The lower frequency is more difficult to interpret. Because it vanishes where bedrock reaches the surface, it may correspond to the signature of the clay-marly limestone interface located at 61 m by inclinometer I3 (fig. 9b). For the frequency to depth conversion, we used a velocity profile that was derived from (S)-wave refraction analysis [Guéguen *et al.*, 2004] and surface waves analysis (fig. 10). Both showed that the undisturbed clays exhibit a velocity $V_{\text{undisturbed clays}}$ around 550 m.s^{-1} . Using an equivalent velocity based on equivalent time propagation ($V_{\text{Sequivalent}} = (H_{\text{disturbed clays}} + H_{\text{undisturbed clays}}) / (H_{\text{disturbed clays}}/V_{\text{disturbed clays}} + H_{\text{undisturbed clays}}/V_{\text{undisturbed clays}})$), the low frequency maximums were picked and converted to depth, in order to obtain an image of the bedrock topography. It is consistent with the bedrock depth measured at borehole I3 and fits remarkably with an electrical tomography profile that reaches the bedrock at a depth of 80 m [Guéguen *et al.*, 2004]. Collectively, these results suggest that the slip surface develops first at the clay/bedrock interface

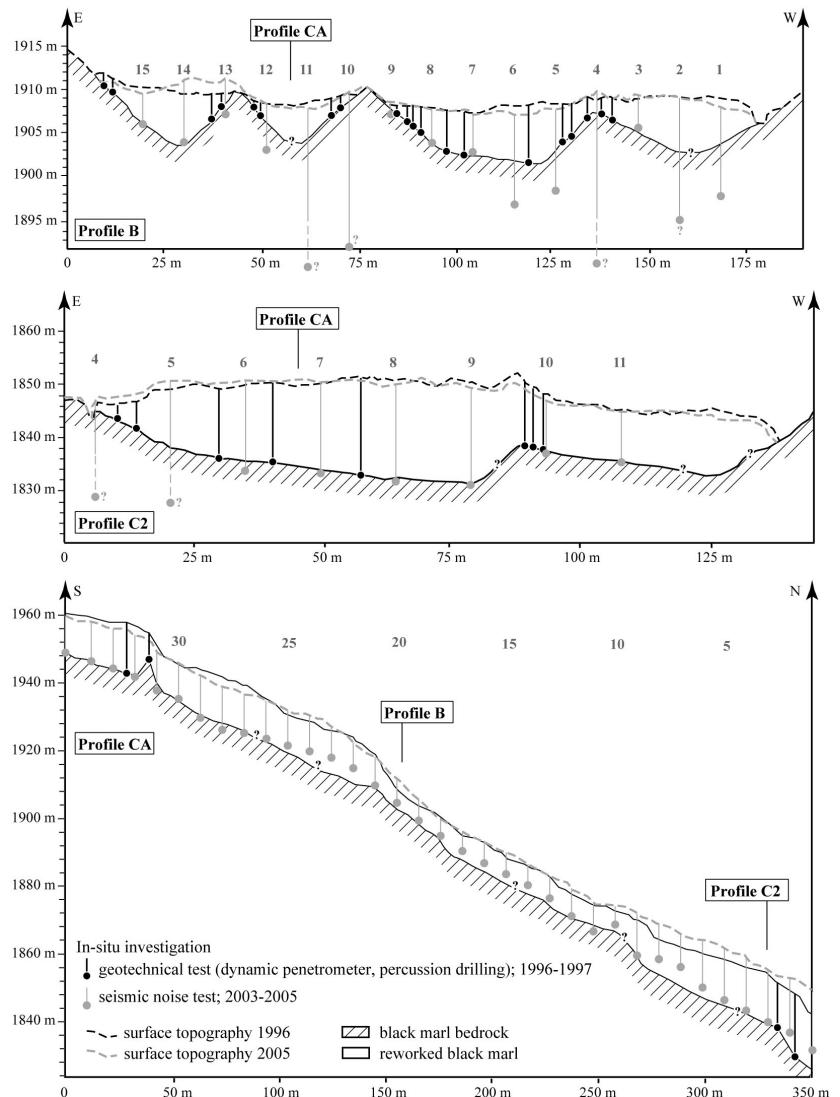


FIG. 6. – Interpretation of H/V picked frequencies on the “Super-Sauze” mudslide for the three profiles B, C1 and CA, assuming an average (S)-wave velocity of 260 m.s^{-1} . Results from geotechnical and electrical data are also shown for comparison. The interface between sliding material and stable ground was drawn considering all the results, except electrical tomography profile. The presence of two peaks in some H/V ratios (figs. 5b and 5c) resulted into two possible interpretations, although lower frequencies are expected to be due to the presence of deeper interfaces (former coarse mudslide), acquisition problems or local heterogeneity. FIG. 6. – *Interprétation des fréquences pointées des mesures H/V sur le glissement-coulée de “Super-Sauze” considérant une vitesse de 260 m.s^{-1} . Ces interprétations sont comparées aux données géotechniques et électriques. L’interface a été dessinée considérant tous les résultats, exceptés ceux de la tomographie électrique.*

when bedrock is close to the surface and then within the clay layer (as confirmed by inclinometer monitoring). Compared to the “Super-Sauze” mudslide, the frequency picking

was easier because structures are less complex and less laterally heterogeneous.

Seismic noise network

Seismic noise measurements with station arrays were carried out near the location of inclinometer I3. They involved three arrays with radius of 20, 40 and 60 m (fig. 8). Similarly to the “Super-Sauze” mudslide study, this investigation was combined with an active seismic experiment using 24 4.5 Hz-vertical geophones. The data were processed in the same way as for the “Super-Sauze” investigation. Figure 10 shows the results derived from both passive and active seismic surveys. The frequency range of the dispersion curves largely differs depending on the method. Indeed, the passive method provided useful information in the [2.5-6.5 Hz] frequency range and the active method in the [4-12 Hz] frequency range. In the [4-6.5 Hz] frequency range, the dispersion curves are remarkably similar, (fig. 10e). This observation confirms again that the largest part of the energy contained in the seismic noise is carried by surface waves. The inversion process was also performed using the H/V constraint for the passive network.

The best models (lowest RMS) for the active and passive experiments are consistent with the geotechnical and geophysical data. The (S)-wave velocity of the topmost layer is well constrained for both experiments, ranging from 260 to 280 m.s⁻¹. It corresponds to the unstable clayey zone affected by deformation, with a thickness between 31 and 34 m from the passive method and between 28 and 30 m from the active method. The difference may results from the 3D smoothing property of the array, which integrates information from a larger volume zone. Moreover, the surface wave acquisition was carried out at the N-W edge of the array.

As discussed before, (S)-wave velocities are close to 550 m.s⁻¹ (Vp=1800 m.s⁻¹) in the stable clay layer and reach more than 800 m.s⁻¹ (Vp 2500 m.s⁻¹) in the marly limestone bedrock. Figure 10 indicates that both methods yielded (S)-wave velocity of around 600 m.s⁻¹ in the second layer (stable clay). However, they were unable to detect and characterize the bedrock top, due to the limited range of the dispersion curve at low frequency and the large data uncertainty.

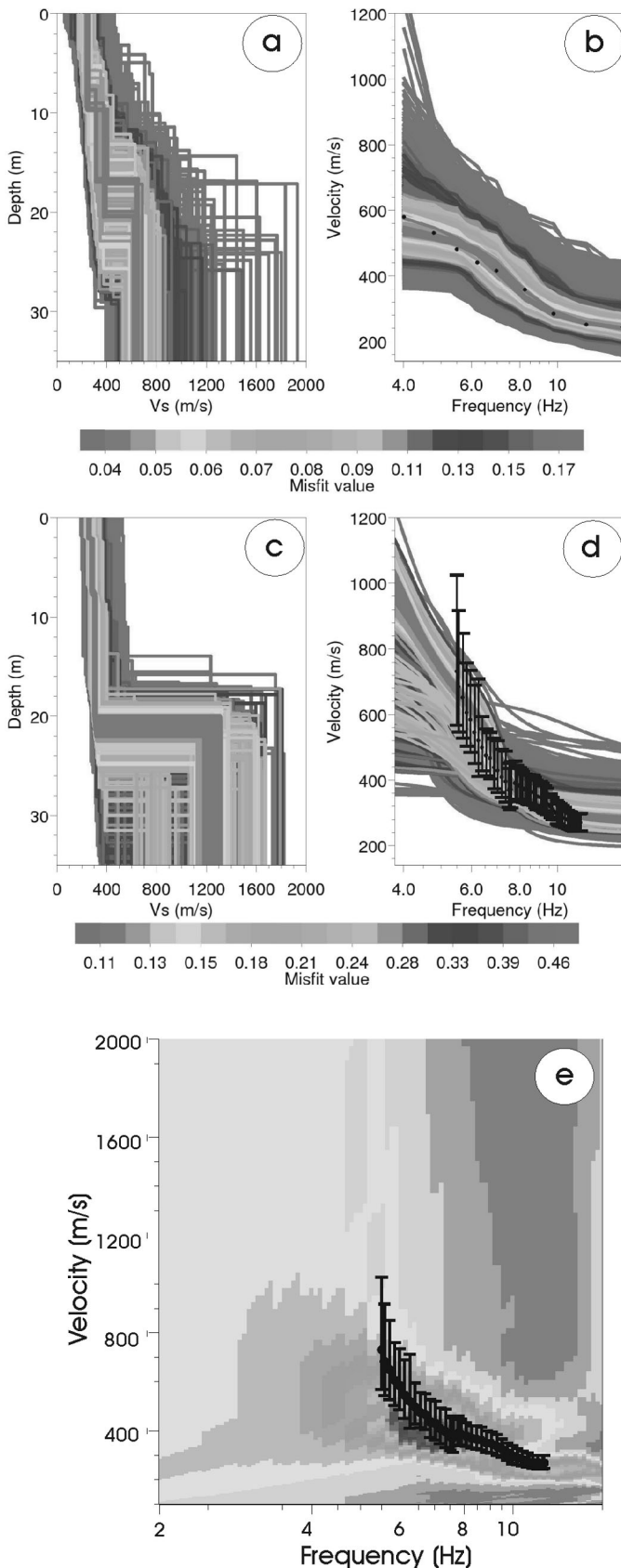
CONCLUSIONS

Electrical tomography and two seismic noise experiments were carried out on two landslides with different characteristics: (1) a mudslide characterized by abrupt 3D variations



FIG. 7. – Inversion results of the dispersion curve obtained from the seismic noise network and from surface wave measurements at the “Super-Sauze” mudslide. Shear-wave velocity (Vs) models as a function of depth and of RMS error (colour scale) for a) the surface-wave data and c) the seismic noise network; b) Superimposition of the measured dispersion curve with the models derived from the surface-wave profile and d) the seismic noise array; e) superimposition of the seismic noise dispersion curve and of the semblance map of surface waves.

FIG. 7. – Résultats de l'inversion de la courbe de dispersion du réseau de bruit de fond sismique et des mesures d'onde de surface sur le glissement-coulée de “Super-Sauze”. Modèles de Vs en fonction de la profondeur et de l'erreur (échelle de couleur) pour a) les ondes de surface et pour ; c) le bruit sismique ; b) surimposition de la courbe de dispersion avec les modèles dérivés des ondes de surface et d) du bruit de fond sismique ; e) surimposition de la courbe de dispersion issue du réseau de bruit de fond sismique et de la carte de vraisemblance des ondes de surface.



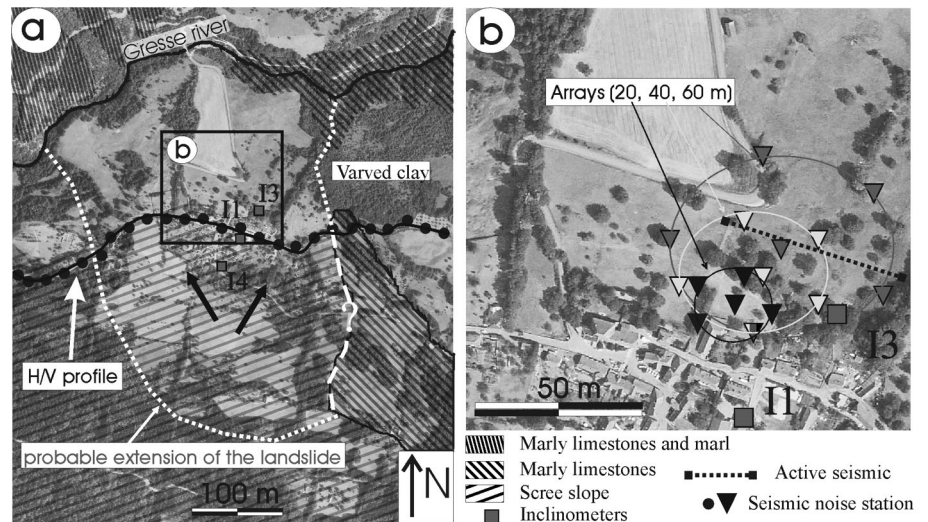


FIG. 8. – Aerial view and investigation of the “Saint-Guillaume” landslide. a) Aerial photograph including locations of the three inclinometers, the locations of seismic stations and a schematic view of the geology; b) enlargement of the zone (right) where seismic noise investigations were carried out.

in the bedrock geometry and large (S)-wave velocity contrasts, and (2) a translational landslide where the slip surface geometry as well as the (S)-wave contrasts are smoother. The 2D electrical tomography sections provided valuable and continuous information about the pseudo-3D geometry of the mudslide. H/V measurements showed their efficiency in characterizing the contact between the stable

and unstable material in both landslides, as well as the bedrock interface for the translational landslide. Difficulties in H/V data interpretation arose on the mudslide, because of multiple resonance frequencies. Some of them are perhaps due to deeper interfaces, heterogeneities or bad coupling effects during acquisition. Our study on H/V measurements on landslides demonstrates that they have to be performed

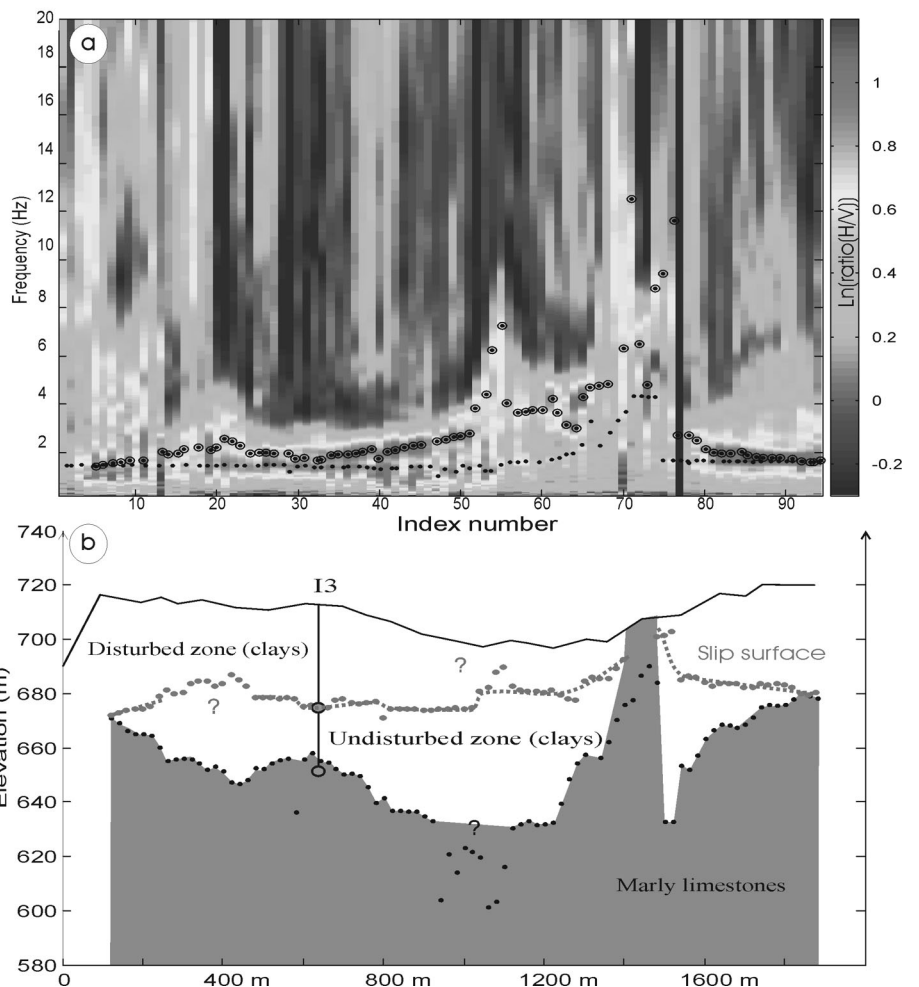
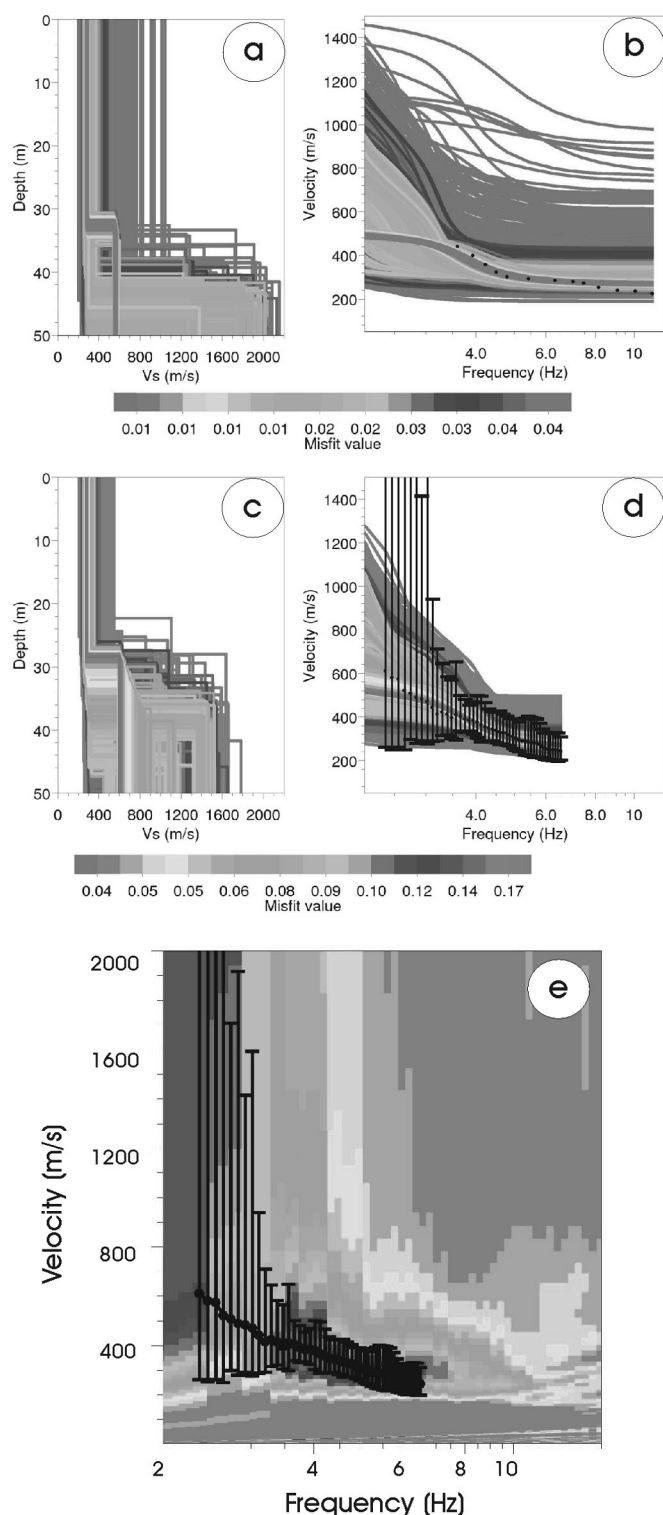


FIG. 9. – H/V measurements at “Saint-Guillaume” landslide. a) Ratio of the vertical and horizontal component (H/V) of seismic noise analysis measured along the H/V profile (fig. 8), with the two picked frequencies (circle and black dots for higher frequency f_1 , black dots for lower frequency f_0); b) interpretation of the picked frequencies in term of slip surface geometry (red dots deduced from f_1) and bedrock geometry (black dots deduced from f_0). The grey dots represent the slip surface and bedrock depths derived from inclinometer I3 and borehole measurements.



along profiles in order to follow frequency peaks, which can dramatically vary in heterogeneous conditions. Also the spatial sampling has to be dense enough and be adapted to the 3D geometry.

Vs profiles deduced from the seismic noise array measurements on both sites were compared to geotechnical data, as well as to results provided by active surface-wave investigations. First, the obvious similarity in the dispersion curves of the active and passive methods at the two sites indicate that the seismic noise was mainly made of surface waves. Secondly, we observed, particularly on the “Super-Sauze” site, that large arrays are not always efficient due to 2D/3D effects on surface waves. The largest array enabled us to record consistent dispersive waves at low frequencies on the “Saint-Guillaume” landslide.

In the two studied landslides large (S)-wave velocity contrasts were found across the slip surfaces, which were detected and measured by seismic noise methods. Consequently, combined to numerical simulations, seismic noise methods may be of high interest to identify and map slip surfaces in 3D.

Acknowledgements. – Support of this work was partially provided by the French National Institute for Universe Sciences (INSU) in the framework of the ‘ACI – Prévention des Catastrophes Naturelles’ Program (Project SAMOA) and the ‘ACI-Aléas et Changement Global’ Program (Project GACH2C). The investigations carried out at “Saint-Guillaume” were supported by Conseil Général de l’Isère within a ‘Pôle Grenoblois des Risques Naturels’ Project. We express our gratitude to the ‘Service de Restauration des Terrains en Montagne’ (RTM38) and particularly to Mrs. C. Moulin for providing geotechnical data on the “Saint-Guillaume” landslide. We also thank all the colleagues who helped us during the field investigations, as well as the people from the city office of “Saint-Guillaume” and particularly Mrs. E. Paquet. We gratefully thank M. Wathélet for providing access to his inversion software SESARRAY. The authors are grateful to two anonymous reviewers for their improvements of the manuscript.

FIG. 10. – Inversion results of the dispersion curve obtained from the seismic noise network and from surface wave measurements at the “Saint-Guillaume” landslide. Shear-wave velocity (Vs) models as a function of depth and of RMS error (colour scale) for a) the surface-wave data and c) the seismic noise network; b) superimposition of the measured dispersion curve with the derived models from the surface-wave profile and d) the seismic noise array; e) superimposition of the seismic noise dispersion curve and of the semblance map of surface waves.

FIG. 10. – Résultats de l’inversion de la courbe de dispersion du réseau de bruit de fond sismique et des mesures d’onde de surface sur le glissement de “Saint-Guillaume”. Modèles de Vs en fonction de la profondeur et de l’erreur (échelle de couleur) pour a) les ondes de surface et pour c) le bruit sismique ; b) surimposition de la courbe de dispersion avec les modèles dérivés des ondes de surface et d) du bruit de fond sismique ; e) surimposition de la courbe de dispersion issue du réseau de bruit de fond sismique et de la carte de vraisemblance des ondes de surface.

References

- ANTOINE P., GIRAUD A. & MONJUEVENT G. (1981). – Les argiles litées du Trièves (Isère), conditions de glissement de terrain et exemples de propriétés géotechniques. – *Bull. Soc. géol. Fr.*, **XXIII**, 117-127.
- ASTEN M.W. (2004). – Passive seismic methods using the microtremor wave field for engineering and earthquake site zonation. – *Proc. 74th SEG Annual Meeting*, Denver, USA, Session NGS-1.
- BARD P.-Y. & BOUCHON M. (1985). – The two-dimensional resonance of sediment-filled valleys. – *Bull. Seism. Soc. Am.*, **75**, 519-541.
- BONNEFOY-CLAUDET S. (2004). – Nature du bruit de fond sismique : implications pour les études des effets de site. – Thèse de Doctorat, Univ. J. Fourier, Grenoble, France, 241 p.
- CHATELAIN J.-L., GUÉGUEN P., GUILLIER B., FRECHET J., BONDOUX F., SARRAULT J., Sulpice P. & NEUVILLE J.-M. (2000). – CityShark: A user-friendly instrument dedicated to ambient noise (microtremor) recording for site and building response studies. – *Seism. Res. Lett.*, **71**, 698-703.

- COMMEND S., GEISER F. & TACHER L. (2004). – 3D numerical modelling of a landslide in Switzerland. *In: Proc. NUMOG IX*, Ottawa, Canada. – Balkema, Rotterdam, B6.
- CORNOU C., KRISTEK J., OHRNBERGER M., DIGUILIO G., SCHISSELE E., GUILLIER B., BONNEFOY-CLAUDET S., WATHELET M., FAEH D., BARD P.-Y. & MOCZO P. (2004). – Simulation of seismic ambient vibrations – II: H/V and array techniques for real sites. – *In: Proc. 13th World Conf. Earth. Eng.*, Vancouver, Canada. – IAEE, Tokyo, Paper 1130, 6 p.
- CRAVOISIER S., GARAMBOIS S., GUEGUEN P., MARAND A. & MONNET J. (2004). – Combined geophysical and seismological experiments on a landslide developing in varved clays. – *EGU, Geophys. Res. Abstr.*, **6**, 04065.
- DAHLIN T. & ZHOU B. (2004). – A numerical comparison of 2D resistivity imaging with ten electrode arrays. – *Geophys. Prospect.*, **52**, 379-398.
- FIELD E. & JACOB K. (1993). – The theoretical response of sedimentary layers to ambient seismic noise. – *Geophys. Res. Lett.*, **20**, 2925-2928.
- FIELD E. & JACOB K. (1995). – A comparison and test of various site-response estimation techniques including three that are not reference-site dependent. – *Bull. Seism. Soc. Am.*, **85**, 1127-1143.
- FLAGEOLLET J.-C., MALET J.-P., SCHMUTZ M. & MAQUAIRE O. (2004). – Integrated investigations on landslides: example of the “Super-Sauze” earthflow. *In: Natural disaster and sustainable development.* – Springer-Verlag, Berlin, 213-238.
- GALLIPOLI M., LAPENNA V., LORENZO P., MUCCIARELLI M., PERRONE A., PISCITELLI S. & SDAO F. (2000). – Comparison of geological and geophysical prospecting techniques in the study of a landslide in southern Italy. – *European J. Env. Eng. Geophys.*, **4**, 117-128.
- GIRAUD A., ANTOINE P., VAN ASCH T.W.J. & NIEUWENHUIS J.D. (1991). – Geotechnical problems caused by glaciolacustrine clays in the French Alps. – *Eng. Geol.*, **31**, 185-195.
- GUÉGUEN P., CHATELAIN J.-L., GUILLIER B. & YEPES H. (2000) – An indication of the soil topmost layer response in Quito (Ecuador) using H/V spectral ratio. – *Soil Dyn. and Earthquake Eng.*, **19**, 127-133.
- GUÉGUEN P., GARAMBOIS S., CRAVOISIER S. & JONGMANS D. (2004). – Geotechnical, geophysical and seismological methods for surface sedimentary layers analysis. *In: Proc. 13th World Conf. Earth. Eng.* Vancouver, Canada. – IAEE., Tokyo, Paper 1777, 6 p.
- HASKELL N.A. (1960). – Crustal reflection of plane SH waves. – *J. Geophys. Res.*, **65**, 4147-4150.
- ISRAIL M. & PACHAURI A.K. (2003). – Geophysical characterisation of landslide site in the Himalayan foothill region. – *J. Asian Earth Sc.*, **22**, 253-263.
- JONGMANS D. & GARAMBOIS S. (2007). – Geophysical investigation of landslides: A review. – *Bull. Soc. géol. Fr.*, **178**, 2, 101-112.
- KVAERNA T. & RINGDAHL F. (1986). – Stability of various f-k estimation techniques. – Report 1. 86/87, NORSAR Scientific Report, Kjeller, Norway, 29-40
- LACHET C. & BARD P.-Y. (1994). – Numerical and theoretical investigations on the possibilities and limitations of the “Nakamura's” technique. – *J. Phys. Earth (Japan)*, **44**, 377-397.
- LACOSS R.T., KELLY E.J. & TOKSÖZ M. N. (1969). – Estimation of seismic noise structure using arrays. – *Geophysics*, **34**, 21-38.
- LEBRUN B., HATZFELD D. & BARD P.-Y. (2001). – A site effect study in urban area: experimental results in Grenoble (France). – *Pure & App. Geophys.*, **158**, 2543-2557.
- LERMO J. & CHÁVEZ-GARCÍA F. J. (1993). – Site effect evaluation using spectral ratios with only one station. – *Bull. Seism. Soc. Am.*, **83**, 1574-1594.
- LOKE M.H. & BARKER R.D. (1996). – Rapid least-squares inversion of apparent resistivity pseudosections by a quasi-Newton method. – *Geophys. Prospect.*, **44**, 131-152.
- MALET J.-P. (2003). – Les “glissements de type écoulement” dans les marnes noires des Alpes du Sud. Morphologie, fonctionnement et modélisation hydro-mécanique. – Thèse de Doctorat, Univ. Louis Pasteur, Strasbourg I, France, 394 p.
- MALET J.-P. & MAQUAIRE O. (2003). – Black marl earthflows mobility and long-term seasonal dynamic in southeastern France. – *In: Proc. 1st Int. Conf. on Fast Slope Movements*, Naples, Italy, Patron Editore, Bologna, 333-340.
- MALET J.-P., VAN ASCH T.W.J., VAN BEEK L.P.H. & MAQUAIRE O. (2005). – Forecasting the behavior of complex landslides with a 2-5D spatially distributed hydrological model. – *Nat. Haz. and Earth Sys. Sc.*, **5**, 1-15.
- MAQUAIRE O., FLAGEOLLET J.-C., MALET J.-P., SCHMUTZ M., WEBER D., KLOTZ S., ALBOUY Y., DESCLOÏTRES M., DIETRICH M., GUÉRIN R. & SCHOTT J.-J. (2001). – Une approche multidisciplinaire pour la connaissance d'un glissement coulée dans les marnes noires du Callovien-Oxfordien (Super-Sauze, Alpes de Haute Provence, France). – *Rev. Fr. Géotech.*, **95/96**, 15-31.
- MERIC O., GARAMBOIS S., JONGMANS D., WATHELET M., CHATELAIN J.-L. & VENGEON J.-M. (2005). – Application of geophysical methods for the investigation of the large gravitational mass movement of Séchillienne, France. – *Can. Geotech. J.*, **42**, 1105-1115.
- NAKAMURA Y. (1989). – A method for dynamic characteristics estimation of subsurface using microtremor on ground surface. – *Quar. Report. Railway. Tech. Res. Institute*, **30**, 25-33.
- NIEUWENHUIS J.D. (1991). – The lifetime of a landslide: investigation in the French Alps. – Taylor & Francis, London, 160 p.
- NOGOSHI M. & IGARASHI T. (1971). – On the amplitude characteristics of microtremor (part 2). – *J. Seism. Soc. Japan*, **24**, 26-40.
- OHRNBERGER M. (2001). – Continuous automatic classification of seismic signals of volcanic origin at Mount Merapi, Java, Indonesia. – PhD Thesis, Univ. of Postdam, Potsdam, Germany, 168 p.
- ROTEN D., CORNOU C., STEIMEN S., FAEH D. & GIARDINI D. (2004). – 2D resonances in Alpine valleys identified from ambient vibration wavefield. *In: Proc. 13th World Conf. Earth. Eng.*, Vancouver, Canada. – IAEE., Tokyo, Paper 1787, 6 p.
- SAMBRIDGE M. (1999a). – Geophysical inversion with a neighbourhood algorithm - I. Searching a parameter space. – *Geophys. J. Int.*, **138**, 479-494.
- SAMBRIDGE M. (1999b). – Geophysical inversion with a neighbourhood algorithm-II. Apprising the ensemble. – *Geophys. J. Int.*, **138**, 727-746.
- SATOH T., KAWASE H. & MATSUSHIMA S. (2001). – Estimation of (S)-wave velocity structures in and around the Sendai Basin, Japan, using array records of microtremors. – *Bull. Seism. Soc. Am.*, **91**, 206-218.
- SCHERBAUM F., HINZEN K.G. & OHRNBERGER M. (2003). – Determination of shallow shear wave velocity profiles in the Cologne/Germany area using ambient vibrations. – *Geophys. J. Int.*, **152**, 597-612.
- SCHMUTZ M., ALBOUY Y., GUÉRIN R., MAQUAIRE O., VASSAL J., SCHOTT J.-J. & DESCLOÏTRES M. (2000). – Joint electrical and time domain electromagnetism (TDEM) data inversion applied to the Super Sauze earthflow (France). – *Surv. Geophys.*, **21**, 371-390.
- STEIMEN S., FÄH D., KIND F., SCHMID C. & GIARDINI D. (2003). – Identifying 2-D resonance in microtremor wave fields. – *Bull. Seism. Soc. Am.*, **93**, 583-599.
- TACHER L., BONNARD C., LALOUI L. & PARRIAUX A. (2005). – Modelling the behaviour of large landslide with respect to hydrogeological and geomechanical parameter heterogeneity. – *Landslides*, **2**, 3-14.
- TOKIMATSU K. (1997). – Geotechnical site characterization using surface waves. *In: Earthquake Geotechnical Engineering.* – Balkema, Rotterdam, 1333-1368.
- UEBAYASHI H. (2003). – Extrapolation of irregular subsurface structures using the horizontal-to-vertical spectral ratio of long-period microtremors. – *Bull. Seism. Soc. Am.*, **93**, 570-582.
- VAN ASCH T.W.J., HENDRICKS M., HESSEL R. & RAPPANGE F.E. (1996). – Hydrological triggering conditions of landslides in varved clays in the French Alps. – *Eng. Geol.*, **42**, 239-251.
- VAN ASCH T.W.J., MALET J.P., VAN BEEK L.P.H. & AMITRANO D. – Techniques, issues and advances in numerical modelling of landslide hazard. – *Bull. Soc. géol. Fr.*, **178**, 2, 65-88.
- WATHELET M., JONGMANS D. & OHRNBERGER M. (2004). – Surface wave inversion using a direct search algorithm and its application to ambient vibration measurements. – *Near Surf. Geophys.*, **2**, 221-231.
- WEBER D. & HERRMANN A. (2000). – Contribution de la photogrammétrie numérique à l'étude spatio-temporelle de versants instables: l'exemple du glissement de terrain de Super-Sauze (Alpes-de-Haute-Provence, France). – *Bull. Soc. géol. Fr.*, **171**, 6, 637-648.

3.3. Exemples de l'intérêt d'un suivi sismologique temporel sur les mouvements de terrain de type rocheux

3.3.1 L'Observatoire OMIV et écoute sismologique sur le mouvement de Séchilienne

Nous présentons dans ce paragraphe l'observatoire OMIV (Résumé EGU, Grasso et al., 2010) puis l'intérêt du suivi sismologique du mouvement de terrain de Séchilienne (site présenté dans le paragraphe 3.2).

The OMIV Observatory on landslides – Observing with Multi-parameters the Instability of Versants

J.-R. Grasso (1), S. Garambois (1), D. Jongmans (1), A. Helmstetter (1), T. Lebourg (2), J.-P. Malet (3), W. Berolo (2), R. Bethoux (1), L. Daras (1), and P. Ulrich (3)

(1) LGIT, UMR5559, OSUG, University Joseph Fourier of Grenoble & CNRS, France, (2) GeoAzur (UMR6526), University of Nice Sophia-Antipolis, (3) School and Observatory of Earth Sciences, Institute of Earth Physics, CNRS UMR 7516, University of Strasbourg, Strasbourg, France.

The OMIV Observatory on landslides (Multidisciplinary Observatory on Slope Instabilities) is a French-research initiative clustering five research institutes in earth sciences under the auspices of INSU (Institut National des Sciences de l'Univers) since 2007. The primary objectives of OMIV are (1) to deploy and maintain permanent instrumental networks in order to be able to (2) to provide robust, long-lasting multi-parameter, open datasets to the international geosciences community. Such continuous monitoring of ongoing landslides are missing and they will provide constrains on the processes that lead to slope instabilities. Worldwide, the societal impact of landslides is one of the most important natural hazard in mountainous and rocky coastal areas. The variability in time and space of the slope structures and their susceptibility to external forcing (weathering, earthquake, climatic triggers) restrain our ability to simulate and forecast slope instabilities. Four active large landslides are monitored by the OMIV observatory group; these sites have been chosen according to their past history of monitoring, to the risk they may create and to the scientific challenges they raise up. The four studied landslides are: the Avignonet landslide (30 km South of Grenoble) and the Super-Sauze landslide (5 km South to Barcelonnette) which are soft-rock slides developed in clays for which the susceptibility to rainfalls and earthquake is the main open question; the La Clapière (100 km North of Nice) and the Séchilienne landslide (25km East of Grenoble) which are typical mature and immature large scale rock mass gravitational instabilities, respectively.

On these four pilot sites, the OMIV research group is monitoring in continuous three types of observations: landslide kinematics (deformation and displacements), landslide seismic activity (through passive seismic auscultation), and landslide slope hydrology (hydrodynamics and hydro-geochemistry). These observables are open datasets which are available through the OMIV websites (<http://www-lgit.obs.ujf-grenoble.fr/observations/omiv/>). If kinematics, hydrology and seismic activity are the main observables for many monitored landslides worldwide, only a few of them combines the three types of observables at relevant spatial and temporal scales. It is hypothesized by the OMIV observatory group that the combination of these three measurements will give access to a better knowledge on the physical processes controlling landslide behavior, such as the generation of brittle damage in the landslide material during sliding, the recognition and characterization of slip surface(s), the characterization of the hydrological behavior of the slope before and after failure. It opens possible routes toward characterizing the macro-scale rheology of the systems (e.g. brittle plastic transition for hard rock slopes, slide to flow transition for soft-rock landslides). The cross analysis of the monitoring data will bring new insights on the kinematics and dynamics of unstable slopes. In this study, we present (i) the technical organization of the multi-parameter monitoring datasets, and (ii) preliminary results from the ongoing monitoring.



1 Seismic monitoring of Séchilienne rockslide (French Alps): 2 Analysis of seismic signals and their correlation with rainfalls

3 Agnès Helmstetter¹ and Stéphane Garambois¹

4 Received 14 September 2009; revised 22 December 2009; accepted 4 February 2010; published XX Month 2010.

5 [1] In the French Alps, Séchilienne rockslide is one of the natural phenomena that
6 presents one of the highest levels of risk in terms of socioeconomical outcomes. This
7 rockslide has been active for a few decades and has been instrumented since 1985.
8 The current very active volume of this rockslide is estimated to be up to 5 million m³,
9 located on the border of a slowly moving mass reaching 50–100 million m³. The velocity
10 of the most active zone reached 1.4 m/yr in 2008, about twice the value of 2000. A
11 seismic network was installed on this rockslide in May 2007 to supplement the monitoring
12 system. It has now recorded several thousand events, mostly rockfalls but also hundreds
13 of local and regional earthquakes, which can be distinguished and classified from their
14 signal characteristics. Rockfalls and microseismicity, which occur in bursts of activity, are
15 found to be weakly, but significantly, correlated with rainfall. Rockfall occurrence
16 increases linearly with precipitation, with however strong fluctuations of the numbers of
17 rockfalls per day for the same rainfall intensity. No threshold was found for rainfall
18 triggering, with even 1 mm of rain being enough to trigger rockfalls. Rockfall activity
19 starts immediately during a rainfall episode and lasts for several days after the rainfall.
20 Rain also induces strong accelerations of the rockslide movement, which also start quasi-
21 instantaneously and last for about a month.

22 **Citation:** Helmstetter, A., and S. Garambois (2010), Seismic monitoring of Séchilienne rockslide (French Alps): Analysis of
23 seismic signals and their correlation with rainfalls, *J. Geophys. Res.*, 115, XXXXXX, doi:10.1029/2009JF001532.

24 1. Introduction

25 [2] Landslides can be triggered by many different causes,
26 including intense or extended rainfall and earthquakes.
27 Understanding of the mechanisms influencing landslide
28 dynamics is limited by the lack of dense and multiparameter
29 data, as very few active rockslides are nowadays instru-
30 mented with continuous measurements. Although there exists
31 an extensive literature about the triggering of shallow land-
32 slides or rockfalls by rainfall (see *Guzzetti et al.* [2007] for a
33 recent review), the catalogs used in these studies often exhibit
34 imprecise times (about 1 day), because they were generally
35 constructed from discrete field observations or aerial and
36 satellite images. In contrast, seismic monitoring presents the
37 opportunity to study the triggering mechanisms of land-
38 slides with very precise event times, but in a small area.
39 This method is also highly sensitive, allowing one to record
40 several thousand events per year. Finally, seismometers also
41 detect microearthquakes induced by the slope movement, in
42 addition to those generated by debris flows and rockfalls.
43 Seismology thus appears to be a promising technique to
44 complement classical techniques for landslide monitoring.

[3] Local seismological networks have been occasionally 45
used for monitoring active landslides. Most seismological 46
studies have used regional networks, primarily dedicated to 47
monitor seismicity [*McSaveney and Downes*, 2002]. Seis- 48
mology has been used for studying landslide propagation, 49
detecting precursory signals, or analyzing site effects. *Norris* 50
[1994] used seismic stations to detect rock avalanches at 51
three Cascade Range volcanoes. *McSaveney* [2002] and 52
McSaveney and Downes [2002] estimated the onset time, 53
duration, volume and propagation velocity of rockfall ava- 54
lanches in New Zealand from seismic signals. *Deparis et al.* 55
[2008] investigated ten rockfalls recorded in the French 56
Alps by a regional seismic network and tried to link seismic 57
parameters to rockfall properties. *Brodsky et al.* [2003] used 58
seismic waves to characterize landslide basal friction for 59
three huge landslides. *Del Gaudio et al.* [2008] analyzed 60
seismic site amplification from microtremors in a landslide 61
prone area (central Italy). Permanent networks were also 62
installed in Norway on the Åknes landslide [*Roth et al.*, 63
2006] and in Swiss Alps on the Randa landslide [*Spillmann* 64
et al., 2007] in order to characterize microseismicity of 65
these active rockslides. At a smaller scale, *Amitrano et al.* 66
[2005] observed precursory microseismicity before a cliff 67
collapse in Normandy (France). 68

[4] In this study, we present the results obtained from the 69
seismic monitoring of a large active rockslide. In the French 70
Alps, Séchilienne rockslide presents one of the highest levels 71
of risk in terms of socioeconomical outcomes. The failure of 72

¹Laboratoire de Géophysique Interne et Tectonophysique, Université Joseph Fourier, CNRS, Grenoble, France.

73 this landslide (3 to several tens of millions m³) is likely to
 74 form a natural dam which could potentially block the
 75 Romanche River located just below [Panet, 2000]. Its
 76 subsequent rupture would have devastating consequences
 77 downstream for people and facilities. For these reasons,
 78 this area has been extensively instrumented since 1988 for
 79 surveillance purposes using a multitechniques displacement
 80 network (noncontinuous GPS, laser, radar, extensometers)
 81 and a meteorological station.

82 [5] In May 2007, this monitoring system was supple-
 83 mented with a seismological network. The main objective is
 84 to detect microseismicity activity associated with fractures
 85 within the rock mass and/or rockfalls occurring within the
 86 rockslide, and to characterize these events (location, mag-
 87 nitude and mechanisms of microearthquakes, volume and
 88 propagation velocity of rockfalls). This network also allows
 89 study of small local earthquakes generated by the nearby
 90 Belledonne Border fault [Thouvenot *et al.*, 2003], and
 91 characterization of the properties and heterogeneities of
 92 seismic site amplification of the landslide. It will also permit
 93 seismic noise analyses to monitor very weak temporal
 94 changes in seismic wave velocities between each sensor due
 95 to fracture openings or fluid flow.

96 [6] In less than 2 years, several thousands seismic events
 97 have been recorded. In this paper, we first focus on the
 98 various types of signals which were acquired and on their
 99 characteristics. Most events have been identified as rock-
 100 falls, but hundreds of microearthquakes and distant earth-
 101 quakes have also been detected. The microseismicity and
 102 rockfall activity appear very variable, from zero to more
 103 than 100 events per day during seismic crises. Most of these
 104 peaks are correlated with rainfall and are also associated
 105 with accelerations of the movement.

106 [7] Landslides triggered by rainfall are generally caused
 107 by the buildup of subsurface water pressure. Many investiga-
 108 tions on rainfall-induced landslides have attempted to estimate
 109 minimum thresholds for initiation of landslides [Guzzetti
 110 *et al.*, 2007]. Our monitoring network gives us the opportu-
 111 nity to investigate the relation between rockfalls and rainfall,
 112 using a large data set of events with very accurate times. This
 113 study suggests the absence of any triggering threshold, and
 114 also allows us to analyze the time delay between rainfall,
 115 rockfall activity and slope movement dynamics.

116 2. Séchilienne Rockslide

117 [8] The Séchilienne landslide is located in the south-
 118 western Belledonne massif, one of the Paleozoic external
 119 crystalline massifs of the French Alps, which is divided in
 120 two major tectonic blocks: the external domain to the west
 121 and the internal one to the east. These two blocks are sep-
 122 arated by a major Late Paleozoic subvertical fault, known as
 123 the Belledonne Middle Fault. The southern part of the
 124 Belledonne massif is deeply incised by the east-west striking
 125 lower Romanche River valley (Figure 1). This incision results
 126 from the alternate activity of the Romanche River and the
 127 Romanche glacier, which developed repeatedly during the
 128 Quaternary glaciations [Montjuvent and Winistorfer, 1980].
 129 The resulting morphology displays very steep slopes, around
 130 35° to 40°, which are affected by large active or past gravi-
 131 tational movements in the micaschists. Eight major land-

slides have been reported in the area, including the large
 Séchilienne landslide which is affecting the south facing
 valley flank of the Romanche River.

[9] In the Séchilienne area, the valley slope consists
 mainly of micaschists with interbedded quartz-feldspar-rich
 layers, which were affected by both the Hercynian and
 Alpine orogenies. Due to this tectonic history, the micaschist
 bedrock is cut by several faults and three sets of near-
 vertical fractures [Pothérat and Alfonsi, 2001]. The global
 geometry of the hill displays a nested slide delimited at the
 top by a 20 to 40 m high scarp (the Mont-Sec scarp). This
 scarp presents a corner shape on the northeast limit of the
 landslide, and extends several hundred meters to the west
 and a few hundred of meters to the south. This scarp was
 studied using cosmic ray exposure dating data to provide
 chronological constraints on the failure time and kinematics
 [Le Roux *et al.*, 2009]. The part of the slope that exhibits
 more signs of current instability (high-motion zone; Figure 2)
 is located in the middle of the hill at an elevation of 600–
 900 m, and involves a rock volume estimated from geometric
 constraints to be about 3 to 5 million m³ [Giraud *et al.*, 1990].

[10] Sismalp seismological network has shown a con-
 centration of seismic sources along a strip which is parallel
 to the western edge of the Belledonne massif [Thouvenot
et al., 2003] and extends for more than 50 kilometers.
 Earthquakes are located at depths shallower than 10 km
 and focal solutions reveal a dextral strike-slip seismotec-
 tonic regime. Since the installation of Sismalp network in
 1989, the largest event detected on this fault is a $m_l = 3.5$
 earthquake, which occurred in 1999 only 7 km southwest
 of Séchilienne.

[11] The rockslide has been extensively instrumented and
 studied since 1988 thanks to the presence of a displacement
 monitoring system designed for surveillance and alert pur-
 poses [Evrard *et al.*, 1990; Duranthon *et al.*, 2003]. This
 instrumentation was supplemented by modeling computa-
 tions [Vengeon *et al.*, 1999; Pothérat and Alfonsi, 2001] and
 hydrological [Guglielmi *et al.*, 2002] and geophysical studies
 [Meric *et al.*, 2005]. In 1993–1994, a 240 m long gallery was
 excavated at an elevation of 710 m in a zone to the west
 of the high-motion zone (Figure 2) characterized by a dis-
 placement rate of about 5 cm/yr. Displacement measurements
 and observations inside the gallery showed a succession of
 rigid moving blocks delimited by highly fractured zones
 parallel to the main fracture set. These blocks exhibit differ-
 ential normal faulting movement. Unfortunately, the gallery
 did not reach sound rock, and the presence of a sliding
 surface is still an open question.

[12] All these studies suggest that the slope movements at
 Séchilienne are controlled by the principal discontinuities.
 The mass breaks into blocks, which are toppling or sliding.
 The rockslide has evolved from progressive damage to a
 potential large slide of unknown characteristics. Several
 investigation campaigns using geotechnical, geophysical,
 hydrogeological and dating methods were performed on this
 rockslide (see Meric *et al.* [2005] and Le Roux *et al.* [2009]
 for reviews). Guglielmi *et al.* [2002] used isotopic and
 hydrogeochemical methods to investigate groundwater flows.
 This study showed that the deep groundwater in the low part
 of the slope is partly recharged from a perched sedimentary
 aquifer, and that water flows very quickly (several cm/d)

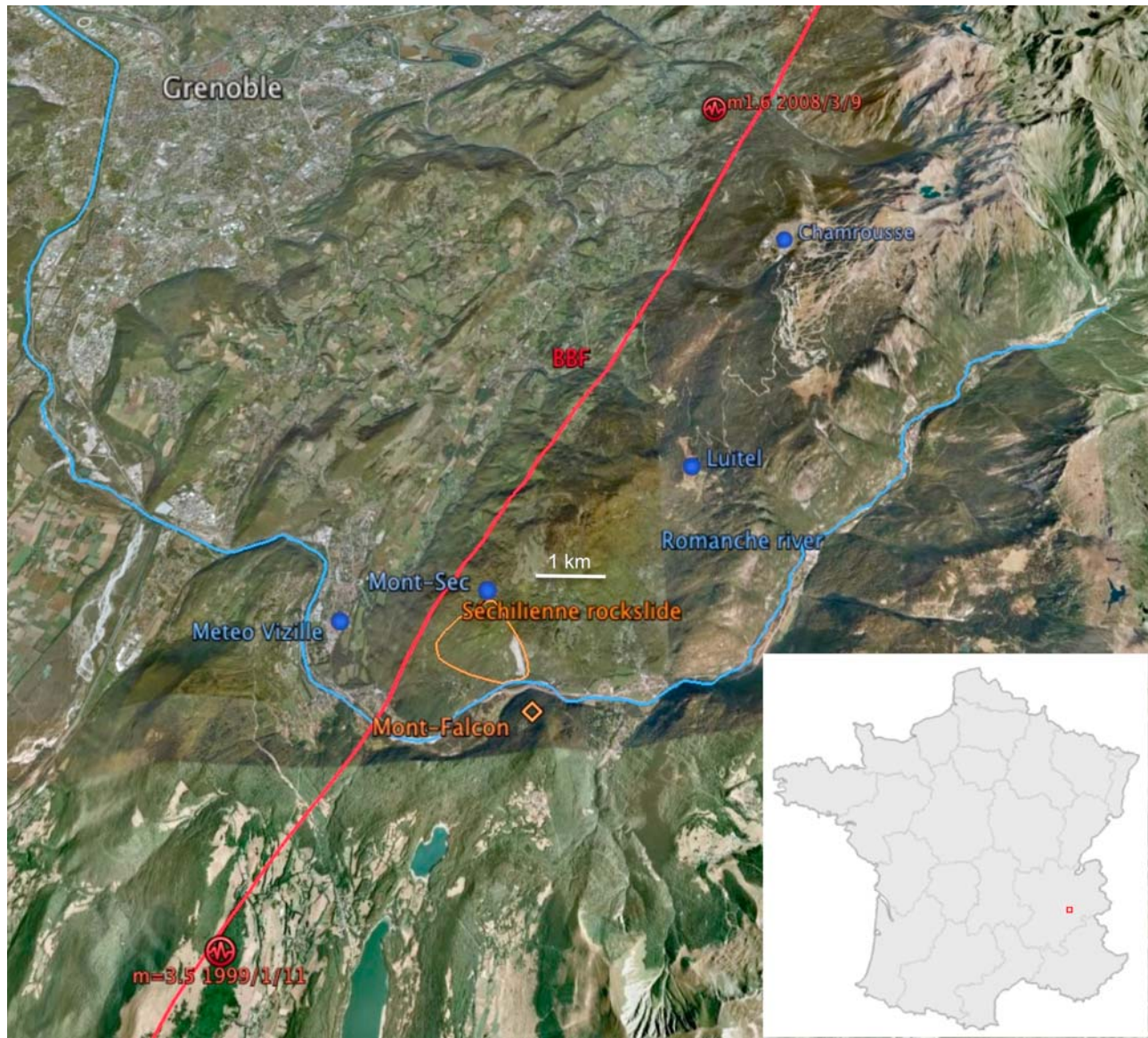


Figure 1. Location of Séchilienne rockslide, in the French Alps, about 15 km southwest of Grenoble, and contour of the rockslide. Also shown are the Belledonne Border Fault (solid line) and weather stations in the proximity of the rockslide (circles). The inset shows the location of Grenoble in France.

193 through the major fault set (oriented 20°N) affecting the rock
 194 mass. This analysis showed the existence of a deep saturated
 195 zone extending into the fractured metamorphic bedrock, with
 196 a probable 100 m thick vadose zone above. In case of inten-
 197 sive rainfall and prolonged water recharge, this vadose zone
 198 could be saturated for a short time, increasing the displace-
 199 ment rate. A major outcome of a multimethod geophysical
 200 study performed along various profiles [Meric *et al.*, 2005] is
 201 that all zones exhibiting signs of present-time or previous
 202 movements (collapse, toppling, sliding) are characterized by
 203 high electrical resistivity values ($\geq 3 \text{ k}\Omega.m$) and low P wave
 204 velocity values (2000 m/s), compared with the undisturbed
 205 zones (between a few hundred and 800 $\Omega.m$ for resistivity and
 206 more than 3000 m/s for P wave velocity). Combining surface
 207 observations and the geophysical results clearly shows that

the resistivity increase and the velocity decrease are associ- 208
 ated with a high degree of fracturing and with the formation of 209
 air-filled voids inside the mass. 210

[13] Despite all these studies, many questions are still 211
 open, particularly those related to the volume and the 212
 geometry of the rockslide, the deep hydrological context and 213
 the possibility of precursory events such as rockfalls and 214
 microseismicity. To address these issues, deep boreholes 215
 ($\geq 120 \text{ m}$) have recently been drilled and instrumented with 216
 inclinometers, piezometers and seismometers. Piezometers 217
 measure fluid pore pressure and water level. Seismometers 218
 at depth could help to better constrain the depth of seismic 219
 events and consequently to locate more precisely seismo- 220
 genic zones. In addition, the Séchilienne rockslide is part of 221
 a National Observatory in France (denoted “OMIV”), which 222

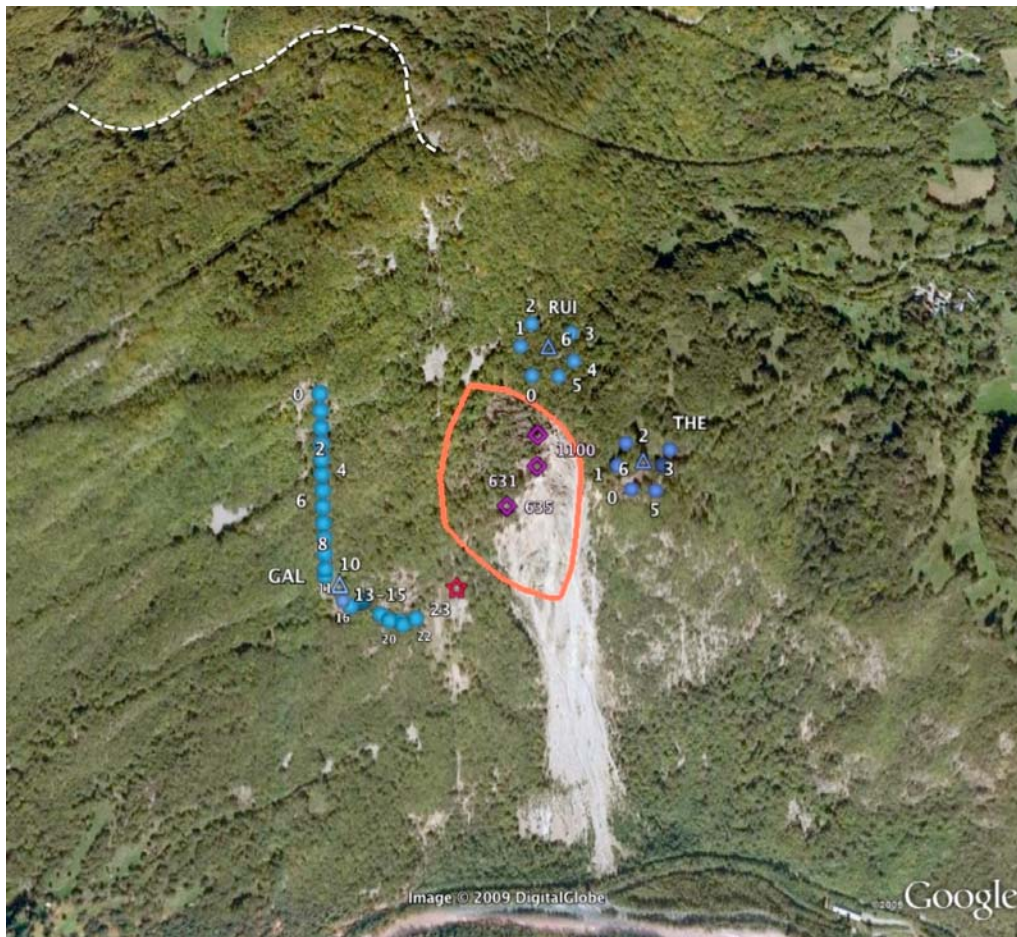


Figure 2. Seismic network: vertical sensors (circles) and 3-component seismometers (triangles) for the 3 stations. Also shown are the locations of benchmarks of the displacement network (diamonds) and the location of a shot on 24 June 2008 (red star). The orange contour shows the limit of the most active zone. The white dashed line shows the Mont-Sec scarp.

223 aims at continuously monitoring several active landslides
 224 with different techniques (seismology, geodesy, remote
 225 sensing, hydrology).

226 3. Monitoring Network

227 3.1. Displacement

228 [14] A surveillance and alert system based on displacements
 229 measurements (laser, radar, extensometers, inclinometers,
 230 strainmeters, GPS) was set up and progressively suppl-
 231 mented from 1985 [Evrard *et al.*, 1990; Effendiantz and
 232 Duranthon, 2002; Duranthon *et al.*, 2003; Duranthon and
 233 Effendiantz, 2004; Lemaitre *et al.*, 2004; Kasperski, 2008].
 234 This very dense system has allowed delimitation of zones in
 235 movement and their evolution for more than 20 years. It
 236 notably has shown that the displacement rate of the most
 237 active zone has increased up to 1.4 m/yr in 2008, more than
 238 twice the mean rate observed before 2000. The other regions
 239 exhibit displacements generally lower than 10 cm/yr. In
 240 addition, a camera and video have been installed in June 2009
 241 to detect and characterize rockfalls, and to estimate dis-
 242 placement from the comparison of successive images.

3.2. Seismic Network

[15] The seismic network was progressively installed from
 May 2007. It consists of three seismological stations and
 various receivers, whose locations are shown in Figure 2.
 Two stations denoted “THE” and “RUI” were first installed
 in May 2007. Each station was connected to 6 vertical 2 Hz
 velocity sensors and one 3-component 2 Hz velocimeter.
 Station RUI is now located just above the most active zone.
 Before April 2008, it was located 50 m downward, and one
 sensor was located below the scarp which borders the main
 active zone. This sensor displayed a very large resonance
 around 15 Hz, which made it difficult to correlate the signals
 with the other sensors outside the active zone. To enlarge
 their frequency sensitivity toward low frequencies, all sen-
 sors were replaced in April 2009 by broadband 0.05 Hz
 NoeMax velocimeters. The typical distance between sensors
 for these two stations is 50 m. In addition, a 24-channel
 station, denoted “GAL” (Figure 2), was later installed in
 April 2008 in the 240 m long survey gallery on the western
 side of the most active zone. It was connected to 4.5 Hz
 geophones (21 vertical sensors and one 3 component), with
 an intertrace of 20 m. Among them, 11 sensors were installed

265 within the gallery and 10 outside the gallery in the eastern
 266 direction (Figure 2).

267 [16] Stations THE and RUI were first recording data in
 268 triggering mode, with a STA/LTA threshold fixed to 3, and
 269 a 250 Hz sampling frequency. This setting was changed in
 270 April 2008 to a continuous mode. Sampling tests conducted
 271 over a short period with a higher sampling frequency (1 kHz)
 272 showed the near absence of seismic energy above 100 Hz.
 273 For station GAL, due to the larger number of channels, the
 274 station is working in trigger mode to limit the amount of
 275 data recorded. However, a higher sampling rate of 500 Hz is
 276 being used, because we thought that small high-frequency
 277 microearthquakes may occur close to the end of the 240 m
 278 gallery near the base of the rockslide. Until now, however,
 279 most events were first detected by the channels located out-
 280 side the survey gallery and present little energy above 50 Hz.

281 4. Detection and Classification of Seismic Signals

282 [17] Since the installation of the first two stations in May
 283 2007, several thousands events have been recorded by each
 284 station. A semiautomatic software has been developed to
 285 detect and classify events. All events are then visually ana-
 286 lyzed to separate natural local events from regional or
 287 worldwide earthquakes, and to reject events classified as
 288 noise (helicopters, industrial noise, storms). The catalogs of
 289 events are available on the OMIV web site: <http://www-iglit.>
 290 [obs.ujf-grenoble.fr/observations/omiv/SECHILIENNE](http://www-iglit.obs.ujf-grenoble.fr/observations/omiv/SECHILIENNE).

291 4.1. Detection of Seismic Signals

292 [18] The detection of seismic signals is based on the
 293 spectrogram of the signal, averaged over all sensors of a
 294 seismic antenna (see Figure 3, right). We estimate the
 295 amplitude of the spectrogram stacked in the frequency range
 296 1–50 Hz, as a function of time. An event is identified when
 297 this function exceeds 3. The event starting time and duration
 298 are first defined by the time interval during which the spec-
 299 trogram amplitude stays above the noise level. This definition
 300 leads to a large number of events with very short interevent
 301 times. For instance, a rockfall event may be divided into
 302 several events corresponding to successive rock impacts.
 303 Consequently, all events with interevent time smaller than
 304 their duration are regrouped as a single event.

305 4.2. Location of Seismic Signals

306 [19] Event location is difficult because most recorded
 307 signals lack impulsive waves so that a satisfying time
 308 picking of first arrivals is almost impossible (see Figure 3),
 309 even for large amplitude signals. Instead, one can use cross
 310 correlation of signals recorded at different sensors in order
 311 to precisely measure time delays between sensors, or beam-
 312 forming methods [Almendros *et al.*, 1999]. The latter
 313 amounts to looking for the source point which maximizes the
 314 intertrace correlation, averaging over all couples of sensors
 315 and after shifting traces in time by the travel time. A second
 316 difficulty concerns distinguishing P from S waves, because
 317 of the small distances between the source and the sensors
 318 and of the lack of high-frequency waves. For distances of a
 319 few hundred meters, the time delay between P and S waves
 320 is a few hundredths of a second, of the order or even shorter
 321 than the dominant period of the signal (generally between

10 and 20 Hz), so that P and S waves overlap. In the absence
 of a precise 3-D velocity model, a uniform velocity was used.
 The source depth was constrained to lie at the ground surface
 and velocity was inverted in the interval 1000–4000 m/s.

[20] Clearly, a uniform velocity model is not realistic in
 such an heterogeneous rockslide, and in many cases this
 simple model was not able to correctly explain the observed
 time delays between sensors. Indeed, 2-D seismic tomog-
 raphy studies realized by *Meriç et al.* [2005] have shown a
 very complex structure. P wave velocity varies laterally and
 with depth, ranging from about 500 m/s to almost 4000 m/s
 in undisturbed areas. A correct 3-D velocity model is thus
 required in the future to better locate seismic signals. This
 represents a challenging task in such an heterogeneous and
 mountainous area and will be obtained from supplemental
 active seismic profiles, which must be performed on a larger
 scale in order to build a deeper 3-D velocity model. In this
 work, we do not present the preliminary results on event
 location. Nevertheless, event location was routinely esti-
 mated and used to better discriminate seismic signals. For
 instance, distant earthquakes can be recognized by their high
 apparent velocity due to their large dip angle. Rockfalls can
 be identified by their azimuth evolving during their propa-
 gation, which is consistent with a source moving downward
 along the rock debris corridor [*Helmstetter et al.*, 2008].
 Events which could not be successfully located (averaged
 intertrace correlation less than 0.5) were rejected as probable
 noise events.

4.3. Different Types of Signals

[21] Figure 3 presents a selection of ten signals of dif-
 ferent types. Data have not yet been deconvolved by the
 instrument response so signal amplitude is given in counts
 (see peak amplitude in the caption of each plot). For each
 signal, we show the seismogram for the whole event dura-
 tion and for a window of 5 s around the peak amplitude, and
 a spectrogram. The first four examples are rockfalls. Events
 from Figures 3f–3i are local microearthquakes. Seismic
 signals displayed in Figure 3e originated from an explosion
 performed using a charge of 1 kg located at 1 m depth, 350 m
 away from the sensor across the most active zone (Figure 2).
 The charge used corresponds to a magnitude of about 0.3
 [*Brocher*, 2003]. The peak amplitude for this shot was $A =$
 6620 counts, about half the amplitude of the largest recorded
 microearthquake, shown in Figure 3g with $A = 14100$.
 Because this event was likely located in the most active zone,
 closer to the sensor but with an amplitude twice as large, its
 magnitude should be close to the one deduced from the shot,
 around 0.3. The last signal is an earthquake of magnitude
 $m_l = 1.6$, detected by Sismalp and located about 12 km
 north of the rockslide. None of the local signals recorded at
 Séchilienne has been detected by Sismalp, although the
 closest station is about 20 km away. Even the 23 November
 2006 rockfall, with a volume of about 40,000 m³ [*Kasperski*,
 2008], was not detected by Sismalp.

4.3.1. Rockfalls

[22] Most natural local seismic events recorded corre-
 spond to rockfalls, which are frequent at Séchilienne,
 especially in the rock corridor located around the frontal
 zone. A 40,000 m³ rock avalanche occurred in this area in
 November 2006 [*Kasperski*, 2008]. Since the installation of

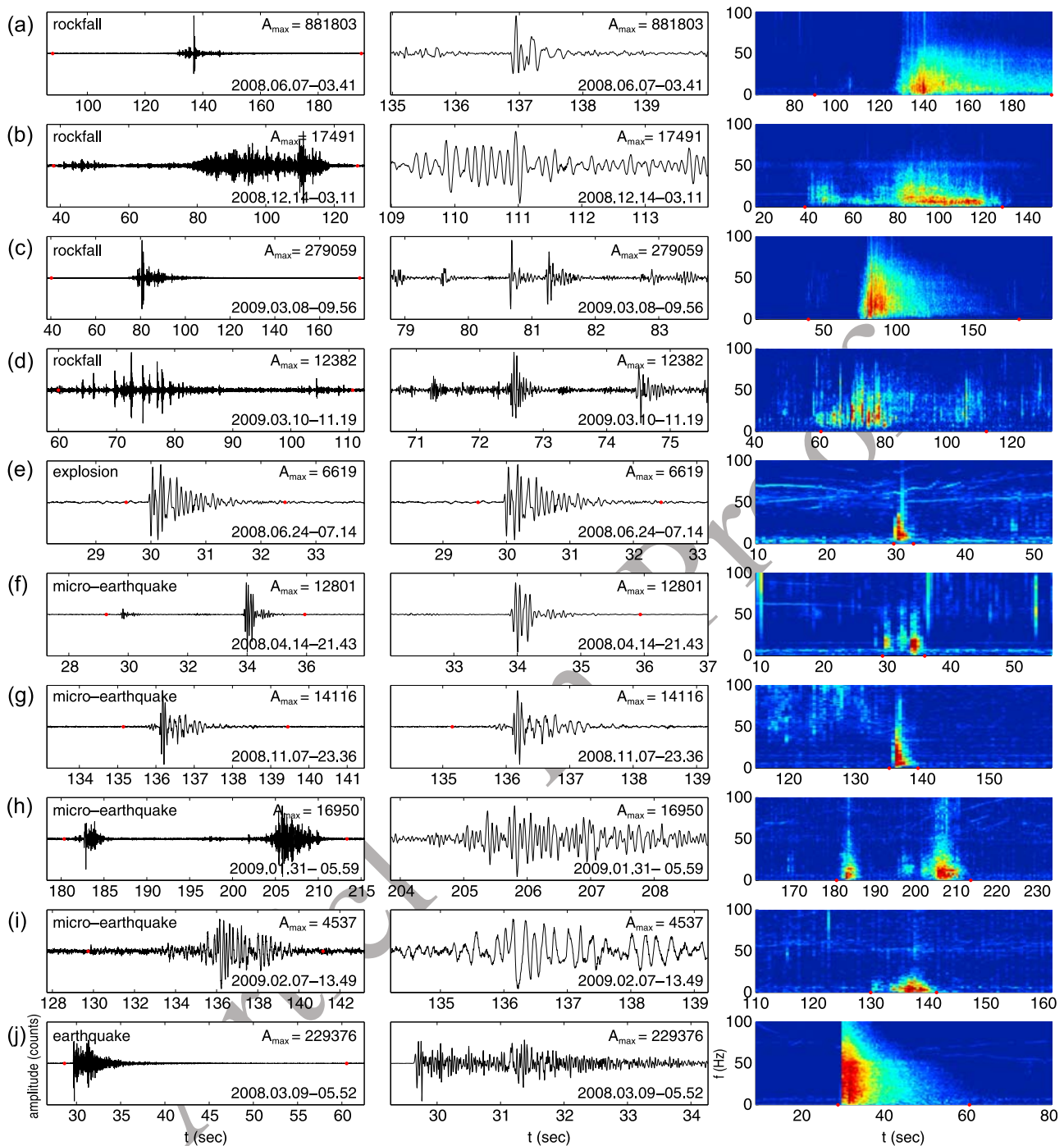


Figure 3. (a–j) A selection of different types of signals. (left) Seismograms recorded for channel 0 of station THE and (middle) zoom for a window of 5 s around the peak of amplitude. The maximum amplitude (in counts) is given in the top right corner of each plot. (right) Spectrograms (log amplitude scale) averaged over all vertical channels of station THE. Dots indicate the start and end of each event.

382 the seismic network, only a rockfall of about 250 m³ has
 383 been observed by people in charge of the surveillance and
 384 though reported as having occurred in July 2008, the exact
 385 date of this event is unknown. It may correspond to one of
 386 the largest events, recorded on 14 July with a peak ampli-
 387 tude of $A = 165,000$. Other rockfalls of this size may have
 388 occurred without having been reported, particularly if they

occurred in zones with dense vegetation or if they presented
 389 less spread. The largest rockfall recorded occurred on 7 June
 390 2008, with an amplitude $A = 882,000$ (see Figure 3a), but
 391 there was no reported observation of rockfall around this
 392 date. Seismic signals present generally a broad spectrum,
 393 sometimes spanning the full 1–125 Hz available range. 394
 Smaller events exhibit the highest energy around 20 Hz, 395

396 while larger events present a peak below 10 Hz. Some
 397 events, such as the one in Figure 3b, have little energy above
 398 20 Hz. The low-frequency spectral content of these events
 399 may be due to the larger distance from the stations, because
 400 they are located further down the debris corridor and high-
 401 frequency waves are attenuated faster, particularly in such a
 402 fractured and heterogeneous medium. Low-frequency events
 403 are generally located south of station THE, while the large-
 404 band signals are generally located west or southwest from
 405 this station, likely within the upper part of the debris cor-
 406 ridor. The differences in frequency content may also be
 407 explained by differences in entrained materials, i.e., debris
 408 flows instead of rockfalls or by different propagation con-
 409 ditions. Indeed, in the upper part of the corridor, rocks often
 410 hit the ground and rebound, producing distinct impulsive
 411 peaks in the seismograms, while in the lower part of the
 412 corridor rocks tend to roll and to trigger other small rock-
 413 falls, or burst into smaller rocks.

414 [23] In general, event durations are of the order of several
 415 tens of seconds. Some events are shorter either because
 416 rocks do not fall all the way down the corridor or because
 417 later impacts are too weak to be detected. The longest events
 418 lasted for several minutes, because several avalanches
 419 overlap, or because rocks fall continuously from the upper
 420 slopes. The smallest events are difficult to distinguish from
 421 microearthquakes because there is only one or a few peaks.
 422 By default, local natural events were classified as rockfalls,
 423 so the classification is often inaccurate for low-amplitude
 424 signals.

425 [24] With the intention of calibrating our network for
 426 small events, a small rock of dimensions about $0.5 \times 0.5 \times$
 427 0.2 (small volume of 0.05 m^3 selected for security reasons)
 428 was thrown from the upper part of the rock corridor in order
 429 to compare the recorded signal with natural events. The
 430 corresponding seismogram is shown in Figure 3d. In terms
 431 of amplitudes, the peak was 12,000, much smaller than the
 432 largest recorded rockfall. The corresponding seismogram
 433 shows several distinct events associated with successive
 434 rock impacts. The rock fell for about 30 s over a distance of
 435 about 400 m. The following peaks in the seismograms (after
 436 100 s) are due to other small rocks falling down another part
 437 of the rock corridor. Compared with the natural events
 438 shown in Figures 3a–3c, this event does not show a long-
 439 period prolonged ringing. This could be because it involved
 440 only one block, while large natural events likely involve
 441 many blocks. However, we also observed natural events
 442 which displayed characteristics similar to those of the
 443 experimental rockfall.

444 [25] Assuming rockfall volume is proportional to peak
 445 amplitude, as suggested by *Norris* [1994], the largest recorded
 446 rockfall would have a volume around 4 m^3 . This volume
 447 appears very small because much larger events are known
 448 to have occurred since the network installation. This vol-
 449 ume may be underestimated if either natural events occurred
 450 farther away from the seismometer (most probable) or if
 451 rockfall volume increases more rapidly than seismic peak
 452 amplitude. The video camera, installed in June 2009 and
 453 facing the landslide, should enable us to calibrate the seismic
 454 network. It will allow us to estimate the nature of the materials
 455 involved (rockfalls or debris flow) and to study the relation
 456 between the involved volume and the recorded signal

amplitude and frequency content. This requires events large
 enough to be observed with the video camera, occurring
 during a day without clouds.

4.3.2. Local Microearthquakes

[26] Microearthquakes can be distinguished from rockfalls
 by their shorter duration, typically a few seconds. Examples
 are shown in Figures 3f–3i. They have about the same fre-
 quency content, although the largest events exhibit generally
 more energy at low frequencies (below 10 Hz) than rockfalls.
 There is also a large variability of signal waveform, duration
 and frequency content. Some events, such as the one shown
 in Figure 3g, exhibits waveform characteristics rather similar
 to the shot shown in Figure 3e in terms of duration, fre-
 quency content and amplitude. The largest arrival of this
 quake is preceded by an emergent signal, starting about 0.2 s
 before, of much weaker amplitude. Other events consist of
 several subevents, separated by about 1 s or longer. Examples
 are shown in Figures 3f and 3h.

[27] Compared to distant earthquakes (see the largest one
 recorded in Figure 3j), microearthquakes lack high-frequency
 waves. This low-frequency content may be due to the source
 of these events or to the strong attenuation of high-frequency
 waves within the fractured zone. These events may be asso-
 ciated with water flow within the fractures, similar to long-
 period earthquakes induced by magma flow on volcanoes.
 Another possibility is that this unusually low frequency
 content results from low rupture velocities combined with
 strong path effects due to their shallow sources, as first sug-
 gested by *Harrington and Brodsky* [2007] for volcanic
 earthquakes. Other microearthquakes exhibit a broadband
 spectrum, comparable with distant earthquakes. They occur
 either individually or as a sequence of a few events, with
 interevent times of about 1 s (see Figure 3g). Micro-
 earthquakes can be distinguished from distant earthquakes by
 their absence of distinct P and S waves and by their lower
 apparent velocities, because of their shallower depth. Most
 local events (microearthquakes or rockfalls) have an apparent
 velocity of about 2 km/s, while for earthquakes $V > 4 \text{ km/s}$
 due to their higher dip angles.

4.3.3. Distant Earthquakes

[28] Many small earthquakes have been recorded, 773 in
 less than 2 years. About half of these events have also been
 detected by the Sismalp regional network. Most of the
 missing events are nearby earthquakes, with interevent times
 between P and S waves in the range of 0.5–2 s, corresponding
 to a distance of about 4–16 km. Their magnitudes are likely
 smaller than 1, which is the detection threshold of Sismalp
 network in this area. As mentioned before, the Séchilienne
 rockslide is located within an active seismogenic zone close
 to the Belledonne Border fault [*Thouvenot et al.*, 2003]. So
 far, the largest signal recorded by our network is the 2008/3/9
 $m_l = 1.6$ earthquake, located about 12 km to the northwest.
 It is displayed in Figure 3j. Before the installation of the
 seismic network, a $m_l = 3.5$ earthquake occurred about 7 km
 southwest of Séchilienne, on the southwestern ending of the
 Belledonne fault, followed by a $m_l = 2.8$ event in October
 2005 [*Thouvenot et al.*, 2003]. The mean recurrence time of
 a $m \geq 6$ earthquake on this fault has been estimated to be
 about 10,000 years. As it could occur only 1 km away from
 the landslide, any risk assessment study should account for
 possible triggering of the rockslide by an earthquake.

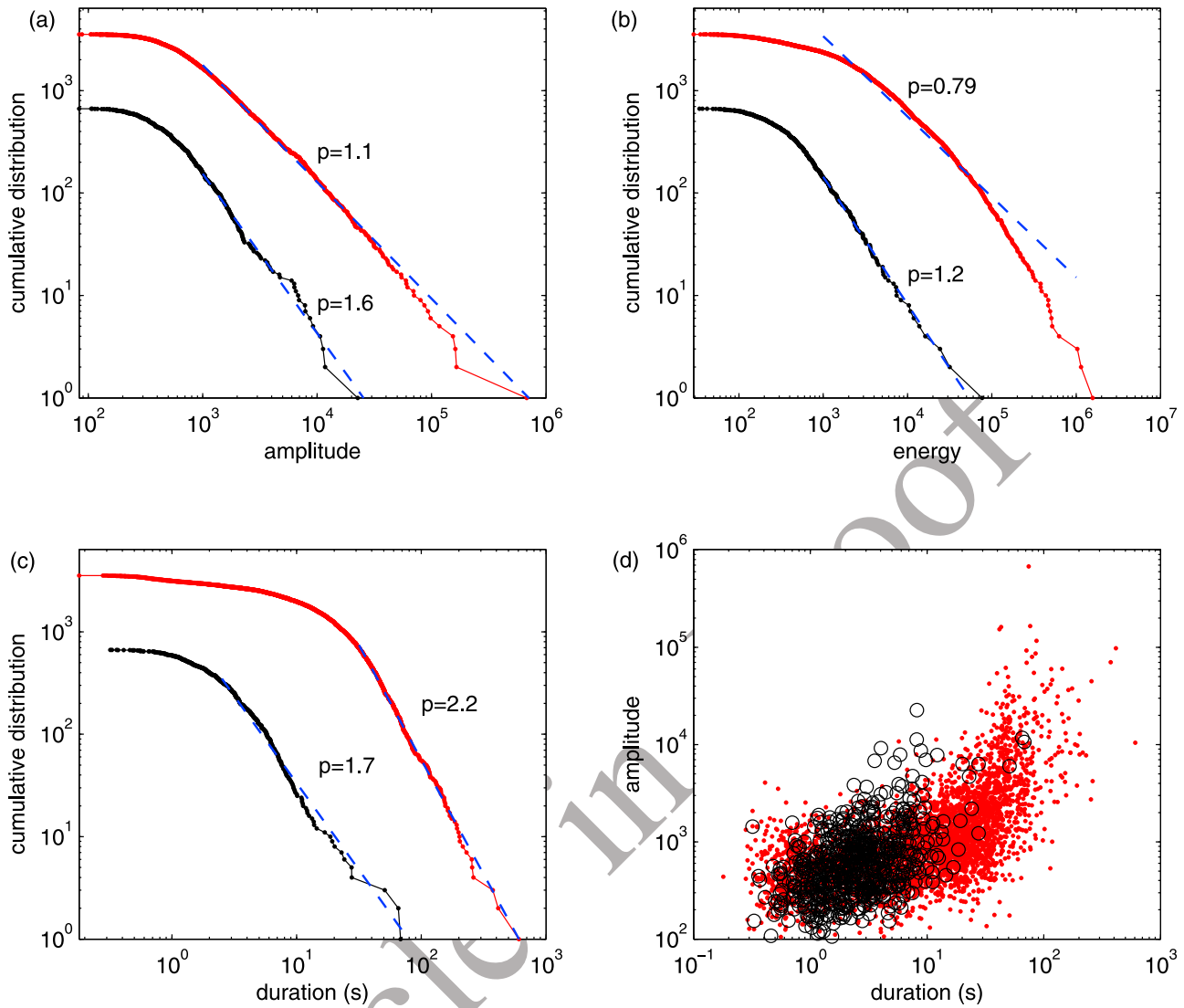


Figure 4. (a) Distribution of the peak amplitude A of rockfalls (red curve) and microearthquakes (black) and fit by a power law for $A > 1000$ (slope exponent is given in the plot), (b) distribution of signal energy (signal envelope integrated in time) for rockfalls (red curve) and microearthquakes (black) and fit by a power law for $E > 1000$ (see slope exponent in the plot), (c) distribution of event duration for rockfalls (red curve) and microearthquakes (black) and fit by a power law, and (d) relation between peak amplitude and signal duration for rockfalls (red dots) and microearthquakes (black circles).

518 **4.4. Distribution of Signal Amplitude, Duration,**
 519 **and Energy**

520 [29] Figure 4a presents the distribution of signal amplitudes
 521 for rockfalls (type R) and microearthquakes (type Q). The
 522 amplitude was estimated after low-pass filtering seis-
 523 grams below 50 Hz, and after averaging maximum amplitude
 524 of all 7 vertical channels of station THE. The distribution
 525 follows a power law for amplitudes larger than 1000. For
 526 smaller events, the curvature is likely due to the incom-
 527 pleteness of the catalog because of temporal fluctuations of
 528 the noise level. The slope exponent is 1.1 for rockfalls and
 529 1.6 for quakes. These exponents can be compared to the b
 530 value of the Gutenberg-Richter distribution of earthquake
 531 magnitudes, $b \approx 1$, if we assume that most events are

532 located at about the same distance from the station so that
 533 amplitude variations according to distance from the source
 534 are limited and do not modify the shape of the distribution
 535 [Weiss, 1997].

536 [30] Figure 4b shows the distribution of energy, defined as
 537 the envelope of the signal integrated over event duration.
 538 For quakes, the distribution can be fitted by a power law of
 539 exponent 1.4, while for rockfalls, the distribution is curved
 540 in a log-log plot over the whole interval, and cannot be
 541 fitted by a power law.

542 [31] The distribution of signal durations is shown in
 543 Figure 4c. It can be fitted by a power law over a limited
 544 interval; for microearthquakes longer than 2 s and for rock-
 545 falls with duration larger than 30 s. For rockfalls, this duration

546 of 30 s corresponds to the time taken for a rock to fall from
 547 the upper part of the corridor down to the valley. Longer
 548 events are sequences of rockfall avalanches with interevent
 549 times smaller than their duration (which were therefore
 550 counted as a single event). Microearthquakes with duration
 551 longer than 5 s are generally sequences of shorter subevents.
 552 The relation between peak amplitude and duration for quakes
 553 and rockfalls is shown in Figure 4d. Rockfall duration may
 554 be underestimated for small rockfalls, because only the
 555 more energetic impacts are above the detection threshold.
 556 Also, as distinguishing quakes from rockfalls is difficult for
 557 small events, they were classified as rockfalls by default.
 558 The amplitude-duration relation is rather similar for quakes
 559 and rockfalls, but the largest quakes exhibit a shorter duration
 560 than rockfalls with the same peak amplitude.

561 **5. Influence of Rainfall on the Rockslide**
 562 **Dynamics**

563 **5.1. Meteorological Data**

564 [32] At least 5 meteorological stations or rain gauges are
 565 located within 10 km of the rockslide (Figure 1). The closest
 566 station (maintained by CETE Lyon) is located at Mont-Sec,
 567 but presents several gaps in the data, and has a large sampling
 568 time of 1 day, leading us to preferentially use other rain
 569 gauges. The Luitel rain gauge is located 4 km northeast from
 570 the landslide at a higher elevation (1280 m). It is maintained
 571 by the “Laboratoire d’étude des Transferts en Hydrologie
 572 et Environnement,” and data are available since July 2007.
 573 This is our preferred station because it has a fast sampling
 574 time of 15 min with few gaps in the data. Another gauge
 575 is located at Vizille, about 3 km west from the rockslide
 576 at an elevation of 290 m. It has a sampling time of 5 min
 577 and was placed in operation in September 2007 ([http://
 578 pagesperso-orange.fr/meteo.vizille](http://pagesperso-orange.fr/meteo.vizille)). The last station is located
 579 at Chamrousse, about 10 km to the northeast of the rockslide
 580 at an elevation of 1860 m. It is part of Meteo France network
 581 and has been working with few gaps since the installation of
 582 our network, with a sampling rate of 1 h. It was used to fill in
 583 the gaps observed at other stations. We tested every meteo-
 584 rological station to analyze the influence of station location on
 585 the correlation between landslide dynamics and precipitation.
 586 Only weak differences were found.

587 **5.2. Temporal Evolution of Microseismicity, Rockfall**
 588 **Activity, Rockslide Movement, and Weather**

589 [33] Figure 5 illustrates the temporal variability of the
 590 rockslide dynamics since the installation of the seismic
 591 network in May 2007. All events detected by station THE
 592 are shown in Figure 5a, but only events with amplitude
 593 larger than 500 were used to estimate the daily rate dis-
 594 played in Figure 5b. Quakes and rockfalls occur in bursts of
 595 activity, lasting for a few days, and appear very often cor-
 596 related with rainfall (Figure 5d) and acceleration of the
 597 rockslide displacement (Figure 5c). Quakes generally occur
 598 during episodes of rockfalls, but rockfalls were relatively
 599 more frequent in June 2007 and June 2008, and quakes
 600 occurred more frequently and continuously in the winter
 601 2008 (see cumulative number of events in Figure 5b). This
 602 may be due to continuous snowmelt inducing continuous
 603 water flow within the rockslide.

[34] Rockslide movement also fluctuates with time. 604
 Figure 5c shows the displacement rate of benchmark 635, 605
 located in the most active zone (Figure 2). This is one of the 606
 most rapidly moving targets that presents no gaps during the 607
 time period considered, except after March 2009, because 608
 data are not yet available. Daily displacement rate increases 609
 almost instantaneously following rainfall [Alfonsi, 1997; 610
Duranthon and Effendiantz, 2004], and decreases back to its 611
 mean value within about 2 months. The temporal evolution 612
 of displacement rate has been successfully modeled by 613
Alfonsi [1997], assuming that velocity increases with the 614
 amount of water (rainfall or snow, decreased by evapotrans- 615
 piration) received by the rockslide, and that the groundwater 616
 table decreases exponentially with time in the absence of 617
 precipitation. However, seasonal variations of the hydrolog- 618
 ical parameters are required in order to correctly model the 619
 observations. 620

5.3. Thresholds for Rainfall Triggering? 621

[35] Correlation between rainfall and rockfalls is not 622
 striking when looking at the temporal evolution of rainfall 623
 and daily rates of rockfall in Figure 5. Using traditional dia- 624
 grams showing rainfall intensity versus duration, introduced 625
 by *Caine [1980]*, is not very helpful. *Caine [1980]* first 626
 plotted each landslide occurrence in a diagram showing the 627
 precipitation at the time of each event as a function of the 628
 rainfall duration, for a catalog of worldwide shallow land- 629
 slides and debris flows. He observed that all events occurred 630
 above a threshold I_r (in mm/h) defined by $I_r = 14.82 D^{-0.39}$, 631
 where D is the storm duration in hours. Such a plot is 632
 shown in Figure 6 (circles) for all rockfalls recorded with 633
 amplitude greater than 500. A rainfall episode is considered 634
 finished as soon as there is a gap of 1 day without rain. It is 635
 impossible to define a minimum threshold for triggering from 636
 Figure 6. Most events occur for zero or very small rainfall 637
 intensities, and consequently no apparent relation can be 638
 derived between the density of events and the rainfall inten- 639
 sity or duration. 640

[36] Other types of thresholds have been proposed using 641
 the rain accumulated from the beginning of the rainfall until 642
 the landslide occurs, or the total rainfall stacked over a period 643
 of a few days up to a year before the landslide occurs, or more 644
 complex physically based thresholds (see *Guzzetti et al.* 645
 [2007] for a recent review). Similar results were found 646
 when replacing the hourly rainfall by the cumulated rainfall 647
 before the event. A problem arising with these thresholds is 648
 that, when new data are added to the database, landslides 649
 may be observed for rainfall conditions lower than the min- 650
 imum threshold, so that a new threshold has to be defined 651
 [Chleborad et al., 2006]. Thresholds describe the mini- 652
 mum rainfall above which landslides may occur. A maximum 653
 threshold is sometimes introduced to give the maximum 654
 rainfall above which landslides always occur. But this 655
 approach does not tell us how likely landslides are between 656
 the minimum and maximum thresholds. Also, only landslides 657
 triggered by rain are considered in these studies, giving up 658
 those which were triggered by earthquakes or by an unknown 659
 mechanism. 660

[37] Few studies have attempted to quantify the probability 661
 of landslide occurrence as a function of rainfall properties 662
 (either rainfall duration, intensity, or cumulated rainfall, or a 663

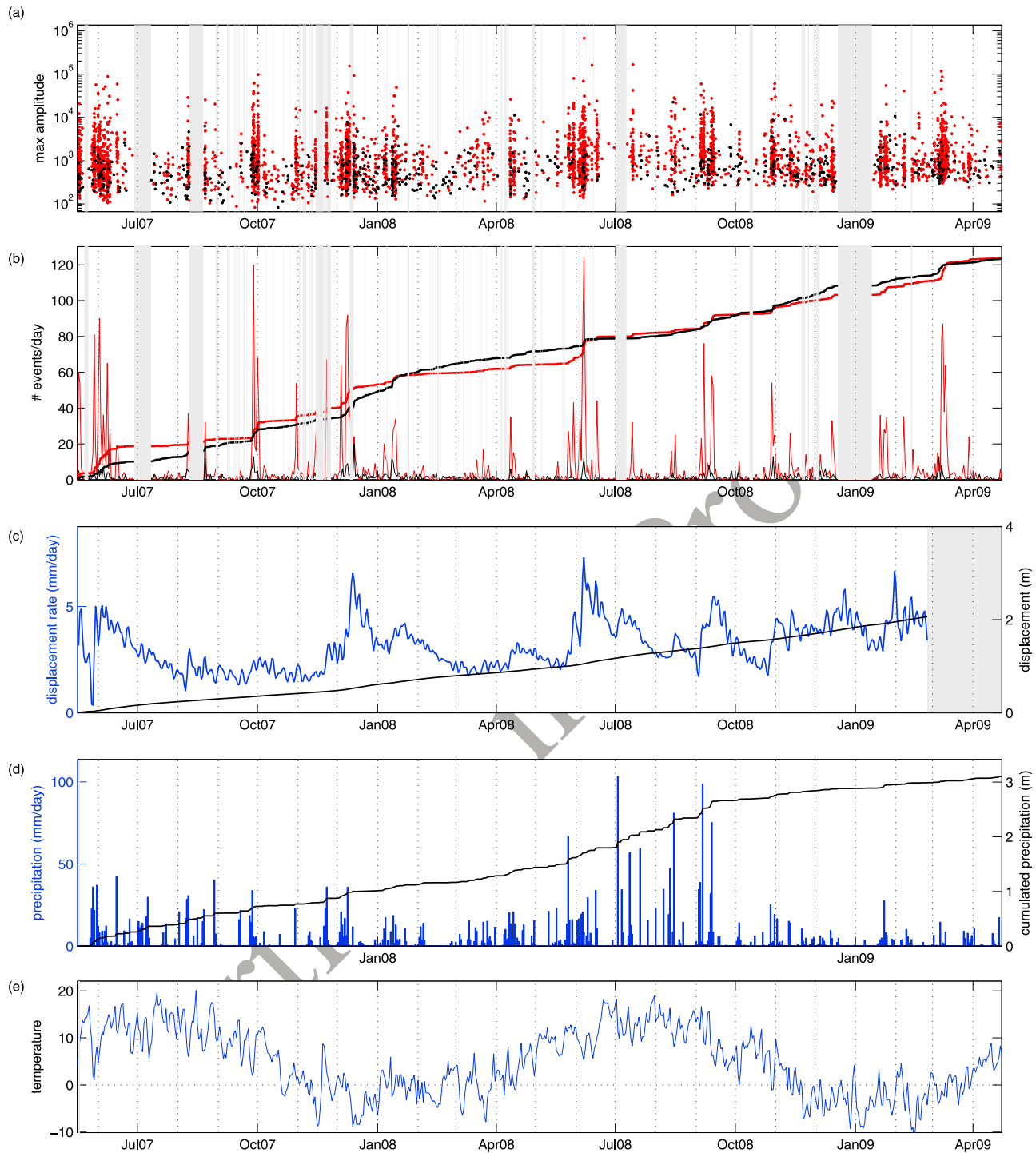


Figure 5. (a) Time series of event peak amplitude for rockfalls (red dots) and microearthquakes (black dots). Gray areas indicate gaps in the monitoring. (b) Daily rates of rockfalls (red) and microearthquakes (black) and normalized cumulated number (smooth red and black lines). (c) Displacement rate (blue line) and displacement (black) of benchmark 635 (data are not yet available after March 2009). (d) Daily and cumulated rainfall and (e) daily average temperature recorded at Luitel meteorological station.

664 combination of these parameters). *Glade et al.* [2000] have
 665 estimated this probability as a function of daily rain at the
 666 time of the landslide and as a function of the “antecedent
 667 daily rainfall index.” *Guzzetti et al.* [2007] also estimated
 668 the probability of landslide occurrence as a function of rain-

fall duration and intensity. In section 5.4, we use a model
 669 inspired by the “Antecedent Daily Rainfall” model of
 670 *Glade et al.* [2000] in order to quantify the probability of
 671 rainfall triggering at Séchilienne.
 672

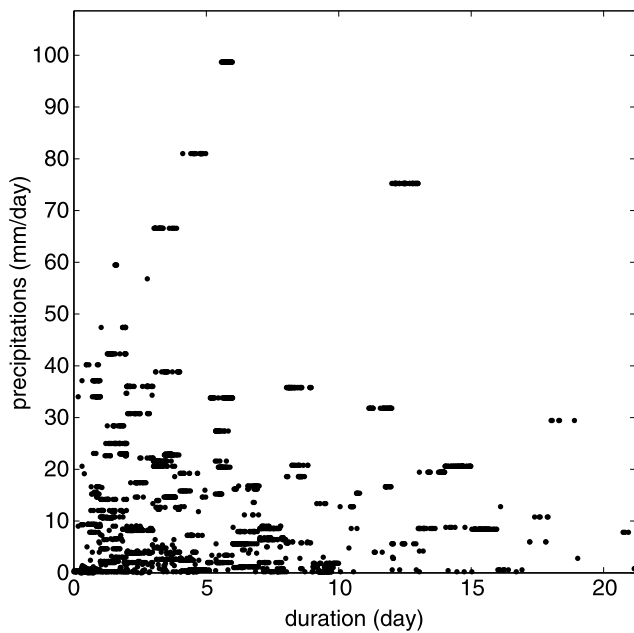


Figure 6. Rockfall occurrence (events with $A > 500$) as a function of the duration of the rainfall episode until each event and of the daily rainfall at the time of the event.

673 5.4. Antecedent Rainfall Water Model

674 [38] We have modeled the observed temporal variations
 675 of rockfall activity using a method inspired by the Ante-
 676 cedent Daily Rainfall model [Crozier and Eyles, 1980;
 677 Glade et al., 2000]. We define the cumulated rainfall index
 678 P_c at time t_i by

$$P_c(t_i) = \sum_{j=0:i} P(t_j) \exp(-(t_i - t_j)/t_c). \quad (1)$$

679 P_c is the sum of hourly rainfall, and rainfall of all previous
 680 hours with a weight exponentially decreasing with time.
 681 This model accounts for the decay of the amount of water
 682 with time due to drainage. The rate of rockfall activity $R(t)$
 683 is then assumed to vary linearly with P_c . Only events with
 684 $A > 500$ were used together with rainfall data measured at
 685 Luitel meteorological station, with a sampling rate of 1 h.
 686 We estimate the characteristic time $t_c = 0.25$ day by maxi-
 687 mizing the linear correlation coefficient between $R(t)$ and
 688 $P_c(t)$.

689 [39] Results are shown in Figures 7 and 8. Figure 7 compares
 690 the time series of rainfall, cumulated rainfall, and number of
 691 rockfalls per hour, for a time window of one month in
 692 September 2008. Peaks of rockfall activity are rather well
 693 correlated with cumulated rainfall, although some events
 694 have occurred in the absence of rainfall. Figure 8 shows
 695 the correlation between the number of events per hour and
 696 rainfall. When looking at the raw rainfall data as a function
 697 of number of rockfalls (hourly rainfall or $P_c(t)$, shown as
 698 crosses in Figures 8a and 8b), the correlation is not obvious.
 699 There are indeed large fluctuations of the number of rockfalls
 700 for the same rainfall value. But when averaging the number
 701 of rockfalls for different classes of rainfall (using a sam-

pling bin size of 1 mm), we now better observe an increase
 in rockfall activity with precipitation (dots in Figures 8a and
 8b), which becomes stronger when looking at cumulated
 rainfall rather than hourly rainfall.

[40] Using all hourly values of rate and rainfall (crosses in
 Figures 8a and 8b), the correlation between $R(t)$ and $P_c(t)$ is
 0.36, a little larger than the correlation with hourly precipi-
 tation, equals 0.25. Taking into account antecedent rainfall
 in the model thus improves the correlation between rockfall
 activity and rainfall. In both cases this correlation is highly
 significant, the probability of getting the same correlation by
 chance being almost zero. However, if we fit the data after
 averaging in classes of rainfall values (i.e., fitting the red
 curve with dots in Figures 8a and 8b), the correlation is then
 only significant for cumulated rainfall. This approach gives
 the same weight to any rainfall interval, while fitting the raw
 data of $R(t)$ and $P_c(t)$ gives the same weight to each time
 interval, so mostly to small rainfall values. After increasing
 for rainfall smaller than 10 mm/h, the number of events per
 hour appears to stabilize or even decrease. We think that this
 is mostly due to the limited number of observations for large
 rainfalls. Rockfall rate increases from 0.14 per hour up to
 about 2.5 events per hour when rainfall increases from 0 to
 10 mm/h. Figure 8c shows the cumulated distribution of
 rainfall at the time of a rockfall event. About 49% of events
 have occurred when the hourly rainfall was zero, and 94%
 when rainfall was less than 5 mm/h. Only 2% have occurred
 when rainfall was larger than 10 mm/h.

5.5. Cross Correlation of Microseismicity, Rockfall Activity, and Weather

[41] In order to study the correlation between rainfall and
 rockfalls at Séchillienne, we have used the cross-correlation
 function between the rate of rockfalls R and the precipita-
 tion P , defined by $C_{R,P}(t) = \sum_i R(t_i)P(t_i + t)$. The variables R
 and P were first detrended (removing average value) and
 normalized by their standard deviation, so that $C_{R,P}(0)$ (for
 zero time lag t) denotes the linear correlation coefficient
 of P and R (equals 1 for perfect correlation, -1 for anti-
 correlation). The cross correlation of R and P can be inter-
 preted as the average precipitation as a function of time
 before and after a rockfall occurrence. This method allows
 comparison between rockfall occurrence and previous rain-
 fall. It is useful to quantify the correlation and to estimate the
 time delay between precipitation and triggered rockfalls.
 Figure 9a shows the cross correlation between hourly precipi-
 tation recorded at Luitel and the number of rockfalls per
 hour. We used 3098 rockfalls recorded by station THE with
 peak amplitude above 500. In order to minimize the influ-
 ence of gaps in the seismic monitoring, the precipitation
 was set to zero during gaps before computing $C_{R,P}(t)$. The
 cross correlation displays a maximum value of 0.27 for a
 time delay of 1 h (sampling rate) between precipitation and
 rockfall activity. The peak amplitude is much larger than the
 average value, indicating that the correlation is weak but
 significant. A zoom for shorter time delays is shown in
 Figure 9b. The peak of the cross-correlation function is
 asymmetric. It is wider for negative times (rain precedes
 seismicity) than for positive times. This shows that rockfalls
 are not only sensitive to hourly rain, but also to previous
 rainfall, due to water infiltration or snowmelt. Rockfalls

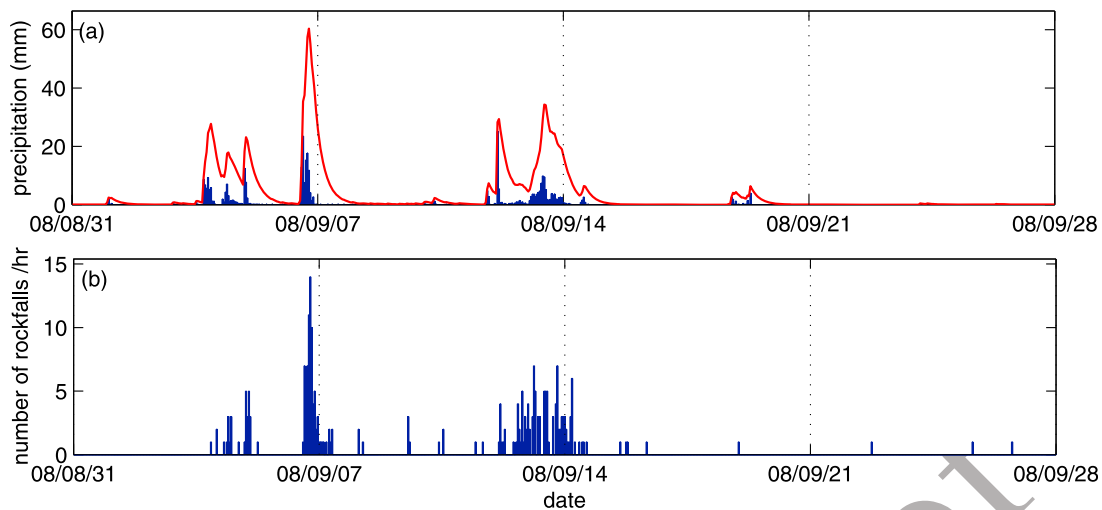


Figure 7. (a) Hourly rainfall (blue bars) and cumulated rainfall (red curve) and (b) hourly number of $A > 500$ rockfalls in September 2008.

762 may also trigger future events, thus increasing the duration
 763 of rockfall crisis after the end of the rainfall episode. The
 764 correlation function for short time delays can be fitted by
 765 an exponential law $C(t) \sim \exp(-|t|/t_c)$, with a correlation time
 766 $t_c = 1.3$ days for negative times, and 0.26 days for positive
 767 times. The fit is however not perfect as the curvature of the
 768 data is stronger than the fit. But in a log-log plot, $C_{R,P}(t)$
 769 exhibits a convex shape, so that it cannot be fitted by a
 770 power law over a significantly large time interval. The vari-
 771 ation of $C_{R,P}$ with time is thus intermediate between an
 772 exponential and a power law function.
 773 [42] To access shorter times delays, we used Vizille rain
 774 gauge, with a sampling time of 5 min. We found that the
 775 peak of $C_{R,P}(t)$ occurs at $t = -25$ minutes. Using Luitel
 776 rainfall data, sampled at 15 min, the correlation peaks
 777 for $t = -45$ minutes. It is not clear at present if there is a finite
 778 time delay for triggering rockfall, due for instance to the time
 779 necessary for water infiltration, or if this delay is due to the

distance between the rain gauges and the rockslide. Using
 780 rain gauge data sampled every 5 min at Vizille, the peak
 781 value is only 0.12, much smaller than when using Luitel
 782 hourly data, but this effect is due to the higher sampling rate.
 783 Using hourly data recorded at Vizille, the maximum correla-
 784 tion is 0.29, close to the value obtained with Luitel rain
 785 gauge. Peak correlation further increases up to 0.47 when
 786 using daily rain recorded at Luitel. The same approach was
 787 used to study microearthquakes (Figure 10a), using 376
 788 events with $A > 500$. The shape of the cross-correlation
 789 function between rate of quakes and precipitations is similar
 790 to the results obtained for rockfalls, but the correlation is
 791 weaker, and has a peak for $t = -3$ h. Using hourly data, the
 792 peak is 0.06, compared to 0.27 with rockfalls, but it is still
 793 above the noise level.
 794 [43] There is also a weak but significant negative correla-
 795 tion between temperature and rockfall activity (Figure 9c).
 796 Maximum of activity coincides with a decrease of tempera-
 797

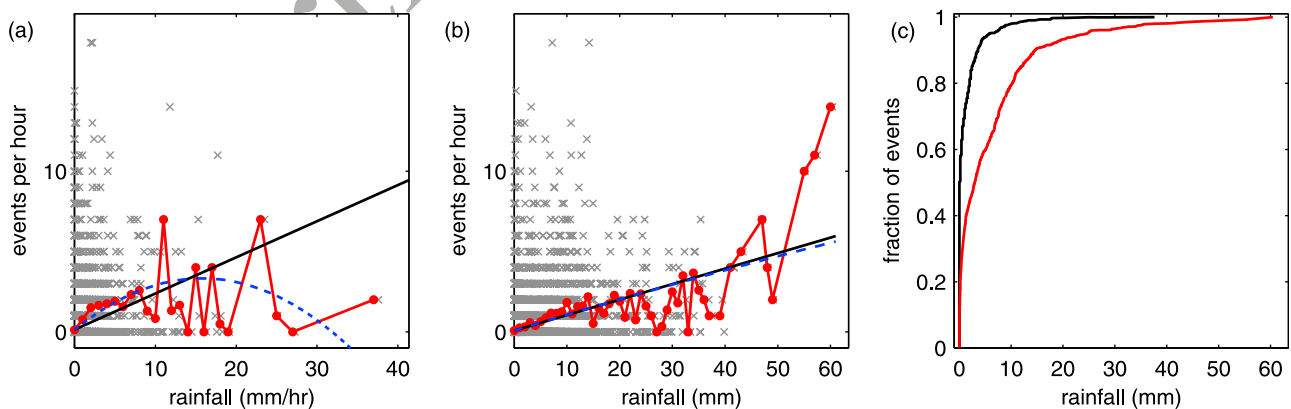


Figure 8. Number of rockfalls per hour with $A > 500$, as a function of (a) hourly precipitation and (b) cumulated precipitation (crosses). The solid line is a linear fit of all hourly values, and the dashed line is a fit by a second-order polynomial. Dots represent the average value of rockfall rate, obtained by binning the rainfall data with a bin width of 1 mm. (c) Fraction of events that have occurred for precipitation smaller than a given value as a function of this threshold. Black line is for hourly precipitation, and red line is using cumulated precipitation.

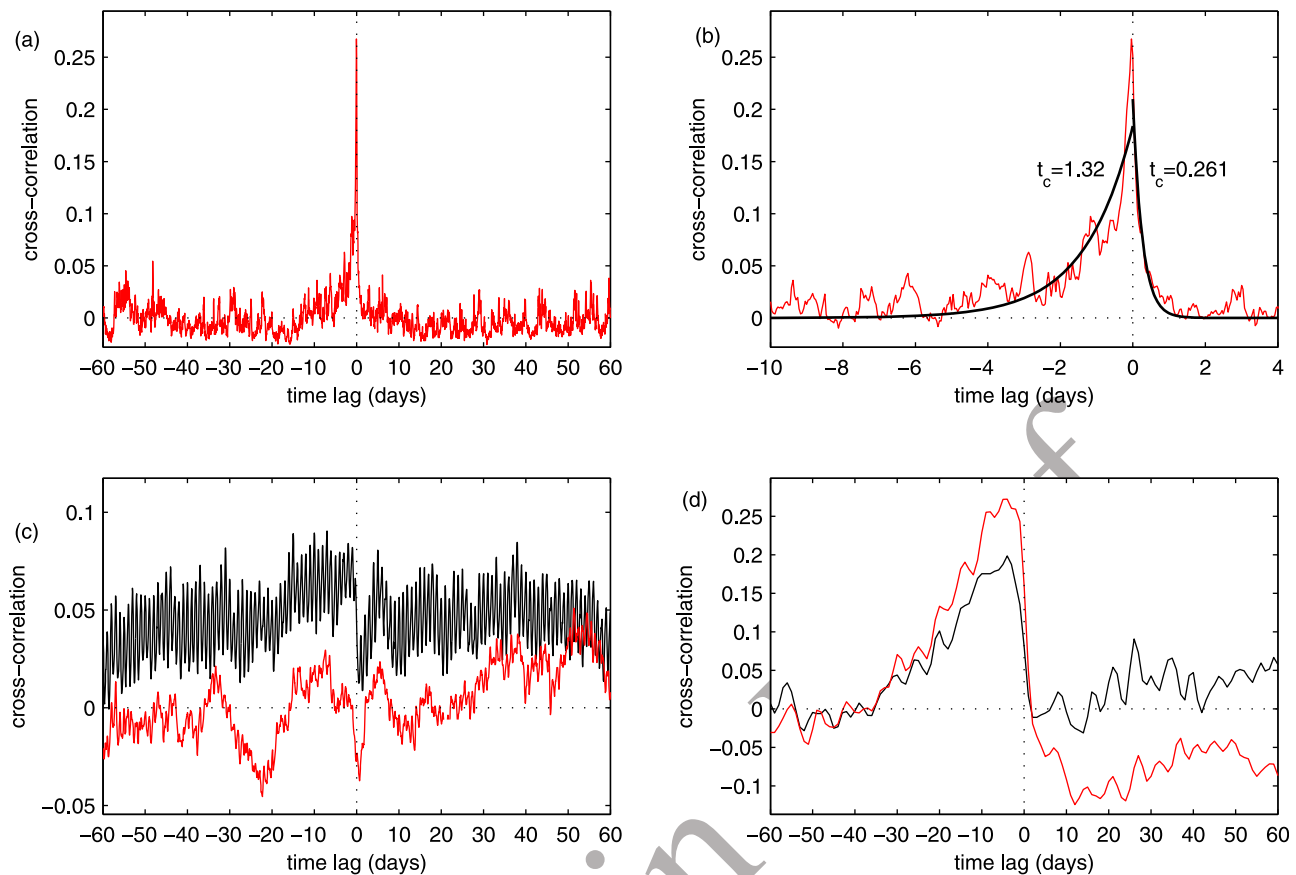


Figure 9. (a) Cross-correlation function of hourly rate of rockfalls and hourly precipitation recorded at Luitel rain gauge; (b) zoom for short time delays, and fit by an exponential law $\sim \exp(-|t|/t_c)$, for both negative and positive times; (c) cross-correlation function of hourly rate of rockfalls and temperature (red line) and of temperature and rainfall (black); and (d) cross correlation of daily precipitation and displacement rate of benchmark 635 (black curve) compared with the cross correlation of displacement rate and daily rate of rockfalls (red line).

798 ture. While a decrease of temperature below 0°C is known
 799 as a potential mechanism for rockfall triggering [e.g.,
 800 *Frayssines and Hantz, 2006*], we do not think that freeze-
 801 thaw cycles can explain the correlation between rockfalls
 802 and decreasing temperature at Séchilienne. The largest
 803 peaks of rockfall activity have been observed in October
 804 2007 and June 2008, when temperatures always remained
 805 positive. We rather suggest that this correlation results from
 806 the correlation between temperature and rainfall (red curve
 807 in Figure 9c), because precipitation is usually associated
 808 with a temperature drop. Indeed, the cross correlation
 809 between rainfall and temperature is very similar to $C_{R,P}(t)$,
 810 for both the shape and the peak value.

811 5.6. Cross Correlation of Rockfalls, Microearthquakes, 812 and Displacement

813 [44] Both rockfalls and microearthquakes were found to
 814 be significantly correlated with accelerations of the rock-
 815 slide displacement (Figures 9d and 10b). For rockfalls, the
 816 peak occurs for $t = -4$ days; that is, peak of rockfall activity
 817 precedes peak of landslide velocity by about 4 days. The
 818 cross correlation is very asymmetric, as it is above zero for

$-36 < t < 2$ days. Peak velocities are thus delayed by a few
 819 days relative to a crisis of rockfall activity, and velocity
 820 relaxes more slowly. This correlation probably mainly results
 821 from the correlation of rockfalls with rain, and of rain with
 822 displacement. The cross correlation of precipitations and
 823 displacement, shown in Figure 9d, is also positive in the time
 824 interval $-36 < t < 2$ days, with a peak at $t = -4$ days. The
 825 maximum value of 0.2 is however smaller than the peak of
 826 cross correlation between rockfalls and displacement rate,
 827 equal to 0.26. We have used the data for benchmark 635 in
 828 Figures 9d and 10b, because it has no gap since the installa-
 829 tion of the seismic network. Benchmarks 1011 and 631 are
 830 also located within the most active zone, and move slightly
 831 faster than benchmark 635 (see Figure 1). However, bench-
 832 mark 631 was destroyed in July 2008 after a rock collapse,
 833 and no data are available for benchmark 1011 in January
 834 2009. These two benchmarks produce a higher correlation
 835 with precipitation and rockfall activity. Data are also avail-
 836 able for other benchmarks located outside the frontal zone,
 837 but the correlation with rockfalls and rainfall is very weak.
 838 The result that correlation increases with average landslide
 839 velocity probably only results from the higher signal-to-noise
 840

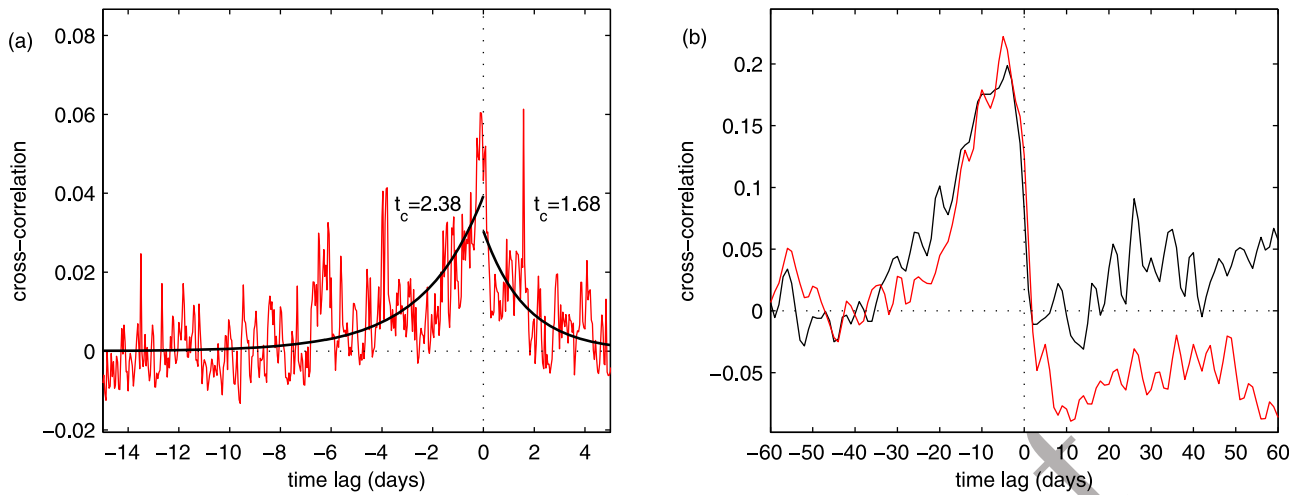


Figure 10. Same as in Figures 9b and 9d for microearthquakes.

841 ratio available in hourly displacement data. This suggests that
 842 precipitation is not the only forcing controlling rockslide
 843 dynamics. For microearthquakes, the time of the peak is
 844 -5 days, slightly larger than for rockfalls, but the correlation
 845 decreases faster to zero (Figure 10b). Also, the peak value is
 846 slightly smaller, about equal to the maximum cross correla-
 847 tion between precipitation and displacement rate.

848 6. Discussion and Conclusions

849 [45] The seismic network installed in 2007 at the
 850 Séchillienne landslide has now recorded several thousands
 851 events, mostly rockfalls, and also hundreds of local micro-
 852 earthquakes and regional earthquakes. Local microearthquakes
 853 generally exhibit less high-frequency energy than distant
 854 earthquakes, but the frequency content appear very variable
 855 among those events. The lack of high-frequency waves may
 856 be due to the strong attenuation of seismic waves in the
 857 damaged zone, as shown by recorded signals generated by
 858 active shots in this area. Another explanation can also
 859 originate from the source, which may generate few high-
 860 frequency waves if they are induced by fluid flows, or
 861 because of low rupture velocities or strong path effects. The
 862 source of these signals is not well understood, in part
 863 because their location is presently inaccurate. A deeper and
 864 more dense active seismic tomography study is in progress,
 865 which will permit derivation of a realistic 3-D P wave
 866 seismic velocity model and better location of a few hundred
 867 events recorded by all 3 stations. This will help us to
 868 understand the nature of the signals recorded, and will also
 869 illuminate the most active fractured zones of the rockslide
 870 and assess the potential presence (or absence) of a sliding
 871 surface. Rockfall volumes are currently unknown, the largest
 872 event having likely a volume of about 100 to 1000 m³, and
 873 the smallest ones being much smaller than 0.05 m³. Seismic
 874 monitoring is thus a very sensitive method for monitoring
 875 rockfall activity as it provides a continuous monitoring,
 876 with accurate event times and durations. In the near future,
 877 we hope to estimate rockfall volume, location, and propa-
 878 gation velocity from seismic signals. A video camera will
 879 be a good complement to better understand the nature of the

material involved (rock avalanches or debris flows) and
 calibrate their volumes. However, video will only work
 during daylight and will be inefficient if the weather is too
 cloudy, which is frequent during episodes of rockfall activity,
 or because of dust clouds during rockfalls.

[46] Rockfall activity and microseismicity were found to
 be weakly, but significantly, correlated with rainfall. No
 threshold was found for rainfall triggering: even 1 mm of
 rain is enough to trigger rockfalls, and most rockfalls occur
 spontaneously in the absence for any precipitation or any
 other forcing. The probability of rockfall occurrence was
 found to linearly increase with rainfall (either daily rainfall or
 antecedent rainfall). Taking into account antecedent rainfall
 clearly improves the correlation between rockfall occurrence
 and rainfall. From the cross correlation of rainfall and rock-
 fall, we suggest that rockfall activity starts immediately
 during a rain episode and lasts for a few days after the end of
 the rainfall. This time delay can be explained by water infil-
 tration or snowmelt, or by a nucleation process (time taken for
 motion to displace portions of the toe enough to affect toe
 stability, or time delay in the conversion of aseismic toppling
 to seismic rockfall). The relaxation of rockfall activity fol-
 lowing rainfall may also be due to the triggering of rockfalls
 by previous events.

[47] Although rockfall occurrence increases with rainfall,
 only a small proportion of rockfall events have occurred
 during the largest rain episodes. Indeed, only 2% of events
 have occurred when precipitation was larger than 1 cm/h.
 Thus the probability of a moderate rockfall being triggered
 by a large rainfall is very small because the probability of
 rockfall occurrence increases more slowly with the rainfall
 intensity than the decrease of the rainfall distribution.

[48] If these observations, based on moderate rainfall and
 small rockfall volume, can be extrapolated to much bigger
 events and intense precipitation, then these results could have
 implications for estimating the coupled hazard of a flood
 resulting from a slope failure. Hazard assessment studies
 generally assume that slope failure will occur during an
 exceptional rainfall, thus resulting in destructive floods if
 the river is dammed by the rockslide and the dam fails. Our
 observations suggest that the occurrence of a slope failure

921 during an exceptional rainfall is rather unlikely, and that
 922 the coupled risk of flood due to a slope collapse may be
 923 overestimated.
 924 [49] Finally, we showed that rockfall occurrence is cor-
 925 related with accelerations of the rockslide, the displacement
 926 rate being delayed by a few days relative to rockfall activity,
 927 and decreases more slowly to its mean value after about one
 928 month, compared to only 5 days for rockfall activity trig-
 929 gered by rainfall. This correlation is likely indirect, due to
 930 the influence of precipitation on both slope displacement
 931 and rockfall activity. Our interpretation is that rainfall
 932 immediately triggers rockfalls and also produces an acceler-
 933 ation of the rockslide displacement which lasts longer than
 934 triggered rockfalls due to inertial effects.

935 [50] **Acknowledgments.** We acknowledge CETE for providing dis-
 936 placement and meteorological data. METEO FRANCE, LTHE laboratory,
 937 and METEO VIZILLE also provided meteorological data, and François
 938 Thouvenot gave us the Sismalp earthquake catalog. This research was sup-
 939 ported by the European Commission under grant TRIGS-043251, by “Pôle
 940 Grenoblois d’Etudes et de Recherches pour la Prévention des Risques
 941 Naturels,” and by French “Agence Nationale pour la Recherche” and
 942 “Institut des Sciences de l’Univers.” We thank Pascal Lacroix and Jean-
 943 Robert Grasso for useful discussions. This work could not have been pos-
 944 sible without the help from many technicians, engineers, students, and
 945 researchers from LGIT: we are grateful to Rémi Bethoux, Glenn Cougoulat,
 946 Sophie Cravoisier, Fabrice Doré, Jean-Robert Grasso, Armand Mariscal,
 947 Yves Orenge, Pascal Lacroix, Catherine Pequegnat, Sandrine Roussel, Laura
 948 Sanchez, Mohamed Tahir, Lucile Tatar, and Christophe Voisin for helping
 949 with installation and maintenance of the seismic network and data proces-
 950 sing. We also thank Mauri McSaveney and an anonymous reviewer for their
 951 careful reading and for interesting suggestions, which helped improve the
 952 quality of the manuscript. Finally, we thank the editor who carefully read
 953 the manuscript and proposed corrections to improve the English.

954 **References**

955 Alfonsi, P. (1997), Relation entre les paramètres hydrologiques et la
 956 vitesse dans les glissements de terrains: Exemples de La Clapière
 957 et de Séchillienne, *Rev. Fr. Geotech.*, 79, 3–12.
 958 Almendros, J., J. M. Ibáñez, G. Alguacil, and E. Del Pezzo (1999), Array
 959 analysis using circular-wave-front geometry: An application to locate the
 960 nearby seismo-volcanic source, *Geophys. J. Int.*, 136, 159–170.
 961 Amitrano, D., J. R. Grasso, and G. Senfauté (2005), Seismic precursory
 962 patterns before a cliff collapse and critical point phenomena, *Geophys.*
 963 *Res. Lett.*, 32, L08314, doi:10.1029/2004GL022270.
 964 Brocher, T. M. (2003), Detonation charge size versus coda magnitude rela-
 965 tions in California and Nevada, *Bull. Seismol. Soc. Am.*, 93, 2089–2105,
 966 doi:10.1785/0120020185.
 967 Brodsky, E. E., E. Gordeev, and H. Kanamori (2003), Landslide basal fric-
 968 tion as measured by seismic waves, *Geophys. Res. Lett.*, 30(24), 2236,
 969 doi:10.1029/2003GL018485.
 970 Caine, N. (1980), Rainfall intensity-duration control of shallow landslides
 971 and debris flows, *Geogr. Ann., Ser. A*, 62, 23–27.
 972 Chleborad, A. F., R. L. Baum, and J. W. Godt (2006), Rainfall thresholds
 973 for forecasting landslides in the Seattle, Washington, area: Exceedance
 974 and probability, *U.S. Geol. Surv. Open File Rep.*, 2006-1064.
 975 Crozier, M. J., and R. J. Eyles (1980), Assessing the probability of rapid
 976 mass movement, in *Proceedings of Third Australia-New Zealand Con-*
 977 *ference on Geomechanics*, edited by N. Z. Geomech. Soc., *Proc. Tech.*
 978 *Groups N. Z. Inst. Eng.*, 6, 247–251.
 979 Del Gaudio, V., S. Coccia, J. Wasowski, M. Gallipoli, and M. Mucciarelli
 980 (2008), Detection of directivity in seismic site response from microtremor
 981 spectral analysis, *Nat. Hazards Earth Syst. Sci.*, 8, 751–762.
 982 Deparis, J., D. Jongmans, F. Cotton, L. Baillet, F. Thouvenot, and D. Hantz
 983 (2008), Analysis of rock-fall seismograms in the western Alps, *Bull.*
 984 *Seismol. Soc. Am.*, 98, 1781–1796.
 985 Duranthon, J.-P., and L. Effendiantz (2004), The unstable “Ruines de
 986 Séchillienne” slope: State of site activity and presentation of the
 987 new remote-monitoring management system, *Bull. Lab. Ponts Chaussées*,
 988 252, 29–48.

Duranthon, J.-P., L. Effendiantz, M. Memier, and H. Previtali (2003),
 989 Apport des méthodes topographiques et topométriques au suivi du versant
 990 rocheux instable des “Ruines” de Séchillienne, *Rev. XYZ*, 94, 31–38.
 991
 992 Effendiantz, L., and J.-P. Duranthon (2002), Risques majeur d’éboulement
 993 des Ruines de Séchillienne Point des mesures de suivi et de surveillance
 994 du site de 1985 au 31 Mars 2002, LRPC Rhône-Alpes, CETE de Lyon,
 995 Lyon, France.
 996 Evrard, H., T. Gouin, A. Benoit, and J.-P. Duranthon (1990), Séchillienne:
 997 Risques majeurs d’éboulements en masse: Point sur la surveillance du
 998 site, *Bull. Liaison Lab. Ponts Chaussées*, 165, 7–16.
 999 Frayssines, M., and D. Hantz (2006), Failure mechanisms and triggering
 1000 factors in calcareous cliffs of the Subalpine Ranges (French Alps),
 1001 *Eng. Geol.*, 86, 256–270.
 1002 Giraud, A., L. Rochet, and P. Antoine (1990), Processes of slope failure in
 1003 crystallophyllian formations, *Eng. Geol.*, 29, 241–253.
 1004 Glade, T., M. Crozier, and P. Smith (2000), Applying probability determi-
 1005 nation to refine landslide-triggering rainfall threshold using an empirical
 1006 antecedent daily rainfall model, *Pure Appl. Geophys.*, 157, 1059–1079.
 1007
 1008 Guglielmi, Y., J. Vengeon, C. Bertrand, J. Mudry, J. Follacci, and A. Giraud
 1009 (2002), Hydrogeochemistry: An investigation tool to evaluate infiltration
 1010 into large moving rock masses (case study of La Clapière and Séchillienne
 1011 alpine landslides), *Bull. Eng. Geol. Environ.*, 61, 311–324.
 1012 Guzzetti, F., S. Peruccacci, M. Rossi, and C. P. Stark (2007), Rainfall
 1013 thresholds for the initiation of landslides in central and southern Europe,
 1014 *Meteorol. Atmos. Phys.*, 98, 239–267, doi:10.1007/s00703-007-0262-7.
 1015
 1016 Harrington, R. M., and E. E. Brodsky (2007), Volcanic hybrid earthquakes
 1017 that are brittle-failure events, *Geophys. Res. Lett.*, 34, L06308,
 1018 doi:10.1029/2006GL028714.
 1019 Helmstetter, A., L. Sanchez, S. Garambois, J. Grasso, F. Doré, Y. Orenge,
 1020 J. Duranthon, P. Pothérat, and J. Kasperski (2008), Multidisciplinary
 1021 monitoring of a huge rocky landslide (Séchillienne, the Alps, France),
 1022 *Eos Trans. AGU*, 89(53), Fall Meet. Suppl., Abstract H51F-0899.
 1023
 1024 Kasperski, J. (2008), Confrontation des données de terrain et de l’imagerie
 1025 multi-sources pour la compréhension de la dynamique des mouve-
 1026 ments de versants, Ph.D. thesis, 268 pp., Univ. Claude Bernard-Lyon I,
 1027 Villeurbanne, France.
 1028 Lemaitre, F., J.-C. Duranthon, and L. Effendiantz (2004), L’utilisation du
 1029 radar au sol pour la surveillance des mouvements de terrain, *Bull. Lab.*
 1030 *Ponts Chaussées*, 249, 19–34.
 1031
 1032 Le Roux, O., S. Schwartz, J. F. Gamond, D. Jongmans, D. Bourles,
 1033 R. Braucher, W. Mahaney, J. Carcaillet, and L. Leanni (2009), CRE dating
 1034 on the head scarp of a major landslide (Séchillienne, French Alps), age con-
 1035 straints on Holocene kinematics, *Earth Planet. Sci. Lett.*, 280, 236–245.
 1036
 1037 McSaveney, M. J. (2002), Recent rockfalls and rock avalanches in Mount
 1038 Cook National Park, New Zealand, in *Catastrophic Landslides: Effects,*
 1039 *Occurrence, and Mechanisms*, edited by S. G. Evans and J. V. DeGraff,
 1040 *Rev. Eng. Geol.*, 15, 35–70.
 1041
 1042 McSaveney, M. J., and G. Downes (2002), Application of landslide seis-
 1043 mology to some New Zealand rock avalanches, in *Landslides*, edited
 1044 by J. Rybář, J. Stemberk, and P. Wagner, pp. 649–654, A. A. Balkema,
 1045 Lisse, Netherlands.
 1046
 1047 Meric, O., S. Garambois, D. Jongmans, M. Wathélet, J. L. Chatelain, and
 1048 J. M. Vengeon (2005), Application of geophysical methods for the
 1049 investigation of the large gravitational mass movement of Séchillienne,
 1050 France, *Can. Geotech. J.*, 42, 1105–1115.
 1051
 1052 Montjuvent, G., and J. Winistorfer (1980), Glaciations quaternaires dans les
 1053 Alpes Franco-Suisses et leur piedmont, *Geol. Alp.*, 56, 251–282.
 1054
 1055 Norris, R. D. (1994), Seismicity of rockfalls and avalanches at three cas-
 1056 cade range volcanoes: Implications for seismic detection of hazardous
 1057 mass movements, *Bull. Seismol. Soc. Am.*, 84, 1925–1939.
 1058
 1059 Panet, M. (2000), Expertise relative aux risques d’éboulement du versant
 1060 des Ruines de Séchillienne, 24 pp., Préfecture de l’Isère, Grenoble,
 1061 France.
 1062
 1063 Pothérat, P., and P. Alfonsi (2001), Les mouvements de versant de
 1064 Séchillienne (Isère): Prise en compte de l’héritage structural pour leur
 1065 simulation numérique, *Rev. Fr. Geotech.*, 95, 117–131.
 1066
 1067 Roth, M., M. Dietrich, L. H. Blikra, and I. Lecomte (2006), Seismic
 1068 monitoring of the unstable rock slope site at Åknes, Norway, in *19th*
 1069 *Annual Symposium on the Application of Geophysics to Engineering*
 1070 *and Environmental Problems (SAGEEP)*, edited by J. Gamey, pp. 184–
 1071 192, Environ. and Eng. Geophys. Soc., Denver, Colo.
 1072
 1073 Spillmann, T., H. Maurer, A. G. Green, B. Heincke, H. Willenberg, and
 1074 S. Husen (2007), Microseismic investigation of an unstable mountain
 1075 slope in the Swiss Alps, *J. Geophys. Res.*, 112, B07301, doi:10.1029/
 1076 2006JB004723.
 1077
 1078 Thouvenot, F., J. Fréchet, L. Jenatton, and J.-F. Gamond (2003), The
 1079 Belledonne Border Fault: Identification of an active seismic strike-slip
 1080 fault in the western Alps, *Geophys. J. Int.*, 155, 174–192.

1067 Vengeon, J.-M., A. Giraud, P. Antoine, and L. Rochet (1999), Contribution
1068 à l'analyse de la déformation et de la rupture des grands versants rocheux
1069 en terrain cristallophyllien, *Can. Geotech. J.*, 36, 1123–1136,
1070 doi:10.1139/cgj-36-6-1123.

Weiss, J. (1997), The role of the attenuation on acoustic emission amplitude 1071
distributions and *b*-values, *Bull. Seismol. Soc. Am.*, 87, 1362–1367. 1072

S. Garambois and A. Helmstetter, Laboratoire de Géophysique Interne 1073
et Tectonophysique, Université Joseph Fourier, CNRS, F-38041 1074
Grenoble, France. (stephane.garambois@ujf-grenoble.fr; ahelmste@obs. 1075
ujf-grenoble.fr) 1076

Article in Proof

3.3.2. Spatial and azimuthal variabilities of seismic site effect patterns due to a landslide located in a high-seismicity region: The Utiku landslide (New-Zealand).

By S. Garambois, A. Quinterro, C. Massey & C. Voisin
To be submitted

A. INTRODUCTION

Landslide triggering by large earthquakes is responsible for about half of the human losses during an earthquake. It is therefore important to deepen the present understanding of the triggering factor(s) controlling earthquake-induced landslides and its distribution. Several back-analysis studies pinpointed the characteristics of the earthquakes able to trigger landslides. A convenient way to consider both magnitude and distance is to consider the Peak Ground Acceleration (PGA) or any other parameter that characterizes the ground movement. *Keefer* (1984; 2002 for a review) compiled information from various databases and established empirical triggering thresholds in Arias intensity for different types of landslides. Focusing on the Chi-Chi earthquake (Mw=7.6, Taiwan) that occurred in a country equipped with a dense accelerometric and seismological network, *Khazai and Sitar* (2003) showed that 81 % of Chi-Chi coseismic landslides occurred in regions presenting mean horizontal PGA greater than 0.15 g. *Meunier et al.* (2007) established a linear correlation between the density of coseismic landslides and both the vertical and horizontal PGA after the Chi-Chi earthquake. However, the PGA maps deduced from regional networks underestimate the real PGA at the site of the landslide. Local conditions such as topography locally increase the PGA of a given earthquake and probably play a major role in the triggering of the landslide. A well described example of topographic amplification of the ground movement is the destruction of the Rognes village (France) during the 1909 Lambesc earthquake. Using co-seismic landslide maps compiled after the Northridge (Mw=6.7, California), the Chi-Chi (Mw 7.6, Taiwan) and the Finisterre mountains (Mw 6.9, Papua New Guinea) earthquakes, *Meunier et al.* (2008) showed that earthquake-triggered landslides were clustered near ridge crests, where PGA are likely to have been greatest. Beside the topography effect, a second amplification mechanism also occurs on slopes affected by a gravitational slide. The movement of the landslide continuously deteriorates the mechanical properties of the surface material, leading to a large and growing contrast of seismic impedance between the landslide body and the host rock (*Meric et al.*, 2007). As a consequence, incoming seismic waves are trapped within the landslide body and this phenomenon leads to the amplification of the ground movement accompanied by an increase in the duration of the shaking. This amplification is not random and presents some characteristics in terms of frequency bandwidth controlled by the geometry and the mechanical properties of the landslide. The evolving sliding process combined with the seismic amplification pattern defines a specific site effect of the landslide. It is consequently an important factor that increases the susceptibility of these slopes to earthquake triggering.

The characterization of seismic site effects on landslides is limited to few studies, although site effects have been largely studied for seismic risk assessment and vulnerability (*Anderson et al.*, 1986). *Del Gaudio and Wasowski* (2007) and *Del Gaudio et al.* (2008) investigated the peri-urban slopes of Caramanico Terme – central Italy – to determine how the seismic response is affected by the presence of topographic features and by pre-existing landslides. Here, our study focalizes on the Utiku active landslide located in central North Island (New-Zealand), a region characterized by a moderate to strong seismic activity. The landslide

was monitored for 14 months (November 2008 – January 2010) using five seismological stations (four on the landslide and one reference site). The main purpose is to assess the variability of site effect patterns along the landslide, which is well studied and monitored, notably in terms of displacements and pore pressure thanks to the presence of boreholes. In a first part, the study was dedicated to compare different site effect assessment methods, i.e. those which use weak motion generated by the ambient seismic noise and those which use others dynamic sources (railway and earthquakes), where particles motions are higher. Spatial variability in seismic site effect properties (frequency, amplification) observed along the landslide is due to deformation differences of the landslides (different shear wave contrasts). It represents a major outcome of this study together with the consistency between the assessment methods, a result that del Gaudi and Wasowski (2007) could not achieve. These observations indicate that the impact of earthquakes can differ a lot along the landslide and also that dynamic properties of seismic waves should play a major role in the triggering. In a second part, we show a large azimuthal anisotropy of the site effect pattern, independent on the analysis used, and which also varies along the site.

B. THE UTIKU LANDSLIDE AND THE MONITORING NETWORK

The Utiku landslide (Fig. 3.4) is a complex reactivated, translational block slide-earth flow, which initiated prehistorically, probably triggered by a major seismic and/or rainfall event, following removal of lateral/toe support resulting from the incision of the Hautapu River. Landslide movement is being driven by the large mass overlying the slide surface and elevated piezometric levels, as well as the loss of toe support caused by erosion along the Hautapu River. Current monitored landslide movements are much lower (in magnitude and rate), than those recorded pre-1973. This change is attributed to a lowering of piezometric levels in the upper landslide, possibly as a result of the mitigation works installed between 1965 and 1972.

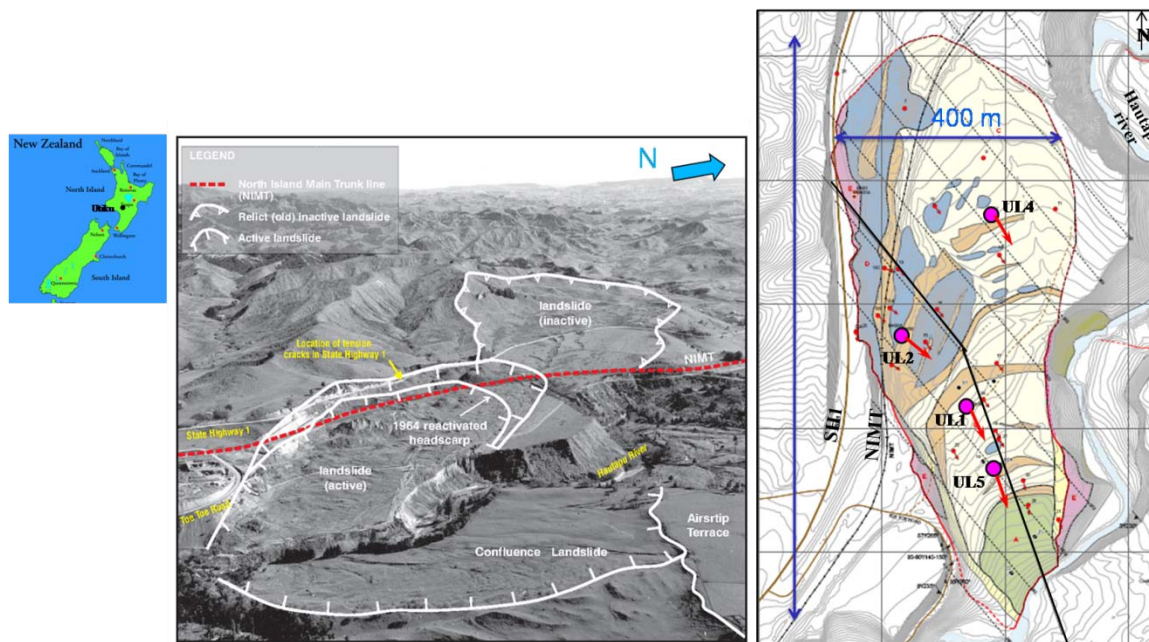


Fig. 3.4. Aerial oblique photograph of the Utiku area (left) taken in 1965. Limits of the landslide and location of the seismological stations within the landslide area (right).

The seismological network was composed of five broadband (30s – 40 Hz) velocimeters, which recorded ambient vibrations as well as thousand of earthquakes over a period of 14 months from November 2008 to January 2010. Four of them were placed within the landslide area near GPS

monitoring stations and boreholes (Fig. 3.4), while one was located outside the landslide and acted as a reference station.

C. VARIABILITY IN SITE EFFECT PATTERN: A COMPARATIVE STUDY

Figure 3.5 presents the N-S component of the seismograms recorded during an $M_l=4.73$ earthquake located 18 km from the landslide for the four stations placed within the landslide and for the reference site (UL3).

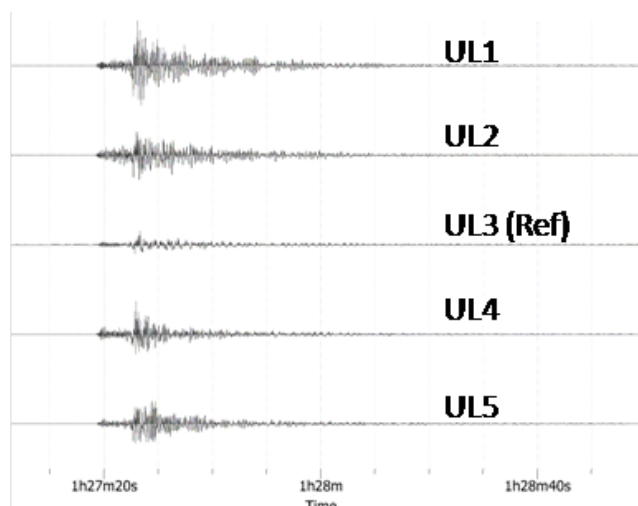


Fig. 3.5. Seismograms of the N-S horizontal component for the different stations recorded the 16th October 2009 for an earthquake ($M_l=4.73$) located 18 km from the landslide.

These seismograms show the large site effect produced by the landslide, as attested by the lower amplitude recorded at the reference site. This site effect seems to present significant variability depending on the location of the seismometers along the landslide. The maximum of amplification appears at the middle of the landslide (UL1), while the lower amplification appears on the edge of the landslide (at UL4, the landslide is more superficial and presents a 3D geometry). In order to analyze and characterize these site effect patterns, two assessment methods have been compared: the H/V method, which uses seismic noise and the spectral ratio method, computed for earthquakes between the given seismometers and the reference site. If they present consistent results in term of spectral characteristics, the level of amplification at peak frequencies is always underestimated using the H/V method. Figure 3.6 (left) presents the results of H/V computations derived from the Geopsy software (Wathelet et al., 2004) with different time windows, while, on the right, the directional distribution have been computed. Fig. 3.7 show the mean spectral ratio between the four stations located along the landslide and the reference site, for 20 selected earthquakes.

The H/V computations first show that the reference site does not display any site effect and that the spectrum is rather constant between 1 and 10 Hz. It also highlights the changes in the peak frequency, ranging from 1.8 Hz (UL2) to 4.1 Hz (UL4). A comparison with borehole measurements show that these peak frequencies are related to the local thicknesses of the landslide (49 m for UL2, 15 m for UL4, 27 m for UL1 and 21 m for UL5). However, Nakamura's famous relation ($f_0=VS/4H$) is not able to explain the observed frequencies if using a constant shear wave velocity all along the landslide body. As thicknesses and fundamental frequencies are precisely known, it is possible to invert Nakamura's relation to derive local shear wave velocities: 350 m/s for UL2, 250 m/s for UL4, 240 m/s for UL1 and 230 m/s for UL5. Not surprisingly, shear wave velocity appears correlated with observed deformation, lower velocities

being observed in the high disturbed zones. Another observation is that UL4 and UL2 H/V results do not present a clear Dirac-shape in terms of peak frequency but a more stretched and lower response, for both assessment methods. This must be due to 2D or 3D effects, these stations being located near abrupt lateral changes of shear-wave velocities (limits of the landslide). Both methods show consistent results, which underline the large level of amplification reaching 10 in amplitude for UL1. It is noticeable that H/V method tends to under-estimate the level of amplification compares to the more robust spectral ratio method.

Finally, no simple linear relationship between shear-wave velocity contrasts and levels of amplification could be directly derived. One could expect that when the Vs contrast is large, amplification will be higher. Here amplification is larger for UL1 at the peak frequency than for UL5, which is however located in a higher weathered zone. Numerical analyses should be performed to better understand this relation and the role of seismic attenuation and geometry of the landslide in these results.

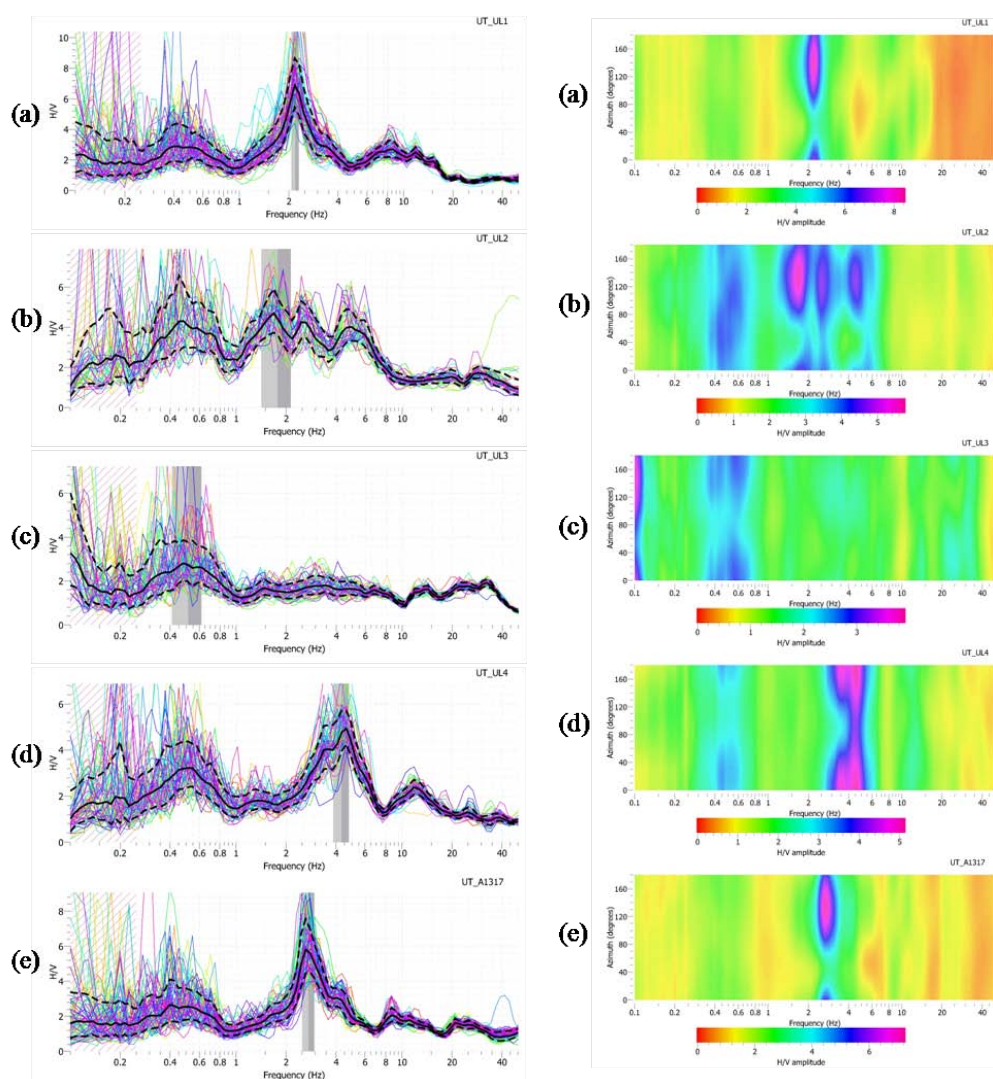


Fig. 3.6. H/V computations performed on various 25 s time windows for each stations (left) and their directional sensitivity (right).

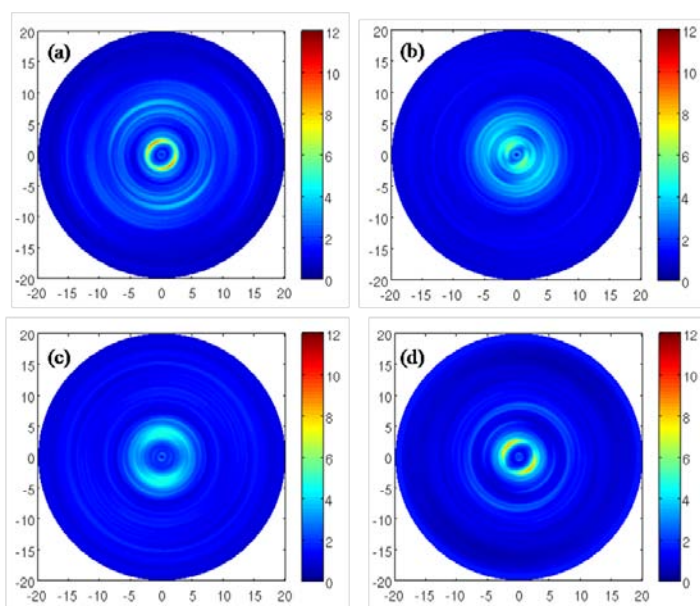


Fig. 3.7. Mean spectral ratios obtained from the average response of 20 earthquakes for UL1 (a), UL2 (b), UL4 (c) and UL5 (d) and their directional anisotropy.

All these observations indicate that the impact of earthquakes can differ a lot along the landslide as site effects are far from being constant and also that dynamic properties of seismic waves should play a major role in the triggering of different parts of the landslide.

D. DIRECTIONAL ANISOTROPY

Both Figures 3.6 (right) and 3.7 show a large anisotropy in the site effect pattern: the maximum of amplification at peak frequencies is far from being isotropic, i.e. it varies as a function of rotation of the horizontal components. This anisotropy effect will be very large on UL1 and UL5 (maximum of amplification above 10 and minimum under 4) and appears weaker on UL2 and UL5, i.e. in stations located on the edges of the landslide. Del Gaudio et al. (2008) have also shown that slope response to seismic shaking can be characterized by directional variations of a factor of 2–3 or larger, with maxima oriented along local topography features (e.g. maximum slope direction). The authors state that the maximum amplification occurs at almost constant direction regardless the origin of the recorded events (back-azimuth of the epicenters). The fact that both assessment methods show the same anisotropic patterns for all stations indicate that this effect cannot be explained source properties (back-azimuth of earthquakes, source frequency content). This anisotropy seems to be correlated with the main displacement direction of the landslide, maybe due to anisotropy in material mechanical properties due to anisotropy in the deformation or to the global 3D shape of the landslide, which presents large directional properties. Further analyses will be made considering a large number of earthquakes presenting large variabilities in terms of back-azimuths and distance/magnitude properties. The anisotropy problem may be important in term of hazard assessment, as the susceptibility of slopes to earthquake induced failures can be increased by the phenomenon of site response directivity, especially when the direction of maximum shaking is close to that of the maximum slope (del Gaudio et al., 2008).

The effect of the 3D shape of the landslide will be studied using a 3D numerical modeling software (SPECFEM3D), based on spectral elements method to simulate the seismic displacements generated by earthquakes inside and outside the landslide. This approach will help a better quantitative understanding of the observed site effect patterns, both in terms of amplitude, shape and anisotropy.

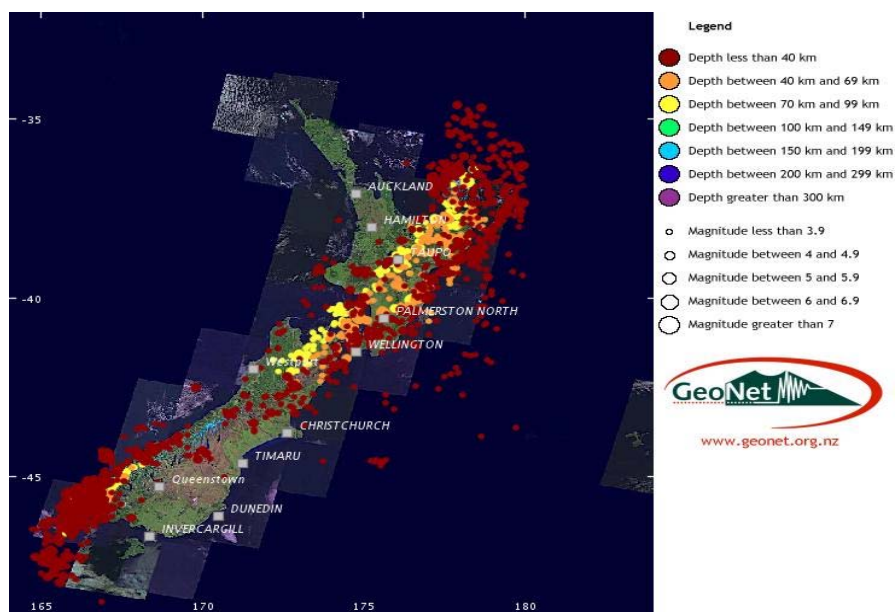


Fig. 3.8. Available Earthquake dataset. In 14 months more than 3,000 earthquakes ($M_I > 3$, $D < 100$ km) have been recorded, with a wide range of source parameters: magnitude, depth, epicentral distance, back-azimuth (GEONET data).

E. CONCLUSIONS - FUTURE WORK

This ongoing work conducted in a high seismicity area aims at better estimate the site effect patterns due to material weathering on a landslide and how it should be taken into account in all risk assessment study. Spatial variability in seismic site effect properties (frequency, amplification) observed along the landslide seems to be due to deformation differences within the landslide body, which generates lateral shear wave contrasts. We also showed the consistency between two assessment methods, one based on the seismic noise method and a second using spectral ratio computed when recording an earthquake. 2D or 3D effects decrease the quality of the peak frequency as well as the level of amplification.

These observations indicate that the impact of earthquakes can differ a lot along a landslide and also that dynamic properties of seismic waves should play a major role in the triggering of different zones of the landslides. This study also suggests that seismic noise methods can be used for a first description of peak frequencies in moderate or low seismic activity areas, but amplitudes of amplification are underestimated. We observed a clear directional variation of the amplification (from 10 to less than 4 on station UL1), which is dependent on the local properties of the landslide. Origin of this anisotropy is presently unclear, even if it seems to be correlated with anisotropy of the deformation within the landslide or with the 3D shape of the landslide. A numerical study should be performed in the near-future to better understand the origin of this large anisotropy as well as the different observed patterns.

Hundreds of earthquakes have been recorded during the experiment (Fig. 3.8), which present a wide range of back-azimuth, magnitudes and distances. Future work will focus on the analysis of site effect pattern as a function of different source characteristics (energy within the landslide, back-azimuth) to establish the variability of site effect assessment. Such analyses may be crucial when site effect assessment is needed in low to moderate seismic activity regions, i.e. are seismic site assessment methods robust when they are computed from a single earthquake?

4. Perspectives Générales

4.1. Imagerie Géophysique.

J'espère continuer à m'investir dans les années à venir sur l'imagerie géophysique des mouvements de terrain, mais en menant un effort vers la quantification, que ce soit au niveau des propriétés mécaniques (porosité, fracturation) que celles des fluides qui jouent un rôle considérable dans la dynamique des mouvements de terrain. Pour cela, il faudra essayer d'appliquer les lois pétrologiques ou d'homogénéisation (Mavko et al., 2003) à des images multi-méthodes (tomographies sismiques et électriques), qui permettront de lever des ambiguïtés lorsque c'est possible, par exemple entre la présence de zones saturées ou d'argiles dans les mouvements visqueux. La sismique réflexion 2D est actuellement une méthode jugée trop difficile à mettre en œuvre et à traiter (voir paragraphe 3.2.1), malgré son potentiel pour l'imagerie haute résolution de subsurface et de l'intérêt évident que peuvent constituer des analyses plus quantitatives des vitesses et des amplitudes (AVO par exemple. Si dans les milieux rocheux et fracturés, les nombreuses hétérogénéités peuvent constituer un obstacle pour l'applicabilité de cette technique en raison de nombreuses diffractions et guides d'ondes potentiels (Musil et al., 2002), la sismique réflexion haute résolution pourra être appliquée sur des mouvements plus homogènes (Bruno et Marillier, 2000).

Dans ce contexte, les développements méthodologiques envisagés sur les techniques d'inversions du champ d'onde sismique complet, détaillées dans le Chapitre 1, permettraient une imagerie plus fine que les méthodes tomographiques et une caractérisation plus complète des paramètres. En effet, une approche élastique permettrait d'utiliser à la fois les variations latérales des ondes de surface et les formes d'ondes des premières arrivées sismiques (ainsi que d'éventuelles réflexions). Ceci permettrait d'obtenir la distribution 2D des vitesses d'ondes P et surtout d'ondes S au sein du glissement, paramètre très sensible à la déformation (Socco et Jongmans, 2004). Dans cette problématique d'imagerie quantitative, l'approche poroélastique développée actuellement (thèse B. Dupuy) et surtout l'approche de double porosité (cf. chapitre 1), permettraient de retrouver directement des paramètres de l'espace poreux et fracturé. Bien évidemment, si l'on parvient en plus à retrouver la distribution de l'état de saturation et de la perméabilité, cela serait un plus pour mieux contraindre les couplages hydro-mécaniques et leur évolution.

4.2 Suivi hydrogéophysique

L'eau est un facteur aggravant de déstabilisation d'un massif. En particulier, les infiltrations d'eaux modifient le niveau des nappes phréatiques en profondeur ce qui génère des déformations hydromécaniques importantes le long des fractures, abaisse la résistance effective des roches et des fractures, et produit donc une déstabilisation générale de l'ensemble du massif (Cappa et al., 2004; Guglielmi et al., 2005). On rejoint ici les problématiques entrevues au sein du Chapitre 1 portant sur l'hydro-géophysique, mais sans doute avec d'autres méthodes que le GPR ou l'acoustique développées dans le Chapitre 1, les milieux étant souvent trop conducteurs et/ou trop fracturés. L'installation permanente de matériels géophysiques choisis en fonction de leur sensibilité à l'eau sera sans doute encouragée à l'avenir. Ce suivi temporel, déjà largement utilisé par les pétroliers et l'imagerie différentielle 4D (Chapitre 1), a déjà été initiée sur les mouvements de terrain par Susuki et Higashi (2003, Fig. 3.9), Supper et Romer (2003) et Lebourg et al. (2005) avec des méthodes de suivi par tomographies électriques d'infiltrations forcées ou naturelles.

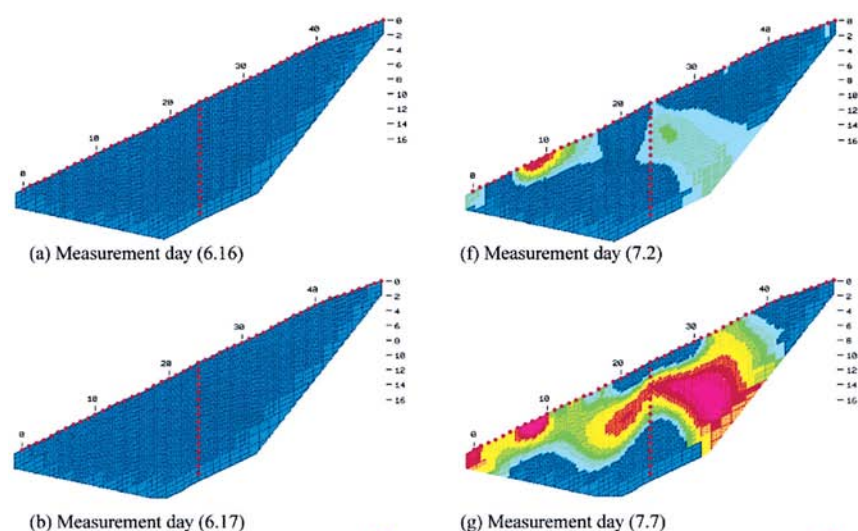


Fig. 3.9. Suivi temporel pour 4 périodes par tomographie électrique différentielle d'un glissement de terrain à risque situé au Japon (Suzuki et Higashi, 2003).

Méric (2006) a installé un réseau d'électrodes sur Séchilienne afin de mesurer les évolutions de potentiel spontané et effectué un travail d'interprétation préliminaire, ce réseau tournant en continu depuis 4 ans maintenant. Si je ne pense pas jouer un rôle majeur dans l'interprétation des méthodes potentielles à l'avenir, j'aimerais encourager une démarche pluridisciplinaire collaborative permettant de rassembler les compétences sur un même site cible, peut-être Séchilienne. Il faudrait par exemple adapter des codes d'interprétation des données de polarisation spontanée basés sur différentes techniques spatiales de traitement du signal pour identifier la position des sources électrocinétiques (Gibert & Pessel, 2001, Jardani et al., 2007) et utiliser la technique de résonance magnétique protonique (présentée au chapitre 1, Legchenko et Valla, 2002).

4.3. Observatoire et Suivi sismologique

Comme cela a été entrevu sur deux sites instrumentés différemment (Séchilienne et Utiku, paragraphe 3), les objectifs d'une écoute sismologique d'un mouvement de terrain sont multiples suivant les contextes (rocheux, visqueux) et les conditions extérieures (pluviométrie, sismicité). Il s'agit de : i) détecter et analyser l'activité micro-sismique (localisation, énergie, durée, mécanismes) associée au mouvement. La localisation permettrait notamment de caractériser l'existence de zones de fractures actives et le volume mis en jeu, voire d'une surface de rupture éventuelle ; ii) enregistrer et caractériser les chutes de blocs sur les sites rocheux. Ceux-ci restent actuellement indétectables autre que visuellement pour les plus gros événements, alors qu'ils pourraient constituer des précurseurs d'éboulements plus importants ; iii) Enregistrer les séismes très locaux pour mieux appréhender la sismicité locale ; iv) Caractériser de possibles effets de site dus à la déstabilisation du massif. Ils sont susceptibles d'amplifier l'accélération des mouvements du sol en cas de séisme (cf. paragraphe 3) ; v) Utiliser le bruit de fond sismique afin de caractériser les fonctions de Green entre deux capteurs, ce qui permettrait de détecter des variations très faibles de vitesse des ondes sismiques dues à l'endommagement du massif.

Dans le cadre de l'ANR SLAMS [2010-2013] que je coordonne (présentée ci-après dans sa dimension interdisciplinaire), le site choisi d'études multi-disciplinaire est le mouvement de Séchilienne (paragraphe 3.2.2), intégré à l'observatoire OMIV. Une thèse, financée dans le cadre de cette ANR (L. Chaumond), doit permettre d'avancer sur les points précédemment évoqués

concernant l'écoute sismologique sur Séchilienne et peut-être sur d'autres mouvements instrumentés de manière pérenne (la Clapière) ou de manière temporaire dans des régions où les forçages climatiques et sismiques sont forts (Nouvelle-Zélande, Pérou). Les principaux points dans lesquels j'aimerais m'investir sur cette problématique concernent la localisation des signaux sismiques et l'amplification des ondes sismiques et leur impact sur la dynamique du glissement.

En ce qui concerne le premier point, nous allons tirer partie du fait que le réseau sismologique déployé à Séchilienne est constitué d'antennes, ce qui permet une localisation des événements proches et peu impulsifs par des techniques quasi-automatiques de beam-forming, basées sur l'inter-corrélation entre traces (Almendros et al., 1999). Cette méthode a été récemment employée sur Séchilienne par Lacroix et Helmstetter (2010), ce qui a permis de fournir une première carte de localisation d'événements (chutes de blocs et micro-séismes). Les erreurs associées à la localisation restent importantes à l'heure actuelle, sans doute en raison du fait que l'inversion permet de déterminer une vitesse constante, alors que la structure est fortement hétérogène à petite échelle, et 3D. Ainsi, l'effet de structures 3D sur la localisation devra être caractérisée à l'aide de modélisations synthétiques, et renforce le besoin d'avoir une structure 3D de la distribution des vitesses. Celle-ci pourra être déduite d'expériences actives classiques ou du déploiement de réseau denses temporaires (IHR). Également, d'autres méthodes de pointés des arrivées plus classiques (pointés manuels) ainsi que l'utilisation de l'amplitude sont envisagées, qui pourraient être couplées à d'autres méthodes d'inversions, du type algorithme de voisinage, qui permettraient une investigation complète d'un plus grand nombre de paramètres.

Pour le second objectif d'étude des effets de site, des accéléromètres du Réseau national Accélérométrique Permanent (RAP) viendront compléter le réseau existant et permettront d'étudier l'amplitude des vitesses ou des accélérations générées en différents points de mouvement et la distribution d'éventuels effets de site (et leur propriétés) dus à la déstructuration du mouvement. Cette approche instrumentale pourra être complétée par des expériences temporaires (IHR) si un besoin d'échantillonnage spatial plus important est nécessaire. Pour comprendre ces données, E. Chaljub (LGIT) propose d'utiliser un code de calcul en 3D (SPECFEM3D, <http://www.geodynamics.org/cig/software/packages/seismo/specfem3d/>) basé sur la méthode des éléments spectraux pour simuler les vibrations sismiques dans et en dehors du mouvement de Séchilienne. Ceci permettra de quantifier les effets de site et les caractéristiques des vibrations (amplitude, durée, fréquence) auxquelles on peut s'attendre, puis de les intégrer dans un code dynamique qui essaiera de caractériser la dynamique du mouvement en réponse à des séismes synthétiques. Cette approche numérique sera validée à partir des déplacements superficiels significatifs (et hétérogènes) générés par le séisme de Laffrey (2005/10/02, $M_L=2.8$, à 5 km du mouvement étudié).

4.4. Interaction avec les Sciences Humaines et Sociales : ANR SLAMS

En collaboration avec d'autres équipes de recherches, je coordonne depuis février 2010 un projet de recherche interdisciplinaire sur le mouvement de terrain de Séchilienne, qui tentera de répondre à la fois à des questions qui restent en suspens au niveau des mécanismes contrôlant la dynamique du mouvement, au niveau de sa gestion et ses conséquences sociales et de gouvernance. Il m'est apparu intéressant de terminer cette partie prospective par un résumé en anglais de cette thématique qui propose une ouverture vers des questions opérationnelles et de gestion du risque, souvent peu abordées dans les problématiques plus techniques évoquées précédemment.

SLAMS : Séchilienne Land movement : Multidisciplinary Studies from Hazard assessment to associated risk and consequences

Par S. Garambois et al., 2010

Huge landslides induce dramatic socio-economical consequences within the world. The various and complex mechanisms at the origin of mass movements and the external factors modifying their internal dynamics are various and complex, leading to large uncertainty in prediction in both space and time domains. This last triggers a lot of misunderstanding between the scientific community and people in charge of civil society, because the management of uncertainties is approached according to various protocols, which are actor dependent. This is the main reason why quantitative risk assessment of this hazard and its time evolution requests the participation of these different actors.

This project proposes to federate these different actors on a emblematic site, the Séchilienne landslide. Indeed, in metropolitan French territory, the Séchilienne landslide is by far the natural phenomenon that does yield the strongest potential combined risk in term of socio-economical consequences. Indeed, the failure of this huge landslide can dam the Romanche valley. It induces the impoundment of the ongoing lake, which rupture could generate large flood flowing along the Romanche valley and threatening the town of Grenoble and the downstream chemical factories of Jarrie. This site is an emblematic example of the prickly questions raised for 25 years after administrative, scientific and political managements, notably owing to its multidisciplinary dimension. The considerable investment performed these last 25 years favoured the management of risk, notably via a competitive and dense system of surveillance (based on the temporal monitoring of displacements). In the opposite, this site suffered from the lack of projects of fundamental and interdisciplinary research. We offer so an ambitious projects, which aims at studying at the same time hazard and organizational vulnerability, but also to offer a better structuring of the risk governance. Major problems, which are still highly debated, are: (1) the physical cause and the history of the slope mechanical deformation, (2) the present-day structure of the landslide and hence the implied volume, (3) the identification of the main parameters controlling the destabilization and the prediction of the slope evolution before, during and after the rupture, and (4) the uncertainty on vulnerability and the political governance in the context of the societal risk acceptance. An analysis of the past, present and potential future risk management at different levels will be performed from human and social point of views. For hazard assessment, we propose a multidisciplinary based on the surveillance system, coupled to new measurements, which will contribute to a better knowledge of deep mechanisms (present and passed), of new potential surveillance techniques and of fluid flows and hydro-mechanical coupling mechanisms, which seems to control the present-day dynamics. These data will constitute the input parameters of different types of numerical modelling which will aim at reconstructing the past kinematics of movement, at reproducing actual dynamics and at assessing the effects of external factors. Different rock falls scenarios will be modelled considering a benchmark of numerical methods. All this work will be considered as inputs for creating decision-tree models, which take into account uncertainties at each step. These obtained results of this project will be able to be applied to other similar cases, and to other types of risks, especially considering risk governance and management studies.

5. REFERENCES (texte principal)

- Antoine, P., Giraud, A., Evrard, H., and Rochet, L. 1994. A huge slope movement at Séchilienne, Isère, France. *Landslide News*, 8: 15–18.
- Bard, P. (1997). "Local effects on strong ground motion: basic physical phenomena and estimation methods for microzoning studies". *Proceedings of the Advanced Study Course on Seismic Risk "SERINA –Seismic Risk : an integrated seismological, geotechnical and structural approach* , pp. 229-299.
- Bonnefoy-Claudet S. (2004). – Nature du bruit de fond sismique : implications pour les études des effets de site. – Thèse de Doctorat, Univ. J. Fourier, Grenoble, France, 241 p.
- Bruno F. & Marillier F. (2000). – Test of high-resolution seismic reflection and other geophysical techniques on the Boup landslide in the Swiss Alps. – *Surv. Geophys.*, 21, 333-348.
- Campillo, M., and A. Paul (2003), Long - range correlations in the diffuse seismic coda, *Science*, 299, 547{549.
- Glastonbury, J., and Douglas, K. 2000. Catastrophic rock slope failures: observed characteristics and behaviour. *In GeoEng2000: An International Conference on Geotechnical and Geological Engineering*, Melbourne, Australia, 19–24 November 2000. Technomic Publishing, Lancaster, Pa. Vol. 2.
- Cornou C., Kristek J., Ohrmberger M., Diguilio G., Schissele E., Guiller B., Bonnefoy-Claudet S., Wathelet M., Faeh D., Bard P.-Y. & Moczo P. (2004). – Simulation of seismic ambient vibrations – II: H/V and array techniques for real sites. – *In: Proc. 13th World Conf. Earth. Eng.*, Vancouver, Canada. – IAEE, Tokyo, Paper 1130, 6 p.
- Del Gaudio, V. and Wasowski, J.: Directivity of slope dynamic response to seismic shaking, *Geophys. Res. Lett.*, 34, L12301, doi:10.1029/2007GL029842, 2007.
- Del Gaudio V., Coccia S., Wasowski J., Gallipoli M. R., and M. Mucciarelli, Detection of directivity in seismic site response from microtremor spectral analysis, *Nat. Hazards Earth Syst. Sci.*, 8, 751–762, 2008.
- Duranthon, J.-P., Effendiantz, L., Mémier, M., and Prévitali, I. 2003. Apport des méthodes topographiques et topométriques au suivi du versant rocheux instable des Ruines de Séchilienne. *Revue XYZ*, 94: 31-38.
- Durville J.-L., P Potherat, R Russo, The Séchilienne Slope-Romanche Valley (ISERE), France, IMIRILAND
- Evrard, H., Gouin, T., Benoit, A., Duranthon, J-P. 1990. Risques majeurs d'éboulements en masse, Point de surveillance du site. *Bulletin de liaison des Laboratoires des Ponts et Chaussées*, 165: 7-16.
- Field E. & Jacob K. (1993). – The theoretical response of sedimentary layers to ambient seismic noise. – *Geophys. Res. Lett.*, 20, 2925-2928.
- Garambois S., Quinterro A., Massey C. & C. Voisin, 2010, Variability in seismic site effect response of a landslide: results from a one-year monitoring of the Utiku landslide (North Island, New-Zealand), to be submitted to *JGR – Earth surface*.
- Gibert D. , Pessel M., 2001, Identification of sources of potential fields with the continuous wavelet transform : application to self-potential profiles. *Geophysical Research Letters*, vol 28, num 9, pp 1863-1866/
- Grasso J.-R., Garambois S.; Jongmans D., Helmstetter A., Lebourg T., Malet J.-P., Berolo W., Bethoux R., Darra, L. & P. Ulrich, 2010, The OMIV observatory on landslides – Observing with multiparameters the Instability of Versants, *EGU*, Vienna, May 2010.
- Guglielmi, Y., Vengeon, J.M., Bertrand, C., Mudry, J., Follacci, J.P., Giraud, A., 2002. Hydrogeochemistry: an investigation tool to evaluate infiltration into large moving rock masses (case study of La Clapière and Séchilienne alpine landslides). *Bull. Eng. Geol. Env.*, 61 (4), 311-324.
- Helmstetter A. and S. Garambois, 2010, Seismic monitoring of Séchilienne rockslide (French Alps): analysis of seismic signals and their correlation with rainfalls, *J. Geophy. Res.*, In press.
- Hutchinson, J.N. 1988. General report: Morphological and geotechnical parameters of landslides in relation to geology and hydrogeology. *In Proceedings of the 5th International Symposium on landslides*, Lausanne, Switzerland, Vol. 1, pp. 3-35.
- Jardani A., A. Revil, A. Bolève, J.P. Dupont, W. Barrash, and B. Malama, 2007, Tomography of groundwater flow from self-potential (SP) data *Geophysical Research Letters*, 34, L24403, doi:10.1029/2007GL031907L.
- Jongmans D. & S. Garambois, 2007, Surface geophysical investigation and monitoring of landslides: a review, *BSGF*, n2, pages 101-112.
- Kasperski J. (2008), Confrontation des données de terrain et de l'imagerie multi-source pour la compréhension de la dynamique des mouvements de terrain, PhD thesis, univ. De Lyon.
- Keefer, D.K., 1984. Landslides caused by earthquakes. *Bull. Geol. Soc. Am.* 95, 406–421.
- Keefer, D.K., 2002. Investigating landslides caused by earthquakes—a historical review. *Surv. Geophys.* 23, 473–510.
- Khazai, B. and Sitar, N., 2004, *Evaluation of Factors Controlling Earthquake-Induced Landslides Caused by Chi-Chi Earthquake and Comparison with the Northridge and Loma Prieta Events*, *Engineering Geology*, Volume 71, Issues 1-2, January 2004, Pages 79-95.
- Lachet C. & Bard P.-Y. (1994). – Numerical and theoretical investigations on the possibilities and limitations of the "Nakamura's" technique. – *J. Phys. Earth (Japan)*, 44, 377-397.
- Lacroix P., A. Helmstetter, 2010, Localization of seismic signals associated with micro-earthquakes and rockfalls on the Séchilienne landslide, French Alps, *BSSA*, in press.

- Lebourg T., Binet S., Tric E., Jomard H. & El bedoui S. (2005). – Geophysical survey to estimate the 3D sliding surface and the 4D evolution of the water pressure on part of a deep-seated landslide, *Terra Nova*, 17, 399-406.
- Lebrun B., Hatzfeld D. & Bard P.-Y. (2001). – A site effect study in urban area: experimental results in Grenoble (France). – *Pure & App. Geophys.*, 158, 2543-2557.
- Legchenko A., Valla P. (2002) – A review of basic principles for magnetic resonance sounding measurements. *Journal of Applied Geophysics*. 50 : p. 3-19.
- Lermo J. & Chavez-Garcia F. J. (1993). – Site effect evaluation using spectral ratios with only one station. – *Bull. Seism. Soc. Am.*, 83, 1574-1594.
- Leroux O. , Schwartz S., Gamond J-F, Jongmans D, Bourles D., Braucher R. and Carcaillet J., 2009, Cosmic ray exposure dating on the head scarp of a major landslide (Séchilienne, French Alps), age constraints on Holocene kinematics, *EPSL*, doi:10.1016/j.epsl.2009.01.034
- Mavko G., Mukerji J. and J. Dvorkin, 2003, The rock physics handbook: tools for seismic analysis in porous media, Cambridge University Press.
- Meunier, P., Hovius, N., Haines, A.J., 2007. Regional patterns of earthquake-triggered landslides and their relation to ground motion. *Geophys. Res. Lett.* 34, L20408. doi:10.1029/2007GL031337.
- Meunier, P., Hovius, N., & Haines, J. (2008). "Topographic site effects and the location of earthquake induced landslides". *Earth and Planetary Science Letters* , pp. 221-232.
- Méric O., 2006, Etudes de mouvements de terrain par méthodes géophysiques, PhD thesis, Univ. J. Fourier, Grenoble, 249 p.
- Méric O, Garambois S, Jongmans D, Wathelet M, Chatelain JL, Vengeon JM (2005). Application of geophysical methods for the investigation of the large gravitational mass movement of Séchilienne, France . *Canadian Geotechnical Journal*, 42:1105-1115.
- Méric O., Garambois S., Malet J.-P., Cadet H., Gueguen P. & D. Jongmans, 2007, Seismic-noise based methods for soft-rock landslides characterization, *Bull. Soc. géol. france*, 2007, n 2, pages 137-148.
- Musil M., Maurer H., Green A., Horstmeyer H., Nitsche F., Mühlz D., and S. Springman, 2002, Shallow seismic surveying of an alpine rock glacier, *Geophysics*, 67, 1701-1710.
- Nakamura Y. (1989). – A method for dynamic characteristics estimation of subsurface using microtremor on ground surface. – *Quar. Report. Railway. Tech. Res. Institute*, 30, 25-33.
- Nakamura, Y. (2000). "Clear identification of fundamental idea of Nakamura's Techniques and its applications". In: *Proceedings of the 12th world conference of earthquake engineering*.
- Papadopoulos G. & A. Plessa, 2000, Magnitude–distance relations for earthquake-induced landslides in Greece, *Engineering Geology*, 58, 377-386.
- Pothérat P and Alfonsi P (2001). Les mouvements de versant de Séchilienne (Isère). Prise en compte de l'héritage structural pour leur simulation numérique. *Revue Française de Géotechnique*, 95/96:117-131.
- Renalier F., Jongmans D., Campillo M. & P.-Y. Bard, 2010, Vs imaging of the Avignonet landslide (France) using ambient noise cross-correlation, *J. of Geophys. Res.*, in press.
- Satoh T., Kawase H. & Matsushima S. (2001). – Estimation of (S)-wave velocity structures in and around the Sendai Basin, Japan, using array records of microtremors. – *Bull. Seism. Soc. Am.*, 91, 206-218.
- Scherbaum F., Hinzen K.G. & Ohrnberger M. (2003). –Determination of shallow shear wave velocity profiles in the Cologne/Germany area using ambient vibrations. – *Geophys. J. Int.*, 152, 597-612.
- SESAME Project, 2004, <http://sesame-fp5.obs.ujf-grenoble.fr/>.
- Shapiro, N., and M. Campillo (2004), Emergence of broadband Rayleigh waves from correlations of the ambient seismic noise, *Geophysical Research Letters*, 31, L07,614.
- Socco V. & Jongmans D. (2004). – Special issue on seismic surface waves, *Near Surf. Geophys.*, 2, 163-258.
- Supper R. & Römer A. (2003). – New achievements in developing a high-speed geoelectrical monitoring system for landslide monitoring. In: *Proc. 9th Meeting Env. Eng. Geophys.*, Prague, Czech Republic. – EAGE Publications, EEGS, Houten, Paper O-004, 6 p.
- Susuki K. & S. Higashi, 2003, Groundwater flow after heavy rain in landslide-slope area from 2-D inversion of resistivity monitoring data, *Geophysics*, 66, 733-743.
- Tokimatsu K. (1997). – Geotechnical site characterization using surface waves. In: *Earthquake Geotechnical Engineering*. – Balkema, Rotterdam, 1333-1368.
- Vengeon, J.-M. 1998. Déformation et rupture des versants en terrain métamorphique anisotrope, PhD Thesis, University of Joseph Fourier, Grenoble.
- Wathelet M., Jongmans D. & Ohrnberger M. (2004). – Surface wave inversion using a direct search algorithm and its application to ambient vibration measurements. – *Near Surf. Geophys.*, 2, 221-231.

CHAPITRE 4

Intérêt du Géoradar pour l'imagerie et la caractérisation des fractures dans le contexte de stabilité des falaises

4.1 Introduction. Problématique

Les éboulements en masse issus de falaises posent un problème particulièrement aigu pour les autorités responsables de la gestion et de l'aménagement du territoire en zone de montagne. D'une part, il est difficile de localiser spatialement les secteurs à risque en raison des incertitudes sur la continuité des discontinuités affectant un massif rocheux. D'autre part, l'occurrence temporelle d'un éboulement est difficile à prévoir en raison de la soudaineté du phénomène, de l'absence de signaux précurseurs et de la multiplicité des causes potentielles de déclenchement. Au niveau spatial, une écaïlle potentiellement instable affectée par des réseaux de fractures reste rattachée au massif rocheux en certains endroits appelés ponts rocheux. Ces derniers, qui peuvent être constitués de la roche saine ou liés à une recristallisation locale, assurent avec la friction la stabilité de l'écaïlle. L'analyse en retour de cicatrices post-éboulements a montré que c'était la rupture des ponts rocheux qui entraînait l'instabilité gravitaire, mais qu'une proportion de l'ordre de quelques % était en général suffisante pour assurer la stabilité d'un compartiment rocheux (Frayssines & Hantz, 2006). Comme souligné par Deparis (2007), l'analyse de la stabilité gravitaire peut être réalisée par des méthodes géomécaniques simples d'équilibre limite (Hoek et Bray, 1981), ou par des méthodes de modélisations numériques, telle que les éléments distincts (Hart, 1993). Ceux-ci présentent l'avantage d'analyser les interactions mécaniques des blocs à l'aide de relations liant les forces et les déplacements au niveau des contacts. D'autres méthodes, plus complexes qui sont basées sur la mécanique de la rupture (Scavia, 1995), dérivent des concepts décrits par Griffith (Atkinson, 1989). Ces travaux lient à la fois une approche géomécanique classique et une approche microscopique de propagation de la fissure, bien décrite dans les milieux continus tels que les aciers, alliages et matériaux polymères. Le problème lié à ces approches réside dans le manque de connaissance des paramètres d'entrée, cruciaux pour toute tentative d'évaluation de la stabilité. Les principaux paramètres étant liés à la connaissance en trois dimensions des discontinuités (extension, continuité, orientation, pendage...) affectant le massif rocheux, ainsi que leurs propriétés géomécaniques (ouverture, remplissage, rugosité) et leur évolution temporelle.

Pour mieux appréhender la géométrie tridimensionnelle d'un compartiment rocheux potentiellement instable (limites externes et fracturation interne), trois techniques d'observations et de mesures complémentaires peuvent être mises en œuvre :

1. la prise détaillée d'observations géologiques et structurales (sur le plateau supérieur, en paroi de falaise, dans les fissures ouvertes)
2. la morphologie numérique à partir d'images et de scannerisation laser (lidar), permettant une description précise de la géométrie superficielle des compartiments rocheux, une prise de mesures structurales et une localisation 3D de toutes les autres mesures effectuées directement le long de la paroi.
3. les reconnaissances géophysiques depuis la surface et/ou en paroi (tomographie électrique, radar géologique, sismique) pour localiser et/ou imager en surface et en profondeur les fractures

principales et leurs caractéristiques (ouverture, remplissage, continuité d'éventuels ponts de matière...).

Les analyses géologiques classiques ou de morphologie numérique peuvent apporter des informations primordiales sur ces discontinuités, mais seulement à partir d'observation superficielles qui sont ensuite extrapolées à l'intérieur du massif. Ainsi, de nombreuses incertitudes subsistent quand à la continuité de ces réseaux, leur extension en profondeur et sur l'existence d'autres réseaux qui n'impactent pas la surface. Pour améliorer la connaissance de la géométrie de ces réseaux de fractures au sein du massif, plusieurs méthodes géophysiques sont disponibles, qui diffèrent par leur sensibilité, leur résolution et leur profondeur de pénétration.

De fait, si de nombreuses investigations géophysiques ont été menées pour caractériser la géométrie des mouvements de terrain, et dans certains cas leurs propriétés (cf. Chapitre 3), très peu d'études ont concerné la problématique des éboulements de falaises et la reconnaissance des discontinuités, sans doute en raison des difficultés de mise en œuvre. Pourtant, de nombreuses observables géophysiques sont sensibles à la déstructuration d'un massif. La présence de micro-fractures va entraîner une décroissance des vitesses sismiques qui peut être accessible à partir d'images des vitesses déduites de tomographies sismiques actives (Dussauge-Peissier, 2003), images malheureusement fortement lissées. De même, Hack (2000) a montré qu'une forte anisotropie des vitesses sismiques (50 %) était corrélée à la présence de fractures. Les techniques basées sur le bruit de fond sismique ont été testées par Gallipoli et al. (2000) qui ont considéré les pics de résonance H/V (cf. chapitre 3) pour mettre en évidence des compartiments présentant des propriétés distinctes en termes de déstructuration. Ces mêmes techniques de bruit sismique sont actuellement utilisées pour estimer l'évolution temporelle des modes de résonance d'une paroi rocheuse (Levy et al., 2010). La résistivité électrique est également sensible à la présence de fractures (Deparis, 2007), mais le processus d'inversion et le lissage des images rendent également difficile leur localisation précise et leur extension.

Pour ces raisons, c'est la méthode géoradar qui a été popularisée pour l'imagerie des fractures au cours de ces dernières années, les milieux traversés étant en général plutôt résistifs (calcaires, gneiss, grés, granite) ce qui rend efficace le géoradar en termes de profondeur de pénétration tout en conservant une résolution adéquate. Celui-ci a été appliqué avec succès pour l'imagerie 2D de failles et de fractures (Benson, 1995; Stevens et al., 1995; Rashed et al., 2003). Avec le même objectif, Grasmueck (1996) a développé une technique d'imagerie radar 3D, qui a été appliquée dans une carrière de gneiss et a permis d'imager aussi bien les fractures subhorizontales que les failles subverticales. Grandjean et Gourry (1996) ont également imagé un réseau de fractures dans une carrière de marbre, à partir de mesures radar 3D.

Notre démarche a consisté à appliquer cette technique géophysique dans un contexte réel d'imagerie et de caractérisation des fractures, principalement à partir de mesures en paroi. Ces travaux ont fait l'objet des thèses de M. Jeannin (2005) et de J. Deparis (2007). Dans un premier temps, nous nous sommes intéressés uniquement au problème d'imagerie en testant le potentiel de différentes configurations d'acquisitions : réflexion à offset constant, CMP et tomographie radar (Jeannin et al., 2007). Ces travaux ont permis de sélectionner les configurations les plus efficaces (modes réflexion et CMP), ce qui a entraîné une autre étude se positionnant dans un contexte plus opérationnel sur un site sensible : les Gorges de la Bourne. Des images multi-fréquences, permettant de détecter des couches fines d'épaisseurs différentes, ont été combinées à une analyse de vitesse électromagnétique pour contraindre la décision de miner une paroi potentiellement instable. En retour, des forages horizontaux et le minage de la paroi ont permis de valider a posteriori les approches géoradar proposées (Deparis et al., 2007). Ces deux cas sont présentés sous la forme d'articles dans le paragraphe suivant.

En parallèle, nous avons considéré une approche plus quantitative en essayant d'utiliser les propriétés de la réflectivité des ondes radar pour caractériser à la fois les fractures et le milieu environnant. En effet, si les vitesses électromagnétiques donnent une information quantitative sur les milieux traversés, celle-ci n'est accessible que lorsque les fractures sont suffisamment ouvertes par rapport à la longueur d'onde pour permettre de distinguer des réflexions sur les deux bords de la couche fine. Dans un premier temps, nous avons validé l'approximation analytique de la réflectivité pour des couches fines, en la comparant avec des radargrammes obtenus par des modélisations par différences finies. Nous avons ainsi pu proposer, à partir de données synthétiques, une méthodologie originale basée sur l'inversion de la signature dispersive des variations de l'amplitude et de la phase de la réflectivité dans le contexte de couches minces (DAPVO). Cette approche a ensuite été appliquée avec succès à différents jeux de données réelles provenant d'acquisitions CMP acquises sur différentes parois rocheuses (Deparis et Garambois, 2009 ; 2010). Cette méthodologie est présentée dans le paragraphe 3 (Deparis & Garambois, 2009). Elle débouchera sur des perspectives qui concerneront à la fois toute problématique de contact (couche fine), mais devront être également élargies à des milieux plus complexes pour lesquels l'ensemble des données CMP devront être inversées, en 1D puis en 2D.

4.2 Imagerie des fractures dans le contexte de stabilité des falaises

Davis et Annan (1989) ont montré que la réflectivité des ondes radar au contact de deux unités était proportionnelle à la différence de contraste diélectrique entre ces deux unités, ce qui a ouvert la voie à de nombreuses applications du GPR de part son fort pouvoir de résolution comparé aux autres méthodes géophysiques. Pour la détection et l'imagerie de fractures et de failles subhorizontales, Grasmueck (1996) a obtenu un jeu de données quasi 3D, depuis un plateau, dans une carrière de gneiss (Fig. 2.1).

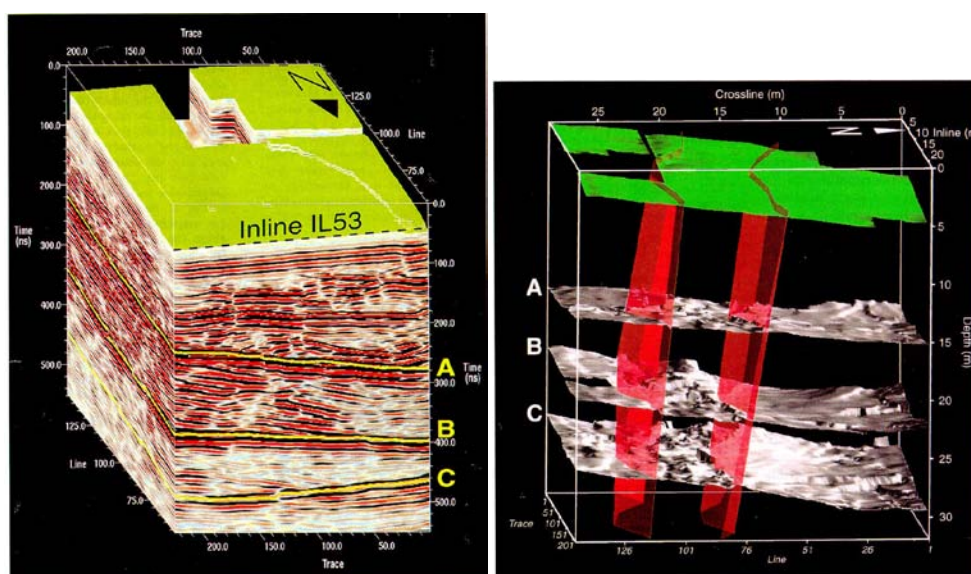


Fig. 2.1. Cube GPR 3D avec les failles principales (droite) et géométries 3D détaillées des principales discontinuités (A, B, et C) obtenues à partir d'une procédure d'analyse des amplitudes des ondes réfléchies (Grasmueck, 1996).

Ceci lui a permis de montrer une géométrie 3D des principales discontinuités à partir d'analyses des amplitudes réfléchies. Dans une carrière de granite, Seol et al. (2001) ont détecté l'orientation des fractures (azimut) en comparant les données radar obtenues avec trois modes d'acquisition

différents pour un même profil. Dérobert et Abraham (2000) ont réalisé des profils géoradars dans une carrière de gypse qui ont permis de caractériser l'endommagement de certains piliers rocheux en analysant la profondeur et l'inclinaison des fractures, tandis que la tomographie sismique n'a pu qu'imager de faibles vitesses sismiques dans les zones endommagées. Martinez et al. (1998) ont imagé de fines couches d'argiles présentes au sein de dépôts calcaires, prouvant le fort pouvoir de résolution du GPR dans le cas de couches minces. De leur côté, Pettinelli et al. (1996), Toshioka et al. (1995) et Pipan et al. (2003) ont montré à partir de données 2D et 3D que les remplissages de couches minces (eau, argiles, air) étaient toutes visibles lorsqu'un choix judicieux de la fréquence d'antenne était effectué. Dans les roches saines (non fracturées), considérées comme étant de bonne qualité, la plupart de l'énergie du signal radar est transmise, tandis que pour des roches de mauvaise qualité, l'énergie est très diffuse en raison de la présence de fractures, de joints et de cavités (Orlando, 2003). L'auteur a ainsi pu définir une méthode d'évaluation semi-quantitative en quantifiant la quantité d'énergie rétro-diffusée comme un critère de qualité des roches. Plus récemment, Roch et al. (2006) ont acquis des données GPR en pseudo-3D depuis une paroi de falaise pour des problèmes de stabilité et ont fourni une interprétation quantitative en termes de discontinuités (Fig. 2.2).

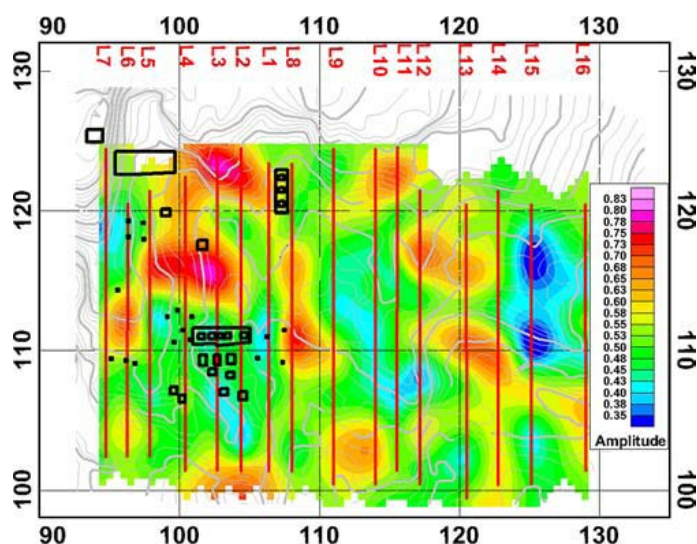


Fig. 2.2 Energie réfléchie entre 1.5 et 5 m de profondeur obtenue à partir de profils verticaux acquis le long d'une paroi rocheuse (Roch et al., 2006).

Suite à ces travaux de 1996, Grasmueck et al. (2005) ont développé une méthode d'acquisition GPR 3D qui permette réellement la migration 3D des données dans un contexte fracturé (sans repliement ni interpolation), la résolution latérale approchant le quart de longueur d'onde. Enfin, Tsoflias et al. (2004) ont étudié les propriétés de polarisation des ondes électromagnétiques en mode TE et TM pour différentes positions des antennes. A partir de mesures GPR de surface sur une carrière de calcaires dolomitiques affectés par une série de fractures verticales, leur étude a montré qu'il est possible de caractériser la position et l'azimut des fractures verticales, par analyse du déphasage entre les modes TE et TM

Dans cette problématique, deux études sont présentées ci-après qui visent à imager des fractures au sein de parois rocheuses. Celles-ci ont été menées à l'aide d'un système RAMAC (Mala Geosciences) que nous avons du adapter au contexte difficile de mesure que constitue les falaises. Nous avons notamment testé différentes acquisitions (réflexions, CMP, transmission) sur un site test ne présentant pas de vulnérabilité particulière (Jeannin et al., 2006). Pour assister l'interprétation des données, nous avons modélisé les données de transmission à l'aide d'un code

2D en différences finies. Puis, nous avons inversé les premières arrivées à la fois pour les données réelles et synthétiques ce qui a permis de fournir la distribution 2D des vitesses GPR au sein du massif par tomographie GPR, mais cette procédure n'a pas permis de localiser précisément les fractures subverticales principales. Des analyses CMP ont permis d'avoir accès à un profil de vitesses, nécessaire pour les traitements de migration et de conversion des temps en profondeur. Celle-ci n'a pas été capable de caractériser directement les propriétés des fractures, leurs ouvertures étant trop faibles. Nous verrons dans un paragraphe suivant que ce sont les attributs de la réflectivité déduites des acquisitions CMP qui permettront l'obtention des propriétés des fractures (ouverture, remplissage), par un processus d'inversion original. Finalement, ce sont les profils réflexion à offset constant, acquis directement le long de la paroi (avec des orientations à la fois verticales et horizontales), qui ont permis de fournir des images haute résolution des discontinuités, jusqu'à 20 m de profondeur, avec une résolution de 25 cm et de préciser leur localisation pseudo-3D. Il faut noter que des variations dans leurs propriétés ont entraîné des variations observables de la réflectivité associée sur les profils à offset constant.

Dans un deuxième temps, c'est une étude plus opérationnelle qui est présentée (DeParis et al., 2007). Celle-ci a été effectuée dans les gorges de la Bourne, localisées à 25 km environ au sud ouest de Grenoble dans le massif du Vercors. La roche en place est peu altérée, présente une porosité inférieure à 1% et une faible teneur en argile. La route de la Bourne, qui a été construite entre 1861 et 1872, est sujette à de fréquents éboulements et chutes de blocs. Par exemple, un éboulement dramatique de 2000 m³ s'est produit durant la nuit du 29 janvier 2004 et a causé la mort de deux personnes. L'observation de la cicatrice de la fracture après l'éboulement a exposé une surface de pont rocheux de 5% (Frayssines, 2005). A quelques dizaines de mètres de l'éboulement de 2004, une autre falaise surplombe la route sur une hauteur de 2.5 m. Une étude géologique de cette masse rocheuse a montré qu'elle est découpée par des plans de stratification faiblement inclinés et des fractures sub-verticales parallèles à la route. En particulier une fracture ouverte de quelques décimètres a été localisée 5 mètres en arrière de la falaise et semble délimiter une écaille instable de part en part. Dans le but d'estimer le pourcentage de ponts rocheux encore présents et la continuité et l'extension des fractures au sein de cette masse rocheuse, une étude géophysique basée sur le Géoradar comprenant deux profils réflexion multi-fréquences et un profil CMP a été proposée. Les données ont été acquises à l'aide d'antennes de fréquences centrales égales à 200, 500 et 800 MHz, positionnées directement le long de la paroi. Outre son aspect opérationnel en termes de risque, un des intérêts de cette étude réside dans le fait que la reconnaissance du site a fait l'objet a posteriori de plusieurs sondages horizontaux destructifs. Ceux-ci ont été effectués au marteau fond de trou avec enregistrement de la vitesse de rotation de l'outil, paramètre sensible aux changements de propriétés du matériau. Dans notre cas, les faibles vitesses traduisent un matériau dur (roche) tandis que les vitesses importantes traduisent un matériau tendre (argile, sable dans les fractures...). Les fractures ponctuelles détectées ont ainsi pu être confrontées aux réflecteurs apparaissant sur les traces radar adjacentes. Cette comparaison illustre le potentiel et les limites du Géoradar pour la caractérisation des fractures. Les fractures principales ont été correctement détectées et localisées à condition qu'elles aient été suffisamment ouvertes et séparées les unes des autres. L'ensemble de ces données, et notamment la présence d'une fracture relativement continue à 2 m de profondeur, non reconnue depuis la surface, a amené les autorités locales à miner la paroi rocheuse afin de sécuriser la route. Cette technique d'assainissement a permis de comparer avec succès les cicatrices des fractures qui ont été exposées après minage avec celles déduites des images obtenues avec le GPR, et notamment leur continuité.

Multiconfiguration GPR measurements for geometric fracture characterization in limestone cliffs (Alps)

Mathieu Jeannin¹, Stéphane Garambois¹, Colette Grégoire², and Denis Jongmans¹

ABSTRACT

Rock-mass fracturing is a key parameter in rock-fall hazard assessment. However, traditional geologic observations can provide information only about discontinuities at the surface. In this case study, detailed ground-penetrating-radar (GPR) measurements (with antennas of 50 MHz, 100 MHz, 200 MHz, and 400 MHz) were conducted on a test site, using different acquisition configurations deployed on vertical cliff faces. Conventional 2D profile data, common-midpoint (CMP) survey data, and transmission data were acquired to evaluate the potential use of radar waves to characterize the geometry and properties of the major discontinuities (fractures) within a Mesozoic limestone massif. Results showed that the continuity and geometry (orientation and dip) of the major observed fractures, which are crucial parameters for assessing rock stability, can be obtained by combining vertical and horizontal profiles measured along the cliff. We used 100-MHz antennae and reached a maximum penetration of 20 m, which limits the technique to rock volumes of a few tens of thousands of cubic meters. We observed significant differences in reflectivity along the detected fractures, which suggests that the fractures' characteristics vary in the rock mass. We used transmission data to obtain a radar velocity image. Although the results were consistent with radar profiles on the cliff, they showed that the technique has little utility, beyond that of more traditional GPR methods, for delineating fractures in a rock mass.

their suddenness and difficulty of prediction. Increasing urbanization in mountainous areas requires better assessment of the hazards linked to rock falls and precise determination of the locations and volumes of rock masses that are likely to fall.

Rock-mass stability assessment is a complex problem generally addressed from surface observations, such as slope morphology, mass fracturing, and/or deformation measurements (Hoek and Bray, 1981; Rouiller et al., 1998). Such observations lack information concerning the geometric relationships among discontinuities in the rock mass. Drilling can be used to supply subsurface information, but it is dangerous near fractured cliffs and merely provides point-source data. Geophysical methods use continuous transects to provide information about the discontinuity geometry within a rock mass. However, geophysical techniques have been applied only rarely to vertical cliffs or steep rock slopes, probably because of logistical difficulties in carrying out geophysical experiments in such difficult conditions.

The ground-penetrating-radar (GPR) method has been applied successfully in easier field conditions to solve comparable geologic problems. Examples are dimensional fault and fracture mapping in electrically resistive rocks, both from surface acquisitions (Benson, 1995; Stevens et al., 1995; Demanet et al., 2001; Rashed et al., 2003) and in boreholes (Zhou and Sato, 2000). To image subhorizontal fractures as well as subvertical faults, Grasmueck (1996) developed a 3D radar technique, which he promisingly applied in a gneiss quarry, even if its data sets were spatially aliased and required interpolation. More recently, Grasmueck et al. (2005) developed a full-resolution 3D GPR imaging method, resulting in migrated imaging approaching quarter-wavelength resolution. In a gypsum quarry, Dérobert and Abraham (2000) collected radar profiles on pillars to characterize fracture depth and inclination and used seismic tomography to image damaged zones as low P-wave velocities. Similarly, Toshioka et al. (1995) detected the distribution and continuity of fractures from radar data acquired on the vertical wall of a welded tuff rock. Seol et al. (2001) developed a

INTRODUCTION

Among the many natural hazards in mountainous regions, rock falls are frequently occurring phenomena that are characterized by

Manuscript received by the Editor July 30, 2004; revised manuscript received October 26, 2005; published online May 26, 2006.

¹LIRIGM, Maison des Géosciences, Université Joseph Fourier, BP 53, 38041 Grenoble Cedex 9, France. E-mail: Mathieu.Jeannin@ujf-grenoble.fr; Stephane.Garambois@ujf-grenoble.fr; Denis.Jongmans@ujf-grenoble.fr.

²Department of Civil Engineering, Katholieke Universiteit Leuven, Kasteelpark Arenberg 40, B-3001 Heverlee, Belgium. E-mail: colette.gregoire@bwk.kuleuven.ac.be.

© 2006 Society of Exploration Geophysicists. All rights reserved.

method to find the strike direction from three different acquisition modes for the same survey line in a granite quarry. The computed reflector azimuths correlated closely with those of observed fractures and joints. In limestone formations, Pettinelli et al. (1996) and Pipan et al. (2003) showed, from 2D and 3D radar measurements, that open fractures, joints, or discontinuities filled with clay or water are clearly visible when an appropriate signal wavelength is used.

Orlando (2003) defined a semiquantitative evaluation method that was based on the amount of backscattered energy as an index of rock quality. In fact, in high-quality rock, most of the radar-wave energy is transmitted, whereas in low-quality rock, energy is backscattered from fractures, strata joints, and cavities. In a more quantitative way, Grégoire et al. (2003) studied the GPR reflection coefficient of fractures in the frequency domain. They deduced the aperture and the filling material of fractures from multifrequency reflection data, but they needed a known reference signal to do so.

Recently, Dussauge-Peisser et al. (2003) used antennae and geophones set against a 12-m-high limestone cliff to conduct radar measurements and collect seismic tomography data. Their results indicate that vertical 120-MHz GPR profiles performed on the cliff face were efficient in detecting and imaging subvertical discontinuities as far as 10 m in from the cliff face. Discontinuities correlated closely with fractures deduced from surface observations. In contrast, their seismic tomography, performed with sources and geophones deployed on the cliff-top surface and on the cliff face, was incapable of detecting and characterizing individual fractures but did provide a low-resolution image for rock-mass stability.

Similarly, Cardarelli et al. (2003) used both GPR and seismic data for tunnel-stability assessment. Radar data supplied information about the number and location of discontinuities in the investigated zone, while seismic methods provided estimates of the distribution of mean elastic properties.

This paper advances the use of multiconfiguration GPR experiments applied to a 10-m- to 15-m-high limestone cliff located in a subalpine massif near Grenoble (France). This site does not present any specific rock fall hazard and was chosen mainly for its accessibility and relatively simple geologic structure. Conventional 2D profiles, common midpoint (CMP) data, and transmission data were acquired to evaluate the potential for characterizing the geometry and properties of fracture networks in vertical cliffs and for assessing the stability of those cliffs.

We conducted GPR measurements using a RAMAC/GPR system (MALÀ Geosciences), which we adapted to the difficult conditions along vertical cliff faces. Because the main fracture networks at our study site are almost vertical, only profiles in which at least one antenna was positioned directly on the cliff surface were able to image the possible interfaces created by these discontinuities. For that reason, and to optimize the coupling between the rock surface and the antennae, an operator climbed down the cliff with the antennae and suitable cables. All profiles were acquired with unshielded antennae and using the transverse electric (TE) mode.

To assist interpretation, we modeled transmission data using a 2D full-waveform modeling code and inverted the first-arrival time picks for both real and synthetic data. Seismic and GPR tomography have been used widely to investigate rock masses (e.g., Ivanson, 1987; Hollender, 1999; Demanet, 2000; Jongmans et al., 2000). Although crosshole transmission tomography is the most widespread method (Ivanson, 1987; Bois et al., 1972; Corin et al., 1997), surface tomography (all sources and receivers located

at the ground surface) is used increasingly, to avoid expensive drilling costs or destructive investigations (Lanz et al., 1998; Liu et al., 1998). Radar tomography also can be used to study attenuation (Hollender, 1999), as well as diffraction or dispersion (Olhoeft, 1993). In this study, we apply radar tomography to map velocity distribution inside the investigated zone.

DESCRIPTION OF THE TEST SITE

Limestone cliffs surrounding the urban area of Grenoble (Isère, France) extend over a cumulative length of 120 km (Figure 1a) and can be as high as 400 m (Figure 1b). They are part of the Chartreuse and Vercors subalpine massifs and are made of sedimentary rocks of the late Jurassic and early Cretaceous ages (limestone and marls). Most of the cliffs are located in Tithonian and Urgonian limestone beds, which dip slightly cliffward (Figure 1b).

Because of the cliff morphology, this region has been subject to extensive risk of rock falls (ranging from block fall to major slope failure). That risk has been studied using a probabilistic approach (Dussauge-Peisser et al., 2002).

During the thirteenth century, the Chartreuse massif experienced a major rock fall, with an estimated volume of 500 million m³ and a transport distance of 7.5 km from the cliff face (Goguel and Pa-choud, 1972).

Our test site is a 12-m-high cliff made of Tithonian limestone (upper Jurassic) that forms a subhorizontal plateau covered by organic soil. Detailed structural studies, carried out from surface observations on the cliff and on the plateau, showed that the rock mass is affected by three main discontinuity sets (Figure 2): The bedding planes (labeled S_0) dipping gently inside the massif (N30°E/20°NW) and two vertical fracture sets (N140°E/90° and N30°E/90°, Figure 2c).

The first fracture set is predominant and clearly visible on the entire cliff. Open fractures are filled with a mix of clay and organic

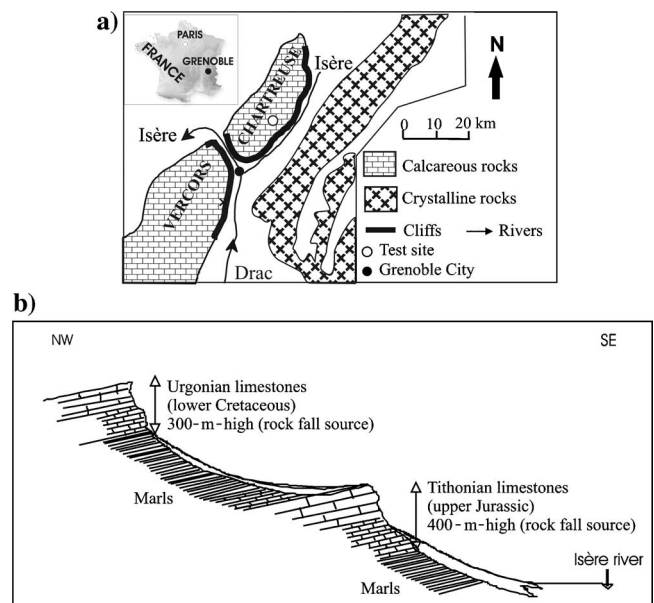


Figure 1. (a) Geologic map of the city of Grenoble (France), and location of the study site in the Chartreuse massif. (b) Typical geologic cross section of the limestone cliffs surrounding the city of Grenoble.

soil. The surface locations of the observed fractures are displayed in Figure 2b (labeled F1 to F5) along an A-B axis perpendicular to the fracture strike (Figure 2a).

The secondary fracture set, oriented N30°E, is mainly visible in the western part of the site (Figure 2a) and is locally exposed on the cliff face. An organic soil horizon, above the limestone cliff face and on the horizontal plateau, covers the extension of the different fracture sets inside the rock mass, so they cannot be observed from the surface.

In order to evaluate the potential of GPR to detect the 2D/3D geometry of the fracture sets, different GPR acquisition patterns were carried out. Because of the attenuating organic soil on top of the cliff and the subvertical orientation of the main fractures, all measurement configurations had at least one antenna placed directly on the cliff face. Figure 3 displays the design of a typical vertical profile acquisition in TE mode. We also performed vertical and horizontal 2D profiles, a CMP survey, and a transmission experiment between the vertical cliff face and the plateau.

PROFILES ACROSS THE CLIFF FACE (VERTICAL AZIMUTH)

The reflection-mode configuration is the most common choice for subsurface measurements. In our study, GPR data were acquired along vertical profiles with antennae placed directly on the cliff face. The 1-m-long transmitter-receiver pair was moved in increments of 20 cm. Figure 4 shows an example of raw (4a) and processed (4b) profiles acquired using 100-MHz-unshielded antennae along the vertical cliff. The main events identified from the raw data are the direct airwave (between 3 and 20 ns) and reflected events down to 75-ns two-way traveltime, which present high-reflectivity variations as a function of vertical location.

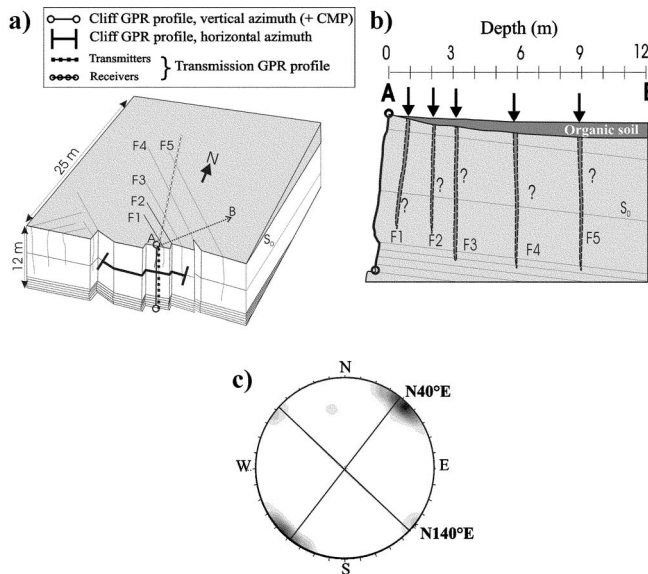


Figure 2. Schematic representation of the test site (Chartreuse massif). (a) Location of the main fractures (F1 to F5) deduced from structural observations and different GPR tested configurations. Direction A-B is orthogonal to the fracture strike direction. (b) Hypothetical view of the fractures along the A-B profile. (c) Stereogram of the observed fractures, showing two main networks.

To increase the amplitude of late (distant) events, the data were processed and filtered. First, a 10- to 200-MHz band-pass zero-phase Butterworth filter was applied, followed by a top-mute of direct-airwave arrival and notch filters designed to attenuate multiple monofrequency reverberations (ringing). Then, an automatic gain control (AGC) was applied, which enhanced the late arrivals but caused the loss of the original amplitude information. The processed radargram (Figure 4b) shows several reflected signals down to 280 ns (two-way traveltime).

VERTICAL-AZIMUTH CMP PROFILE

To obtain a velocity profile as a function of distance behind the cliff face, a CMP profile was made by varying the radar-antenna



Figure 3. Photograph of GPR-data acquisition on a vertical cliff face (TE mode).

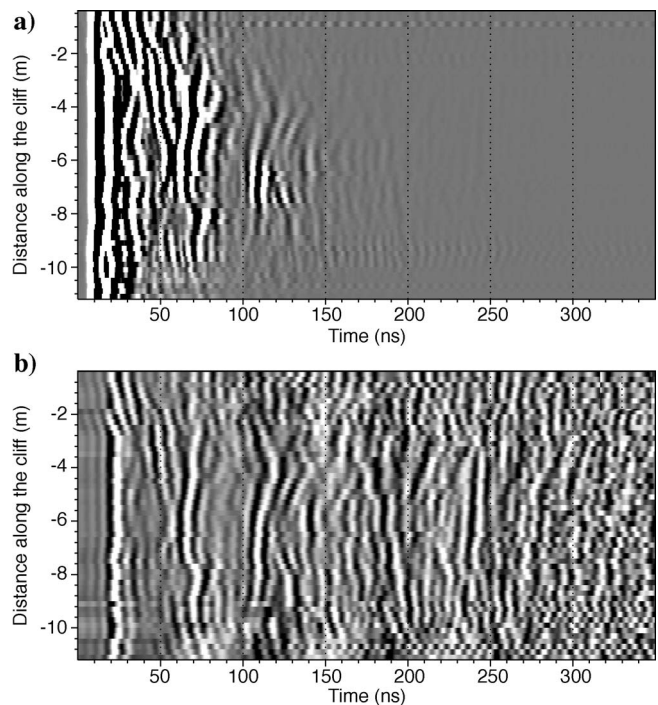


Figure 4. An example of a vertical GPR profile: (a) raw data and (b) processed data acquired along the cliff, using 100-MHz antennae.

spacing across a central location 5 m from the top of the cliff. Two operators carrying one antenna each traversed up and down the cliff face from this central location. Antennae with a 200-MHz center frequency were chosen to enhance the resolution, although penetration depth decreased. The CMP profile (Figure 5a) was filtered using a 30- to 300-MHz band-pass Butterworth filter, and amplitudes were equalized with AGC. The normal move-out (NMO) was analyzed using the semblance maxima approach (Yilmaz, 1987), which is used commonly in seismic processing and yields the stacking velocity (Figure 5b). Only the onsets of the main reflected waves were picked because of the difficulty in identifying reflections from closely spaced reflectors (for example, the reflected waves occurring at 55-ns two-way traveltime). The corresponding interpretation (reflections at fractures F2 and F3) was made possible by the data displayed later in Figure 6c, which shows that fracture F2 dips within the rock mass toward fracture F3. Five reflected events were picked on the basis of the combined semblance image and on CMP gather panels (Figure 5b). Four of the five reflected events (F1, F2, F3, F4, and F5) correspond to the location of observed fractures (Figure 6), the picked F6 fracture was not seen from surface observations. A deeper reflected wave can be distinguished around 230 ns, but only for low offsets, thus preventing any hyperbola fitting. Figure 5c displays the data after

NMO corrections, which were computed using the velocity presented in Figure 5b. Almost all reflected events have been correctly flattened, thereby indicating that the NMO velocity profile is well constrained.

The average interval velocities $V_{i,j}$ between times t_i and t_j were computed from the NMO velocity using the Dix formula (Dix, 1955). Although that process may suffer from numerical problems when reflections are spaced closely or when rms velocities vary rapidly (Clapp, 2001), it allows an approximate derivation of the interval velocities. The computed interval-velocity profile (Figure 5d) shows moderate 1D velocity variations inside the rock mass (ranging from 8–10 cm/ns). This interval-velocity profile presents a slight increase in velocity, moving downward, from 10.5 cm/s at the surface to 12 cm/s at 1.9 m deep. This latter value is characteristic of unaltered limestone with no cracks (e.g., Davis and Annan, 1989). Below 3 m, the velocity decreases, reaching 8 cm/ns between 5.4 and 7.6 m in depth. This velocity reduction is probably linked to filling of the main fractures F2 to F5. Below 7.6 m in depth, the velocity increases to 10 cm/ns.

Figure 5e presents the stack of NMO-corrected data (Figure 5c), which amplifies the reflections and allows a correlation of the reflected events with the observed fractures.

VERTICAL-AZIMUTH RADAR PROFILE RECORDED AT DIFFERENT FREQUENCIES

Four different antennae with center frequencies of 50 MHz (Figure 6a), 100 MHz (Figure 6b), 200 MHz (Figure 6c), and 400 MHz

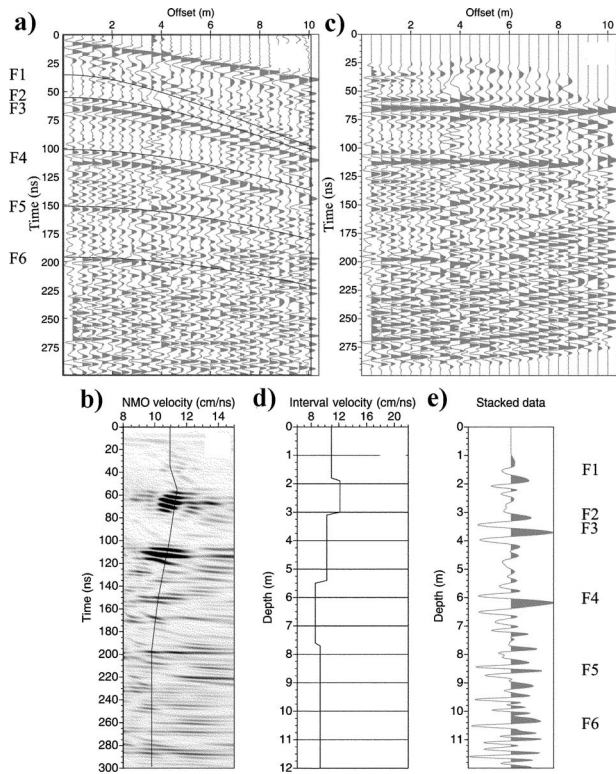


Figure 5. (a) Filtered CMP data with a direct airwave (velocity of 30 cm/ns), a poor signal-to-noise ratio linear-wave arrival propagating directly into the limestone, as well as several reflected waves and their corresponding picked hyperbolae. The hyperbolae are labeled according to their fracture correspondence. (b) Semblance analysis of reflected events and deduced NMO velocity profile as a function of time. (c) CMP data after NMO corrections. (d) Interval-velocity profile deduced from the NMO velocity profile using the Dix formula. (e) GPR trace after NMO corrections and stack of CMP data.

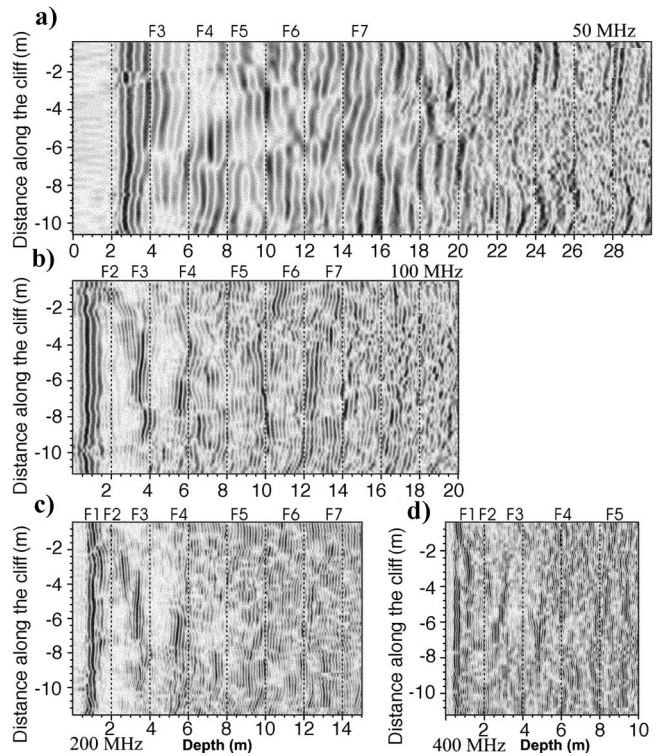


Figure 6. Comparison of the same GPR vertical-azimuth profile, acquired with different antenna frequencies: (a) 50 MHz, (b) 100 MHz, (c) 200 MHz, and (d) 400 MHz. All GPR sections were filtered and migrated using the velocity profile presented in Figure 5d. The main fractures (observed from structural surface investigations or deduced from GPR data) are labeled F1 to F7.

MHz (Figure 6d), were used along the same profile on the cliff face. They had a vertical azimuth and a trace spacing of 20 cm. The four radargrams shown in Figure 6 were filtered and processed the same as the data in Figure 4, except for the band-pass filter, which was adapted here to the center frequency of each antenna. The four radar sections also were migrated using the velocity profile deduced from the CMP analysis (Figure 5d). Numerous vertical reflectors are apparent and are approximately parallel to the cliff wall. The exception is F2, which dips toward the rock mass (Figures 6a–6d). Most of the vertical reflectors correspond to the main fractures observed from the surface (F1, F2, F3, F4, and F5, see Figure 2b), which are located at 0.9, 2.0, 3.2, 5.5, and 9.0 m, respectively, along the plateau moving away from the cliff face (Figure 2b). These fractures correlate well with reflected events, both in the CMP data and in the profile with a vertical azimuth. Two deeper fractures (F6 and F7) were detected with these measurements, but probably were masked from observation at the surface by the organic cover located on the horizontal plateau. Fracture F6 also appeared on the CMP measurements (Figure 5a).

The four radar sections show information about these fractures, with a trade-off between resolution and depth of penetration. Some shallow reflectors (F1 and F2) are observable only with the higher-frequency antennae (Figures 6c and 6d), whereas deeper events (F6 and F7) are imaged using lower-frequency antennae (Figures 6a and 6b). No multiple reflected waves were identified. The penetration depth of the radar waves ranges between 21 m with the 50-MHz antenna (Figure 6a) and 10 m with the 400-MHz antenna (Figure 6d). The 100- and 200-MHz radar sections (Figures 6b and 6c, respectively) appear to be the best compromise between resolution and penetration.

Maximum vertical imaging resolution is usually considered to be one-quarter of the predominant wavelength (Yilmaz, 1987). This formula leads to an approximate resolution of 50 cm, 25 cm, 12.5 cm, and 6.25 cm, respectively, for the different antennae used in this study (50-MHz, 100-MHz, 200-MHz, and 400-MHz antennae). Note that 50-MHz antennae do not provide the required resolution to accurately position the discontinuities.

Using Annan's (1996) reflection-coefficient threshold of 0.1 (considered as a frame of reference) and the thin-layer approximation, one can compute the maximum detection power of each antenna for low incidence angles in the TE mode. In our case, using a mean velocity of 12 cm/ns for limestone and 7 cm/ns for the clay filling, the derived detection power equals approximately 3 cm (50 MHz), 1.5 cm (100 MHz), 0.75 cm (200 MHz), and 0.375 cm (400 MHz).

Amplitude variations are clearly visible along the same reflector (e.g., fracture F3) and are a function of frequency (second-order changes) at a given location. Such variations can result either from fluctuations in topographic relief and electrical properties of the cliff face, which will affect radiation properties of antennae (Lampe and Holliger, 2003), or from reflectivity changes.

In a given frequency range, fracture detection with GPR depends on the material filling the fracture and on the thickness of the discontinuities. Fractural dispersive properties, which can be modeled using the Jonscher formulation (Jonscher, 1977), were used successfully by Grégoire et al. (2003) to locate a fracture opening in a salt mine (Grégoire et al., 2003). For this, they used thin-layer approximation and needed a known reference signal.

In our data, a key interpretational problem concerns the origin of the amplitude variations of the radar echoes along a given reflector.

First, one can see that these variations are not observed at the same vertical location for all reflectors and that they were detected identically using different antennae of various frequencies, which presented different coupling properties with the rock face. Second, the roughness of the cliff face exhibits small amplitudes. Consequently, the observed reflectivity changes along a given reflector seem to be linked directly to changes in fracture properties (aperture and/or filling), and antennae coupling effects appear to generate only second-order disturbances.

3D VISUALIZATION USING INTERSECTING PROFILES

For a better characterization of the spatial fracture geometry, we recorded a horizontal-azimuth GPR profile on the cliff wall using 200-MHz antennae with a trace spacing of 20 cm. The horizontal profile was 13 m long and was 5 m from the top of the cliff, whereas the vertical profile was 11 m long. We filtered and migrated the raw data in the same manner that we used for the other 2D profiles.

Figure 7 shows a pseudo-3D view of the 200-MHz vertical and horizontal profiles. The combination of the two profiles allows one to define potentially unstable masses for rock-stability assessment. In this example, two sets of reflectors are clearly visible (primary and secondary fracture sets). Knowing the cliff-wall direction (N100°E), one could deduce the azimuths of the two sets of fractures from the GPR data, which correspond to the orientations observed in the outcrop. On the two profiles, each reflected wave exhibits variations in reflectivity, suggesting that the fracture properties (aperture and filling) may vary in space.

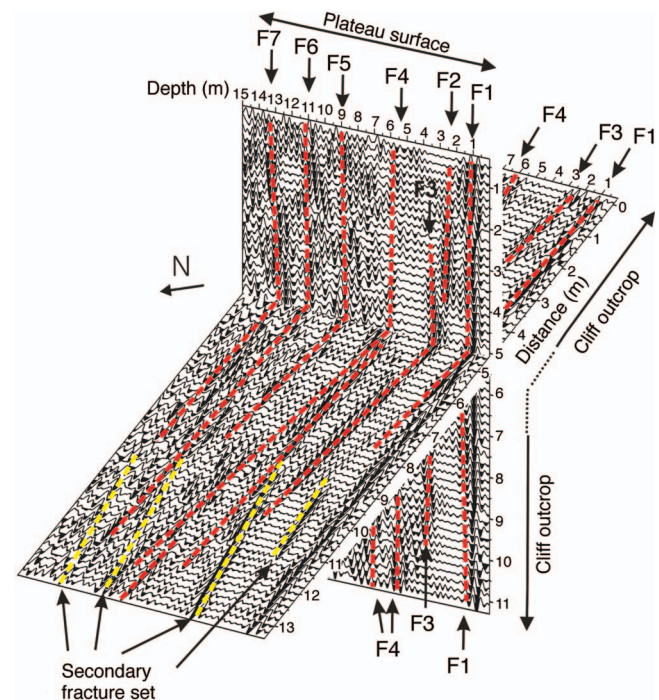


Figure 7. Vertical and horizontal 200-MHz profiles, showing the orientation and dip of the main fractures. The data were filtered and migrated.

TRANSMISSION EXPERIMENT

The potential value of GPR velocity tomography in characterizing discontinuities within the rock mass was tested with 100-MHz antennae in transmission mode.

The GPR antenna configuration and the preliminary locations of the fractures are shown in Figure 8a. The transmitting antenna was moved vertically in increments of 1 m along the cliff surface (transmitters T1 to T11). For each transmitter position, the receiving antenna was displaced along the plateau at 1 m intervals (receivers R1 to R20) along a profile that was roughly orthogonal to the cliff wall (Figure 2a). According to our structural study and GPR data presented before, fractures F1 through F5 cross the profile on the plateau near receivers R1, R3, R5, R11, and R15, respectively. Figure 8b displays a typical radar section for transmitting antenna T7.

We used a finite-difference numerical modeling code, GPR-MAX2D, (Giannopoulos, 2002) to identify the different waves by comparing synthetic and real data. We characterized the modeled media by linear and isotropic properties and by the frequency-dependent permittivity described by the Debye formula (e.g., Jonscher, 1977). The transmitting antenna is modeled as a line source.

Figure 9a displays the model's geometry, as deduced by trial-and-error tests. Our strategy was to start the modeling with a homogeneous medium presenting a limestone velocity of 11 cm/ns and to gradually include an increasing number of fractures with various properties. We repeated this process until the derived synthetic radargram corresponded to the observed one. Note that the three main vertical fractures of the model correspond to those deduced from the 100-MHz vertical-azimuth profile (Figure 6b).

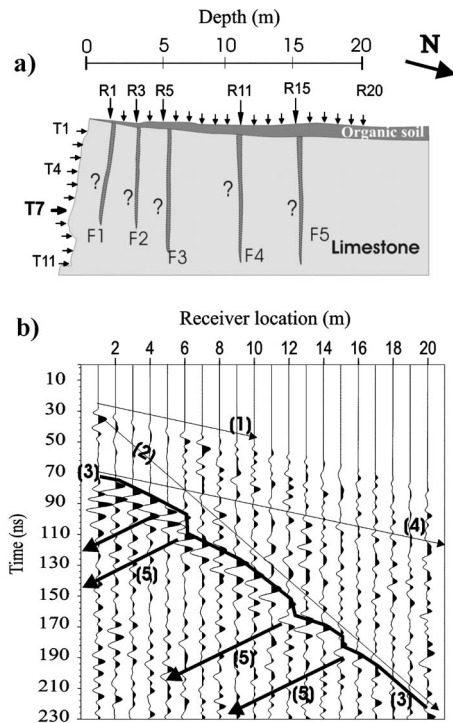


Figure 8. The transmission experiment. (a) Layout of the field experiment and location of the main observed fractures (F1 through F5). (b) Real-transmission radargram obtained for transmitter T7, and main EM events, labeled 1 to 5. Synthetic data and associated raypaths shown in Figure 9 helped in the interpretation.

This comparative study permitted a schematic characterization of the fracture properties (aperture, velocity of 7.5 cm/ns), and of the geometry and velocity of the upper soil. It also underlined the effectiveness of 2D modeling in this geometry. The synthetic radargram for transmitter T7 is presented in Figure 9b. On both real and synthetic data (Figures 8b and 9b), five types of waves can be identified: (1) the direct airwave (in blue in Figures 9a and 9b), which had a velocity of 30 cm/ns, followed by (2) a ground wave (in yellow in Figures 9a and 9b) that propagated from the transmitter to each receiver, with an apparent velocity of 10.5 cm/ns. The third wave (3, in red in Figures 9a and 9b) had a velocity similar to that of the direct wave (30 cm/ns) but arrived with a 40-ns delay on the plateau. This wave propagated in limestone along the surface of the cliff wall and was diffracted in the air at the corner of the cliff. Also shown are the reflected waves from the fractures (5, in black in Figures 9a and 9b), which can be used for imaging, and the direct ground wave transmitted inside the rock mass (4, in green in Figures 9a and 9b).

The systematic delay of a few nanoseconds between the synthetic signals and the real one is undoubtedly a consequence of not including fracture F1 in the model. The wave transmitted in the rock mass (labeled 3 in Figures 8 and 9) exhibited time delays locally, observed at receivers R6, R12, and R15 on the real data and at receivers R4, R7, and R13 on the synthetic data. These delays are the result of crossing through low-velocity zones that also generated reflected events (labeled 5). Those low-velocity zones correlate with fractures F2, F3, F4, and F5 (Figure 8a) and a CMP velocity decrease (Figure 5), thereby indicating that the fractures probably are filled with clay material (or organic soil).

Two-dimensional modeling helped us identify the direct waves transmitted in the ground, which we then used to obtain a velocity tomogram of the rock mass. Next we picked first-break arrival times on all radargrams and inverted them using the simultaneous

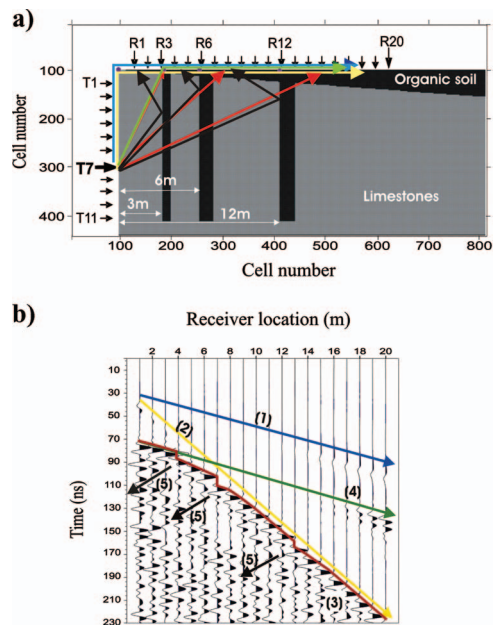


Figure 9. (a) Geologic model used in the GPR transmission modeling, and raypaths associated with each identified event. (b) Synthetic transmission radargram obtained for transmitter T7 from the geologic model shown in (a).

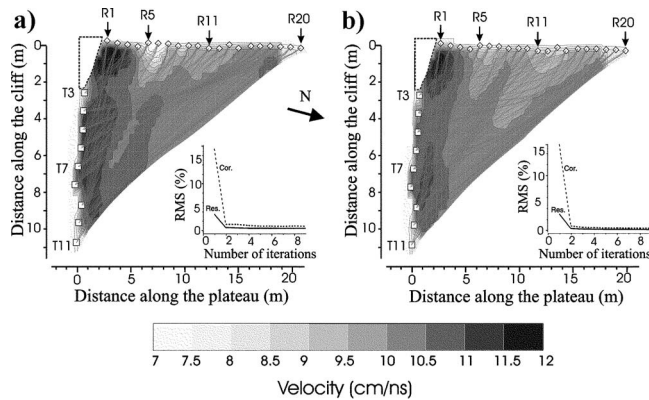


Figure 10. (a) Real and (b) synthetic GPR tomograms of the investigated rock mass. The raypaths indicate the spatial resolution of this image. Note that the rms error decreases as a function of the number of iterations.

iterative reconstruction technique (Dines and Lyttle, 1979), which was implemented in 3D software for seismic velocity tomography analysis (Demagnet, 2000).

Using that technique, in a given cell, the slowness correction (at each iteration) is a weighted sum of the time residuals for the rays crossing the cell. In the software, the weighting factors are the ratios of the ray length in the cell and the total ray length, to favor the rays that cross few cells. To ensure a stable convergence of the iteration process, the slowness correction was limited to 50% of the slowness value in the cell (Demagnet, 2000). The velocity of the homogeneous starting model was 12 cm/ns. To avoid possible non-uniqueness problems, we focused attention on the final velocity distribution's low sensitivity to the starting model by considering different starting velocities (Demagnet, 2000).

To evaluate the efficiency of the tomography method, the transmitted waves generated from the synthetic model described in Figure 9a were also analyzed using the same layout. Figure 10a shows the computed 2D real tomogram, and Figure 10b shows the synthetic velocity tomograms, both of which were obtained after 9 iterations. The same figure also displays the evolution of rms errors, with the number of iterations and the raypaths.

The resulting images appear smoothed and exhibit similar features: a low-velocity zone, ranging from 7 to 8 cm/ns near the surface (related to the soil cover); a gradual velocity decrease at the fracture locations (F3 and F4 for the real case), with limited vertical extension; and a 3-m-thick homogeneous zone with a velocity of approximately 11.5 cm/ns, close to the cliff. All these features correlate well with the velocity analysis deduced from the CMP data (Figure 5) and the model used for the simulation (Figure 9a). However, the transmission technique appears to be of little utility for accurately detecting and characterizing the fracture network, because it is labor intensive and produces gradational contacts that make identification of localized fractures difficult.

CONCLUSIONS

GPR measurements with different configurations were performed on a limestone cliff, with the aim of imaging the discontinuities inside the rock mass. Because the plateau above the cliff is covered with a conductive weathered layer and the two main sets of fractures are nearly vertical, GPR reflection profiles were car-

ried out on the vertical cliff face. In the geologic context of Mesozoic limestone massifs such as this one, a maximum penetration of 20 m was reached with 100-MHz antennae that gave a satisfactory resolution (approximately 25 cm) and detection power (approximately 1.5 cm). Although this work required a complex data-acquisition effort, particularly for the horizontal-azimuth profile, the results showed the presence of several reflectors. The location and orientation of those reflectors coincided with the fractures observed at the surface.

Additional valuable information obtained by GPR measurements was imaging of the fracture network with a resolution of a few centimeters using the high-frequency antenna (200 MHz). At the present time, such high-resolution GPR measurements probably are the only technique that allows a detailed 3D investigation inside the rock mass (Grasmueck et al., 2005). Its application in rock fall assessment could be of great interest for defining potentially unstable blocks. Because of the relatively low depth of penetration, however, the technique is limited to volumes of a few tens of thousands of cubic meters. The high cost of such experiments probably will restrict the use of the technique to cases in which the risk is high.

Improvements must be made to the acquisition system in such difficult contexts. Wireless technology should be developed to move the instruments efficiently on the cliff. Data from GPR should also be coupled with laser-scanning techniques to position the GPR traces on a numerical model of the cliff and to define the 3D geometry of potentially unstable blocks. All the data acquired during this study exhibit reflectivity variations, both with distance along the same fracture and with frequency. That reflectivity variation suggests that GPR measurements are sensitive to fracture properties (e.g., to filling and aperture).

In the future, reflection coefficient versus frequency should be inverted to characterize the fractures, as has already been proposed. At present, the main difficulty to overcome is to accurately compute the reflection coefficient, which depends on the source signal and is likely to vary from one trace to the next. Amplitude and phase variation with offset (APVO) curves derived from CMP data acquired both in TE and TM modes should also help characterization, as should polarization studies (Tsoflias et al., 2004).

ACKNOWLEDGMENTS

All data were processed using Seismic Unix. The authors acknowledge the contribution from Dr. A. Giannopoulos, who made the 2D modelling code available to everyone (GprMax2D can be downloaded from the address: <http://www.see.ed.ac.uk/~agianno/GprMax/>.) This work was supported partially by the "Pole Grenoble des Risques Naturels" through funding from the Conseil General de l'Isère (France) and by the Parc Régional de Chartreuse. We thank everyone who helped us during the field experiments, and particularly Michel Sintès for providing us with topographic data. We wish to thank the editor and the reviewers who provided helpful comments to improve the manuscript.

REFERENCES

- Annan, A. P., 1996, Ground penetrating radar: Workshop notes: Sensors and Software, Inc., Mississauga, Ontario.
- Benson, A. K., 1995, Application of ground penetrating radar in assessing some geological hazards: Examples of ground water contamination, faults, cavities: *Journal of Applied Geophysics*, **33**, 177–193.

- Bois, P., M. la Porte, M. Lavergne, and G. Tomas, 1972, Well-to-well seismic measurements: *Geophysics*, **37**, 471–480.
- Cardarelli, E., C. Marrone, and L. Orlando, 2003, Evaluation of tunnel stability using integrated geophysical methods: *Journal of Applied Geophysics*, **52**, 93–102.
- Clapp, R. G., 2001, Geologically constrained migration velocity analysis: Ph.D. thesis, Stanford University.
- Corin, L., I. Couchart, B. Dethy, L. Halleux, A. Monjoie, T. Richter, and J. P. Wauters, 1997, Radar tomography applied to foundation design in a karstic environment: *Modern Geophysics and Engineering Geology: Geological Society of London, Special Publication, Engineering Geology* 12, 167–173.
- Davis, J. L., and A. P. Annan, 1989, Ground penetrating radar for high-resolution mapping of soil and rock stratigraphy: *Geophysical Prospecting*, **37**, 531–551.
- Demagnet, D., 2000, Tomographie 2D et 3D a partir de mesures géophysiques en surface et en forage: Ph.D. thesis, University of Liege.
- Demagnet, D., F. Renardy, K. Vanneste, D. Jongmans, T. Camelbeek, and M. Meghraoui, 2001, The use of geophysical prospecting for imaging active fault in the Roer Graben, Belgium: *Geophysics*, **66**, 78–89.
- Dérobot, X., and O. Abraham, 2000, GPR and seismic imaging in a gypsum quarry: *Journal of Applied Geophysics*, **45**, 157–169.
- Dines, K., and J. Lytle, 1979, Computerized geophysical tomography: *Proceedings of the IEEE*, 1065–1073.
- Dix, C. H., 1955, Seismic velocities from surface measurements: *Geophysics*, **20**, 68–86.
- Dussauge-Peisser, C., A. Helmstetter, J.-R. Grasso, D. Hantz, M. Jeannin, and A. Giraud, 2002, Probabilistic approach to rock fall hazard assessment: Potential of historical analysis: *Natural Hazards and Earth System Sciences*, **2**, 1–13.
- Dussauge-Peisser, C., M. Wathelet, D. Jongmans, D. Hantz, B. Couturier, and M. Sintès, 2003, Investigation of a fractured limestone cliff (Chartreuse Massif, France) using seismic tomography and ground penetrating radar: *Near Surface Geophysics*, **1**, 161–170.
- Giannopoulos, A., 2002, GPRMAX2D/3D User's guide: <http://www.gprmax.org>.
- Goguel, J., and A. Pachoud, 1972, Géologie et dynamique de l'écroulement du Mont Granier, dans le massif de la Chartreuse en novembre 1248: *Bulletin du Bureau de Recherches Géologiques et Minières*, III (1), 29–38.
- Grasmueck, M., 1996, 3-D ground penetrating radar applied to fracture imaging in gneiss: *Geophysics*, **61**, 1050–1064.
- Grasmueck, M., R. Weger, and H. Horstmeyer, 2005, Full-resolution 3D GPR imaging: *Geophysics*, **70**, K12-K19.
- Grégoire, C., L. Halleux, and V. Lukas, 2003, GPR capabilities for the detection and characterisation of open fractures in a salt mine: *Near Surface Geophysics*, **1**, 139–147.
- Hoek, E., and J. W. Bray, 1981, *Rock slope engineering*: Elsevier Science.
- Hollender, F., 1999, *Interprétation de la distorsion des signaux géoradar propagés et réfléchis — Développement d'une tomographie par bandes de fréquences*: Ph.D. thesis, Institut National Polytechnique de Grenoble.
- Ivanson, S., 1987, Crosshole transmission tomography, *in* G. Nolet, ed., *Seismic tomography with applications in global seismology and exploration geophysics*: Reidel Publishing Company, 159–188.
- Jongmans, D., P. Hemroulle, D. Demagnet, F. Renardy, and Y. Vanbrabant, 2000, Application of 2D electrical and seismic tomography techniques for investigating landslides: *European Journal of Environmental and Engineering Geophysics*, **5**, 75–89.
- Jonscher, A. K., 1977, The "universal" dielectric response: *Nature*, **267**, 673–679.
- Lampe, B., and K. Holliger, 2003, Effects of fractal fluctuations in topographic relief, permittivity and conductivity on ground-penetrating radar antenna radiation: *Geophysics*, **68**, 1934–1944.
- Lanz, E., H. Maurer, and A. G. Green, 1998, Refraction tomography over a buried waste disposal site: *Geophysics*, **63**, 1414–1433.
- Liu, L., J. W. Lane, and Y. Quan, 1998, Radar attenuation tomography using the centroid frequency downshift method: *Journal of Applied Geophysics*, **40**, 108–116.
- Olhoeft, G. R., 1993, Velocity, attenuation, dispersion and diffraction hole-to-hole radar: 4th Tunnel Detection Symposium on Subsurface Technology, *Proceedings*, 26–29.
- Orlando, L., 2003, Semiquantitative evaluation of massive rock quality using ground penetrating radar: *Journal of Applied Geophysics*, **52**, 1–9.
- Pettinelli, E., S. Beaubien, and P. Tommasi, 1996, GPR investigation to evaluate the geometry of rock slides and buckling in a limestone formation in northern Italy: *European Journal of Environmental and Engineering Geophysics*, **1**, 271–286.
- Pipán, M., E. Forte, F. Guangyou, and I. Finetti, 2003, High-resolution GPR imaging and joint characterisation in limestones: *Near Surface Geophysics*, **1**, 39–55.
- Rashed, M., D. Kawamura, H. Nemoto, T. Miyata, and K. Nakagawa, 2003, Ground penetrating radar investigations across the Uemachi fault, Osaka, Japan: *Journal of Applied Geophysics*, **53**, 63–75.
- Rouiller, J. D., M. Jaboyedoff, C. Marro, F. Philipposian, and M. Mamin, 1998, *Pentes instables dans le Pennique valaisan: MATTEROCK: une méthodologie d'auscultation des falaises et de détection des éboulements majeurs potentiels*: Final Report PNR31, Verlag der Fachvereine.
- Seol, S. Y., J.-H. Kim, Y. Song, and S.-H. Chung, 2001, Finding the strike direction of fractures using GPR: *Geophysical Prospecting*, **49**, 300–308.
- Stevens, K. M., G. S. Lodha, A. L. Holloway, and N. M. Soonawala, 1995, The application of ground penetrating radar for mapping fractures in plutonic rocks within the Whiteshell Research Area, Pinawa, Manitoba, Canada: *Journal of Applied Geophysics*, **33**, 125–141.
- Toshioka, T., T. Tsuchida, and K. Sasahara, 1995, Application of GPR to detect and map cracks in rock slopes: *Journal of Applied Geophysics*, **33**, 119–124.
- Tsoflias, G. P., J.-P. Van Gestel, P. L. Stoffa, D. D. Blankenship, and M. Sen, 2004, Vertical fracture detection by exploiting the polarization properties of ground-penetrating radar signals: *Geophysics*, **69**, 803–810.
- Yilmaz, O., 1987, *Seismic data processing*: SEG.
- Zhou, H., and M. Sato, 2000, Application of vertical radar profiling technique to Sendai castle: *Geophysics*, **65**, 533–539.



On the potential of Ground Penetrating Radar to help rock fall hazard assessment: A case study of a limestone slab, Gorges de la Bourne (French Alps)

Jacques Deparis, Stéphane Garambois*, Didier Hantz

LIRIGM-LGIT, Université Joseph Fourier, Grenoble, France

Received 8 November 2006; received in revised form 19 July 2007; accepted 26 July 2007
Available online 3 August 2007

Abstract

The stability of a potentially unstable rock mass is highly sensitive to the continuity of the joints cutting it. The rock fall hazard assessment, generally based on surface geological observations and on a simple geomechanical model, suffers from the lack of information on the 3D geometry and the properties of the joints. This case study investigates the potential of Ground Penetrating Radar (GPR) measurements regarding hazard assessment in hard rock. GPR was used to detect and characterize joints that could cause the failure of an overhanging rock mass located above a road in the “Gorges de la Bourne” (France). GPR data were acquired using high frequency shielded antennae (500 and 800 MHz) to assess the extension of these joints and to detect other possible fractures. Combined with a velocity profile deduced from a Common Mid-Point (CMP) analysis, these measurements provided detailed images of the fracture network, which were locally consistent with turn rate velocity measurements performed within two horizontal boreholes. The rock bridge percentage in the critical joints was estimated from GPR data to be too low to ensure the stability of the overhanging rock mass. Consequently, mining of the rock mass was decided on. Afterwards, a comparison between GPR images and the real joints observed after mining also confirmed the GPR interpretation for the location and the extension of the joints.

© 2007 Elsevier B.V. All rights reserved.

Keywords: Rock fall; Stability; Hazard assessment; Ground Penetrating Radar; Fractures; Common mid-point; 3D geometry

1. Introduction

For the last few decades, growing urbanization in mountainous areas has generated an increase in natural risks. Possible natural hazards such as rock falls are difficult to predict, as instability precursors are rather limited and pre-failure rock mass displacements are very slow. To face up to socio-economical pressure as well as growing safety

needs, long term hazard assessment is necessary. It requires systematic detection and evaluation of potential rock falls at the massif scale (Hantz et al., 2003).

Nowadays, detection is usually limited to the visual search for typical configurations that favor a failure mechanism. Once a potentially unstable mass has been detected, its failure probability, which both depends on the present state of stability and on its evolution over time, has to be estimated. For the first point, well known limit equilibrium methods can be used to derive a safety factor, but they require mechanical and geometric data (e.g. Hoek and Bray, 1981).

* Corresponding author. Tel.: +33 476 82 80 46; fax: +33 476 82 80 70.

E-mail address: Stephane.Garambois@ujf-grenoble.fr (S. Garambois).

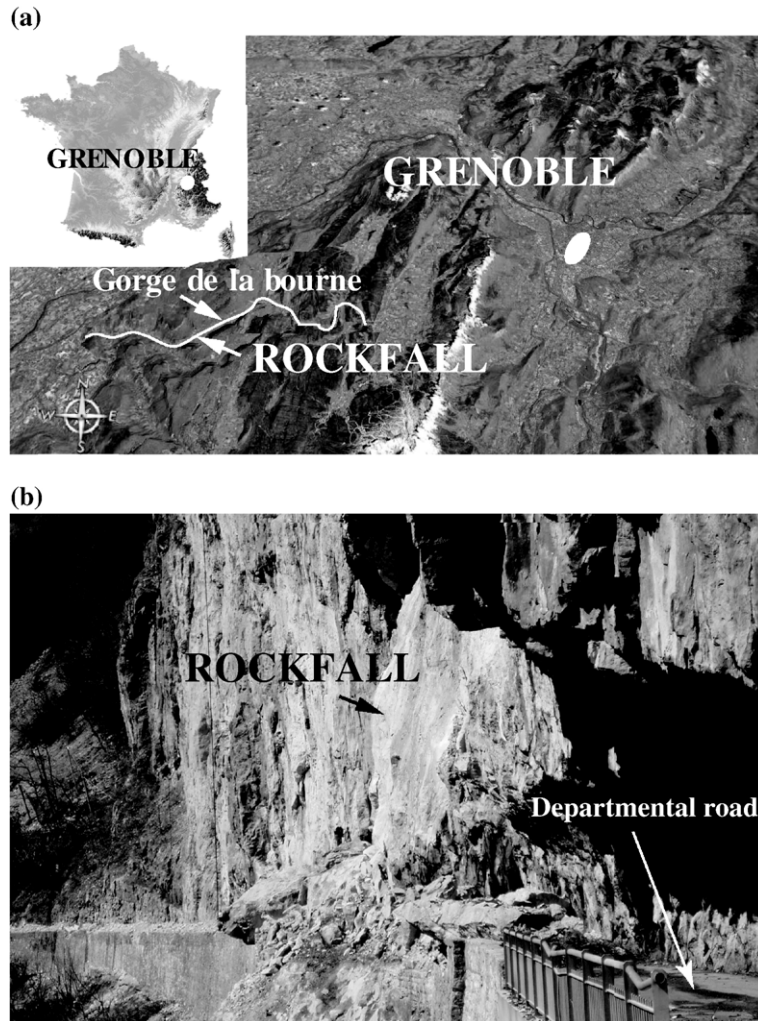


Fig. 1. (a) Satellite view of Grenoble area and location of the Gorges de la Bourne rock fall (French Alps). (b) Photograph of the 2004 rock fall event.

The mechanical properties of intact rock specimen and of small portions of joints can be determined from laboratory experiments. The joint orientations are generally extrapolated from surface measurements. However, the overall strength of a potential failure surface depends on the strengths of both joints and intact rock, as well as on the size and location of intact rock bridges along the failure surface. For example, back analysis of past rock falls in the calcareous cliffs of the Grenoble area (French Alps) has shown that the safety factor is sensitive to the rock bridge proportion in the potential failure surface, and that a proportion of a few percent is generally sufficient for the stability (Fraysines and Hantz, 2006). Unfortunately, the rock bridge proportion and location cannot be determined from surface observations, as they are generally entirely hidden from the surface.

It ensues that the key point for a better evaluation of the present stability of potentially unstable rock masses lies in better knowledge of their internal structure, particularly of the persistence of the joints. Traditional investigation methods, like boreholes, are not suitable because they provide only 1-D local information on the depth of a joint, but do not assess its spatial continuity. Among the wide range of geophysical methods available, Ground Penetrating Radar (GPR) is the most suitable to provide precise information about the near surface structures of the underground. This is due to i) its good vertical and horizontal resolution, which depends on the rock characteristics and the frequency of the antenna chosen, ii) its good penetration depth in resistive materials to detect deeper fractures, iii) its sensitivity to complex dielectric permittivity contrasts and iv) the low weight of the GPR equipment. In the last

decade, GPR has been used extensively for fault and fracture mapping in 2D (Benson, 1995; Toshioka et al., 1995; Stevens et al., 1995; Demanet et al., 2001; Rashed et al., 2003) and in 3D (Grasmueck, 1996; Pipan et al., 2003; Grasmueck et al., 2005). Pettinelli et al. (1996) and Pipan et al. (2003) showed, from 2D and 3D radar measurements, that discontinuities filled with clay, water or air are clearly detectable when an appropriate signal frequency is used.

Considering these results, GPR experiments conducted along vertical cliffs have emerged in the last couple of years. Jeannin et al. (2006) studied different acquisition configurations (reflection, tomography) on a limestone cliff, which did not present any rock fall risk. They notably, presented 100 MHz GPR reflection profiles, which reached a penetration depth of 20 m with a vertical resolution of 25 cm. They showed that location and orientation of several reflectors coincide with the fractures observed from the surface. Roch et al. (2006) acquired 3D GPR data, which were combined with photogrammetric data to derive a quantitative 3D interpretation in terms of discontinuities. They notably imaged a major fracture, which presents an extent of 350 m² partly at the surface of the rock wall. However, neither of these interpretations were validated by independent measurements nor directly served hazard assessment and mitigation.

In this paper, we illustrate how GPR measurements taken on a potentially unstable rock slab overhanging a road can help hazard assessment and mitigation decision. GPR measurements consisted in two vertical reflection profiles acquired from the cliff wall using 500 MHz and 800 MHz shielded antennae. They were supplemented by a Common Mid-Point survey (200 MHz unshielded antennae) designed to derive velocities within the rock mass. The images obtained, which were confronted to independent structural investigations based from two horizontal borehole measurements, permitted to assess the distribution of rock bridges and consequently to directly estimate the rock fall hazard and finally to propose a mitigation method (mining). Furthermore, the originality of this study also lies in the possibility of late confronting GPR images to fracture scars visible after mining.

2. Description of the site studied

The "Gorges de la Bourne" area is located in the Vercors massif (French Alps, Fig. 1), about 25 km south-west from Grenoble. The Bourne River cut through massive limestone of lower Cretaceous age (Urgonian facies), forming vertical cliffs up to 200 m in height. The intact rock is not weathered, as demonstrat-

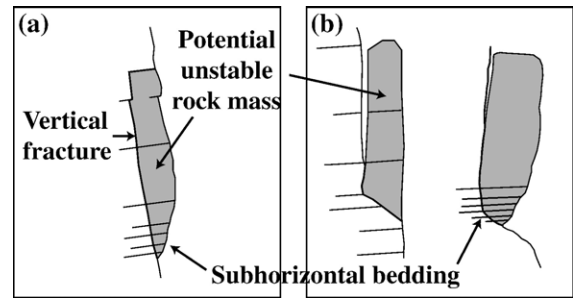


Fig. 2. Typical failure configurations in the limestone cliffs with subhorizontal bedding. A-type: bedding dips less than 30° and joints define a translational sliding (a). B-type: bedding dips less than 30° and joints define a composite sliding surface (b) (after Frayssines and Hantz, 2006).

ed by a longitudinal seismic P-wave velocity measured at around 6000 m/s at the scale of a 80 mm rock sample and by a uniaxial compressive strength of about 140 MPa. It presents a porosity lower than 1% and low clay content, allowing for karstification and dry conditions. The 10-km road (D531), which was built between 1861 and 1872, runs through the gorges and often undercuts the steep limestone cliff. It frequently experienced collapses in the past.

On the 29th January 2004, 2000 m³ of rock collapsed during the night (Fig. 1b), which caused the death of two people in a car. At this point, the road undercuts the cliff by 4 m. The observation of the scar showed that the fallen rock mass was bounded to the stable part of the cliff by rock bridges, which represented only 5% of the total surface of the scar (Frayssines, 2005). The other part of the scar is formed of pre-existing fractures, whose surface is coated with a calcite crust. It indicates that it was opened enough (probably a few centimeters) for water to seep inside. Consequently, freeze and thaw cycles in winter combined with thermal cycles in summer certainly reduced stability according to time. The geometrical configuration corresponds to the first of the typical rock fall configurations (A-type) which were identified by Frayssines and Hantz (2006) in the calcareous steep cliffs of the French Subalpine Ranges, with subhorizontal bedding (Fig. 2a). A steep potential translational sliding surface is defined by joints, more or less perpendicular to bedding. This sliding surface may be a planar or a wedge surface. In the second type (Fig. 2b, B-type), the potential failure surface is made up of a combination of a steep rearward part and a flatter sole. For both types, the failure mechanism may be a slide or topple, depending on the presence and the size of an overhang.

Some tens of meters upstream from the 2004 event, the road again undercuts the cliff, forming a 2.5 m deep

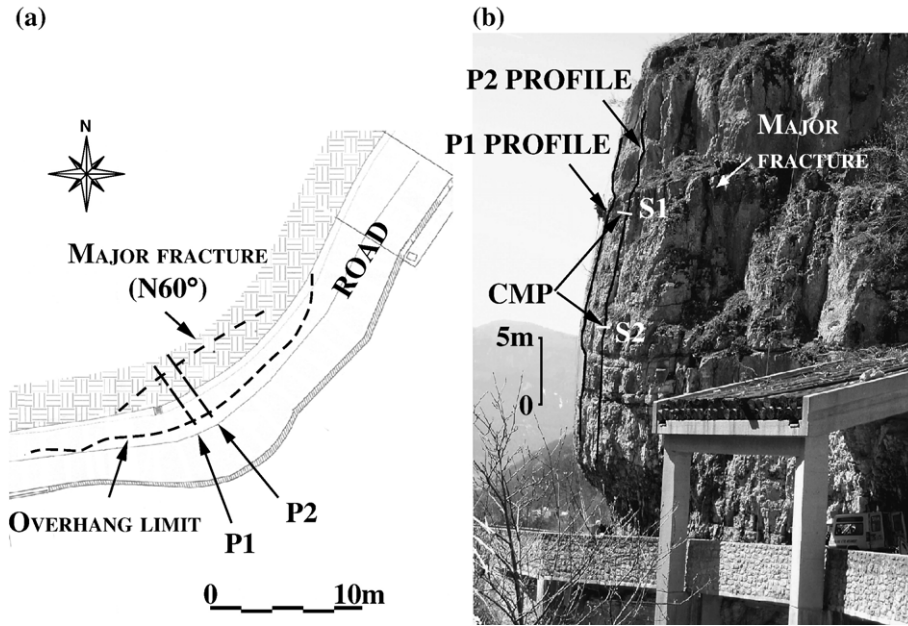


Fig. 3. Schematic view (a) and photograph (b) of the potentially unstable rock slab studied, with location of the main fracture. The locations of the GPR vertical profiles and CMP survey are displayed.

overhang under a slightly marked spur (Fig. 3). A geological survey of the overhanging rock mass showed it was cut by subhorizontal bedding planes and subvertical joints, parallel to the cliff, forming vertical rock slabs or scales. In this way, potential failure

mechanisms of both types (displayed on Fig. 2) can occur. The state of stability of the cliff depends greatly on the three-dimensional location and persistence of joints. In particular, a vertical joint striking N60°, which is opened to several decimetres and located 5 m behind

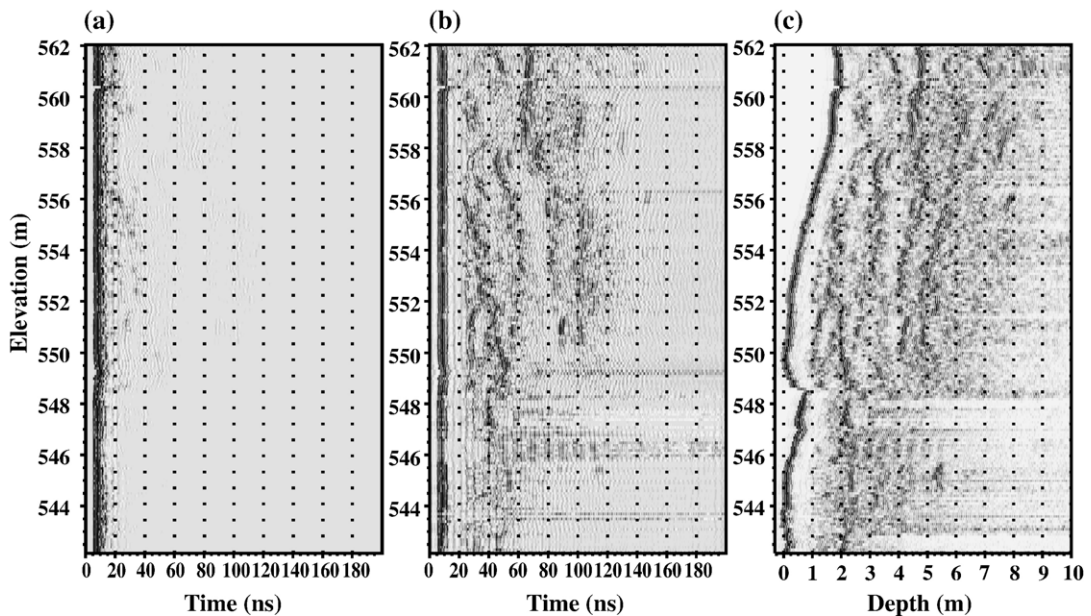


Fig. 4. Illustration of the processing chain applied to GPR data using the 500 MHz P1 profile. (a) Raw data. (b) Processed data using i) a DC removal, ii) a zero-phase band-pass filter and iii) an AGC time equalization. (c) Static corrections for topography and time to depth conversion were applied compares to (b).

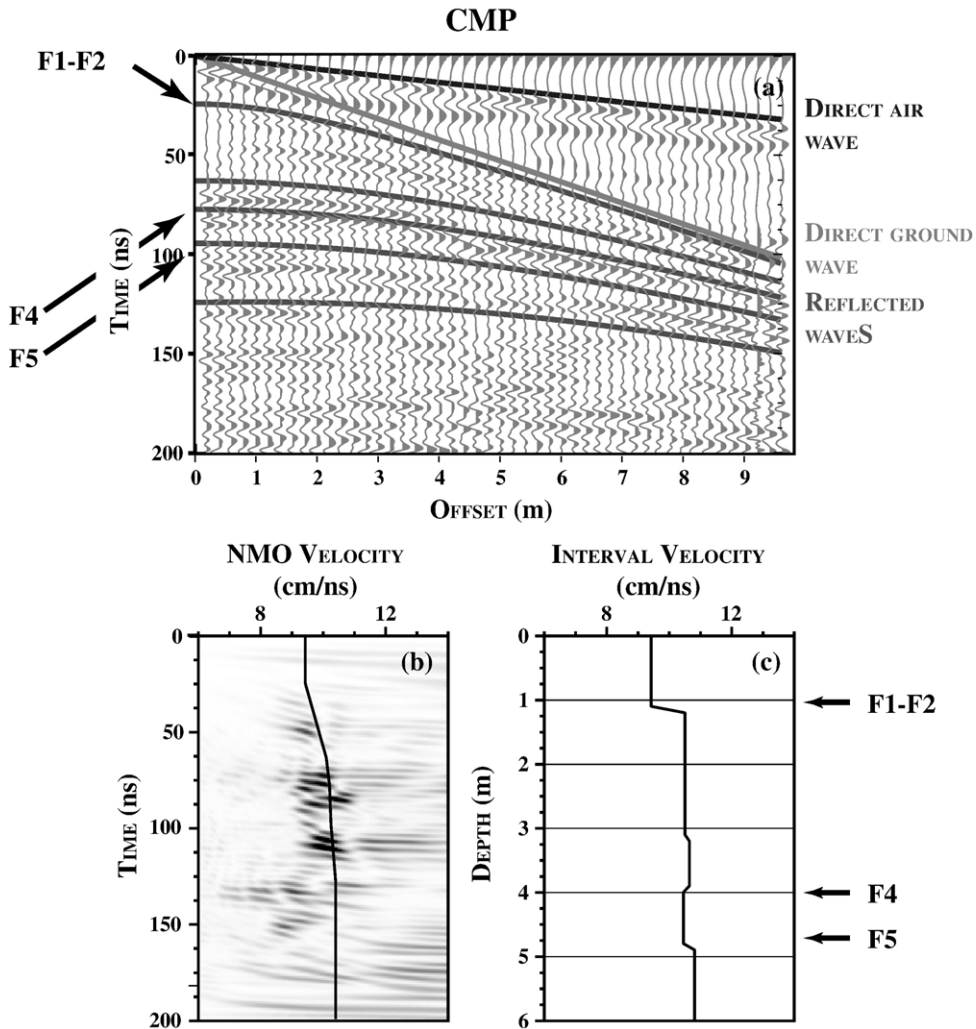


Fig. 5. (a) Filtered CMP data showing the direct air wave (velocity of 30 cm/ns), the direct wave propagating in the limestone and several reflected waves whose corresponding hyperbolae picking was superimposed. (b) Semblance analysis of reflected events and deduced NMO velocity profile as a function of time. (c) Interval velocity profile deduced from the NMO velocity profile using the Dix (1955) formula.

the cliff wall, was visible on the upper right part of the spur, what worried decision-makers in charge of the road security. Indeed, the fact that its lateral and vertical extension was unknown illustrated well the difficulty in estimating the associated rock fall hazard without any other available information. In this context, only a large number of boreholes or GPR investigations may provide the required information.

3. GPR acquisition and processing

GPR measurements were acquired with a RAMAC GPR system (Malâ Geosciences) along two vertical reflection profiles (P1 and P2), 2 m apart and whose locations are displayed in Fig. 3b. These profiles were

supplemented by a 200 MHz Common Mid-Point (CMP) survey located along the P2 profile. The 200, 500 and 800 MHz data were acquired using a sampling frequency of respectively 2000, 4000 and 5000 MHz, and during 420, 230 and 200 ns. All measurements were stacked 128 times. As the fractures are almost vertical, antennas had to be placed on the cliff wall. An operator had to go down the cliff to ensure a satisfying antenna/rock coupling.

3.1. Vertical radar profiles

Two vertical profiles were acquired using 500 MHz and 800 MHz shielded antennas (P1 and P2, Fig. 3a). An illustration of the main GPR data processing steps needed to derive a representative image of fractures is

displayed in Fig. 4 for profile P1, acquired with 500 MHz antennas. The processing and images were produced using Seismic Unix software (Stockwell, 1999). The processing chain of raw data (Fig. 4a) includes: i) DC removal (continuous current), zero-phase band-pass filtering (depending of antenna frequency) and Automatic Gain Control (AGC) time equalization (Fig. 4b), followed by ii) static corrections of surface topography and time to depth conversion (Fig. 4c). The velocity used for time to depth conversion was derived from the analysis of CMP data presented afterward. As reflectors are almost vertical and no diffracted waves are visible, no migration process was applied to the data, to avoid the appearance of undesirable noise. Fig. 4c clearly shows various reflectors, which present more or less continuity on the entire vertical profile. This example underlines also the necessity to compute static corrections of topography when high-resolution images are desired.

3.2. Velocity analysis

To convert time (two-way traveltimes) to depth on GPR profiles acquired in a reflection mode, a CMP survey is required, which provides the Normal Move-Out (NMO) velocity as a function of the distance behind the cliff face. As the distance between the transmitting and receiving antennas varied during the survey, we were forced to use 200 MHz unshielded antennae, which were the highest frequency antennae available. The CMP survey was carried out from the middle of the P2 profile (Fig. 3). As the dispersive effect of the effective permittivity is low in limestone formations within the [100–1000 MHz] frequency range (Hollender, 1999), it is reasonable to extend the obtained 200 MHz velocity field to velocity used for time to depth conversion of 500 MHz and 800 MHz GPR data.

Acquisition of a CMP on a vertical cliff is not an easy task and requires two operators, carrying one antenna each, who moved respectively up and down the cliff face from the central point. In our study, the distance between the transmitting and receiving antenna increased by 10 cm steps from the central point, until a 10 m offset was reached. The CMP section was first filtered using a [50–300 MHz] band pass Butterworth filter and processed using an AGC time equalization.

Several different waves can be observed on the CMP section (Fig. 5a). The direct air wave appears first with a velocity of 30 cm/ns, followed by the direct ground wave propagating in the limestone. The amplitude of the latter is very low at large offsets compared to the reflected wave amplitude, due to antenna radiation

pattern, which preferentially focalizes energy downward (Lampe et al., 2003). Later, different hyperbolic events (denoted F1–F2, F4 & F5) can be observed, which correspond to deep reflected waves. The main crack (F4), which is visible on the right upper edge of the spur (Fig. 3), corresponds to the event arriving at 80 ns on the CMP. The origin and extension of the other waves will be discussed afterwards.

The normal move-out (NMO) was analyzed using the semblance maxima approach (Yilmaz, 1987), which is commonly used in seismic processing and yields the stacking velocity (Fig. 5b). This approach shows a small increase of NMO velocity between 25 ns and 70 ns. The validity of this increase remains dubious because of the undesirable inherent stretching in this method (Perroud and Tygel, 2004), what causes a drop in the precision with ± 0.5 cm/ns. To improved that point, five reflected events were picked on the basis of the combined semblance image and on CMP gather panels, where hyperbola adjustment refined the NMO velocity profile with a precision of ± 0.3 cm/ns (Fig. 5a–b). The picked events were selected on the basis of the 500 MHz image, which permitted to better distinguish and identify the different reflectors, by taking into account their spatial continuity. For example, this strategy permitted to identify the event occurring around 50 ns at zero-offset like a multiple of reflector F1–F2 (see next section), and consequently not to include it in the velocity analysis. That also made it possible not to take into account hyperbolas of low amplitudes on the CMP whose continuity clearly does not appear on 500 MHz image. The precision of this approach was deduced from a sensitivity study which consisted in superimposing hyperbolas of different velocities on the maximum amplitude of studied reflected waves. This approach clearly showed that a shifting of velocity of 0.3 cm/ns diverged too much from the reflected hyperbolas.

The average interval velocities $V_{i,j}$ between times t_i and t_j , were computed from the NMO velocity using the Dix formula (Dix, 1955). This process may suffer from numerical problems when reflections are closely spaced or when RMS velocities vary rapidly (Clapp, 2001). These limitations are not encountered in our case and this process allows the interval velocities to be approximately derived when reflectors are almost parallel. The computed velocity profile (Fig. 5c) shows a 1 m thick rock layer presenting a velocity at around 9 cm/ns near the cliff face, followed by a higher velocity layer within the rock mass, characterized by an almost constant velocity around 10 cm/ns between 1 and 6 m in depth. Deeper small velocity changes are not sufficiently significant to be interpreted. The velocity contrast between the layers may be explained by different amounts, openings and

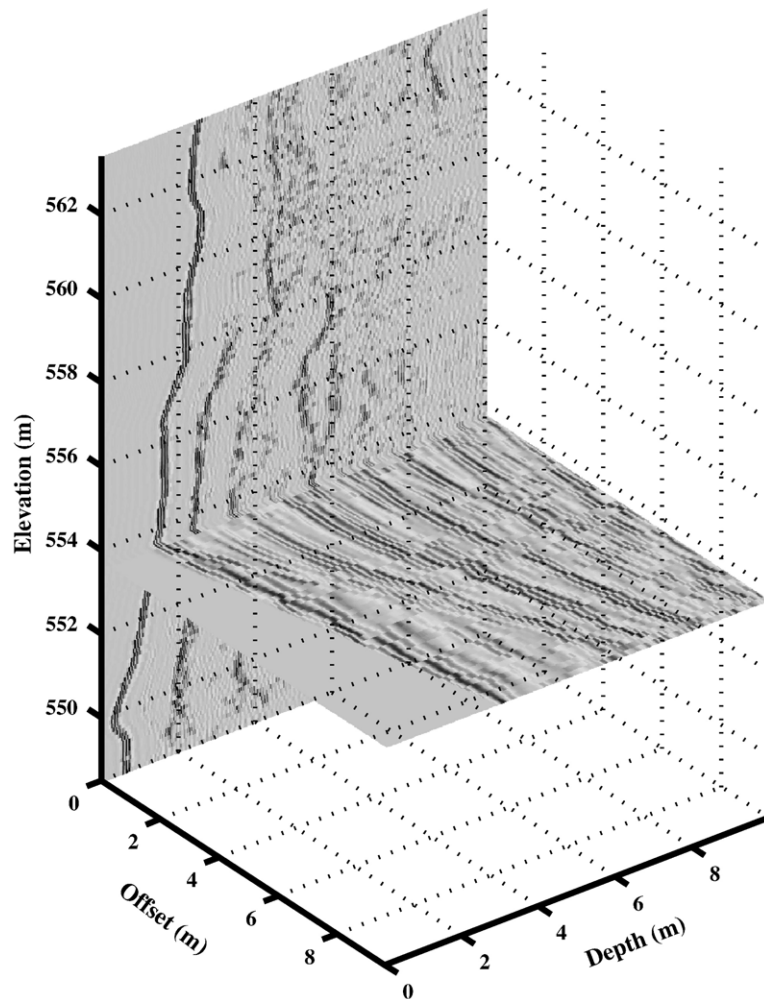


Fig. 6. Combined view of the vertical 500 MHz P2 profile and the 200 MHz CMP survey.

fillings of micro-fractures in each block. Here, the higher amount of micro-fractures would be located within the first layer if their filling is clay or water (lower GPR velocity) or within the second one if their filling is air (higher GPR velocity). The first assumption is the most likely as there should be higher rates of micro fracturing in the superficial part of the rock mass due to its higher sensitivity to thermal cycles. To conclude this velocity analysis, it is noticeable that in our case, this process was unable to directly retrieve fracture properties (aperture, velocity). This is due to the impossibility of distinguish two reflections coming from both fractures surfaces with the 200 MHz antennas, which moreover present lower resolution.

Fig. 6 presents a superimposition of the vertical GPR image acquired along the P2 profile (with 500 MHz shielded antenna) and the CMP section (with 200 MHz unshielded antenna). Such a perspective view shows the

continuity of all reflections and the consistency of reflected events over frequency, thus confirming that dispersive effects are negligible in these rocks. It is also noticeable that the 200 MHz CMP exhibits a larger penetration depth, which permitted to detect fractures deeper than 6 m, but with a lower resolution.

3.3. Multifrequency vertical profiles

Figs. 7 and 8 present GPR images acquired on the cliff wall on P1 and P2 profiles respectively, using 500 MHz and 800 MHz antennas. The images are presented after filtering (with an adapted band-pass frequency filter depending on antenna) and processing, as illustrated in Fig. 4. For both profiles, penetration depth can be estimated at around 6 m for the 500 MHz antenna with a resolution of 5 cm and 5 m for the 800 MHz antenna with a resolution of 3 cm. Resolutions

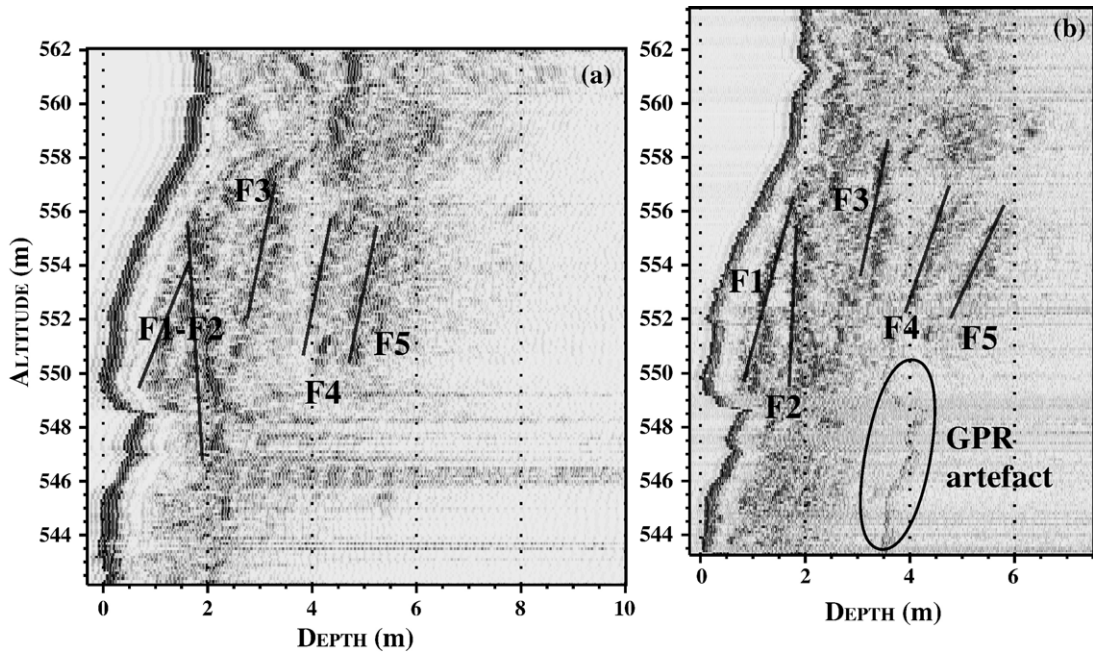


Fig. 7. GPR images of profile P1 acquired at 500 MHz (a) and at 800 MHz (b) after processing and filtering.

were computed considering the quarter GPR wavelength (Reynolds, 1997). The time to depth conversion was applied using a constant velocity of 10 cm/ns, which was deduced from the CMP analysis.

On profile P1, numerous events present more or less continuity within the rock mass, which can be character-

ized precisely. The first two (F1 and F2) are almost parallel to the cliff face. Although they are barely separated on the 500 MHz image, their continuity and separation between elevations 550 and 560 m are more precisely estimated using the 800 MHz image. These fractures meet at around 557 m of elevation, at 1 m in

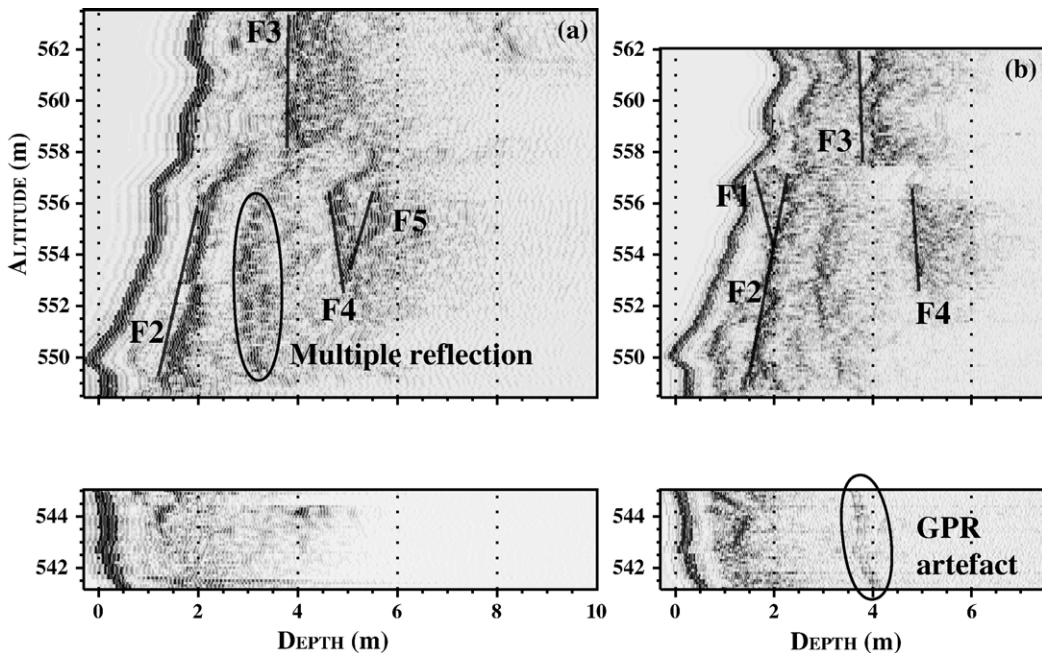


Fig. 8. GPR images of profile P2 acquired at 500 MHz (a) and at 800 MHz (b) after processing and filtering.

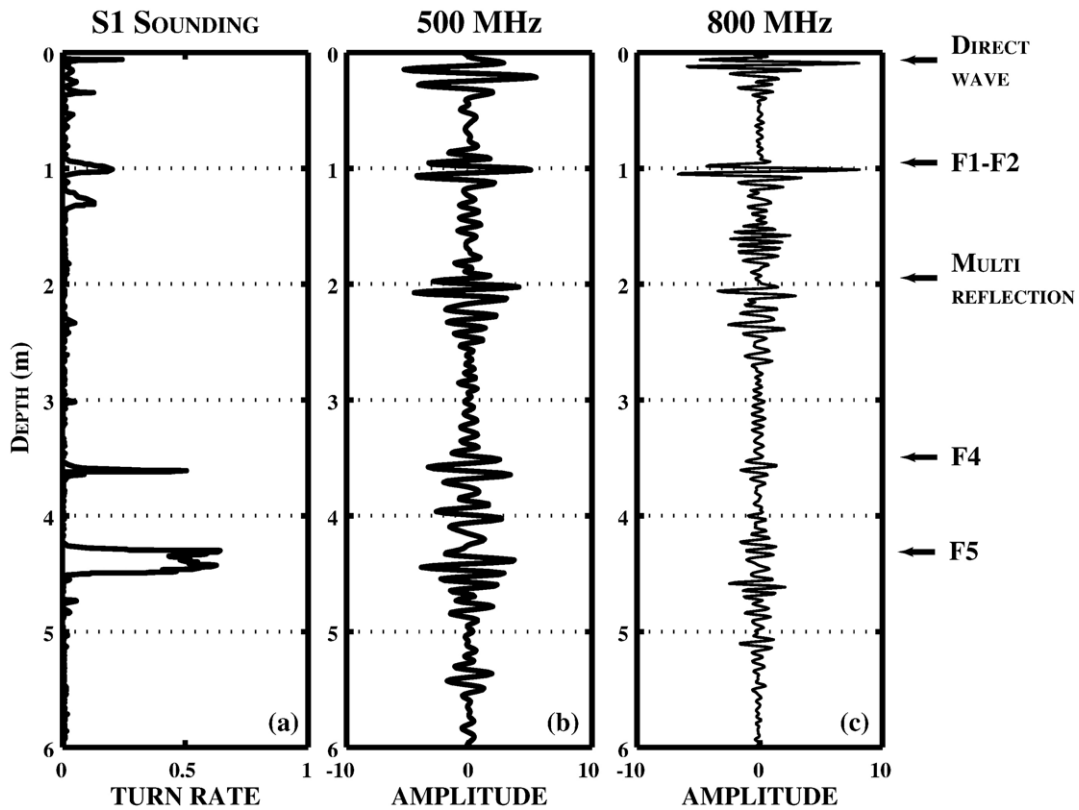


Fig. 9. (a) Borehole measurements displaying the turn rate velocity as a function of depth (elevation 555, profile P2). Corresponding GPR traces acquired before drilling and presented after processing and filtering for the 500 MHz antenna (b) and for the 800 MHz antenna (c).

depth. The extension of the F2 fracture between elevations 543 m and 548 m is better imaged on the 500 MHz vertical GPR profile. The F3 fracture is also almost parallel to the cliff face but is less persistent than fractures F1 and F2, especially between elevations 558 m and 560 m. That can be an indication of the closing of the fracture or of the presence of large rock bridges. It seems to join the F2 fracture at an elevation of around 549 m, at 2 m in depth. The event observed at 3.5 m of depth and parallel to the cliff wall on the lower part of the 800 MHz image corresponds to an artefact of the source antenna, which emitted a secondary pulse. Finally, two deeper events (F4 and F5) between 4 m and 5 m in depth are well defined in the upper part of the profile (between elevations 563 and 550 m) with both antennae. The F4 event corresponds to the main crack observed on the right upper edge of the spur. The fact that no reflected event was detected in the lower part (below 550 m) is an indication of the closing or vanishing of the fractures F4 and F5, i.e. they may be too thin to be detectable using these antennae or they may end at 550 m elevation. A careful observation of the complex waveforms of most of the reflected signals indicates interferences between reflections occurring on

both sides of the fractures, which cannot be separately imaged. Consequently, no quantitative information on fracture aperture can be obtained directly from the images because of their low thicknesses compared to the wavelength.

Profile 2 was not acquired continuously due to the presence of an overhang on the cliff face. However, the obtained images also present numerous events, whose reflectivity highly depends on the location within the rock mass. They have been supposed to be the continuation of the fractures identified on the profile 1. Located directly behind the cliff wall, the F1 fracture was well imaged only on the 800 MHz image due to a better resolution. It is not really continuous, except in the lower part of the profile (between elevations 550 and 556 m) where it shows a common section with the F2 fractures. The second fracture F2, which is located between 1 m (upper part) and 2 m (lower part) behind the cliff face, is almost continuous all along the profile. Fracture F3 is imaged only in the upper part of the profile (between elevation 558 and 564 m), at 2 m of depth. The event imaged in the lower part (at the same depth) seems to correspond to a multiple of F2 (following classical

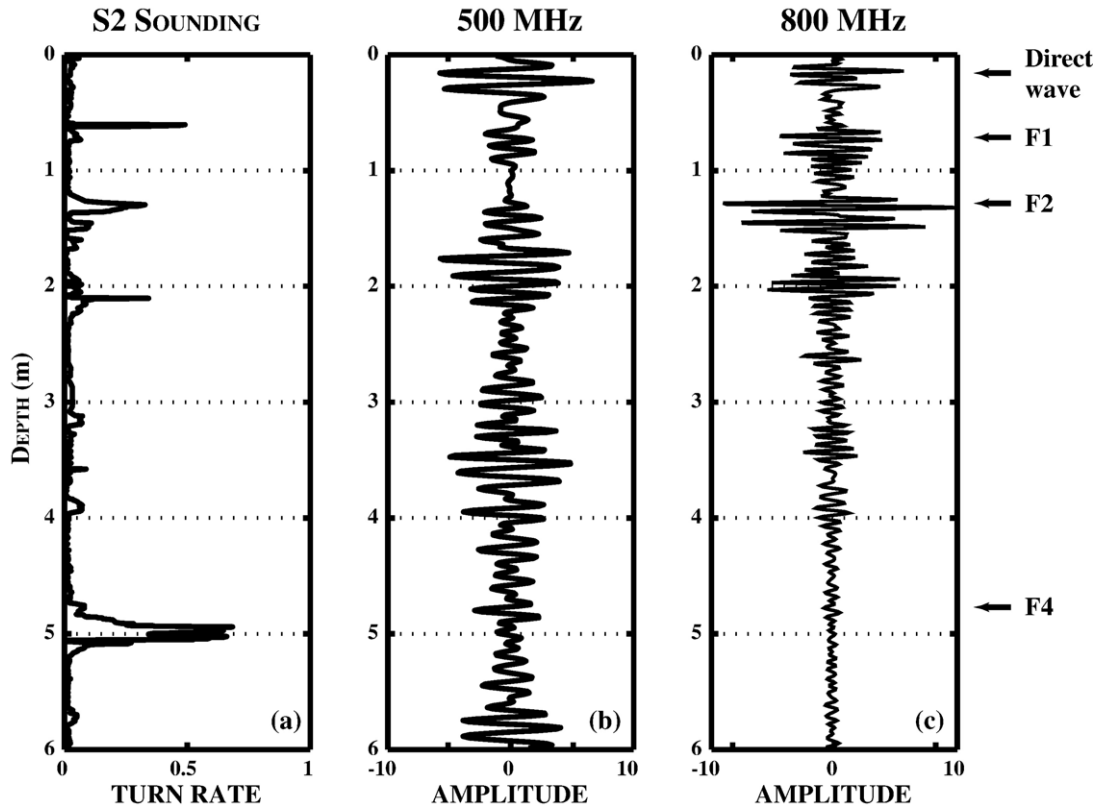


Fig. 10. (a) Borehole measurement displaying the turn rate velocity as a function of depth (elevation 549, profile P2). Corresponding GPR traces acquired before drilling are presented after processing and filtering for the 500 MHz antenna (b) and for the 800 MHz antenna (c).

considerations of time and dip of the reflected wave, Reynolds, 1997), extended in the 800 MHz image by the source artifact discussed above. This interpretation was confirmed afterwards with borehole investigations showing the absence of fractures in this part. As on the P1 profile, the F4 fracture does not appear under the elevation of 550 m. Separation between F4 and the deeper F5 fracture is better imaged with the 500 MHz antenna (F5 is almost invisible on the 800 MHz image, due to depth penetration limits). Given that the cliff wall strikes at N60° between the two profiles, the fact that the F4 joint appears at the same depth in both profiles shows that it also strikes at N60° and that it corresponds to the main fracture observed at the edge of the spur (Fig. 3).

4. Comparison with borehole investigations and post-mining observations

4.1. Borehole investigations

In order to estimate locally and precisely fracture locations and apertures, two horizontal 70 mm diameter boreholes were drilled along the P2 profile at elevations

555 m and 549 m respectively (S1 and S2, Fig. 3). They were performed using the down-the-hole hammer destructive technique, which recorded the turn rate velocity (S1, Fig. 9; S2, Fig. 10), a parameter sensitive to changes in material properties: in our case, a low turn rate velocity corresponds to a hard material (limestone), and a high one to a soft material (clay, sand or air inside the fracture).

On the S1 borehole, four fractures were detected, located at depths of 1, 1.20, 3.60 and 4.30 m. Their aperture varies from a few cm to 20 cm. On the S2 borehole, we can distinguish four principal events, located at depths of 0.5, 1.20, 2.1 and 4.9 m. Their aperture varies from a few cm to 15 cm. Smaller events, which are present on both soundings, were not considered because of their unreliability. Figs. 9 and 10 compare borehole measurements (a) and processed GPR traces acquired prior to drilling at the borehole locations for the 500 MHz antenna (b) and 800 MHz antenna (c). These images make a direct comparison between both techniques possible. It is clear that the four main fractures intersected by the S1 sounding correspond to those detected by GPR (F1, F2, F4 and F5). On

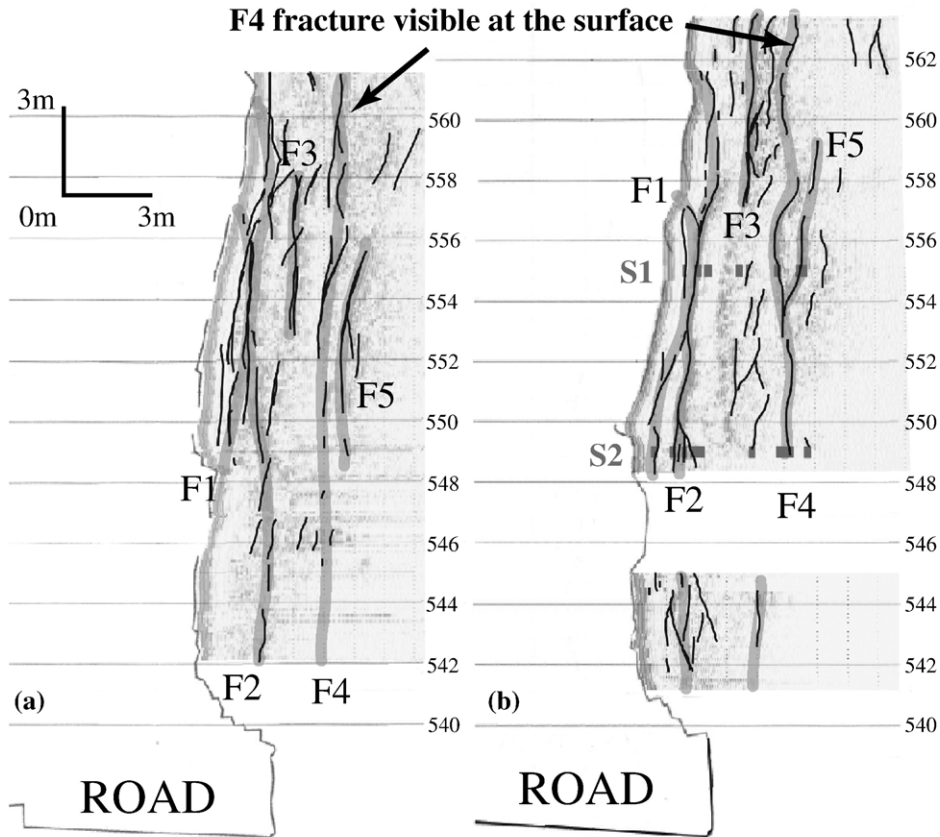


Fig. 11. Interpretation of vertical GPR profiles P1 (a) and P2 (b) in terms of fracture continuities and rock bridges. Thin black lines correspond to fractures detected by GPR, while thick grey lines correspond to interpreted structural model.

the S1 sounding, fractures F1 and F2 appear a few centimetres apart, a resolution which is not provided by either GPR antenna. Fractures F4 and F5 are correctly detected and located with the 500 MHz antenna but the F5 fracture is too far from the surface to be clearly detected by the 800 MHz antenna. It is noticeable that a complex reflection appears for the thick F5 fracture, certainly due to interferences between multiple reflections generated from both sides of the crack (thin-layer case). Both antennas show an unexplained reflection at a depth of 1.6 m, which does not appear in borehole measurements. This event may be related to 2D or 3D local geometry of the F1–F2 fractures (visible at 550 to 555 m on Fig. 8), generating multi-reflections from a single rough interface.

On the S2 sounding, the three main fractures are well correlated with those identified from GPR images (F1, F2 and F4). There exists another fracture on S2 sounding at a depth of 2 m, which also appears on GPR traces. However, as its continuity is rather limited on GPR profiles, this event was not considered in the structural interpretation. Contrary to the S1 sounding,

F1 and F2 fractures are well separated both on S2 sounding and on GPR traces. On the other hand, at this location, F4 and F5 fractures do not appear well separated, on S2 borehole measurements and on GPR corresponding traces. Numerous reflections appear between 2 and 4 m in depth in the 500 MHz image. They probably correspond to small fractures, which were not interpreted on the vertical GPR images due to their lack of continuity. They are correlated with a small increase in the turn rate velocity between 3 and 4 m in depth, indicating the presence of a softer material.

This comparison shows the potential and limits of GPR for fracture characterization: the main fractures were correctly detected and located on condition that they are sufficiently opened and separated from each other. Otherwise the fractures create a complex reflectivity pattern and cannot be distinguished anymore. It is noticeable that, although 2D or 3D geometrical effects as well as the presence of multi-reflected or diffracted waves could worsen GPR images, the consistency between GPR images and borehole measurements is remarkable.

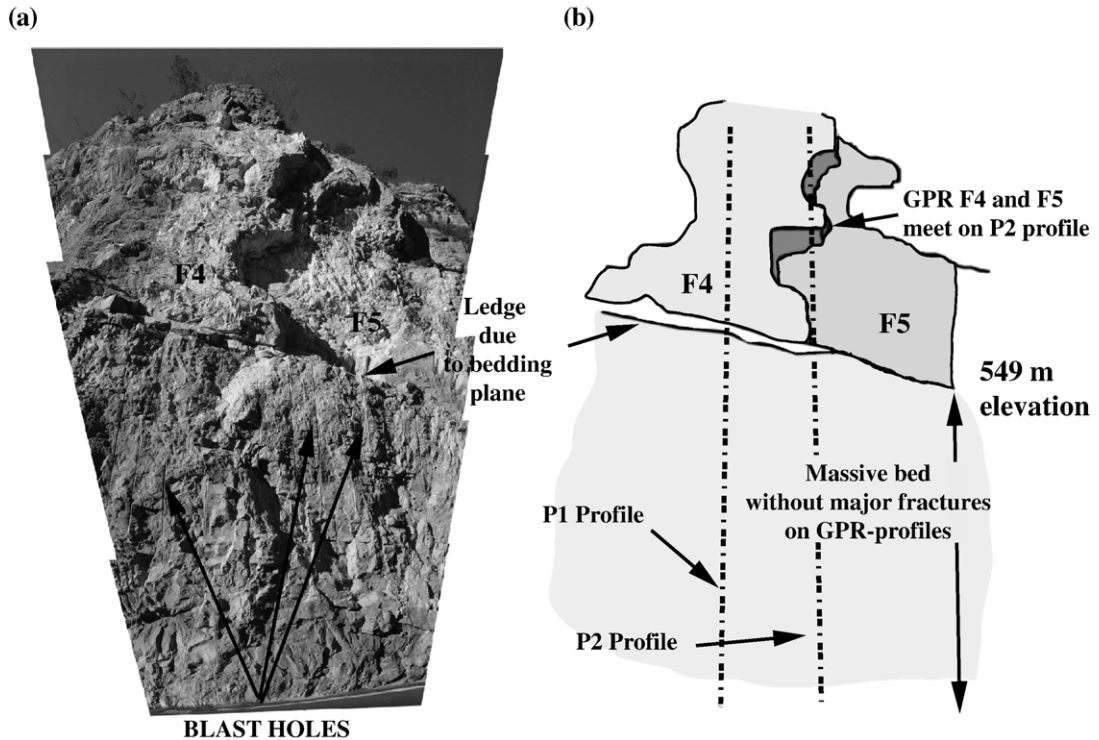


Fig. 12. Photograph (a) and diagram (b) of the rock scale after mining.

4.2. Post-mining observations

By considering GPR and borehole interpretation in terms of rock bridges presented below (Fig. 11), the authorities decided to mine the rock slab in order to improve the safety of the road. This remediation technique made it possible to compare fractures scars, which were exhibited after mining, with GPR images obtained before. Fig. 12 displays a photograph of the rock wall after mining and the linked interpretation. The surface which was exposed after mining appears in a light colour, in contrast to the patina which covers the surrounding rock surface. Above the elevation of 549 m, the surface corresponds to the pre-existing F4 and F5 fractures, which were exposed by blasting. No evidence of clay or sand filling, nor of rock bridges was visible on their surface, which is coated with a calcite crust. Under the elevation of 549 m, where blast holes are visible, no pre-existing fracture was opened by blasting, but a fresh fracture surface in the rock material was created, which is highlighted in Fig. 12b. This suggests that the F4 and F5 fractures do not extend under this elevation, as first deduced from GPR images. This is confirmed by the fact that these fractures seem to vanish under the same elevation, when viewed from the right edge of the spur.

In the area where the P2 profile was acquired, observation after mining shows a more complex structure:

at 554 m elevation, the F4 and F5 fractures meet, as first shown on the P2 GPR profile (Fig 11b). This remarkable consistency also confirms the reliability of obtained GPR images.

5. Discussion

5.1. Potential of GPR for precise fracture detection and location

Based on this study, it is clear that a single GPR profile combined with a CMP acquisition, makes it possible to determine the extension of a fracture observed locally at the surface (F4 in this case) in the direction of the profile. It also appears that an invisible fracture parallel to the cliff can be located using two GPR vertical profiles (F2 in this case). However, a horizontal profile is required to better assess the horizontal continuity of this fracture. Ideally, a complete 3D determination of the fractures would require a set of close parallel and perpendicular GPR profiles as well as 3D processing (migration) and interpretation.

In our case study conducted in massive limestone, the penetration depth of EM waves is estimated to be 6 m with a 500 MHz antenna and 5 m with a 800 MHz antenna, with corresponding theoretical vertical resolutions of 5 cm and 3 cm.

There is a minimal aperture for a fracture to be detected by GPR, according to the filling material in the fracture, the propagating medium and the frequency acquisition (Deparis and Garambois, 2006). Due to this limitation, the method provides information on the minimal extension of the fractures and reciprocally, on the maximal extension of the rock bridges, which link the potentially unstable compartments to the stable rock mass. CMP acquisition is a crucial part of GPR investigations when other information is not available. It allows the velocity of the EM waves to be established and to locate the fracture precisely on the reflection profile, with a simple time to depth conversion. The remarkable consistency between borehole measurements, GPR images and post-mining observations, confirms the potential of GPR investigations, but also underlines a few limits: multi-reflections and possible 3D geometrical effects. In our case, no geometrical 2D effects (non-vertical fractures or having a roughness of strong amplitude) were identified in the data. In regions where 2D or 3D effects are possible, a complex 2D or 3D migration process should be applied to the data. Finally it is important to note that GPR is unable to distinguish fractures separated by a distance lower than a half-wavelength.

5.2. Contribution of GPR to hazard assessment

GPR surveys have highlighted the fractures which define potentially unstable rock compartments. The F1, F2 and F3 fractures, located less than 3 m behind the cliff wall, define a type A failure configuration (Fig. 2a), with a possible translational slide or a topple, depending on the exact three-dimensional morphology of the rock surface. The F4 fracture, located 4 to 5 m behind the cliff wall, defines a type B failure configuration, with a possible compound slide or hyperstatic topple (Fig. 2b). For the A-type configuration, given the steep slope of the failure surface, the present stability mainly depends on the cohesion and tensile strength of the failure surface, rather than on its friction angle. These parameters are proportional to the proportion of rock bridges on the potential failure surface. As EM waves are not able to detect fractures that are too thin, the default estimation of the fracture extension can lead to a maximal value for the safety factor. Theoretically, such an estimation is appropriate to justify mitigation measures, but not to guarantee the stability of a cliff. However, the regional geological context can be used to decide if the disappearance of a fracture on a GPR profile is due to a lower aperture or to the end of the fracture (occurrence of a rock bridge). In a karstic limestone, intact rock bridges are frequently encountered even in largely open karstic frac-

tures. Consequently, disappearances of fractures on a GPR profile may be preferentially attributed to the occurrence of a rock bridge.

Geomechanical modelling makes it possible to analyze the present state of stability for slide or topple of an overhang (Frayssines, 2005), but is unable to predict its future evolution. This is the reason why rock fall hazard assessment is usually a qualitative assessment, based on expert judgement. In the present case, the main parameter which was taken into account is the proportion of rock bridges. The maximal linear percentage of rock bridges for the F1 fracture reaches 8 and 10% respectively along P1 and P2 profiles, and for the F2 fracture, it reaches 6 and 8% respectively along P1 and P2 profiles. These maximal values, derived from GPR interpretation, were considered too low to ensure the long term stability of the overhang, and mitigation measures were decided on. For the B-type configuration, the possible failure mechanisms are more complex than for the A-type and require additional discontinuities compared to those detected from GPR. As the cliff is made of Urgonian limestone, which is sensitive to dissolution, there is a little chance that the F4 fracture is connected to another fracture dipping towards the road, without the latter being enlarged by dissolution and so, visible on GPR images. For this reason, a B-type failure was considered as improbable. Consequently, estimation of the potentially unstable volume was reduced thanks to GPR measurements. From this study, the choice in term of mitigation focused on mining the overhanging slabs. A pre-splitting plane was designed to obtain a vertical wall above the road. The blast holes are now visible along the road, under the elevation of 549 m (Fig. 12).

6. Conclusion

This case study illustrates well how GPR measurements acquired on a limestone cliff can be of primary interest to characterize continuity and extension of fractures and consequently to take part in hazard evaluation. All required GPR data were acquired during one single day along two vertical profiles located on the wall of a limestone cliff. Combined with a Common Mid-Point survey, which provided GPR velocities within the rock mass investigated, they provided detailed images within the first 6 m behind the cliff face. These images made it possible to detect several vertical fractures and to study their continuity with a satisfactory vertical resolution, as two high frequency antennae were used here. The interpretation derived, which was locally consistent with borehole measurements and post-mining observations, was the input to compute a maximal linear percentage of

rock bridges. This property is the crucial parameter for stability assessment. The maximal percentage of rock bridges along a non observed 2 m deep fracture was low enough to justify remedial measures to prevent the fall of a 2 m thick slab. On the other hand, the probable percentage of rock bridges still in place on a deeper potential failure surface was considered high enough to reject the possibility of the fall of a 4 to 5 m thick slab. As a result, the rock volume to be mined was reduced. In the future, such a study can be easily performed in 3D with multi-channel GPR systems now available, in order to obtain reliable 3D GPR images and 3D information about rock bridges. In addition to its efficiency to image the fracture network, GPR data exhibited sometimes complex fracture reflectivities, which may contain information about fracture properties (aperture, filling). These data will be used in the future, considering two different inversion approaches to help for quantitative characterization. The first one uses the frequency sensitivity of the reflectivity (Grégoire et al., 2003), while the second uses Amplitude and Phase Variations of the reflection coefficient versus Offset computed from CMP data (Deparis and Garambois, 2006). Using these quantitative information and 3D surveys, one can expect to obtain a global 3D view of the fracture network and of its properties.

Acknowledgements

This work was partially supported by the General Council of Isère, who provided the financial support for the borehole measurements performed by the HYDRO-KARST company. We thank the S.A.G.E (Société Alpine de Géotechnique) geotechnical company for its help in the acquisition and the PERAZIO company for the topographical data. The original manuscript benefited from corrections carried out by two anonymous reviewers and the editor of this journal, whom we thank sincerely.

References

- Benson, A.K., 1995. Application of ground penetrating radar in assessing 440 some geological hazards: examples of ground water contamination, faults, cavi. *Journal of Applied Geophysics* 33, 177–193.
- Clapp, R.G., 2001. Geologically constrained migration velocity analysis. PhD thesis, Stanford University.
- Demagnet, Donat, Renardy, François, Vanneste, Kris, Jongmans, Denis, Camelbeeck, Thierry, Meghraoui, Mustapha, 2001. The use of geophysical prospecting for imaging active faults in the Roer Graben, Belgium. *Geophysics* 66 (1), 78–89.
- Deparis, J., Garambois, S., 2006. Fracture imaging and characterization from apvo gpr data. 11th Int. Conf. on Ground Penetrating Radar, Columbus, Ohio, USA.
- Dix, C.H., 1955. Seismic velocities from surface measurements. *Geophysics* 20, 68–86.
- Frayssines, M., 2005. Contribution à l'évaluation de l'aléa éboulement rocheux (rupture). PhD thesis, Université Joseph Fourier.
- Frayssines, M., Hantz, D., 2006. Failure mechanisms and triggering factors in calcareous cliffs of the subalpine ranges (french alps). *Engineering Geology* 86, 256–270.
- Grasmueck, M., 1996. 3-d ground penetrating radar applied to fracture imaging in gneiss. *Geophysics* 61, 1050–1064.
- Grasmueck, M., Weger, R., Horstmeyer, H., 2005. Full-resolution 3d gpr imaging. *Geophysics* 70, K12–K19.
- Grégoire, C., Halleux, L., Lukas, V., 2003. Gpr capabilities for the detection and characterisation of open fractures in a salt mine. *Near Surface Geophysics* 1, 139–147.
- Hantz, D., Vengeon, J.M., Dussauge-Peisser, C., 2003. An historical, geomechanical and probabilistic approach to rock-fall hazard assessment. *Natural Hazards and Earth System Sciences* 3, 693–701.
- Hoek, E., Bray, J., 1981. *Rock Slope Engineering* (revised third edition). Institution of Mining and Metallurgy London, London.
- Hollender, F., 1999. Interprétation de la distorsion des signaux georadar propagés et réfléchis- Développement d'une tomographie par bande de fréquence. PhD thesis, Université Joseph Fourier.
- Jeannin, M., Garambois, S., Jongmans, D., Grégoire, C., 2006. Multiconfiguration gpr measurements for geometric fracture characterization in limestone cliffs (alps). *Geophysics* 71, B85–B92.
- Lampe, B., Holliger, K., Green, A.G., 2003. A novel algorithm for estimating the responses of diverse georadar antennas. *Geophysics* 68, 971–987.
- Perroud, H., Tygel, P., 2004. Nonstretch NMO. *Geophysics* 69, 599–607.
- Pettinelli, E., Beaubien, S., Tommasi, P., 1996. Gpr investigation to evaluate the geometry of rock slides and buckling in a limestone formation in northern Italy. *European Journal of Environmental and Engineering Geophysics* 1, 271–286.
- Pipan, M., Forte, E., Guangyou, F., Finetti, I., 2003. High-resolution gpr imaging and joint characterisation in limestones. *Near Surface Geophysics* 1, 39–55.
- Rashed, M., Kawamura, D., Nemoto, H., Miyata, T., Nakagawa, K., 2003. Ground penetrating radar investigations across the Uemachi Fault, Osaka, Japan. *Journal of Applied Geophysics* 53, 63–75.
- Reynolds, J.M., 1997. *An Introduction to Applied and Environmental Geophysics*. Wiley.
- Roch, K.H., Chwatal, E., Brückl, E., 2006. Potential of monitoring rock fall hazards by gpr: considering as example of the results of Salzburg. *Landslide* 3, 87–94.
- Stevens, K.M., Lodha, G.S., Holloway, A.L., Soonawala, N.M., 1995. The application of ground penetrating radar for mapping fractures in plutonic rocks within the Whiteshell Research Area, Pinawa, Manitoba, Canada. *Journal of Applied Geophysics* 33, 125–141.
- Stockwell, J.W., 1999. The cwp/su: seismic unix package. *Computers & Geosciences* 25, 415–419.
- Toshioka, T., Tsuchida, T., Sasahara, K., 1995. Application of gpr to detect and map cracks in rock slopes. *Journal of Applied Geophysics* 33, 119–124.
- Yilmaz, O., 1987. *Seismic Data Processing*. SEG.

4.3 Caractérisation des fractures : inversion des courbes AVO dispersives

Le paragraphe précédent a montré que l'imagerie radar depuis une paroi pouvait fournir des informations intéressantes en vue de la localisation des fractures (orientation, pendage) et de leur continuité, même en 3D. Dans certaines conditions – si l'ouverture de la fracture est assez grande devant la longueur du milieu contenant cette dernière - il est aussi possible de connaître les propriétés diélectriques ainsi que l'ouverture de la fracture grâce à l'analyse des vitesses déduites d'acquisitions CMP, de manière ponctuelle. Ceci est vrai pour tous les problèmes d'interface (exemple de contact glacier-bedrock, Sénéchal *et al.*, 2003). Cependant, les caractéristiques des couches minces ne sont pas accessibles directement lorsque leurs ouvertures sont petites devant la longueur d'onde du signal. En effet, il devient alors impossible de séparer les réflexions se produisant sur chacun de ses bords (fig. 3.1).

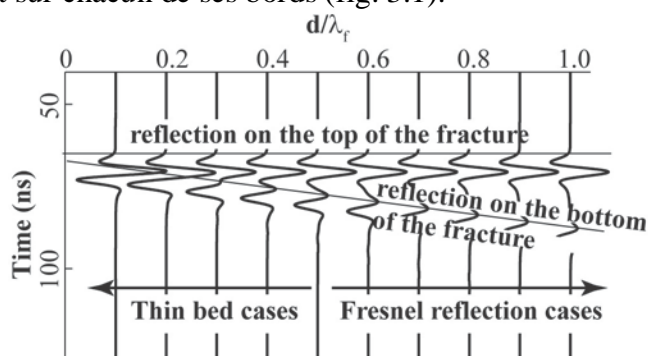


Fig. 3.1 Signaux GPR réfléchis synthétiques sur les bords d'une fracture en fonction du rapport ouverture sur longueur d'onde (d/λ_r) (d'après Deparis et Garambois, 2010).

Dans ce cas, le signal réfléchi résultant est la somme de réflexions multiples, qui vont dépendre de la nature, de l'épaisseur et de la nature du remplissage de la fracture. La réflectivité est alors elle-même contrôlée par le contraste de permittivité complexe ainsi que par l'épaisseur de la fracture (Annan, 2001). Elle présente à la fois des variations fréquentielles (dispersion) et angulaires (Annan, 2001).

Lane *et al.* (2000) ont montré à partir de données synthétiques et réelles que des fractures saturées d'eau génèrent des amplitudes de réflexion plus grandes que les fractures ouvertes remplies d'air, et qu'un déphasage était observable. Pettineli *et al.* (1996) avaient également montré que dans le cas de joints rocheux séparant un contact calcaire/calcaire, aucune réflexion du signal radar n'était observable sauf si les contacts étaient remplis par de l'argile ou de la calcite. Ainsi, les propriétés de la réflectivité de couches minces (amplitude, déphasage) sont sensibles à leur remplissage (ainsi qu'à leur ouverture), quelque soit l'offset considéré. A partir de cette observation, Grégoire (2001), Grégoire et Hollender (2004) et Jeannin (2005) ont proposé une méthode de caractérisation des fractures basée sur les propriétés dispersives de la réflectivité, en utilisant des données à offset unique mais multi-fréquentielles (Fig. 3.2).

Cette stratégie leur a permis d'utiliser des données classiques en imagerie géoradar, c'est-à-dire à offset constant, sur une grande échelle spatiale, pour retrouver les propriétés des fractures. Dans le cadre de la thèse de M. Jeannin (2005), nous avons proposé une méthode d'inversion des rapports spectraux des coefficients de réflexion radar mono-offset, basée sur un algorithme de voisinage (Sambridge, 1999a,b). Si celle-ci semble efficace sur des données synthétiques pour retrouver les paramètres d'épaisseur et de remplissage des fractures (Fig. 3.3), cette méthode nécessite un signal de référence (pour le rapport spectral), qui peut être obtenu soit

par transmission, soit par réflexion sur une couche de propriétés connues. Cette difficulté a freiné l'applicabilité de la méthode en contexte réel

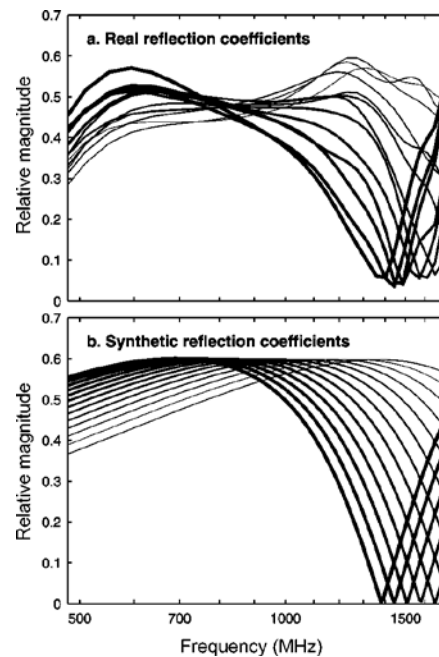


Fig. 3.2 Propriétés dispersives de la réflectivité d'une fracture séparant deux milieux homogènes (d'après Grégoire et Hollender, 2004). Comparaison entre données de laboratoire (haut) et modèle théorique (bas) utilisant le paramétrage de Jonsher (1977).

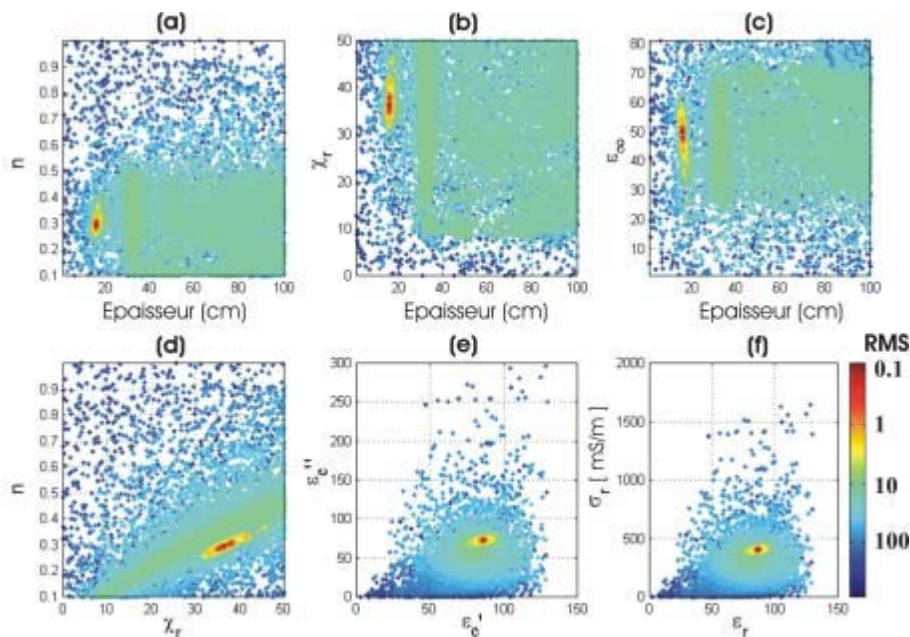


Fig. 3.3. Résultats d'inversion du coefficient de réflexion par algorithme de voisinage en considérant la méthode du rapport spectral. Illustration de la convergence avec une fracture de 16 cm d'épaisseur remplie d'argile (100 MHz). Les paramètres du modèle de Debye pour l'argile sont : $n=0.25$, $\chi_r=30$, $\epsilon_\infty=55$ et les permittivités diélectriques $\epsilon\epsilon'=\epsilon_r=85$, $\epsilon\epsilon''=72.42$ et les conductivités $\sigma\epsilon'=\sigma_r=402$ mS/m.

Pour contourner cette limitation, nous avons proposé d'utiliser les données acquises en Point Milieu Commun (CMP), certes plus lourdes et ponctuelles par rapport aux profils à offset constant, mais qui ont l'avantage d'apporter une contrainte supplémentaire : les courbes de

variation de la réflectivité en fonction de l'offset (AVO). Dans le cas des méthodes sismiques pétrolières, les analyses AVO ont été appliquées pour permettre l'accès aux contrastes de propriétés élastiques (Ostrander, 1984 ; Castagna, 1993). Ceux-ci peuvent être liés à des transitions lithologiques (Kindelan et al., 1989) ou de nature du fluide (Simmons and backus, 1994 ; Hall and Kendall, 2003 ; Mahob and castagna, 2003, Stovas et al., 2006). Au niveau des données radar, les premiers tests AVO ont été appliqués de manière qualitative pour caractériser la présence de contaminants dans la subsurface (Baker, 1998 ; Jordan and Baker, 2002, Deeds and Bradford, 2002). Des études synthétiques ont également montré la plus-value que constituent les informations AVO provenant des deux modes de propagation indépendants TE et TM en électromagnétisme (Lehmann, 1996 ; Carcione et al., 2006). Dans les cas de couches fines, Bradford et Deeds (2006) ont analysé une solution analytique des variations angulaires de la réflectivité, pour une fréquence donnée, qu'ils ont appliquée à des cas réels de contaminants.

Dans l'article présenté ci-après (Deparis et Garambois, 2009) nous présentons une approche originale qui consiste à inverser à la fois l'amplitude et la phase de la réflectivité en fonction de l'offset et en fonction de la fréquence, ceci dans le contexte de couches fines. Cette inversion menée par un algorithme de voisinage (Sambridge, 1999 a,b) possède la particularité que chaque solution analysée est corrigée des effets de propagation et du diagramme de rayonnement des antennes durant le processus d'inversion et avant la comparaison avec les données réelles. Cette approche spectrale effectuée en utilisant le modèle de Jonsher (1977), permet non seulement d'inverser les caractéristiques de la couche fine (profondeur, remplissage, ouverture) mais également celles du milieu environnant. Elle est par contre à l'heure actuelle limitée à un milieu homogène dans lequel une seule fracture est analysée (la première). Une description de la stratégie d'inversion est fournie pour des données synthétiques (figure 3.4).

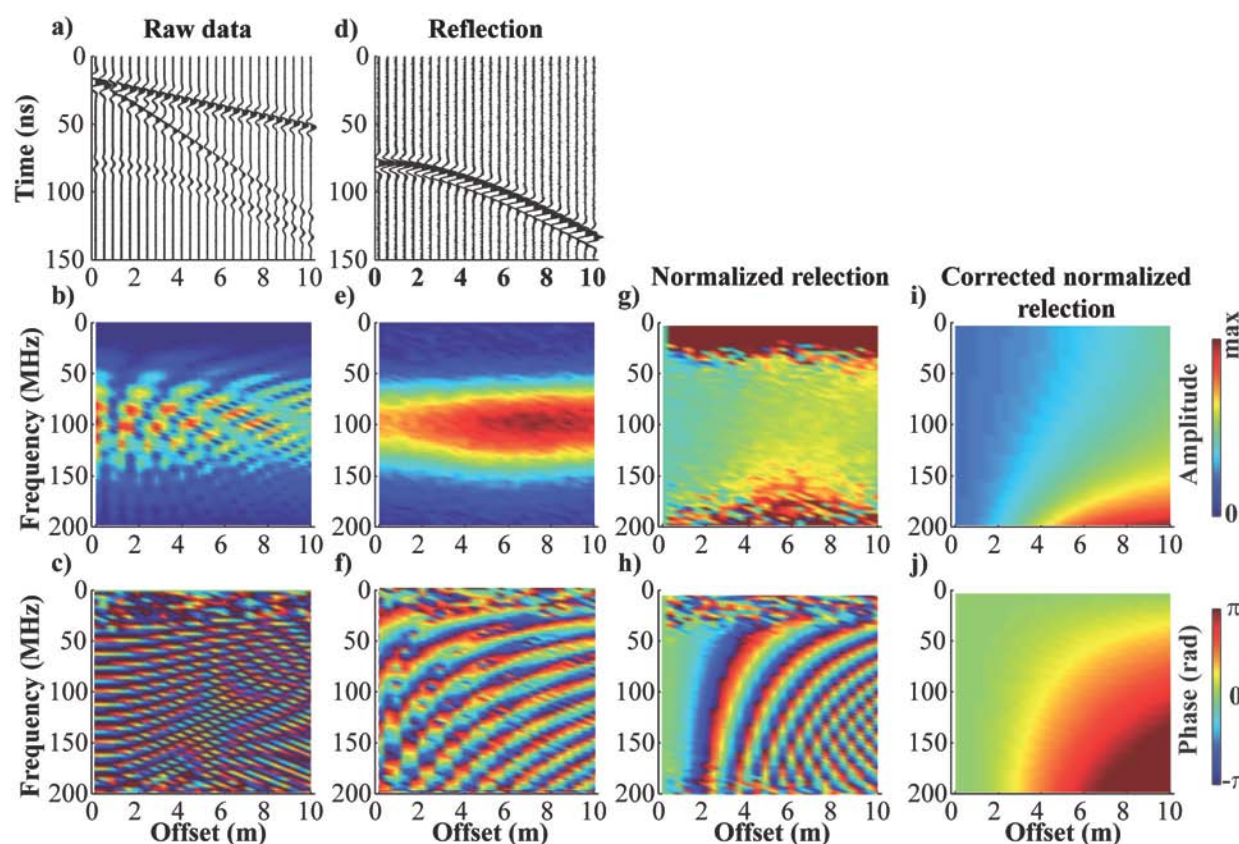


Fig. 3.4. Illustration de la stratégie d'inversion (Deparis et Garambois, 2010). Les données CMP sont représentées dans les domaines temporel (a) et fréquentiel pour l'amplitude (b) et la phase (c). Après sélection du signal réfléchi (d, e, f) les données sont normalisées dans le domaine fréquentiel (g, h) puis corrigées au cours du processus d'inversion de la propagation et du diagramme de rayonnement (i, j).

L'ensemble de la procédure d'inversion a été testé avec succès sur des données synthétiques bruitées (Deparis et Garambois, 2010) pour un grand nombre de remplissages présentant de propriétés différentes (ouvertures, nature du remplissage). Elle a été appliquée à deux cas différents de fractures réelles, acquis le long de parois rocheuses, et les solutions trouvées montraient une convergence intéressante. L'article présenté ci-après (Deparis et Garambois, 2009) présente cette méthodologie en détail et son applicabilité.

Les limites actuelles font qu'elle n'a été appliquée que dans un milieu encaissant homogène et que dans le cas d'une seule fracture, ceci afin de limiter les corrections, notamment au niveau de la transmission à une interface. Par la suite, ces limites devront être surpassées et des milieux variant latéralement être envisagés. L'approche envisagée serait l'inversion du champ d'onde complet, si la résolution de la méthode s'avère suffisante pour être appliquée aux couches fines.

On the use of dispersive APVO GPR curves for thin-bed properties estimation: Theory and application to fracture characterization

Jacques Deparis¹ and Stéphane Garambois¹

ABSTRACT

The presence of a thin layer embedded in any formation creates complex reflection patterns caused by interferences within the thin bed. The generated reflectivity amplitude variations with offset have been increasingly used in seismic interpretation and more recently tested on ground-penetrating radar (GPR) data to characterize nonaqueous-phase liquid contaminants. Phase and frequency sensitivities of the reflected signals are generally not used, although they contain useful information. The present study aims to evaluate the potential of these combined properties to characterize a thin bed using GPR data acquired along a common-midpoint (CMP) survey, carried out to assess velocity variations in the ground. It has been restricted to the simple case of a thin bed embedded within a homogeneous formation, a situation often encountered in fractured media. Dispersive properties of

the dielectric permittivity of investigated materials (homogeneous formation, thin bed) are described using a Jonscher parameterization, which permitted study of the dependency of amplitude and phase variation with offset (APVO) curves on frequency and thin-bed properties (filling nature, aperture). In the second part, we discuss and illustrate the validity of the thin-bed approximation as well as simplify assumptions and make necessary careful corrections to convert raw CMP data into dispersive APVO curves. Two different strategies are discussed to correct the data from propagation effects: a classical normal-moveout approach and an inverse method. Finally, the proposed methodology is applied to a CMP GPR data set acquired along a vertical cliff. It allowed us to extract the characteristics of a subvertical fracture with satisfying resolution and confidence. The study motivates interest to use dispersion dependency of the reflection coefficient variations for thin-bed characterization.

INTRODUCTION

Detection of prone-to-fall rock masses often proves to be undependable, owing to lack of information about the main discontinuities that cut through the mass and that may lead to potential instability. Recently, ground-penetrating radar (GPR) investigations conducted directly on various cliff faces successfully provided images of fracture continuity with a satisfying resolution (Jeannin et al., 2006; Roch et al., 2006; Deparis et al., 2007, 2008). In some cases, these images were quantitatively interpreted in terms of maximum rock-bridge percentage (Deparis et al., 2007). Even if it constitutes a large projection to approach the stability factor in terms of hazard assessment, we need more quantitative information about discontinuities (aperture and filling properties) to determine the stability factor.

When fractures are large compared to wavelength, it is possible to detect and individualize reflections coming from the two surfaces of a single fracture and deduce its aperture and filling properties when electromagnetic (EM) velocity is known from common-midpoint (CMP) surveys. Such an approach is, however, impossible to apply when fracture aperture is lower than half of the dominant wavelength (of the wave propagating in the filling material). In this case, multiple reflections coming from the two sides of the fracture create interferences and generate complex reflection patterns.

EM reflection properties, which have been widely studied for GPR purposes (Annan, 2001; Grégoire et al., 2003; Carcione et al., 2006), are sensitive to several contributing properties such as dielectric permittivity, electrical conductivity, and magnetic permeability (Annan, 2001). They also depend on the antenna polarization (Lehmann, 1996; Lutz et al., 2003), on the incident angle of the GPR wave (Annan, 2001), and on the frequency of the studied wave. In

Manuscript received by the Editor 5 October 2007; revised manuscript received 17 June 2008; published online 12 December 2008.

¹Université Joseph Fourier and CNRS, LGIT, Maison des Géosciences, Grenoble Cedex, France. E-mail: deparis.jacques@gmail.com; stephane.garambois@ujf-grenoble.fr.

© 2009 Society of Exploration Geophysicists. All rights reserved.

seismic interpretation, amplitude variation analyses of the seismic reflectivity as a function of offset (AVO) proved to be a useful tool to access the contrasts in elastic properties. These variations were related to lithological (Kindelan et al., 1989) and fluid content changes (Simmons and Backus, 1994; Hall and Kendall, 2003; Mahob and Castagna, 2003; Stovas et al., 2006).

AVO tests were successfully performed on GPR data to qualitatively characterize the presence of nonaqueous-phase liquid (NAPL) contaminants in the subsurface (Baker, 1998; Deeds and Bradford, 2002; Jordan and Baker, 2002; Jordan et al., 2004). Work was supplemented by numerical analyses of Lehmann (1996) and Carcione et al. (2006), who studied transverse electric (TE) and transverse magnetic (TM) reflection variations with offset for different contrasts of EM properties such as NAPL concentrations. All these studies were based on the Fresnel reflection coefficient curves (Griffiths, 1998), which were derived assuming monochromatic EM incident plane waves on a boundary separating two homogeneous and isotropic media. These assumptions are contradicted to some degree when applied to field data, particularly in the event of the presence of a thin bed, which affects reflectivity caused by interferences between reflections generated on both sides of the thin bed. A direct consequence is that the Fresnel reflection equation is no longer valid when the aperture of the thin bed is less than 75% of the dominant wavelength of the signal (Bradford and Deeds, 2006).

For seismic applications, the pioneering work of Widess (1973), which showed how the composite reflection amplitudes from a thin bed vary as a function of its aperture for a cosine wavelet, was generalized and more thoroughly studied (e.g., Schoenberger and Levin, 1976; Koefoed and de Voogd, 1980; Stephens and Sheng, 1985). Recently, AVO response of a single thin bed was discussed by Liu and Schmitt (2003) in terms of its capability to characterize a seismic reservoir. For GPR data, Grégoire and Hollender (2004) compared the spectral ratio between measured reflected wavelets and a reference wavelet for the case of thin-bed reflectors to estimate the dispersive dielectric permittivity of the reflectors and their apertures. This frequency-sensitive approach was only applied to constant-offset sections and not to AVO data. In addition, Bradford and Deeds (2006) analyzed AVO curves using an analytical solution of the thin-bed reflectivity and successfully applied their modeling to two case studies dealing with NAPL-contaminated zones. However, the authors did not account for the dispersive properties of constitutive parameters.

In this paper, amplitude and phase variation with offset (APVO) analyses of GPR data are conducted to characterize fracture properties (filling, aperture). The procedure is restricted to a homogeneous medium in which a thin bed is embedded. The study is extended to a dispersion analysis of these APVO curves within a useful frequency band. Dispersion of dielectric properties is taken into account using a Jonscher formulation (Jonscher, 1977). We first briefly recall the main characteristics of EM thin-bed reflection coefficient variations with offset and frequency and on their sensitivities to thin-bed properties (aperture, filling). In the second part, the validity of the thin-bed approximation is numerically studied and discussed together with the problem of raw data corrections, a delicate process necessary for getting reflectivity properties. In the last part, this frequency-dependent APVO methodology is applied to CMP data acquired on a cliff face. It permitted us to derive with satisfactory resolution quantitative properties of the main fracture that cuts through the studied rocks. Such methodology, which can be extended to all

thin-bed problems, constitutes the preliminary results of inversion of dispersive APVO curves.

THIN-BED EM REFLECTION AND PROPERTIES

Fresnel reflection and transmission equations quantify amplitude and phase distribution of EM waves on both sides of an interface for two different polarization planes, the TE mode (electric field vector is parallel to the strike of a dipping fracture plane) and the TM mode (electric field vector is perpendicular to the strike of a dipping fracture plane) (Griffiths, 1998). Snell's law expresses the relationship between incidence θ_i , transmission θ_t , and reflection θ_r angles for a wave impinging on an interface between two media presenting different EM properties (Griffiths, 1998).

Dispersion effects of constitutive dielectric properties can be described using various theoretical models. The complex dielectric permittivity characterizes the redistribution of local connected charge under the action of an electric field. There are different relaxation phenomena associated with relaxation frequencies. For the frequency range used in GPR surveys, the dominant polarization phenomena may be the electronic, atomic, and molecular dipole processes, depending on the investigated material. Several authors (Debye, 1929; Cole and Cole, 1941; Jonscher, 1977) propose different models to account for this dispersion, which are thoroughly presented and discussed in Bano (2004). Among them, Jonscher parameterization (Jonscher, 1977) is well adapted to describe complex permittivity ε_e of GPR systems (Hollender and Tillard, 1998), particularly when the signal frequency is higher than the relaxation frequencies. This model, which is not suitable when the signal frequency is lower than the relaxation peak, only uses three Jonscher parameters (ε_∞ , χ , and n):

$$\varepsilon_e(\omega) = \varepsilon_0 \chi_r \left(\frac{\omega}{\omega_r} \right)^{n-1} \left(1 - i \cot \frac{n\pi}{2} \right) + \varepsilon_\infty, \quad (1)$$

where ε_0 is the permittivity of free space ($8.854 \cdot 10^{12}$ F/m) and ω_r (Hz) is a reference frequency (arbitrarily chosen).

Thin-bed reflectivity

The validity limit of standard Fresnel equations describing reflection and transmission across individual interfaces was established by Bradford and Deeds (2006) at approximately 0.75 of the characteristic wavelength λ of the signal propagating within the second layer. When the layer aperture is less than 0.75λ , multiple reflections between both sides of the thin bed generate frequency-dependent interferences, which create a complex reflectivity pattern.

Considering the restricted case of the thin bed embedded within a homogeneous medium (Figure 1), an analytical solution of the thin-bed reflectivity R is given by (see Appendix A and Liu and Schmitt, 2003)

$$R(\omega) = \frac{R_{12}(\omega) - R_{12}(\omega)e^{-i\phi(\omega)}}{1 - R_{12}^2(\omega)e^{-i\phi(\omega)}}, \quad (2)$$

with $\phi(\omega) = 2dk_2(\omega)\cos(\theta_i)$ and $k_{1,2} = \omega\sqrt{\mu_{1,2}\varepsilon_{e1,2}}$. In this expression, $R_{12}(\omega)$ denotes the TE or TM Fresnel reflection coefficient between layers 1 and 2, k is the wavenumber, and d is the thin-bed aperture. Equation 2 shows that thin-bed reflectivity depends on the dielectric properties of the propagating medium (homogeneous) and of the filling material, on the aperture of the thin bed, on the incidence angle of the wave, and finally on the frequency of the signal.

Dispersion of the thin-bed reflection coefficient

To illustrate the reflectivity sensitivity of a thin bed, APVO curves were computed for the TE mode as functions of frequency (Figure 2a and b) for vertical incidence and as functions of the incidence angle at a frequency of 100 MHz (Figure 2c and d). These computations were performed considering an air-filled (solid line) and clay-filled (dashed line) thin bed of various apertures embedded within a limestone formation.

These examples highlight the dispersive variations of both amplitude and phase of a thin-bed reflection coefficient for two different fillings. It underlines the existence of a critical normalized aperture of the thin bed ($d = \alpha\lambda_2/2$, where α is a positive integer) for which the amplitude of the reflection coefficient is null (for air) or minimum (for clays). The phase exhibits large fluctuations around this value. The amplitude of the reflection coefficient is maximum for a thin-bed aperture of $\alpha\lambda_2/4$. Figure 2 also highlights the variation of amplitude and phase of the reflectivity according to the incidence angle. The amplitude increases more or less gradually (depending on the aperture) up to one for large incidence angles, contrary to phases, which present weak fluctuations according to incidence angle. Finally, these computations also show large reflectivity fluctuations according to the filling material.

These simple computations illustrate well the potential of the proposed global approach to characterize the thin-bed properties by using all reflection-coefficient variations (dispersion and APVO).

Comparison between numerical and analytical thin-bed reflection coefficients

The validity of the analytical form of the thin-bed approximation is studied using a numerical model generated from a finite-difference time-domain (FDTD) numerical modeling code (GprMax2d, Giannopoulos, 2005). The purpose is to compare reflection coefficient properties derived from the thin-bed approximation to those derived from the numerical modeling. This process also allows us to evaluate the efficiency of the methodology chosen to correct the data from propagation effects (geometric spreading and attenuation effects). At this stage, radiation pattern effects were not considered because the EM source was an infinitesimal dipole embedded in a homogeneous medium. Data were computed in the H -plane (with a central frequency around 100 MHz). The grid resolution ($N = \lambda/\delta_x$) is larger than 10, with a cell size δ_x of 0.33 cm, to keep numerical dispersion low (Holberg, 1987; Bergmann et al., 1996).

The geometric model is made up of a thin bed located at a depth of 3 m, embedded within homogeneous limestone. As GprMax software does not use Jonscher parameterization, we modelled the limestone matrix with the following parameters: $\epsilon_r = 9$, $\sigma = 10^{-3}$ S/m. The CMP acquisition was computed as a realistic survey, i.e., with a maximal offset of 10 m, which provides incidence angles ranging from 0 to 60°. As the source waveform is difficult to determine in field conditions, all APVO analyses were normalized in the Fourier domain using a low-offset trace for all studied frequencies.

Figure 3 presents reflection-coefficient properties for an air-filled thin bed with an aperture of 30 cm ($\lambda_2/10$ for a frequency of 100 MHz) as functions of frequency and incidence angle. Numerical data were corrected from 2D FDTD propagation effects by dividing them by $e^{-ik_1(\omega)r/\sqrt{r}}$, using the 2D geometric spreading factor $1/\sqrt{r}$. These computations show the good consistency between analytical (Figure 3a and d) and numerical modeling (Figure 3b and e) results for both the amplitude and phase within the investigated fre-

quency range (50–200 MHz) and the incidence-angle range. For frequencies up to 200 MHz, the relative amplitude error (Figure 3c) is always below 1.6% and the phase difference (Figure 3f) below 0.3 rad. The maximum errors, which are observed for large frequencies and large incidence angles, are essentially because of numerical dispersion coupled with phase-velocity errors generated during FDTD computations. Indeed, phase-velocity error is maximum when the wave direction under the cell equals 45° for square cells (Zhao, 2002, 2004) and numerical dispersion increases with the propagation distance of the waves, resulting in larger dispersion errors at the largest incidence angles. For greater frequencies (200–300 MHz), the relative amplitude error and phase difference increase to 2.8% and 0.6 rad, respectively, thus highlighting the influence of numerical dispersion resulting from the decreasing cell resolution in relation with frequency.

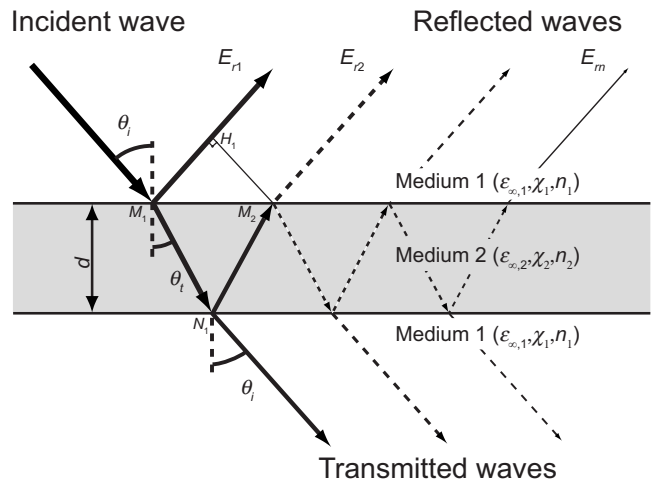


Figure 1. Schematic representation of a thin bed embedded between two identical layers, which create wave interferences resulting from multiple reflected and transmitted waves coming from both sides of the thin bed.

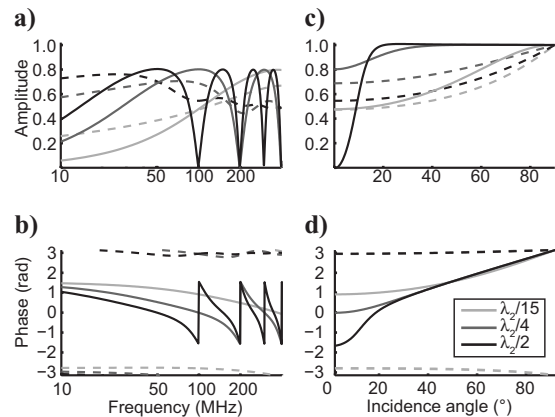


Figure 2. Reflection coefficient between limestone ($\epsilon_{s1}/\epsilon_0 = 8.14$; $\chi_1 = 0.94$; $n_1 = 0.82$) and a thin bed filled with different materials (air in solid lines: $\epsilon_{s2}/\epsilon_0 = 1$; $\chi_2 = 0$; $n_2 = 1$; clays in dotted lines: $\epsilon_{s2}/\epsilon_0 = 55$; $\chi_2 = 30$; $n_2 = 0.25$) as functions of frequency and incidence angle for the TE mode. The modulus and phase-sensitivity curves were computed for different apertures of the thin bed at zero offset for (a) and (b) (with $\lambda_2/2$, $\lambda_2/4$, and $\lambda_2/15$ computed at a frequency of 100 MHz) and at 100 MHz for (c) and (d).

This satisfying consistency obtained considering a low dispersive filling material can be extended to different situations. For the two first cases (Figure 4a and b), the real part of the effective permittivity of the filling material is lower than that of the matrix. It represents air and a more conductive material (dry sands). For the last two cases (Figures 4c and d), the real part of the effective permittivity of the filling material is larger than that of the matrix. It represents a conductive material (clays or soil) and fresh water.

For the air filling (Figure 4a), the comparison between analytical and numerical reflection coefficients is consistent as long as the aperture is lower than 80 cm ($\lambda_2/3.75$). Beyond this aperture, the absolute variation of amplitude differs slightly. This result highlights the influence of critically refracted waves when fracture aperture is greater than 80 cm for air filling at 100 MHz. For the sandy filling (Figure 4b), the comparison is satisfactory for all apertures. For clay and water fillings (Figure 4c and d), the comparison of amplitudes is quite consistent for all apertures, contrary to the phases, where differences appear for large incidence angles (greater than 40°) and when the aperture of the thin bed is greater than $\lambda_2/2$. The phase differences are essentially from phase-velocity error and numerical dispersion. Indeed, in these two last cases, the associated grid-resolution decreases caused by the increase of the real part of permittivity in the thin bed. When the aperture is lower than $\lambda_2/2$, errors between numerical and analytical reflection coefficients always remain below 5%. These results suggest that the thin-bed approximation can be used in all cases as long as thin-bed aperture remains lower than $\lambda_2/2$, except for air filling, which requires an aperture lower than 80 cm (corresponding to $\lambda_2/3.75$).

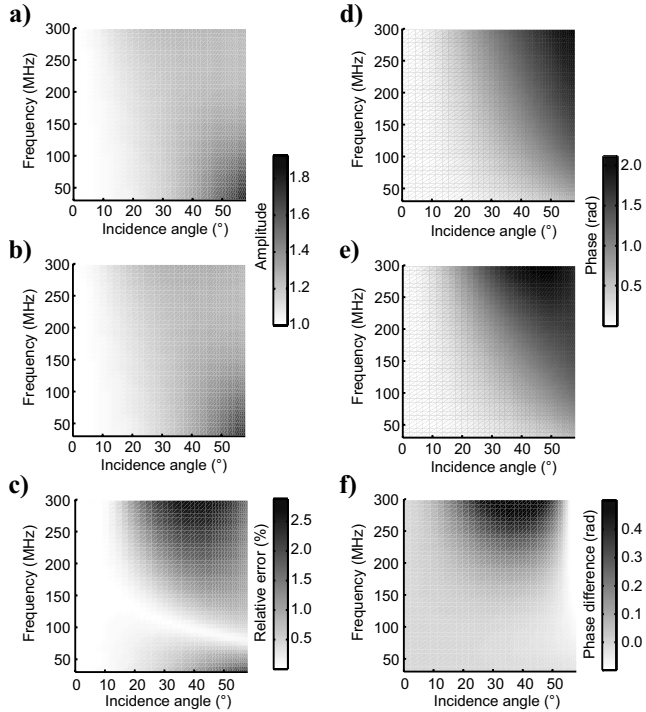


Figure 3. Comparison between amplitude A and phase P of analytically (a, d) and numerically (b, e) computed reflection coefficients for an air-filled thin bed (aperture of 30 cm) as functions of frequency and incidence angle. The relative amplitude error ($|A_{\text{mod}} - A_{\text{syn}}|/|A_{\text{mod}}| \times 100$) and phase difference ($P_{\text{mod}} - P_{\text{syn}}$) are presented in (c) and (f), respectively.

FROM CMP DATA TO REFLECTION-COEFFICIENT PROPERTIES

The conversion of field GPR data into reflectivity properties (APVO, dispersion) is a delicate operation that requires several corrections. Bradford and Deeds (2006) discuss several issues related to this point. The reflected electric field $E_{\text{mes}}(\omega, x)$ recorded at an offset x (incidence angle θ_i) and at an angular frequency ω can be expressed from the electric field source for a homogeneous medium:

$$E_{\text{mes}}(\omega, x) = E_0(\omega) \frac{D(\omega, \theta_i) C(\omega, \theta_i) T(\omega, \theta_i) e^{-ik_1(\omega)r}}{r} R(\omega, \theta_i), \quad (3)$$

where $D(\omega, \theta_i)$ describes the influence of the transmitter and receiver antenna radiation patterns, $C(\omega, \theta_i)$ describes the influence of transmitter and receiver/soil couplings, $T(\omega, \theta_i)$ describes possible energy losses caused by interfaces located between the free surface and the studied thin bed, r is the length of the travel path studied ($r = x/\cos(\theta_i)$), and x is the distance between the emitting and receive-

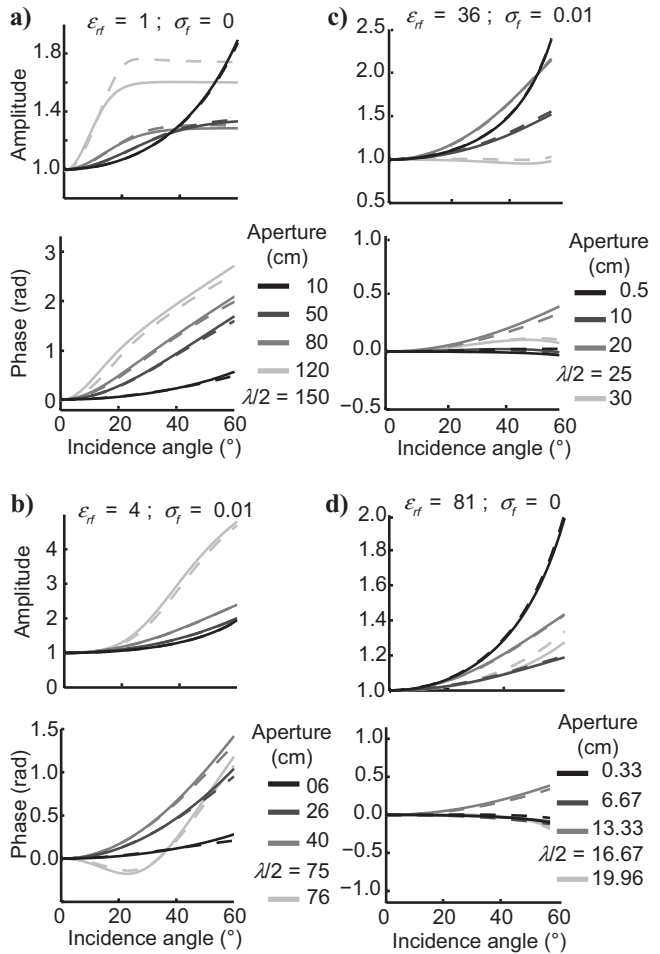


Figure 4. Comparison between analytically (solid lines) and numerically (dashed lines) computed reflection coefficients as a function of incidence angle for different apertures and filling materials: air (a), sand (b), clays (c), and water (d). All curves were computed for a 100 MHz frequency.

ing antennas. The factor $e^{-ik_1 r}$ is the propagation term, which includes the intrinsic attenuation and dephasing for a plane wave.

The emitting source waveform depends highly on the acquisition system (antennas and electronic system), and this information is difficult to obtain, especially for commercial GPR systems. As a consequence, there is no possibility to access absolute properties of the reflection coefficient. This problem can be circumvented by normalizing equation 3 with a trace acquired at a given offset x_2 . Equation 3 also shows the necessity of making simplifying assumptions and necessary corrections to access the relative reflection properties $R(\omega, \theta_1)/R(\omega, \theta_{i2})$ (i.e., dispersive APVO effects) generated by a thin bed from the recorded reflected signals $E(\omega, x)$.

Simplifying assumptions are thoroughly discussed by Bradford and Deeds (2006). They assume that the coupling factor does not vary significantly over the offset range for a uniform surface with laterally homogeneous material and that the transmission losses do not vary significantly with offset. They conclude that the error generated by omitting these phenomena is less than 5% and that it may generate problems only for large angles. These two assumptions, with the normalization, make it possible to simplify equation 3:

$$\frac{R(\omega, \theta_i)}{R(\omega, \theta_{i2})} = \frac{E_{\text{mes}}(\omega, x)}{E_{\text{mes}}(\omega, x_2)} \frac{r}{r_2} \frac{D(\omega, \theta_{i2})}{D(\omega, \theta_i)} \frac{e^{-ik_1(\omega)r_2}}{e^{-ik_1(\omega)r}} \quad (4)$$

Propagation corrections

To access the relative reflection coefficient properties, the signal has to be corrected from propagation effects, a process that implies knowing precisely r , r_2 , and $k_1(\omega)$. Two distinct strategies can be envisaged to achieve this goal.

The easier one requires additional measurements. It consists of (i) analyzing CMP data in terms of normal-moveout (NMO) velocity or migration inversion (Kuhl and Sacchi, 2003) and (ii) obtaining electrical measurements of the homogeneous medium (here, limestone). CMP analysis provides both the depth of the reflector (and so r and r_2) and the real part of k_1 at various frequencies. Rock materials generally show a low dispersion of the real part of k_1 in the GPR frequency range; consequently, this dispersion can be considered as negligible. The imaginary part of k_1 can be deduced from electrical measurements acquired at the test site using electrical tomography, EM methods, or laboratory measurements on rock samples. Field measurements generally are performed at low frequency (quasi-static conditions) but can be extended to GPR frequencies for low dispersive media. The drawback of such an approach is that there is a trade-off between phase shift because of propagation, relaxation, and reflection. The contribution of each phenomenon is not easily distinguishable. For this reason, Bradford and Deeds (2006) study only the amplitude of the reflected wave by considering the envelope of the signal. Although relaxation effects are very weak in limestone formations, this trade-off may result in minor velocity changes.

Another approach, studied by Deparis and Garambois (2007) and derived from Deparis and Garambois (2006), consists of inverting all parameters together to take into account the above-mentioned trade-off. This method is described hereafter.

Radiation pattern effects

The second correction concerns radiation patterns of the antennas. Currently, only radiation pattern studies for antennas placed in free space have been carried out for the RAMAC unshielded GPR anten-

nas used in our experiments (Streich and van der Kruk, 2007). As no study has reproduced radiation patterns of these antennas at the contact between a free surface and a half-space, we modeled them.

Figure 5a compares the normalized radiation-pattern amplitude in the H plane (for TE mode) deduced from three different methods: (i) the analytical far-field solution of an infinitesimal horizontal EM dipole located at the boundary of a half-space (Engheta et al., 1982), (ii) a semiempirical radiation pattern presented by Bradford and Deeds (2006), which gives similar results to those obtained in the laboratory, and (iii) a numerical study at 140 MHz carried out using the software developed by Lampe and Holliger (2005), based on FDTD approximation of Maxwell's equations. As the latter simu-

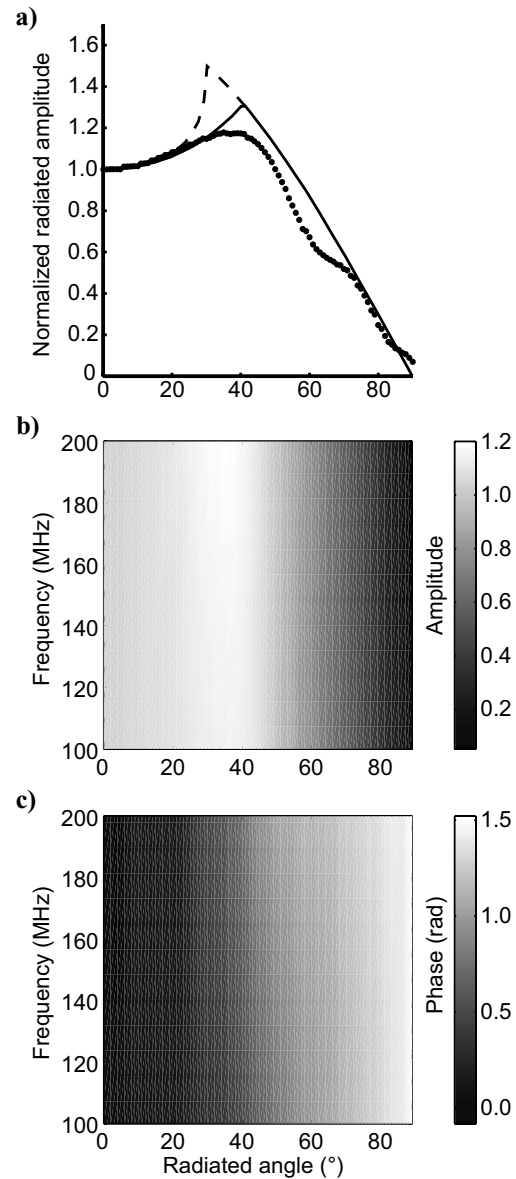


Figure 5. (a) Normalized amplitudes of half-space radiation patterns for the far field of an infinitesimal dipole (dashed line), a semiempirical model (solid line), and a model obtained from a numerical modeling (dotted line) at a frequency of 140 MHz and radius of 30° for bow-tie antennas. Radiation patterns normalized by the propagation term $e^{-ik_1(\omega)r}/r$ between 100 and 200 MHz obtained from numerical modeling for (b) amplitude and (c) phase.

lates the radiation characteristics of a wide variety of typical surface GPR antenna systems, it permitted us to compare different types of bow-tie GPR antennas and to conclude that a scaled Wu and King (1965) profile is a possible loading criterion applicable for GPR antennas (Lampe and Holliger, 2005). Streich and van der Kruk (2007) show that a profile scaled to roughly one-fourth of the nonreflecting Wu-King load explained reasonably well laboratory measurements of RAMAC antenna radiation. Our radiation pattern was extracted from model data on a circle located around the source at a distance of 2.8 m and was corrected from propagation effects by dividing them by $e^{-ik_1(\omega)r}/r$. This computation used a size of cells of 3 cm to achieve a grid resolution ($N = \lambda/\delta_z$) above 10 for frequencies up to 300 MHz.

Figure 5 shows the good correlation between the different proposed radiation patterns for low (lower than 20°) and high (greater than 70°) incidence angles. The infinitesimal horizontal dipole model strongly diverges between these two limits. Semi-empirical and numerical radiation patterns present slight differences above 30° . This is resulting from the presence of a less smoothed near-field contribution with numerical modeling. Figure 5b and c shows the frequency dependency of radiation pattern for, respectively, the amplitude and phase for the present FDTD modeling. The amplitude shows a weak frequency dependence in the 100–200 MHz frequency range. Phase exhibits small variations according to the incidence angle and also a weak frequency dependence. Considering all the results, GPR data will be corrected from radiation-pattern effects using the FDTD results presented in Figures 5b and c.

INVERSION OF FREQUENCY APVO CURVES

Inversion scheme

This inversion scheme is based on the neighborhood algorithm (Sambridge, 1999a, 1999b), which consists of searching an ensemble of best models inside a given parameter space that fit experimental data well. The search in this space is performed using the nearest neighbor regions defined under a suitable distance norm. It is first initialized by a random seed number; the algorithm requires solving a large number of forward problems. The advantage of the neighborhood algorithm compared to classical random inversion methods (e.g., Monte Carlo) lies in the fastness of investigation of space parameters, especially when the number of unknowns is greater than three. The inversion process makes a direct comparison in the frequency domain between the normalized field data and synthetic data generated using equation 4. The main advantage of this strategy is that the algorithm corrects the data from propagation and radiation pattern effects for each cell of the investigated parameter space. Finally, the normalization by the nearest-offset trace also eliminates the problem of the source wavelet, which is unknown in field conditions.

Parameters investigated by inversion

Dielectric parameters, which are complex, can be decomposed into Jonscher parameters, both for the matrix and the fracture: $\varepsilon_{z,m}/\varepsilon_0$, $n_m\chi_m$, $\varepsilon_{z,f}/\varepsilon_0$, n_f , χ_f . As the $\varepsilon_{z,m}/\varepsilon_0$ ratio can be roughly estimated directly from the interval velocity profile deduced from the CMP analysis, the related parameter space that must be investigated can be highly reduced. In the same way, the n_m and χ_m parameter spaces were reduced to limestone formation properties presenting high electrical resistivity values. According to the thin-layer

limit, the thickness d of the thin bed can only vary from zero to $\lambda/2$. Finally, the incident angle θ introduces one supplemental hidden unknown, the depth of the reflector z . This value can be roughly deduced from the CMP analysis. In sum, there are eight unknowns for the inversion process, four of them having a broad variation range ($\varepsilon_{z,f}/\varepsilon_0, n_f, \chi_f, d$) and four having a reduced variation range ($\varepsilon_{z,m}/\varepsilon_0, n_m, \chi_m, z$).

Studies on synthetic data

The inversion program was first tested on analytical signals computed using equation 3 for parameters describing sand-filled material within a (50–150 MHz) frequency range. For each inversion, five runs that correspond to different seed numbers were computed to get more reliable results. The investigated parameter space is given in Table 1.

To reproduce a classical CMP acquisition, analytical APVO curves were inverted after normalization, considering a maximal offset of 10 m and an increment between traces of 20 cm. Different fracture apertures were tested, ranging from $\lambda/100$ to $\lambda/2$ (λ denotes the wavelength of the filling material, i.e., wet sand). Corresponding inversion results are displayed in Figure 6. The Jonscher parameters were transformed into complex permittivity parameters at a frequency of 100 MHz using equation 1. The error between each model of the parameter space and the data was computed in the root mean square (rms) sense. Low rms values (dark) represent the models that best fit the analytical APVO curves.

Figure 6 shows the very good characterization of the fracture parameters ($\varepsilon_{r,f}$, $\varepsilon_{i,f}$, d , z) and matrix parameters ($\varepsilon_{r,m}$, $\varepsilon_{i,m}$) for TE acquisition mode. It is particularly true as long as the ratio d/λ is greater than or equal to 0.1. This preliminary result also illustrates the high sensitivity of dispersive APVO curves to fracture properties.

APPLICATION TO FRACTURE CHARACTERIZATION: A FIELD DATA SET ACQUIRED ON A VERTICAL CLIFF

The proposed methodology was tested on a field data set that was part of a multiconfiguration and multifrequency study (Jeannin et al., 2006) conducted on a 12-m-high cliff composed of Tithonian limestone (Upper Jurassic) that forms a subhorizontal plateau covered by organic soil. A detailed structural study (Jeannin et al., 2006) was performed from surface observations on the cliff face and on the

Table 1. Investigation range for the parameter space during inversion of synthetic data.

Parameters	Model value	Investigated range
$\varepsilon_{z,m}/\varepsilon_0$	8.14	7–10
n_m	0.84	0.5–1
χ_m	0.94	0–1.5
$\varepsilon_{z,f}/\varepsilon_0$	2.5	1–100
n_f	0.85	0.1
χ_f	2.0	0.80
d (m)	Variable	0– $\lambda/2$
z (m)	3.0	2.5–3.5

plateau. It mainly showed that the rock mass is affected by three main discontinuity sets: the bedding planes S_0 , dipping gently inside the massif (N30°E/20°NW) and two vertical fracture sets (N140°E/90° and N30°E/90°). The first fracture set is predominant and clearly visible on the entire cliff. The secondary fracture set, oriented N30°E locally, appears along the cliff.

Common-offset GPR data

GPR measurements were acquired using a RAMAC/GPR system (MALA Geosciences) that was suited for the difficult conditions along vertical cliff faces. As the main fracture networks are almost vertical, only profiles where antennas were directly positioned on the cliff surface were able to image the possible interfaces created by these discontinuities. For this reason, and to optimize the coupling between the rock surface and the antennas, an operator had to climb the cliff with the antennas and suitable cables. The 200-MHz data were acquired using a sampling frequency of 2000 MHz and acquisition time of 420 ns. All measurements were stacked 128 times. Figure 7 shows common-offset GPR data acquired on the cliff face using 200-MHz unshielded antennas in TE mode. The 1-m-long offset transmitter-receiver pair was moved in increments of 20 cm.

To increase the amplitude of late (distant) events, the common-offset data were processed and filtered. First, a 10–400-MHz band-pass zero-phase Butterworth filter was applied, followed by notch filters designed to dampen multiple monochromatic reverberations (ringing). Then, automatic gain control (AGC) was applied for display purposes. The processed GPR image shows several reflected signals down to 280 ns (only the first 150 ns are presented here). This image shows the direct airwave, followed by different reflected events, whose amplitudes vary considerably along the same reflector. These reflectors are approximately parallel to the cliff face except for the first one, which dips toward the rock mass. It appears that two clearly separate reflectors at the top of the cliff, which correspond to different fractures observed at the surface, coalesce around 4 m to form a single fracture, which is studied hereafter.

CMP data

The CMP survey (Figure 8) was performed by increasing the distance between transmitting and receiving antennas in increments of 40 cm. The central location of CMP acquisition is 6 m from the top of the cliff in Figure 7. Two operators carried the 200-MHz antenna up and down the cliff face from this central location. The CMP profile was filtered using a 30–300-MHz band-pass Butterworth filter and amplitudes were equalized with AGC for visualization only. The CMP data exhibit the direct airwave followed by reflected events. The signal-to-noise ratio is satisfactory except for traces ranging between 3.6 and 4 m (bad rock/antenna coupling), which were muted in the dispersive APVO analysis. In this paper, we only study the highlighted wave ($t_0 \approx 60$ ns), which corresponds to the main reflector in the common-offset data (between 50 and 78 ns).

We tested the two strategies to correct these data for propagation effects. The NMO analysis performed on the CMP data yielded a mean velocity estimated around 12 cm/ns at 140 MHz between the cliff face and the fracture (real permittivity of 6.2) and a depth of the

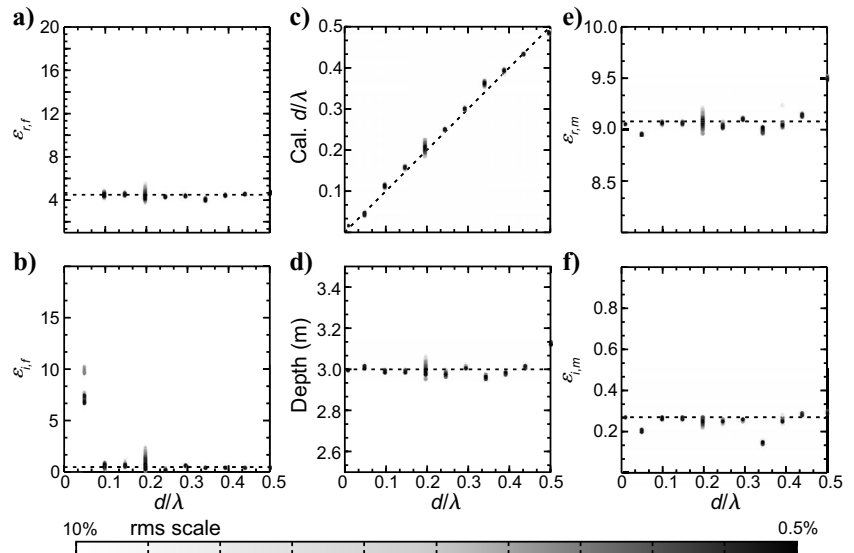


Figure 6. Inversion results for a crack filled with wet sand embedded in a limestone formation for (a) the real part ($\epsilon_{r,f}$) and (b) imaginary part ($\epsilon_{i,f}$) of the effective permittivity of the filling material, (c) the calculated aperture, (d) the depth, (e) the real part ($\epsilon_{r,m}$), and (f) imaginary part ($\epsilon_{i,m}$) of the effective permittivity of the matrix in function of d/λ for the TE mode. Dotted lines represent the theoretical solution.

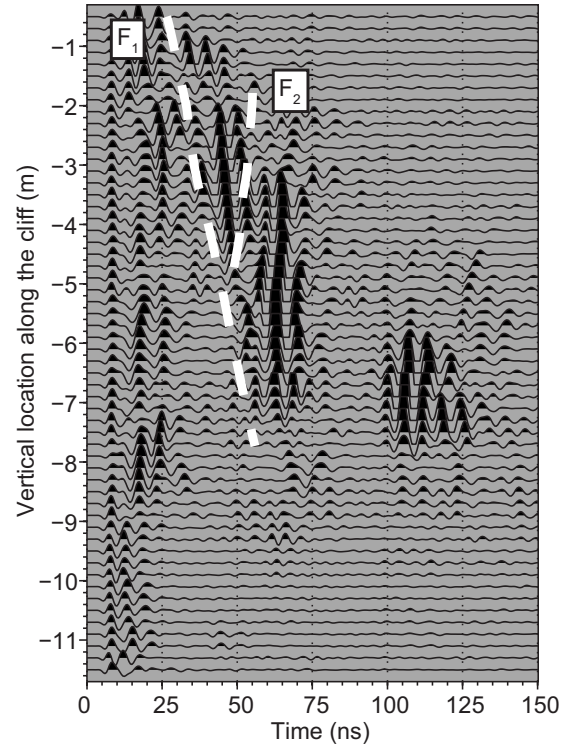


Figure 7. GPR vertical azimuth profile acquired with a 200-MHz unshielded antenna along the cliff. Data were filtered using a 10–400 MHz–Butterworth band-pass filter, notch filters to eliminate ringing effects, and an AGC process. Reflections F_1 and F_2 are referred to in the text.

fracture around 2.8 m. Low-frequency EM data (EM31, Geonics) acquired on the plateau showed a resistivity of 800 Ωm for the limestone formations.

Figure 9a and b shows the data corrected using the permittivity and resistivity values deduced from NMO and EM31 analysis, respectively. The data were transformed to the frequency domain using a fast Fourier transform, and the frequency range of 100–200 MHz was extracted for this study. For all frequencies, a sudden and major change is observed for offsets greater than 5 m (incidence angle of 40°), marked by a large decrease of the amplitude of the reflection.

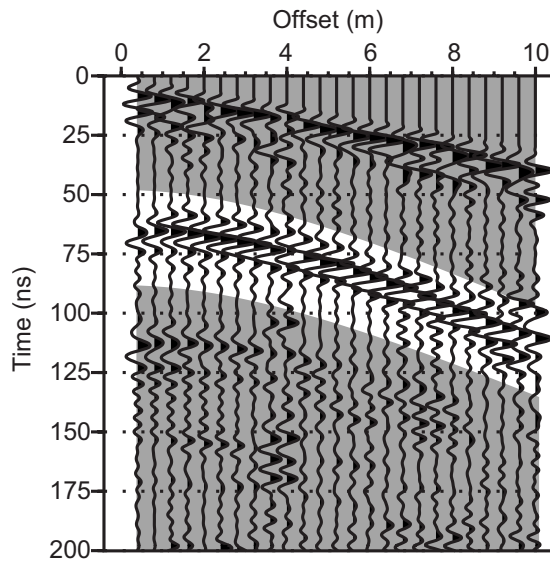


Figure 8. CMP data acquired using a 200-MHz unshielded antenna on the wall of a limestone cliff. The studied reflected event is high-angled.

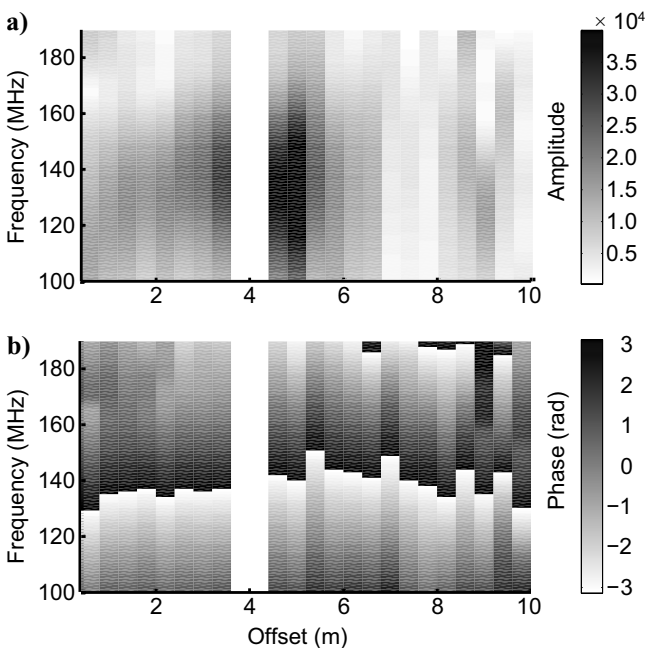


Figure 9. (a) Amplitude and (b) phase of the studied reflected wave after propagation and radiation-pattern corrections (for inversion solution) for all frequencies and incidence angles investigated.

No theoretical thin-bed or Fresnel reflection coefficient model is able to reproduce this observation. Multiple reasons may cause this distortion, such as interferences between various waves for large-offset data (airwave reflections, scattering at the edges of the cliff) or 2D effects (presence of a weathered zone at the edge of the cliff). In our case, the presence of a second bedding reflector at the top of the cliff (F_1 in Figure 8), which is located above the studied thin bed (F_2), may be the principal cause of continuity loss of the factor $T(\omega, \theta_i)$ (transmission losses above the thin bed), which was assumed to be constant all along the CMP acquisition. For this reason, only low-offset data (lower than 5 m) will be taken into account for the following analysis.

For the second approach, the inversion process presented before, the Fourier-transformed data of the studied reflection are the input of the inversion software. The signals above and below the reflection (shaded in gray on Figure 8) were muted. Because of the sudden large amplitude decrease (Figure 9), we used only the first 5 m for the inversion process. Prior to inversion, the data were normalized with respect to the second trace. The inversion results are plotted in Figure 10. The Jonscher parameters are transformed into complex permittivity parameters at a frequency of 140 MHz.

Figure 10 shows a satisfying focusing of solutions toward a minimal error solution, which was obtained for the following parameters: $n_f = 0.94$; $\chi_{r,f} = 0.5$; $\epsilon_{\infty,f}/\epsilon_0 = 5.5$. The Jonscher relation computed with these parameters results in a complex permittivity of $6 + 0.05i$ for a frequency of 140 MHz and a reflector depth of 2.84 m. For the fracture, the best solution found an aperture of 40 cm, and the Jonscher parameters of the filling are $n_f = 0.86$, $\chi_{r,f} = 2.29$, $\epsilon_{\infty,f}/\epsilon_0 = 3.1$, corresponding to a complex permittivity of $5.2 + 0.5i$.

Figure 11a shows the reflected wave in the time domain after correcting propagation effects. This figure underlines that NMO effects

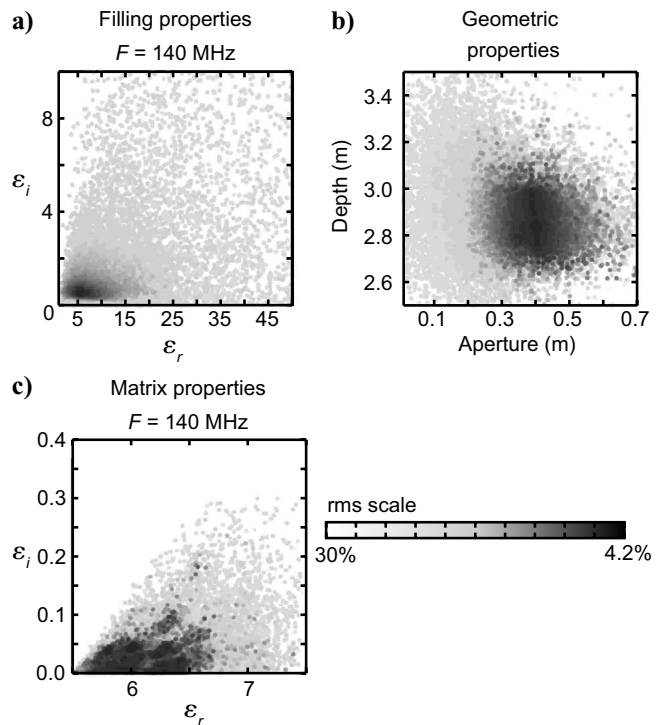


Figure 10. Results of the inversion: (a) thin-bed complex permittivity, (b) depth of the fracture as a function of its aperture, and (c) limestone complex permittivity.

were properly corrected using the best solution deduced from the inversion process, especially for low-offset traces, and that interesting amplitude variations are visible as a function of offset. These variations are better displayed in Figure 11b and c. It is clear that the chosen approach for the propagation effect corrections presents low influence on the final APVO curves in this case. Figure 11c shows that the raw data exhibit a wraparound of phase, which highlights the propagation effects, contrary to the processed data whose phase variation appears smoother and exhibits low sensitivity to offset. This confirms that propagation effects were properly corrected.

Analyses of results

The low complex-permittivity values of filling properties, which were deduced from the inversion process, seem to indicate the presence of dry sands in the fracture at this elevation ($n_f = 0.86$; $\chi_{r,f} = 2.29$; $\epsilon_{\infty,f}/\epsilon_0 = 3.1$; $d = 0.4m$) and the absence of clays and organic materials. This result is in good agreement with preliminary observations of the fracture from the plateau surface located 5 m above, which indicate that clay and organic material are present only near the surface, caused by local weathering.

Figure 12 shows the comparison between normalized data after propagation and radiation-pattern-effect corrections and five theoretical normalized thin-bed reflection coefficients for different thin-bed apertures or filling properties and associated errors: (1) best model deduced from the inversion process (rms = 4.2%), (2) the same but for an aperture 1 of 30 cm (rms = 5.6%; black dashed-dotted line), and (3) aperture 2 of 50 cm (rms = 7.9%; black dashed line), (4) model 1 with a value of $\epsilon_{\infty,f}/\epsilon_0$ equal to 2.1 (rms = 8.3%; permittivity 1, gray dashed-dotted line), and (5) model 1 with a value of $\epsilon_{\infty,f}/\epsilon_0$ equal to 4.1 (rms = 6.7%; permittivity 2, gray dashed line). Figure 12a and b represents amplitude and phase for an incidence angle equal to 26° as a function of frequency for the same data and models. It is clear that the best model derived from inversion correlates well and presents the lowest rms value with experimental data in the 120–190-MHz frequency range, whereas the four others exhibit a higher rms. Figure 12c and d compares normalized field data at a frequency of 140 MHz for incidence angles ranging from 0 to 40° with those computed from the five theoretical models. The same conclusions can be drawn: only the best model is able to explain correctly the field data. Changes of the parameters n_f and $\chi_{r,f}$ influence directly the real and imaginary parts of the effective permittivity. If the imaginary part increases, variations in normalized amplitude and phase with frequency and incidence angle are reduced. These comparisons show that frequency and APVO data are highly sensitive to thin-bed aperture and the parameter $\epsilon_{\infty,f}$.

Figure 13 generalizes the comparison between a normalized theoretical reflectivity model obtained using the best model deduced from the inversion process and field data after propagation and radiation-pattern corrections as functions of frequency and incidence angle. It displays amplitude (a and c) and phase (b and d). Data were too noisy to be presented between 32° and 38° caused by the roughness of the cliff surface in this area that generated a bad antenna coupling. This figure clearly generalizes the very good consistency between the model and data for all frequencies and incidence angles. In particular, one can note that amplitude maximum and large phase variations appear at far offsets around 165 MHz, for both field and modelled data. The normalization process conducted using a low-incidence-angle trace implies that this maximum corresponds to a minimum of reflectivity at low offsets. From theoretical considerations

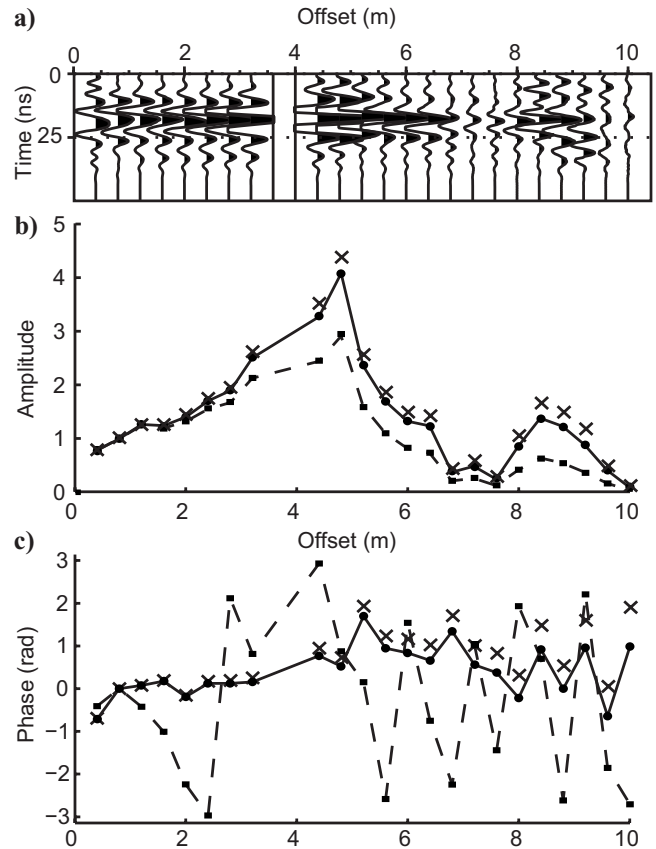


Figure 11. (a) The investigated reflection after propagation and radiation pattern corrections. (b) Amplitude and (c) phase variations of the event studied as a function of offset at 140 MHz (dominant frequency) without any corrections (squares) and with propagation and radiation pattern-effect corrections using the NMO (crosses) and inversion (circle) approaches. Amplitudes are normalized with respect to the trace acquired at offset 0.8 m.

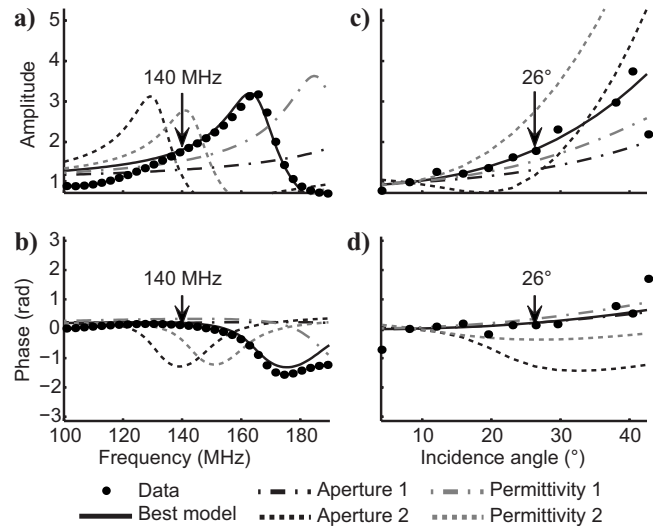


Figure 12. Comparison between the reflectivity coefficients obtained from the experimental data set and those deduced from five theoretical thin beds. (a) Amplitude and (b) phase curves, respectively, to frequency derived at an incidence angle of 26°. (c) Amplitude and (d) phase curves according to the incidence angle derived at a frequency of 140 MHz.

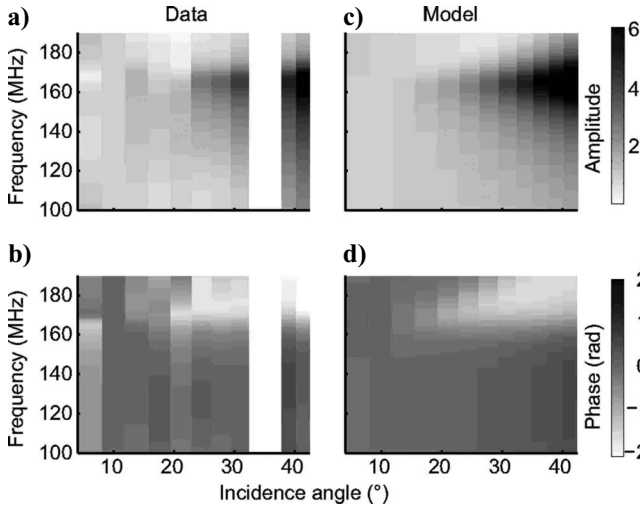


Figure 13. Comparison of normalized corrected data (a, b) with theoretical thin-bed reflection coefficients (c, d) derived for the best model found by the inversion process.

about thin-bed properties presented above, this minimum is reached when thin-bed aperture equals a multiple of $\lambda/2$. One can note that dispersion analysis of the reflection coefficient imposes large constraints about the velocity on aperture ratio $f_{\min} = v/(2d)$, which dramatically reduces the number of acceptable solutions. Subsequently, APVO curves will select the best solutions among them. For the best solution deduced from the inversion process, Jonscher parameters give a velocity of 13 cm/ns for the filling and a fracture aperture of 40 cm was found. These values indicate that the frequency for which destructive interference occurs at low incidence angles (low offsets) should be 162.5 MHz, which is very close to the value obtained from our data.

CONCLUSIONS

CMP GPR data contain important information on the ground investigated. Velocity assessment is the basic and traditional analysis of these data for time-to-depth conversion and data migration. It can also enable layers to be characterized when the aperture is greater than half of the wavelength of the reflected signal. For thinner layers, thin-bed analysis can be used to obtain valuable information. Such analyses consist generally of retrieving the amplitude of the thin-bed reflection coefficient as a function of offset and attempting to reproduce the AVO curve with theoretical models. In the particular case of a thin bed embedded within a homogeneous medium, we showed that AVPO analyses can be performed according to frequency, a process that dramatically reduces the possible range of solutions and also permits characterizing the homogeneous formation where the thin bed is embedded. Conversion of CMP raw data into reflection-coefficient properties (according to offset and frequency) is a very delicate operation that can be performed only under certain conditions: (i) contact between GPR antenna and investigated soil must be almost constant throughout the survey and (2) transmission losses between the acquisition surface and the studied reflected event must be constant. Propagation-effect corrections can be performed in a classical manner (NMO corrections and electrical resistivity measurements) if properties of the homogeneous medium are not dispersive. Otherwise, relaxation effects should be included in the correc-

tions and can be retrieved only using a global and complex inversion process. Finally, radiation-pattern corrections can be computed from numerical modeling.

This methodology was applied to fracture characterization (aperture, filling) in the context of rock fall assessment. It has been shown that the frequency dependency of reflection coefficient is of major importance for obtaining satisfactory and unique solutions. As all contributing properties are described using a Jonscher parameterization, this frequency-dependent approach opens up the possibility toward a global inversion. Such an inversion process will allow thin beds embedded within dispersive homogeneous media to be characterized. The next step consists of developing a new methodology dealing with the case of a thin layer separating two different formations. Such developments should help to characterize all contact surface problems.

ACKNOWLEDGMENTS

We are grateful to M. Sambridge, who allows the free distribution of his inversion code for research purposes. We are grateful to K. Hollinger who provided the FDTD modeling code to study the radiation-pattern of GPR antennas. We thank John H. Bradford and two anonymous reviewers who provided helpful comments that improved the manuscript.

APPENDIX A

THIN-LAYER REFLECTION

Considering the model presented in Figure 1, the amplitude of the electric field for each reflection is given by

$$\begin{aligned} E_{r1} &= E_i \times R_{12} \\ E_{r2} &= E_i \times T_{12} \times T_{21} \times R_{23}^1 \times e^{-i\phi} \\ &\dots \\ E_{rn} &= E_i \times T_{12} \times T_{21} \times R_{23}^n \times R_{21}^{n-1} \times e^{-in\phi}. \end{aligned} \quad (\text{A-1})$$

Reflection from the thin bed is equal to the sum of all these individual reflected waves:

$$\begin{aligned} E_r &= E_i \times \left[R_{12} + T_{12}T_{21}R_{23}e^{-i\phi} \left(\sum_{n=1}^{+\infty} q^{n-1} \right) \right] \\ &\text{with } q = R_{23}R_{21}e^{-i\phi}. \end{aligned} \quad (\text{A-2})$$

The sum of equation A-2 is a geometric continuation of common ratio lower than one and can thus be rewritten as

$$R = - \frac{R_{12} + R_{23}e^{-i\phi}}{1 + R_{12}R_{23}e^{-i\phi}}. \quad (\text{A-3})$$

The presence of a fracture embedded in a homogeneous half-space imposes that the dielectric properties of the first and third media are equal; thus,

$$R_{23} = R_{21}. \quad (\text{A-4})$$

The Fresnel reflection coefficient for a wave propagating in the first and reflected at the second medium is written (for TE mode)

$$R_{12} = \frac{\mu_2 k_1 \cos \theta_i - \mu_1 k_2 \cos \theta_t}{\mu_2 k_1 \cos \theta_i + \mu_1 k_2 \cos \theta_t} \quad (\text{A-5})$$

For the same geometric characteristic, the angle of reflection and refraction between the second and first media are, respectively, θ_i and θ_t , such that

$$\begin{aligned} R_{21}(\theta_t, \theta_i) &= \frac{\mu_1 k_2 \cos \theta_t - \mu_2 k_1 \cos \theta_i}{\mu_1 k_2 \cos \theta_t + \mu_2 k_1 \cos \theta_i} \\ &= \frac{-(-\mu_1 k_2 \cos \theta_t + \mu_2 k_1 \cos \theta_i)}{\mu_1 k_2 \cos \theta_t + \mu_2 k_1 \cos \theta_i} \\ &= -R_{12}(\theta_i, \theta_t) \end{aligned} \quad (\text{A-6})$$

Equation A-3 becomes

$$R = \frac{R_{12} - R_{12} e^{-i\phi}}{1 - R_{12}^2 e^{-i\phi}} \quad (\text{A-7})$$

The term ϕ denotes the phase difference of the waves travelling within the thin bed. Figure 1 plots the geometric characteristic of a thin layer. We pose

$$\phi = \delta_i. \quad (\text{A-8})$$

The phase difference between the waves conveyed by the first two emergent rays is written

$$\delta_i = \overline{M_1 N_1 M_2} \times k_2 - \overline{M_2 H_1} \times k_1 \quad (\text{A-9})$$

with

$$\begin{aligned} \overline{M_1 N_1 M_2} &= \frac{2 \times d}{\cos \theta_i} \\ \overline{M_2 H_1} &= \sin \theta_i \times 2 \cdot d \cdot \tan \theta_i. \end{aligned} \quad (\text{A-10})$$

Replacing equation A-10 with equation A-9 results in

$$\delta_i = \frac{2d}{\cos \theta_i} \times k_2 - \sin \theta_i \cdot 2 \cdot d \cdot \tan \theta_i \times k_1. \quad (\text{A-11})$$

Considering trigonometric simplification, phase difference is given by

$$\phi = \delta_i = 2 \cdot d \cdot k \left(\frac{1 - \sin^2 \theta_i}{\cos \theta_i} \right) = 2 \cdot d \cdot k_2 \cdot \cos \theta_i. \quad (\text{A-12})$$

REFERENCES

- Annan, A., 2001, Ground penetrating radar workshop notes: Sensors and Software Inc.
- Baker, G., 1998, Applying AVO analysis to GPR data: *Geophysical Research Letters*, **25**, 397–400.
- Bano, M., 2004, Modeling of GPR waves for lossy media obeying a complex power law of frequency for dielectric permittivity: *Geophysical Prospecting*, **52**, 11–26.
- Bergmann, T., J. O. A. Robertsson, and K. Holliger, 1996, Numerical properties of staggered finite-difference solutions of Maxwell's equations for ground-penetrating radar modeling: *Geophysical Research Letters*, **23**, 45–48.
- Bradford, J., and J. Deeds, 2006, Ground-penetrating radar theory and application of thin-bed offset-dependent reflectivity: *Geophysics*, **71**, no. 3, K47–K57.
- Carcione, J., M. Botelho, A. Osella, and M. de la Vegas, 2006, Fresnel reflection coefficients for GPR-AVO analysis and detection of sea water and NAPL contaminants: *Near Surface Geophysics*, **71**, 253–263.
- Cole, K., and R. Cole, 1941, Dispersion and absorption in dielectrics: *Journal of Chemical Physics*, **9**, 341–351.
- Debye, P., 1929, *Polar molecules*: Dover Press.
- Deeds, J., and J. H. Bradford, 2002, Characterization of an aquitard and direct detection of LNAPL at Hill Air Force Base using GPR AVO and migration velocity analysis: *Proceedings of the 9th International Conference on Ground Penetrating Radar*.
- Deparis, J., B. Fricout, D. Jongmans, T. Villemin, T. Effendiantz, and A. Mathy, 2008, Combined use of geophysical methods and remote techniques for characterizing the fracture network of a potentially unstable cliff site (the “Roche du Midi,” Vercors massif, France): *Journal of Geophysics and Engineering*, **5**, 147–157.
- Deparis, J., and S. Garambois, 2006, Fracture imaging and characterization from APVO GPR data: *Proceedings of the 11th International Conference on Ground Penetrating Radar*.
- , 2007, Inversion of dispersive APVO GPR curves: A thin-layer approach for fracture characterization on a vertical cliff: *Proceedings of the 4th International Workshop on Advanced Ground Penetrating Radar*, 49–55.
- Deparis, J., S. Garambois, and D. Hantz, 2007, On the potential of ground penetrating radar to help rock fall hazard assessment: A case study of a limestone slab, Gorges de la Bourne (French Alps): *Engineering Geology*, **94**, 89–102.
- Engheta, N., C. Pappas, and C. Elachi, 1982, Radiation patterns of interfacial dipole antennas: *Radio Science*, **17**, 1557–1566.
- Giannopoulos, A., 2005, Numerical modeling of ground penetrating radar using GprMax: *Proceedings of the 3rd International Workshop on Advanced Ground Penetrating Radar*, 10–15.
- Grégoire, C., L. Halleux, and V. Lukas, 2003, GPR capabilities for the detection and characterisation of open fractures in a salt mine: *Near Surface Geophysics*, **1**, 139–147.
- Grégoire, C., and F. Hollender, 2004, Discontinuity characterization of the spectral content of ground penetrating radar (GPR) reflections — Application of the Jonscher model: *Geophysics*, **69**, 1414–1424.
- Griffiths, D., 1998, *Introduction to electrodynamics*: Prentice Hall.
- Hall, S. A., and J. M. Kendall, 2003, Fracture characterization at Valhall: Application of P-wave amplitude variation with offset and azimuth (AVOA) analysis to a 3D ocean-bottom data set: *Geophysics*, **68**, 1150–1160.
- Holberg, O., 1987, Computational aspects of the choice of operator and sampling interval for numerical differentiation in large-scale simulation of wave phenomena: *Geophysical Prospecting*, **35**, 629–655.
- Hollender, F., and J. Tillard, 1998, Modeling ground-penetrating radar wave propagation and reflection with the Jonscher parameterization: *Geophysics*, **63**, 1933–1942.
- Jeannin, M., S. Garambois, D. Jongmans, and C. Grégoire, 2006, Multiconfiguration GPR measurements for geometric fracture characterization in limestone cliffs (Alps): *Geophysics*, **71**, no. 3, B85–B92.
- Jonscher, A., 1977, The universal dielectric response: *Nature*, **267**, 673–679.
- Jordan, T., and G. S. Baker, 2002, Field testing amplitude and phase variation with offset (APVO) analysis of ground penetrating radar data: *Proceedings of the 72nd Annual International Meeting, SEG, Expanded Abstracts*, 10.1190/1.1816954.
- Jordan, T., G. S. Baker, K. Henn, and J.-P. Messier, 2004, Using amplitude variation with offset and normalized residual polarization analysis of ground penetrating radar data to differentiate an NAPL release from stratigraphic changes: *Journal of Applied Geophysics*, **56**, 41–58.
- Kindelan, M., G. Seriani, and P. Sguazzero, 1989, Elastic modeling and its application to amplitude versus angle interpretation: *Geophysical Prospecting*, **37**, 3–30.
- Koefoed, O., and N. de Voogd, 1980, The linear properties of thin layers, with an application to synthetic seismograms over coal seams: *Geophysics*, **45**, 1254–1268.
- Kuhl, H., and M. Sacchi, 2003, Least-squares wave-equation migration for AVP/AVA inversion: *Geophysics*, **68**, 262–273.
- Lampe, B., and K. Holliger, 2005, Resistively loaded antennas for ground-penetrating radar: A modeling approach: *Geophysics*, **70**, no. 3, K23–K32.
- Lehmann, F., 1996, Fresnel equations for reflection and transmission at boundaries between two conductive media, with applications to georadar problems: *Proceedings of the 6th International Conference on Ground Penetrating Radar*, 555–560.
- Liu, Y., and D. Schmitt, 2003, Amplitude and AVO responses of a single thin bed: *Geophysics*, **68**, 1161–1168.
- Lutz, P., S. Garambois, and H. Perroud, 2003, Influence of antenna configurations for GPR survey: Information from polarization and amplitude versus offset measurements: *Geological Society, London, Special Publications*, **211**, 295–308.
- Mahob, P., and J. Castagna, 2003, AVO polarization and hodograms: AVO

- strength and polarization product: *Geophysics*, **68**, 849–862.
- Roch, K., E. Chwatal, and E. Brückl, 2006, Potentials of monitoring rock fall hazards by GPR: Considering as example the results of Salzburg: *Landslide*, **3**, 87–94.
- Sambridge, M., 1999a, Geophysical inversion with a neighbourhood algorithm — I. Searching a parameter space: *Geophysical Journal International*, **138**, 479–494.
- , 1999b, Geophysical inversion with a neighbourhood algorithm — II. Apprising the ensemble: *Geophysical Journal International*, **138**, 727–746.
- Schoenberger, M., and F. Levin, 1976, Reflected and transmitted filter functions for simple subsurface geometries: *Geophysics*, **41**, 1305–1317.
- Simmons, J., and M. Backus, 1994, AVO modeling and the locally converted shear wave: *Geophysics*, **59**, 1237–1248.
- Stephens, R. B., and P. Sheng, 1985, Acoustic reflections from complex strata: *Geophysics*, **50**, 1100–1107.
- Stovas, A., M. Landrø, and P. Avseth, 2006, AVO attribute inversion for finely layered reservoirs: *Geophysics*, **71**, no. 3, C25–C36.
- Streich, R., and J. van der Kruk, 2007, Characterizing a GPR antenna system by near-field electric field measurements: *Geophysics*, **72**, no. 5, A51–A55.
- Widess, M., 1973, How thin is a thin bed?: *Geophysics*, **38**, 1176–1180.
- Wu, T. T., and R. P. King, 1965, The cylindrical antenna with non-reflecting resistive loading: *IEEE Transactions on Antennas and Propagation*, **13**, 369–373.
- Zhao, A., 2002, Analysis of the numerical dispersion of the 2-D alternating-direction implicit FDTD method: *IEEE Transactions on Microwave Theory and Techniques*, **50**, 1156–1164.
- , 2004, Rigorous analysis of the influence of the aspect ratio of Yee's unit cell on the numerical dispersion property of the 2-D and 3-D FDTD methods: *IEEE Transactions on Antennas and Propagation*, **52**, 1630–1637.

4.4 Perspectives

Pour les problèmes classiques d'imagerie des couches fines, l'avènement récent de systèmes GPR multi-traces (jusqu'à 16 canaux) permet maintenant d'envisager des acquisitions et des traitements 3D plus routiniers, ce qui devrait augmenter les reconnaissances des fractures ou de toute zone de contact depuis la surface ou depuis des pentes faiblement inclinées. Ce type de matériel, à l'heure actuelle disponible seulement en mode TE, devra être adapté à la reconnaissance en paroi, mais cette limite technique ne paraît pas insurmontable. On peut également penser que le développement d'acquisitions aéroportées pourrait également apporter des facilités d'acquisition permettant des investigations de grande échelle à l'avenir, même si la proximité de la paroi restera un problème. Si ces avancées permettaient de suivre l'extension des fractures ou des zones de contact, elles ne permettraient pas de résoudre le problème de la caractérisation.

La présence d'objets fortement anisotropes va modifier la polarisation des ondes EM incidentes. Ainsi, comme discuté par Sassen et Everett (2009) toute méthode GPR qui se focalise sur la détection de changements de formes d'ondes et de polarisation peut améliorer la détection et la discrimination de fractures, par exemple en utilisant des algorithmes de cohérence de polarisation. Pour la caractérisation des fractures, ils proposent également une méthode d'inversion du champ d'onde complet, pour des acquisitions en transmission. De même, Tsoflias et Becker (2008) suggèrent, après des études expérimentales de sensibilité au remplissage de la couche fine, que les données APVO (Amplitude and Phase versus offset) combinées avec des analyses de dispersion peuvent permettre une caractérisation du remplissage, même en utilisant des données plus basses fréquences, ce qui permet une reconnaissance quantitative à plus grande profondeur.

Vers une inversion en champ d'onde complet

L'ensemble des travaux présentés ci-avant indique clairement la potentialité des données GPR pour la caractérisation des zones de contact, à condition d'utiliser le maximum d'informations disponibles (multi-modes, multi-fréquences, multi-offset). Notre approche d'inversion proposée ci-avant ne s'applique à l'heure actuelle que sur la première interface rencontrée, les corrections successives à apporter pour accéder aux propriétés d'une seconde interface s'avérant trop délicates et sans doute instables. De plus, des simplifications fortes ont dû être proposées, notamment concernant l'absence de variations latérales du milieu et du diagramme de rayonnement (hypothèse 1D). Tout ceci indique qu'il faut se diriger vers l'utilisation du champ d'onde complet, sans doute en élargissant cette approche à différentes fréquences et différents modes d'acquisition à l'avenir. Cette utilisation a été proposée par Ernst et al. (2007) dans le cas de données GPR acquises entre forages. Ils comparent notamment des images synthétiques obtenues par tomographie (méthode des rais) et une inversion en champ d'onde complet. Cette exemple montre bien l'intérêt de l'approche du champ d'onde complet, notamment pour une bonne reconstruction de la distribution de la conductivité électrique (très liée à l'atténuation et la dispersion) et une localisation fine d'interfaces abruptes ou d'hétérogénéités ponctuelles au sein d'un milieu homogène (Fig. 4.1). Pour cela, ils ont utilisé un code d'inversion basé sur la solution des équations de Maxwell dans le domaine temporel et des techniques de gradient conjugué pour l'optimisation.

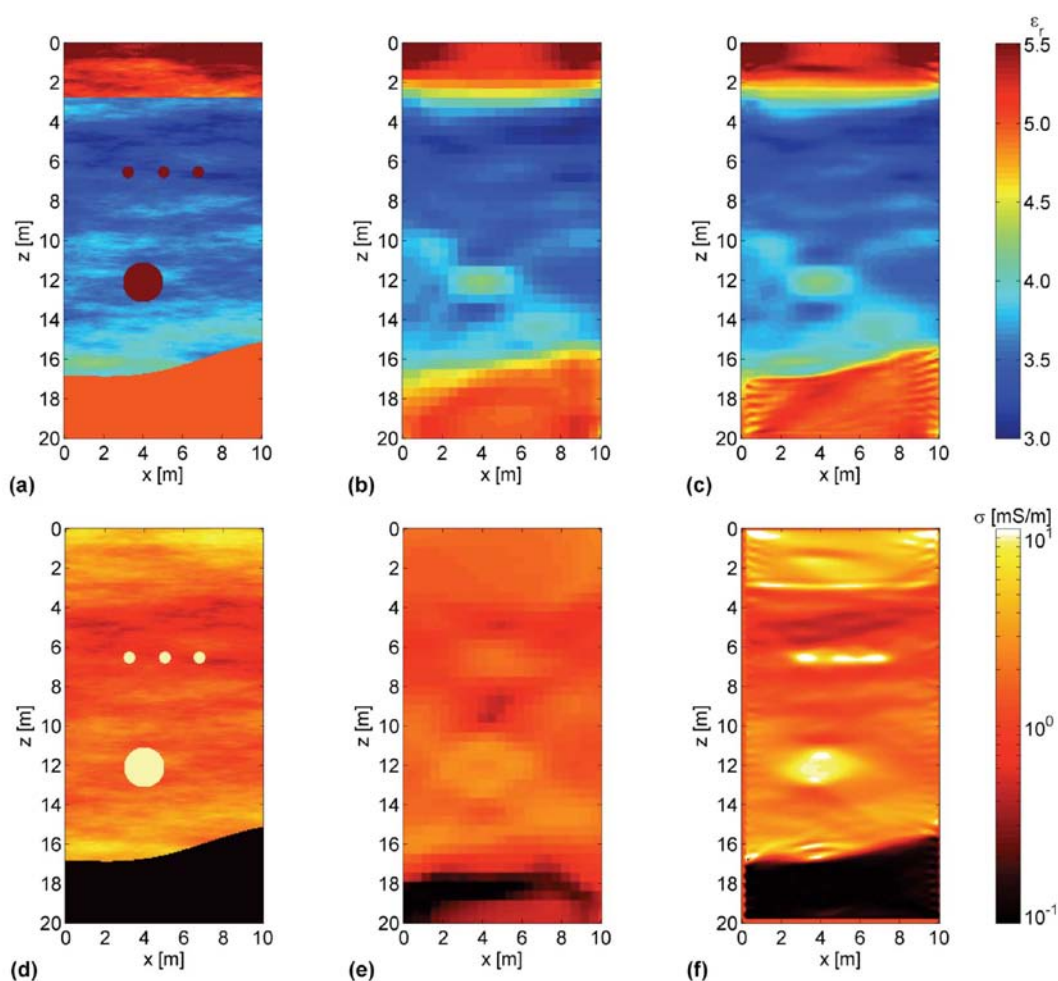


Fig. 4.1. Résultats d'inversion sur des données synthétiques présentant différents objets et différentes interfaces (abruptes et incluses dans un milieu homogène), d'après Ernst et al., (2007). A gauche, modèle à reconstruire, au milieu modèle reconstruit par tomographie des rais à droite par inversion du champ d'onde complet. En haut, permittivité diélectrique, en bas conductivité électrique.

Nous avons déjà abordé l'intérêt du développement de techniques d'inversion du champ d'onde complet pour les méthodes sismiques, et présenté les travaux en cours pour les milieux poreux et/ou les techniques différentielles (Chapitre 1). Très récemment des inversions en champs d'onde complets ont été entrepris (Ernst et al., 2007 ; Lopes, 2009 ; Minet & Lambot, 2010) en utilisant des techniques de modélisation directe effectuées dans le domaine temporel. Nous proposons d'adapter des algorithmes modélisant la propagation des ondes sismiques en 2D et 3D aux équations électromagnétiques et à leur spécificité, notamment en termes de modes de propagation (TE & TM) et de sources (diagrammes de rayonnement). Ce travail sera conduit dans le domaine fréquentiel, ce qui permet une prise en compte correcte et immédiate des effets de relaxation, par une modélisation Galerkin-Discontinu pour l'approche 2D (Virieux et Operto, 2009). Les premiers tests d'inversion seront conduits sur des données synthétiques dans un premier temps (modes TE et TM indépendants puis couplés) et permettront de déterminer les configurations optimales d'acquisitions (offset maximal, espacement entre chaque CMP, nombre de traces/CMP) suivant les buts recherchés et présentés tout au long de ce mémoire (zones de contact, géotechnique, failles, glaciers, hydrologie). Par la suite, des données réelles seront acquises en 2D (failles actives, glaciers, géotechnique, fractures) puis en 3D sur des cibles ciblées et de taille raisonnable.

Pour la problématique d'imagerie des fractures au sein de falaises instables, un effort d'instrumentation devra être mené pour optimiser l'acquisition des données multi-offsets à ce contexte difficile. Celles-ci seront inversées d'une part et migrées d'autre part, afin de permettre des comparaisons effectives en termes d'imagerie. Pour cela, une thèse a été acceptée récemment (F. Lavoué), qui devrait débiter à l'automne 2010.

En parallèle à ces développements, nous étudierons l'intérêt de combiner les deux approches de caractérisation évoquées ci-avant, à savoir les techniques DAPVO reposant sur l'acquisition de données multi-offset et celles employant des rapports spectraux, mono-offset. Ceci permettrait de caractériser un réflecteur complet, en utilisant les résultats de l'inversion DAPVO pour reconstruire le signal de référence. De même, nous tenterons d'étendre les analyses DAPVO à plusieurs couches fines horizontales d'une part, et à une seule couche fine séparant deux milieux différents d'autre part. Cette dernière approche pourrait permettre résoudre nombres de problèmes de contact (interface glacier-bedrock par exemple).

4.5. REFERENCES (texte principal)

- Annan, A., 2001, Ground penetrating radar workshop notes: Sensors and Software Inc doi:10.1190/1.1543212.
- Atkinson, B. K., 1989, *Fracture mechanics of rock*. Academic press geology.
- Baker, G., 1998, Applying AVO analysis to GPR data: *Geophysical Research Letters*, **25**, 397–400.
- Benson, A. K., 1995, Application of ground penetrating radar in assessing some geological hazards: Examples of ground water contamination, faults, cavities: *Journal of Applied Geophysics*, **33**, 177–193.
- Bradford, J., and J. Deeds, 2006, Ground-penetrating radar theory and application of thin-bed offset-dependent reflectivity: *Geophysics*, **71**, no. 3, K47–K57.
- Carcione, J., M. Botelho, A. Osella, and M. de la Vegas, 2006, Fresnel reflection coefficients for GPR-AVO analysis and detection of sea water and NAPL contaminants: *Near Surface Geophysics*, **71**, 253–263.
- Cardarelli, E., C. Marrone, and L. Orlando, 2003, Evaluation of tunnel stability using integrated geophysical methods: *Journal of Applied Geophysics*, **52**, 93–102.
- Castagna, J. P., 1993, AVO analysis — Tutorial and review, in J. P. Castagna and M. M. Backus, eds., *Offset-dependent reflectivity—Theory and practice of AVO analysis: Investigation in Geophysics*, SEG, 3–36.
- Davis, J. L., and A. P. Annan, 1989, Ground penetrating radar for highresolution mapping of soil and rock stratigraphy: *Geophysical Prospecting*, **37**, 531–551.
- Deeds, J., and J. H. Bradford, 2002, Characterization of an aquitard and direct detection of LNAPL at Hill Air Force Base using GPR AVO and migration velocity analysis: *Proceedings of the 9th International Conference on Ground Penetrating Radar*.
- Dérobot, X., and O. Abraham, 2000, GPR and seismic imaging in a gypsum quarry: *Journal of Applied Geophysics*, **45**, 157–169.
- Deparis J., « Etude des éboulements rocheux par méthodes Géophysiques » *Thèse de doctorat*, Université Joseph Fourier, Grenoble 1, 2007.
- Deparis J., Garambois S., Hantz D., 2007, On the potential of ground penetrating radar to help rock fall hazard assessment: A case study of a limestone slab, Gorges de la Bourne French Alps » *Engineering Geology*, **94**, 89–102.
- Deparis, J., and S. Garambois, 2009, On the use of dispersive APVO GPR curves for thin-bed properties estimation: Theory and application to fracture characterization: *Geophysics*, **74**, no. 1, J1-J12.
- Deparis J. & S. Garambois, 2010, Inversion methodology of dispersive amplitude and phase versus offset curves (DAPVO) for thin-beds, SEG reference publication on *Advances in Near Surface Seismology and Ground-Penetrating Radar*, in press.
- Deparis, J., B Fricout, D Jongmans, T Villemin, L Effendiantz and A Mathy., 2008, Combined use of geophysical methods and remote techniques for characterizing the fracture network of a potential unstable cliff site (the 'Roche du Midi', Vercors massif, France): *J. Geophys. Eng.* **5**, 147-157.
- Dussauge-Peisser, C., M. Wathelet, D. Jongmans, D. Hantz, B. Couturier, and M. Sintès, 2003, Investigation of a fractured limestone cliff Chartreuse Massif, France_ using seismic tomography and ground penetrating radar: *Near Surface Geophysics*, **1**, 161–170.
- Ernst, J.R., Maurer, H.R., Green, A.G., and Holliger, K., 2007. Full-waveform inversion of crosshole georadar data based on 2-D finite-difference time-domain solutions of Maxwell's equations, *IEEE Trans. Geosc. Rem. Sens.*, **45**, 2807-2828.

- Frayssines M., 2005, Contribution à l'évaluation de l'aléa éboulement rocheux (rupture) *Thèse de doctorat*, Université Joseph Fourier, Grenoble 1.
- Frayssines M., Hantz D., 2006, Failure mechanisms and triggering factors in calcareous cliffs of the Subalpine Ranges (French Alps), *Eng. Geology*, **86**, 256–270.
- Gallipoli, M., V. Lapenna, P. Lorenzo, M. Muccialrelli, A. Perrone, S. Piscitelli et F. Sdao, 2000, Comparison of geological and geophysical prospecting techniques in the study of a landslide in southern Italy. *Eur. J. Env. Eng. Geophysics*, **4**, 117–128.
- Grangjean G., and Gourry J.C., 1996. GPR data processing for 3D fracture mapping in a marble quarry (Thassos, Greece). *Applied Geophysics*, vol. 36/1, 19-30.
- Grasmueck, M., 1996, 3-D ground penetrating radar applied to fracture imaging in gneiss: *Geophysics*, **61**, 1050–1064.
- Grasmueck, M., R. Weger, and H. Horstmeyer, 2005, Full-resolution 3D GPR imaging: *Geophysics*, **70**, K12–K19.
- Grégoire, C., and F. Hollender, 2004, Discontinuity characterization of the spectral content of ground penetrating radar (GPR) reflections — Application of the Jonscher model: *Geophysics*, **69**, 1414–1424.
- Giannopoulos, A., 2005, Numerical modeling of ground penetrating radar using GprMax: *Proceedings of the 3rd International Workshop on Advanced Ground Penetrating Radar*, 10–15.
- Hack R., 2000, Geophysics for slope stability. » *Surveys in Geophysics*, **21**, 423–448.
- Hall, S. A., and J. M. Kendall, 2003, Fracture characterization at Valhall: Application of P-wave amplitude variation with offset and azimuth (AVOA) analysis to a 3D ocean-bottom data set: *Geophysics*, **68**, 1150–1160.
- Hart R. D., 1993, An Introduction to Distinct Element Modelling for Rock Engineering. In 7th International Congress on Rock Mechanics.
- Hoek, E., and J. W. Bray, 1981, Rock slope engineering: Elsevier Science.
- Holberg, O., 1987, Computational aspects of the choice of operator and sampling interval for numerical differentiation in large-scale simulation of wave phenomena: *Geophysical Prospecting*, **35**, 629–655.
- Jeannin M., 2005, Etude des processus d'instabilités des versants rocheux par prospection géophysique. Apport du radar géologique. Thèse de doctorat, Université Joseph Fourier, France.
- Jeannin M., Garambois S., Grégoire C., Jongmans, D., 2006, Multiconfiguration measurements for geometrical fracture characterization in limestone cliffs, *Geophysics*, **71**, B85–B92.
- Jonscher, A., 1977, The universal dielectric response: *Nature*, **267**, 673–679.
- Jordan, T., and G. S. Baker, 2002, Field testing amplitude and phase variation with offset (APVO) analysis of ground penetrating radar data: *Proceedings of the 72nd Annual International Meeting, SEG, Expanded Abstracts*, 10.1190/1.1816954.
- Jordan, T., G. S. Baker, K. Henn, and J.-P. Messier, 2004, Using amplitude variation with offset and normalized residual polarization analysis of ground penetrating radar data to differentiate an NAPL release from stratigraphic changes: *Journal of Applied Geophysics*, **56**, 41–58.
- Koefoed, O., and N. de Voogd, 1980, The linear properties of thin layers, with an application to synthetic seismograms over coal seams: *Geophysics*, **45**, 1254–1268.
- Kindelan, M., G. Seriani, and P. Sguazzero, 1989, Elastic modeling and its application to amplitude versus angle interpretation: *Geophysical Prospecting*, **37**, 3–30.
- Lane, J.W., Buursink, M.L., Haeni, F.P., Versteeg, R.J. (2000) Evaluation of ground-penetrating radar to detect free-phase hydrocarbons in fractured rocks - results of numerical modeling and physical experiments, *Ground Water*, v.38, no.6, p. 929-938.
- Lehmann, F., 1996, Fresnel equations for reflection and transmission at boundaries between two conductive media, with applications to georadar problems: *Proceedings of the 6th International Conference on Ground Penetrating Radar*, 555–560.
- Levy C., L. Baillet, D. Jongmans, P. Mourot, and D. Hantz, 2010, Geophysical methods to investigate and survey unstable volumes along a cliff. EGU, Vienna, Austria, 02 – 07 May.
- F. Lopes F., 2009, Inversion des formes d'ondes électromagnétiques de données radar (GPR) multioffsets. Thèse de doctorat, Institut de Physique du Globe de Paris.
- Liu, Y., and D. Schmitt, 2003, Amplitude and AVO responses of a single thin bed: *Geophysics*, **68**, 1161–1168.
- Mahob, P., and J. Castagna, 2003, AVO polarization and hodograms: AVO strength and polarization product: *Geophysics*, **68**, 849–862.
- Martinez A., Franseen E.K., and Beaty D.S., 1998a. Application of Ground-Penetrating Radar to sedimentologic and stratigraphic studies –Examples from Pennsylvanian siliciclastics and carbonates in Kansas. *GPR'98, Proceedings of the Seventh international conference on ground-penetrating radar, USA, may 27-30*, 687–692.
- Minet J., Lambot S., Slob E.C., Vanclooster M., 2010, *Soil surface water content estimation by full-waveform GPR signal inversion in presence in thin layers*, *IEEE Transactions on Geoscience and Remote Sensing*, **48**, N°3, part I/II, p. 1138–1150.
- Orlando, L., 2003, Semiquantitative evaluation of massive rock quality using ground penetrating radar: *Journal of Applied Geophysics*, **52**, 1–9.
- Ostrander, W. J., 1984, Plane-wave reflection coefficients for gas sands at nonnormal angles of incidence: *Geophysics*, **49**, 1637–1648.

- Pettinelli, E., S. Beaubien, and P. Tommasi, 1996, GPR investigation to evaluate the geometry of rock slides and buckling in a limestone formation in northern Italy: *European Journal of Environmental and Engineering Geophysics*, 1, 271–286.
- Pipan, M., E. Forte, F. Guangyou, and I. Finetti, 2003, High-resolution GPR imaging and joint characterisation in limestones: Near Surface *Geophysics*, 1, 39–55.
- Rashed, M., D. Kawamura, H. Nemoto, T. Miyata, and K. Nakagawa, 2003, Ground penetrating radar investigations across the Uemachi fault, Osaka, Japan: *Journal of Applied Geophysics*, **53**, 63–75.
- Sambridge, M., 1999a, Geophysical inversion with a neighbourhood algorithm — I. Searching a parameter space: *Geophysical Journal International*, **138**, 479–494.
- Sambridge, M., 1999b, Geophysical inversion with a neighbourhood algorithm — II. Apprising the ensemble: *Geophysical Journal International*, **138**, 727–746.
- Sassen, D.S. and M.E. Everett, 2009, 3D polarimetric GPR coherency attributes and full-waveform inversion of transmission data for characterizing fractured rock: *Geophysics* **74**, J23-J34.
- Scavia, C., 1995, A method for the study of crack propagation in rock structures. *Geotechniques*, 45, 447–463, 1995.
- Schoenberger, M., and F. Levin, 1976, Reflected and transmitted filter functions for simple subsurface geometries: *Geophysics*, **41**, 1305–1317.
- Seol, S. Y., J.-H. Kim, Y. Song, and S.-H. Chung, 2001, Finding the strike direction of fractures using GPR: *Geophysical Prospecting*, **49**, 300–308.
- Simmons, J., and M. Backus, 1994, AVO modeling and the locally converted shear wave: *Geophysics*, **59**, 1237–1248.
- Stevens, K. M., G. S. Lodha, A. L. Holloway, and N. M. Soonawala, 1995, The application of ground penetrating radar for mapping fractures in plutonic rocks within the Whiteshell Research Area, Pinawa, Manitoba, Canada: *Journal of Applied Geophysics*, **33**, 125–141.
- Stovas, A., M. Landrø, and P. Avseth, 2006, AVO attribute inversion for finely layered reservoirs: *Geophysics*, **71**, no. 3, C25–C36.
- Toshioka, T., T. Tsuchida, and K. Sasahara, 1995, Application of GPR to detect and map cracks in rock slopes: *Journal of Applied Geophysics*, **33**, 119–124.
- Tsoflias, G. P., J.-P. Van Gestel, P. L. Stoffa, D. D. Blankenship, and M. Sen, 2004, Vertical fracture detection by exploiting the polarization properties of ground-penetrating radar signals: *Geophysics*, **69**, 803–810.
- Tsoflias G. and M. W. Becker, 2008, Ground-penetrating-radar response to fracture-fluid salinity: Why lower frequencies are favorable for resolving salinity changes, *Geophysics*, VOL. 73, NO. 5, P. J25–J30.
- Virieux J. and S. Operto, 2009, An overview of full waveform inversion in exploration geophysics, *Geophysics*, 74(6), 74, 6.
- Widess, M., 1973, How thin is a thin bed?: *Geophysics*, **38**, 1176–1180.

PERSPECTIVES

Ce mémoire constituant un sorte de bilan, je me suis aperçu que je m'étais fortement investi au cours de ces dernières années dans l'acquisition et le traitement de données de terrain (et en collaboration pour des données de laboratoire), leur interprétation parfois quantitative voire leur inversion. Ceci a été fait sur un grand nombre d'objets et de milieux différents en utilisant également une grande variété de méthodes géophysiques voir sismologiques. Un des avantages de cette approche a parfois été son caractère opérationnel, certains projets ou développements ayant eu un impact au niveau socio-économique, notamment vers des applications concrètes sur les risques. Sur les sites à enjeux politiques importants (Séchilienne, glacier de Tete Rousse), la question de la place du scientifique étudiant l'aléa par rapport à la problématique de la gestion du risque, de la gouvernance politique et de la prise de décision (transparence, communication, incertitudes) sera une problématique secondaire que j'aimerai aborder à l'avenir avec des sociologues et des services opérationnels (RTM, CETE) en charge de la surveillance de ces risques (projet ANR SLAMS).

En tant que géophysiciens, nous sommes souvent sollicités dans des projets pour apporter des réponses fondamentales à d'autres problématiques (glaciers, tectoniques, géotechniques) simplement par une imagerie classique qui ne nécessite pas de développements particuliers. Si cette ouverture (ou dispersion selon le point de vue) est intéressante, elle s'est sans doute faite au détriment d'une approche plus focalisée en termes de méthode qui permettrait des développements plus théoriques voire numériques. Je suis convaincu que c'est la comparaison entre données réelles, développements théoriques et approches numériques qui permet de mieux comprendre les images qualitatives voire quantitatives obtenues et ouvre de nouvelles portes en termes de potentialité de caractérisation. C'est donc dans cette voie que j'aimerais me tourner à l'avenir, notamment en utilisant plus systématiquement voir en développant des codes de calculs numériques directs simulant la propagation des ondes (sismiques, sismo-EM, GPR) dans des milieux toujours plus complexes (2D, 3D, multiphasiques). Ceci sera fait sur différentes problématiques et en liaison avec des expériences en laboratoire, lorsque cela s'avérera nécessaire.

A court terme, je suis impliqué dans plusieurs projets de recherches et d'encadrements de thèses, qui ont été déclinés dans les chapitres précédents. Pour mémoire, je citerai les projets ANR HPPP-CO2 (coordinateur Y. Guglielmi, ondes sismiques en milieu bi-phasique), SLAMS (coordinateur S. Garambois, recherches multi-disciplinaires sur le mouvement de terrain de Séchilienne), CENTURISK (coordinatrice I. Manighetti, apports des méthodes GPR et sismiques Haute Résolution pour identifier des marqueurs enfouis au voisinage des failles actives). Un projet INTERREG IV portant sur les risques glaciaires (GLARISKALP, coordinateur Fondation montagne sure, GPR sur glaciers tempérés) et un projet collaboratif avec Total (imagerie sismique différentielle) complètent les orientations des travaux à court terme. Ceux-ci ont bénéficié de financements de thèse, en cours, que je co-encadre : B. Dupuy (HPPP-CO2, J. Virieux), A. Asnaashari (Total, J. Virieux), L. Chaumond (SLAMS, A. Helmstetter), S. Beauprêtre (CENTURISK, I. Manighetti). Il faut rajouter un financement de l'école normale Supérieure (F. Lavoué, inversion GPR, J. Virieux).

L'ensemble de ces travaux envisagés à court terme a été présenté au cours de ce mémoire, dans les chapitres concernés, mis à part la thématique faille active, qui avait donné lieu à la thèse de F. Nguyen (2005, université de Liège). Je n'ai pas repris cette thématique sous la forme d'un chapitre, mais je pense intéressant de présenter un court résumé du projet CENTURISK [2010-2014], en annexe ci-après. En effet, les méthodes géophysiques et notamment les méthodes

sismiques hautes résolutions et GPR sont fortement impliquées dans ce projet pour identifier et reconnaître des marqueurs – décalés – par les séismes qui se sont produits le long d'une faille (en décrochement pour la Nouvelle-Zélande et normale pour l'Italie centrale). L'analyse quantitative des images obtenues (attributs de la réflectivité, paramètres constitutifs, lien avec la topographie de surface) seront des développements à creuser.

Un grand nombre de perspectives techniques a déjà été avancé dans chacune des parties développées dans ce mémoire, que ce soit pour la constitution multi-phasique de la subsurface, les conversions sismo-électromagnétiques, les mouvements de terrain et la caractérisation de couches fines par géoradar. Je ne reprendrai que globalement celles-ci dans ce paragraphe.

Une problématique générale sur la subsurface et les objets étudiés, qui concerne à la fois les problèmes de fluides (sols, mouvements de terrain, glaciers) que les problèmes mécaniques (fractures, milieux poreux) concerne le besoin croissant de quantification des propriétés complexes décrivant les milieux étudiés. En effet, en plus de l'imagerie à proprement parlé, il devient maintenant nécessaire de recouvrer quantitativement la distribution des observables concernées (vitesses et atténuations sismiques et GPR) qui sont sensibles à la structure poreuse (ou fracturée) des matériaux étudiés ainsi qu'à la partie fluide (saturation, nature du fluide, porosité, contenu en eau, conductivité de l'eau).

La méthode commune d'approche proposée sera l'inversion 2D des champs d'ondes complets, GPR et sismiques, avec une description de plus en plus complexe du modèle direct (poro-élastique non-saturé et fracturé pour les ondes sismiques, prise en compte de la dispersion pour les ondes radar). Idéalement, cette approche pourrait permettre de décrire parfaitement les milieux traversés de manière quantitative. En pratique, chacune des étapes envisagées (modèle direct complexe, inversion, pré-conditionnement des données, choix d'un modèle initial) sera d'abord testé sur des données synthétiques et leur applicabilité à des données réelles restera un challenge qui montrera sans doute des limites plus ou moins importantes (problème de la source, du diagramme du rayonnement, de stabilité). Pour contourner ce problème, je pense nécessaire d'avoir en parallèle une approche simplifiée pour des milieux stratifiés, ce qui permettra également d'utiliser des jeux de données plus accessibles au monde universitaire, en terme de volume et de lourdeur d'acquisition. Également, il me semble nécessaire de continuer à travailler sur des méthodes d'analyses des attributs (amplitude, phase, contenu spectral) de la réflectivité, que ce soit en sismique ou en GPR. En effet, si l'on peut élargir la méthode d'inversion proposée pour les couches fines (Chapitre 4) à plusieurs réflecteurs et à des zones de contact plus complexes (milieu encaissant hétérogène), on pourra obtenir de l'information quantitative sur les milieux. Cette problématique « simplifiée » pourra être appliquée à l'ensemble des objets décrits dans ce mémoire qui respectent une approche 1D.

La compréhension des phénomènes dynamiques se produisant dans les milieux poreux classiques, que ce soit en sismique qu'en sismo-électromagnétisme nécessitera l'acquisition de données contrôlées en laboratoire. Ce travail, qui se fera en collaboration avec d'autres équipes spécialisées, permettra de mieux comprendre certains phénomènes à différentes fréquences (couplage sismo-électromagnétique par exemple), et leur sensibilité à certains paramètres, comme la saturation des formations. Il permettra en outre de tester les approches numériques citées auparavant pour des milieux simples, contrôlés et qu'on peut facilement faire évoluer dans le temps. Dans certains cas, le développement spécifique de codes de modélisation en milieu cylindrique pourra être envisagé.

Nous avons également montré que le suivi temporel des structures, des fluides et des processus actifs qui se produisent dans la subsurface devient d'une importance stratégique, que

Perspectives

ce soit pour les problèmes de ressources, de risques ou environnementaux. L'acquisition de données géophysiques discrètes dans le temps sera sans doute une des missions des investigations futures. Dans ce contexte, une prospective à moyen terme, qui s'inscrit en continuité des développements envisagés ci-avant en imagerie GPR ou sismique, portera sur la quantification de l'évolution des paramètres par les méthodes de propagation d'ondes, en différentiel.

La seconde problématique importante dans laquelle je compte m'investir, au moins à moyen terme, concerne la notion d'observatoire des mouvements de terrain, et notamment leur suivi sismologique et géophysique. Le suivi temporel des observables géophysiques, en particulier sismiques, s'inscrit naturellement dans la démarche quantitative proposée ci-avant et rejoint d'autres thématiques, en particulier hydrogéophysiques. Par contre, il faut reconnaître que le suivi sismologique des mouvements de terrain s'inscrit a priori dans une démarche plus éloignée. Pourtant, que ce soit pour l'écoute sismologique qui vise à localiser des événements sismiques internes (chutes de blocs, micro-séismes) ou pour la caractérisation des effets de sites sismiques potentiels générés par les zones déformées, le manque de reconnaissance géophysique rend difficile toute interprétation quantitative. En particulier, nous avons montré que dans ces deux problématiques, la connaissance des vitesses sismiques en 3D s'avérerait nécessaire dans ces milieux fortement hétérogènes pour mieux localiser les événements internes enregistrés ou pour mieux comprendre et définir les effets de sites enregistrés ponctuellement sur des stations sismologiques. Il faudra d'une part étudier la relation entre la distribution hétérogène de ces observables dans le milieu et la déformation superficielle enregistrée, ce qui permettra de mieux caractériser le mouvement. D'autre part, il faudra quantifier le caractère anisotrope des ces observables, que ce soit pour les ondes P que pour les ondes S, en vitesse et en atténuation. Celui-ci pourrait contrôler à la fois la dynamique différentielle actuellement observée de certains mouvements, mais également l'anisotropie des effets de site, observée sur plusieurs mouvements différents.

ANNEXE : THE CENTURISK PROJECT

“A novel method to identify the faults prone to break in the coming century, hence posing the most immediate risk”

By I. Manighetti et al., 2010

Abstract. Most populated regions worldwide are dissected by numerous active faults. The question we address is: within such dense networks of faults, can we recognize those that are prone to break in a large earthquake during our lifetime that is over the next century? Those ‘ready-to-break’ faults are those posing the most immediate hence highest risk to populations. We suggest that, if we can characterize (age, location, magnitude) the large earthquakes that have broken a fault over the last 1000s of years, then we can construct the empirical occurrence frequency curve of those earthquakes. This empirical function should reveal whether the fault is presently in a paroxysmal phase of seismic activity (many large earthquakes occurring in a narrow, <100-200 yrs, time window) hence prone to break over the next century, or rather in a more quiescent phase. At present, there exists no technique that allows recovering the long past earthquake histories that we need to reconstruct the above functions. We thus develop a novel approach that we expect successful to recover the traces of the 10-20 past large events on some target faults. We suggest that the memory of past large earthquakes has to be searched in the first 10s meters of the ground, where it is preserved as buried offset morphological markers. We thus would like combine three complementary, non-invasive, up-to-date geophysical techniques (3D GPR, Electric Tomography, and High-Resolution Seismic Imaging) to investigate at high-resolution the first 10s meters of the ground, along a few target faults chosen as best candidates for success. Doing so, we expect detecting the traces of a large number of past earthquakes, while measuring the displacements produced by those earthquakes hence estimating their magnitude. Combined with the dating of the identified events, our work should allow constructing the empirical occurrence frequency functions that we seek, and help identifying the faults most prone to break during our lifetime.

An example of GPR data acquired on the different parts of the fault area is displayed figure A1. It underlines the complexity to identify identical buried markers on each compartment and to measure their horizontal shift. Here, the markers are quite evident as erosion created large superficial features.

Other experiments will be conducted on the normal Central Italy faults, both with High-resolution seismic (to test full-waveform inversion in this context) and GPR measurements. On normal faults, the potential shift will be vertical, hoping that different markers (porosity, compaction) have been embedded at the fault foot.

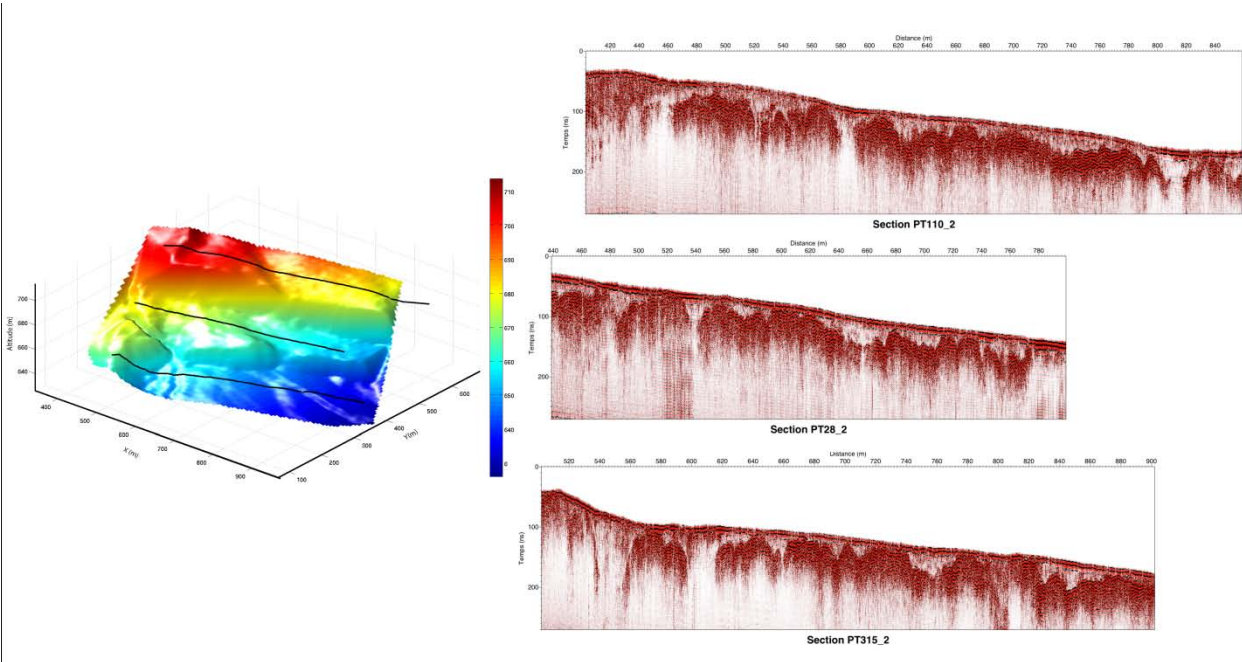


Fig. A1. MNT of the Terako site (Hope fault, South island, NZ) underlying the two vertical scarps due to the fault movement and GPR profiles acquired within each of the compartment.